FLOW FIELD DYNAMICS IN A HIGH-G ULTRA-COMPACT COMBUSTOR

DISSERTATION

Andrew E. Cottle, Captain, USAF

AFIT-ENY-DS-16-D-037

DEPARTMENT OF THE AIR FORCE
AIR UNIVERSITY

AIR FORCE INSTITUTE OF TECHNOLOGY

Wright-Patterson Air Force Base, Ohio

AFIT-ENY-DS-16-D-037

FLOW FIELD DYNAMICS IN A HIGH-G ULTRA-COMPACT COMBUSTOR

DISSERTATION

Presented to the Faculty

Department of Aeronautics and Astronautics

Graduate School of Engineering and Management

Air Force Institute of Technology

Air University

Air Education and Training Command

In Partial Fulfillment of the Requirements for the

Degree of Doctor of Philosophy

Andrew E. Cottle, BS, MS

Captain, USAF

December 2016

AFIT-ENY-DS-16-D-037

FLOW FIELD DYNAMICS IN A HIGH-G ULTRA-COMPACT COMBUSTOR

Andrew E. Cottle, BS, MS
Captain, USAF

Committee Membership:

Dr. Marc D. Polanka
Chair

Dr. Mark F. Reeder
Member

Maj Darrell S. Crowe, PhD
Member

Dr. Kevin C. Gross
Member

Dr. Andrew W. Caswell
Member

Dr. Adedeji B. Badiru
Dean, Graduate School of Engineering and Management

Abstract

The Ultra Compact Combustor (UCC) presents a novel solution to the advancement of aircraft gas turbine engine performance. A "high-g" UCC design operates by diverting a portion of the axial compressor flow into a circumferential combustion cavity positioned about the engine outer diameter over a hybrid guide vane (HGV) that combines the effects of compressor exit and turbine inlet geometry. The circumferential cavity (CC) provides the necessary residence length and time for combustion within substantially reduced axial lengths; furthermore, high rates of centrifugal acceleration – termed "high-g loading" – are imposed upon the swirling cavity flow. These high-g conditions are hypothesized to significantly increase flame speed, reduce flame length, and improve lean blow-out performance.

The objectives of the AFIT test program were to investigate the trade space presented by the mating of the high-g combustion cavity, a common-source upstream flow diffuser, and a complex hybrid guide vane design. This research capitalized on the availability of advanced flow diagnostic data such as Particle Image Velocimetry (PIV), Particle Streak Emission Velocimetry (PSEV), and high-speed video imagery. Furthermore, high-fidelity temperature data was enabled – within the CC and within the HGV passages – through the technique of Thin-Filament Pyrometry (TFP). These experimental measurements were coupled with a computational fluid dynamics (CFD) model to provide additional insight into the flow field and combustion dynamics. Three specific research objectives were addressed:

1. Performance of the UCC with the common-source upstream diffuser was analyzed, and the problem of uneven pressure distribution was identified and resolved with a hardware fix.

2. Combustion cavity flow dynamics were analyzed with respect to fundamental changes in air/fuel delivery and mixing as well as cavity aspect ratio. Dramatic improvements to the combustion event were demonstrated experimentally and numerically.
3. Intermediate and dilution-zone dynamics within the HGV passages were analyzed. The temperature profile at the exit was investigated for several geometric configurations. Implementation of a radial vane cavity (RVC) was demonstrated to improve the characteristics of the exit flow.

Table of Contents

List of Figures

List of Tables

TABLE Page

I. Introduction

From their origins in steam, to the breakthroughs of Whittle and von Ohain, to the refined technological marvels of today, gas turbine engines have truly revolutionized power generation. That effect has perhaps been most prominently manifest in the evolution of powered flight. As reciprocating engines slowly gave way to turbine power plants in the mid-20th century, air transportation began its unprecedented advance to become the safest, most convenient, and most reliable form of long-distance travel currently employed. Gas turbine engines allowed more efficient operation at high altitudes with superior power-to-weight and reliability as compared to piston-driven counterparts. Those core advantages have driven the engineering of turbine engines for the past six decades, and the motivation for continued development remains stronger than ever.

Modern challenges to gas turbine engineering abound, and modern solutions continue to rise to meet them. Of these, environmental impacts are foremost in the minds of the public and the policy makers as evident in the most recent National Security Strategy (NSS) [1]. Therein, the needs for reduced carbon emissions and increased energy efficiency are expressed both explicitly and implicitly. The security and prosperity of the nation, and indeed global society at large, are fundamentally linked to the conscientious, judicious use of fossil fuels. In addition, the NSS continues its call for leadership in science, technology, and innovation. Tenacious pursuit of solutions to the challenges of environmentally-conscious design therefore has the second-order effect of sustaining the nation's position on the forefront of technological skill and expertise.

Designers, integrators, and users of gas turbine engines are as attentive to energy efficiency as ever, due in part to policy guidance as demonstrated above, but due as well to the simple fact that increased efficiency is economically desirable in any circumstance. In fact, most modern gas turbine engine combustors operate at over 99% efficiency; that design space being stretched to its limit has driven innovators to seek alternative methods to improve engine performance, either by achieving more power output with equivalent weight and fuel consumption, or by achieving equivalent power output in smaller, more fuel efficient packages. Those ever-present pressures to increase power while concurrently reducing engine weight and fuel consumption have given rise to a wealth of new technologies intent on increasing compressor pressure ratios, optimizing combustor economy, increasing turbine inlet temperatures, strengthening and protecting engine components, reducing noise and emissions, and decreasing overall engine size.

Ultimately, as in any technological field, the mutual strain between cost and performance results in a taut, thin line that must be balanced for any incremental improvement to transition from theory to practice. Nowhere is that balance more precarious than in the domain of aerospace; and nowhere in aerospace is the stress more keenly felt than in the realm of military aviation. In addition to a uniquely complex economic environment, military aerospace technology is subject to many of the most demanding performance requirements while still beholden to the same efficiency and environmental constraints as their civilian counterparts.

1.1. The Ultra Compact Combustor

It is in this context that work is progressing at the Air Force Institute of Technology (AFIT) and the Air Force Research Laboratory (AFRL) on a novel concept for efficient combustion in a gas turbine engine. Traditional combustor sizing is driven by the need for sufficient axial length to inject fuel, mix and ignite the fuel with high pressure air, sufficient

residence time for the combustion process, and sufficient additional mixing to complete the combustion and dilute the products prior to entry into the turbine inlet guide vane. Work at AFIT has focused on development of a concept that employs a circumferential – rather than an axial – combustion chamber. A portion of the high-pressure air from the compressor is diverted to a cavity that is recessed around the outer diameter of the engine. The recessed cavity serves as the primary combustion zone where both air and fuel are introduced, mixed, and ignited. Bohan and Polanka [2] provide an illustration of a notional UCC design compared to a traditional combustor as shown in Figure 1.1, where the potential engine length reduction is demonstrated.

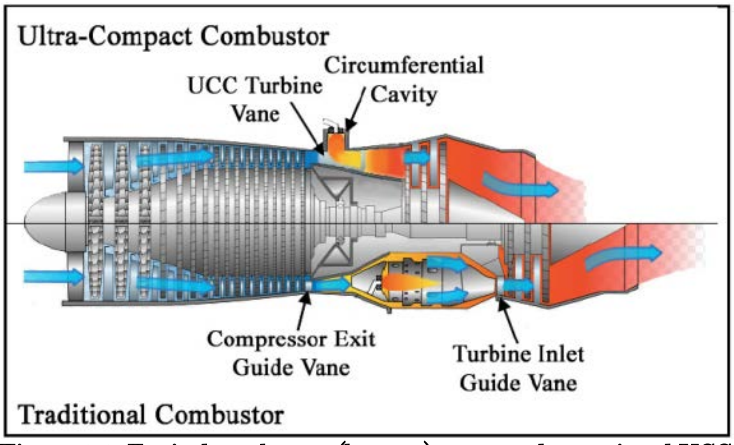

Figure 1.1. Typical combustor (bottom) compared to notional UCC configuration (top). [2]

Introduction of fluid into the recessed circumferential cavity (CC) may be done in one of two ways. First, air and fuel may be injected from the upstream and downstream walls in such a way as to stabilize a cavity vortex whose axis of rotation is tangent to the circumference of the engine. This technique has been termed "trapped-vortex combustion" (TVC), and it has been researched extensively by AFRL as outlined in Chapter 2. Secondly, air and/or fuel may be injected from the upstream or outer-diameter cavity walls with tangential angle, thereby inducing bulk circumferential swirl within the CC. The velocity of that bulk swirl is such that an outward centrifugal force is applied to the cavity fluid. That force can be expressed in terms of the earth's gravitational constant – as a "g-load"; typical operating conditions in combustors

of this design attain g-loads, g, in the range of $300g_0 < g < 3000g_0$. This technique has been termed "high-g combustion" (HGC). Research on the HGC concept has been pursued at both AFIT and AFRL. In both techniques, the potential exists for realization of a rich-burn quick-quench lean-burn (RQL) combustion process where the hot primary zone combustion occurs fuel-rich, then migrates back into the cold core flow to continue with intermediate and dilution burning in a fuel-lean state. In the HGC technique, the strong density gradients induced by the high-g loading have the potential to improve combustion efficiency through enhanced mixing and increased flame speed. More details on the evidence for those behaviors are introduced in Chapter 2.

Benefits to the realization of an operational UCC design extend beyond primary combustion. Interest exists in a viable method for combustion between turbine stages, a concept known as inter-turbine burning. Fundamental cycle analyses have shown that use of an inter-turbine burner (ITB) can yield substantial benefits through improved thrust-specific fuel consumption; however, implementation of an effective combustion scheme in the constrained space between turbine stages has always presented a significant challenge. The UCC concept has the potential to resolve that challenge by virtue of its compact design. Research considerations at AFIT have encompassed both primary combustion and ITB roles. Furthermore, implementation of a UCC could be accomplished in such a way as to reduce engine hardware requirements and thereby increasing the potential thrust-to-weight performance.

While the theoretical benefits to a UCC design are indeed attractive, many challenges remain to be overcome before such a design can be practically implemented in a real engine. That statement essentially encompasses the primary mission of UCC research at AFIT; that is: **to achieve combustion performance and efficiency competitive with traditional axial combustors while capitalizing on the space- and weight-saving characteristics of the UCC.** To that end, the details of the aerodynamics, combustion chemistry, and heat transfer within the UCC must be

thoroughly understood. To be presented as a viable alternative to a traditional combustor, the combustion efficiencies within the UCC must at least be comparable. Efficient combustion in the UCC is dependent on the combustion cavity air and fuel injection schemes. Re-introducing the combustion products into the core engine flow must be done so that uniform velocity and temperature profiles are presented to the first turbine stage. Last but far from least, emissions from the combustion process must again be comparable to traditional combustors.

Work at AFIT has progressed toward the realization of those goals. A full-annular test rig has been designed, developed, and put through multiple iterations of testing. Variations in hardware, air/fuel supply, and instrumentation have been produced and tested in order to better understand the various factors that influence the UCC combustion characteristics. The following section presents the detailed objectives proposed by this current doctoral program toward accomplishment of the UCC goals.

1.2. Research Objectives

The current work is focused on continuing the effort to understand and characterize the AFIT UCC test rig, and to identify optimum designs to achieve the overarching goal outlined previously. Thus, the foundational goal to which the present research will be anchored is: **to understand and address the challenges of enabling efficient combustion within and hot gas migration out of a high-g combustion cavity.** The specific objectives that will lead to accomplishment of that goal shall be

1. Develop the aerodynamic mechanisms to deliver the proper air and fuel to the high-g cavity from a common flow source.
2. Determine the effects of the complex flow environment on flame dynamics within the high-g combustion cavity.

3. Investigate the parameters that influence and promote hot gas migration into the core flow to enable control over the exit temperature profiles

1.2.1. Objective 1: Common Flow Source

Previous work with discrete control over the air flow into the combustion cavity identified an optimal ratio of air mass-flow between the combustion cavity and the core flow. Initial follow-on studies utilizing a diffuser to attain the same mass-flow ratio from a single source were unsuccessful. Performance of the diffuser is crucial, as effective combustion within the cavity is highly dependent on effective flow injection. Thus, the first objective of this research is to analyze the factors that influence how flow is efficiently diverted between the two streams. The desired flow split must be obtained through all operating regimes while minimizing system pressure loss. Thus, the existing diffusion system will be examined in detail. Design issues will be identified and resolved experimentally and computationally, and an effective diffusion system will be demonstrated. Upon completion, it will be proven that the UCC can be operated with a common flow source as would be required in a real aircraft engine.

1.2.2. Objective 2: Cavity Flame Dynamics

Once effective operation with a common flow source has been attained, the second objective shall be to undertake a detailed evaluation of the dynamics of the combustion flame within the circumferential cavity. The aerodynamics alone present many novel challenges. Prior UCC work with discrete air sources utilized a cavity injection scheme wherein both the fuel and the air were injected from the outer diameter. In contrast, the use of the common air source necessitates air injection from the upstream cavity sidewall, while fuel injection remains on the outer circumference. Air is injected at a tangential angle to induce swirl in the cavity, and pressure gradients induced by the high-velocity core flow exert an additional force on the cavity flow. In other words: the effects of (1) two transverse sources of multiple round-jet injections, (2) bulk circumferential swirl, and (3) transverse bulk core flow all combine in an as-

yet poorly understood, highly complex flow field in which mixing and combustion must then occur. It will be an endeavor of this study to qualify and quantify the nature of those aerodynamic effects, their influence on the combustion process, and the resultant effect on exit temperature profiles and emissions (as detailed in the following section). Variations to combustion cavity geometry and air/fuel injection schemes will be implemented, including changing the cavity cross-sectional area, modifying the jet injection angles, and integrating diffuser modifications as involved in Objective 1.

1.2.3. Objective 3: Hot Gas Migration

Complementary to knowledge of the dynamics in the cavity, the next objective seeks to understand how these hot cavity combustion gases are distributed across the exit span. Efforts to modify the distribution will be undertaken to understand the effect on exit temperature profiles and emissions. The mechanism of flow entrainment from the UCC combustion cavity into the core currently consists of a set of hybrid guide vanes, and it is proposed in this work to modify the configuration of those vanes in order to improve exit profile characteristics. Modifications will include means to encourage the proper cavity residence time – while combustion products must be entrained, uncombusted fluid must be encouraged to continue circulation within the cavity. Additional modifications will seek to optimize the radially-inward component of the migrating flow such that the exit temperature profile meets with convention without producing any hot-spots on the hybrid-vane side walls or the inner diameter. Specifically, the following hybrid-vane variations are hypothesized to have an effect on combustion characteristics and exit temperature profile:

i. Operating conditions
ii. Refinement of the vane edge geometry, i.e.: fillets, scoops, grooves, and channels to better distribute entrained flow from the cavity
iii. Refinement of vane wall characteristics: added channels, steps, and contours

1.3. Uniqueness of Research

While a great variety of work has been done with the UCC concept, this current proposal will be the first of its kind in three important aspects. First, the AFIT test hardware is unique in that it is a full annulus as opposed to a sectional design. In this study, the integration of the full-annular hardware with the common-flow-source interface will make it one of two known test rigs with such capability. Second, the methodology for achieving the foregoing research objectives will include the use of a computational fluid dynamics (CFD) model of the test hardware. Currently, there is minimal published work on the simulation of the complex reacting environment that will be represented by the AFIT model. Upon satisfactory validation with experimental measurements, that model has the potential to provide novel insight into the behavior of a diffusion flame in a highly turbulent, swirling flow. The model will also enable the testing of an important hypothesis: that buoyant phenomenon in a high-g combustion environment increase the effective flame speed of the reacting flow. To this end, model results will be compared to and validated against high speed video flame structure tracking. Third and finally, as will be discussed further, the experimental setup enables combinations of optical flow interrogation that are both unique and cutting-edge in terms of the spatial and temporal resolution they are able to obtain.

II. Literature Review

The literature review presented herein is done so with the goal of providing a broad perspective, not only on the historical context of compact combustor technology, but also on its basis in the fundamental sciences. The problem at hand is complex and multi-faceted; many of the physical phenomena addressed are complex in their own right; implementation of the geometry requirements for high-g ultra-compact combustion compounds those complexities exponentially. As a consequence, the tools utilized for investigation of those interactions of hardware and fluid behaviors are themselves complex in their theory and execution. The literature review will provide summary information on all those topics and – more importantly – pertinent references to which the reader is encouraged to turn for more thorough treatment.

Section 2.1 addresses the issue of fundamentals by summarizing much of the textbook-level understanding that governs the applied science of gas turbine engine and combustor design. Section 2.2 discusses science of arguably equivalent importance to this work and to engineering research at large: the practical modeling and simulation of fluid phenomena, especially those fields of interest to this current study. Section 2.3 introduces specific details on experimental methods for optical analysis of reacting flows, and Section 2.4 then offers a rigorous summary and evaluation of recent work performed in the name of compact combustion. Finally, Section 2.5 presents a background of AFIT's role in compact combustion research. Results of early analytical work will demonstrate the impetus for compact combustion research. A variety of compact combustion schemes will be described, leading ultimately to the body of research in high-g combustion.

2.1. Turbulent Combustion in Gas Turbine Engines

As a combustion system, the Ultra Compact Combustor must fit within the established framework of aircraft combustor design that has evolved over nearly a century of research and development. To provide the necessary context, this section presents a brief synopsis of the foundational principles of combustion and fluid dynamics. First, the governing principles of gas turbine engine design and operation are summarized. Subsequently, focus is given to the combustor assemblies in those same engines. The nature of flames, aspects of combustor design, and a background on emissions are then presented.

2.1.1. Gas Turbine Engines

While combustion science alone is a rich field of study, all combustors of practical use must operate in concert with other, equally complex components designed to supply air and fuel, and then extract the resultant energy in various forms. A system-level view is essential. Fundamentally, a propulsion system is defined by Mattingly [3] as "a unit submerged in a fluid medium about and through which fluid flows." A mechanism defined as an "engine" increases the kinetic energy of the fluid passing through the system. In aircraft, the primary purpose of the engine is to generate thrust by increasing the pressure and velocity of incoming air, and the primary means to that end is a gas generator. The theoretical framework for a gas generator, as described in Boyce [4], is the ideal air-standard Brayton cycle as shown in Figure 2.1. A conceptual configuration appears at the top of the figure and plots of pressure versus volume (left) and temperature versus entropy (right) appear at the bottom. The ideal compressor stage (1 – 2) and the turbine stage (3 – 4) are represented as isentropic (constant entropy), adiabatic (no heat transfer) compression and expansion processes, respectively. The ideal combustor stage (2 – 3) is an isobaric (constant pressure) heat addition process.

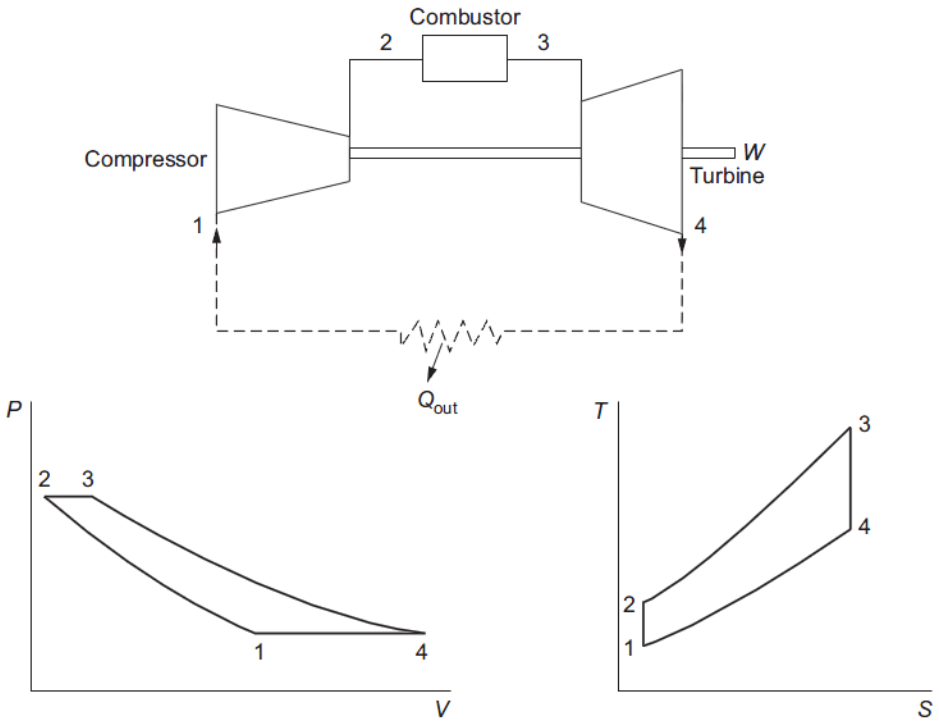

Figure 2.1. Air-standard Brayton cycle [4]

Following the development of Mattingly [3], the performance of an aircraft engine is fundamentally expressed in terms of its thrust generation. From a simplified thermodynamic analysis, the uninstalled thrust, F, generated by a jet engine with a single inlet and a single exhaust is shown in Equation (1). Here, the mass flow rate of the inlet air and the fuel are denoted by $\dot{m}_0$ and $\dot{m}_f$, respectively; the velocity and pressure at the engine inlet are V_0 and P_0, and at the exit V_e and P_e; exit area is given by A_e. Installed thrust, T, accounts for losses induced by inlet and nozzle drag as shown by Equation (2). Fuel consumption is generally given as the ratio of the fuel mass flow to the engine thrust; uninstalled fuel consumption, S, and installed, or thrust-specific fuel consumption, $TSFC$, are related to the inlet and nozzle losses in a similar manner as shown in Equation (3):

$$F = \frac{(\dot{m}_0 + \dot{m}_f)V_e - \dot{m}_0 V_0}{g_c} + (P_e - P_0)A_e \tag{1}$$

$$T = F(1 - \phi_{\text{inlet}} - \phi_{\text{noz}}) \tag{2}$$

$$S = TSFC(1 - \phi_{\text{inlet}} - \phi_{\text{noz}}) \tag{3}$$

The heat added to the system can be described by Equation (4) where LHV_{fuel} is the fuel lower heating value. The work output of a simple turbojet engine is defined by the net rate of change of kinetic energy of the fluid through the engine as shown by Equation (5); the engine thermal efficiency is then the ratio of the work output to the heat addition, Equation (6). The propulsive efficiency, Equation (7), then describes how effectively the engine power is transferred to the aircraft. For the case where the mass flow rate of fuel is much less than that of the air, and when the installation losses are relatively small, the propulsive efficiency can be simplified to the alternative expression shown as well by Equation (7). Overall engine efficiency is then the product of the propulsive and thermal efficiencies expressed in various forms by Equation (8).

$$\dot{Q}_{in} = \left(\dot{m}_f\right)\left(LHV_f\right) \tag{4}$$

$$\dot{W}_{out} = \frac{1}{2g_c}\left[\left(\dot{m}_0 + \dot{m}_f\right)V_e^2 - \dot{m}_0 V_0^2\right] \tag{5}$$

$$\eta_T = \frac{\dot{W}_{out}}{\dot{Q}_{in}} \tag{6}$$

$$\eta_P = \frac{TV_0}{\dot{W}_{out}} = \frac{2}{V_e/V_0 + 1} \tag{7}$$

$$\eta_O = \eta_P \eta_T = \frac{TV_0}{\dot{Q}_{in}} = \frac{TV_0}{\dot{m}_f LHV_f} = \frac{V_0}{TSFC\left(LHV_f\right)} \tag{8}$$

Among the more important system-level design constraints that an integrated combustion system must reconcile is simply the conservation of mass. Compressor design limits will dictate the overall mass flow rate presented to the combustor, absent any bleed air removed from the compressor stage for other purposes. That air mass flow rate will dictate the fuel mass flow rate into the combustor, thereby driving the design combustor heat release. Similarly, compressor design will dictate the geometric sizing of the entrance area to the combustor.

Annular flow areas at each compressor stage are a function of mass flow, flow angle, and total temperature and pressure. At the final stage of a typical high-pressure compressor, the ratio of the hub radius to the tip radius of the blades is on the order of 0.9 [3]; in other words, the passage is very narrow. A simple, representative four-stage compressor design is illustrated in Figure 2.2 for a representative case of 114 kg/s mass flow at sea-level conditions and an inlet Mach number of 0.5. Total engine diameter is driven by blade material and blade tip speed constraints; the case for the corresponding turbine is similar in many respects, with inlet geometry analogous to that of the compressor exit. The combustor system must interface between these two components, and much of the nature of aircraft gas turbine combustor engineering is driven by those interfaces.

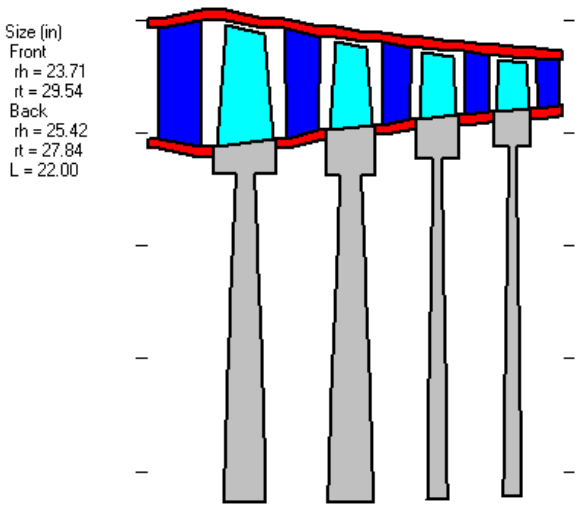

Figure 2.2. Example four-stage compressor design; flow is left-to-right, stators are dark blue, rotors are light blue

2.1.2. Combustor Development and Design

Combustion systems for aircraft gas turbine engines are generally comprised of main burners and afterburners (also called augmenters or reheaters). Their purpose is to fulfill the heat-input role of the Brayton cycle in order to increase the thermal energy of the air/fuel mixture. Aircraft combustors differ from their land-based counterparts primarily in the premium imposed on space and weight. Thus, it is necessary for the combustion process to be

accomplished as quickly as possible in a very restrictive volume. Consequently, the combustion intensity for the main burner of a turbojet is often in the realm of 11,000 MW/m^3, while a typical ground-based steam power plant comes in around 3.0 MW/m^3 [3]. To achieve that level of output from an aircraft gas turbine combustor while meeting concurrent demands of operating conditions and reliability, Mattingly [3] outlines a comprehensive set of desirable combustor properties while noting that many of them, unfortunately, present mutually conflicting requirements:

1) Complete combustion
2) Low total pressure loss
3) Stability
4) Proper exit temperature distribution
5) Short length and small cross section
6) Freedom from flameout
7) Relightability
8) Operation over a wide range of mass flow rates, pressures, and temperatures.

Add to the above the need for fuel efficiency and reduced emissions, and combustor design becomes a very complex trade space. The following subsections describe specific aspects of those challenges, beginning with the fundamental requirements of the combustion process. Selected design parameters are then introduced, and emissions are discussed in further detail.

2.1.2.1. Fundamentals

Combustion is itself a complex phenomenon, but the science is well developed, and many fundamental behaviors are well characterized. A definition from Webster's Dictionary describes combustion as "rapid oxidation generating heat, or both light and heat; also, slow oxidation accompanied by relatively little heat and no light." All practical combustion involves the

former, rapid oxidation process. Combustion can occur in both flame and non-flame modes, and the flame modes can involve either premixed or non-premixed (diffusion) flames [5].

Combustion requires a mixture of fuel and oxidizer to proceed. The chemical processes governing real combustion are complex, but are often represented by a single, global chemical reaction. Turns [5] provides an example as shown below in Equation (9) for an unspecified hydrocarbon reacting in air. Air is assumed to be composed of 21 percent O_2 and 79 percent N_2 (by volume), and the coefficient a is given in terms of the subscripts x and y, which are in turn specific to the particular hydrocarbon under consideration. From that result, the stoichiometric air-fuel ratio can be similarly found as a function of the chemical composition and the molecular weights (MW), as shown in Equation (11).

$$C_xH_y + a(O_2 + 3.76N_2) \rightarrow xCO_2 + \left(\frac{y}{2}\right)H_2O + 3.76aN_2 \tag{9}$$

$$a = x + \frac{y}{4} \tag{10}$$

$$\left.\frac{A}{F}\right|_{stoic} = \left(\frac{mass_{air}}{mass_{fuel}}\right)_{stoic} = 4.76a\left(\frac{MW_{air}}{MW_{fuel}}\right) \tag{11}$$

An important parameter in the characterization of combustion processes is the equivalence ratio. It is defined in Equation (12) as the stoichiometric air-fuel ratio divided by the actual air-fuel ratio of the mixture under consideration. Mixtures with $\phi > 1$ contain more fuel than is necessary for complete combustion and are termed "fuel-rich." Similarly, mixtures with $\phi < 1$ have excess air and are considered "fuel-lean." All mixtures have lower and upper limits of equivalence ratio within which combustion can be sustained; for hydrocarbon-air mixtures that range is roughly $0.4 < \phi < 2.0$. The lower and upper bounds are sometimes referred to as the lean blowout and rich blowout limits, respectively. Theoretical temperatures for a given mixture typically peak at equivalence ratios of just over one.

$$\phi = \frac{(A/F)_{stoic}}{(A/F)} \tag{12}$$

2.1.2.2. Flame Characteristics

Turns [5] defines a flame as a self-sustaining propagation of a localized combustion zone at subsonic velocities. Flames propagate through a mixture in discrete "waves." Propagation speeds at subsonic velocities place a flame in the category of a deflagration; supersonic combustion waves are termed detonations. While detonations are being harnessed in current aircraft propulsion research, gas turbine engines are all designed to operate in the deflagration regime. Specifically, reactions in a gas turbine combustor are highly turbulent and typically involve combinations of premixed and non-premixed flames. Turbulent flames share many characteristics with laminar flames, and are indeed identical in their core mechanisms. The most important parameters characterizing flames in either category are the flame speed, and the flame thickness. Simple one-dimensional relationships for those quantities for laminar flames are found in Turns [5] and are reproduced below:

$$S_L = \left[-2\alpha(\nu+1)\frac{\bar{\dot{m}}_F'''}{\rho_u}\right]^{1/2} \tag{13}$$

$$\delta = \frac{2\alpha}{S_L} \tag{14}$$

The term α represents the thermal diffusivity, ν, represents the mass oxidizer-to-fuel ratio, $\bar{\dot{m}}_F'''$ the mean volumetric mass production rate, and ρ_u the density of the unburned gasses.

The effects of turbulence essentially amount to wrinkling and distorting a laminar flame front to varying degrees based on the turbulence intensity. An important note in that regard is that a distinction is seldom made between the laminar and the turbulent flame thickness. Turbulent flames nearly always appear thicker, but that visual effect is due to the corrugation, disruption, and scattering of the otherwise laminar flame front. The human eye integrates these rapid flame movements, thereby leading to the impression of an increased flame

thickness. The laminar flame thickness itself, however, remains unchanged. Thus, the terms "flame thickness" and "laminar flame thickness" are effectively interchangeable.

The nature of the flame front distortion is a function of the flame thickness and the turbulent length scales. Two particular length scales define the upper and lower bounds of the regime of turbulent motion: the integral length scale, ℓ_0, represents the largest scales of turbulent motion; in other words, it is the approximate size of the largest eddies in the flow. Such sizes are of the same order of magnitude of the boundary geometry dimensions such as hole diameter or channel height. At the other end of the spectrum is the Kolmogorov length scale, ℓ_K, which represents the smallest eddies of the flow wherein the fluid viscosity results in dissipation of the eddy rotational energy into thermal energy. Three categories of turbulent flames are defined by the turbulent length scales and the flame thickness:

Wrinkled laminar flames: $\delta \leq \ell_K$ (15)

Flamelets in eddies: $\ell_0 > \delta > \ell_K$ (16)

Distributed reaction: $\delta > \ell_0$ (17)

Equation (15) is also referred to as the Williams-Klimov criterion. At that scale, the flame thickness is much thinner than the smallest turbulent scale, to the turbulent motions can at most distort the flame front. Equation (17), then, is referred to as the Damköhler criterion. If the scales of turbulent motion are much smaller than the flame thickness, then those turbulent motions begin to contribute – along with molecular processes – to transport within the reaction zone [5].

Another important parameter in combustion is the Damköhler number, defined by Turns [5] as the ratio of a characteristic flow or mixing time (τ_{flow}) to a characteristic chemical time (τ_{chem}):

$$Da \equiv \frac{\tau_{flow}}{\tau_{chem}} \tag{18}$$

The condition of $Da \gg 1$ represents a fast chemistry regime wherein the chemical reaction rates are fast relative to fluid mixing rates; the converse holds for $Da \ll 1$.

The analysis in Turns [5] for a turbulent premixed flame results in an expression for Da in terms of the integral length scale, root-mean-square (RMS) velocity, flame speed, and flame thickness. The turbulent Reynolds number is defined similarly as a function of the RMS velocity, integral scale, and viscosity. An important figure results, and is shown in Figure 2.3. The conditions for each of the three combustion regimes previously defined are highlighted and bounded by the solid black lines representing $\ell_K = \delta_L$ and $\ell_0 = \delta_L$. The boxed region contains experimental data from spark-ignition engine combustion. The two dashed lines are additional constant values of ℓ_K/δ_L; the dot-dash line is another constant value of ℓ_0/δ_L; and the thin solid lines are lines of constant v'_{rms}/S_L.

In Anthenien and Zelina [6], the combustion regimes of an ultra-compact combustor test rig were analyzed, and the combustion process was found to exist primarily in the regime of distributed reactions, therefore implying that turbulent transport is an important factor in UCC operation. Applications of the current research will include evaluation of similar characteristics of the test rig at AFIT.

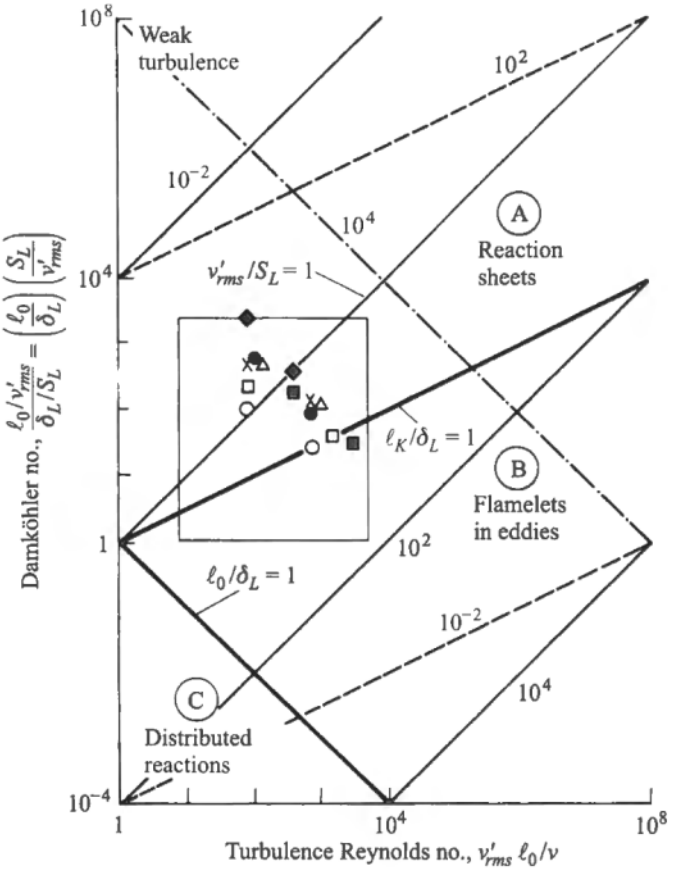

Figure 2.3. Parameters characterizing turbulent premixed combustion [5]

2.1.2.3. Combustor Design Characteristics

A representative, modern combustor design, as presented by Lefebvre [7], is illustrated in Figure 2.4. High pressure compressor air enters from the left and passes through a diffuser to reduce its Mach number. Main burner air is typically imparted with high degrees of swirl and injected alongside an atomized liquid fuel stream in order to facilitate fast, efficient mixing. Ignition occurs in the primary zone. The primary zone is where the flame is anchored, and it is designed to provide sufficient time, temperature, and turbulence to achieve nearly complete combustion [7]. The primary-zone holes are designed to inject air in a manner that the flow recirculation zones in the upper and lower halves of the primary zone merge and blend, thereby strengthening one another. This primary zone flow pattern is illustrated in Figure 2.5. Such a pattern has been found to provide wide stability limits, good ignition performance, and freedom

from pulsation- and noise-type combustion instabilities. Following the primary zone, the intermediate zone exists to begin diluting the combusted mixture incrementally; if dilution occurs too quickly then the composition of the freshly-reacted mixture would become "frozen" and CO would be discharged from the combustor unburned. Dropping the temperature to an intermediate level with small amounts of air via the secondary holes encourages burnout of soot as well as the combustion of any remaining unburned hydrocarbons (UHC). Finally, typically 20 to 40% of the total combustor air is devoted to the dilution zone. The primary purpose of this zone is a final reduction in temperature of the combustion products and optimization of the exit temperature pattern factor – a very important performance parameter that shall be discussed in Section 2.1.2.4.

Overall, the conceptual configuration discussed here has changed very little over the decades. Its nature lends to three basic engineering configurations of gas turbine combustors as highlighted in Figure 2.6. Tubular configurations, while relatively cheap to develop, incur length and weight requirements that generally preclude their use in aircraft engines. Tuboannular configurations make better use of the limited space within the engine casing by placing the inner combustion cans within a single outer annular liner. It is more challenging, however, to achieve consistent airflow patterns within such a design. An annular design is considered an ideal form in many ways due to the low pressure losses associated with its clean aerodynamic layout. A main disadvantage is the heavy buckling load imposed on the outer liner. Development and testing of such configurations is also challenging due to the need to test the entire assembly versus individual cans.

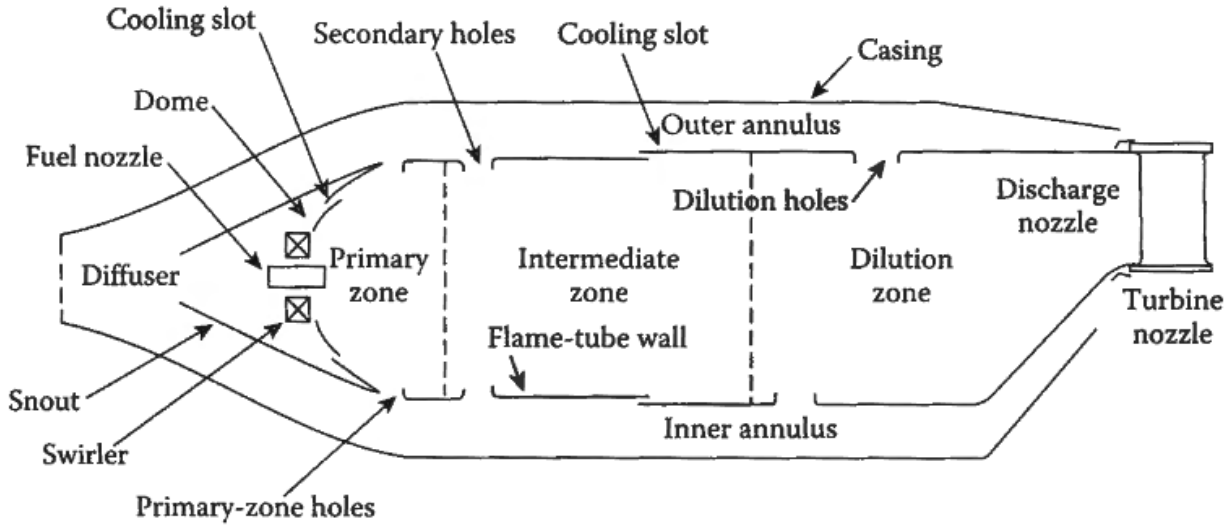

Figure 2.4. Main components of a conventional combustor [7]

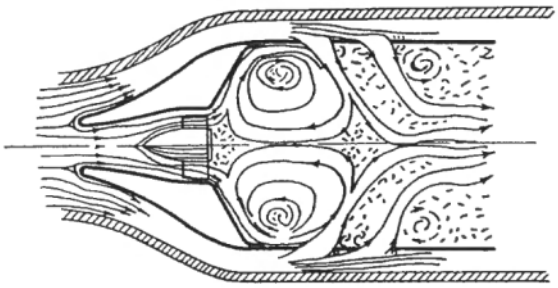

Figure 2.5. Desirable primary-zone airflow pattern [7]

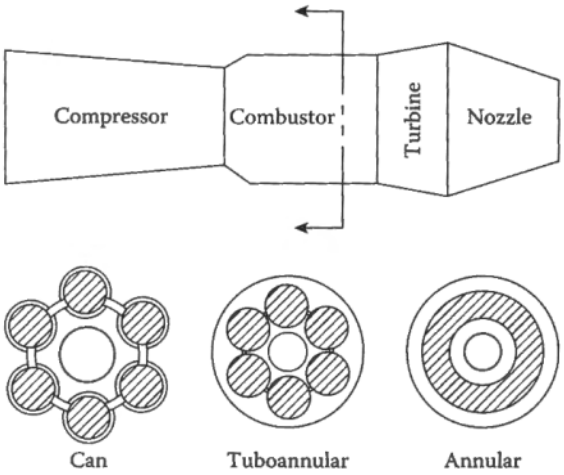

Figure 2.6. Three main combustor types [7]

2.1.2.4. Combustor Performance Parameters

From Mattingly [3], the ability of the combustion process to continuously sustain itself is called combustion stability. Stability is influenced by the equivalence ratio, as discussed earlier, since operation near rich- and lean-blowout limits is inherently destabilizing. An additional parameter used to characterize combustion stability is the combustor loading parameter, defined in terms of the mass flow rate, combustion volume, and pressure:

$$\text{CLP} \equiv \frac{\dot{m}}{P^n(V)} \tag{19}$$

For hydrocarbons in air, the pressure exponent has been experimentally determined to be $n = 1.8$. Experiments with hydrocarbons in well-stirred reactors have found loading parameter stability limits of 90 lbm/(s*atm$^{1.8}$*ft^3) at $\phi = 1$ and 10 lbm/(s*atm$^{1.8}$*ft^3) at $\phi = \{0.5,1.7\}$ [3].

In Anthenien *et al.* [8], loading in the cavity of a high-g combustor is considered with a parameter derived from well-stirred reactor studies called the Longwell Parameter:

$$\theta = \frac{P^{1.75} V e^{T/300}}{\dot{m}_{Acav}} \tag{20}$$

The units of *P, V,* and *T* are Pa, m^3, and K, respectively, and $\dot{m}_{Acav}$ is defined as the mass flow rate of air supplied to the cavity. Note as well that the Longwell parameter represents a reciprocal to the loading parameter described in Equation (19); thus, lower θ corresponds to higher cavity loading. At high efficiency, conventional annular combustors operate at Longwell values of about 10^8; in contrast, the high-g test rig of Anthenien *et al.* [8] demonstrated operation with comparable efficiency at Longwell values of about 10^7. Furthermore, combustion efficiency was found to increase with increased loading, while typical combustors see reduced efficiency as loading is increased [8].

Combustor cross-sectional area is generally determined by one-dimensional analysis of the engine components as alluded to earlier. Combustor length, however, is driven by length scaling, which is in turn based on the required chemical residence time. Fluidic residence time within the combustor is a simple matter of combustor length divided by a mean flow velocity. That residence time must be sufficient for the chemical reactions to occur. Reaction rates can be approximated in many situations by a form of the Arrhenius equation, as shown in Equation (21), where $f(T)$ is a function that relates the reaction rate to the forms of energy the molecules have, and the exponential term accounts for the number of molecular collisions in which the

energy of one molecule relative to another exceeds the activation energy E. $\mathcal{R}$ is the universal gas constant. As the reaction time is inversely proportional to the reaction rate, Mattingly [3] derives the combustor length, L, scaling law as shown in

$$Reaction\ Rate \propto P^n f(T) \exp\frac{-E}{\mathcal{R}T} \tag{21}$$

$$L \propto \frac{P_{t3}^{-r}}{\sqrt{T_{t4}}} \tag{22}$$

where $r = 1.51$ for $n = 1.8$.

As far as actual combustion efficiency, detailed theoretical treatment is beyond the scope of most references due to the highly complex environment within the combustion zone. Thus, empirical approaches are therefore generally relied upon. One of the more common of such approaches is the burning velocity model in which the burner efficiency, η_b, is a function of the reaction rate parameter, θ, as shown in Mattingly [3]:

$$\eta_b = f(\theta) = f\left[\left(\frac{P_{t3}^{1.75} A_{ref} H \exp\left({}^{T_{t3}}/_{b}\right)}{\dot{m}_3}\right) \times 10^{-5}\right] \tag{23}$$

where

P_{t3} = main burner inlet pressure [psi]

A_{ref} = main burner reference area [in^2]

H = height of main burner [in]

T_{t3} = main burner inlet temperture [°R]

$\dot{m}_3$ = main burner inlet airflow [lbm/s]

$b = 382\left(\sqrt{2} \pm \ln\frac{\phi}{1.03}\right)$

The function b uses a plus when the equivalence ratio is $\phi < 1.03$, and a minus when $\phi > 1.03$. Values of the combustion efficiency versus the reaction rate parameter are shown in Figure 2.7

for varying values of b. Industry standards for overall combustion efficiency have long been in excess of 99%, and a no point in the operating cycle less than 90% [7]. In fact, modern standards mandate off-design efficiencies in excess of 98.5% in consideration of regulations on exhaust CO and unburned hydrocarbons [3].

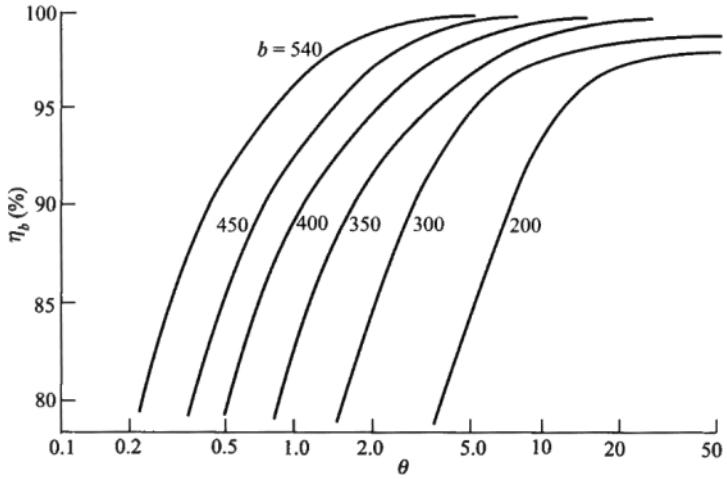

Figure 2.7. Combustion efficiency versus reaction rate parameter [3]

The total pressure loss across the combustor is another important characteristic. Two distinct parameters are of interest: first is the overall pressure loss, $\Delta P_{3-4}/P_3$, and second is the ratio of the total pressure drop to the reference dynamic pressure or the pressure-loss factor, $\Delta P_{3-4}/q_{ref}$ [7]. The latter term is of prime importance as it denotes flow resistance introduced into the airstream between the compressor outlet and the turbine inlet. While the overall pressure loss is dependent on operating condition, the pressure-loss factor is solely a property of the combustion chamber. It can be thought of in two components: the pressure drop across the diffuser, and the pressure drop across the liner. The challenge, however, is that a high liner pressure drop is actually desirable since it aids with penetration of the secondary jets into the combustion chamber, thereby promoting good mixing and facilitating a shorter liner. Pressure loss factors for representative designs range from 20 to 40 [7].

The exit temperature profile, or "temperature traverse quality" [7], is considered one of the most important combustor performance parameters, and represents one of the greatest

challenges. All elements of the combustor design from dimensions, geometry, and airflow distribution, to fuel spray characteristics play a role in the exit flow patterns. For overall engine performance, the turbine inlet temperature, T_4, is considered the most important governing temperature characteristic of the engine. Since the turbine inlet guide vanes must be designed to withstand the maximum combustor exit temperature, the primary metric of interest is the pattern factor, shown in Equation (24). Conversely, turbine blade design is most dependent on the average radial temperature profile, characterized by the profile factor as shown in Equation (25). Values of the pattern factor for modern combustors range from 0.25 to 0.45; increased durability requirements could push the lower limit as low as 0.15. A common design goal for the profile factor is about 1.06, while a range of 1.04 to 1.08 is common in modern systems [3].

$$\text{Pattern factor} = \frac{T_{max} - T_4}{T_4 - T_3} \tag{24}$$

$$\text{Profile factor} = \frac{T_{mr} - T_4}{T_4 - T_3} \tag{25}$$

$$\text{Turbine profile factor} = \frac{(T_{4.r} - T_{4.des})_{max}}{T_4 - T_3} \tag{26}$$

Importantly, modern engine designs do not generally call for a perfectly uniform temperature profile. Instead, the most desirable shape is curved with the peak temperature just above the midheight of the blade and the lowest temperatures at the blade root and tip. Thus, the turbine profile factor shown in Equation (26) takes that design profile into account, where $(T_{4.r} - T_{4.des})_{max}$ is the maximum temperature difference between the average temperature at any given radius around the circumference and the design temperature for that same radius [7].

2.1.2.5. Emissions

Pollutant emissions from all energy sources have become an issue of global significance. As described by Turns [5], specific pollutants of concern include

1) Particular matter such as soot, fly ash, metal fumes, aerosols
2) Sulfur oxides SO_2 and SO_3
3) Unburnt/partially burnt hydrocarbons
4) Oxides of nitrogen, or "NO_x", including NO and NO_2
5) Carbon monoxide, CO
6) Greenhouse gasses, CO_2, CH_4, N_2O

Emissions of a given species, i, are traditionally quantified by an emission index, defined as the ratio of the mass of the species emitted to the mass of the fuel burned as shown in Equation (27). Though it is technically a dimensionless quantity, it is often assigned units such as g/kg to avoid working with very small numbers. For a hydrocarbon in air, the emission index can be found from concentration measurements of the species of interest together with those of all the carbon-containing species, shown as well in Equation (27) (all fuel carbon is assumed to be present as either CO or CO_2). Note that χ_i is the mole fraction, and x is the number of moles of carbon in a mole of a given fuel C_xH_y, and MW_i are the respective molecular weights [3].

$$EI_i = \frac{m_{i,emitted}}{m_{F,burned}} = \left(\frac{\chi_i}{\chi_{CO} + \chi_{CO_2}}\right)\left(\frac{xMW_i}{MW_F}\right) \tag{27}$$

Standards for aircraft engine emissions are set forth by the International Civil Aviation Organization (ICAO) for rated thrust levels above 26.7 kN (6000 lbs). The standards are based on typical operating cycles around airports below 3000 feet, thus including descent, approach, landing, taxi, and takeoff engine power settings and timescales; that operational cycle is referred to as the ICAO landing-takeoff cycle (LTO) [7]. An example of typical mass distributions of modern engine emissions from Bahr [9] is shown in Table 1. The bulk of emissions are in the form of NO_x, particularly at cruise conditions.

Table 1. Distribution of total emission mass quantities generated during a typical flight profile of a twin-engine transport over a 500 nautical mile range

Category	Percent of Total Emission Mass		
	During ICAO LTO Cycle	During Climbout, Cruise, and Descent	Overall
Smoke	-	0.1	0.1
UHC	0.6	1.0	1.6
CO	5.4	7.0	12.4
NOx	7.8	78.1	85.9
Total	13.8 (56.5 % NOx)	86.2 (90.6% NOx)	100.0

Formation mechanisms for CO have been found to dominate at low-power conditions where burning rates and peak temperatures are relatively low; this contradicts predictions of equilibrium theory, which states that CO is produced during fuel-rich or stoichiometric conditions. Factors influencing CO production are similar to those that influence combustion efficiency: engine/combustor inlet temperatures, combustion pressure, equivalence ratio, and liquid fuel mean drop size. Experimental levels of CO have been found to reach a minimum at around $\phi = 0.8$ with typical values ranging between 8 and 80 g/kg of fuel; lower emissions were noted at higher combustion pressures. Furthermore, the generation of unburned hydrocarbons (UHC) was found to follow trends similar to CO [7]. Formation of soot – and thereby smoke – generally occurs in the primary combustion zone, while consumption of soot occurs in the intermediate and dilution zones. Formation is most severe at high pressures. Fuel type also plays a role, as smoke production increases with increased aromatic content of typical hydrocarbon fuels [7]. Oxides of nitrogen (including NO and NO_x) are formed by one of four mechanisms including thermal, prompt, and fuel NO_x as well as nitrous oxide mechanism. Thermal NO is controlled by temperature with little formation observed below 1850 K. Thus, as expected, formation peaks around stoichiometric equivalence ratios where temperatures are highest. Increasing residence time generally increases formation except in very lean conditions (ϕ~0.4). Emissions data for a premixed propane-air system is presented in Lefebvre [7], where a residence time of 2 ms at $\phi = 0.6$ results in a concentration of approximately 5 g of NO_x per kg

of propane. Reducing NO_x production is primarily accomplished through reduction of the combustion temperature; reducing the formation of hot spots is a coupled objective in that regard. Better mixing and reduced residence time are additional reduction strategies. However, as a general rule, any tactic employed to reduce NO_x emissions will result in increased production of CO and UHC. Thus, trade studies are often required to find an acceptable balance for any given combustor design. In high-g combustion research, Anthenien *et al.* [8] demonstrated CO emissions at levels between 20 and 180 g/kg of liquid JP-8 fuel. Zelina *et al.* [10] combined those results with NO_x emissions that ranged from 1.5 to 3.0 g/kg.

2.2. Analytical and Modeling Approaches

The idiom always goes "all models are wrong, some are useful." In theory, the physical principles of fluid flow and combustion are understood. The coupling of turbulence and the chemistry of reactions is developed as well. A more common desire amongst engineers and designers of practical systems, however, are approaches that can address the theoretical complexities with experimentally and numerically tractable approximations. Models are a primary tool of engineering approximation in numerous senses, be they sectional representations, scaled-down geometries, approximations to fluid condition and composition (i.e. – using kerosene to represent jet fuel), and the ubiquitous computational-numerical models. No model – numerical or otherwise – can hope to be a perfect representation of its real-world counterpart. However, with judicious use and careful understanding of the information that can be reliably obtained, as well as the information that is known to be lost, a model can provide invaluable insight into the characteristics of the system that it represents.

This current study will rely heavily on the science of computational fluid dynamics (CFD). To that end, this section devotes itself to the various techniques that exist for representing flow fields, particularly as applicable to the development of the ultra-compact combustor (UCC). Requisite analytical foundations in fluid flow and combustion are first given

to provide an appropriate context, after which common numerical variants of those foundations will be discussed. The current study will utilize the commercial CFD platform Fluent for all flow simulations; therefore, this section will also serve to summarize the implementation of the relevant models in Fluent. The models will be presented in the context of the current application to UCC development, and a summary of recent trends will be included.

2.2.1. Analytical Foundations

Fluids are differentiated from "non-fluids", generally speaking, by their propensity to flow under an applied shear force. The properties of a fluid, then, are founded in its molecular composition. Indeed, detailed understanding of the complex molecular interactions in homogenous and heterogeneous media is a science in and of itself. For problems of practical interest, however, pressures and temperatures are such that the spatial and temporal scales of fluid motion are several orders of magnitude greater than those of molecular motion. That notion is typically expressed with the Knudsen number, which quantifies that separation of length scales, where λ represents the molecular mean free path and l the smallest geometric length scale:

$$\mathrm{Kn} \equiv \lambda / l \tag{28}$$

For practical flows, $\mathrm{Kn} \ll 1$, therefore the discrete nature of a fluid can be neglected in favor of a continuum view. This fundamental continuum hypothesis allows the assumption that the fluid properties may be defined at any arbitrary location within the fluid. Therefore, vectors defining the fields of fluid flow are in all places differentiable [11].

Fundamental properties of a fluid are described in terms of three conservation laws governing the mass, momentum, and energy characteristics of the fluid in terms. The momentum conservation equation may be further developed by incorporating Newton's viscosity law, which states that the stress on a fluid element is proportional to the rate of strain: the results are the Navier-Stokes equations. Similarly, energy conservation may include Fourier's

law, which states that the heat flux is proportional to the temperature gradient. Those relations are presented in nearly every fluid dynamics reference; they are shown below in the form of ANSYS [12], which itself draws from Batchelor [13]:

$$\frac{\partial \rho}{\partial t} + \nabla \cdot (\rho \boldsymbol{u}) = S_m \tag{29}$$

$$\frac{\partial}{\partial t}(\rho \boldsymbol{u}) + \nabla \cdot (\rho \boldsymbol{u}\boldsymbol{u}) = -\nabla p + \nabla \cdot (\bar{\bar{\tau}}) + \rho \boldsymbol{g} + \boldsymbol{F} \tag{30}$$

$$\frac{\partial}{\partial t}(\rho E) + \nabla \cdot \big(\boldsymbol{u}(\rho E + p)\big) = \nabla \left(k_{eff} \nabla T - \sum_j h_j \boldsymbol{J}_j + \big(\bar{\bar{\tau}}_{eff} \cdot \boldsymbol{u}\big) \right) + S_h \tag{31}$$

Equation (29) is the general mass conservation equation for both compressible and incompressible flows where ρ is the density, t is time, and $\boldsymbol{v}$ the velocity field. The term S_m is specific to Fluent, and is included to account for multi-phase interaction as well as user-defined source terms. Equation (30) describes the conservation of momentum in an inertial reference frame. The term p represents the static pressure, $\bar{\bar{\tau}}$ the stress tensor, $\rho \boldsymbol{g}$ the gravitational force, and $\boldsymbol{F}$ any external or Fluent-user-defined sources. The stress tensor is further defined as

$$\bar{\bar{\tau}} = \mu \left[(\nabla \boldsymbol{v} + \nabla \boldsymbol{v}^T) - \frac{2}{3} \nabla \cdot \boldsymbol{v} I \right] \tag{32}$$

where μ is the molecular viscosity and I is the unit tensor. The term involving the unit tensor is the effect of volume dilation. In the energy equation, Equation (31), k_{eff} is the effective conductivity, which is itself defined as the sum of the thermal conductivity and the turbulent conductivity. The term $\boldsymbol{J}_j$ is the diffusion flux of species j, and the first three terms on the right-hand side represent energy transfer due to conduction, species diffusion, and viscous dissipation, respectively. The term S_h is again specific to Fluent, and it includes the heat of chemical reaction as well as any additional user-defined sources.

2.2.2. Turbulence

There are many classes of flows for which direct analytical methods; that is, Equations (29) - (31) may be solved directly, and the state of the flow at the given conditions determined precisely. Such classes are limited, however, to mostly academic exercises. Nearly all flows of interest to aerodynamics are turbulent. The onset of turbulence in a flow can generally be predicted by the flow Reynolds number, defined as the ratio of the product of a characteristic velocity ($\mathcal{U}$) and a characteristic length scale ($\mathcal{L}$) to the kinematic viscosity of the fluid (ν):

$$\mathrm{Re} = \frac{\mathcal{U}\mathcal{L}}{\nu} \tag{33}$$

For example, in the case of flow through a straight pipe, $\mathcal{U}$ is defined as the axial flow velocity and $\mathcal{L}$ as the pipe diameter. It has been found for such pipes that the flow is laminar for $\mathrm{Re} < 2{,}300$, and turbulent for $\mathrm{Re} > 4{,}000$ [11]; the exact mechanism of the transition from laminar to turbulent, though, depends on the details of the experiment. At the inlet to the test section of the AFIT UCC, the flow is approximated by traditional pipe flow characteristics. At air mass flow rates of around 0.1 kg/s with a 7.62 cm diameter, Reynolds number estimates are on the order of 2×10^5.

2.2.2.1. Reynolds-Averaging

In a turbulent flow, the velocity is random; the velocity vector is defined in statistical terms as a random variable. As such, it is expedient to analyze the velocity and other quantities with the technique of Reynolds averaging, wherein they are decomposed into their mean and fluctuating components. For velocity,

$$u_i = \bar{u}_i + u_i' \tag{34}$$

If the expression in Equation (34) is substituted into the mass and momentum conservation equations shown in (29) and (30), and if those relations are subsequently time- (ensemble-) averaged, then the ensemble-averaged momentum equations result as shown below in

Cartesian tensor form [12]. Note as well the definition of the Kronecker delta included for reference as Equation (37).

$$\frac{\partial \rho}{\partial t} + \frac{\partial}{\partial x_i}(\rho u_i) = 0 \tag{35}$$

$$\frac{\partial}{\partial t}(\rho u_i) + \nabla \cdot (\rho u_i u_j) = -\frac{\partial p}{\partial x_i} + \frac{\partial}{\partial x_j}\left[\mu\left(\frac{\partial u_i}{\partial x_j} + \frac{\partial u_j}{\partial x_i} - \frac{2}{3}\delta_{ij}\frac{\partial u_l}{\partial x_l}\right)\right] + \frac{\partial}{\partial x_j}\left(-\rho\overline{u_i' u_j'}\right) \tag{36}$$

$$\delta_{ij} = \begin{cases} 1 & \text{if } i = j \\ 0 & \text{if } i \neq j \end{cases} \tag{37}$$

Equations (35) and (36) are called the Reynolds-averaged Navier-Stokes (RANS) equations. The last term on the right-hand side of Equation (36), specifically the product $\overline{u_i' u_j'}$, is a second-order tensor whose components are referred to as the Reynolds stresses (though not technically stresses in the physical sense, their behavior is analogous to the point that the description has become customary). It is a product of the averaging process, and it introduces a new term to the momentum equation. For a general three-dimensional flow, there are four equations (continuity and the three components of momentum) coupled with four unknowns (pressure and the three components of the velocity vector). Introduction of the Reynolds stresses result in a closure problem: no analytical solution to the RANS equations is possible without additional information. The dominant approach to resolve that issue is to model the Reynolds stresses, and many decades of research have been devoted to that end.

2.2.2.2. Wall Spacing

A fundamental issue to analysis of turbulent flows is the precise nature of wall-bounded flow behavior. Turbulent flow near a wall can be described by two basic non-dimensional parameters. The first parameter defines the spatial dimension perpendicular to the wall. If the dimensional unit is defined as y in units of length, then the non-dimensional unit is defined by Equation (38) in terms of the viscous length scale (Equation (39)) and the friction velocity

(Equation (40)). Other terms introduced are the viscosity, ν, the density, ρ, and the shear stress at the wall, τ_w. The latter is detailed by Equation (41) as the product of the density, viscosity, and the change in the mean velocity, $\bar{U}$, at the wall. The significance of y^+ is its ability to describe the relative importance of viscous and turbulent processes independent of the flow Reynolds number. At the wall, due to the no-slip condition, contributions of turbulent motions to the total Reynolds stress is zero, and viscous stresses therefore contribute 100%. The viscous contribution at $y^+ \approx 12$ is only 50%, and is less than 10% by $y^+ \approx 50$.

$$y^+ \equiv \frac{y}{\delta_\nu} = \frac{u_\tau y}{\nu} \tag{38}$$

$$\delta_\nu \equiv \nu \sqrt{\frac{\rho}{\tau_w}} = \frac{\nu}{u_\tau} \tag{39}$$

$$u_\tau \equiv \sqrt{\frac{\tau_w}{\rho}} \tag{40}$$

$$\tau_w = \rho \nu \left(\frac{d\bar{U}}{dy} \right)_{y=0} \tag{41}$$

Similarly, a non-dimensional description of velocity near the wall can be defined by Equation (42).

$$u^+ \equiv \frac{\bar{U}}{u_\tau} \tag{42}$$

$$u^+ = \frac{1}{\kappa} \ln y^+ + B \tag{43}$$

Turbulent wall flow is classified according to ranges of wall units wherein the behavior of u^+ follows certain patterns. For $y^+ < 5$, it has been shown that $u^+ = y^+$. This region is called the viscous sublayer. From a range of approximately $5 < y^+ < 30$ a transitory behavior presents, following which a fairly consistent behavior occurs in the so-called "log-law" region from approximately $30 < y^+ < 5{,}000$; behavior in that region follows Equation (43) where the constants are known to be within 5% of $\kappa = 0.41$ and $B = 5.2$. Generally, $y^+ \sim 10{,}000$ represents

the limits of the boundary-layer thickness, after which freestream conditions dominate [11]. The practical importance of the viscous sublayer and the log-law region are related to the resolution to which computational numerical models are constructed. That discussion will be presented in Section 2.2.3.2.

2.2.3. Turbulence Modeling

In addition to the inherent difficulties of the closure problem, turbulence modeling is beset by numerous additional challenges that have even in modern times confounded the limits of computational power. As Pope [11] states, the turbulent velocity field is three-dimensional, time-dependent, and random. Fluid motion must be resolved at multiple length and time scales that span many orders of magnitude. The largest length scales reflect the boundary geometry, and therefore are not universal. The smallest length scales decrease as $\mathrm{Re}^{-3/4}$, and similarly the smallest time scales decrease as $\mathrm{Re}^{-1/2}$; thus increasing Reynolds numbers impose orders of magnitude increases in complexity.

2.2.3.1. Summary of Approaches

Pope [11] makes a distinction between a turbulent-flow simulation and a turbulence model. In the former, Equations are solved for a time-dependent velocity field representative of one realization of the turbulent flow. The latter involves solutions for mean quantities. However, the term "models" is often used to refer to both classifications.

Two common simulation techniques are direct numerical simulation (DNS) and large-eddy simulation (LES). In DNS, all length scales and time scales are resolved through direct solution to the Navier-Stokes Equations for one realization of the flow. This is the highest-fidelity approach, and DNS results are often held in similar regard as experimental results as validating authorities for less accurate models. However, the computational cost is also greatest since it increases as $\mathrm{Re}^{9/4}$ [11]. As Pope [11] notes, though, 99% of the effort of a DNS computation is involved in resolution of the smallest length and time scale – the "dissipation

range". Flow characteristics of practical interest often do not require such resolution. In contrast, LES involves the solution of a filtered velocity field that is representative of the larger-scale turbulent motions, and the influence of the small-scale motions is modeled rather than being directly represented.

Turbulence models are those solutions obtained for the RANS Equations as shown by Equations (35) and (36). The mean velocity field is determined through various approaches to representing the Reynolds stress, either through algebraic models or from turbulent quantity transport Equations. These models are typically grouped according to the number of additional Equations involved. Simple approaches such as the Spalart-Allmaras model involve only one additional transport equation to determine the turbulent viscosity. More rigorous two-equation developments such as the $k-\varepsilon$ and the $k-\omega$ models introduce two additional transport Equations; computing costs are greater, but the benefits to accuracy outweigh those costs in some classes of flows. More detail is given in Section A of the Appendix.

2.2.3.2. Wall Functions

To account for the behavior of a turbulent flow field in the presence of walls, there are two traditional approaches. Near-wall modeling involves constructing a grid with sufficient density so that the inner layers of the turbulent boundary layer are fully resolved. That involves having at least one point within the viscous sublayer, and multiple points within the range of $y^+ < 50$. The advantage of that approach is fidelity of the turbulence models throughout the near-wall region, while the disadvantage is the dramatic increase in cell count induced by the requisite wall spacing. Alternatively, semi-empirical formulae called "wall functions" may be invoked as bridges between the wall and the fully-turbulent region. Contrary to the near-wall modeling approach, wall functions cannot be used if the resolution is too fine; the first grid point is typically desired at $y^+ = 30$. There are seven options for implementing wall functions in Fluent: standard, scalable, non-equilibrium, enhanced wall treatment (EWT)

for the ε-equation, EWT for the ω-equation, LES near-wall treatment, and user-defined. In general, the use of EWT is recommended with the $k-\varepsilon$, though scalable wall functions are also endorsed. In application to skin friction calculations in a boundary layer over a flat plate, Mongia [14] documents successful use of standard wall functions with the first grid point located anywhere from $30 < y^+ < 500$. When enhanced wall treatment was used instead, a range of $1 < y^+ < 500$ was found to be appropriate. Thus, current and future computational work encompassed by this document will ensure that grid resolution and model application both adhere to those spacing requirements.

2.2.3.3. Model Application Discussion

As noted, the two-equation models are notionally the best balance between computational expense and flow representation. Especially when their attributes are combined as in the SST $k-\omega$ model, their range of applicability is broad. Pope [11], however, notes that the benefits of computational efficiency are often not realized, as the models are composed of coupled nonlinear Equations, often with multiple roots. Thus, although the cost of comparable RSM approaches is greater, the differences can become hard to distinguish for complex flows, especially as the increased capability of the RSM approach begins to outweigh its increased cost. Pope [11] offers a similar conclusion as noted by ANSYS [12] in Section A.2.iv: that the RSM approach can be far superior to the turbulent viscosity models in calculating flows with significant mean streamline curvature, strong swirl or mean rotation, secondary flows in ducts, and flows with rapid mean-flow variations. For many complex internal geometries, the $k-\varepsilon$ turbulence model is often utilized. By incorporating various wall function schemes, the $k-\varepsilon$ model produces accurate results with grid spacing in the realm of $30 < y^+ < 400$ [12]. The $k-\omega$ model, in contrast, requires grid resolution within the viscous sublayer, requiring the first grid point to be at a value of $y^+ \sim 1$. Thus, the later approach is much more intensive in its grid requirements.

In Mongia [14] and Mongia [15], the issue of modeling in gas turbine combustion is addressed in detail. The performance of several turbulence models in a swirl-cup combustor is compared; those models include the standard, RNG, and realizable variations of the $k-\varepsilon$ model, the $k-\omega$ model, and the Reynolds stress model. The standard and realizable $k-\varepsilon$ models are shown to have the best agreement with experiment, although they are still unable to satisfactorily predict the complex flows downstream of the cooling injection point. Mongia [14] concludes that RANS modeling for confined swirling flow is best utilized as a screening tool, and that LES is required for more advanced stages of the design process.

Early computational work on the Ultra Compact Combustor (UCC) was performed by Ehret [16], where a standard $k-\varepsilon$ model was implemented with some success, although only qualitative comparisons were made with the experimental data. The standard $k-\varepsilon$ model was used as well in the computational work of Greenwood [17] and Anisko [18]. Moenter [19] performed a comparative study between the standard and the renormalization group (RNG) $k-\varepsilon$ variant, concluding that the later was more successful at accurately resolving detailed turbulent flow structures. In the work of Mawid *et al.* [20], Mawid *et al.* [21], and Thornburg *et al.* [22], the realizable $k-\varepsilon$ model was used exclusively. In simulation of a trapped-vortex compact combustor (TVC-UCC), Briones *et al.* [23] also utilized the realizable variant. In the work of Briones *et al.* [24], premixed high-g combustion in a tube was simulated using Fluent's SAS turbulence models.

2.2.4. Combustion Models in Fluent

In this section, specific Fluent reacting flow schemes of interest to the current research are summarized and their applications are discussed. Unless otherwise noted, the reference for all subsections is ANSYS [12]. Further detail is given in the Appendix, Section A.2.

2.2.4.1. Summary of Approaches

The simplest method for implementing reactions is known as the Species Transport model. Mixing and transport of chemical species can be modeled by solving conservation Equations describing convection, diffusion, and reaction sources for each component species. Reactions occur in the bulk phase, or in other words, the reactions are volumetric. The local mass fractions for a given species are obtained through the solution of its specific convection-diffusion equation. Specific models can also be implemented for premixed and non-premixed combustion processes; laminar flamelet models are also implemented in these categories. Information is typically preprocessed into assumed-shape probability density functions (PDFs), and species properties are obtained via table lookup during the computation. In many cases – including the environment in the UCC – partially-premixed conditions exist, necessitating the use of a combined model. Modeling of emissions is often accomplished as a post-processing step after the initial flow field has been computed to convergence. Discrete models are utilized to predict formation of NO_x (including thermal, prompt, and fuel variants), SO_x, and soot. The presence of unburned hydrocarbons, in contrast, can generally be observed through species concentrations from the initial flow solution.

2.2.4.2. Reacting Model Applications

Applications of the Fluent models to Ultra-Compact Combustor simulations have been somewhat consistent. The calculations of Ehret [16], Greenwood [17], Anisko [18], and Moenter [19] utilized the non-premixed combustion model with the mixture-fraction PDF lookup and single-step global kinetics. Although the flow solver was different, Mawid *et al.* [20] and Thornburg *et al.* [22] employed a similar rate-of-progress variable for combustion calculations with single-step kinetics; an eddy-dissipation scheme was used. Mawid *et al.* [21] employed a similar approach but with a two-step reaction scheme. Briones *et al.* [24] utilized a two-step global reaction scheme for propane-air with the premixed combustion model. In Briones *et al.*

[23], detailed results are presented from computations of a trapped-vortex combustor flow field. A flamelet PDF was computed external to Fluent, then imported for use in the main computation with the non-premixed combustion scheme. Results indicated that both non-premixed and premixed conditions likely existed, so a combined scheme was recommended for future work. The most advanced UCC simulation to date was documented by Briones *et al.* [25] wherein flamelet modeling methods were coupled with a customized user-defined-function (UDF) to account for variability in the mixture molecular viscosity and thermal conductivity.

In Mongia [15], a single laminar-flamelet approach similar to Briones [23] is recommended for comprehensive gas turbine combustor design processes. Mongia [14] maintains that the flamelet model is the optimum approach for combustor calculations. However, it is also noted that such models still fall short in the presence of both premixed and non-premixed combustion. The benefit of LES was again emphasized for detailed numerical analysis of designs that have progressed beyond the screening stage.

2.3. Optical Interrogation

The mainstays of the aerospace research toolset have been probe measurements. In their various forms, probes collect information from the field of interest by physically "intruding" to some degree into some part of the system in order to reach the point of interest. The intrusive impact of these probes is largely insignificant, as the conditions of the field downstream are seldom of interest. Furthermore, the size of the probes relative to the size of the experiment generally renders their influence on the regions of interest negligible. Spatial and temporal resolution is often sufficient in larger, relatively simpler test rigs. With decreasing size and increasing complexity, requirements drive the development of alternatives to the traditional probe designs. In this respect, optical measurements – those that may be acquired via a camera and lens with minimal or zero intrusion on the region of interest – have

become commonplace. The following subsections detail the use of several such techniques, particularly as applied to combustion experiments.

2.3.1. Particle Image Velocimetry

Modern Particle Image Velocimetry (PIV) techniques have grown out of early applications of particle tracking and laser illumination to the point where it is nearly ubiquitous in academic and industrial research into fluid fields. The literature is consequently vast; the intent of this section will be to provide only an introduction to the technique and the methods that will be directly applied to this research. The primary reference for the fundamentals was Dantec [26].

The PIV technique provides instantaneous velocity vector measurements within a cross-section of a flow. An illustration of the various components and steps in the process is provided by Figure 2.8. First, appropriate seed particles are selected and introduced into the fluid upstream of the desired measurement location. Many criteria determine the desired seed type, but ultimately it needs to be (1) robust to the flow conditions, (2) small enough to flow along the same general path as the flow. (In combustion applications a widely accepted material for flow seeding is silicon carbide (SiC) with diameters of about 1 μm.) A laser beam is then configured to pass through a sheet-forming lens. Such lenses are generally semi-circular or full-circular cylinders; the cylinder diameter determines the width of the beam sheet at the region of interest. The laser is pulsed twice per measurement with some separation between the pulses, Δt, and the pulses are then captured as two image frames by an imaging system. In modern applications that system consists of a charge-couple device (CCD) camera; these systems have long been the standard due to their ability to capture successive high-resolution frames over extremely short intervals. The objective is to capture two frames of particle motion where individual particles can be tracked between the frames. Thus, the laser pulse (and image acquisition) must be timed appropriately based on reasonable knowledge of the flow

characteristics and the expected velocity of the seed particles as they traverse the measurement region. If the image frames are too far apart, then particles present in the first image will have left the region entirely by the time the second image is taken. If the frames are too close together, however, seed particles will appear stationary.

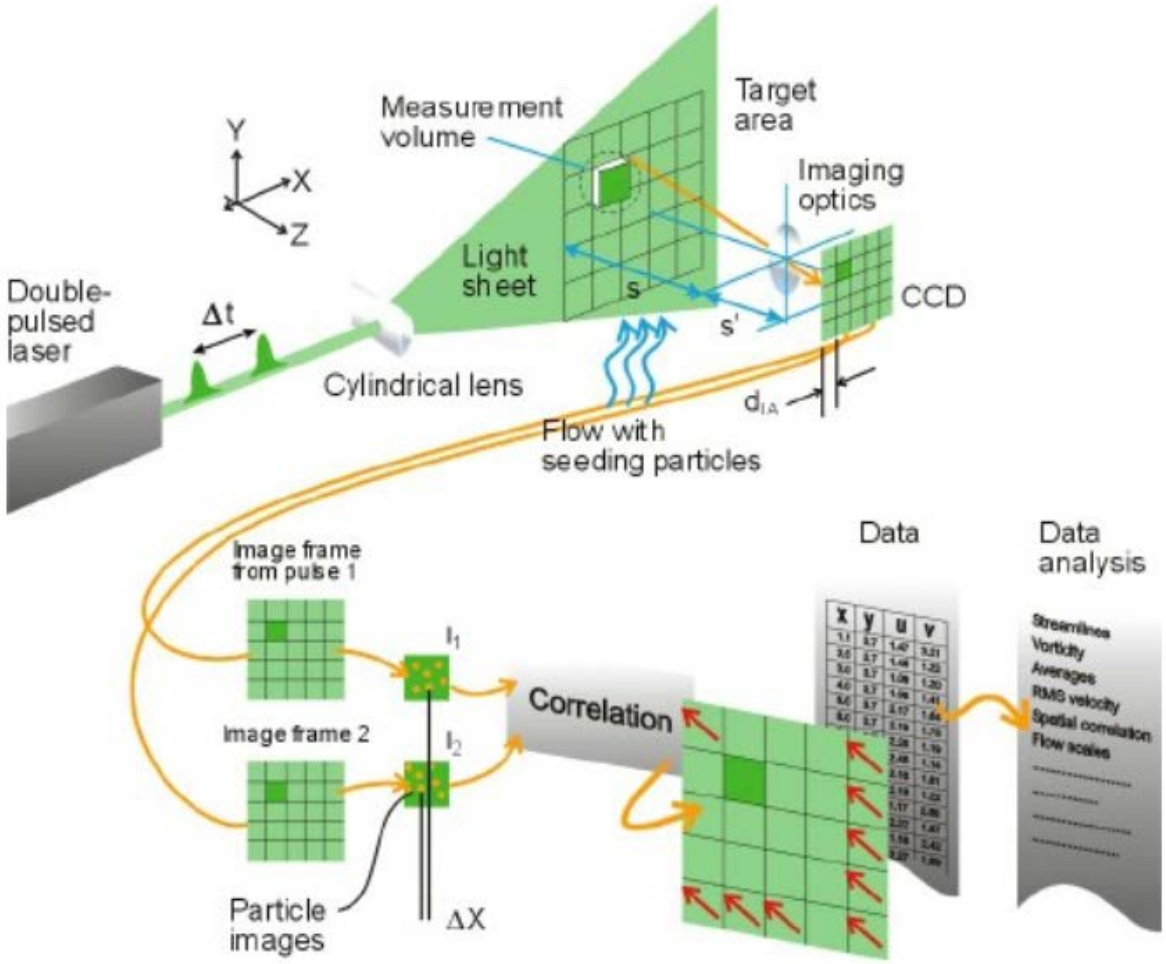

Figure 2.8: Illustration of the PIV measurement and analysis process [26]

After acquisition, the images are divided into small subsections called interrogation areas (IA). The interrogation images from each image frame, I_1 and I_2, are cross-correlated with each other pixel by pixel. Cross-correlation is a signal-processing operation that measures the similarity of two series as a function of the lag of one relative to the other. In PIV processing the cross-correlation formula has a form as shown by Equation (44).

$$C(s) = \iint_{IA} I_1(X) \cdot I_2(X - s)\, dX \tag{44}$$

The output of the correlation is a signal peak at each instance of common particle displacement. An accurate measure of the displacement is attained using sub-pixel interpolation. The displacements are then converted to velocities with knowledge of the time separation between the image pairs. A velocity vector map over the entire region of interest is then obtained by repeating the cross-correlation for each interrogation area [26].

Three rules of thumb are generally used to govern proper setup of a PIV measurement region. First, the number of particles visible in each image is important to obtain a good cross-correlation signal peak – 10 to 25 particles are recommended. Second, the side length of the interrogation area d_{IA} and the image magnification s'/s (both parameters are shown in Figure 2.8) should be balanced against the size of the flow structures to be resolved. One way to ensure this quality is to require the velocity gradient to be small within the interrogation area as shown by Equation (45). Finally, the highest measureable velocity is constrained by particles travelling further than the size of the interrogation area within the time Δt (as alluded to earlier). A rule of thumb to guard against this is shown in Equation (46).

$$\frac{\frac{s'}{s} \cdot |v_{max} - v_{min}|_{IA} \cdot \Delta t}{d_{IA}} < 5\% \tag{45}$$

$$\frac{\frac{s'}{s} \cdot v \cdot \Delta t}{d_{IA}} < 25\% \tag{46}$$

The traditional technique outlined above permits the measurement of two components of the fluid velocity with the third component "hidden" due to the imaging geometry. Modern developments, however, have seen the employment of dual-camera setups so that, by comparing the displacement measurements between the two cameras, the third velocity component can be resolved. Three- and four-camera setups have even been used for volumetric velocimetry, and

advances in both camera and laser technology currently permit time-resolved velocity measurements of the most complex flow environments. Most recent work in the literature involving gas turbine combustor interrogation invokes at least one of those modern PIV techniques. As examples: Slabaugh *et al.* [27] combined stereoscopic PIV, planar laser-induced fluorescence, chemiluminescence, and simultaneous integration to resolve spatially- and temporally-variant helical vortex structures in both stable and unstable operating modes of a swirl-stabilized burner, and Meadows and Agrawal [28] used time-resolved PIV with a repetition rate of 4.2 kHz to identify the acoustic instability modes and effects within a lean premixed burner with and without a porous inert media insert.

2.3.2. Thin Filament Pyrometry

Thin Filament Pyrometry (TFP) is a technique for obtaining temperature measurements within combustion environments. Thin filaments of highly emissive material are installed perpendicular to the flow. Upon exposure to high temperatures, the natural blackbody radiation of the filaments can be captured and correlated to obtain time-resolved temperature values with spatial resolution along the entire visible length of the filament. Early work demonstrating the TFP technique is documented by Vilimpoc *et al.* [29]. In their application SiC filaments 15 μm in diameter were utilized. The material was chosen due to its high melting point (2673 K) and its higher resistance to oxidation and catalytic effects as compared to traditional thermocouples. More recently, the TFP technique has been applied at the Air Force Research Laboratory (AFRL) as part of their SABER-Rig experimental campaign [30]. Therein, larger 125 μm filaments were employed due to their increased durability in hostile flow environments (SABER was an afterburner experiment). In fact, many of the lessons and practices from those experiments fed directly into the test that will be discussed later in this document.

The TFP technique can be implemented either by the intensity-ratio method or the two-color method. At AFRL and AFIT, the intensity-ratio method was used. The filament is a greybody whose emissivity is not a function of wavelength; therefore, the intensity of its emission is given by Planck's law. The intensity ratio of the filament at a measured temperature as compared to a reference temperature is thus defined as in Equation (47) where $I_b(\lambda, T)$ is the spectral radiance calculated by Planck's equation at the central wavelength λ of the interference filter and filament temperature T. C_2 is Planck's second constant and T_0 is the reference filament temperature [30].

$$I_R = \frac{\epsilon I_b(\lambda, T)}{\epsilon I_b(\lambda, T_0)} = \exp\left(\frac{C_2}{\lambda}\left(\frac{1}{T_0} - \frac{1}{T}\right)\right) \tag{47}$$

Filament temperatures are therefore determined by measuring the intensity ratio and comparing to the ratio predicted by Equation (47). The reference temperature represents filament greybody emission at a known temperature. It can be obtained by using a calibrated burner (such as a Hencken flame) or a calibrated pyrometer. The latter approach was used both at AFRL and at AFIT to ensure that the reference temperature was obtained under the same flow and environmental conditions as the experimental temperatures. That aided reduction in uncertainty due to large radiation correction factors inherent in low-speed calibration flames. Thus, a disappearing-filament pyrometer can be used to measure the color temperature of the filament at a fixed flame condition during testing. The color temperature can then be corrected for transmission losses and filament emissivity (0.9 for the SiC material) allowing the establishment of reference values of temperature and intensity at experimental operating conditions [30].

A radiation correction factor must be calculated due to the fact that the filament temperature is lower than the gas temperature. This is a result of excessive heat loss due to radiation versus convective heat transfer between the surrounding hot gasses and the filament. In most instances conductive heat transfer from the filament can be ignored due to its relatively

low thermal conductivity. In a simple thin flame with no surrounding hot walls the gas temperature can be defined as shown in Equation (48) where T_g, T_f, and T_∞ are the gas-phase temperature, the filament temperature, and the ambient temperature, respectively. Additionally, σ is the Stefan-Boltzmann constant and h is the convective heat transfer coefficient. Finally, the temporal response of a filament can be calculated by Equation (49) where τ is the response time, D_f is the filament density, R_f is the filament radius, C_f the filament heat capacity, and H_g the gaseous heat transfer [30].

$$T_g = \frac{\epsilon\sigma\left(T_f^4 - T_\infty^4\right)}{h} + T_f \tag{48}$$

$$\tau = \frac{D_f R_f C_f}{H_g} \tag{49}$$

An example of other recent research is the work of Ma *et al.* [31] wherein, among other things, the color-ratio and intensity-ratio methods for TFP were compared. Excellent agreement was found with both methods in a calibrated flame against coherent anti-Stokes Raman scattering measurements; overall uncertainty using the intensity-ratio approach was found to range between 15 and 32 K and using the color-ratio approach it was between 30 and 50 K.

2.3.3. Laplacian Convolution Filtering for PSEV

A new technique will be introduced in Chapter 3 for optical diagnostics: Particle Streak Emission Velocimetry (PSEV). As it is a novel approach developed recently by Innovative Scientific Solutions, Inc. (ISSI), it does not appear in direct terms within the literature. However, in application it is a fairly simple blend of particle tracking techniques (as in PIV) and the capture of natural blackbody radiation (as in TFP). One essential underlying component upon which PSEV relies, however, is an image-processing technique called a Laplacian convolution filter, which is itself an application of the discrete Laplace operator. While

examples of the use of this technique can be found in the literature such as in Reuter *et al.* [32], the online reference provided by the Fisher *et al.* [33] provides the top-level primer necessary for the current discussion.

A Laplacian is a 2D isotropic measure of the 2nd spatial derivative of an image. It highlights regions of rapid intensity changes and is therefore useful when edge detection is required (or, in the case of PSEV, for the detection of high-intensity streaks). The Laplacian operator typically takes greyscale images as input and gives greyscale as output. The general form of the Laplacian of an image with pixel intensity values $I(x, y)$ is shown in Equation (50).

$$L(x, y) = \frac{\partial^2 I}{\partial x^2} + \frac{\partial^2 I}{\partial y^2} \tag{50}$$

The Laplacian is generally calculated by way of a convolution filter. In an image processing context, a convolution consists of two input arrays: one greylevel image, and a second much smaller "kernel," both are illustrated in Figure 2.9. The convolution is performed by sliding the kernel over the image, generally starting in the upper left corner, such that the kernel transits all positions where it fits entirely in the image. Each kernel position corresponds to a single output pixel, the value of which is calculated by multiplying together the kernel value and the underlying image pixel value for each of the cells in the kernel and then adding all those numbers together. In the given example, the value of the bottom right pixel in the output image will be defined by Equation (51). If the image has M rows and N columns and the kernel is similarly sized $m \times n$ then the size of the output image will be $(M - m + 1) \times (N - n + 1)$. The general form of the convolution can thus be written as in Equation (52) [33].

I_{11}	I_{12}	I_{13}	I_{14}	I_{15}	I_{16}	I_{17}	I_{18}	I_{19}
I_{21}	I_{22}	I_{23}	I_{24}	I_{25}	I_{26}	I_{27}	I_{28}	I_{29}
I_{31}	I_{32}	I_{33}	I_{34}	I_{35}	I_{36}	I_{37}	I_{38}	I_{39}
I_{41}	I_{42}	I_{43}	I_{44}	I_{45}	I_{46}	I_{47}	I_{48}	I_{49}
I_{51}	I_{52}	I_{53}	I_{54}	I_{55}	I_{56}	I_{57}	I_{58}	I_{59}
I_{61}	I_{62}	I_{63}	I_{64}	I_{65}	I_{66}	I_{67}	I_{68}	I_{69}

K_{11}	K_{12}	K_{13}
K_{21}	K_{22}	K_{23}

Figure 2.9: An example small image (left) and kernel (right) to illustrate convolution [33]

$$O_{57} = I_{57}K_{11} + I_{58}K_{12} + I_{59}K_{13} + I_{67}K_{21} + I_{68}K_{22} + I_{69}K_{23} \tag{51}$$

$$O(i,j) = \sum_{k=1}^{m}\sum_{l=1}^{n} I(i+k-1, j+l-1)K(k,l) \tag{52}$$

Two commonly used simple Laplace kernels appear as the left and center images in Figure 2.10. As they are approximating a second derivative measurement on the image, however, they can be very sensitive to noise. To counter this, the image is often Gaussian smoothed before applying the Laplacian filter to reduce components of high frequency noise prior to the differentiation step. Furthermore, as the convolution operation is associative, the Gaussian smoothing filter can be convolved with the Laplacian filter first, and the hybrid filter can subsequently be applied to the image. This approach is termed a "Laplacian of Gaussian," or "LoG." The 2D LoG function centered on zero with Gaussian standard deviation σ has the form shown by Equation (53); a discrete kernel approximating the function (with $\sigma = 1.4$) is shown as the right image of Figure 2.10.

0	−1	0
−1	4	−1
0	−1	0

−1	−1	−1
−1	8	−1
−1	−1	−1

0	1	1	2	2	2	1	1	0
1	2	4	5	5	5	4	2	1
1	4	5	3	0	3	5	4	1
2	5	3	-12	-24	-12	3	5	2
2	5	0	-24	-40	-24	0	5	2
2	5	3	-12	-24	-12	3	5	2
1	4	5	3	0	3	5	4	1
1	2	4	5	5	5	4	2	1
0	1	1	2	2	2	1	1	0

Figure 2.10: Two common simple Laplace kernals (left and middle) and the discrete LoG kernel (right) [33]

$$LoG(x,y) = -\frac{1}{\pi\sigma^4}\left[1 - \frac{x^2+y^2}{2\sigma^2}\right]\exp\left(-\frac{x^2+y^2}{2\sigma^2}\right) \tag{53}$$

In execution, the LoG response will be zero where the image has constant intensity. In the vicinity of a change in intensity, the LoG response will be positive on the dark side and negative on the light side. Thus, at a reasonably sharp edge between two regions of uniform but different intensities, the LoG response will be (a) zero at a long distance from the edge, (b) positive just to one side of the edge, (c) negative just to the other side of the edge, and (d) zero at some point in between, on the edge itself. This is illustrated by the LoG response to a step function as shown by Figure 2.11 [33].

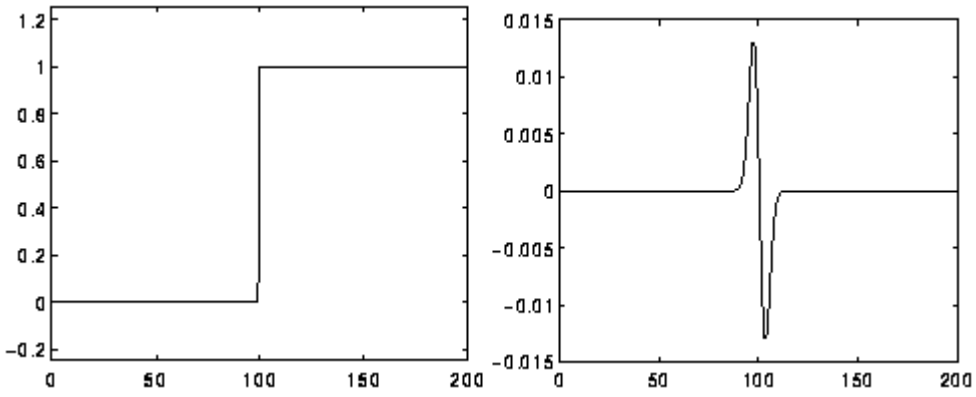

Figure 2.11: Response of 1D LoG filter to a step edge with Gaussian $\sigma = 3$ pixels [33]

2.3.4. Laser-Induced Breakdown Spectroscopy

Laser-Induced Breakdown Spectroscopy (LIBS) is an established technique for measuring the local equivalence ratio in combustion environments. Several textbook references exist; this review will utilize Noll [34] for a summary of the fundamentals. The bulk of modern applications for LIBS involve sampling of solid surfaces although it may be equivalently applied to liquid and gaseous targets. Thus, to illustrate the basic development, a notional LIBS measurement event on a solid surface is shown in Figure 2.12. A pulsed laser beam is focused upon the surface (or location in space) to be analyzed as in Image (1) in the figure. Radiation energy is locally coupled into the media (2) that subsequently begins to evaporate (3). A plasma is then generated within the resulting vapor and the surrounding atmosphere (4) leading to the excitation of the material constituents and thus their spontaneous emission of element-specific radiation as they decay (5-7). In solid samples a crater is then formed as evaporated material is partially removed by the intrinsic dynamics. One note is that the term "evaporation" is used deliberately as generally there is no direct sublimation from the solid phase to the gas phase [34].

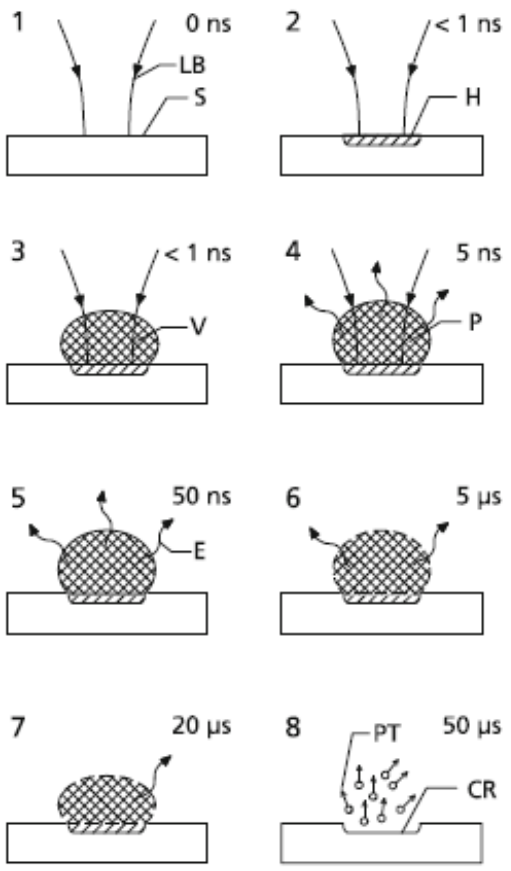

Figure 2.12: LIBS principle phases of measurement depicting temporal evolution in eight phases; LB = incoming laser beam, S = sample, H = region of energy deposition, V = material vapor, P = plasma, E = element-specific emission, CR = crater, PT = particles [34]

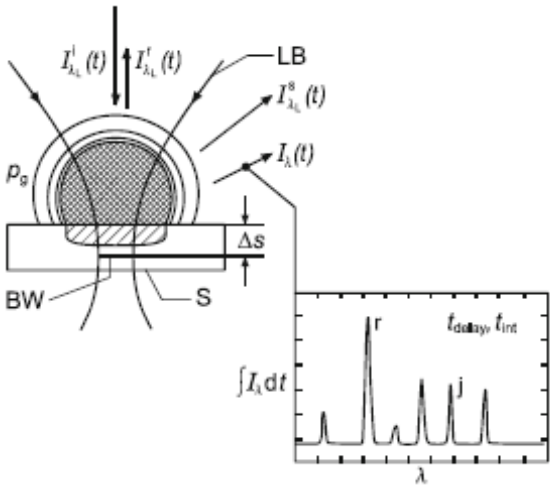

Figure 2.13: Illustration of measuring parameters at the emitted spectrum [34]

In Figure 2.13 typical measurement parameters associated with the plasma emission are illustrated along with a sample emissions spectrum. The parameters are the incident laser irradiance $I^i_{\lambda_L}(t)$ at the wavelength λ_L. Portions of the incident laser energy are reflected by the sample and the plasma, $I^r_{\lambda_L}$, while the remainder is scattered, $I^r_{\lambda_L}$. The ambient gas pressure, p_g, as well as the type of ambient gas also influence the plasma dynamics. Finally, the emitted plasma spectrum, $I_\lambda(t)$ is also a function of time. The two primary metrics for LIBS measurements are therefore (1) the intensity of the plasma emission at discrete wavelengths as a function of time, $I(\lambda = \lambda_i, t)$, and a spectrum that is integrated over a time interval

$[t_{delay}, t_{delay} + t_{int}]$: $S(\lambda) = \int_{t_{delay}}^{t_{delay}+t_{int}} I(\lambda, t)dt$. A sample spectrum with a number of emission lines is illustrated in the left image of Figure 2.14. The spectral position of the lines is allocated to the respective elements based on literature data. The height of a line is a measure of the concentration of the respective element, but numerous other factors affect the intensity of a given line including laser pulse energy, plasma temperature, plasma size, atomic parameters of the line transition, sample surface, and detector response function. In general, the influence of those extraneous factors can be diminished by taking the ratio of the intensity of an analyte line to the intensity of a dominant element of the sample. That dominant line thus acts as an internal standard or reference. To translate the measured ratio into quantitative results, a calibration is required using identical intensity measurements from samples with known chemical composition [34]. Examples applying the LIBS technique to hydrocarbon combustion systems include Do and Carter [35] and Kotzagianni and Couris [36].

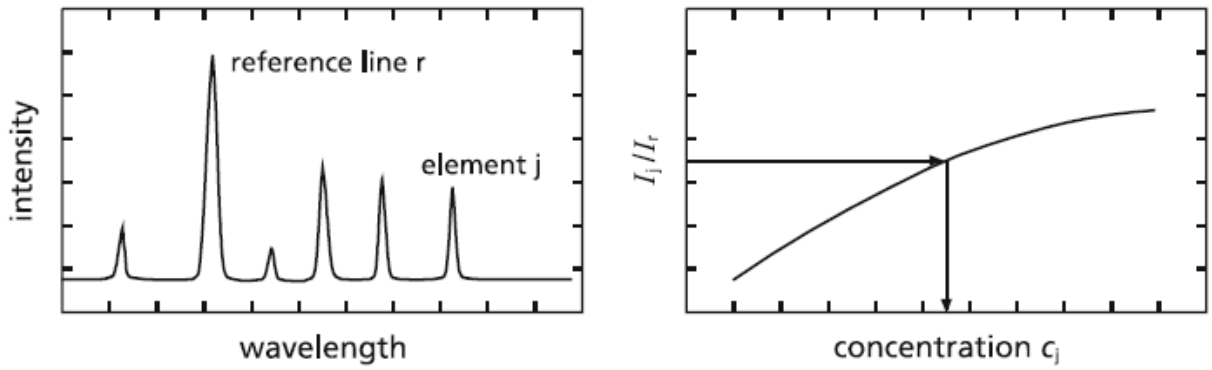

Figure 2.14: Emission spectrum of laser-induced plasma with analyte and reference line (left) and calibration curve (right) [34]

2.4. Compact Combustion

The science of compact combustion itself is still quite young. The focus of objective two, understanding the flame dynamics in the cavity, is largely dependent upon the underlying science and governing physical phenomena of compact combustion. Much of the literature

encompassed in this section consists of detailed, rigorous work with direct applications to the understanding of the fundamental scientific questions that are required to engineer a gas turbine compact combustor in its various forms.

2.4.1. Cycle Analysis

Sirignano, *et al.* [37] presented a seminal document wherein they first introduced their concept of a turbine burner; the concept was then the focus of a more detailed follow-up in Sirignano, *et al.* [38]. Their motivation was the persistent pressure for increased engine thrust-to-weight ratios, decreased specific fuel consumption, and wider ranges of engine operation. Their concept revolved around continual heat addition while extracting energy out of the cycle within the turbine – termed turbine burning. They extended the standard Brayton cycle by including secondary combustion within the turbine stage. In Figure 2.15, a turbofan engine schematic is shown with conventional station numbering; a complementary Brayton cycle is shown in Figure 2.16 in the form of a temperature-entropy (T-s) diagram. In considering secondary combustion, Sirignano noted a number of different locations that might serve similar purposes; those locations are marked in Figure 2.15, and they include the traditional combustor at stage 3 $(\dot{Q}_b)$, a fan burner at stage 3f $(\dot{Q}_{fb})$, and a conventional afterburner at stage 5 $(\dot{Q}_{ab})$. Figure 2.16 demonstrates the theoretical cycle differences between traditional afterburning augmentation and one with a turbine burner at stage 4 $(\dot{Q}_{tb})$. The solid and dashed line path represents a traditional engine cycle with afterburner, and the all-solid path represents an engine cycle with both turbine burning and afterburning. A traditional afterburner adds power to the engine, but since it does so at a lower pressure than the main burner, overall cycle efficiency is reduced. Conversely, in a notional turbine-burner, fuel would be burned while simultaneously doing work to the rotor. Ideally, the heating could be organized such that the stagnation temperature stays constant (as in an ideal Carnot cycle).

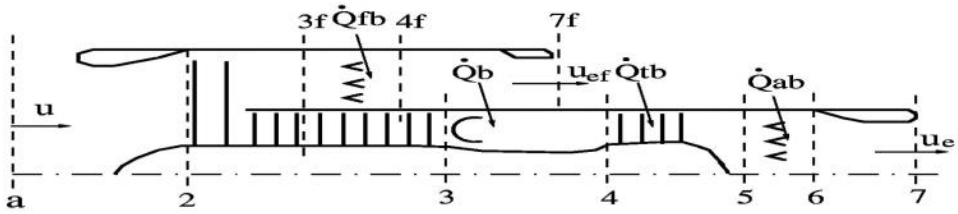

Figure 2.15: Schematic for a notional turbofan engine marked with possible combustor locations [37]

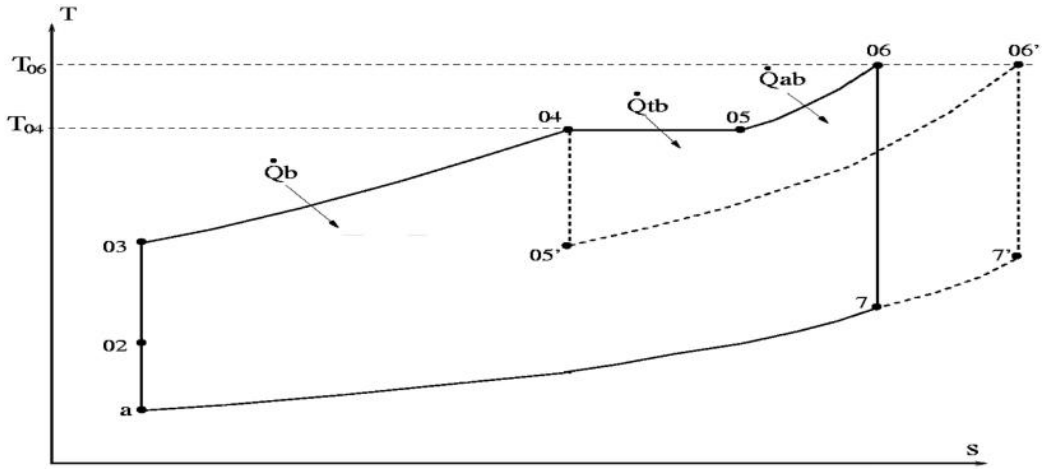

Figure 2.16: Ideal Brayton cycle highlighting impact of turbine burning [37]

In Sirignano *et al.* [37], a simple cycle analysis was performed comparing a baseline engine, turbine-burner augmentation, afterburning augmentation, and a combination of a turbine-burner and a reduced afterburner (AB). It was shown that the latter option attained greater specific thrust with less thrust-specific fuel consumption (TSFC) than the case of a simple AB. Those results imply that a turbine burning configuration, compared to a simple AB, can generate the same amount of thrust with a shorter engine length, or greater thrust with the same engine length. In Sirignano [38] the turbine burner concept was extended to include the notion of discrete combustion stages between the turbines, or confined to the turbine stators. As shown in Figure 2.17, increasing the number of ITB stages tends to approximate the theoretical performance of a continuous turbine burner (CTB).

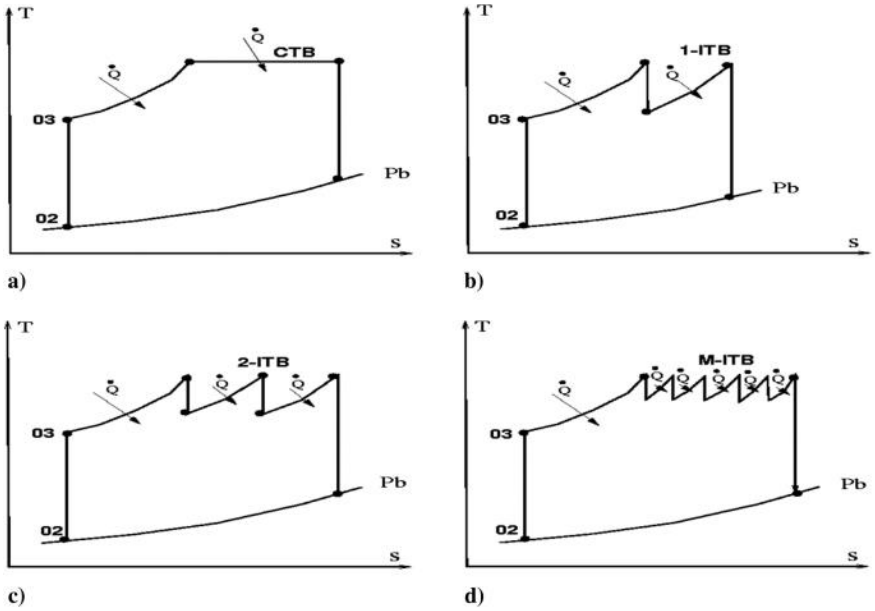

Figure 2.17: Cycle comparisons of CTB and ITB configurations (no afterburner) [38]

2.4.2. Accelerating, Reacting Mixing Layers

For practical applications, a continuous turbine burner (CTB) is not feasible; thus, building on the thermodynamic foundations outlined above, a variety of work has progressed to address the challenges of integrating discrete secondary combustion stages between turbine stages or within a turbine stator. The latter option was pursued by Sirignano and colleagues, beginning with an endeavor to understand the fundamental behavior of multidimensional flows with mixing and chemical reaction in the presence of strong pressure gradients. In Sirignano and Kim [39] and Fang *et al.* [40], solutions were obtained for a laminar, two-dimensional, reacting mixing layer subject to a stream-wise acceleration induced by a non-zero pressure gradient assuming infinite-rate and finite-rate chemical kinetics, respectively. Mehring *et al.* [41] introduced turbulent effects to the same analysis. It was shown that the spreading of the transverse velocity and temperature profiles were from 5 to 23 times that of the laminar case, depending on downstream location and whether on the air or fuel side of the flame.

Conclusions from the prior studies informed progressively more complex research. Simulations of reacting, accelerating, transitional channel flow with a mixing layer were

performed by Cheng *et al.* [42]; representative results are shown in Figure 2.18. The passage is meant to represent flow through a notional airfoil passage, such as a turbine stator stage. Reference locations along the passage length are marked by s as a function of δ_θ. The variable δ_θ is a measure of the mixing layer thickness at the inlet and is a constant set to $\delta_\theta = 1.25 \times 10^{-4}$ m. A faster, hotter air stream is on the outside of the curve, while the slower colder fuel stream (methane in these studies) is on the inside; similar behavior was observed when the stream locations were flipped. An important conclusion of this work may be noted in Figure 2.18: the flame "roll-ups" induced by the onset of instability cause flames to impinge directly onto the sidewalls; "sidewall" in this case refers to either the top or bottom surfaces of the curved geometry. The impact of these "hot spots" within a turbine stator passage would impose strenuous cooling requirements to an otherwise innocuous hardware component.

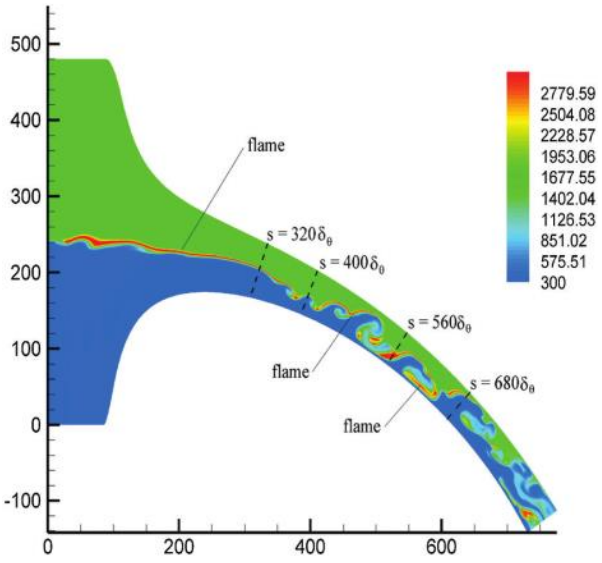

Figure 2.18: Instantaneous temperature contours of a reacting mixing layer in a curved, converging channel [42]

2.4.3. Cavity Flow Interactions

One strategy for effective combustion in a turbine passage is the incorporation of a cavity flameholder wherein fuel and some air may be injected before becoming entrained into the bulk passage flow. The study of flow over a cavity has broader applications with a variety of

work present in the literature, however, Colcord and Sirignano [43] first began a two-dimensional study of such a configuration for application to an inter-turbine burner (ITB). Therein, they concluded that long, shallow cavities would promote mixing better than deep, square cavities. Their simulations included fuel and air injection into the cavity in several arrangements, depicted and labeled in Figure 2.19; the highest burning efficiency was noted in the case of parallel injection. They noted as well that cavities with an aspect ratio of one did not hold a flame beyond a Reynolds number of 5000, whereas cavities with an aspect ratio of two held a flame for all Reynolds numbers studied (up to 10,000). Subsequent studies were performed on three-dimensional variants of the cavity configurations using direct numerical simulation (DNS). Notable differences from the two-dimensional case were observed. Flow around the jet injection streams introduced eddies in the third dimension; length scales were correspondingly smaller.

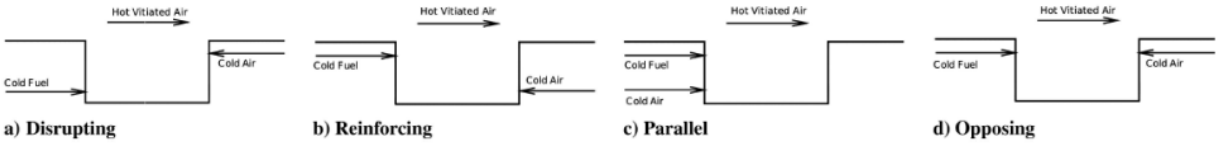

Figure 2.19: Cavity injection configurations simulated by Colcord and Sirignano [43]

In the same study, the analysis extended to 4:1 aspect ratio cavities in curving channels at a Reynolds number of 2000; representative results for reacting flow with parallel injection are shown in Figure 2.20. The parallel injection scheme (Figure 2.19c) was stable, and the disrupting scheme (Figure 2.19a) was unstable, for both the straight-channel and the curved-channel with the cavity on the inside. For the curved channel and the cavity on the outside, the reverse was true: the disrupting injection scheme was stable, and the parallel case was unstable. This was due to the introduction of a centrifugal instability component in addition to the normal Kelvin-Helmholtz instability induced by the cavity itself. Furthermore, when the channels (both straight and curved) were allowed to converge, increases in efficiency were noted

despite the decrease in residence time due to acceleration. Finally, stagnation pressure losses in the case of the converging, turning channel with the cavity on the outside were found to be small: effects of the cavity, injection and mixing, and chemical reaction were found to represent only about 1% of the entering pressure [44].

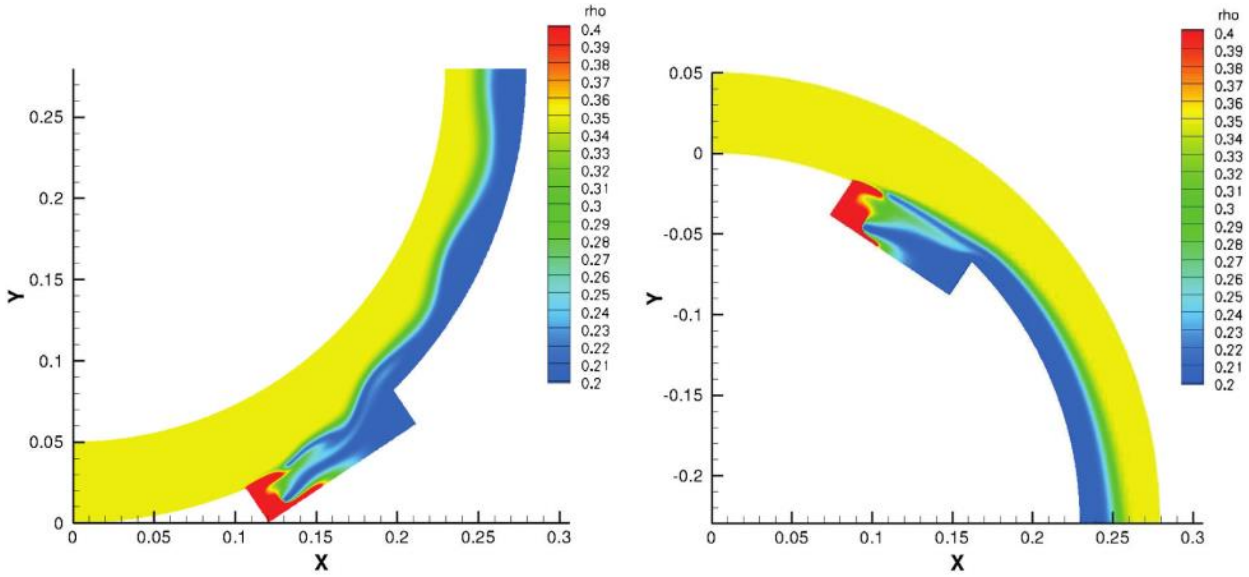

Figure 2.20: Density contours with parallel injection and the cavity on the outer (right) and inner (left) sidewalls [43]

The foregoing computational work has been supplemented by an experimental campaign, for which many of the salient details are summarized in Puranam *et al.* [45]. The test rig was configured with an optimal cavity fuel (propane) injection scheme, and two different cavity aspect ratios (1 and 2.5), with the cavity positioned on the inner wall. One notable conclusion resulting from this work was that three distinct combustion regimes were observed as functions of Reynolds number: low ($Re < 5{,}000$), high ($Re > 40{,}000$) and moderate. In the low regime, insufficient air entered the cavity and the flame was confined to the inner-wall shear layer. In the "high" regime the bulk of the combustion took place in the cavity; this was due to the high-speed bulk flow being too fast to maintain sufficient residence times for sustained flames. The flame was not stable in the moderate regime. Images of each of the three regimes are shown in Figure 2.21, with the "low" image on the left. The low-level shear-layer flame was

observed to behave like a diffusion flame, while the high-level cavity flame performed more akin to a well-stirred reactor. Positioning the cavity on the inner wall was found to produce exit temperature profiles highly skewed toward the inside due to the centripetal forces acting against the flame-to-core migration. It is hypothesized that having the cavity on the outer wall will yield more uniform exit profiles, but explicit results are as yet forthcoming. The Reynolds number regimes are an important conclusion, and it is hypothesized that similar results may be observed in the HGC presented in this current study.

Figure 2.21: Three combustion regimes: Re < 5000 (a), 5000 < Re < 40000 (b) and Re > 40000 (c) [45]

2.4.4. Trapped Vortex Combustion

Trapped vortex combustion (TVC) is a variation of ultra-compact combustor design independent of the so-called "high-g combustion." The latter will be discussed in Section 2.4.5. The former, though different in execution, stems from identical motivations and addressed many similar fundamental physical phenomena. Rather than a single combustion chamber, the trapped vortex combustor consists of two parts: a pilot combustor for stability, and a main combustor for power. The pilot combustor takes the form of a cavity that is sized such that it can contain a stable recirculation zone. Injection of fuel and air into the cavity is arranged to reinforce the recirculation. The cavity encircles the engine casing outer diameter; the main combustor, then, occupies the remaining interior space "beneath" (that is, radially inward) the pilot cavity. Thus, the design benefits from having the primary (pilot) combustion flame removed from the core flow, thereby enhancing stability and efficiency. A process known as

rich-burn quick-quench lean-burn (RQL) combustion can be exploited: the primary combustion (in the cavity) is done fuel-rich, after which the mixture migrates into the core in such a way that it quickly quenches to a fuel-lean condition. Thus, the temperature peak that occurs at stoichiometric conditions can be avoided, thereby reducing the overall thermal load on the system [46].

The notion of creating a stable vortex in a cavity appears early in the works of Mair [47] and Little and Whipkey [48]. Mair [47] noted that, given the success of separated flow pressure recovery devices (such as a ribbed diffuser), the drag on a blunt body of revolution could be reduced by attaching a disc behind the base of appropriate size and displacement. His measurements verified that there were a range of disc configurations that led to drag reduction. A single appropriately sized disc showed a maximum reduction of 35%. Using subsequent pressure measurements, flow visualization techniques, and hot-wire tests, Mair concluded that the minimum-drag configurations represented a condition wherein a toroidal eddy was stabilized between the base of the body and the disc. The stable vortex allowed the streamlines to pass smoothly over the cavity and converge in a stagnation point roughly two body diameters downstream. Defining x as the downstream displacement of the disc from the blunt body, and D_0 as the blunt body diameter, the minimum drag condition was noted at $x/D_0 = 0.6$. Little and Whipkey [48] expanded on those results including smoke visualization and laser velocimetry. It was confirmed therein that, at the minimal drag disc displacement of $x/D_0 = 0.6$, the vortex in the cavity was smooth and steady; mass transfer into and out of the cavity was also at a minimum. They concluded that the optimum cavity dimensions were such that the trapped vortex effectively filled the cavity. That result was verified by Katta and Roquemore [49] in both nonreacting and reacting flow.

Independent work on the officially-dubbed TVC was initiated by the United States Air Force by way of an Air Force Office of Scientific Research program in 1993. In Roquemore *et al.* [46], the cumulated work between 1993 and 2001 was represented with test results from a

notional TVC in realistic conditions. High efficiencies (>99%) and wider operating maps in terms of lean blow-out, altitude relight, and overall equivalence ratio in comparison with traditional combustors were observed. Results and hardware from those experiments set the baseline for the subsequent and on-going work at the Air Force Research Laboratory.

The most recent AFRL TVC work is represented by Erdmann *et al.* [50], and Blunck *et al.* [51]. A representative image of the test hardware, common between the two studies, is shown in Figure 2.22. Dimensions are given in terms of the combustor inlet height, H. Locations of inlet air flow, cavity air and fuel injection, and cooling flow are highlighted. The test rig operates at pressures ranging from 520-1030 kPa with inlet temperatures in the range of 480-620 K. Equivalence ratios in the combustion cavity range from 0.7 to 1.8. The goal of Blunck *et al.* [51] was to examine variation on the inlet air distribution by way of a channel directing the flow either upward, toward the center, or downward toward the cavity (that latter configuration is shown in Figure 2.22). An emissions rake consisting of nondispersive infrared analyzers, chemiluminescent detectors, and flame-ionization detectors was positioned at the trailing edge of the deswirling vanes. Additionally, high-speed images of the visible cavity radiation were processed using coherent-structure velocimetry to obtain path-averaged estimates of the gas velocities. That latter measurement technique facilitated the finding that directing inlet flow downward toward the cavity enabled the most coherent vortex structure within the cavity. High-strength cavity vortices also resulted in the highest combustion efficiency of those configurations tested; efficiencies greater than 99.5% were observed for $0.8 \leq \phi_{cavity} \leq 1.8$.

An important parameter used to characterize performance of the combustion cavity in this and other TVC studies is the cavity air loading, defined as

$$AL = \frac{\dot{m}_{air}}{V_{cavity}\left(\frac{P_{inlet}}{101.325}\right)^{1.75} e^{T_{inlet}/300}} \tag{54}$$

where $\dot{m}_{air}$ is the air mass flow into the cavity in kg/s, V_{cavity} is the volume of the cavity in m^3, P_{inlet} is the plenum total pressure in kPa, and T_{inlet} is the plenum total temperature in Kelvin. Results from Blunck *et al.* [51] are shown in Figure 2.23, where the configurations in each panel cover different ranges of cavity loading. The contour lines are interpolated from the point measurements. Generally speaking, increased air loading with constant cavity equivalence ratio would allow additional chemical energy to be released within the engine. Such a condition would represent increased levels of both air and fuel mass injection enabling increased energy generation. However, as shown in Figure 2.23, increased loading had the effect of shifting the regions of highest combustion efficiency to lower and narrower ranges of equivalence ratios. In addition, excessive air loading was shown to lead to lower flame stability, poorer emissions profiles, and lower combustion efficiencies due to higher flame strain rates [51]. Essentially, though more energy is generally better, there's only so much mass that can be added to the TVC system before your region of stable operation begins to collapse. These results are highlighted as they present an important potential point of comparison between a TVC and a HGC; cavity air loading is a parameter that could be applied to both cases, and this current work will investigate that possibility.

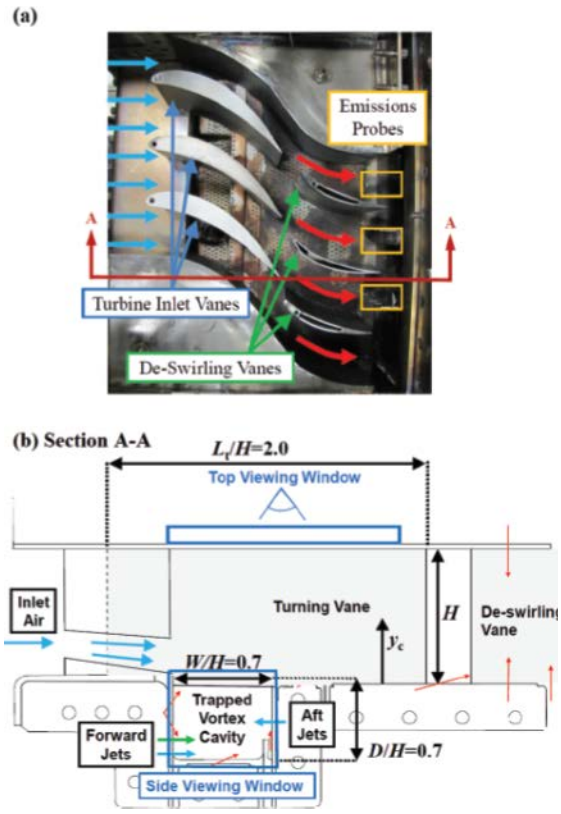

Figure 2.22: Trapped vortex combustion test rig at AFRL; (a) photograph of top view of experimental arrangement, (b) illustration of side view of combustor; air driver jets and inlets are shown in blue, fuel injectors in green, and effusion cooling in red [51]

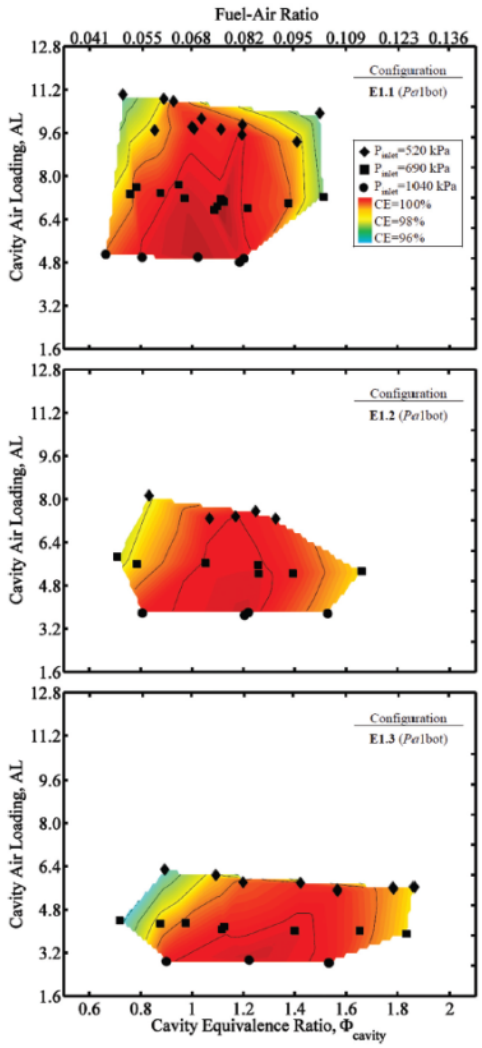

Figure 2.23: Combustion efficiency (colored contours) with varying cavity air loading and equivalence ratio; the three panels correspond to different inlet areas of the driver jets in the cavity [51]

The goal of Erdmann *et al.* [50] was the investigation of variations on the inlet guide vane (IGV) over the combustion cavity, including the addition of a radial vane cavity (RVC) to aid in flow migration. Emissions data were captured as noted in the previous paragraph. Additionally, chemiluminescence images of electronically excited OH radicals (OH*) from the top and side views of the cavity were obtained. Representative results are shown in Figure 2.24, where the three configurations represent no vanes (CDF-2), smooth vanes (CDF-2SV) and vanes with radial cavities (CDF-2RV). While the addition of vanes resulted in lower overall

intensities than the baseline, the converse was true with the addition of vanes with RVCs, as shown by the very bright regions in the lower and middle vane passages. Thus, the RVCs have the effect of increasing the reaction zone length. Furthermore, addition of the smooth vanes caused the exit temperature profile peak to migrate from 70% to 30% of the combustor height. The RVCs, then, produced a profile with the peak nearly exactly at 50% height. Again, there is a strong potential for analogous results to be observed in a HGC configuration, particularly as a sub-objective for this study will be to examine geometric variations to the hybrid vane beneath the combustion cavity to promote radial migration. It is hypothesized that the addition of channels in the vanes, similar to the RVCs below, may have desirable effects on the transport of combustion products from the cavity to the core flow.

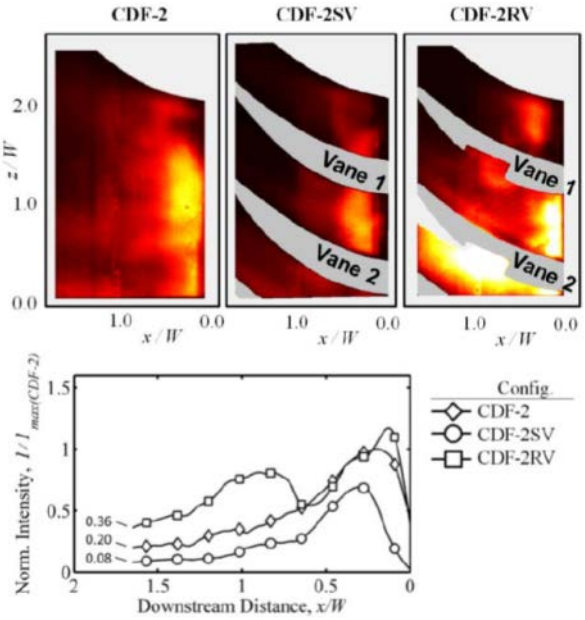

Figure 2.24: Representative top-view chemiluminescence images (top) with normalized downstream intensity profiles (bottom) [50]

2.4.5. High-g Combustion

This section focuses on the recent work pertaining to combustion in fields of high gravitational acceleration. It has been noted that such fields can have profound effects on combustion mechanisms, and it is on that basis that the high-g ultra-compact combustor is

founded. The forthcoming discussion includes the important initial work by George Lewis, followed by a summary of the progress made towards validating his work and incorporating it into a novel compact combustor design.

2.4.5.1. The Bubble Transport Hypothesis

The concept of combustion at "high-g" arose from a set of studies published by Lewis [52], [53], [54]. Lewis filled a six-foot stainless-steel pipe with a fuel-air mixture, and then began rotating the pipe about its centerline to induce varying levels of centrifugal acceleration. After the desired acceleration (expressed in "g's" – that is, as multiples of the earth's gravitational acceleration, $g_0 = 9.81$ m/s) was attained, the mixture in the tube was ignited with a spark plug, and the position of the resulting flame front was tracked with a series of pressure transducers and ionization probes. His results are summarized in Figure 2.25; he observed generally no effect on the flame speed up to accelerations of $500g_0$, followed by an exponential increase, and subsequently a sharp drop-off in the flame speed. He noted different results when using mixtures of hydrogen-air, where the flame speeds in stoichiometric mixtures at atmospheric pressure were unaffected. Lewis developed a theory that he termed "bubble-transport flame spreading," an illustration of which is provided in Figure 2.26. "Bubbles" of flame immersed in a denser fuel-air mixture were acted upon by a buoyant force induced by the centrifugal acceleration, and opposite the direction of that centrifugal force; that is, in the rotating tube, the centrifugal force was directed away from the center of rotation, and the resultant buoyant forces were directed inward. Lewis discussed the theory behind Figure 2.26 as follows:

> *"In an increment of time δT, it moves a distance equal to the product of the time increment multiplied by the velocity S_B, which will be called the "bubble velocity." During the same time, turbulent flame propagation has caused the flame front to advance in all directions by an amount equal to the product of the turbulent*

flame speed S_T multiplied by the same time increment. …The example on the extreme left represents the case where bubble velocity is negligible, as with stoichiometric propane-air combustion in the Earth's gravitational field. The data near the left axis of [Figure 2.25] represent this condition. If a strong centrifugal force field is added, however, the bubble races ahead of the advancing turbulent flame front, as shown in the middle sketch in [Figure 2.26]. To an observer measuring flame propagation, the rate would depend only on centrifugal force intensity. This is the situation represented by the data above about 500 g in [Figure 2.25]. The sketch on the extreme right in [Figure 2.26] represents a case where a centrifugal force field is applied but the turbulent flamespeed still exceeds the bubble velocity."

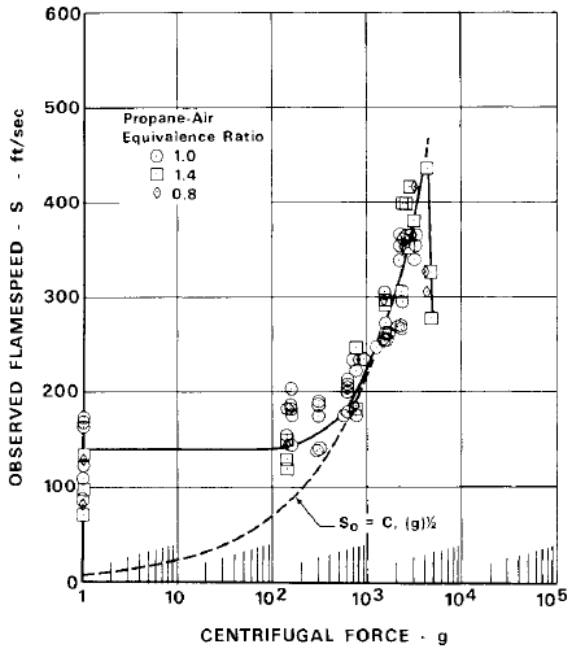

Figure 2.25: Results of Lewis [45] showing propane-air flame speeds increasing with centrifugal acceleration

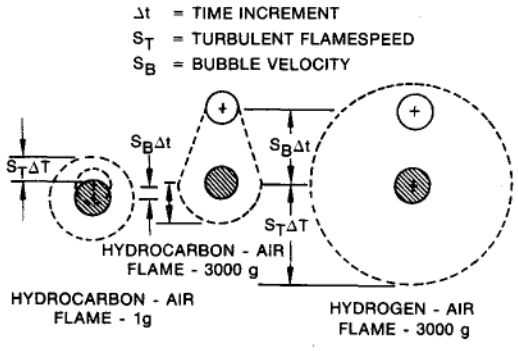

Figure 2.26: Illustration of bubble-transport flame spreading [54]

Lewis explained the sudden drop-off in flame speed as analogous to a condition of extinction behind a flameholder. As the relative velocity around the flameholder (or the

buoyant bubble) exceeded a certain threshold, the flame stretch began to reduce the spreading of the flame until all spreading ceased.

It is important to note, as Lewis emphasizes, that the true flame speed of the reaction front remains unchanged; the progression of the flame front, to an outside observer, is simply the sum of the two sources described above. A relation describing the bubble velocity in the accelerating region was found to be $S_B = 0.38\sqrt{g_0}$. In Lewis *et al.* [54], an experiment was devised in which the buoyant bubble phenomenon was to be demonstrated in subscale and full-scale aircraft augmenter test rigs. They were able to demonstrate efficient combustion via bulk swirl about the longitudinal axis with the traditional augmenter flameholding devices removed. An improvement in total pressure loss was measured, as well as an improvement of about 2% in specific fuel consumption.

Two notable computational studies have since validated the bubble-transport hypothesis. In the work of Zelina *et al.* [55], the experiment of Lewis [53] was validated using a two-dimensional, unsteady, laminar calculation with hydrogen-air. In Figure 2.27, the results clearly demonstrate the buoyant effect in the flame front, confirming the hypothesis. A similar, more recent, and more rigorous study was undertaken by Briones *et al.* [24]. The same experiment of Lewis was modeled in two dimensions using the commercial code Fluent and a transient turbulence model. Premixed propane-air, kerosene-air, and n-Octane-air were considered; representative results are shown in Figure 2.28. Good agreement was found between predicted values of the propane-air flame propagation velocity and those measurements reported in the literature. There were no distinct differences noted between the different fuels in terms of the effect of the centrifugal force on the flame propagation velocity. Significantly, simulations revealed the presence of a pressure wave generated from the ignition process that propagates much faster than the flame front, leading it to reflect from the opposite wall and return to interact with the front in various ways depending on the g-load; that wave generated the corrugation effects observable in Figure 2.28, as well as the region of slightly

elevated temperature at the opposite end of the tube. The conclusion of that work was that the perceived increase in flame speed was not, in fact, due to g-loading but was instead the result of Rayleigh-Taylor instability with thermal expansion. This was a critical finding that influenced later work at AFRL and provided a context for this current work in terms of the complexity of the problem that would be addressed.

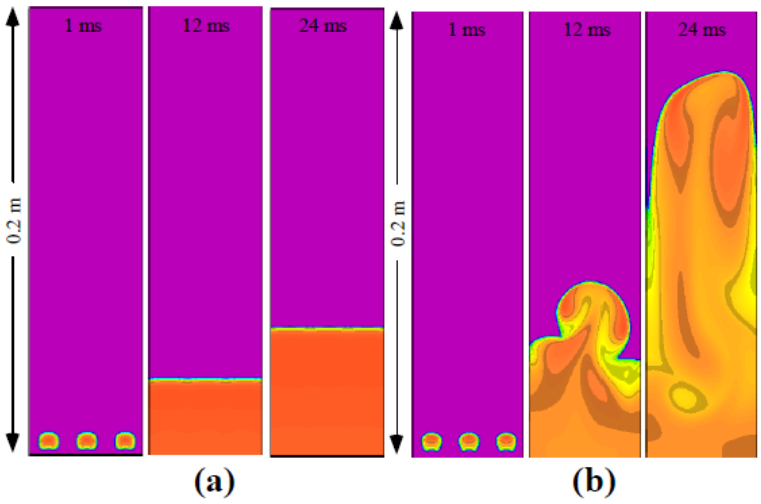

Figure 2.27: Temperature contours showing spreading of a laminar hydrogen-air flame under a gravitational force of (a) 10g and (b) 500g [55]

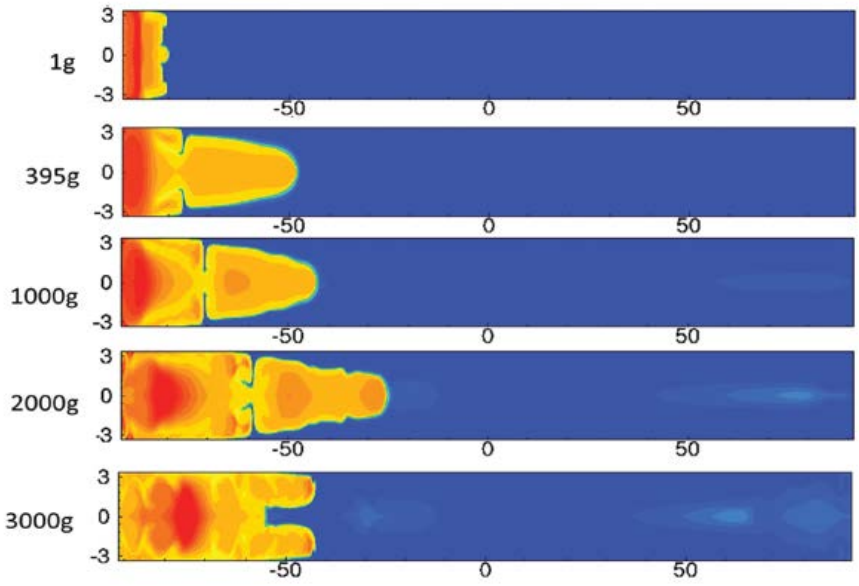

Figure 2.28: Temperature contours showing spreading of a turbulent propane-air flame at t=8 ms under varying gravitational accelerations [24]

2.4.5.2. Comparing High-g and Trapped-Vortex Combustors

In this section, the point of comparison between high-g combustion (HGC) and trapped-vortex combustion (TVC) approaches to compact combustion is emphasized. Section 2.4.4 demonstrated several characteristic facets of the TVC design, and in many ways the system as a whole has analogues to its HGC counterpart. The desire in both cases is to maintain primary combustion apart from the core flow in a recessed cavity encircling the engine outer diameter. Air and fuel injection in the cavity, and their respective influences on the combustion dynamics, are of utmost importance; so too are the mechanisms by which fluid is entrained from the cavity back into the core flow. Circulation is also important to both concepts, but they each differ in the primary axis of rotation. A graphical comparison is made in Figure 2.29 emphasizing the relationships between the respective core and cavity flows. (One important side note is that, from an experimental standpoint, the TVC design allows testing on representative cross-sections, while the HGC concept can only be accurately represented by a full annulus.)

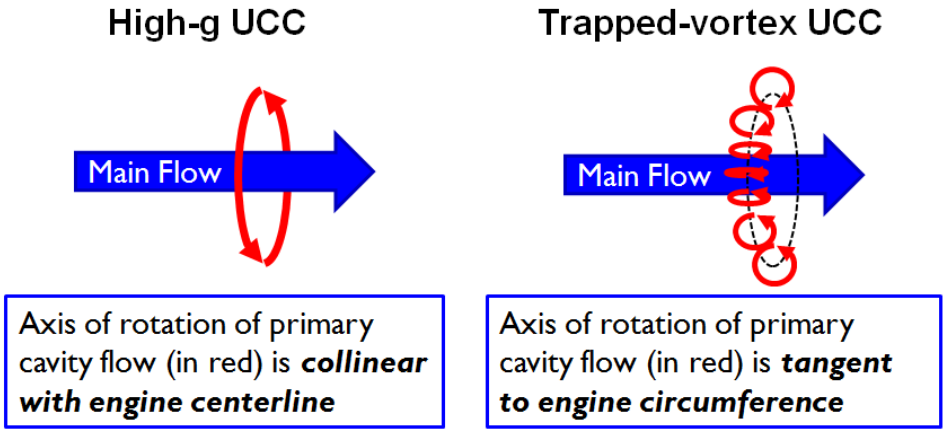

Figure 2.29: Comparison between HGC and TVC concepts

2.4.6. Design, Development, and Evolution of a High-g Combustor

As shown in Figure 2.29, the fundamental architecture of a high-g combustor involves circumferential motion at velocities that imparts centrifugal load upon the circulating fluid. The definition of g-loading in a circumferential cavity is therefore commonly accepted to be in

the form of Equation (55) with tangential velocity in the numerator and the product of the radial coordinate and gravitational constant in the denominator. Thus, cavities of smaller diameter could be expected to produce higher centrifugal loading for the same cavity mass flow rate; conversely, larger diameter cavities would require more mass flow to attain the same loading as a smaller design.

$$g = \frac{v_{tan}^2}{r g_0} \tag{55}$$

All high-g combustion concepts utilize Equation (55) to define their operating regimes in terms of expected centrifugal load on the fluid. However, many other characteristic parameters have been developed along the way. The next sections will introduce a variety of work focused on the design and evaluation of high-g combustion cavities and their performance characteristics.

2.4.6.1. Early Work

The first work aimed at capitalizing on the benefits of high-g combustion in a practical engine design is documented by Yonezawa *et al.* [56]. Therein, a solution was sought to increase combustion loading in order to increase engine thrust-to-weight ratios. To that end, the need was identified for increased combustion efficiency, independent of air-fuel ratio. Primary influence upon the combustion efficiency was asserted to be the parameter defined by Equation (56) as

$$\frac{\tau_m + \tau_c}{\tau_r} \tag{56}$$

where the subscripts *m*, *c*, and *r* represent the fuel-air mixing time, the speed of reaction, and the residence time, respectively, in the primary combustion zone. According to the authors, increases to efficiency, and therefore combustor loading could be attained by (1) accelerating the mixing process, (2) accelerating the reaction process, or (3) increasing the residence time. While paths 1 and 3 had been studied at that point, path 2 was a new avenue enabled by the effects of high g-loading as observed by Lewis [53].

Thus, Yonezawa *et al.* [56] tested an injection concept employing both axial and circumferential deflection angles in order to produce a helical flow pattern within the combustor head. Computational results demonstrated the positive correlation between injector angle and a g-load parameter, thereby validating the high-g quality of the design. An experimental test was then developed with the same geometry. Design point inlet conditions were 5.9 kg/s mass flow at 500 kPa and 500 K. An air-loading parameter was defined as shown in Equation (57) where W_a was the inlet mass flow rate and V_ℓ was the loaded volume.

$$\Omega = \frac{W_a \times 10^9}{P_3^{1.8} \cdot V_\ell \exp(T_3/300)} \tag{57}$$

At the tested conditions, 99.5% efficiency was measured over the loading range $2 \leq \Omega \leq 10$. That was contrasted with a typical combustor loading range at the same efficiencies of $1 \leq \Omega \leq 5$.

In 2009, Lapsa and Dahm [57] tested a step-stabilized flame in three duct configurations as shown in Figure 2.30. The intent was to study the effects on the flame propagation subjected to zero (Configuration **a**), positive (**b**) and negative (**c**) centrifugal loading. The flame propagation was evaluated by observing shadowgraph imagery as shown in Figure 2.31 and chemiluminescence imagery (not shown). The location at which the flame front propagated to the wall opposite the step was used to determine propagation distance. It was found that the propagation length for the straight duct was linearly dependent on the inlet velocity. In the case of positive loading induced by duct **b**, the propagation length was less than the baseline straight configuration at all locations. Furthermore, the propagation length became independent of the inlet velocity as inlet velocity increased. Finally, examination of the blowout limits revealed that there were no differences between configurations **a** and **b** up to a threshold of inlet velocity at about 25 m/s. Beyond that limit, where the straight duct flame experienced blowout, the positive-loaded flame continued to sustain up to about 70 m/s. The threshold

velocity corresponded to a centrifugal acceleration of about $1100g_0$. Thus, the work of Lapsa and Dahm provided a data point in conjunction with Lewis regarding the possible threshold at which the onset of centrifugally-loaded effects could be expected. The theoretical Lapsa criteria was much greater, however, than that observed by Lewis [53] at about $350g_0$.

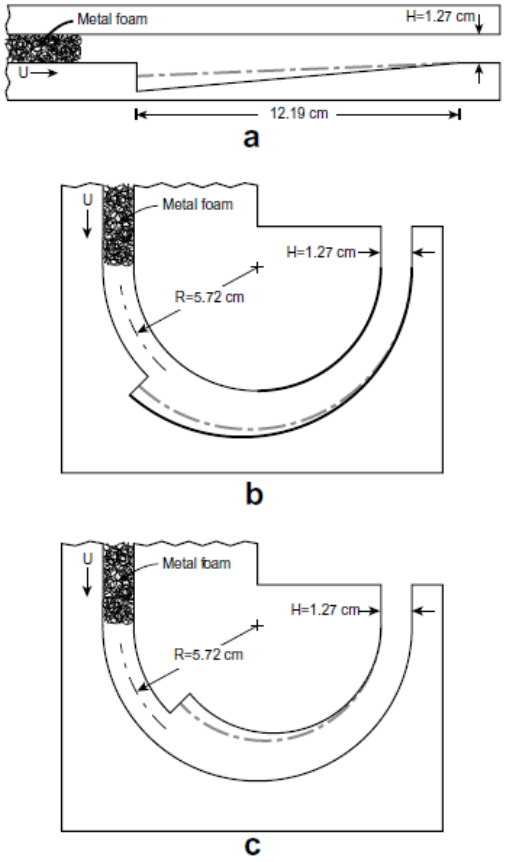

Figure 2.30: Lapsa experiment setup

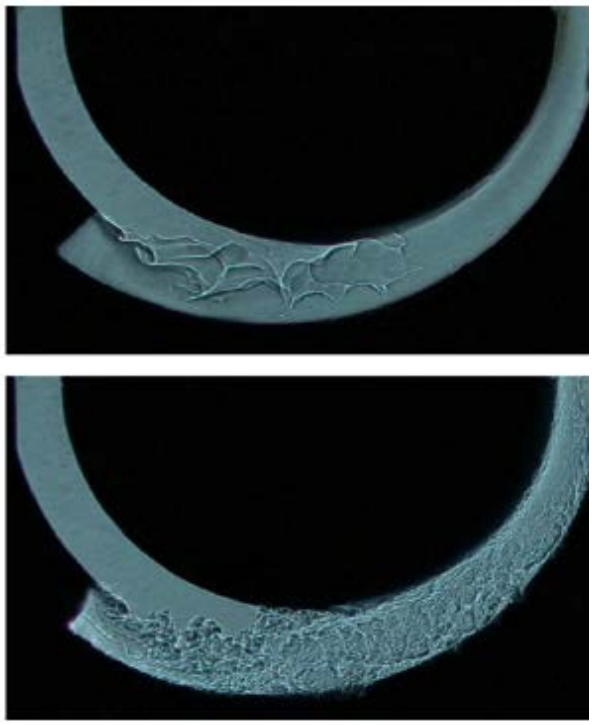

Figure 2.31: Lapsa shadowgraph results at inlet velocities of 4 (top) and 40 (bottom) m/s

2.4.6.2. AFRL Development

Encouraged as well by the analytical results demonstrated by Lewis [53] and Sirignano *et al.* [37], experiments on a compact combustor proof of concept was also initiated by workers at the Air Force Research Laboratory as summarized in reports by Anthenien *et al.* [8], Quaale *et al.* [58], and Zelina *et al.* [59]. One distinct mechanical advantage noted by Anthenien *et al.* [8] was the ability to combine the compressor exit guide vanes and the turbine inlet guide vanes

into a single continuous vane, about which the circumferential combustion cavity would be wrapped; a conceptual illustration is shown in Figure 2.32. The "swirled circumferential cavity" takes the form of an annulus wrapping about the outer diameter of the engine. The red arrows in the figure show (1) the direction of the swirling flow within the cavity, (2) the direction of the bulk core flow, and (3) the notional path that fluid migrating from the circumferential cavity would take as it migrates back into the core flow; the "radial cavities" were integrated into the vanes in order to aid that flow migration. Flow in the cavity is injected in such a way as to induce very high g-loads, thereby reducing the overall required residence time. Finally, as noted in the image, the combustor is designed around the rich-burn quick-quench lean-burn (RQL) process. Initial combustion in the cavity is deliberately rich, with equivalence ratios around 1.3. Fluid migrating from the cavity to the core has sufficient unburned product remaining that combustion continues in the vane assembly, but in a fuel-lean state with equivalence ratios around 0.6. A cutaway of the experimental test rig is shown in Figure 2.33, and details of the fluid injection schemes and flow paths are demonstrated in Figure 2.34 and Figure 2.35.

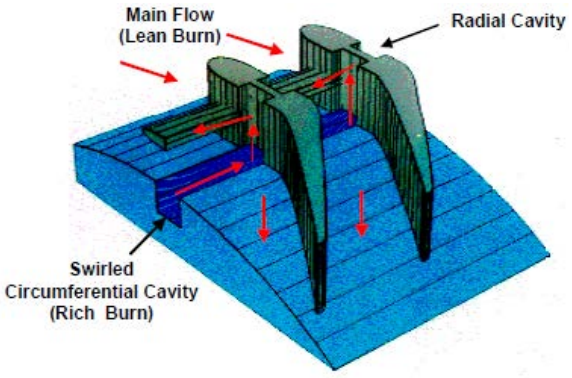

Figure 2.32: High-g combustor concept [8]

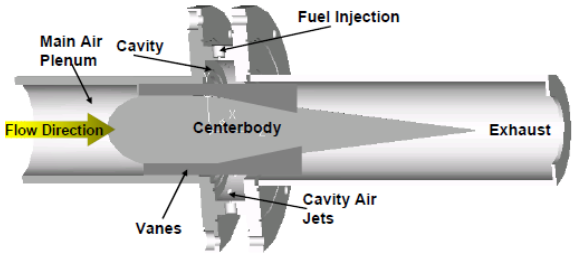

Figure 2.33: High-g combustor experimental setup [10]

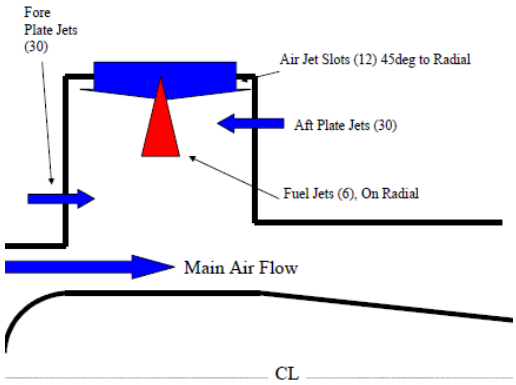

Figure 2.34: High-g combustor experimental setup, side view [8]

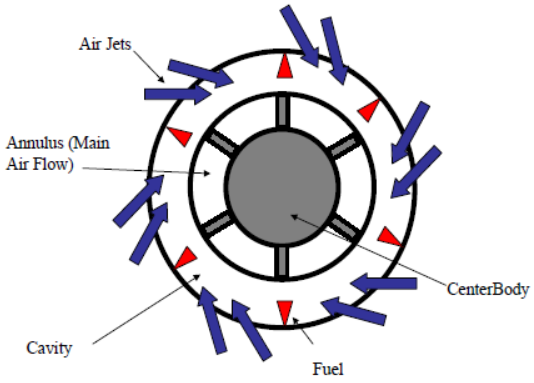

Figure 2.35: High-g combustor experimental setup, front view [8]

The initial work was performed on the test rig without the vanes beneath the cavity. Anthenien *et al.* [8] demonstrated operation of this test rig under a variety of conditions using ethanol and JP-8 fuel; air/fuel injection into the cavity was varied between the "slot jets" shown in Figure 2.34 to "straddle jets" positioned on either side of the fuel injection port. The latter configuration was found to yield efficiencies of 99+%. Cavity loading in these studies was computed using the Longwell parameter, given as follows:

$$\theta = \frac{P^{1.75} V e^{T/300}}{\dot{m}_{Acav}} \tag{58}$$

The variable $\dot{m}_{Acav}$ is the air supplied to the cavity, and P, V, T are in units of Pa, m^3, and K, respectively. Note the similarities to the air loading parameter shown in the trapped vortex combustion (TVC) review in Equation (54). Here, however, the definition has been written such that lower θ is equivalent to higher cavity loading. It was found, as expected, that higher loadings (on the order $\theta = 1 \times 10^7$) were attained with ethanol versus JP-8; importantly, higher cavity loading was found to correspond to higher combustion efficiency, opposite the trend for traditional axial combustors. Qualitative observations of flame length demonstrated about half that of traditional combustors for similar overall equivalence ratios. Quaale *et al.* [58] performed Laser Doppler Velocimetry (LDV) measurements within the combustion cavity. Results indicated velocities corresponding to g-loads as high as $4000 g_0$. Although combustion

efficiency increased with increased g-loading, the concurrently reduced residence times led to increased emissions.

Quaale's results were corroborated with computational fluid dynamics (CFD) analyses performed by Ehret [16]. In Zelina *et al.* [59], additional experimental results are validated against that same CFD with good results. Those experiments examined the overall performance of the test rig in detail, employing three different configurations that varied the total air mass-flow split to the combustion cavity at three levels: 16%, 22%, and 27%. Cavity equivalence ratios ranged from 0.75 to 2.2 using JP-8+100 fuel; tests were performed at atmospheric pressure. Emissions data supported the hypothesis that entrainment from the core air flow into the cavity was present at levels as high as 40%, thereby forcing much of the combustion to take place high in the cavity. It was found that increasing cavity air at constant ϕ had the desirable effect of reducing both NOx and CO emission, whereas in traditional combustors there usually exists a trade between the two. Heat release rates in the cavity were found to be roughly twice that of traditional combustors for similar temperature rise, and efficiency was found to increase with increased cavity air flow at constant loading due to improved mixing.

Additional work on this experimental configuration was documented by Anthenien and Zelina [6], wherein the LDV study of Quaale *et al.* [58] was extended. The combustion regimes of the AFRL UCC test article were analyzed. It was found that turbulent velocity and length scale both decreased with increasing cavity mass injection, resulting in a significant decrease in turbulent Reynolds number. The upper limit of cavity mass flow at which combustion was sustainable was thought to be a result of flow relaminarization and the resulting significant reduction in flame speed. All measured data fell below a Damköhler number (Da) of $Da < 100$, and the bulk of the data fell within the range $1 < Da < 10$. Additionally, all data fell above the Klimov-Williams criterion (that is, the Kolmogorov length scale, l_k, was in all data smaller than

the laminar flame thickness, δ_L). By those criteria, all data fell within the regime of distributed reactions (perturbed flamelets).

Zelina *et al.* [10] extended the prior work to incorporate the vanes beneath the combustion cavity. Though the initial concept as shown in Figure 2.32 shows curved vanes, straight vanes were used in these experiments. A fore-quarter view of the test rig geometry with the vanes included is shown in Figure 2.36, and the vanes themselves are shown in Figure 2.37, detailing the radial vane cavity (RVC) as implemented. Configurations were tested with the RVC and without (flat vanes).

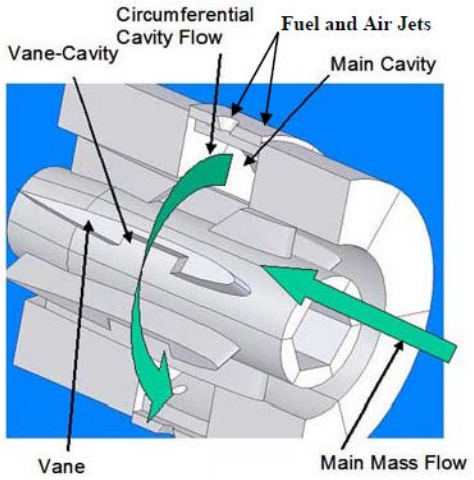

Figure 2.36: High-g combustor experimental geometry, fore-quarter view [10]; image adapted by Drenth [81]

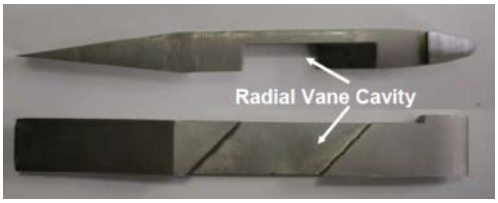

Figure 2.37: High-g combustor experimental setup, side view [10]

Results demonstrated, as expected, that the loading parameter in the UCC was about four times that of traditional combustors. Excellent lean blow-out (LBO) performance was observed; LBO was independent of the loading parameter for the configuration with high cavity air injection and the RVC. This was thought to be due to the RVC entraining the high-velocity cavity air too soon, pulling un-reacted mixture out of the cavity too rapidly. Increasing cavity loading, however, improved mixing due to increased g-loading and bulk circumferential swirl, thereby minimizing the fuel transport from the cavity. Similar trends were noted in combustion efficiency: at low g-loading, excessive migration from the cavity resulted in poor efficiency in

configurations utilizing the RVC. Increased g-load minimized those effects, and efficiencies greater than 95% were realized. Transport of unreacted mixture from the cavity was therefore found to be a strong function of cavity injector air and g-loading. Optimal LBO and emission performance were attained with the configuration utilizing low cavity air-injection with RVCs.

Zelina *et al.* [60] demonstrated operation of the test rig with liquid fuel (JP-8) injection. Combustion efficiency for injectors with zero angle of injection was found to peak at a certain level of cavity g-loading, dependent on cavity equivalence ratio, then decrease. Introducing an injection angle altered that trend. It was found that, at an injection angle of 37 degrees, efficiency remained high at 94+% independent of g-loading, and it increased with increasing cavity equivalence ratio. Equivalence ratios with the highest efficiencies were between 1.2 and 1.4 depending on injector swirl. Based on the bubble transport hypothesis of Lewis, Zelina and coworkers established a relationship to the bubble transport speed such that $S_b \propto (T_b/T_u)(g_0)^{1/2}$ where T_u was taken to be the air inlet temperature and T_b was taken as the adiabatic flame temperature for JP-8/air; the parameter on the right-hand-side of the above equation was termed the "swirl parameter." It was thought that systematic variations in the combustion efficiency could be accounted for by plotting against the swirl parameter, but limited success was attained for baseline (zero-injection-angle) configurations. Examining the non-zero injection angle cases with induced swirl produced slightly better results, leading to the conclusion that the swirl parameter did indeed seem to describe important aspects of the combustor performance.

Zelina *et al.* [55] and Zelina *et al.* [61] further investigated design variations on the same UCC test rig pertaining to fuel injection and vane design at both atmospheric and elevated pressures. One important result of that work, shown in Figure 2.38, was that not only did the UCC have excellent lean blow-out performance, but that a stable flame could be maintained up to g-loads of $8000g_0$. This is corroborated by the data in Lewis [53] that suggest that flame extinction will occur at that same value of $8000g_0$. Furthermore, in light of prior hypothesis

concerning the effect of fuel atomization on the scaling parameter, atomization levels of the injected fuel were increased by reducing the injector flow number, leading to a collapse of the efficiency curves as demonstrated in Figure 2.39. Thus, atomization was indeed a strong driver for system performance; at droplet sizes of ~20 μm, represented by the improved atomization case, the cavity flame speed is dictated only by the cavity reaction temperature and the g-loading. Additional findings from this work included shorter flame lengths (50%) compared to conventional combustors, and the ability of a radial vane cavity (RVC) to improve mixture transport from the cavity into the core flow, thereby improving emissions performance at high cavity equivalence ratios. Finally, a correlation was developed for NOx emissions for the UCC. Previous correlations for conventional combustors did not include a term for residence time. Since experimental results from the UCC demonstrated a marked decrease in residence time as g-loading increased, the final correlation included a term accounting for the cavity g-loading. Estimated values fell within 10% of measured values for pressure levels ranging from one to five atmospheres.

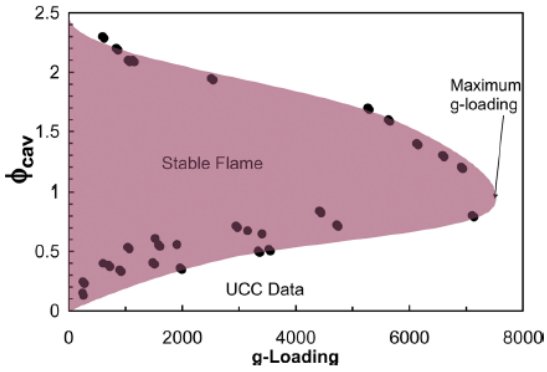

Figure 2.38: AFRL UCC cavity equivalence ratio at blowout as a function of cavity g-loading [55], as adapted in Bohan et al. [2]

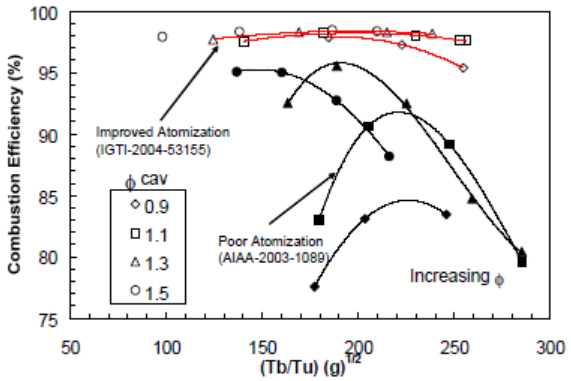

Figure 2.39: Effects of atomization quality on the correlation parameter of high-g combustion [55]

Zelina *et al.* [62] developed the design space by investigating the use of a contoured RVC as compared to the straight-angle RVC in use to that point. The fuel injection scheme was varied as well, allowing different levels of concurrent air flow around the injector nozzle. In

general, the contoured RVC was found to be inferior to the straight-angle due to lack to flameholding ability. Lean blow-out (LBO) performance was substantially better with the straight-angle, and the contoured vane was found to result in higher levels of unburned hydrocarbons (UHC). Thus, the combustion region induced within the straight-angle at high flow rates was found to be fundamental to the effective operation of the UCC. Additionally, it was found that increasing the concurrent injector air flow had a pronounced effect at high cavity equivalence ratios, as it tended to migrate unburned fuel directly into the RVC without first initiating the combustion process within the circumferential cavity. Finally tests at atmospheric pressure were compared to tests in the range of 40 to 60 psi, with the expected results that combustion efficiencies were improved, and LBO performance was not significantly affected.

Mawid *et al.* [21] informed this work through a comprehensive CFD analysis including three different RVC configurations: Configurations one and two represented the angled and contoured steps, respectively, as tested in Zelina *et al.* [62]. Configuration three essentially flipped the orientation of the Zelina's contoured cavity so that the step was forward-facing as opposed to backward-facing. For clarification, the three tested configurations, accompanied by the computational domain, are shown in Figure 2.40. The goals of the study were to investigate effects on flow migration, exit profiles, combustion efficiency, and flame characteristics. The shape of the RVC was found to have profound qualitative and quantitative impacts on the flow characteristics. It was found that Configuration two encouraged higher rates of mixing, but the mixing was accomplished in the shear layer that shed from the aft wall of the circumferential cavity, instead of in the RVC as was desired. Conversely, rates of radial transport were found to be lowest for Configuration two, and similar for Configurations one and three. The comparable performance of Configurations one and three (red and blue lines) can be noted in Figure 2.41; furthermore, the temperature profiles of all three configurations are undesirable by the standards of modern combustor design. Figure 2.42 demonstrates the markedly different

qualities of the flow in each of the three configurations. Configuration one (left-most image) demonstrates a large amount of hot gas along the upper wall of the main flow path, whereas in Configuration three (right-most image) shows the majority of the hot gas against the inner wall. In contrast, Configuration two (center image) shows less uniform flow distribution and more hot-spot attachment at the walls. These results inspired significant work in this study on the impact of guide-vane features such as radial cavities that played prominently in the investigation of Objective 3.

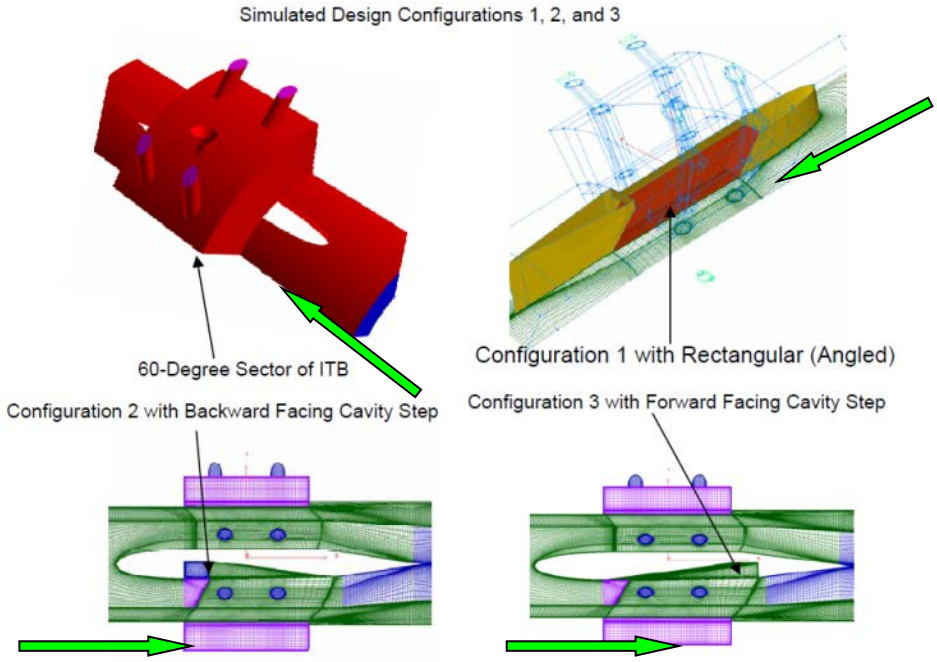

Figure 2.40: Computational configurations evaluated by Mawid et al. [21]; flow direction is indicated by the light green arrow.

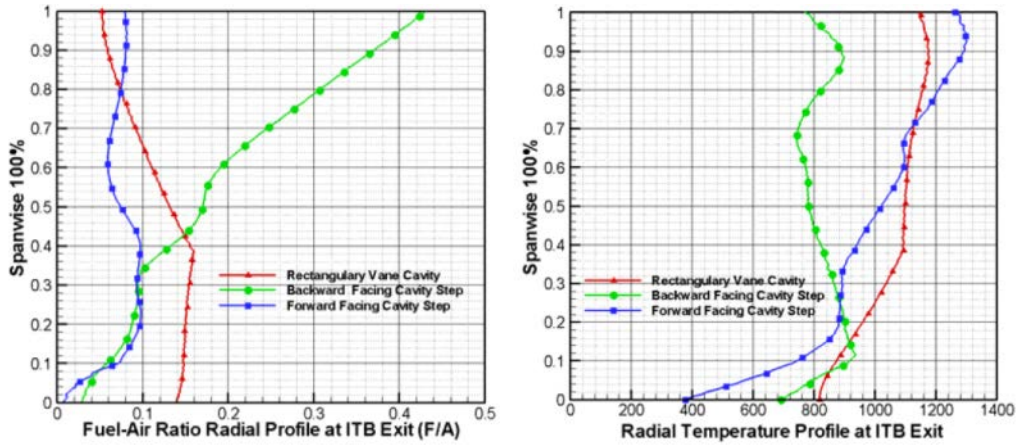

Figure 2.41: Radial exit profiles of fuel-air ratio (left) and temperature (right) [21]

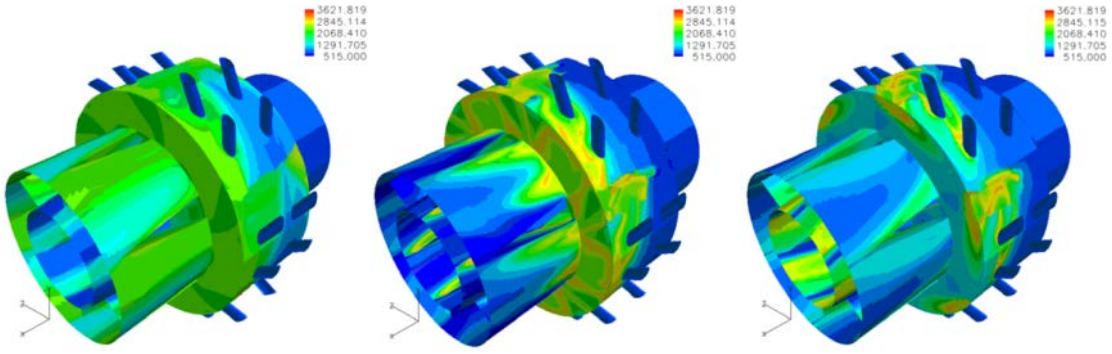

Figure 2.42: Wall temperature contours for configurations one (left), two (middle), and three (right) [21]

Recent computational work by Briones *et al.* [25] represented the first rigorous simulation of the high-g UCC test rig at AFRL. However, prior to discussing the results, some comments must be made regarding the authors' introductory discussion. As it was the first published assessment of the AFRL UCC in nearly a decade, some reflection was offered upon the earlier work by Zelina and colleagues. As posited initially by Briones *et al* [24], it was acknowledged that the g-load may have no effect on the turbulent flame speed. Furthermore, the authors acknowledged upon examination of the Zelina results that claims of shorter flame length were not proven as there were no flame length measurements actually discussed in the relevant publications. The impetus for high-g UCC research was still motivated, however, by the evidence presented by Zelina that higher combustion efficiencies for wider ranges of loading parameter could be obtained in addition to larger static stability and reasonable NO_x emissions.

Briones *et al.* [25] utilized Fluent for their simulations with realizable $k-\varepsilon$ turbulence and partially-premixed flamelet combustion modeling with the JetSurf-1.0 reaction mechanisms. Customized functions were integrated with Fluent in order to account for variability in the mixture molecular viscosity and thermal conductivity, which were by default assumed constant. Inlet conditions reflected the (at the time) ongoing AFRL UCC experimental work with 134 kPa (gauge) inlet pressure and 811 K inlet temperature. The overall mass flow rate for the AFRL rig was 3.4 kg/s. The tested variables were the circumferential cavity (CC) jet injection angles α and the CC-to-core area ratios (where increasing the area ratio directly increased the mass flow ratio $\dot{m}_{cc}/\dot{m}_{core}$). Both factors would impact the g-load in the cavity as they directly influenced the cavity jet injection velocity. Representative temperature contours form the 60° sector model are shown on the left in Figure 2.43 where the core flow direction is from left to right. The outer cold annular region was an air plenum that fed the inner annular region comprising the combustion cavity. Flame length was observed by defining a stoichiometric iso-surface and restricting it to values of the progress variable such that $\tilde{C} \geq 0.5$. Representative results are shown on the right in Figure 2.43. Flame lengths were examined for all cases, but no trends were observed with respect to mass flow split or jet injection angle.

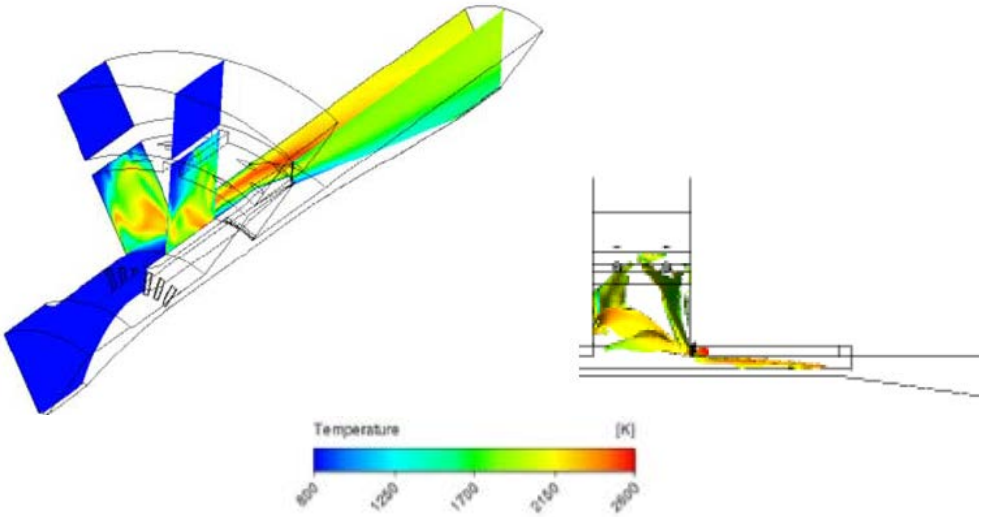

Figure 2.43: Representative temperature contours (left) and flame surface (right) [25]

Area-averaged profiles of g-load in the reacting cavity from Briones *et al.* [25] are shown in Figure 2.44. As expected, the g-loads increased with decreasing α (where the injection angle was defined relative to the outer diameter – so decreased angle meant increased tangential component); g-load also generally increased with increasing $\dot{m}_{cc}/\dot{m}_{core}$. It was noted that high $\dot{m}_{cc}/\dot{m}_{core}$ was more sensitive to changes in α, and the moderate value of α was more sensitive to $\dot{m}_{cc}/\dot{m}_{core}$ than either the low or the high values of α.

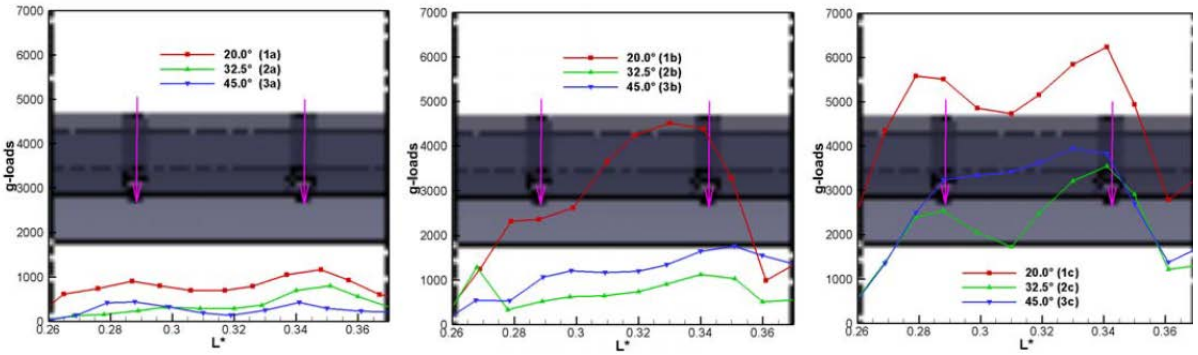

Figure 2.44: Axial area-averaged g-load profiles) [25]

Briones *et al.* [25] acknowledged early in their report that calculation of the turbulent flame speed was problematic. Their solution was to examine the flame speed indirectly by way

of the un-normalized reaction progress variable source term S_C. If turbulent flame speed increased, so too would S_C. Thus, axial area-averaged profiles of S_C are shown in Figure 2.45. The results indicated that S_C was much greater outside the CC, and that therefore more reactions were occurring in the core passage than in the CC; that was consistent with the temperature observations. Comparing the g-load profiles with the S_C profiles suggested that increased g-load led to increased S_C in the CC. The authors asserted, however, that the enhancement of S_C occurred through mean velocity gradients that generated turbulent kinetic energy, and that subsequently wrinkled or corrugated the flame surface area. The low S_C in the CC relative to the core was explained as due to the high stretch rates in the CC. S_C increased as stretch rates diminished in the core. Finally, the exit temperature profiles were examined as shown in Figure 2.46. The best profile was determined to be that at the smallest α and smallest $\dot{m}_{cc}/\dot{m}_{core}$. The profile was found to be more sensitive to α at low $\dot{m}_{cc}/\dot{m}_{core}$ and more sensitive to $\dot{m}_{cc}/\dot{m}_{core}$ at small α.

The Briones [25] results were directly applicable to the research in this document. Many similar techniques were adapted for CFD solutions and analyses, although direct comparisons were not possible due to differences in operating conditions.

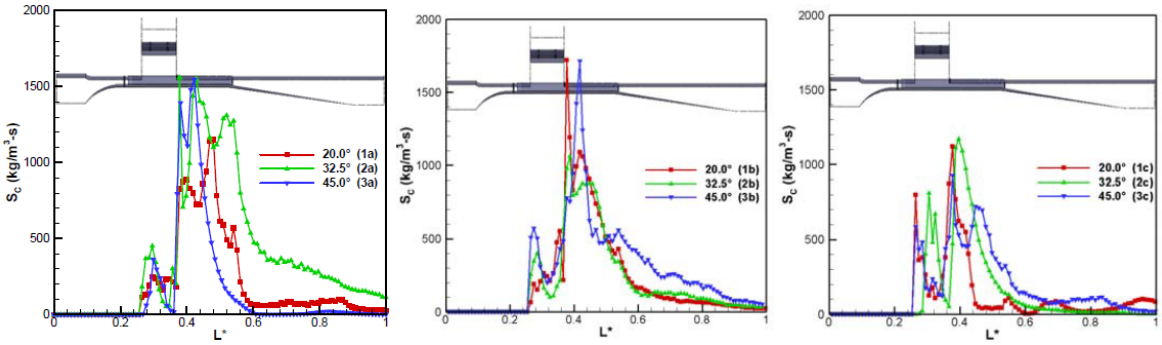

Figure 2.45: Axial area-Sc profiles) [25]

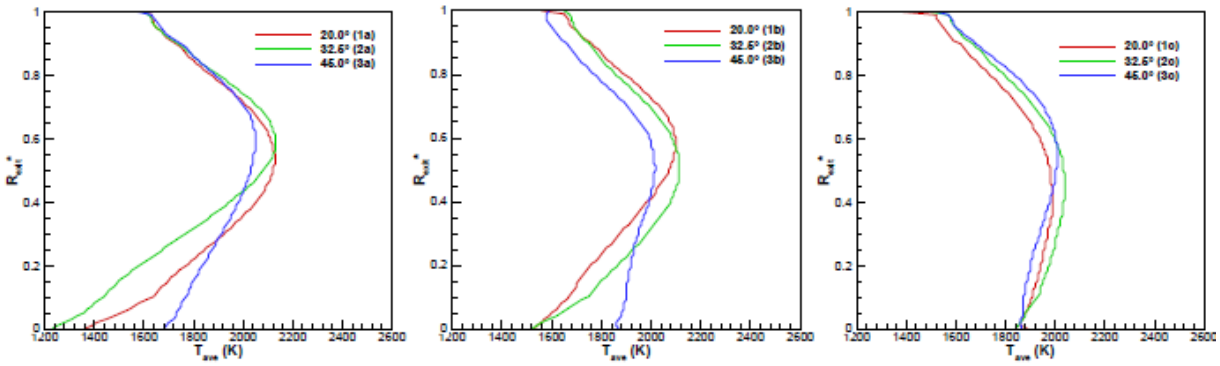

Figure 2.46: Area-averaged radial temperatures just downstream of the IGV trailing edge) [25]

2.4.7. Inter-Turbine Burner Research and Development

The trapped-vortex combustor designs lend themselves well to an inter-turbine burner (ITB) concept. The work of Sirignano, in particular, was focused on the cycle benefits of turbine burning, and subsequently evaluated in great detail the challenges imposed by reactions in the turbine. The trapped-vortex designs of AFRL are very similar, and as such hold similar promise for a turbine-burning application, although their tests were somewhat more generic as to maintain applicability to both a main burner and turbine burner role. A high-g design is equally applicable to an ITB cycle, and this section will summarize the body of literature that has begun to form around that specific research niche.

The appeal of turbine burning has been highlighted by Sirignano in Figure 2.16. Until the advent of compact combustion concepts, however, practical application of a reheat cycle between a turbine stage was untenable for aircraft engines due to the additional length and weight requirements of the added combustor. However, reheat cycles, also called sequential combustion, are already seeing widespread use in land-based gas turbine generators. Beginning in 1995, ALSTOM Power in Switzerland has documented development and deployment of two models of sequential combustion gas turbine engines, the GT24 and the GT26. More recent results are discussed in Hiddeman and Marx [63] and Ciani [64]. A diagram of the engine configuration is shown in Figure 2.47, where the flow is from right to left.

The EV combustor is an annular dry low NOx burner that accomplishes initial heating of the compressed air using roughly 50% of the total fuel at base load. The heated air passed through a high-pressure turbine stage after which the remaining fuel and additional cooling air are injected into the SEV burner to complete the heating up to the maximum turbine inlet temperature; a four-stage low-pressure turbine follows. Hiddeman and Marx [63] note that the vitiated environment in the SEV burner is advantageous from an emissions standpoint because there is less oxygen available for NOx formation. Additionally, less heating is required to reach the required flame temperature.

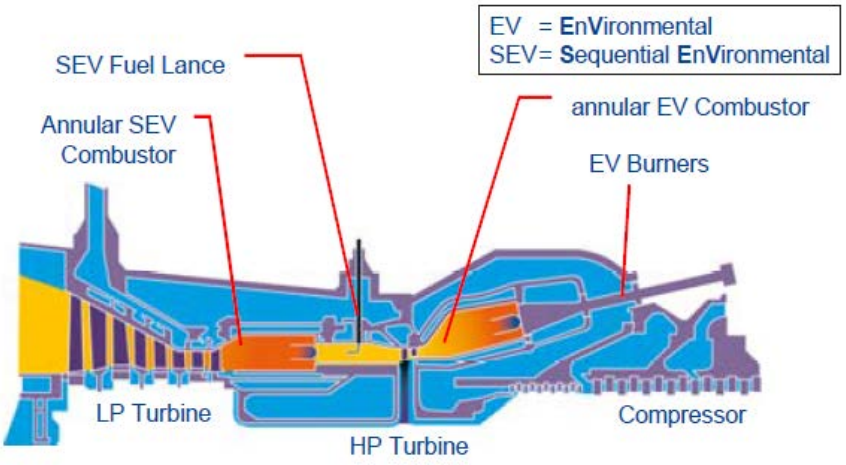

Figure 2.47: ALSTOM GT24/GT26 sequential combustor [63]

In 1998 Vogeler [65] took note of the ALSTOM (then ABB Power Generation) design and proposed application of the sequential combustion cycle (SCC) to aircraft gas turbine engines. Conventional analysis suggested, as it still does, that increased bypass ratio would yield lower specific fuel consumption; however, it came at the expense of decreased core mass flow. A SCC, however, would allow realization of increased cycle energy for the same mass flow (or the same energy at reduced mass flow) without changing the requirement for the maximum turbine inlet temperature. Cycle analysis revealed that the SCC concept, using only a single-spool, delivered 24% higher specific thrust that the baseline dual-spool turbofan. It was shown that applying

the SCC to a dual-spool concept was actually disadvantageous; insufficient energy is released in the first combustor to build appropriate pressure for an economical expansion across the second stage turbine. Liew *et al.* [66] conducted a performance-cycle (or off-design) analysis to contrast with works of Sirignano [38] and Vogeler [65] that consisted of parametric (on-design) analyses. Liew *et al.* [66] examined a dual-spool separate-exhaust turbofan with an ITB at full and partial throttle settings for sea-level and high-altitude (10 km) conditions. A full notional mission analysis was also conducted including simulated combat maneuvers such as high-g turns and supersonic dash. The overall analysis revealed that the ITB engine had increased performance at full throttle, higher thrust at lower specific fuel consumption in partial-throttle, and an estimated 2.6% fuel savings over the notional mission components.

Zelina *et al.* [67] explored the AFRL high-g combustor concept as applied to a reheat cycle. The AFRL UCC was operated in vitiated flow to simulate exhaust from a high pressure turbine stage. Vitiation ranged from 12-20% oxygen levels, and resultant combustion efficiencies ranged between 97-99%. Importantly, the superior lean blowout performance of the high-g combustion concept proved essential, as the low temperature rise across the ITB leads to operation at near-lean-blowout limits of conventional combustors.

Spytek [68] incorporated an ITB into a fully assembled operational gas turbine engine. A 1334 N dual spool turbojet with a conventional (reverse-flow) main combustor was augmented with an ITB between the first and second stage turbine stages. The ITB utilized the high-g combustor concept as demonstrated by Zelina [62]. Mass flow to the ITB cavity was controlled dynamically, and the entrainment of the cavity combustion products back into the core flow was accomplished with a proprietary device. The ITB was fit to an axial booster. An optimal mass flow fraction for the cavity air was found to be 23% with stable operation between equivalence ratios of 0.6 and 0.7. ITB performance yielded up to 22% increased power on-demand with an ITB temperature rise of 590 K. Additional information on ITB work at the Air Force Institute of Technology is presented in Section 2.5.4.

2.5. The AFIT Test Program

Research at the Air Force Institute of Technology (AFIT) began as collaborative efforts with AFRL utilizing the same test hardware. Subsequently, AFIT students designed and fabricated a series of test rigs for use exclusively in their Combustion Optimization Analysis and Laser (COAL) laboratory, with which this current study is primarily concerned. This section highlights that work and describes how the current research objectives are founded therein.

2.5.1. Early Work and AFRL Collaboration

The first collaboration between AFIT and AFRL produced the work in Quaale *et al.* [58], as already cited, wherein Laser Doppler Velocimetry (LDV) measurements of the UCC cavity were accomplished and compared to a CFD solution. In addition, Quaale [69] developed an analytic model of the UCC flow through direct application of the Navier-Stokes Equations, including the Zeldovich formulation for coupling the species and energy relations. One issue he noted was that the combustion process in the UCC could not be accurately described as a diffusion flame since the cavity is a partially-premixed region. Thus, the Zeldovich formulation was rendered ineffective; alternative approaches were recommended for future work.

Armstrong [70] performed chemiluminescence measurements on the AFRL test rig, including the detection of C_2*, CH*, and OH* radicals as well as near-infrared blackbody radiation. Fuel droplet sizes were also measured with a laser diffraction analyzer; results were collected at varying equivalence ratios and g-loads. He observed the buoyant effects of the high g-loads as the unreacted fuel and air mixture tended to remain at the outer diameter of the cavity.

Greenwood *et al.* [71] implemented a computational fluid dynamics (CFD) model for the AFRL test hardware. Initial goals were to compare to traditional combustors in terms of combustion efficiency, emissions, and pressure characteristics. The flow solution was obtained

with Fluent using the $k-\varepsilon$ turbulence model and non-premixed equilibrium combustion. Emissions of CO, CO_2, and O_2 were found to compare well with experiment, while emissions of NO_x did not. This was due to the limitations of the equilibrium combustion model in predicting prompt NO_x and fuel NO_x emissions. (Modern approaches in Fluent include the use of a discrete NO_x model, ANSYS [72]). Variations to the baseline geometry were subsequently investigated. It was thought that increasing the exit area would reduce the back pressure while maintaining low emissions; instead, computations demonstrated minimal difference in pressure drop with significantly higher emissions. The diameter of the cavity air inlet jets was also increased, thereby decreasing the velocity and decreasing the overall angular momentum in the combustion cavity; results were a slight pressure drop with a significant emissions increase. The conclusion was that sufficient air velocity in the cavity must be maintained. Greenwood [17] then extended the above results by investigating the effects of decreasing the cavity length and introducing curved vane geometry. The combination of decreased cavity length and the curved vane resulted in decreased pressure drop with near constant estimates of efficiency and emissions as compared to the AFRL straight-vane rig of Zelina [10].

Anisko *et al.* [73] performed additional analysis on the model of Greenwood *el al.* [71]. Motivations for that investigation included examination of the vortex-shedding behavior from the combustion cavity, as well as optimization of mass extraction from the cavity into the core flow. To further investigate the potential benefits of reduced cavity size as noted in Greenwood [17], three cases with different cavity volumes (i.e. – different axial widths) were examined, as were two different flow rates ("low" and "high"). The axial lengths of each of the three cavities were 25.4, 38.1, and 46.6 mm, respectively; the height of the cavity was held constant at 27.5 mm, thereby yielding cavity aspect ratios (L/H) of 0.92, 1.4, and 1.7. The kerosene-fuel injection was held constant such that its jet velocity was 31 m/s. The flow solution was again obtained with Fluent using the $k-\varepsilon$ turbulence model and non-premixed equilibrium combustion. Estimates of circumferential velocity matched those of the computational work in Quaale *et al.*

[58]. Agreement between the periodic and full-annular models was good in the low-flow case, but less so in the high-flow case. Similarly, agreement between the simulations and experimental results was better in the low-flow case than in the high-flow. This was due to the increased challenge of resolving the higher Reynolds number flow with the chosen modeling scheme. Decreasing the cavity volume was found to increase pressure loss slightly (about 0.7%), but it also had the desirable effect of improving mixing, cavity flow uniformity, and cavity flow migration, thereby leading to improvements in exit pattern factor and emissions. The periodic computational geometry is shown in Figure 2.48. Calculations at an axial plane that intersects the center of the combustion cavity are shown in Figure 2.49, demonstrating the combination of circumferential and radial motion as well as the temperature stratification. Calculations are shown in Figure 2.50 at the circumferential plane as is highlighted by the red boxed region in Figure 2.48. The velocity vectors indicate that the smaller cavities encourage stronger flow migration out of the cavity and into the radial vane cavity (RVC).

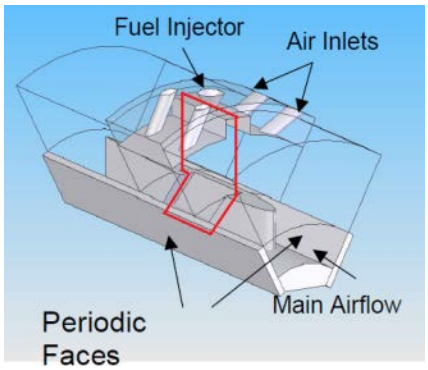

Figure 2.48: Computational geometry of Anisko et al. [73] with contour plane outlined in red

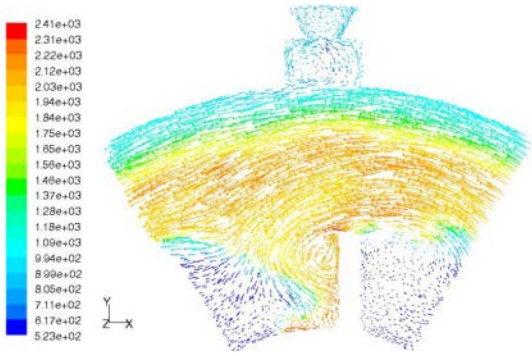

Figure 2.49: Results of Anisko et al. [73] showing velocity vectors colored by temperature with the medium cavity width

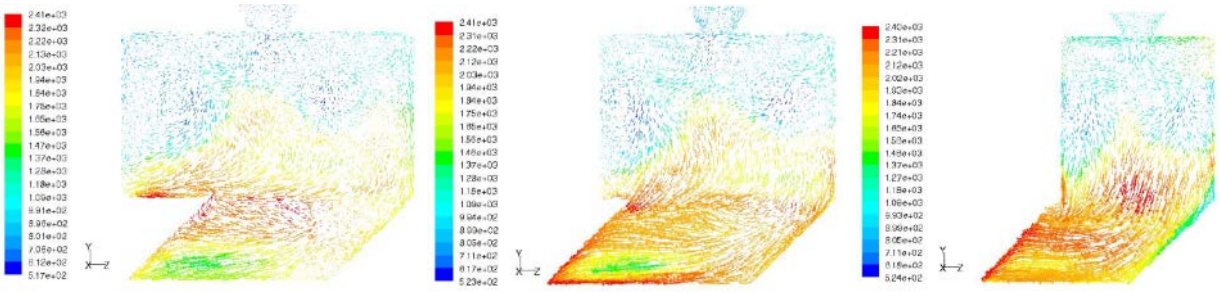

Figure 2.50: Results of Anisko et al. [73] showing velocity vectors colored by temperature for the case of the large cavity (left), medium cavity (middle), and small cavity (right)

Further observations on the previous results are warranted. Although the flow migration is improved, the flame front remains fairly consistent. It should be noted that the simulations show that only the bottom third of the cavity actually contains the flame; it seems that the bulk of the combustion is actually taking place in the RVC in all cases. Thus, as observed in Anisko *et al.* [73], an undesirable consequence of the strong flow migration out of the narrow cavity is a marked increase in the levels of unburned hydrocarbons (UHC) at the exit plane. Additionally, the position of the fuel injector was held constant with respect to the cavity sidewalls, but that meant it shifted with respect to the RVC. That is, in the left-most image of Figure 2.50 the fuel is being injected at an axial location corresponding to roughly 80% of the RVC axial length; conversely, the fuel injection location in the right-most image is just about at 50% of the RVC length. Fuel injection location will certainly impact where the flame exists, but it is unclear from these results whether it is the location with respect to the cavity volume or the location with respect to the entrainment device (in this case the RVC) that has a larger influence. Finally, no certain conclusions may be drawn about the relative proportions of radial and circumferential travel required for mixture and ignition as compared between the different cavity sizes. The implication, however, is that cavities that are taller than they are wide are optimal for flow migration.

In addition to the geometric variations described above, Anisko [18] also investigated the effect of additional curvature on the aft edge of the radial vane, higher air injection angles, and

increased radial vane height. The increased air injection angles were hypothesized to keep more of the reactions in the cavity and thereby alleviate the high levels of UHC previously noted. That hypothesis proved correct, with higher injection angles resulting in lower levels of UHC, CO, and NO_x. However, increased pressure loss resulted from increased drag due to higher cavity velocities. The trailing edge of the straight vanes was rounded to improve aerodynamic performance. It was found that minimal effects upon the parameters of the study resulted, with the exception of pressure loss where reductions up to 25% were observed. Increasing the vane height by roughly two times, while holding mass flux and cavity loading constant, resulted in a pattern factor increase of 70% due to deficiencies in mass transport from the cavity. Pollutant emissions were about 50% higher as well.

Anderson *et al.* [74] introduced bulk swirl into the AFRL UCC test rig. A set of "pre-swirler" vanes were incorporated to simulate the upstream compressor exit flow, and the primary vanes were curved to represent the turbine inlet guide vanes. The revised geometry is shown in Figure 2.51. In the right image, the "normal" operating mode is indicated, with the cavity flow induced in the counter-clockwise (looking from the back) direction. The primary goal of Anderson *et al.* [74] was to evaluate whether clockwise ("reverse") cavity flow or counter-clockwise ("normal") cavity flow yielded the best performance with the given vane curvature. Radtke [75] provided a supporting view of the vane arrangement more clearly explaining the flow nomenclature as shown in Figure 2.52. Experiments were conducted using both JP-8 and Fischer-Tropsch fuels. First, it was noted that all curved-vane configurations demonstrated inferior lean blow-out performance when compared to the earlier straight-vane tests. It was noted as well that there were no significant differences in performance between the two fuels tested. Little distinction was evident between the different cavity flow rotation directions in terms of emissions or efficiency. Qualitatively, normal cavity flow rotation induced a broader flame in both the cavity and the radial vane cavity (RVC). Conversely, the reverse flow rotation created large regions of entrainment from the core flow into the cavity with resultant

recirculation in the same regions. That had the effect of pushing the flame almost entirely into the RVC, thereby degrading lean stability performance. In addition to supporting the above work, Radtke [75] performed Rayleigh loss calculations and concluded that, while the heat addition process conformed to Rayleigh theory, the pressure losses deviated. That was thought to be a consequence of the pressure-drop-driven velocity in the test rig, versus the compressor-driven velocity in a normal engine.

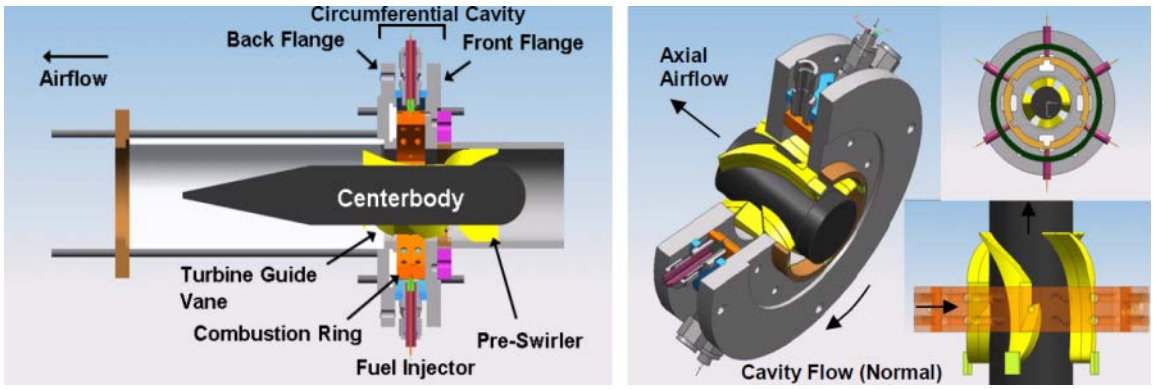

Figure 2.51: Curved-vane UCC test rig from Anderson et al. [74]

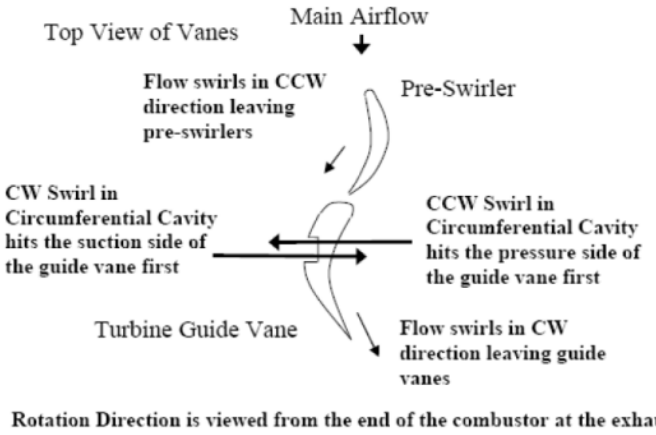

Figure 2.52: Curved-vane flow depiction in Anderson et al. [74] as presented in Radtke [75]

The curved vane geometry was more extensively examined in the computational work of Thornburg *et al.* [22], and the results therein are probably the closest to what may be expected of the numerical studies with which this current document shall be occupied. A full-annular hybrid topology was generated from the AFRL UCC with the pre-swirler and curved vanes.

FLUENT was used for the flow solution, and liquid Jet-A was injected. Multiple combustion zones were noted in the circumferential cavity due to the penetration of the air injection jets. Migration in both the shear layer and the RVC was observed and was deemed satisfactory. A comparison of the radial exit temperature profiles of the curved-vane design versus the straight-vane analysis as performed by Mawid *et al.* [20], and as shown in Figure 2.53, demonstrates considerably improved performance in terms of flow uniformity and peak temperature.

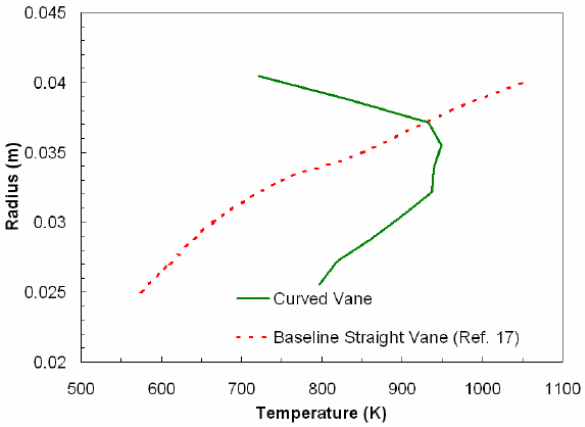

Figure 2.53: Radial exit temperature profile comparison between straight and curved vane UCC designs [22] ("Ref 17" = [20])

2.5.2. Sectional Model Design, Development, and Test

The research of Moenter [19] represents the first independent development effort at AFIT. Based in large part on the work of Greenwood [17] and Anisko [18], a primary objective was to design an experimental apparatus that would enable laser diagnostics into the restrictive vane passageways. Curved-cavity (finite radius) and straight-cavity (infinite radius) sector designs were proposed and modeled. The infinite-radius straight-cavity design would preclude observation of any g-loading effects; the intent, however, was to focus on cavity-vane interactions and the induced trapped-vortex effects that might be present in the flow. The three-dimensional (3D) AFRL geometry was also modeled for additional validation. Comparisons of the standard $k-\varepsilon$ turbulence model and the RNG $k-\varepsilon$ model in Fluent were made; the latter was found to more accurately resolve the detailed turbulent flow structures.

Subsequently, simulations of the sector models were found to be in reasonable agreement with the full axisymmetric model, albeit with decreased turbulence intensity.

Concurrent with the above work, Dittman [76] and Anderson [77] led the design and construction of what has become AFIT's UCC test facility. The product was a highly capable atmospheric test facility incorporating a variety of diagnostic equipment, from emissions analyzers to laser systems such as Coherent Anti-Stokes Raman Scattering (CARS) and Planar Laser-Induced Fluorescence (PLIF). Anderson [77] also utilized the CFD models of Moenter [19] to create practical assemblies for fabrication and installation in the new lab space. The resulting straight and curved designs are shown in Figure 2.54. Koether [78] completed installation of the straight test section with all flow lines and instrumentation in place, tested, and validated. Additionally, he used a Hencken burner to validate performance of the lab's OH PLIF system, resulting in some error in the fuel-rich regime, surmised to be a result of the measurement location relative to the top of the flame.

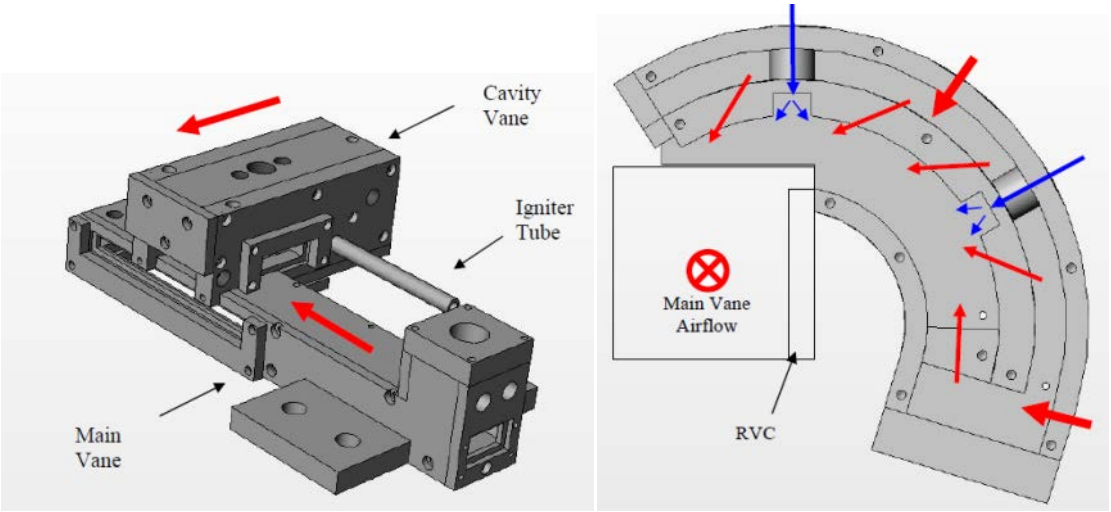

Figure 2.54: AFIT UCC test sections; infinite-radius (left) and finite-radius (right). Air flow is in red, fuel flow in blue [77]

Lakusta [79] and Hankins [80] completed the OH-PLIF calibration with the Hencken burner, and then reassembled the optics and diagnostics to begin measurements on the straight-cavity test rig. Lakusta executed the first OH-PLIF tests on the straight-sectional rig

yielding estimates of flame location. Improved vortex trapping was noted at lower overall equivalence ratios. The initial operating map of the test rig was established. Experimental results compared poorly to the corresponding CFD of Moenter [19], thought to be the result of operational deficiencies including liquid fuel pooling during test runs. Furthermore, representative efficiency calculations were insufficient; fuel exiting the cavity exhaust was treated as UHC, whereas in a true UCC those reactants would circulate continuously until they were eventually burned or drawn into the core. Qualitatively, Hankins [80] observed the presence of a "dual-vortex" structure in the main flow exhaust, indicating the presence of core-to-cavity migration that might induce large regions of recirculating cold flow. Lakusta [79] verified those results with high-speed imagery, and correlated the presence of the dual-vortex behavior with a drop in the presence of OH in the main flow.

Drenth [81] executed further on-line OH-PLIF analysis of the straight test rig with results comparable to previous students. Two-line PLIF was also performed on both the straight and curved sectional models; cavity exit temperature trends with equivalence ratio were similar for the two models, though a systematic bias was present due to the comparatively smaller cavity exit area of the curved rig. In a study of the main flow exit gases, dual-vortex behavior was again noted for the straight model, but was not observed in the curved model. Evidence of more uniform mixing was noted in the curved model as well.

Combustion of synthetic fuel was compared to the JP-8 results from Hankins [80] using the straight model; both fuels produced low emissions at high combustion efficiency, but the synthetic fuel performed better than the JP-8 in all respects. Comparisons between the curved and straight models were made using propane as fuel (to preclude the fuel-pooling issues in the curved rig) with the result that the emissions and efficiency performance of the curved model were inferior to the straight model. Concurrently, Thomas [82] performed 10 Hz PIV measurements of both models (as an aside, the PIV seeding from these tests was found to interfere with the PLIF testing by way of additional scatter induced by residual seeds, in spite

of cleanup efforts between tests). Overall turbulence intensities of 15% and 21% of the main channel velocity were noted for the straight and curved test rigs, respectively. The radial vane cavity (RVC) was observed to be effective at generating flow rotation that increased with streamwise velocity. Boundary layer effects were noted to be significant on the wall opposite the RVC, but insignificant near the RVC. An unexpected negative correlation between turbulence intensity and mass flow rate was noted for the curved model, but was not present in the straight model.

LeBay *et al.* [83] encapsulated some of the results of Thomas [82] with supporting PLIF measurements at the exit plane. Flame locations were qualitatively demonstrated. Flame speeds were calculated; the ratio of flame speeds in the curved model versus the straight model was roughly 2:1, and therefore the impact of the increased g-loading on the observed flame speed was verified. Temporal variations of the OH flame location revealed the effectiveness of the RVC in aiding flow migration and holding a steady flame. Shedding vortices were noted in the straight model; such were the undesirable consequences of operation without g-loading in the circumferential cavity. In LeBay *et al.* [84], the earlier 10 Hz PIV measurements, having been found inadequate to fully capture the flow unsteadiness, was supplemented with a series of time-resolved PIV experiments utilizing a continuous-wave (CW) laser on the AFIT curved UCC model. Velocity and vorticity analyses were completed. Regions of high positive vorticity prevailed near the RVC surface, while regions of negative vorticity were noted near the wall opposite the RVC.

As documented by LeBay *et al.* [85], experiments were conducted using 2-line PLIF and high-speed video (HSV) experiments at varying g-loads and with varying RVC heights with the curved model. Figure 2.55 is included for clarification; the various air and fuel flow paths are highlighted by the arrows, and the viewing regions for the PLIF and HSV tests are denoted by the dark-green and light-green rectangles, respectively. In other words: the PLIF images provided a "bottom-up-view" of the cavity/vane interaction, while the HSV images provided a

"side-view" of the cavity-core interaction region. Note: the PLIF measurement location was physically at the noted plane, while the HSV view was "through" its respective plane. Representative HSV imagery is shown in Figure 2.56 for the baseline case. Overall temporal variation of the cavity-core flow interface is shown to be substantial. Conversely, the "flame migration angle" – the angle that the flame front makes with the horizontal core-flow direction – was temporally insensitive. It did, however, vary with cavity-to-core mass flow ratio, which was defined as the ratio $\dot{m}_{cavity}/\dot{m}_{core}$. The baseline case was considered as a mass flow ratio of 0.2.

Figure 2.57 demonstrates the effects on flame migration at various points with respect to the baseline. With excess core flow (top and middle-top images), the RVC contained little or no flame. The baseline (middle-bottom image) shows the flame filling the RVC; decreased core flow beyond the baseline (bottom image) resulted in the flame overwhelming the RVC and encroaching on the forward surfaces of the radial vane. PLIF temperature measurements verified past results wherein the highest temperatures were noted on the wall opposite the radial vane. The implications were that, in a full annular configuration, peak temperature loading could be expected on the pressure sides of the radial vanes. Radial vane height (measured as the distance of the top surface of the vane from the circumferential cavity) was found to influence the flow migration in a similar manner as the mass flow ratio, though to a lesser degree. Finally, cases with higher g-loading demonstrated greater flame distributions and correspondingly higher temperatures, although the flame injection angle was unaffected.

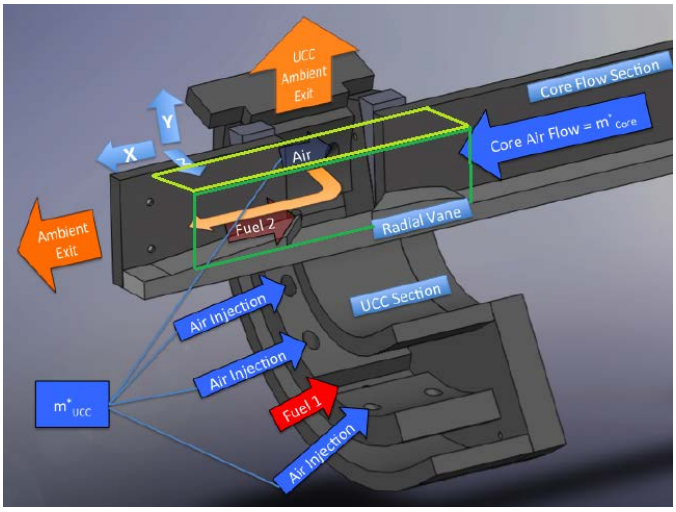

Figure 2.55: AFIT UCC curved test model with flow paths highlighted; HSV viewing section is noted by the light-green rectangle, and PLIF viewing section is noted by the dark-green rectangle; adapted from [86]

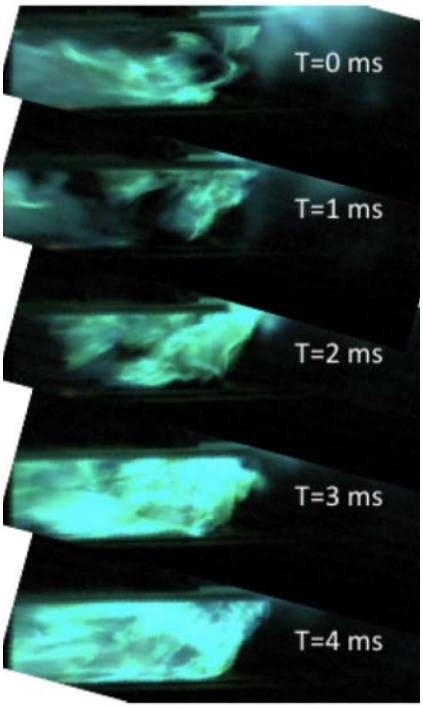

Figure 2.56: HSV image time-sequence; flow is from right to left [85]

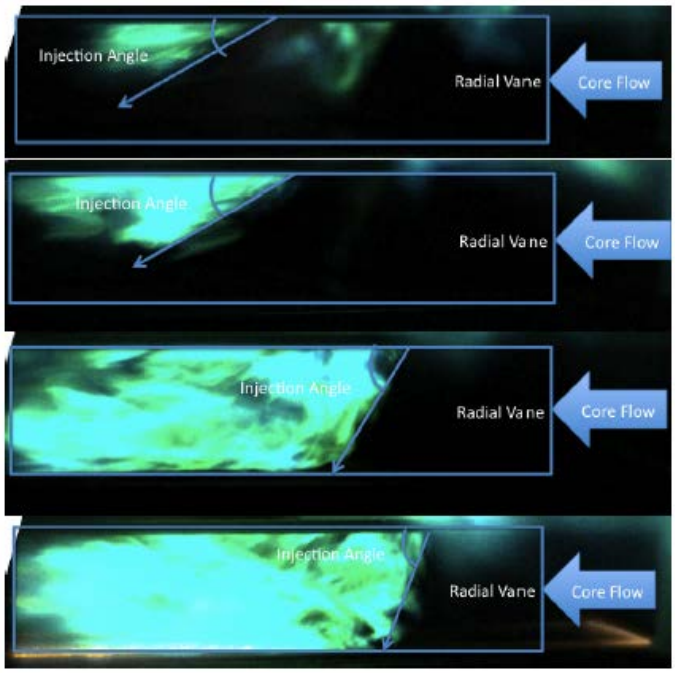

Figure 2.57: HSV images at 1000g and MFR = 0.05 (top), 0.1, 0.2, and 0.3 (bottom) [85]

The doctoral work of LeBay [86] supplemented the previous work through comparison to the straight UCC model. Improved flame migration was demonstrated in the curved model versus the straight model. An analytical model was also developed from which the rate of mass

flow migrating out of the circumferential cavity was determined to be a function of the fluid and geometric properties of the cavity and core flows. The dual-vortex behavior noted earlier was also analyzed, but re-termed as a "v-shaped flame." Whereas prior results demonstrated that the v-shaped flame existed only at the cavity exit of the straight test model, LeBay was able to demonstrate that it existed as well at the exit of the curved model though it was less pronounced. Notably, a previous version of the curved test rig included a circumferential cavity exit area that was much smaller than the straight test rig. The setup of LeBay corrected that issue so that the two models had comparable cavity exit areas; the result was that the flow characteristics – including the v-shaped flame – were more closely comparable. The v-shape was hypothesized to result from the shear layer interface between the cavity and core flows. Subsequent analyses by Parks [87] found that it was more likely an artifact of the test rig geometry.

Concurrent with LeBay, Benhassen [88] implemented a Filtered Rayleigh Scattering (FRS) technique to measure the effects of buoyancy and g-loading on the trajectory and mixing of the jet injectors in circumferential cavity. A stereolithography (SLA) quarter-sector model of a mid-scale UCC cavity (38 cm radius of curvature) was fabricated and jets of CO_2 were introduced into the bulk flow to evaluate whether the buoyancy or the centrifugal acceleration would dominate. Tests were run at g-loads up to 1000g, and at those levels the centrifugal forces were found to dominate. Additionally, the jet profile was altered from a theoretical "bell-shape" to a dual-peaked flow biased away from the center of curvature.

Again concurrently, Parks [87] accomplished modifications to the curved sectional model. Modifications to the centerbody vane were investigated; a smooth vane, an RVC-vane, and a "tiger-claw" design were tested for their ability to evenly distribute flow from the circumferential cavity back into the axial core. The tiger-claw is shown in Figure 2.58; notional circumferential cavity flow would migrate from the bottom edge and out of the left-hand side of the images. Holes visible were for static pressure measurements, which were not included in

the results of Parks. HSV and emissions experiments demonstrated the ability off the tiger-claw to more evenly distribute the hot gases into the core flow, though only at lower core mass flow rates. At higher core mass flow rates (i.e. a mass flow ratio of 0.1), the tiger-claw was less effective, and results between the tiger-claw, the RVC, and the flat vane were similar. Furthermore, the tiger-claw had the intended effect of preventing excess hot gas transport to the far (inner diameter) wall. However, a consequence of that dynamic was a reduction bulk swirl in the core flow, and therefore a reduction in mixing. Thus, the tiger-claw design suffered from lower efficiency than the other two configurations.

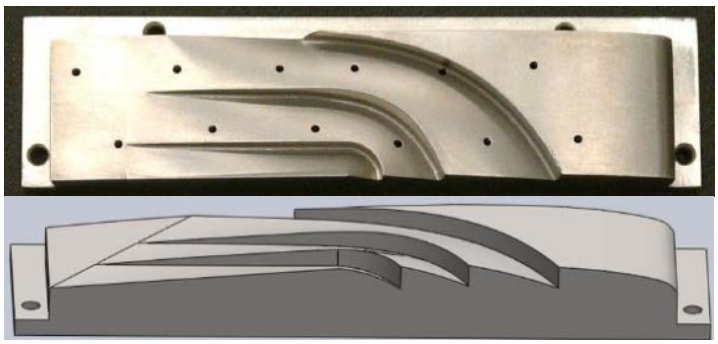

Figure 2.58: The "tiger-claw" variant on the UCC radial vane cavity, top-view (top) and profile (bottom) [87]

2.5.3. Full Annular Design, Development, and Test

The work of Bohan [89] and Bohan and Polanka [2] introduced several important results to the development of the AFIT UCC that contributed to the design of the full-annular test rig. A UCC scaled appropriately for a large fighter-type gas turbine engine was considered; the inner radius at the combustor exit was taken to be 31.75 cm. A unique UCC guide vane was developed as a composite of a traditional compressor exit guide vane (EGV) and a turbine inlet guide vane (IGV). Fluid from the last-stage compressor rotor was permitted to maintain its inlet swirl angle of 36° and turned only slightly to exit at 70°, suitable for a conventional high-pressure turbine rotor stage; thus, the total turning of the vane was only 34°. Vane thickness was maintained at 2 cm to enable introduction of cooling schemes, and due to the steep angle,

chord length was relatively large. A graphical depiction of the design process of the so-called "hybrid vane" is shown in Figure 2.59.

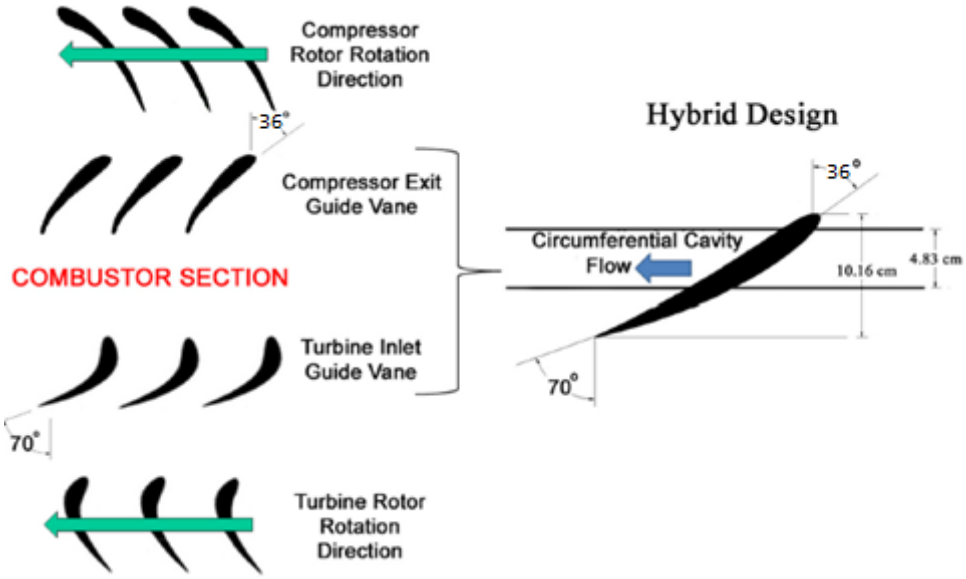

Figure 2.59: Origin and orientation of hybrid vane design [2]

The number of vanes for the full annulus did not exceed 30 due to resultant metallic blockage of the core flow and issues with overlap. A computational study was undertaken on a single vane from a representative annulus, the details of which are presented in Figure 2.60 for the case with a total vane count of 20; a case with 30 vanes was also studied. Nonreacting and reacting flow simulations were performed. In the reacting studies, an engine-representative condition with liquid kerosene fuel was modeled, as well as a lab-representative atmospheric condition with gaseous propane. Fluent 6.3 was implemented with an RNG $k-\varepsilon$ turbulence model; reactions were considered with both a five- and a twelve-species model. Intermediate results drove a study optimizing the cavity air injection ports to produce the desired tangential velocity that would then produce the desired operating g-load of 3500g, the results of which appear in Figure 2.61. The dashed lines represent the required air inlet diameter to achieve a tangential velocity of 114 m/s – then yielding the desired g-load of 3500g. Engine conditions produced slightly higher tangential velocities than rig conditions with the same inlet velocity,

leading in turn to slightly higher temperatures (solid lines in Figure 2.61). Reacting cases resulted in slightly lower tangential velocities with identical inlet velocities. Tangential velocity in the cavity was greater than the cavity air injection velocity in all cases due to fluid circulation and buildup.

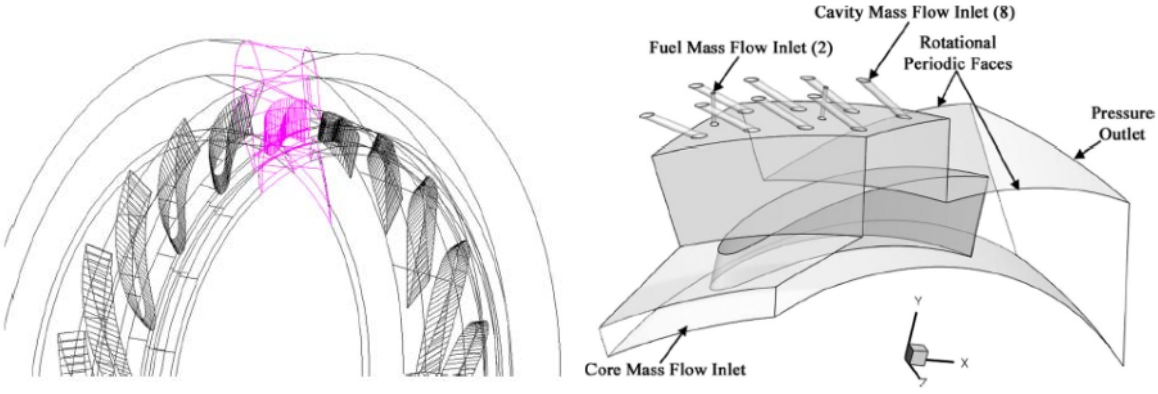

Figure 2.60: Computational sector (left) and domain surfaces (right); unlabeled surfaces are walls [2]

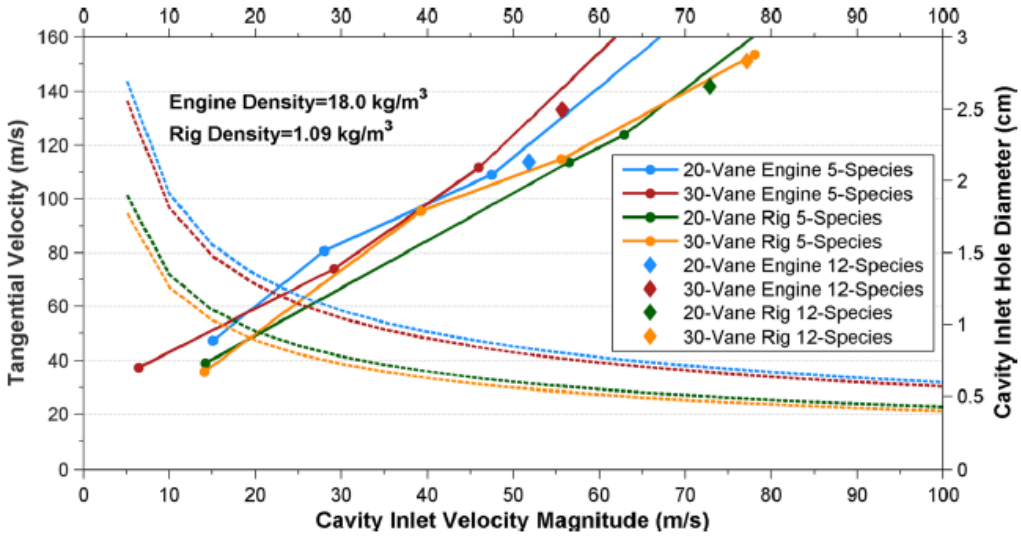

Figure 2.61: Cavity air inlet diameter study [2]

Over a g-load range of 365 to 7000, cavity residence times ranged between 2.4 and 3.8 ms. Pattern factors ranged between 0.37 and 0.45, greater than that of conventional combustors, which come in around 0.2. Inner diameter endwall heating was prevalent, indicating that, while flow migration from the cavity was therefore successful, future work was

needed to better optimize that flow to prevent excess heating at the endwalls. System pressure loss predictions were comparable between the five- and twelve-species reaction models; the largest influence was the number of vanes. Minimum pressure loss was demonstrated with the 20-vane configuration at values of 5.9% static and 4.7% total pressure loss. Traditional combustor pressure loss is around 6%, but Bohan and Polanka note that that metric does not account for the compressor EGV or the turbine IGV as does the UCC model. Therefore, the loss measurements are all the more significant. Combustion efficiency based on species concentrations at the exit plane was calculated to be 98.8%

Subsequent design, manufacturing, and test of a full-annular test rig was led by Wilson as documented in Wilson [90], Wilson and Polanka [91], and Wilson *et al.* [92]. The findings of Bohan and Polanka [2] were synthesized with the greater body of AFRL and AFIT UCC results to determine suitable rig sizing for use in the AFIT COAL lab. The rig was intended for testing in either a main combustor or an inter-turbine burner role. Modularity was a primary design criterion, as was improved optical access and instrumentation capability. The new rig, in addition to being a full annulus, had a larger radius of curvature than the previous curved sectional model. In a main combustor role, the test rig was designed to accept inlet air at Mach 0.35 and 35° swirl. The size of the circumferential cavity was optimized for 8.1 kg/min of core air in order to reach a g-load of 2000g with core flow at 18.9 kg/min. Core and cavity air were injected separately and were discretely controlled, as in nearly all prior UCC work. Design point equivalence ratio was set between 1.5-2.0, resulting in a minimum overall fuel-to-air ratio (OFAR) of 0.45 in order to operate within the stable regime defined by Zelina *et al.* [55]. A centerbody with a hybrid vane based on Bohan and Polanka [2] was incorporated.

A graphical depiction of the rig is shown in Figure 2.62. The hybrid vane centerbody is shown in yellow, and the cavity air and fuel injection ring is in red. The test rig core flow is uniform, so a pre-swirler (in dark blue) turns the incoming flow to simulate the conditions at the exit of a typical compressor stage. The core components were designed to accept cooling flow.

In Figure 2.62a, the front plate is shown with the modular panels removed; a mirrored arrangement is present on the back plate. The panels could be configured with instrumentation (pressure probes and thermocouples), or as windows for optical access (quartz or sapphire) either into or through the circumferential cavity. The diameter of the cavity is 15.85 cm with a cross-sectional area of 2.54 x 2.54 cm – nearly 50% larger than the AFRL high-g test rig. An image of the fabricated inner section, including the nose cone, pre-swirler, centerbody, and tail cone is shown in Figure 2.63 (top). Injection rings were fabricated with varying air injection jet diameters in order to observe similar trends as seen by Bohan and Polanka [2].

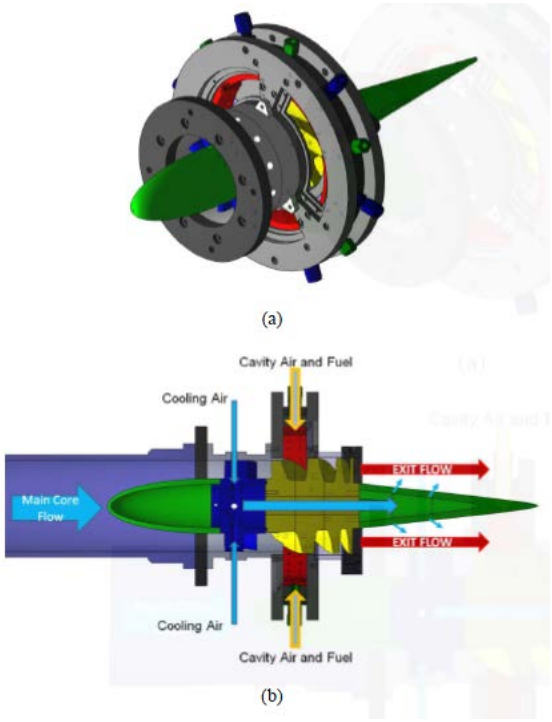

Figure 2.62: Full annular rig design assembly (a) and cross-section (b) [90]

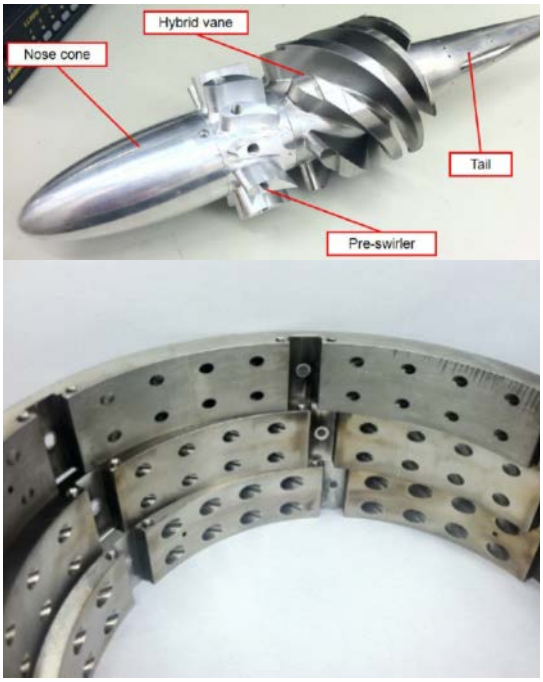

Figure 2.63: Full annular center section hardware (top) and air/fuel injection rings with varying diameters (bottom) [90]

Figure 2.64: Installed fuel baffle (left-most image); installation of fuel baffle addition (right three images)

Liquid fuel injection was executed as in previous work with a cavity-in-cavity scheme (visible in the bottom image of Figure 2.63). However, when gaseous propane was injected, observations indicated that the jet of gaseous fuel actually had a detrimental effect on the cavity flow as it created a pseudo-barrier that forced the flow to circulate around it. A solution was then designed to more evenly disperse the gaseous fuel by way of an eight-hole fuel baffle, as shown in Figure 2.65 (left-most image). Subsequently, Damele [93] noted that gas tended to escape the gap between the injection ring and the fuel baffle, so a baffle addition was designed to create a better seal and coerce the fuel through the baffle holes (Figure 2.64, right three images).

Initial results with the full annular rig, published in Wilson and Polanka [91], document studies regarding Rayleigh loss reduction through the hybrid vane passage. The initial centerbody inner diameter (ID) followed a linear taper from fore to aft; it was found that Rayleigh loss for that configuration exceeded 10%, more than double the accepted state-of-the-art value of 5%. By way of a 2D CFD optimization, the ID of the centerbody was modified to create increased cross-sectional area through the vane passage, thereby reducing the Mach number in the region of high heat release, at the point of cavity-core migration. In Wilson [90], experimental results verified that the low-loss centerbody was successful in reducing Rayleigh loss by as much as 25% when compared to the tapered centerbody. Higher temperatures were also observed, indicating more complete burning.

In Wilson *et al.* [92], the orientation of the cavity air injection scheme was varied between clockwise-swirl (CW) (as viewed from the front) or counter-clockwise (CCW) swirl; the former flow scheme migration that impacts the suction side of the hybrid vane first, while the latter migration scheme impacts the pressure side first. Representative results are shown in Figure 2.65; note that the flow direction appears opposite its label as a mirror was used to collect the image. Qualitatively, the CW (suction-side impact) orientation produced a far more stable flame; measured system pressure loss was also less for all cases of CW swirl versus the CCW configuration. In the same study, lean blowout limits of the test rig were evaluated with results similar to those of Zelina [10]; those results appear in Figure 2.66. A trend line for the blowout conditions is included. Operation close to blowout was possible, but stability was compromised; the flames did not circulate through the entire cavity, thereby resulting in a substantial drop in average cavity temperature. Finally, tests of varied cavity air injection jet diameter produced results that matched the calculations of Bohan and Polanka [2]; larger jet diameters resulted in lower g-loads for a given mass flow. The smallest jet diameter tested was unable to sustain flame at the test point with the highest cavity mass flow (with constant equivalence ratio). Based on measurements at the cavity centerline and quarterline, it was postulated that the smallest jets created a substantially greater velocity gradient across the cavity contributing to increased flow instability.

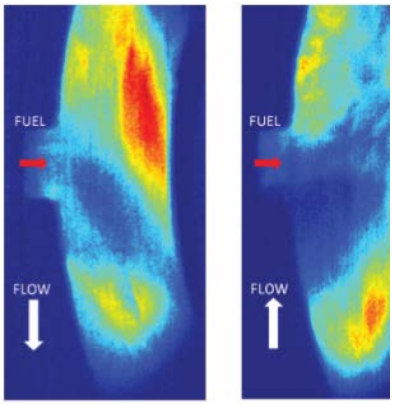

Figure 2.65: Time-averaged flame intensities in the combustion cavity for CW (left) and CCW (right) swirl [92]

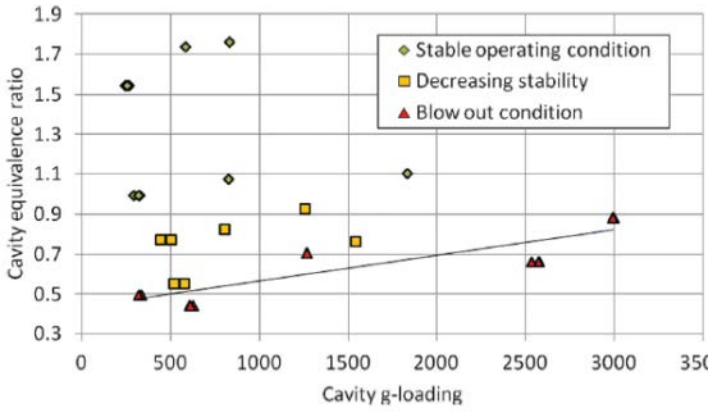

Figure 2.66: Lean blow out with constant core flow rate of 3.24

The work of Damele [93] and Damele *et al.* [94] followed Wilson directly with additional testing and characterization of the new AFIT full-annular rig. The pressure and temperature instrumentation was refined, after which a battery of tests was designed and run. In previous work associated with LeBay [86] and others, the primary metric for evaluating the interaction of the cavity with the core was the ratio of their respective mass flows. In the case of Damele and in subsequent work, that metric was redefined as simply the core/cavity mass-flow split. It will be expressed in all subsequent discussion as a ratio defined by

$$\frac{\%\ of\ total\ mass\ flow\ passing\ through\ the\ core}{\%\ of\ total\ mass\ flow\ passing\ through\ the\ cavity}$$

Thus, a "70/30 split" indicates that 70% of the overall air mass flow passes through the core, and 30% passes through the cavity. In the test matrices of Damele, mass flow splits of 60/40, 70/30, 75/25, and 80/20 were tested at cavity equivalence ratios ranging from 0.56 to 1.65. The effects of those variations on exit temperature profiles, system pressure losses, and exit emissions were evaluated. Initial results supplemented the UCC stability map initiated by Wilson and are shown in Figure 2.66 with the fuel-lean blowout limits. Fuel-rich blowout was noted at cavity equivalence ratios of about 3 at 1100g, and about 2.6 at 3500g. Representative results of temperature exit profile measurements are shown in Figure 2.67. The general trend is

nonuniform with consistent skew toward the outer diameter. However, the trend itself is consistent with increasing cavity equivalence ratio. Further investigation into measurements of pattern and profile factors revealed that neither of those quantities was significantly affected by changes in cavity equivalence ratio. Pattern and profile factors were, however, sensitive to the flow split as shown in Figure 2.68. Both trends were consistent with the results of LeBay [86]: while the cavity equivalence ratio only affects the magnitude of the heat release, the cavity/core mass flux ratio (or the flow split) had a substantial influence on the migration patterns from the circumferential cavity back into the core flow. For these tests Rayleigh losses were computed between 3 and 5% (using the low-loss centerbody). Combustion efficiencies were calculated between 95 and 83% - considered low relative to prior work. Emissions were found to be a strong function of flow split, with increased efficiency noted for higher core mass flow percentages.

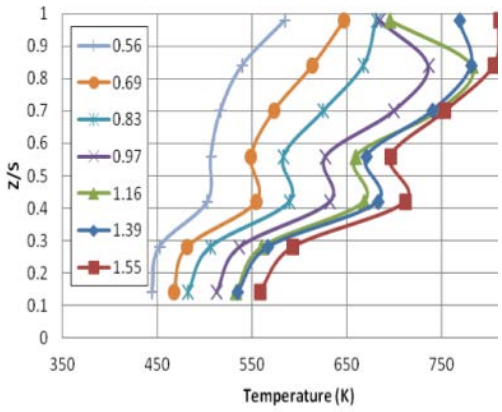

Figure 2.67: Exit temperature profiles for various cavity equivalence ratios [94]

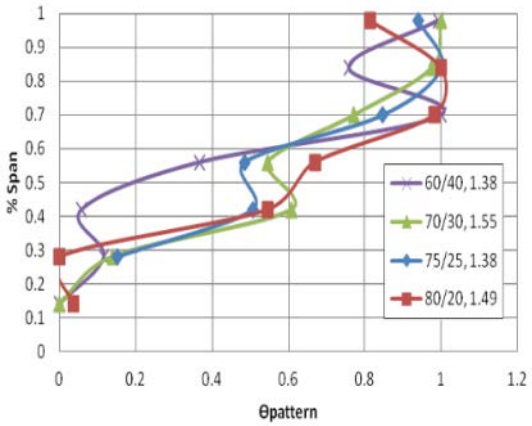

Figure 2.68: Exit pattern factors for various cavity equivalence ratios [94]

2.5.4. Inter-Turbine Burner Development and Spray Testing

Concurrent with Wilson, Conrad [95] and Conrad *et al.* [96] documented the design and development of a hardware interface between the new full annular test rig and a small turbine engine (STE) in order to facilitate operation of the test rig in conditions representative of an inter-turbine burner (ITB). The hardware interface would split flow from a common source

between the core and the cavity, as opposed to the discretely-sourced core and cavity of the baseline design. While the original vision employed the use of the STE to provide vitiated flow, the same hardware could be employed with cold inlet flow as from an upstream compressor stage. The design process resulted in a diffuser that would split the stream from a common upstream source between the core hybrid vane passages and the cavity air injection scheme. Notably, contrary to the radial air injection scheme prevalent in nearly all prior UCC research, the diffuser design called for air to be injected into the combustion cavity from the upstream sidewall while maintaining the same radial fuel injection scheme as designed by Wilson. An illustration of the diffuser attached to the primary UCC components is shown in Figure 2.69. The STE selected to provide the upstream vitiated air source was a JetCat P200; the test configuration with the JetCat attached is shown in Figure 2.70. The diffuser was designed with modular middle diameter (MD) rings so that the splitting ratio of the oncoming flow could be adjusted. Note as well that Figure 2.69 shows a UCC centerbody with straight vanes as opposed to the curved hybrid vanes discussed earlier. The straight-vane design was developed in anticipation of better fitting the needs of an ITB in a thrust augmentor role, but the design was never manufactured.

In addition to the diffuser design, Conrad *et al.* [96] developed a CHEMKIN model and used it to examine the potential emissions performance of an ITB with representative vitiated flow from a JetCat-type STE with varying mass flow splits. Therein, an 80/20 flow split was demonstrated to have the highest combustion efficiency but the worst NO_x and CO emissions. Conrad *et al.* concluded that the 70/30 split represented the best tradeoff between combustion efficiency and emissions performance. Finally, limited testing was accomplished with the liquid fuel injection scheme in the full annular test rig. High-speed imagery of non-reacting fuel injection demonstrated the tendency of the fuel stream to sweep toward the outer diameter of the circumferential cavity with increasing g-load.

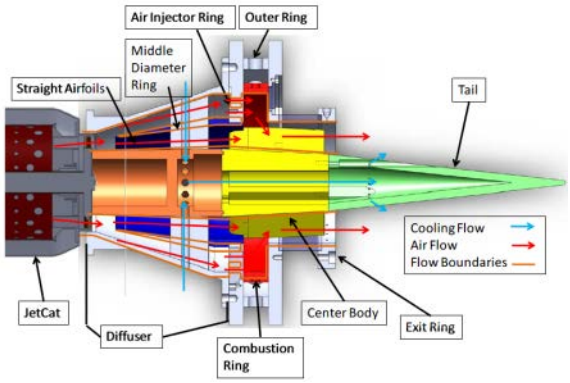

Figure 2.69: Flow paths through ITB configuration

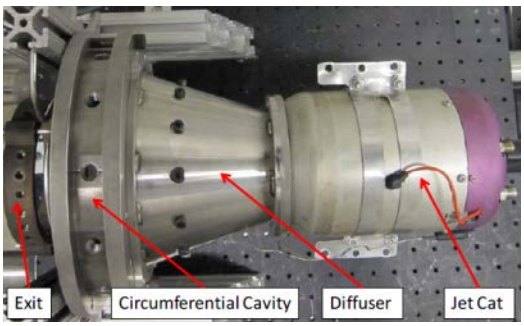

Figure 2.70: ITB integrated with STE [96]

Brinker [97] performed liquid spray characterization of the full-annular rig under high-g loads using Phase Doppler Particle Anemometry (PDPA) as a follow-on study to the qualitative spray test results obtained by Conrad [95]. Water was utilized with the same fuel injection hardware as in previous tests; fuel was not used due to concerns of leakage and proper handling of excess fuel. Three unique modes of atomization were identified in a range of g-loads from 300 to 5000g. Droplet velocity vectors were obtained, and droplet sizes tended to be small. Concentration measurements demonstrated the inherent unsteadiness in the cavity; increased g-loading caused more drops to remain at the cavity outer diameter. It remains to be seen whether liquid fuel exhibits the same characteristics.

Miranda [98] continued the work of Conrad on integrating the JetCat with the UCC. He developed a numerical model using the Numerical Propulsion System Simulation (NPSS), a product of the National Air and Space Administration (NASA), to perform detailed cycle analysis on a notional ITB system as compared to a traditional afterburning turbofan. The primary objective was to evaluate the relative performance of an afterburner and an ITB in thrust augmentation and power extraction (PX) roles. Selected results of the thrust and PX studies are shown in Figure 2.71 and Figure 2.72, respectively. After a short initial interval, the ITB achieves superior thrust-specific fuel consumption (TSFC) for identical thrust demands as compared to an afterburner. The calculated temperature rise across the ITB accompanying a

~4500 N thrust increase was 565K – consistent with the experimental results of Spytek [68]. For the PX study, each model is tasked to maintain constant thrust while increasing shaft power is drawn from the low pressure turbine; Figure 2.72 presents those results with trends similar to Figure 2.71.

Additional work by Miranda [98] involved cold-flow testing of the common-source diffuser of Conrad. Issues resulted, as an adverse pressure gradient was measured in the diffuser outer flow path, and mixing ratios less than unity were calculated between the core and the outer paths. The implication was that the diffuser was not splitting the flow as anticipated, and the majority of the flow (nearly 100%) was passing into the core rather than being partially diverted to the circumferential cavity.

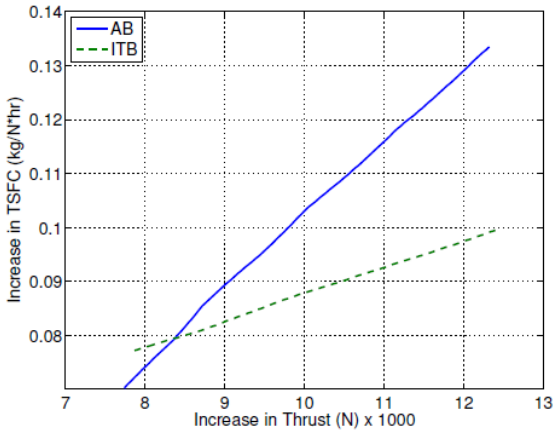

Figure 2.71: TSFC versus Thrust [98]

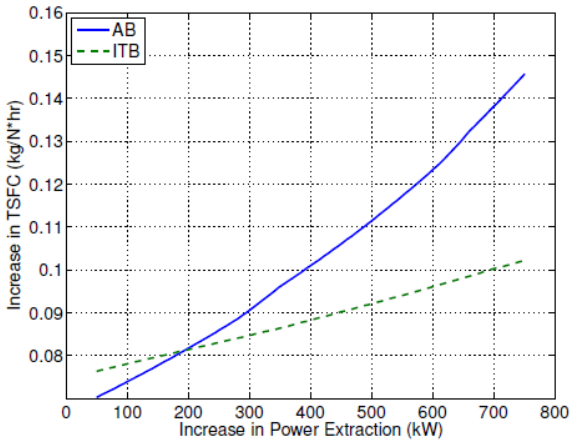

Figure 2.72: TSFC versus power extraction [98]

2.6. Summary

Ultra-Compact Combustion presents some genuinely intriguing possibilities within the context of gas turbine combustion. While the body of work reflected in this review is substantial, many fundamental questions still remain. Most importantly, is the g-effect important? Can its influence be separated from the myriad other influences that govern the

complex circumferential flow environment? How do we design a circumferential combustor for optimal operation?

More specifically, these broad questions have served to inspire the work that shall be presented in the coming pages. The research objectives have evolved into those that were introduced in Chapter 1. To address the problems of design, Objective 1 will endeavor to demonstrate a major change in design philosophy to incorporate features more representative of real engine geometry. To address the physical nature of g-loaded combustion, Objective 2 will demonstrate the most high-fidelity measurements and computations of a fully-annular high-g circumferential combustion cavity in order to understand the parameters that affect g-loading and the combustion process. Finally, the problems of design philosophy and circumferential cavity combustion come together in Objective 3 where the interactions between a circumferential cavity and a complex core flow design are examined. The conditions and variables that most affect system-level behaviors will be identified and further evolutions of design will be tested.

III. Methods

Chapter 3 details the present features of the experimental and computational resources that were utilized to perform the research in this study. The goals of the research, as discussed in Chapter 1, were operation and characterization of the AFIT UCC with specific consideration for (1) common upstream flow delivery, (2) circumferential cavity flow dynamics, and (3) flow migration. A wide variety of tools were necessary to address those objectives as the problem was highly complex in both concept and execution. A general presentation of the experimental facility, test hardware, and measurement methods are given in Section 3.1. Included in that section is discussion of the transition from the "version 2" UCC hardware to "version 3" – that move was the first and most significant geometric variation investigated by this work. A dedicated discussion is then given by Section 3.2 regarding the execution of optical diagnostics for interrogation of UCC flow features in both the CC and the exit plane. Section 3.3 gives extended detail on additional geometry components that were varied for the purposes of this study in order to investigate (1) improved cavity flow distribution and (2) improved flow migration and exit characteristics. Those modifications included the addition of a core restrictor plate in Section 3.3.1, varying the cavity air injection scheme in Section 3.3.2 and adding a surface feature to the HGV in Section 3.3.3. The resulting studies motivated further investigation into the HGV surface feature trade space as presented in Section 3.3.4. Finally, Section 3.4 details the computational resources, methods, and analytic procedures that facilitated the numerical results that accompany and expand the conclusions drawn from the experiments.

3.1. Experimental Facilities

Combustion experiments at the Air Force Institute of Technology were performed in the Combustion Optical Analysis and Laser (COAL) laboratory. COAL lab capabilities evolved over a decade of evolutionary research and upgrades as described in Section 2.5. The current section will outline the present capabilities and equipment that pertain to achieving the goals of this project. A general description of the test hardware is provided in Section 3.1.1. The setup of the test facility is similarly generally described in Section 3.1.2 with some detail as to recent developments. Section 3.1.3 describes the setup of basic temperature and pressure instrumentation and Section 3.1.4 presents the associated data acquisition software. Accomplishment of the research objectives was dependent on reliable flow measurement and visualization; therefore, optical flow interrogation played a significant role and is described in Section 3.2. A number of geometric modifications were pursued as dependent variables in the research for their anticipated influence on the UCC field parameters as detailed in Section 3.3. Finally, computational fluid dynamics (CFD) tools were also employed extensively to supplement and extend the experimental analyses. Model development, solver parameters, and grid independence results are given in Section 3.4.

3.1.1. Test Rig

Two major versions of test hardware were utilized for this work. They are described separately in Sections 3.1.1.1 and 3.1.1.2. The first – version 2 – consisted of the common-source diffuser developed by Conrad [96] and Miranda [98] with the motive of better representing real engine operating conditions. The second – version 3 was designed by Wilson but undocumented with the primary motives being (1) improved mechanical sealing, (2) improved distribution of the cavity air drivers, and (3) investigation of a larger cavity aspect ratio by increasing the diameter of the outer combustion ring. A portion of the current effort

was devoted to finalizing and producing Wilson's design and employing it for the current test campaigns.

3.1.1.1. Version 2

The hardware dubbed "Version 2" or simply UCC v2 was the result of combining the previously-tested discrete-source UCC (as described in Section 2.5.3) with the common-source upstream diffuser. Depictions of the UCC v2 test rig are shown in Figure 3.1 and Figure 3.2. Primary air/fuel flow paths are labeled in Figure 3.1. The entire assembly, including the diffuser, measured 43.2 cm long. At the widest point, the rig was 25.4 cm in diameter. Figure 3.2 outlines the major components of the rig. The circumferential cross section of the combustion cavity was 2.54 x 2.54 cm, and its outer diameter was 15.9 cm. The injection holes in the cavity air injection panels consisted of three plates, each with two rows of ten holes, each hole being 0.45 cm in diameter and angled at 30 degrees relative to the axial direction. Fuel was injected at six equally spaced locations about the outer diameter; the eight-point fuel baffles described by Figure 2.64 remained installed. Injection points in the inner combustion ring correspond to mounting locations on the outer ring. Additional holes in the outer ring existed to serve as air injectors for the discretely-sourced-air configuration of Wilson [90] and Damele [93]; those holes and the plenum location between the outer and inner rings were unused in the common-source configuration shown below.

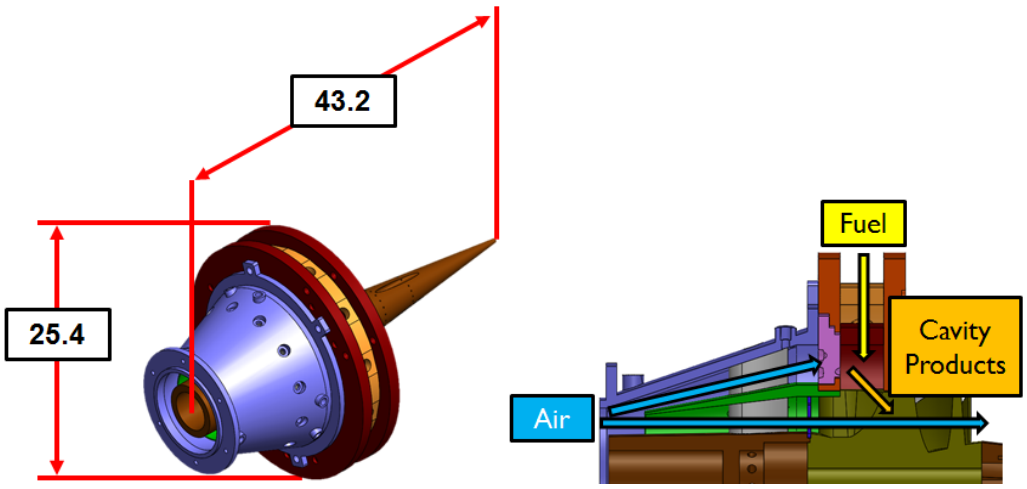

Figure 3.1: AFIT UCC v2 full-annular test rig with attached diffuser; dimensions in cm

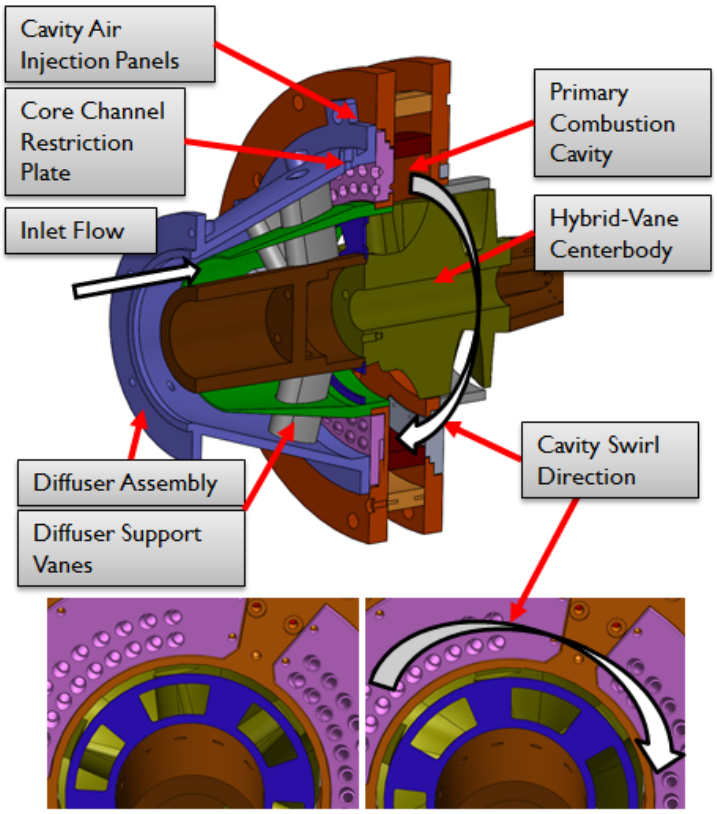

Figure 3.2: Exploded views of UCC combustor assembly (top) and diffuser assembly (bottom)

The diffuser was designed with a modular middle diameter (MD) component so that the location of the flow split could be varied, subsequently varying the proportional mass flow

between the core and the cavity. An exploded view of the diffuser is shown on the left in Figure 3.3, and an illustration of the varying MD is shown on the right. The "Core Open" configuration was so named since it presented more area to the core flow path; "Cavity Open" was similarly named. The design core/cavity mass flow splits for the Core Open, Middle, and Cavity Open configurations were 80/20, 70/30, and 60/40, respectively. The core channel restriction plate was designed to provide additional modular control of the flow distribution, and its design is covered in detail in Section 3.1.2. The diffuser support vanes were designed to be installed as either straight or curved. The straight configuration is seen below, and it is suitable for ITB applications where no additional swirl is desired in the incoming flow. The curved-vane configuration would be notionally utilized when simulating flow from a notional upstream compressor.

The original v2 diffuser design was intended to interface with the turbine exit plane of a JetCat small turbine engine in order to evaluate the UCC with vitiated air. As the objectives of this research required the use of cold inlet air only, the first modification to the v2 design was a simple nose cone to make the diffuser inner diameter more aerodynamically sound. The nose cone is shown in grey in the left image of Figure 3.4. It was designed as the revolution of an ellipse with semi-major and semi-minor axes of 11 and 3 cm, respectively. The diffuser inner diameter was modified with a lip to interface with the nosecone by way of three radial counter-bore #6 machine thread holes. However, the fit between the ID and nosecone was snug enough that only one screw was generally needed; often no screws were used with no ill effect.

Similarly, the leading edge of the hybrid guide-vane (HGV) centerbody is shown below with zero incidence angle with respect to the flow to complement the diffuser straight vanes. If curved diffuser vanes were installed, a complementary curved HGV leading edge component would be installed to match the imparted flow angle. The straight support vanes and straight leading edges were utilized in all cases for this research. The rig was designed to accommodate up to 0.45 kg/s total air flow at atmospheric or vitiated conditions. Components of the rig that

will be introduced and discussed in more detail include the combustion ring and air driver distribution in Section 3.1.1, the channel plate in Section 3.3.1, air driver modifications in Section 3.3.2, and the hybrid guide vane and its modifications in Sections 3.3.3 and 3.3.4.

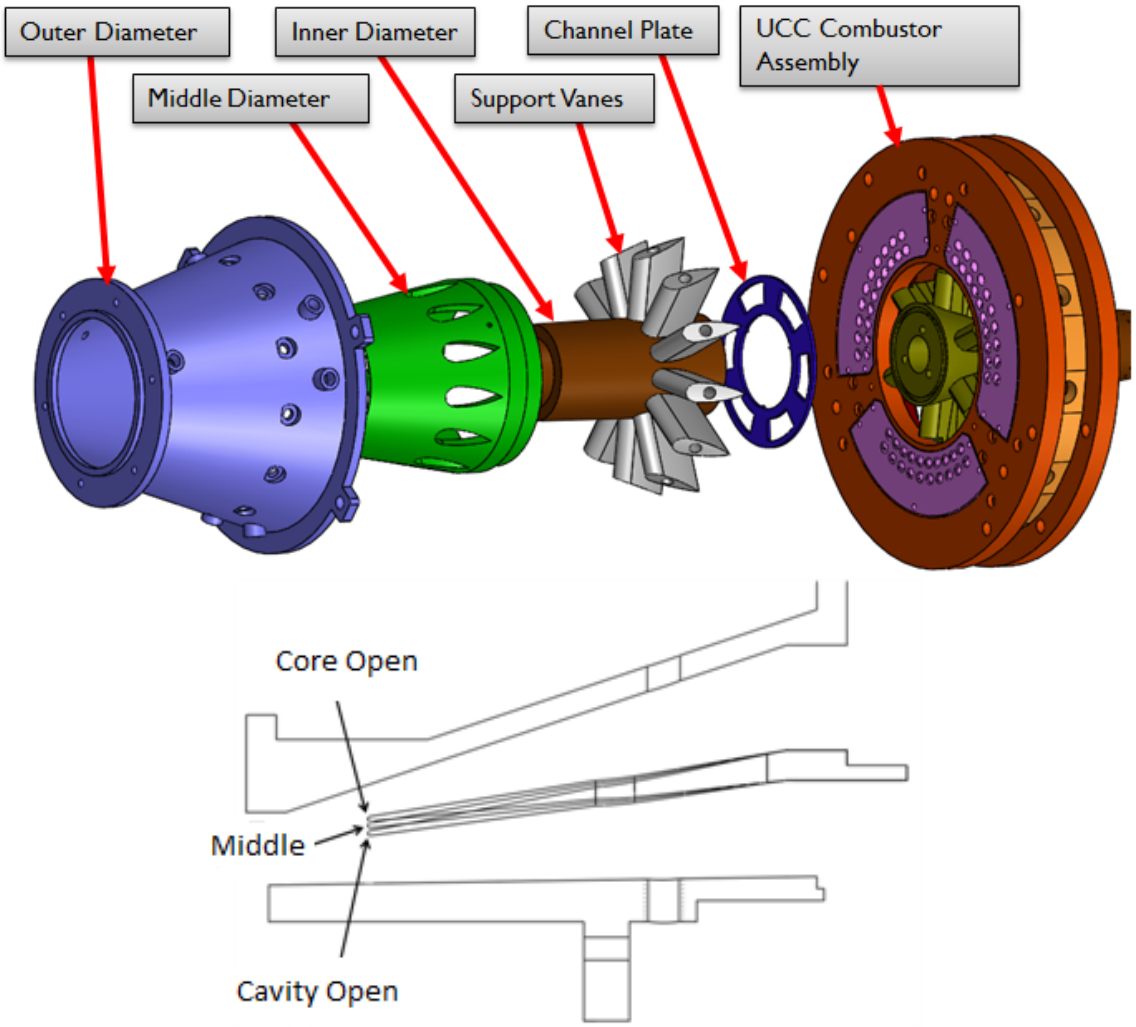

Figure 3.3: Diffuser exploded view (top); middle diameter variations and terms

The v2 design included ports on the aft wall of the cavity for installing instrumentation as illustrated by the left image in Figure 3.4. The ports were tapped for 1/16 inch NPT threads in order to interface with the Swagelok fittings commonly used in the lab. The ports could accept either 1/16 stainless steel tubes, which were used for pressure measurements, or 1/16 inch K-type thermocouples. (More detail on instrumentation is provided in Section 3.1.3.) Similar ports were drilled on the instrument ring such that probes could be installed near the

exit plane. A tail cone was also part of the original design in order to facilitate smooth expansion of the exhaust gases; it was about 20 cm in length thus yielding an expansion angle of about 6°. Small holes were drilled in the tail cone for a notional cooling scheme, but there was no need for cooling to be incorporated during this current research.

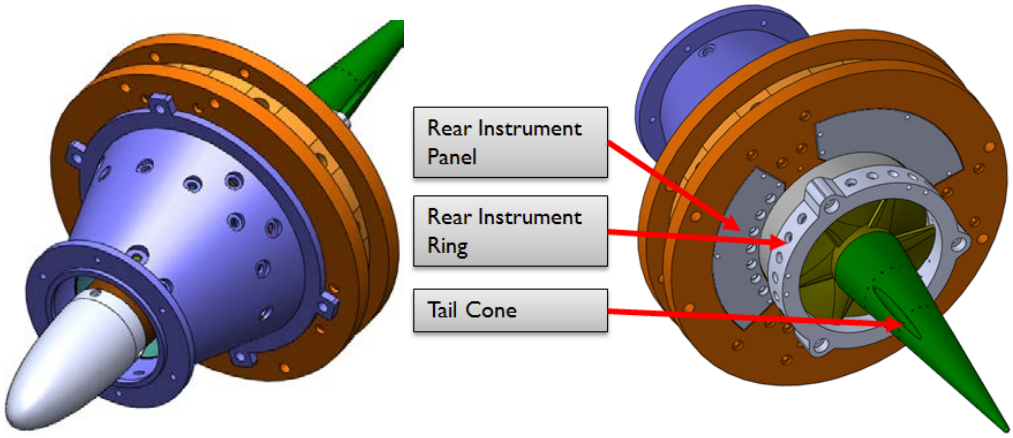

Figure 3.4: Front view with inlet nosecone (left) and aft view with tailcone (right)

The hybrid guide vane (HGV) centerbody was the realization of the hybrid concept first proposed by Bohan [89] and discussed in Section 2.5.3. The fundamental implementation in Solidworks consisted of a revolution of the low-loss profile from Section 2.5.3 coupled with a helical airfoil. The airfoil began as a simple rectangular profile and was subsequently allowed to trace a helical path to the aft; precise details of the relevant parameters are given in Appendix B; the resulting original Wilson design is shown on the left in Figure 3.5. However, due to the relatively small scale of the implementation, the resulting geometry included very high degrees of circumferential turning – almost exactly 180° for a single airfoil – for relatively small turning with respect to the passage of 43° . Comparatively, the original Bohan inception of the HGV called for similar in-passage turning for airfoil circumferential turning between 36° and 54°. The original HGV was designed to accept inlet flow with some swirl as would be the case at the exit of a notional compressor. However, one of the objectives for UCC v2 was to also accept flow from a turbine exit, which would have little – if any – swirl. Thus, the leading edges

of the HGV were modified to be straight as shown on the right in Figure 3.5 with the modified part highlighted in blue.

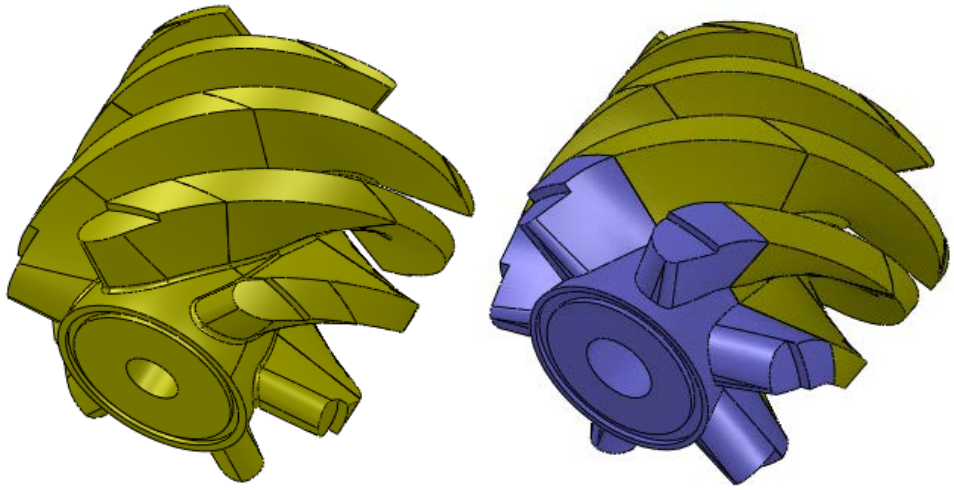

Figure 3.5: Original Wilson centerbody (left) modified for operation with diffuser (right)

3.1.1.2. Version 3

The hardware dubbed "Version 3" or UCC v3 was initially designed by Wilson in a separate effort. The most important changes implemented were (1) replacing the set of three air injection panels with a single solid plate of uniformly distributed air drivers and (2) increasing the outer diameter of the combustion cavity. As will be demonstrated in Chapter 4, those decisions were highly effective in improving the distribution of fuel and air in the cavity. Figure 3.6 presents a qualitative comparison between the two hardware versions in the top set of images; the bottom image shows a side-view cutaway of the diffuser and combustor assembly in order to highlight additional dimensional nomenclature. Constant quantities between the two versions (in cm) included $W = 2.54$, $r_v = 5.33$, and $h_e = 3.0$. The remaining differences are documented in Table 3.1. The ring overall outer diameter was increased in order to provide additional volume in which the fuel momentum could be disbursed and distributed in response to the results of Section 4.2. In those results it was found that the air jets from the discrete panels were not circulating as anticipated. In the case of fuel injectors that fell between air

driver panels, the resultant streams traversed the entire height of the cavity without any circulation. It was hypothesized that the increased outer diameter would resolve that issue. For similar reasons, the air driver distribution was changed to attain more uniform mixing between the air and fuel in the cavity, and the air driver angle was increased in order to increase the bulk swirl velocities. As shown in Table 3.1, the driver angles were increased from 30° to 55° with reference to the UCC centerline axis; that is, increasing air driver angle translated to increased tangency with the circumference. The results in Chapter 4 demonstrated a resultant increase in cavity tangential velocity from centerline-average values around 15 m/s to 25 m/s.

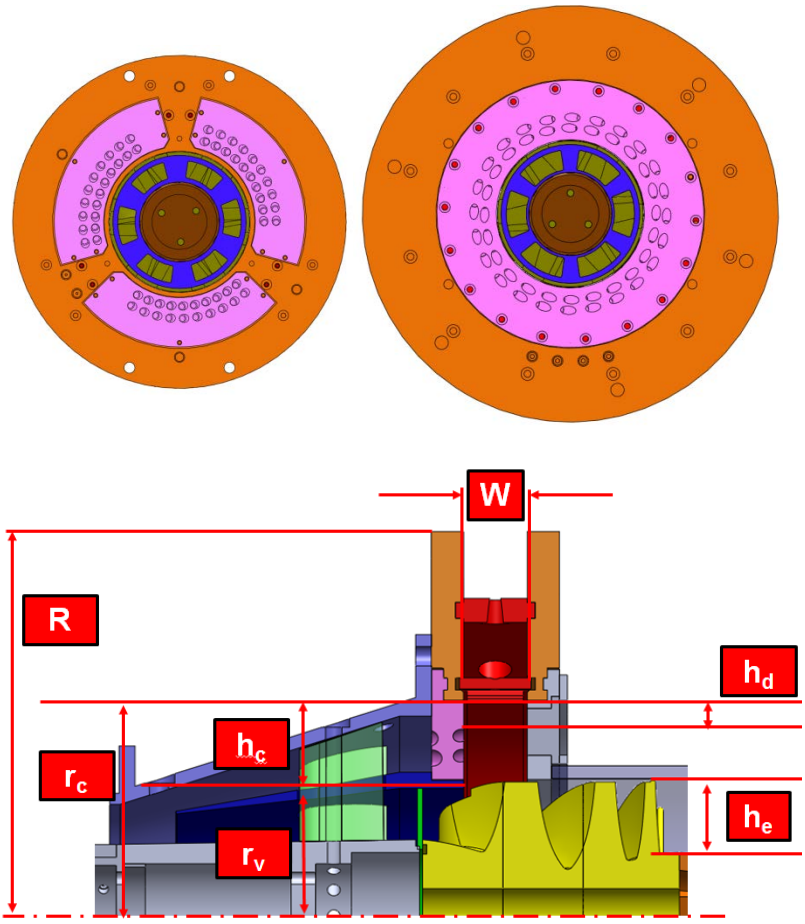

Figure 3.6: Front-view (top) comparison of v2 (left) and v3 hardware (right); dimension nomenclature (bottom)

Table 3.1. Dimension comparison between v2 and v3 hardware

Ring Dimensions			Air Drivers		
	v2	v3		v2	v3
R [cm]	12.7	15.2	Count	60	48
h_c [cm]	2.62	3.17	Total Area [cm^2]	9.52	9.15
r_c [cm]	7.95	8.50	Angle [deg]	30	55
Volume [cm^3]	277	349	h_d [cm]	0.32	1.05

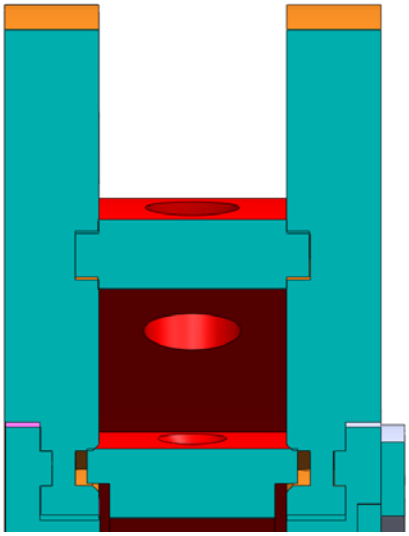

Figure 3.7: UCC v3 cutaway showing the improved mechanical sealing between the side plates and the circumferential rings

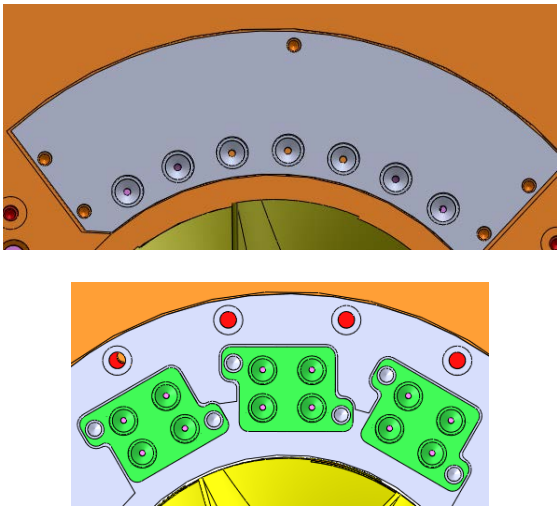

Figure 3.8: Comparing the v2 (top) and v3 aft instrumentation panel concepts

A secondary goal of the v3 hardware was refinement of the cavity design to improve the mechanical sealing and reduce the occurrence of flame leakage between the front and back plates. Whereas in the v2 design the interfaces between the front and back plates and the circumferential inner and outer rings had been simply flat, in the v3 design those parts were design such that the inner/outer rings fit included notches that fit into groves on the side plates; an illustration is shown in Figure 3.7. A minor change was also implemented on the aft instrumentation scheme: the 80° panel was replaced by three smaller panels, each of which could be customized for any particular purpose or just left blank. Figure 3.8 illustrates that

comparison with all three v3 instrumentation panels drilled for 1/16 NPT threads to fit the standard Swagelok interfaces in use in the COAL lab.

3.1.1.3. Optical Access Modifications

The AFIT hardware was unique in its capability to allow optical access to the combustion event by way of a quartz window installed on the CC aft wall. An aft view of the test rig is shown in Figure 3.9 with some components removed for better visibility and other major components highlighted. The aft window was made of quartz with a field-of-view spanning 80° of arc and 1.9 cm of the cavity radial height. Improvements were made to the v2 window design, shown on the top in Figure 3.10. Experience with that early design was that cracking was often induced by the relatively thin "lip" upon which it interfaced with the aft plate, and the issue was exacerbated by the square corners. The v3 window addressed both issues by rounding the corners and increasing the thickness at the interface. The v3 window was still highly susceptible to cracking, however, upon installation. The mounting methods of the v2 and v3 windows were somewhat similar as shown in Figure 3.11. Both required tightening a bracket over the top and to the sides of the quartz. However, whereas the thickness of the v2 window was designed to fit within the axial thickness of the aft wall, the thicker v3 window was offset from the wall by about 0.5 cm. Consequently, tightening the bolts generated a moment on the lip of the v3 window, which would very easily crack the corners if too much torque was applied. It was found that the bolts should be tightened until the bracket just barely contacted the window surface. As visible in the lower image of Figure 3.11, the gap between the window and the wall was subsequently sealed as detailed in Section 3.1.2.4.

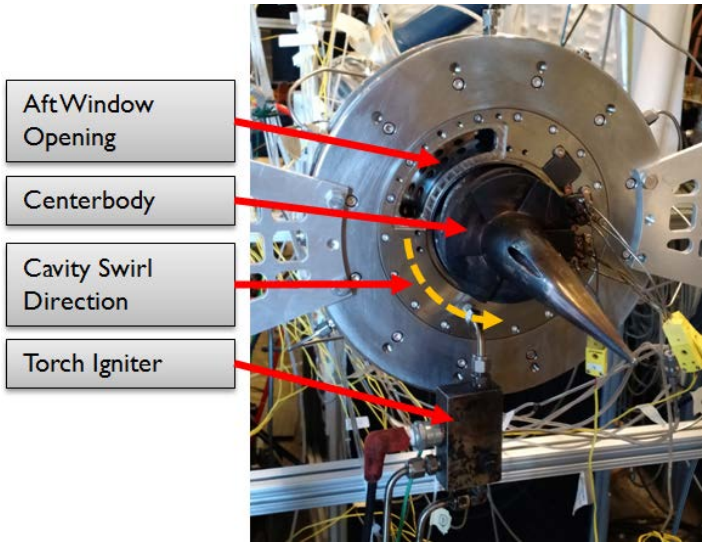

Figure 3.9: Aft view showing location of optical access window

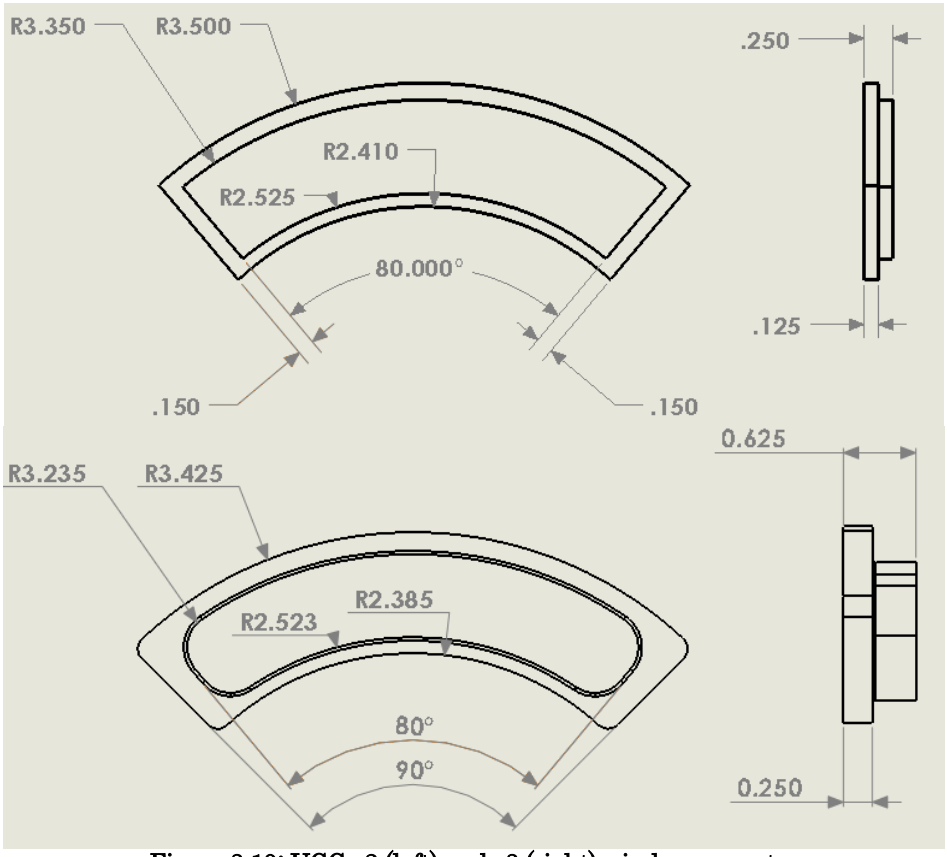

Figure 3.10: UCC v2 (left) and v3 (right) window geometry

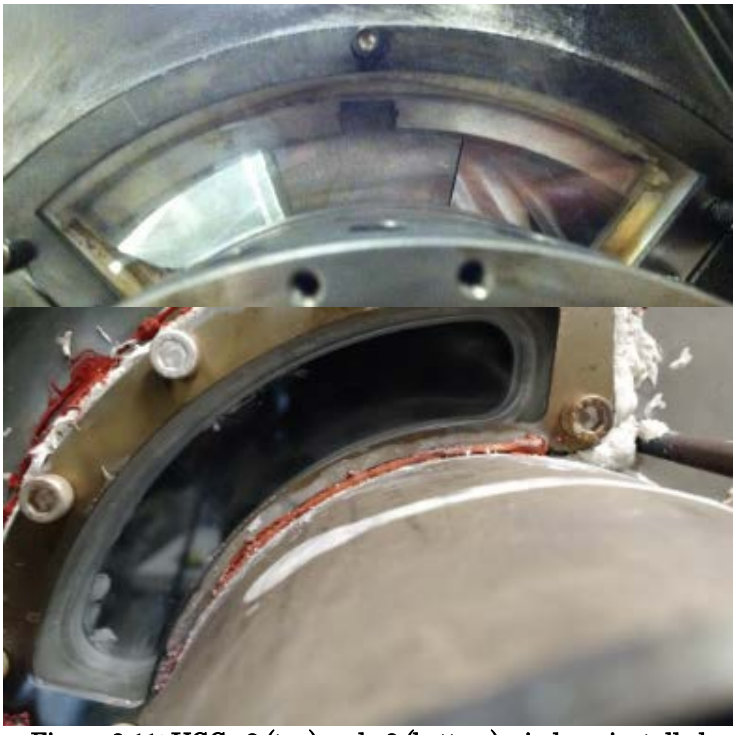

Figure 3.11: UCC v2 (top) and v3 (bottom) windows installed

After the v3 hardware was produced, but before its first run, additional modifications were incorporated in order to allow an access point for a PIV laser. The outer ring was modified by flattening the surface around an unused air injection hole to allow placement of a 20 mm diameter quartz window. A set of concentric holes was then drilled into the inner ring to accept placement of a second 20 mm window. The bracket holding the inner window was also designed to hold a 5 mm diameter rod lens in order to facilitate creation of the beam sheet as required by traditional PIV techniques. If desired, the two window brackets could be swapped so that beam spreading was initiated at the outer ring. Images of the CAD model and window installation are shown in Figure 3.12. Therein, the center image shows the outer ring with a bracket and 20 mm window, and the bottom image shows the inner ring (removed from the rig) with the rod lens and the second 20 mm window. The top image also demonstrates the path of the incoming beam and the resultant formation of the laser sheet.

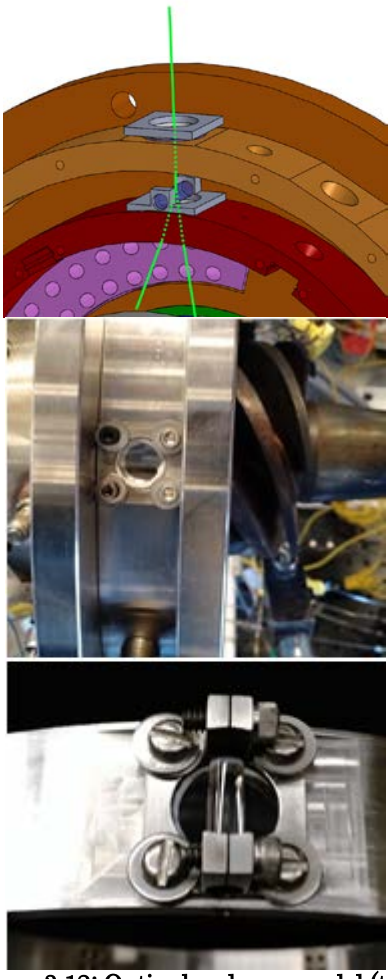

Figure 3.12: Optics hardware model (top), installed outer ring (middle) and installed inner ring (bottom)

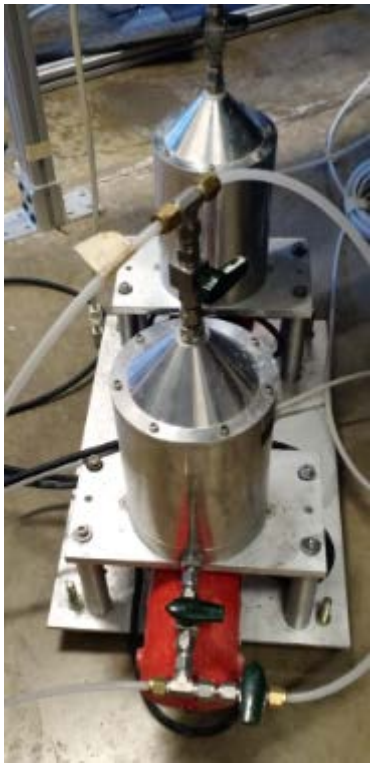

Figure 3.13: SiC seeder

Finally, modifications were made to the upstream air supply duct in order to introduce ~1 μm silicon-carbide (SiC) seed particles from an adjacent drum seeder; an image of the seeder appears in Figure 3.13. The modification consisted of a simple ¼ inch hole; the size of the hole permitted installation of a ¼ inch NPT-threaded Swagelok interface that easily self-tapped its threads when turned into the PVC material. During PIV testing, two operators were required in the back of the lab near the rig exit to accomplish (1) PIV image collection and (2) seeder operation. The seeder was fed by a split from the #4 branch of the air supply that was, in turn, fed from the AFIT compressor. The lower line was plumbed with a pressure regulator; the seed density was metered by adjusting the upstream pressure. In general, higher seed densities

were required for PIV than PSEV, and higher seed densities were also required for higher levels of ϕ_{cav}.

3.1.2. Laboratory Equipment

3.1.2.1. Air Supply

Air was plumbed into the COAL lab via three primary lines labeled with numbers 1, 2, and 3, and sized at 7.62 cm, 3.81 cm, and 1.91 cm, respectively, as shown by Figure 3.14. The lines were fed from either of the two outside sources. The COAL Lab was the sole user of the primary source: an Ingersroll Rand H50A-SD compressor installed by Parks [87]. It was capable of supplying up to 1 kg/s of atmospheric pressure air or 0.1 kg/s at 862 kPa; in practice, however, steady operation with that compressor at atmospheric conditions could not be maintained at rates greater than 0.1 kg/s, and a peak rate of 0.24 kg/s could only be maintained for about ten seconds (that was after the required ~10-15 seconds for the flow meter to control up to that point). A second source was supplied from a pair of AFIT Kaeser BSD-50 compressors that were shared by all AFIT lab users and, in practical testing, were found capable of supplying flow at rates identical to the COAL lab compressor. Each of the three primary lines was equipped with an identical flow control scheme with appropriately sized hardware. In flow order, the control hardware on each line included a pneumatic solenoid valve (controlled via computer interface), a pressure regulator (manually controlled), a flow meter, and a flow control valve (manually or computer controlled). The flow control valves for the two larger lines were MaxFlow 3 models rated at 0.6 kg/s and 0.3 kg/s for lines 1 and 2, respectively, while line 3 used a Badger valve rated at 0.03 kg/s. The flow meters were wired to three Eurotherm 2404 PID controllers that interfaced with the laboratory control station via a Labview program. Signals from the control station were routed through the PID controllers that then interfaced with the control valves based on feedback from the flow meters. During the course of this research, Line 4 was plumbed as shown in Figure 3.14. It was fed to an

independent pressure regulator – the white component in the image – and then proceeded without any further control hardware. Immediately downstream of the regulator a split was added as illustrated by the blue arrows; the downward-arrow indicates the line used to feed the SiC seeder, which was discussed in Section 3.1.1.3.

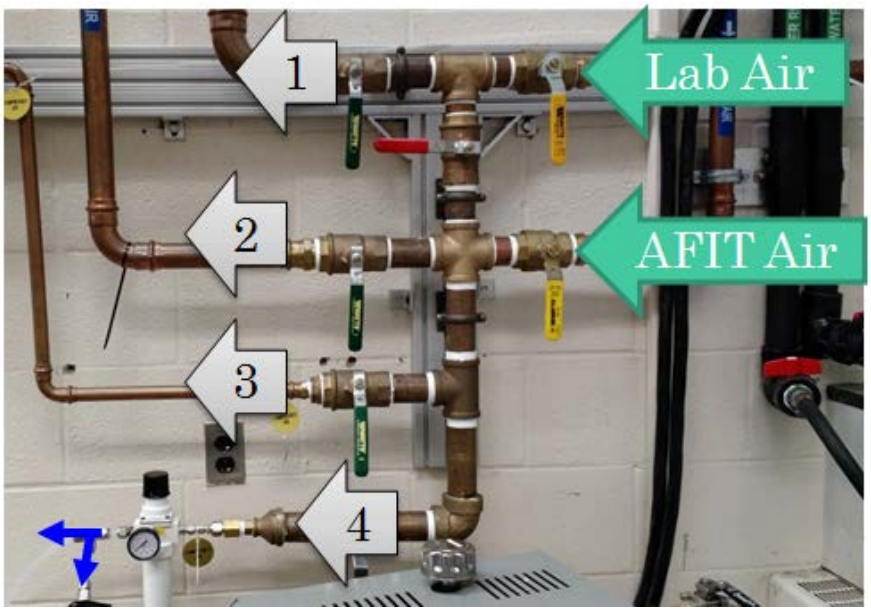

Figure 3.14: Laboratory primary air inlet branching

3.1.2.2. Fuel Supply

Various fuel sources were available to the COAL lab; however, the current study was limited to the use of gaseous propane. All fuel was stored in a dedicated fuel farm outside the lab. Propane was stored in liquid form in four tanks, and was forced through electric Zimmerman LPG liquid-to-gas vaporizers prior to being piped to the lab via four separate 1.27 cm copper lines. Control of the propane was achieved through a single Brooks SLA 5853 flow controller rated for up to 200 standard liters per minute (SLPM) of gaseous propane. This was a change from prior research where the propane was fed into three separate controllers. In Figure 3.15, an image is shown with a view looking toward the back of the lab. The four copper propane lines are highlighted by the red box; flow proceeded in all lines in the direction of the red arrow. The four lines joined into two at the point of the two large valves noted by the two

blue arrows. Downstream of those valves, the two propane lines then combined into a single line. For the Hencken burner tests described in Section 3.2.3, a small split was created in the propane line downstream of the two-to-one join as highlighted by the green arrow. The propane was then fed to the Brooks controller, which is shown by the purple arrow. A detailed image of the Brooks controller is shown in Figure 3.16. The upstream side is at the lower-right; downstream of the controller is a three-way valve that controlled the fuel feed to either the UCC experiment or the COAL lab's well-stirred reactor experiment. From the three-way valve the flow to the UCC was then split into six 1/8 inch steel tubes that fed the six fuel injection locations in the UCC cavity. At each of the six locations the fuel was forced through a baffle plate containing eight smaller holes in order to evenly disburse the gas momentum; a view of a baffle as installed in the combustion ring is shown in Figure 3.17.

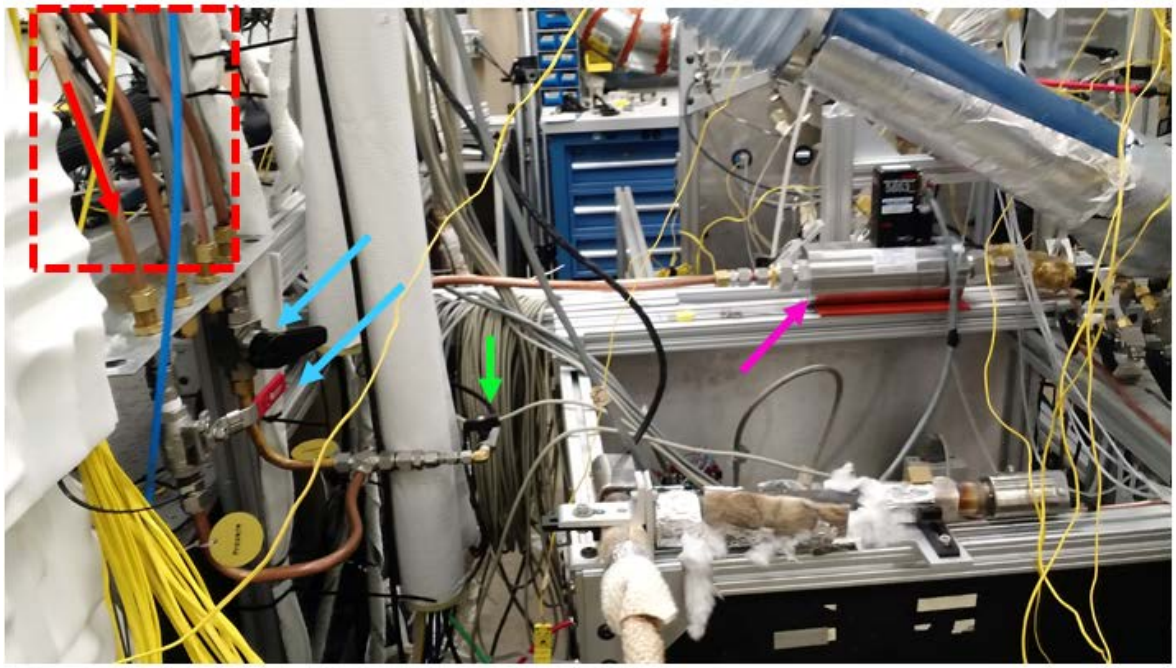

Figure 3.15: Propane lines joining upstream of the Brooks controller

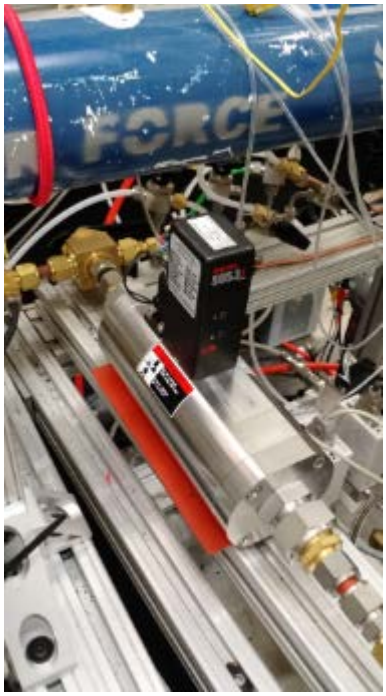

Figure 3.16: Brooks propane flow controller followed by a three-way

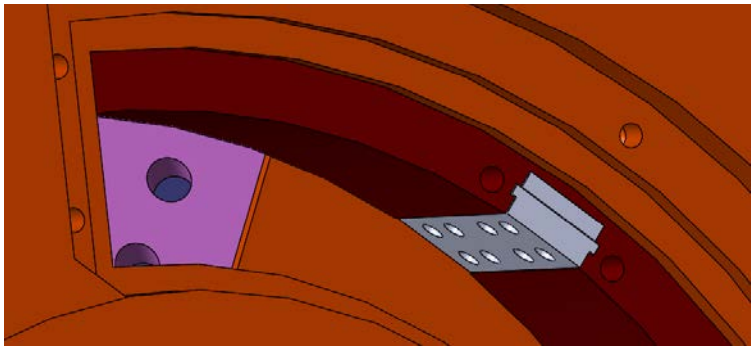

Figure 3.17: Fuel baffle as seen through the cavity aft window

The UCC rig also utilized gaseous ethylene to fuel the torch ignitor. The ignitor is shown in Figure 3.18 as installed on the back of the test rig (left) and fastened to the test frame for independent testing. In the image, the ignitor air line, fuel line, and spark plug are each indicated by blue, red, and yellow arrows. The spark was provided by a standard automotive spark plug. The plug itself was supplied by a Dongan ignition transformer, model A10-LA2. The transformer took 120V input and output 10,000V at 22 mA; power to the transformer and spark plug was controlled through the Labview interface at the control station. The flow rates to the ignitor were controlled with the MKS interface at the control station; rates of 25 SLM air and 3.5 SLM ethylene were consistently used. Notably, prior students observed that at those fuel/air set points the torch would burn self-sustaining after a brief spark. However, in the course of this research, no self-sustaining operation of the torch was achieved. A brief time was spent experimenting with various fuel and air flow rates, but no condition was found at which the torch would burn without continuous application of the spark. For practical purposes,

however, there was no reason to pursue that issue any further, as UCC ignition could generally be accomplished with only 5 – 15 seconds of torch burning; leaving the spark plug on for those durations did not present any operational concerns.

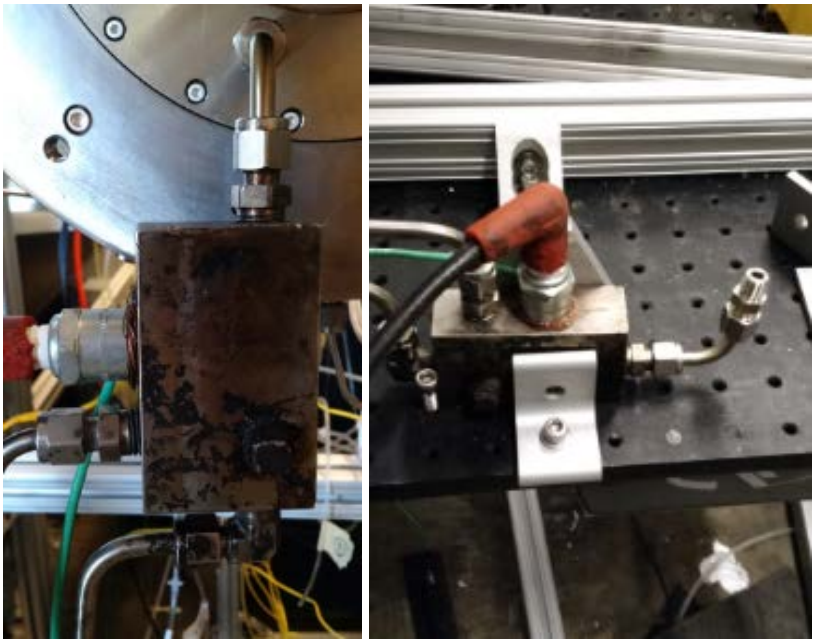

Figure 3.18: Ethylene-air torch ignitor installed on rig (left) and positioned for component testing (right)

3.1.2.3. Ventilation

The COAL lab contains a number of equipment items and tools related specifically to emissions that have evolved substantially over the course of this work. One of the first changes to the lab setup was implemented by the department lab technicians in response to concerns expressed over the emissions levels generated by prior tests. A contractor was hired to install eleven sensors throughout the lab: three to measure raw concentrations of carbon monoxide (CO), three for hydrogen (H), two for oxygen (O), and three to measure propane as a percentage of its lower explosive limit (LEL). In the left image of Figure 3.19 a sample sensor installation is shown just above the UCC rig. The right image shows the sensor control panel that is installed in the hallway, outside and immediately to the right of the lab entrance. In Figure 3.20 the layout of the sensors throughout the COAL lab is illustrated with respect to the three

primary resident experiments: the UCC, the well-stirred reactor (WSR), and a materials testing setup called the HVOF. A black arrow is pointing at the east wall. All three LEL sensors were installed near the floor (propane being heavier than air), while the remaining sensors were installed high. The CO/H/O sensors were distinguished from one another by color. Looking up, a ring of material was visible at the bottom of each sensor as indicated by the red arrow in Figure 3.19. The material colors were white, red, and blue for the CO, H, and O sensors, respectively. The black-boxed "E" points to the East wall, and the yellow and red circles represent wall-mounted alarm lights associated with the alarms, which will be discussed in the upcoming paragraphs.

Figure 3.19: CO sensor above the UCC test stand (left) and hallway control panel (right)

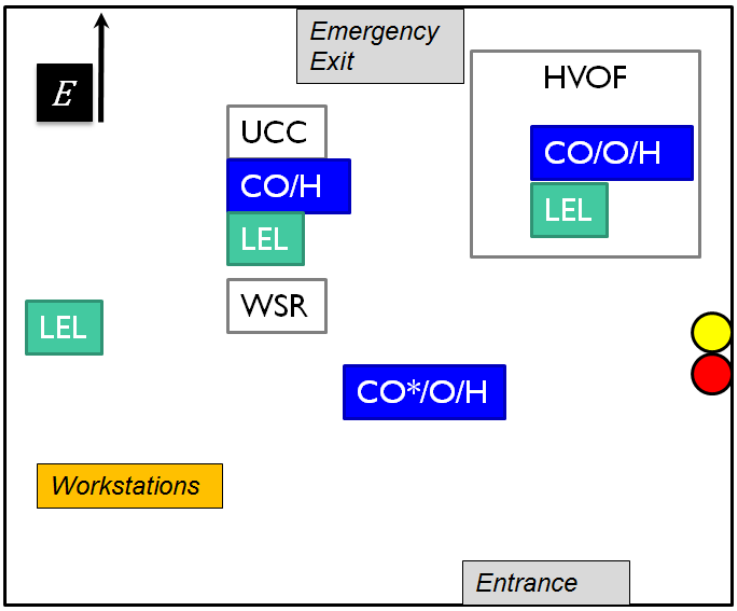

Figure 3.20: COAL lab gas sensor layout

The impact of the sensor installation was immediate. During normal test procedures, the CO sensor on the ceiling (indicated with the asterisk in Figure 3.20) routinely registered CO emissions. During low-flow (< 0.1 kg/s) and fuel-lean operations, the measured quantities seldom rose over 5 ppm. However, during rich, high-flow operations the sensor very quickly exceeded its first threshold of 20 ppm. After exceeding that threshold the system was programmed to begin a continuous strobe of the yellow alarm light on the south wall (shown in the figure). This was accompanied by illumination of the "A1" row on and emission of a low-volume high-pitch alarm noise from the hallway control panel. The A1 illumination appeared above the sensor that was generating the alarm – the ceiling CO sensor, for example, was number 11. The display above the alarm lights was set to scroll continuously, so an observer could see the measured values from all sensors over the course of about ten seconds. If the UCC operating conditions were maintained at those levels, then the second threshold – "A2" – was exceeded at 35 ppm of CO. At the A2 condition the sensor system was program to flash the red alarm light on the south wall and generate an exceptionally loud alarm within the lab. In any

case, if an alarm was activated, lab operators could disable it by pressing the green "OK" button on the hallway control console.

The A2 alarm condition was established to inform personnel of a condition that presented immediate danger and would require evacuation of the lab space. Presumably, the threshold of 35 ppm CO was selected because it was the strictest published limit of CO exposure by the National Institute for Occupational Safety and Health (NIOSH) [99]. However, upon a closer examination of the reference, that recommended exposure limit (REL) is followed by the time-weighted-average (TWA) designation. That indicates an exposure limit averaged over a standard 40-hour work week. That is, exposure to concentrations less than or equal to 35 ppm continuously over a 40-hour work week is considered to have no health or safety effects. Instantaneous exposure to that concentration is therefore harmless. In fact, the recommended instantaneous exposure ceiling is given in the above reference as 200 ppm. At concentrations above 200 ppm, without breathing protection, personnel could expect the onset of the symptoms of harmful CO exposure; levels at or above 1200 ppm are defined as Immediately Dangerous to Life and Health (IDLH).

COAL lab operators raised these issues with the lab technicians and the gas sensor contractor. The contractor stated that the system could be reprogrammed, but it would require a new contract and would be expensive (an exact quote was not obtained). At the time that this issue developed, funding was not immediately available for such an effort. Furthermore, as the workaround was relatively simple (hitting the OK button), it was deemed a somewhat low priority. UCC testing continued, then, with the routine use of "spotters" whose duties entailed watching the CO sensor on the ceiling and going out the hallway to hit the OK button as needed. The caveat to this approach was that the CO sensor displayed an "out of range" value when it exceeded 100 ppm. Therefore, as the CO concentrations could consequently not be known with any certainty at that point, operations ceased to allow the room CO levels to dissipate before resuming. This procedure was approved by lab technicians.

The fundamental reason for the emissions issues was the configuration of the UCC exit plane. The emissions from the HGV were at high velocity with very dominant tangential components. The resultant exhaust was expelled radially from the test rig; while the exhaust ducting was equipped with dual fans and provided high levels of suction, it was not sufficient to capture all of the high-velocity radial components of the fumes. This was deemed acceptable in large part due to the research requirements that dictated access to the HGV exit with emissions probes and optics. However, when planning for PIV testing, the determination was made that expelling the SiC seed into the lab environment would present an unacceptable safety risk. Furthermore, the PIV testing would not require any access to the HGV exit. Therefore, a new outer cowling was designed and installed at the UCC exit in order to feed all of the emissions axially directly into the exhaust duct. The extended cowling is shown in Figure 3.21 during a test run (blue flame is visible through the quartz window). The cowling was designed such that it utilized the existing exit instrumentation ring and a set of on-hand 5.5 inch screws of the same thread type as the shorter instrument-ring screws. It was 10.8 cm (4 ¼ inches) long with ID and OD diameters of 10.9 and 11.9 cm (4.3 and 4.7 inches), respectively. It was effective during operation at eliminating the emissions issues; no instances of seed particle escape were observed, and readings from the lab gas sensors remained at zero.

Figure 3.21: Extended exhaust cowling for PIV/PSEV testing

The final lab modification came to the exhaust ducting itself. As seen in Figure 3.21 and to the left in Figure 3.22, the original ducting consisted of a single 10-inch diameter elbow attached to a vertical duct that fed into the primary lab exhaust system. During late-phase testing, a novel camera placement technique was desired that was hindered by the large vertical component of the duct. In response to that requirement, the single elbow and vertical section were replaced by a series of 6-inch diameter elbows and an angled straight section as shown on the right in Figure 3.22. Also observable in the image is a large rectangular plate mounted nearly flush with the UCC back wall; that part was a component of a "box" that was being designed by a visiting research as an enclosure for the aft portion of the UCC as further guarantee of exhaust capture; the UCC was not run with the full enclosure installed during the research for this document. The new exhaust duct path allowed clearer access for a novel high-speed imagery setup, which is also shown in the figure; one of the Phantom cameras can be seen mounted where the old vertical duct had previously been installed, and a second camera was mounted below out of the frame of the image. Execution of test with that configuration is an item of future work.

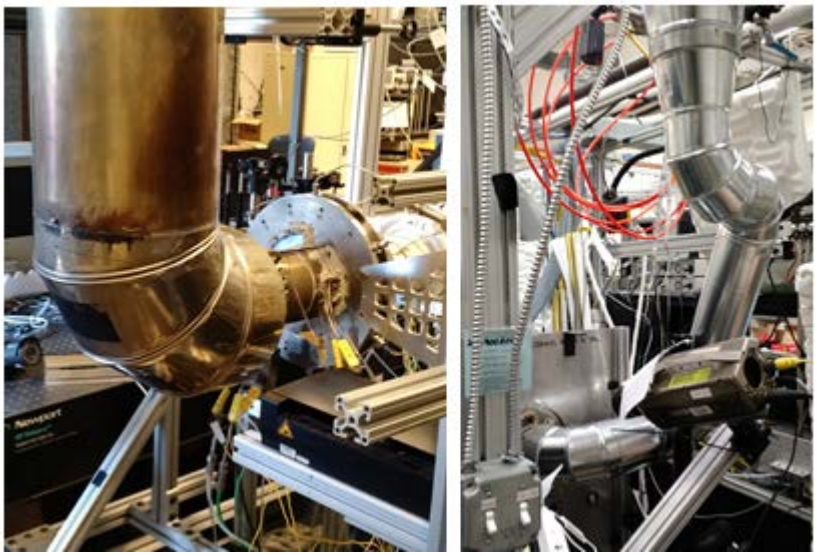

Figure 3.22: Legacy exhaust system (left) and modified system (right)

3.1.2.4. Sealant

As operations began with the new v3 hardware, leakage problems persisted in spite of the attempts at improving the mechanical sealing between the combustion cavity and the front and back plates. Observations of leak events indicated that fumes were escaping around the instrument blocks on the back plate as well as from the outer ring. Flames would develop at the instrument blocks and then proceed to engulf the remaining fumes around the rig. Additional flame leakage was observed from around the quartz window. Initial troubleshooting focused on the window; a variety of dry gasket options were investigated including a mica material that was favored in the combustion test rigs at AFRL; none appeared to resolve the issue. At the recommendation of ISSI, a high temperature muffler and exhaust repair sealant was applied around the window, the exhaust cowling, and the instrument blocks – the application may be observed in Figure 3.21. The sealant was successful at preventing leaks and permitted extended test periods with no flame or emission incidents. The sealant that was used is pictured on the right in Figure 3.23. It was rated for continuous exposure up to 1000 F and

intermittent exposure up to 1500 F. A substantial drawback, however, was that if the test configuration need to be changed then removal of the material was laborious as it cured rigidly. Additional options were subsequently investigated for sealing other components of the rig: the center image of Figure 3.23 shows "Ultra Copper," which is rated up to 700 F, and the left image shows "Ultra Blue," which is rated up to 500 F. Both of those materials are silicone so they remain pliable when cured; removal still required some effort, but risk of damage to parts was greatly reduced and in many cases the sealant was easily "peeled" away. The Ultra-Copper was successfully used on the interfaces between the front/back plates and the combustion rings as well as around the fuel injectors on the outer diameter. The Ultra-Blue was used as a replacement for the Fibrefrax seal that had been the gasket of choice for the interface between the air supply duct and the diffuser; it was used as well at the interface between the diffuser and the front plate. Finally, some seed particle leaking was observed at the numerous joints in the new exhaust ducting arrangement shown in Figure 3.22. The Ultra Copper was therefore applied liberally at the joints and interfaces in the ducting.

Figure 3.23: "Wet-seal" options tested in the COAL lab

3.1.3. Instrumentation

Pressure data were obtained from 0.16 cm stainless steel static and total pressure ports at a variety of locations. Primary pressure data acquisition was facilitated by a 32-channel Esterlin Initium pressure scanner. Additionally, two XT-190 and two XTE-190 Kulite 5 psid

pressure transducers were included to obtain higher fidelity of certain critical measurements. Due to the relatively small scale of the pressure variations within the test rig, capturing differential values between a pair of locations based on independent data from the Initium pressure scanner was susceptible to potentially opposing variations from the two sources. The Kulite transducers combated that error by taking the required delta pressures directly. To illustrate the plumbing for the "deltas," a representative layout is shown in Figure 3.24 and a graphical representation of their locations on the test rig is shown in Figure 3.25. Each measurement retained routing to a discrete channel on the Initium scanner. Selected points, however, were split to the Kulite transducers as well. Three of the paired measurements, represented by the identification numbers K1, K2, and K4, were intended to capture the difference between the total and static measurements at the upstream inlet, the core flow split, and the cavity flow split, respectively. The fourth measurement, K3, measured the drop in total pressure across the cavity air injection panels. The pressure delta $\Delta = P_t - P_s$ from the Kulite probes and other locations was used to calculate the local point velocity from the expression in Eqn. (59). Mass flow can then be estimated based on Eqn. (60). Installation of the Kulite probes was accomplished by mounting them in an existing probe baffle – the white component in Figure 3.26 – and mounting that baffle to the frame near the UCC. As with most pressure transducers, the Kulites had a specific 10V input power requirement. The COAL lab had the necessary conversion boards on hand; two new boards were installed on the instrument rack at the control station as shown in Figure 3.27 and each board powered two Kulite probes.

$$v = \left(\frac{\mathrm{P_t} - \mathrm{P_s}}{\rho}\right)^{1/2} \tag{59}$$

$$\dot{m} = \rho v A \tag{60}$$

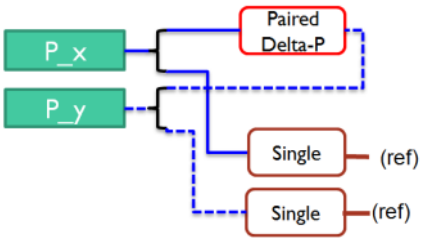

Figure 3.24: Representative pressure probe routing

ID	Description of Differential Pressure Measurement
K1	Inlet Duct Total - Static
K2	Core Flow Total - Static
K3	Outer Flow Total - Cavity Total
K4	Outer Flow Total - Static

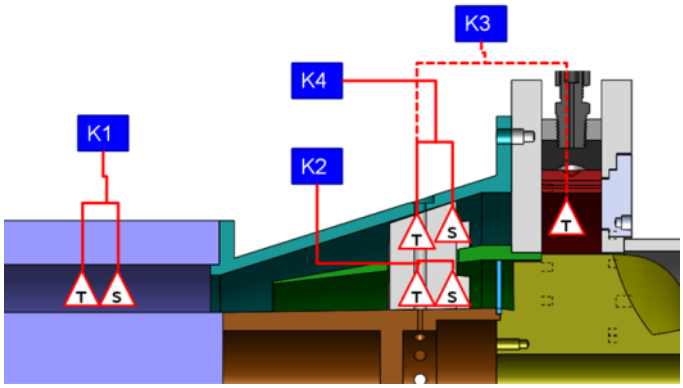

Figure 3.25: Delta-pressure measurement locations

Figure 3.26: Kulite probe installation

Figure 3.27: Kulite power boards

Remaining pressure probe installations consisted of simple tube designs inserted through dedicated ports around the diffuser and in the cavity instrumentation block (Figure 3.8). In Figure 3.28, a view of the diffuser inner diameter, middle diameter, and support vane components is shown. Example total pressure probes are illustrated in yellow at two installation locations: at the front of the diffuser upstream of the flow split, and in the outer

(cavity) flow path; total probes were also installed in the inner (core) flow path at analogous locations. The outer/inner total probes were oriented such that they were radially centered between their passage outer and inner walls and also circumferentially centered between pairs of support vanes. The probe heads were axially positioned to align with the maximum vane thickness. Static probes were installed in similar locations flush with the walls. During the v2 testing as documented in Chapter 4, there were two total pressure probes and one static probe installed at the front of the diffuser, two total probes and one static probe in the outer path, and one total and one static probe in the inner path. Instances of multiple total probes were for redundancy; while they were at different circumferential positions, the symmetry of the diffuser would theoretically give identical measurements at any given axial-radial coordinate around the circumference. Pressure probes in the v2 CC were installed as illustrated in Figure 3.29. One redundant total-probe pair, H1 and H2, was installed to be approximately at the axial halfway point of the CC. A second redundant pair, Q1 and Q2, was installed at the quarter point (relative to the instrument plate), and a fifth probe provided static pressure data. The remaining two access points visible in the instrument block were used for thermocouples (not shown).

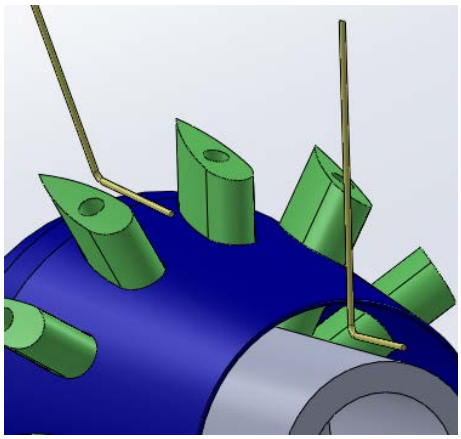

Figure 3.28: Sample diffuser pressure probe installation

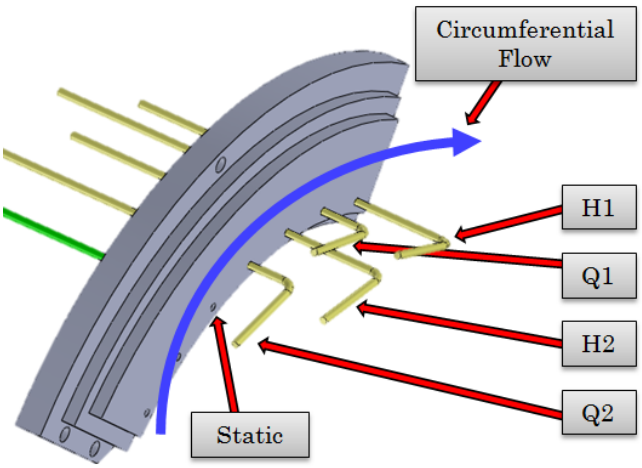

Figure 3.29: v2 cavity probes

A note must be given regarding probe installation in the diffuser. While probes could feasibly be installed at the front of the diffuser and in the outer flow path while the components were apart, installation into the core flow path required the parts to be assembled. The constraints of the installation space therefore required the use of straight tubes that were fed through purpose-drilled holes in the outer and middle diameter pieces. For total pressure probes, the straight tubes were then bent into the flow after being fed through. This became a limiting factor when attempting to improve the pressure measurement scheme as will be discussed next.

In response to initial test and CFD results, which will be discussed in Chapter 4, two major enhancements to the pressure measurement scheme were pursued. First, a set of pitot-static probes were acquired from United Sensor, model PCA-8-KL. However, due to the installation constraints, the new probes could not be installed in the core flow path without significant and difficult machining. By way of a simple ¼ inch hole in the diffuser outer diameter, however, a rake of probes were installed as illustrated in the left image of Figure 3.30. In that image, a view is given from the front of the diffuser looking aft; the middle diameter splitter is visible in the foreground, the diffuser support vanes appear downstream, and in the background the air injection panels can be seen in the outer path. The axial location of the probe heads was about 2.5 cm downstream of the flow split – approximately centered between the flow split and the leading edges of the diffuser support vanes. The new probes were also used at the diffuser entrance and the HGV exit plane.

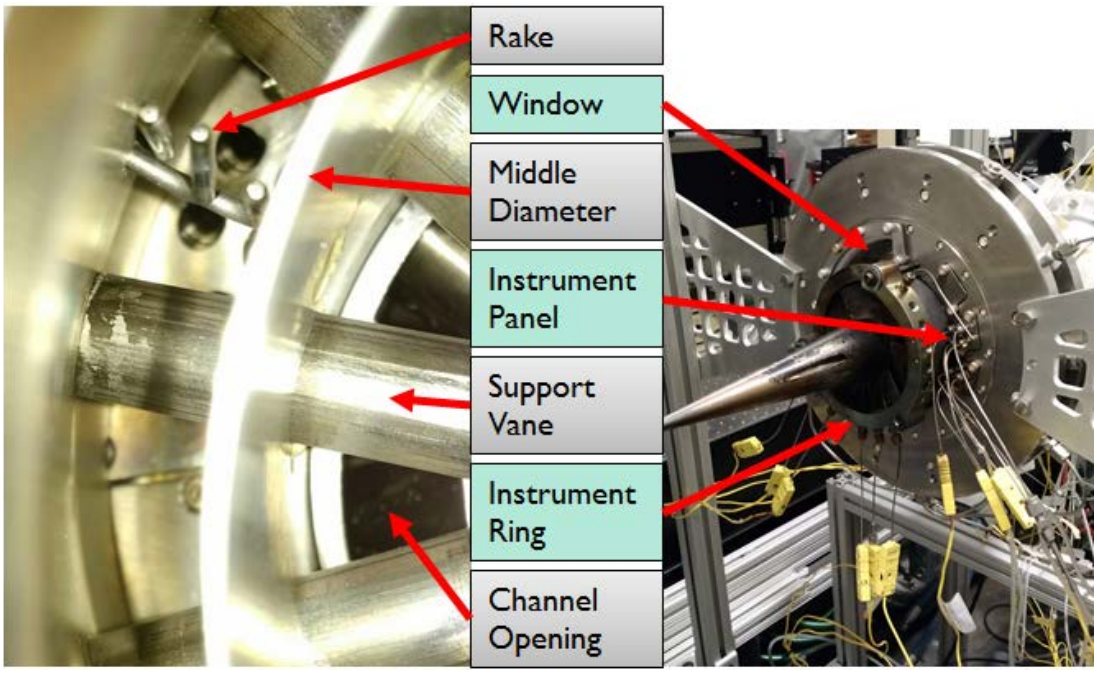

Figure 3.30: Pitot-static probe rake in diffuser outer diameter (left) and aft instrumentation setup (right)

Temperature measurements were provided by 0.16 cm diameter Omega brand K-type thermocouples (range 73 – 1523 K, error 0.75%). The primary thermocouple placement location was on the cavity aft wall by way of modular instrumentation panels as shown in Figure 3.8; an example of a thermocouple illustration on UCC v3 is shown in the right image of Figure 3.30. In that image two of the panels have been drilled for Swagelok instrument interfaces (both temperature and pressure) while the third has been left blank. Also shown is the exit instrumentation ring that was designed to place probes immediately downstream of the HGV exit.

To improve upon that concept, Gilbert [100] designed a thermocouple rake that placed seven probes directly into the exit plane of one of the HGV passages. Figure 3.31 shows a zoomed-in view of the probe heads and documents the method for determining their precise location. The relative pixel location in the image itself for each probe was converted into measured position along the radial height of the HGV passage. For example, the distance of

Probe 1 from the HGV inner diameter was 71 pixels that converted into 15 % of the total radial height.

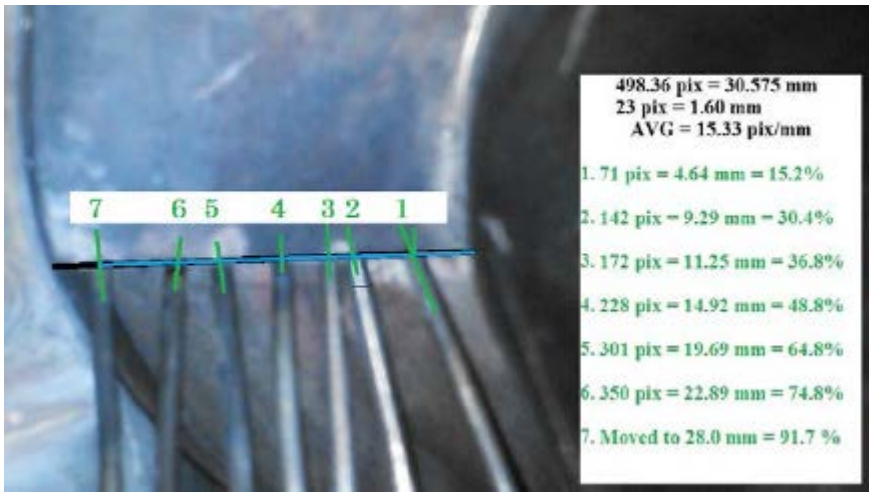

Figure 3.31: Aft view showing detail of thermocouple rake placement

3.1.4. Labview

Labview version 11.0.1 was the primary control mechanism for the laboratory equipment. Flow solenoids and air flow setpoints were linked to the software to enable dynamic manipulation of test conditions. Pressure and temperature data are supplied via standard data acquisition (DAQ) boxes, and data collection was fed to local text files. Text files were post-processed using Microsoft Excel. The functional Labview codes were largely unmodified from that developed by Wilson [90] and Damele [93] with the exception of the introduction of the additional data from the Kulite probes described in Section 3.1.3. Large portions of non-functioning code were removed, however, in attempts to improve performance. Further modifications were undertaken by Gilbert [100] to refine the collection of emissions and temperature data. The result of that work now exists as the primary UCC operation interface.

Labview programs were also called "VI's" as their file names included the ".vi" extension. There were two separate VI's utilized during UCC testing. The first contained all of the control interfaces mentioned above and including the interface with the spark ignitor. The UCC was

often run using that VI alone. However, a separate VI was required to collect pressure data through the Initium pressure scanner. In both cases, the capability was built in to store data to text files during testing. However, that capability was limited at the time of this research to the collection of instantaneous points. That is, pressing the "collect" button stored a single line of data from all available temperature and/or pressure channels to the specified text file that represented the instantaneous conditions. Therefore, to obtain time-averaged results, multiple collection events had to be accomplished.

The primary control VI was also responsible for temperature collection; however due to its complexity, after pressing the collection button several seconds elapsed while the code looped before the button could be pressed again. Thus the maximum data collection rate for temperatures was about 1/5 Hz. The Initium VI was much quicker – the only limit to the data collection rate was the speed at which the mouse button could be clicked. Thus, pressure data rates were typically on the order of 10 Hz. Thus, for a given condition during collection of pressure data (as comprises much of the Chapter 4 results), 30-50 samples were collected. Each line data in the text file included a timestamp and a customizable label that was used to denote the specific test condition. The files were comma-separated thus facilitating import into Excel. All samples for each test condition were then averaged to produce the final results.

3.2. Optical Diagnostics

Objective 2 of this research was to determine the effects of the complex cavity flow environment on the development and progression of the combustion event. Due to the foundational importance of that goal to the UCC as a whole, the decisions regarding rig design and test tool selection were made with interrogating the CC as a top priority. As a result, the UCC was developed with the unique capability of an optically accessible combustion cavity that then permitted application of a series of optical diagnostics; over the duration of this research, four diagnostic techniques were employed. Particle Image Velocimetry (PIV) and Particle

Streak Emission Velocimetry (PSEV) were invoked to measure the cavity velocity fields as will be discussed in Sections 3.2.1 and 3.2.2. Laser-Induced Breakdown Spectroscopy (LIBS) allowed measurement of local equivalence ratio as shown in Section 3.2.3, and Thin-Filament Pyrometry (TFP) provided one-dimensional profile measurements of the temperature as shown in Section 3.2.4. Each technique will be detailed further in the following sections. The relatively robust suite of available optical interrogation techniques was facilitated almost entirely by Innovative Scientific Solutions, Inc. (ISSI) and in particular Dr. Larry Goss and Corey Goss who served as the operators of the laser, cameras, and image processing software.

3.2.1. PIV

Understanding the velocity field in the cavity was an important step in accomplishing Objective 2; therefore, Particle Image Velocimetry was a logical choice as an experimental tool. As established in Section 2.3.1, PIV has long been used for a wide range of applications to produce accurate, planar-resolved velocity vector data. Such results also lend themselves well comparison with analogous computational results.

The COAL PIV system was driven by a Spectra Physics Quanta-Ray PIV400 10 Hz dual-pulsed Nd:YAG laser with frequency doubling to produce dual 532 nm pulses. The laser is currently installed in the lab as shown in Figure 3.32, just to the left of the computer control station. It was dependent on interfaces with the power supply and the AFIT water lines. The laser system itself was actually comprised of two beam generators as illustrated in Figure 3.33. The internal setup could be configured to generate two separate beams at wavelengths of 1064 nm (illustrated by the purple lines); however, in the figure the internal path is configured such that the two beams are combined and "frequency doubled" as they exit together from a single point. Frequency doubling is equivalent to halving the wavelength; thus the resultant beam was at a wavelength of 532 nm.

Figure 3.32: PIV laser power supply (foreground) and laser system (background)

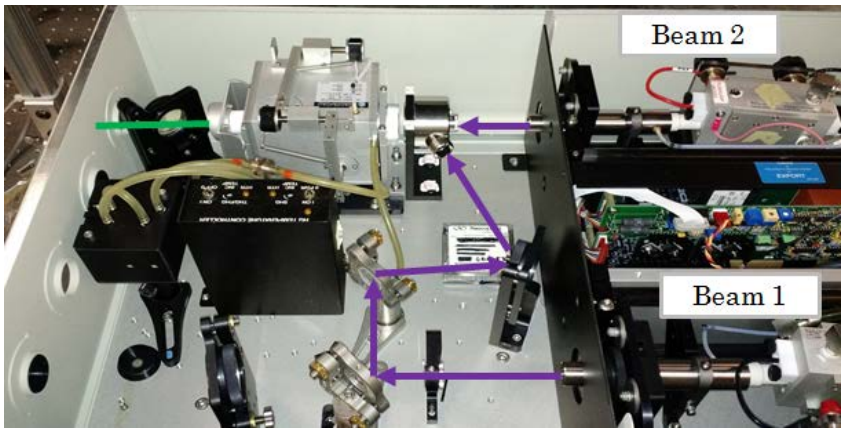

Figure 3.33: PIV laser internal setup

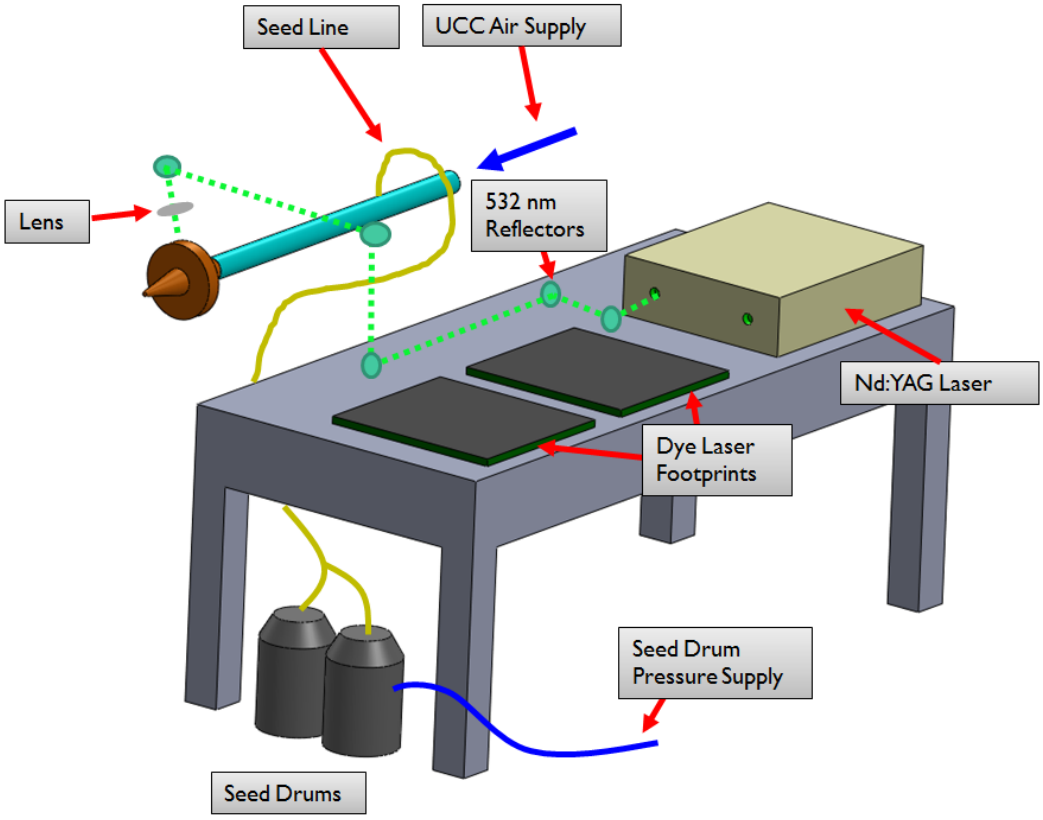

Figure 3.34: PIV laser beam path diagram

The beam was guided to a point over the top of the test rig, then through the modified access ports in the outer and inner rings. The laser beam path for PIV testing is shown in the

drawing in Figure 3.34 as a green dashed line. 532 nm reflectors (only one of which is called out by the label) were used to guide the beam from the exit of the laser casing, around other hardware components, and up to the UCC entry point. The drawing also shows the location of the SiC seeders and the approximate path of the seed plumbing from the seeders to its entry point upstream of the UCC. In terms of laser operation, this document will advise that external consultation with ISSI be maintained for that purpose.

PIV imagery was captured with a PCO 2000 interline transfer camera positioned about 0.6 m aft of the quartz window at a slight angle in order to accommodate the larger 25 cm exhaust duct. The camera was operated in double pulse mode to match the 10 Hz laser pulse rate. Image capture was accomplished with dedicated software provided and operated by Dr. Goss, and a 20 μs time separation between images was utilized for all PIV measurements. The images were processed in batch mode using cross correlation software. The interrogation box utilized during processing was 32x32 pixels or about 1x1 mm. Accuracy was determined from a conversion factor, which was a built-in function of the software; its computation was based on the spatial (or pixel) resolution of each streak signal and the exposure time of each image (1/10 s in this case). For the PIV data reported here, the conversion factor was 1.68 m/s/pixel, thereby yielding an accuracy of <0.1 pixel or 0.17 m/s.

To minimize potential damage to the rod lens, the energy in each laser sheet could not exceed 25 mJ. Additional unique constraints were imposed by the geometry of the UCC test rig. First, the small wall entry windows limited the size of the laser light sheet. The resultant field of view was limited to a trapezoidal region spanning roughly 20° of arc. Secondly, the PIV measurements required a relatively high density of seed particles. As detailed in Section 3.1.1.3, seed particles were introduced into the system in the inlet duct several diameters upstream of the diffuser. As a result, the particles distributed themselves throughout the test rig. They were therefore fed into the cavity from the air drivers immediately opposite the quartz window; consequently, the particles coated the window leading to degraded and

ultimately untenable obstruction of the visible signal. Whereas the seed levels for the PSEV permitted collection of nearly a dozen data points over the course of about 1.5 hours, the seed levels required for the PIV testing resulted in excessive window accumulation after only three test conditions, or about ten minutes. The threshold at which window accumulation was deemed unacceptable was determined by the quality of the image being observed by the PCO camera; when seed traces could no longer be resolved, the testing was stopped. In the specific case of the PIV testing accomplished for this study, the window had already been subject to cracking due to installation errors and prior test cycles. Furthermore, the window had been sealed using the hard-setting exhaust sealant described in Section 3.1.2.4. As a result, the window could not be removed without destroying it completely; unfortunately, it was the last remaining spare at the time. Therefore, only three test conditions were collected in the initial campaign. Further testing with a new window commenced later in the test program.

3.2.2. PSEV

As an alternative to PIV, PSEV measurements were also obtained. PSEV involves capturing particle streaks by way of an appropriate camera exposure. The UCC setup utilized a monochrome Phantom v12 camera with an 80 mm F1.2 micro lens and an exposure rate of 126 μs (7900 fps). Traditional PSEV approaches have relied on a continuous-wave (CW) laser for steady illumination of the seed particles. However, a non-laser approach was chosen for this application. The seed particles emit natural blackbody radiation at the temperatures seen within the UCC combustion cavity. Thus, that radiation may be captured with a relatively simple setup requiring only a single high-speed camera. The resulting spatial resolution was ~130 μm per pixel that, in conjunction with the exposure time, yielded a conversion factor of 1.032 m/s/pixel and a corresponding accuracy of 0.10 m/s.

In Figure 3.35, a typical image processing sequence is presented, beginning with the raw image in the upper left. In the first post-processing step, application of a Laplacian convolution

filter (detailed in Section 2.3.3) separated the flame emission from the particle streaks, thereby yielding clear particle streaks as shown in the top right image. After filtering, analysis was conducted using cross-correlation. Three sequential post-processed frames are shown in the bottom left of Figure 3.35 (colored in order by red, green, and blue, via the post-processing software). Thus, clear velocity vectors are revealed by the streak progression. Finally, a 25-image composite image (colored by frame number) appears in the bottom right. The path lines demonstrate sharp inward turning as they are entrained in the hybrid guide vane (HGV) passage below. The oddly-shaped tracks in the upper right of the image were not particles, but rather an emissive flame structure that was unable to be completely filtered out. There were two important drawbacks to this technique that must be noted. First, with only a single camera, there was no ability to resolve the z-component (into/out-of the page) of the motion of the streaks. Thus, while the resulting images were 2D, they were more accurately discussed as measurements of the bulk velocity, only – there was no resolution of the depth of the field of view. Secondly, the emissivity of the seed particles produces a detectable signal to a visible-spectrum camera only above temperatures of about 900 K. Any particles not heated to at least 900 K will not be visible. There are solutions to each of those drawbacks: (1) to obtain resolution of the axial velocity component, a dual-camera (stereo) setup may be employed, and (2) IR cameras would theoretically be capable of capturing the motion of relatively cooler seed particles.

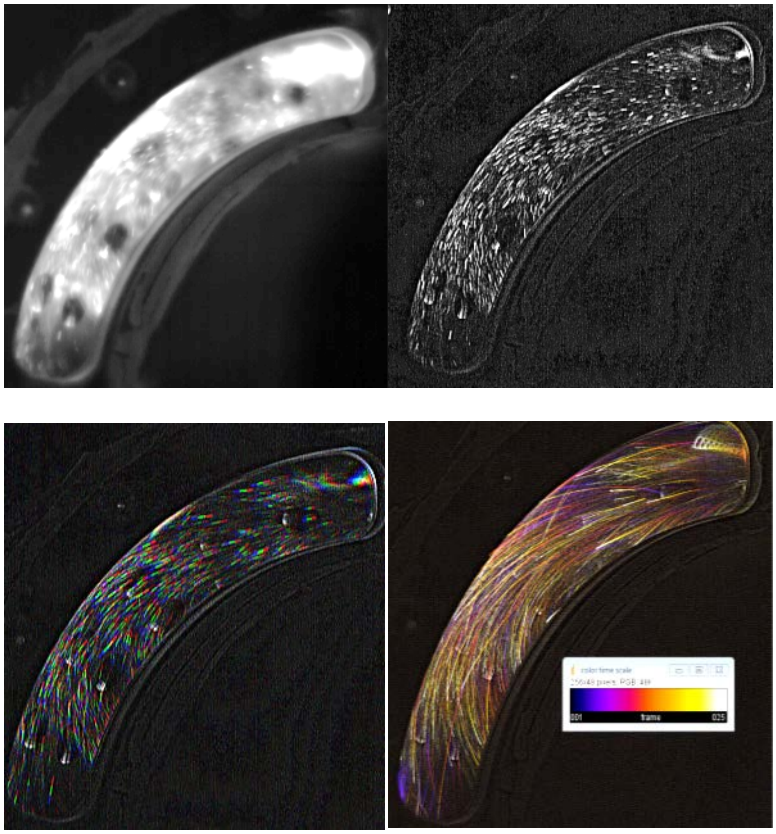

Figure 3.35: Sample PSEV image processing sequence

3.2.3. LIBS

Understanding the velocity field by way of PIV and PSEV was one important step to the accomplishment of Objective 2. The next goal was to understand the interaction of the fuel and air and the environment in which the combustion was occurring. One important parameter describing both those characteristics is the equivalence ratio. While the fuel flow was controlled for each test condition by setting the level of ϕ_{cav}, measuring the local equivalence ratio, ϕ, within the cavity would enable evaluation of exactly where the fuel was going and what the chemical composition was within the flame region. One technique particularly suited for that task is laser-induced breakdown spectroscopy (LIBS).

The LIBS method is well established for composition analysis of solid, liquid, and gaseous media as detailed in Section 2.3.4. In summary, the technique works by introducing a

short, high-powered laser pulse to induce a dielectric breakdown within the test sample. The visible emission from the breakdown can be captured and spectroscopically analyzed for atomic and molecular concentrations. A sample spectrograph from a Hencken flame is shown in Figure 3.36. The relevant spectral lines were clearly observable for atomic nitrogen, hydrogen, and oxygen. In the figure, the dark blue line was a baseline measurement of air only; the light green line was a lean propane-air mixture, and the light blue line was a rich mixture.

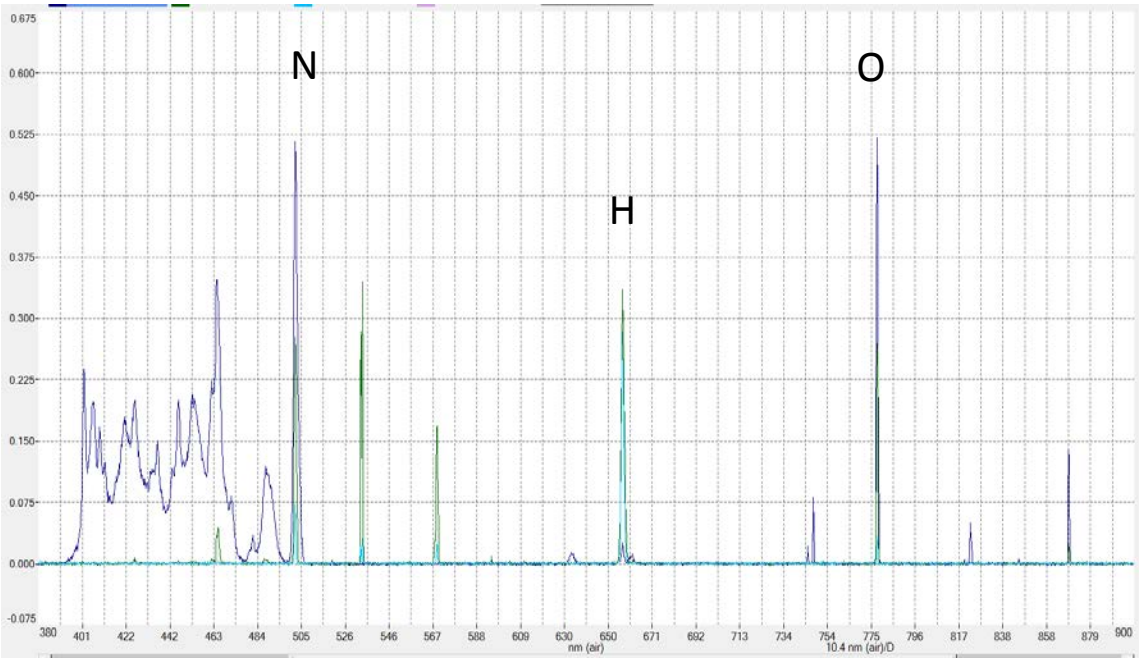

Figure 3.36: Sample LIBS emission spectrum

For application to the AFIT UCC test procedure, the integrated intensity of the H-atom emission at 654 nm was divided by the integrated intensity of the N-atom line at 870 nm. The calibration procedure was performed separately by taking LIBS measurements within a Hencken flame; this was also accomplished in the COAL lab with the setup illustrated in Figure 3.37; therein, the spectrometer is the red component in the foreground, and the Hencken burner is in the center beneath an exhaust guide. Flow rates required for burner operation did not exceed 1 SLM for fuel and 5 SLM for air. The Hencken burner was plumbed for fuel from a branch off of the primary propane lines, downstream of the laboratory valves, but upstream of

the Brooks controller. The fuel was metered with a 5 SLM controller linked to Channel 7 of the MKS control system. The core air was fed from a branch off of the #4 air supply line and metered by a 20 SLM controller linked to Channel 8, while the co-flow air was fed by the ignitor-air controller on Channel 1.

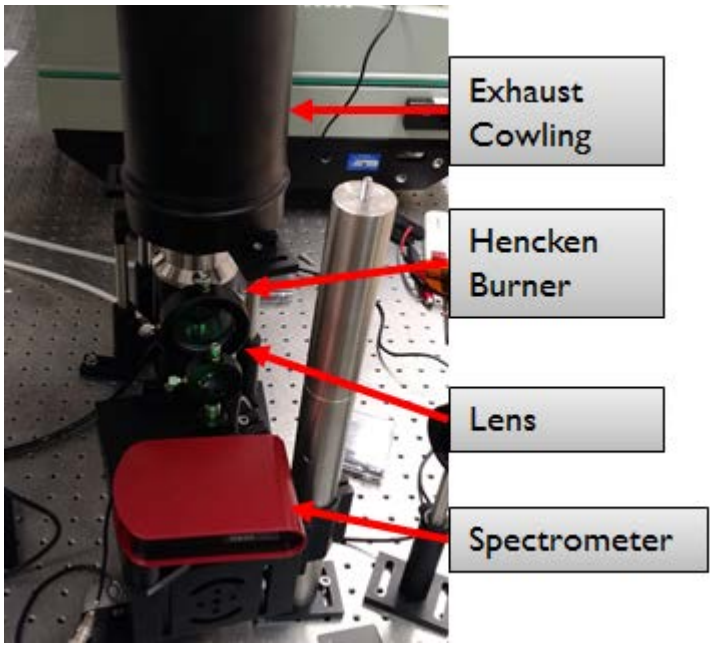

Figure 3.37: Hencken burner setup

LIBS measurements of the atomic H/N ratio were correlated with the known equivalence ratio of the Hencken flame, which was, in turn, computed from MKS inputs. The resulting calibration curve is shown in Figure 3.38. It should be noted that while the ratios of both H/N and H/O were sensitive to ϕ, H/N was selected due to the relatively low sensitivity to laser power that was observed during calibration. Also during the calibration, the Hencken flame consistently blew out at equivalence ratios $\phi < 0.6$; consequently no data were collected in that range. An identical procedure was subsequently applied during UCC operation wherein integrated H/N data were collected. The observed integrated intensity was then correlated to equivalence ratio using the third-order polynomial shown in Figure 3.38. Although the trend line extends beyond the collected data points, the formula was only applied to conditions that

fell within the range of the collected calibration data, $0.65 < \phi < 1.8$ $(2.77 < H/N < 24.78)$. Additional data from the Hencken calibration testing is provided for reference in Appendix C.

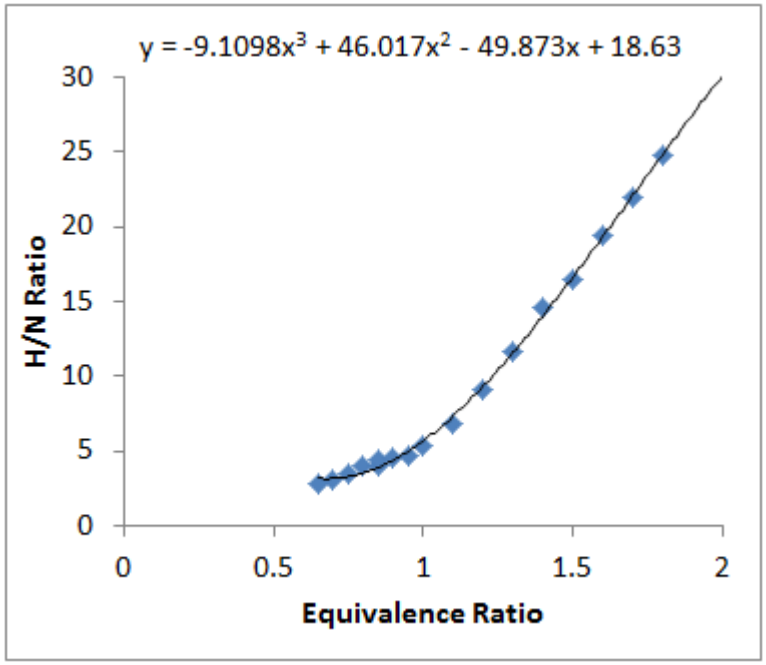

Figure 3.38: Hencken flame calibration curve for integrated H/N atomic emission as a function of equivalence ratio

For application to the UCC, the LIBS laser pulse was initially directed along the PIV beam path previously shown in Figure 3.34. However, due to the high energy required to obtain a readable signal in the UCC environment (~110 mJ), the 20 mm windows were consequently damaged. One proposed fix was to replace the inner window with a 20 mm lens, thereby increasing the beam cross-section as it passed through the window and spreading the energy over a wider area. A second, simpler fix was to direct the pulse through the aft quartz window; that second fix was chosen for its ease of execution. An added benefit of that approach was the ability to obtain measurements from different circumferential positions. However, the axial position of the measurement was limited by (1) proximity to the aft quartz window and (2) proximity to the resultant reflection from the surface of the air injection plate. In the latter case, if the pulse was focused too close to the wall, it would be indistinguishable from its own

reflection. The final location of the LIBS measurement is shown in Figure 3.39. It was selected in such a way that there would be room for experiments to vary in both the radial and the circumferential directions.

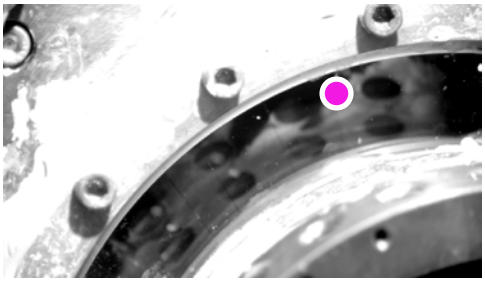

Figure 3.39: LIBS measurement location

3.2.4. TFP

Objectives 2 and 3 require understanding the distribution of the temperature within the UCC cavity and exit plane, respectively. Temperature measurements and analyses provide indications of fuel/air mixing, the location of flame fronts and reaction zones, and cues as to where hardware cooling may be required. One common method for collecting temperatures is a thermocouple, the use of which was discussed previously in Section 3.1.3. However, a higher fidelity measurement in both time and space was discovered in the method of Thin Filament Pyrometry (TFP).

Thin Filament Pyrometry utilizes thin (125 μm) filaments of β-SiC installed perpendicular to the local flow field. Due to the high emissivity of the material (as in the case of PSEV), the natural blackbody radiation of heated filaments may be captured relatively easily. Work acquiring TFP measurements within the combustion cavity and at the exit plane was carried out primarily by Gilbert *et al.* [101]. Data were collected by two Bobcat Imprex monochrome cameras with serial numbers 280072 and 280087, respectively. The cameras were both fitted with 75 mm lenses and 990 nm filters with 10 nm bandwidth. A single point calibration for the filaments was performed at the start of each test at the highest temperature

condition ($\phi_{cav} \cong 1.0$) on both cameras. A DFP 2000 Disappearing Filament Optical Pyrometer from Spectrodyne, Inc. with a central wavelength of 655 nm was attached over the lens of the second camera for the calibration. The pyrometer used a NIST traceable algorithm that allowed simultaneous test point collection and calibration to account for the high degree of fluctuation in the measured flames. Importantly, as with the PSEV technique, the signal to the visible-range camera was only viable at high temperatures – in this case, no temperature lower than 980 K was recorded. As discussed in Section 3.2.2, one solution to that issue in future work would be to employ a high-speed infrared camera for image acquisition. While that would be a simple fix in concept, it would also require replacement of the aft quartz window with a substantially more expensive sapphire equivalent.

The images in Figure 3.40 show the installed filaments in the CC (left) and the HGV exit (right). In the CC the filaments were installed such that they spanned from the top edge of an HGV airfoil to the outer diameter of the cavity; Figure 3.41 provides a more detailed illustration of their placement. They were anchored to the HGV surface with shallow 0.5 mm pilot holes that were drilled via electrical discharge machining (EDM) at the AFIT machine shop; no holes were drilled in the outer ring. They were held in place with Cotronics 907 Regular Grade (fireproof) Adhesive. Their labels were defined by their axial position as a percentage of the total CC axial span with 0% representing the front cavity wall, which contained the cavity air drivers (shown in pink in Figure 3.41); cavity filament numbering began with number one at the fore-most location. As shown in Figure 3.40, the exit plane filaments were installed such that they spanned the passage between the suction side of one HGV airfoil and the pressure side of the next. They were similarly held in place by 0.5 mm EDM-drilled holes; the holes were drilled completely through the trailing edge of one vane and then partially into the surface of the next. The same adhesive was utilized. The filament labels were defined in a similar fashion as percentages of the total exit passage radial height with 0% representing the passage inner

diameter; exit filament number one began closest to the ID. All of the filaments and their definitions are summarized for reference in Table 3.2.

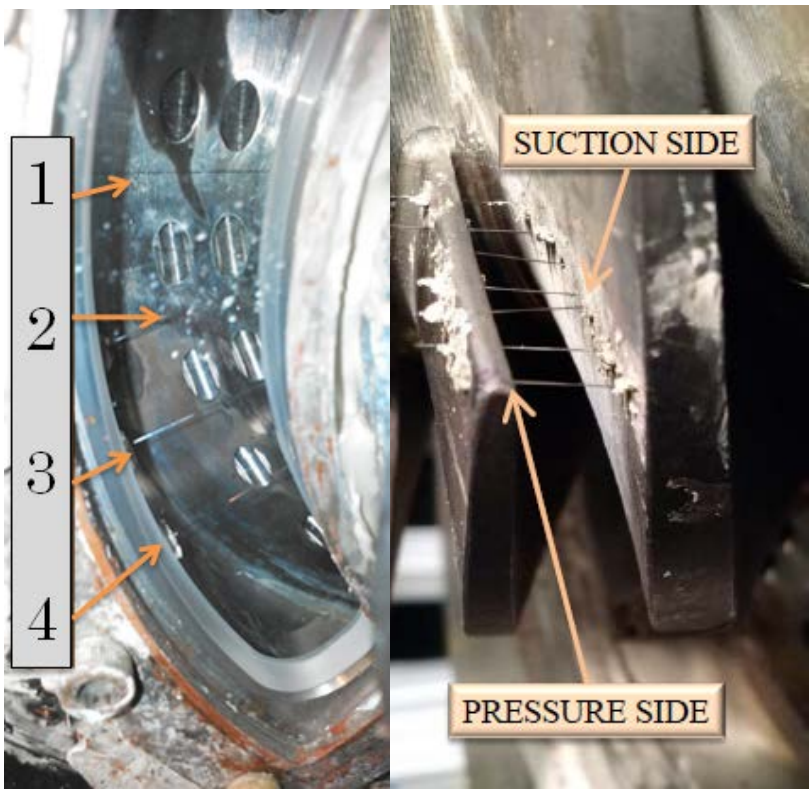

Figure 3.40: Filament installation in the cavity (left) and the HGV exit (right) [100]

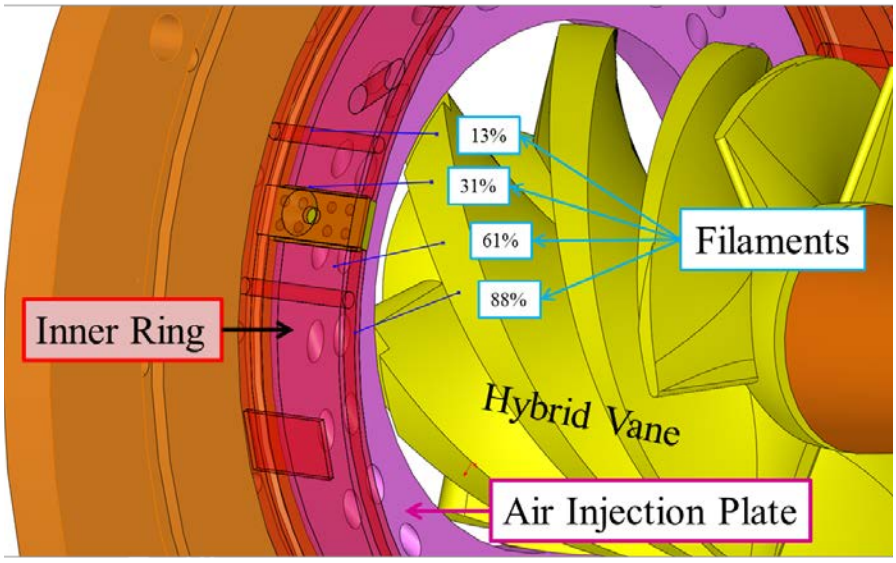

Figure 3.41: Cavity filament installation detail

Table 3.2. Summary of filament positions

Cavity		Exit	
Label	Position [% axial span]	Label	Position [% radial span]
1	13	1	16
2	31	2	29
3	61	3	40
4	88	4	50
		5	60
		6	72
		7	85

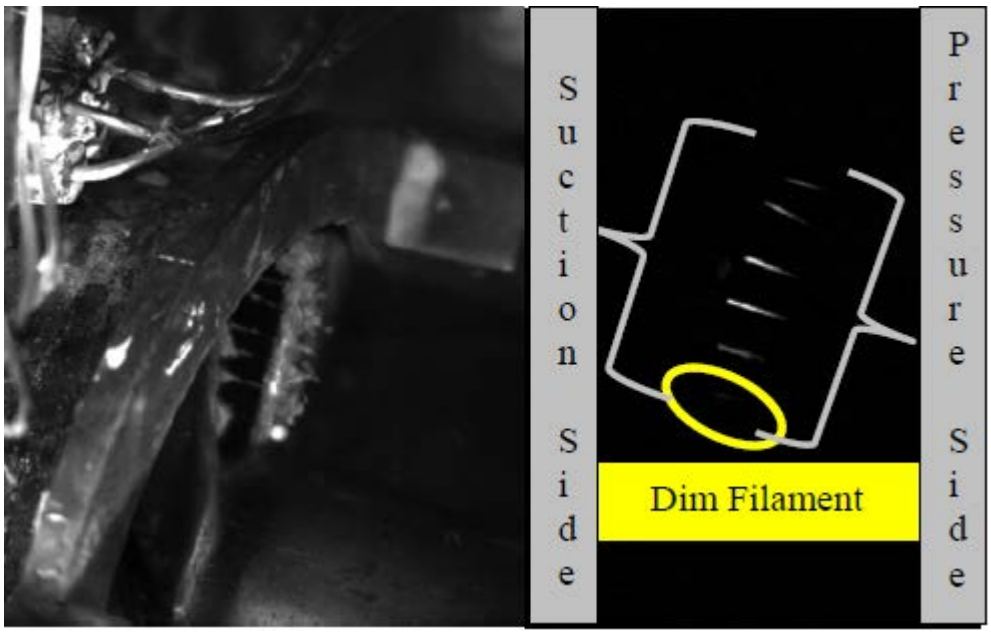

Figure 3.42: Filament image capture at the HGV exit, raw (left) and filtered (right)

Sample acquisition imagery is shown for both the exit plane and the cavity in Figure 3.42 and Figure 3.43 respectively. In both figures, the left image is a raw capture of an actual combustion event. The raw images were processed entirely by Dr. Larry Goss with ImageJ and custom algorithms developed and presented by Vilimpoc *et al.* [29] as summarized in Section 2.3.2. The spatial resolution for that method was determined to be 120 μm per sample point.

Accuracy was then calculated using the methods discussed in Section 2.3.2 to be 36 K. Finally, the highlighted "dim filament" is an example of a region of temperatures too low to register.

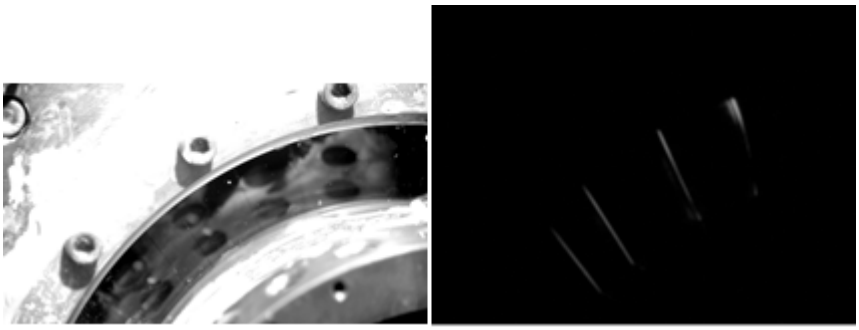

Figure 3.43: Cavity filament image capture, raw (left) and filtered (right) with LIBS measurement location highlighted

3.2.5. TFP Post-Processing Complications

As discussed in Section 3.2.4, the filaments were mounted at the exit plane through the use of pilot holes and a high-temperature adhesive. In Figure 3.40, the exit plane installation is shown in the right-hand images. The pilot holes were drilled via EDM entirely through the trailing edge of one vane, then partially into the surface of the next. In the figure, the vane with the through-holes was also the vane that was closer to the exhaust duct, thus it was labeled as the "outer wall," while the next vane with the partial-holes was the "inner wall." The filaments therefore spanned from the pressure-side of the outer airfoil to the suction-side of the inner airfoil. Numerical results from the TFP experiments were provided by ISSI in the form of text files that were imported into Excel worksheets where each column represented a time-averaged result from one filament at one run condition, and each row represented a pixel along that filament that was resolved and produced good data. In the initial reported results given by Gilbert *et al.* [101] and detailed by Gilbert [100], the results were interpreted such that, in all cases, the provided results were assumed to represent the entire span within which they were installed; "Row 1" was interpreted as being located at the suction-side wall, and the final row, "Row N," was the pressure side wall.

In the course of data analysis for this document, the original source images for the numerical filament data were requested. One representative image is shown in Figure 3.44. The angle of the camera was such that the exit plane was roughly horizontal with the outer wall at the bottom of the image and the inner wall at the top. The filaments appeared as brightly emitting lines. In Figure 3.44, the solid walls of the airfoils are barely visible at the locations indicated by their labels. Finally, and most importantly, unanticipated structures were also present in the image. Those structures in Figure 3.44 have the appearance of "clouds" or "billows" of a sort; they were determined to be filament adhesive that had expanded during the testing. They were present in numerous image samples, and always on the inner wall. The resulting hypothesis was that, as the pilot holes on the inner wall were only partially-drilled, there was air trapped within the holes that expanded at the hot test conditions. Dr. Goss of ISSI affirmed that the test temperatures were approaching the melting point of the filament adhesive, thereby rendering it elastic. Thus, the heated air trapped within the holes expanded the adhesive during each test and subsequently contracted when cooled. The mounting of the filaments was not compromised; none were lost due to flow conditions over dozens of cycles (the only filament losses occurred due to intentional removal/replacement and/or human error). (Importantly, upon similar analysis of the cavity acquisition images, the same effect was not present. This was due to the fact that the partially-drilled mounting holes on the HGV outer surface were outside the field of view offered by the aft quartz window.)

Therefore, to properly interpret the exit-plane TFP data, the relative position of each experimentally viable filament length had to be determined on a case-by-case basis. A summary is provided by Table 3.3. Note that the exit passage span is defined by the variable s where $s = 0$ at the suction side and $s = s_0$ at the pressure side. The spatial extend of each filament for each test case was defined by a starting and ending value of the normalized variable s/s_0. Note that in all experimental cases, no data were available at the inner filament, F1. In the RVC case, data were unavailable at filament F2 as well (as observable in Figure 3.44

by the absence of signal at the F2 location), and in the LLB, CPD, and CMB cases no data were available at the F7 location.

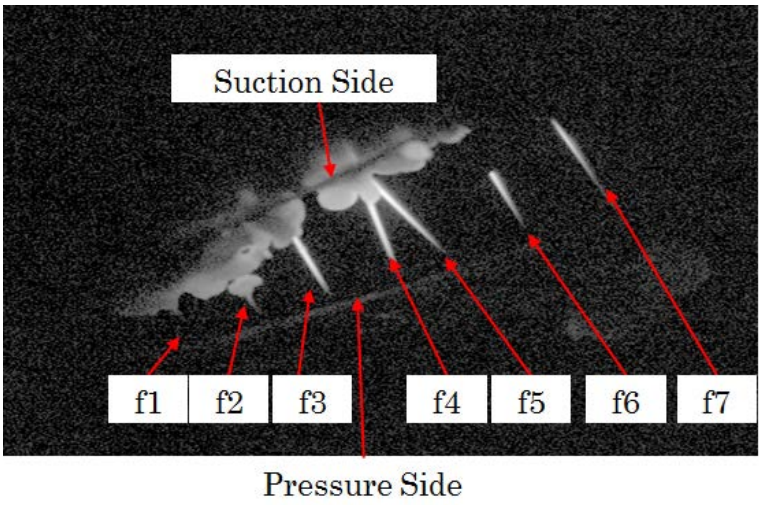

Figure 3.44: Representative image acquisition of the exit-plane filaments during the RVC case testing.

Table 3.3: Summary filament span values

Case	Filament	Start s/s0	End s/s0	Case	Filament	Start s/s0	End s/s0
LLB	2	0.15	1.00	CPD	2	0.31	1.00
	3	0.26	1.00		3	0.50	1.00
	4	0.27	1.00		4	0.40	1.00
	5	0.24	1.00		5	0.32	1.00
	6	0.03	1.00		6	0.29	1.00
RVC	3	0.37	1.00	CMB	2	0.00	0.94
	4	0.31	1.00		3	0.03	0.93
	5	0.24	0.95		4	0.23	0.95
	6	0.36	0.87		5	0.31	0.96
	7	0.29	0.74		6	0.53	1.00

3.3. Geometric Variations

Exploring the geometric trade space was fundamental to all three of the objectives of this study. The UCC remains very much a complex problem with multiple "subsystems" interacting and interfacing in multiple complex ways. It was essential that the design and integration of the various UCC components be investigated in a systematic manner in order to

facilitate more complete understanding of the physical and operational characteristics involved. To facilitate accomplishment of the first objective of evaluating UCC operation with a common flow source, the channel plate as described in Section 3.3.1 became a critical component. In response to the results from the first objective test program, work on Objective two – an investigation of the combustion cavity dynamics – incorporated improvements to the cavity air delivery scheme as described in Section 3.3.2. Finally, Objective three involved investigation of the migration mechanisms from the cavity to the exit. To that end, and based off of reports from the literature, a radial vane cavity (RVC) was designed and implemented as discussed in Section 3.3.3. As a result of initial testing with an RVC design, the RVC was parameterized to allow more detailed development of the accompanying trade space as discussed in Section 3.3.4.

3.3.1. Channel Plate

To fulfill the first objective, the first major geometric change was to augment the diffuser with the core channel plate. As summarized near the end of Section 2.5.4, initial cold-flow testing with the diffuser had been performed by Miranda [98] with results indicating unsatisfactory flow distribution. Specifically, it appeared that no flow at al was present in the outer path and that, in fact, some reverse flow was potentially entering the diffuser through the cavity air drivers. The core channel plate was designed to solve that issue by introducing additional flow blockage in the core path to balance the severe pressure drop associated with the cavity air drivers in the outer path.

The core channel restrictor plate ("channel plate") consisted of a thin (25.4 mm) Hastelloy-X plate with six rectangular channels corresponding to the six HGV airfoils. The design was such that orientation of the channel openings could be centered either in the HGV passages or on the HGV leading edges. The bottom two images of Figure 3.2 demonstrate the channel plate in each of those orientations; the "on-vane" orientation is shown on the left, and the "in-passage" orientation is on the right. The size of the channel opening was determined by

parameterizing the fractional area blockage and comparing it with an analogous measure of the cavity fractional area blockage. The governing formula is shown as Equation (61).

$$\frac{A_{channelPlate}}{A_{core}} = \lambda \frac{A_{injectionHoles}}{A_{cavity}} \tag{61}$$

If $\lambda = 1$, then the core channel passages would be sized such that an equal fractional area would be open to both the core and the cavity flows. Based on experiences from AFRL's TVC testing [51], the decision was made to fix the aspect ratio of the channel passages to 2:1. Therefore, the primary design variable of the channel was the radial height, h, of the channel opening. The total available annular area in the core (A_C) and the cavity (A_V) can be written as follows. For brevity, the term R_i is introduced to describe the radial dimensions such that $R_i = r_{outer}^2 - r_{inner}^2$:

$$A_{core} \equiv A_C = \pi\left(r_{core,outer}^2 - r_{core,inner}^2\right) = \pi R_C \tag{62}$$

$$A_{cavity} \equiv A_V = \pi\left(r_{cavity,outer}^2 - r_{cavity,inner}^2\right) = \pi R_V \tag{63}$$

$$A_{injectionHoles} \equiv A_h = N\pi r_h^2 \tag{64}$$

The flow area through the channels in the core restriction plate can be written in terms of their outer and inner radii (r_1 and r_2, respectively), and the channel angular width, ψ, as shown in Equation (65). The constraint on the aspect ratio is expressed in Equation (66) where the ratio of the mean arc length to the channel height is set equal to two, thereby yielding an expression for the angular width. Utilizing that substitution in Equation (65), and noting that the channel height is defined by $h = r_1 - r_2$, the open area of the core channels can be developed and defined as shown in Equation (67).

$$A_{channelPlate} = \frac{6\phi\pi}{360}(r_1^2 - r_2^2) \tag{65}$$

$$\frac{1}{h}\left[2\pi\left(\frac{\phi}{360}\right)\left(\frac{r_1 + r_2}{2}\right)\right] = 2 \rightarrow \phi = \frac{720h}{\pi(r_1 + r_2)} \tag{66}$$

$$A_P = \frac{\phi\pi}{60}(r_1 - r_2)(r_1 + r_2)$$

$$A_P = \left[\frac{720h}{\pi(r_1 + r_2)}\right]\frac{\pi}{60}h(r_1 + r_2)$$

$$A_P = 12h^2 \tag{67}$$

Equation (61) can therefore be rewritten as

$$\frac{12h^2}{\pi R_C} = \lambda\frac{Nr_h^2}{R_V} \tag{68}$$

Aside from the channel height and the chosen value for λ, the remaining geometric characteristics of the core and cavity passages are constant. Thus, the channel height can be expressed such that

$$h = f\{\lambda, \text{constants}\} \tag{69}$$

Therefore, from selection of a value for λ, a channel height follows immediately; the remainder of the channel dimensions were found from the aspect ratio constraints. Note that the limiting values are $\lambda = 0$, which would correspond to a completely blocked core passage, and the case where the channel height is equal to the core passage height, corresponding to a completely unblocked core. In that latter case, letting $h = r_{core,outer} - r_{core,inner}$ and solving yields $\lambda \cong 8$.

Variations to the channel plate were defined by the sizing parameter, λ. Ultimately, six designs were produced at values of $\lambda = \{0.7, 1.0, 1.3, 3.0, 4.0, 5.0\}$. A mix of cold-flow and reacting-flow testing was performed, and those results will comprise the bulk of the discussion in Chapter 4.

3.3.2. Cavity Air Injection

As presented in Section 3.1.1.2, the new version of the combustion cavity – UCC v3 – comprised one substantial geometric variation. The move from three separate air injection panels to one uniformly spaced panel was shown to have a substantial impact. In the initial simulations of that configuration, it was observed that the increased cavity outer diameter also

tended to hold a relatively thick layer of unburnt fuel. Thus, the cavity volume – while shown to be more effective at mixing – was also not being used as efficiently as possible. A simple solution to this was proposed by including an outward-radial angular component to the air driver holes, therefore moving from a simple tangential injection to a complex "compound angle" injection scheme.

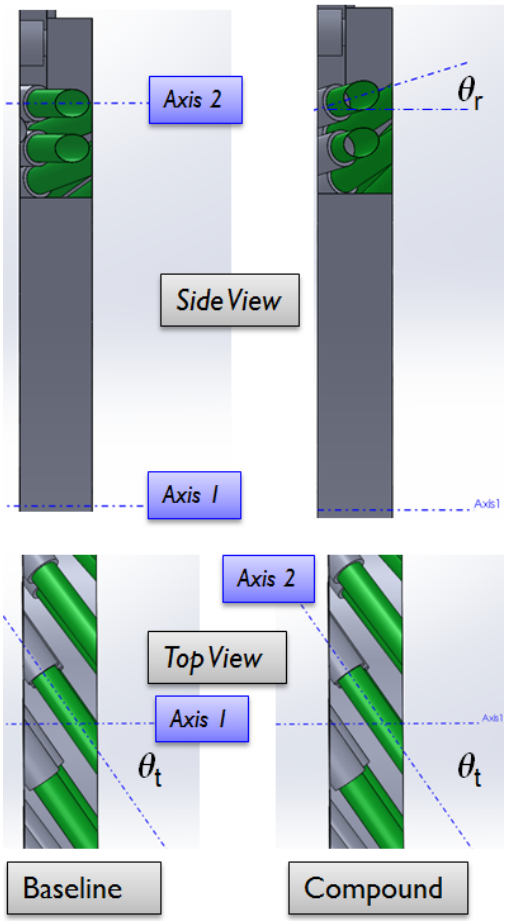

Figure 3.45: UCC v3 air injection holes, baseline (left) and compound-angle (right)

An illustration of the design change is shown in Figure 3.45; the UCC centerline ("Axis 1") and the centerline of one of the air drivers ("Axis 2") are highlighted. The baseline case on the left consists only of a tangential angle $\theta_t = 55°$ relative to Axis 1. The modified case on the right keeps the tangential angle constant, but also includes an outward-radial angle of $\theta_r = 10°$.

The particular value of θ_r was chosen such that the air driver centerline approximately met with the intersection of the cavity inner ring and the back plate.

3.3.3. Radial Vane Cavity

The Radial Vane Cavity was a modification concept applied to the original low-loss centerbody design as detailed in Section 3.1.1. The use of a RVC has been investigated numerically and experimentally by AFRL (see Section 2.4.6.2) as well as AFIT (Section 2.5.2). Its application to the AFIT full-annular test article has been discussed at length. This study – in conjunction with the master's work of Gilbert – endeavored to make that design variation a reality in order to aid accomplishment of this program's third research objective regarding the investigation and optimization of the flow migration behavior to develop optimum conditions at the HGV exit.

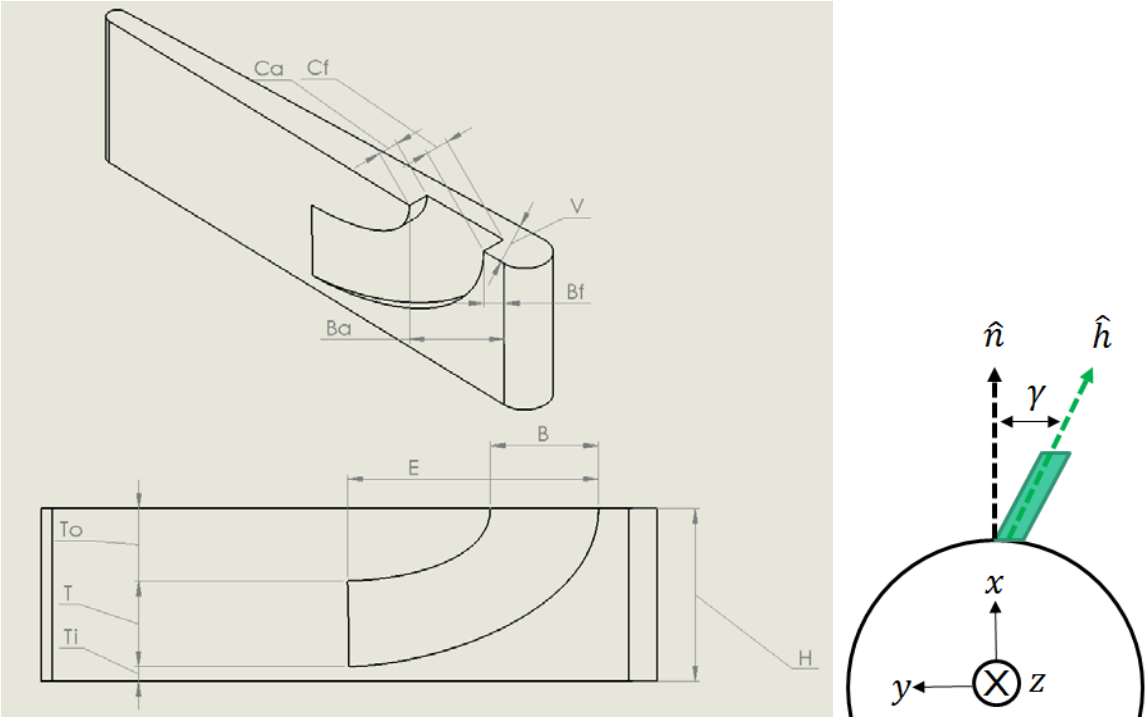

Figure 3.46: RVC design parameters illustrated

To aid discussion and development of the RVC trade space, a set of parameters were defined to describe any potential variations of the RVC profile. An image of a generic guide

vane and RVC is shown in Figure 3.46 with a number of parameters labeled. A front-view conceptual image is also shown to illustrate how HGV vane "tilt" is described. A full list of all the trade parameters and their descriptions is given in Table 3.4.

Table 3.4. RVC design parameters tabulated

B	Outward-facing axial width	V	HGV vane thickness at CC front wall
B_a	Axial distance from CC front wall to RVC aft most point	W	Circumferential cavity (CC) axial width
B_f	Axial distance from CC front wall to RVC foremost point	α	$= C/V$
C_a	Initial lateral width of front-facing step	β	$= B/W$
C_f	Initial lateral width of back-facing step	ξ	$= E/W$
E	Axial extent of RVC	γ	Angle between $\hat{h}$ and $\hat{n}$
H	HGV vane height	$\hat{h}$	Unit vector in the direction of the vane leading edge
T	Termination point radial height	$\hat{n}$	Normal to the circumference at the base of the vane
T_i	Radial distance from vane inner edge to termination point	τ	$= T/H$
T_o	Radial distance from vane outer edge to termination point		

The concept for the initial RVC design was inspired by both Mawid [21] and Parks [87], the end result being a combination of those two. Furthermore, the initial design was deliberately constrained such that it could be implemented on a subsection of the HGV centerbody, thus precluding the need for production of an entirely new piece. The left image of Figure 3.47 demonstrates how the centerbody is subdivided. The first HGV design produced by Wilson – dubbed the LLCB for this study – was generated in three pieces as the geometry was too complex for traditional milling techniques to produce it in one solid piece. This subdivision had the additional benefit of enabling the airfoil leading edges to be modular in order to accommodate varying degrees of inlet flow swirl. In Figure 3.47 the fore, middle, and aft components are colored yellow, orange, and then yellow again, respectively. The separation

point between the fore and middle components occurs at exactly half of the combustion cavity axial width ($W/2$). As the goal of the RVC was to migrate combustion products, it was convenient and logical to begin the RVC in the rear half of the combustion cavity, as the fluid in the front half would notionally not be fully combusted and prepared for an enhanced migration method.

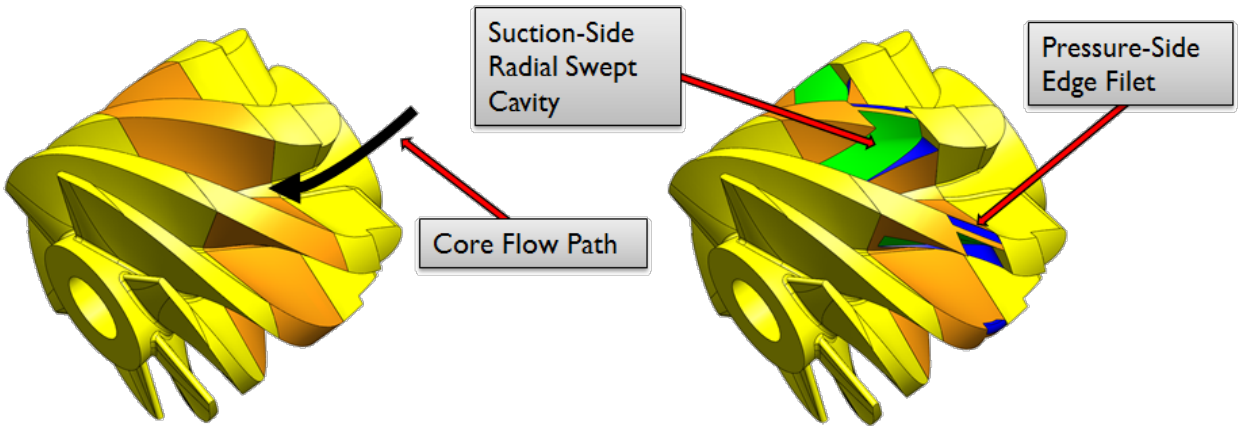

Figure 3.47: Comparison of the smooth HGV versus the RVC

The RVC consisted of both a front-facing and a backward-facing step due to the relative success of that concept in the results of Mawid [21] over the single front- or back-facing step options. Thus, the RVC outward-facing cut axial parameters were defined as $\beta_f = 0.5$, $\beta_a = 1$. The lateral parameters were more challenging to define consistently due to the complexity of the shape being implemented in the solid model, but the end results were $\alpha_f = 0.63$ and $\alpha_a = 0.57$. The RVC began cutting radially inward, but then turned until it merged parallel and smoothly with the HGV airfoil surface. The axial extent parameter was $\xi = 1.15$, while the termination point parameters were held constant at $\tau = 0.45$, $\tau_o = 0.66$, and $\tau_i = 0.19$. In conjunction with the RVC placement on the airfoil suction-side, an edge filet was incorporated on the pressure-side opposite the RVC. The filet was postulated to further benefit flow migration by encouraging more fluid to exit down the pressure side, more completely filling the

HGV passage. The final design was grown through a process of Direct Laser Metal Sintering (DLMS) by Bastech, Inc. The product is shown in Figure 3.48.

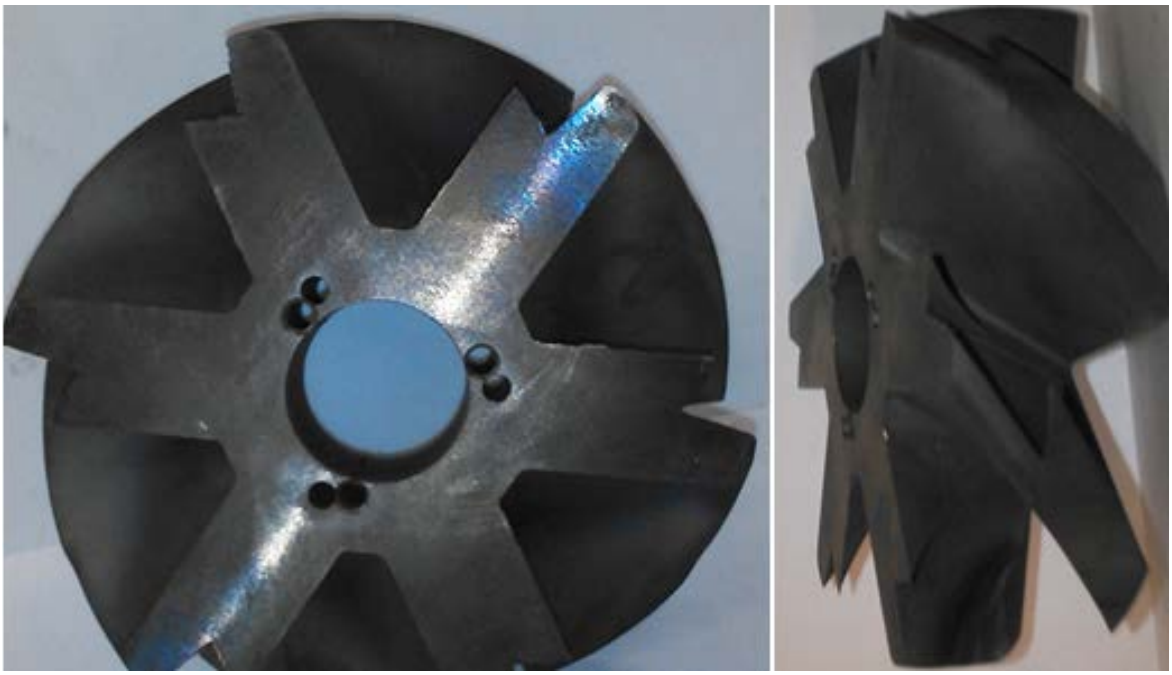

Figure 3.48: As-produced RVC center section from Gilbert [100]

3.3.4. Radial Vane Cavity Iterations

The results of the initial testing with this RVC experiments and simulations, discussed in Section 6.2, prompted additional parametric variations in order to determine which aspects of the RVC most desirably influenced the exit flow. Four additional RVC designs and two additional HGV vane concepts were modeled and simulated in order to down-select for production of another test article. Figure 3.49 illustrates the six proposed designs. First and foremost, based on positive experience producing the required piece for the original RVC design in Figure 3.47 via DLMS, it was proposed that the next iteration be one solid body as opposed to three separate pieces. Thus, in Concept **3** of Figure 3.49, the basic cavity shape is identical, but the initial inward-radial cut occupies nearly the entire axial length of the combustion cavity. Concept **4** utilizes the same cut as **3** but increases the rearward axial extent of the cavity. Concept **5** again utilizes the same basic cut as **3**, but the front-facing step is removed leaving

only the back-facing portion of the cavity. Concept **6** is a dual-cavity variant of **5** with two back-facing steps and no front-facing steps. Concept **7** is a design attributable to Gilbert (though not documented) wherein the baseline vane was modified with a "crescent" shape on the suction-side wall. Finally, Concept **8** modifies the baseline vane with an exaggeration of the pressure-side edge filet described by Figure 3.47; the intent was to seek a stronger migration into the pressure-half of the HGV passage, as current designs (as shall be demonstrated) tend to constrain the hot flow on the vane suction side.

The precise parameters of the designs, based on the definitions in Figure 3.46, are given in Table 3.5. The variations are each labeled with a "Case ID," which will be used for reference during the discussion of the results. A common practice in designed experiments is to present the levels of each variable in "coded" form in order to make the changes between cases more clear. The parameter codes in the table may be matched to their respective maps beneath the "Levels" heading. The "Count" parameter refers to the number of cavities on the vane. Thus, for example, the design parameters of Case 7 are $B/W = 1.0$ (indicating an initial cavity cut across the entire axial cavity span), $E/W = 1.15$ (indicating an axial extent that matches the original Gilbert design, Case 2), $C_a/W = 0$ (indicating removal of the front-facing step), and Count = 2. All other parameters were set to be equal between cases. The results of the investigation into these new designs, as well as all other HGV discussion, will be given in Section 6.3.

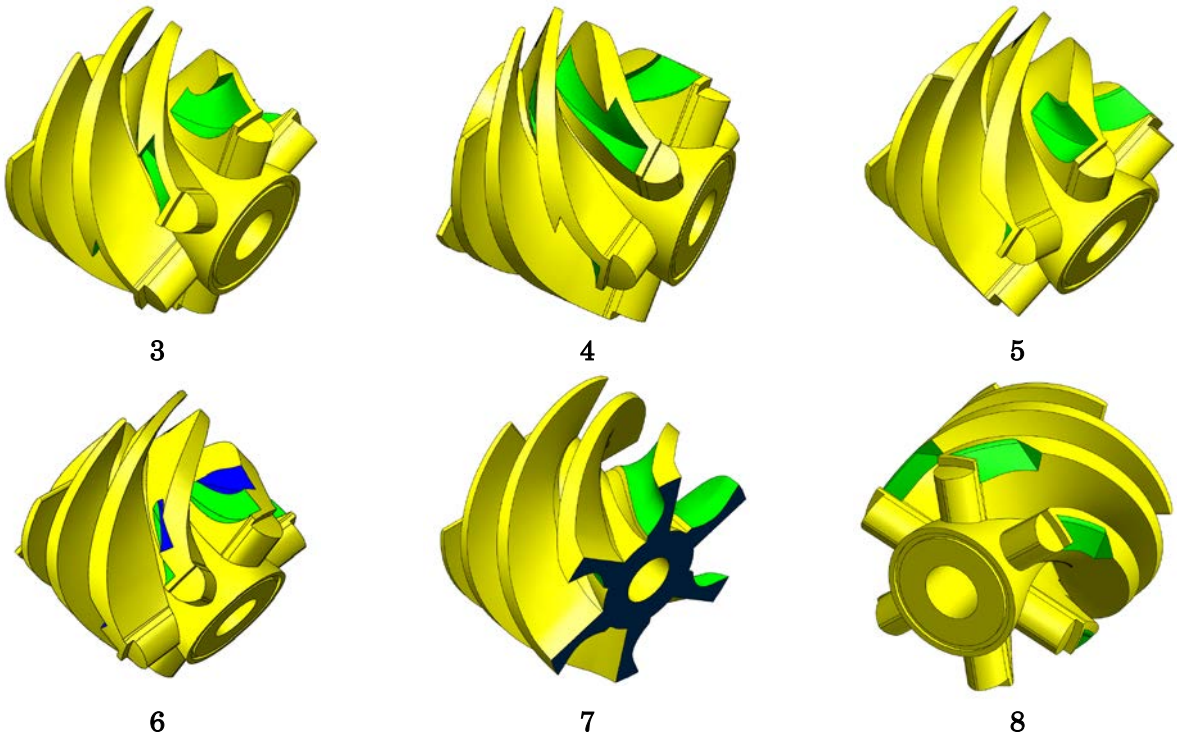

Figure 3.49: Additional HGV designs

Table 3.5. Trade study cases and parameters

Case ID	Description	Parameters					Levels	
		B	E	Ca	Count		0	1
1	Smooth Vane	n/a				B/W	0.5	1
2	Baseline RVC	0	0	0	0	E/W	1.15	2.34
3	Full Cavity Span	1	0	0	0	Ca/W	0.46	0
4	Axially Extended	1	1	0	0	Count	1	2
5	Back Step Only	1	0	1	0			
6	Dual Back Steps	1	0	1	1			
7	Cresent	n/a						
8	Cut	n/a						

3.4. Computational Methods

Computational modeling was a complement to all of the objectives in this project. The power of Computational Fluid Dynamics (CFD) lies within the ability to test numerous hardware variations without requiring actual parts to be manufactured and installed. The

resulting solutions complement the experimental investigations and allow supplemental insight into the physics of the problems leading to improved understanding of the research objectives. The computational work presented in this document is facilitated by both local and remote hardware and software resources. Section 3.4.1 describes the available software, and presents detail as to the capabilities and methods that will be utilized. Section 3.4.1.5 then summarizes the hardware resources that were utilized for these analyses.

3.4.1. Software Tools and Methods

The bulk of the computational work required for this project involved solid modeling, grid generation, and CFD solution generation. Solidworks, Pointwise, and Fluent, respectively, fulfill those roles. Details on grid generation are given in Section 3.4.1.1, while the method for grid independence analysis is discussed separately in Section 3.4.1.2. Section 3.4.1.4 then describes the flow solver and the settings utilized for this study including turbulence models, combustion models, and chemistry, much of which evolved over the course of this research.

3.4.1.1. Grid Generation

Pointwise versions 17.1 and 17.2 were used to create the computational grid from the solid models. Several different approaches were tested, and important results are documented in Chapter 4. Early attempts at two-dimensional studies were lacking for the very important reason that there are no two-dimensional effects to be captured in the UCC. By its very nature, the incoming axisymmetric flow is intentionally turned out-of-plane in order to generate the circumferential swirl. Early attempts were subsequently made to generate functional periodic sector models. Those proved unsuccessful for a variety of reasons, ultimately driving a full-annular approach to the computational model. In the course of that effort, Dr. Konstantin Vogiatzis with the AFRL High-Performance Computing center provided invaluable technical assistance, and his contribution was essential to the early phases of this project.

An early gird configuration is shown in Figure 3.50, oriented such that the flow is from left to right. The initial inlet section and the flared outlet were computational constructs only; the central geometry, however, was hardware-representative. The case used a combination of structured (rectangular) and unstructured (triangular) surface topology; in the Pointwise nomenclature, such surface grids are referred to as "domains." A cutaway view of the combustion cavity and hybrid vane surfaces in Figure 3.51 demonstrates the hybrid topology approach. Structured domains are visible on the hybrid vane walls, and unstructured domains may be observed on the outer diameter of the combustion ring, as well as the inner diameter of the hybrid vane passages. Similarly, hybrid schemes were used to generate the internal volume regions, known as "blocks." The inlet and outlet regions use purely structured (hexahedral) cells. The interior used a particular technique known within Pointwise as "T-Rex" as discussed in detail by Steinbrenner and Abelanet [102].

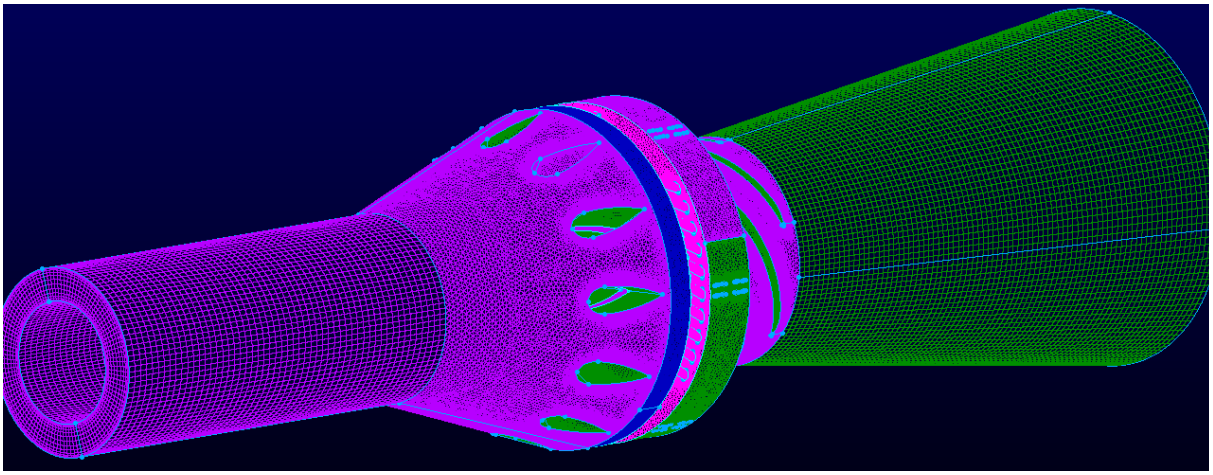

Figure 3.50: Early computational domain

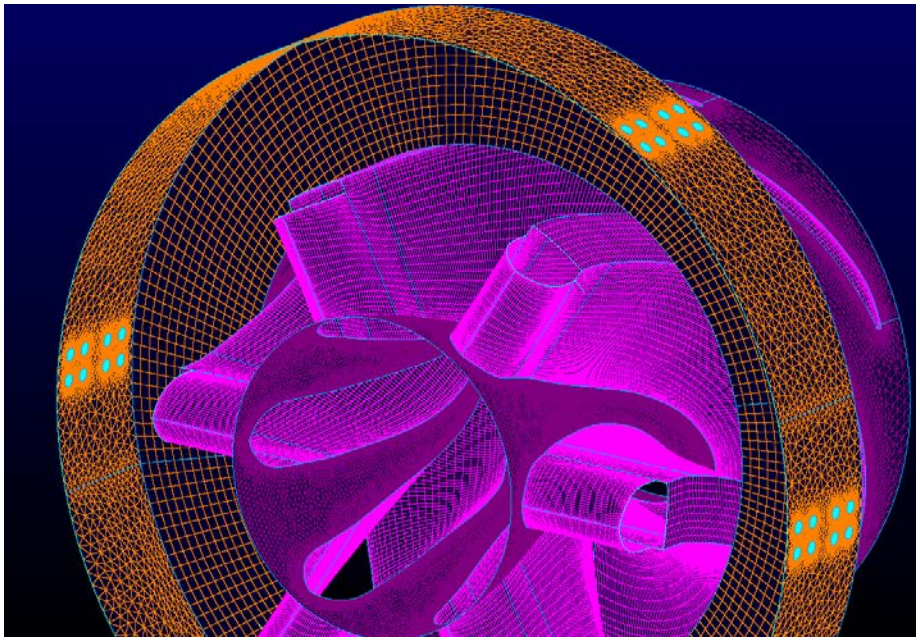

Figure 3.51: Internal view of early surface domains

Anisotropic tetrahedra were layered upon the desired surface domains at specified rates of growth until they achieved isotropy or met other certain criteria, after which standard unstructured tetrahedral were used to fill the remaining volume. This technique allowed the effective resolution of boundary layer regions without the need to design and initialize separate structured blocks. Use of this technique is demonstrated by the cutaway of the diffuser flow path in Figure 3.52 as well as the combustion cavity in Figure 3.53, with the cell colors scaled by skewness: blue indicates minimal skew and red indicates high skew. T-Rex boundary layers are similar to traditional structured boundary layers in that they often suffer from high amounts of skew due to the desire to resolve a boundary layer block while maintaining a coarse surface domain.

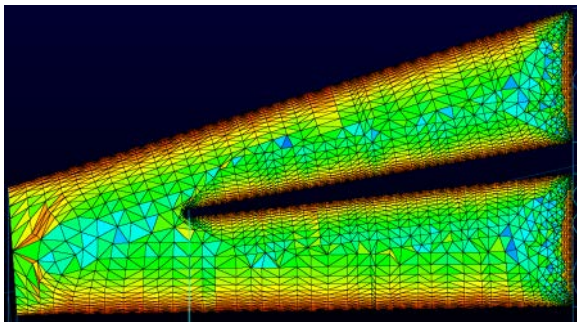

Figure 3.52: Diffuser volume T-Rex cells

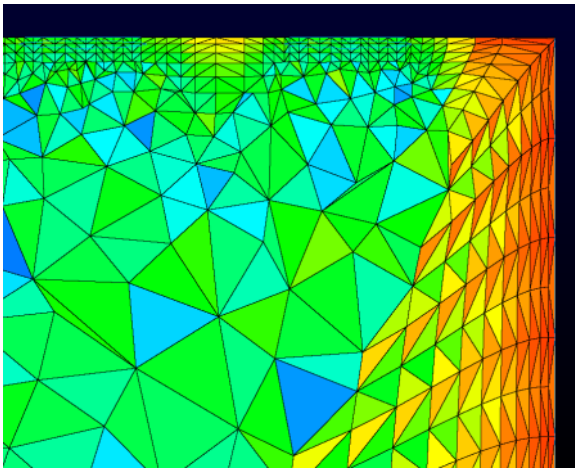

Figure 3.53: Combustion cavity outer and aft walls

In order to attain adequate resolution of the boundary layers, estimates of the required wall spacing were derived from the inlet flow conditions. Based on a representative inlet mass flow rate of 0.1 kg/s, a diffuser annular inlet area of 0.00364 m^3, and the air density of 1.20 kg/m^3, the inlet velocity is approximately 23.0 m/s. The viscosity of air at those conditions is 1.8369×10^{-5} kg/m-s, thereby yielding a kinematic viscosity of $\nu = \mu/\rho = 1.53 \times 10^{-5}$ m^2/s. The radial height of the diffuser annulus is $h =$ 0.0158 m; thus, assuming the flow through the diffuser annulus represents turbulent channel flow, a reference Reynolds number can be found as $Re = hU/\nu = 23{,}700$. Several empirical relations from turbulent boundary layer theory allow the estimation of the skin friction from knowledge of the Reynolds number. One such relation from White [103] (page 434) is shown in Equation (70):

$$C_f \approx 0.027 Re^{-1/7} \tag{70}$$

For the value of Re above, $C_f = 0.006404$. The wall shear stress and friction velocity may then be determined as

$$\tau_w = C_f \left(\frac{1}{2}\rho U^2\right) = 2.010 \tag{71}$$

$$u_\tau = \sqrt{\frac{\tau_w}{\rho}} = 1.292 \tag{72}$$

In practice, determining the resulting wall coordinate from a desired absolute spacing (y) has proven to be a convenient approach. The required formula can be written as

$$y^+ = \frac{u_\tau y}{\nu} \tag{73}$$

The smallest value for wall spacing utilized thus far has been $y = 0.13$ mm, which corresponds to $y^+ = 11$. As discussed in Section 2.2.2.2, that spacing is slightly smaller than recommended for using standard wall functions. However, enhanced wall treatment (EWT) has been utilized in all current calculations. Thus, in general, valid initial spacing from the wall could range from $1 < y^+ < 500$, or $0.0005 < y < 5.9$ mm. However, additional constraints were imposed by the geometry itself as will be illustrated by Figure 3.55 and the associated discussion.

With wall spacing between 0.25 and 1.3 mm, early case sizes ranged from about 20 million to 40 million cells. One available option when exporting completed grids to Fluent, however, allowed anisotropic tetrahedral cells to be combined into hexahedral cells. In other words, the unstructured boundary growth layers created with the T-Rex technique could effectively be merged into prism layers, reducing overall cell counts by roughly 60%. Therefore, early case sizes after processing into Fluent ranged from 8 million to 18 million cells.

Grid development evolved over the course of this effort. Based on results that will be documented in Chapter 4, use of T-Rex cells ceased. The ability to resolve near-wall behavior was found to have marginal impact on the ability to resolve the bulk flow quantities that were of primary interest. Furthermore, the high skew induced by the boundary growth layers led to cell quality problems in the flow solver. Thus, in the face of minimal benefit at high cost, a move was eventually made to a fully-unstructured grid. Though many of the surface domains could have been left as structured grids, such a setup often required careful balancing with grid point spacing in other, more constrained parts of the geometry. Thus, even those domains

eventually became unstructured in order to provide the flexibility to adapt the grid piece-by-piece as the research warranted.

A late-program version of the computational grid is shown in Figure 3.54. Notable changes over the previous version were: (1) the inlet duct was modeled in its entirety, including the nose cone, as was present in the actual test rig, (2) the exit cowling was modeled as a wall rather than as a "pseudo-farfield" with a symmetry boundary condition, (3) all domains and blocks are fully unstructured with the spacing of the first tetrahedral element set to 0.25 mm on average.

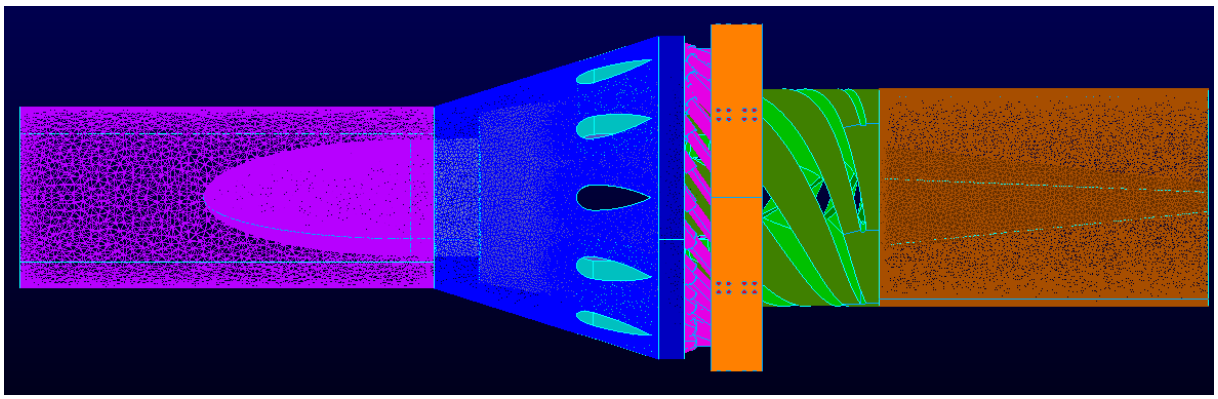

Figure 3.54: Current computational domain

The regions that most benefitted from a fully-unstructured approach were the HGV passages, as it was there where the biggest issues with T-Rex cell quality occurred. A cross-section of an unstructured volume is shown in Figure 3.55; the view is from the side, and the axial direction runs from left to right. The HGV trailing-edge is visible (in pink), and the beginning of the exit expansion cone is also just visible (in grey) at the bottom-left of the image. The cells are colored by skewness as indicated by the color bar/histogram on the left side; values closer to zero are less skewed and therefore higher quality. Notably, the mean value occurs right around 0.4 – this is in contrast to typical T-Rex volumes where the histogram mean occurred as high as 0.9. Furthermore, Figure 3.55 demonstrates the resolution of the HGV passage inner diameter highlighted by the red box. At that point, the passage width at the

inner diameter (i.e. the perpendicular distance between the two vane surfaces) is 3.0 mm. At a minimum (further upstream) the passage width at the inner diameter reaches values as small as 1 mm. At that point there are eight grid nodes across the width of the passage for a representative minimum node spacing of 0.13 mm. These late-phase grid cases had cell counts typically on the order of 65 million.

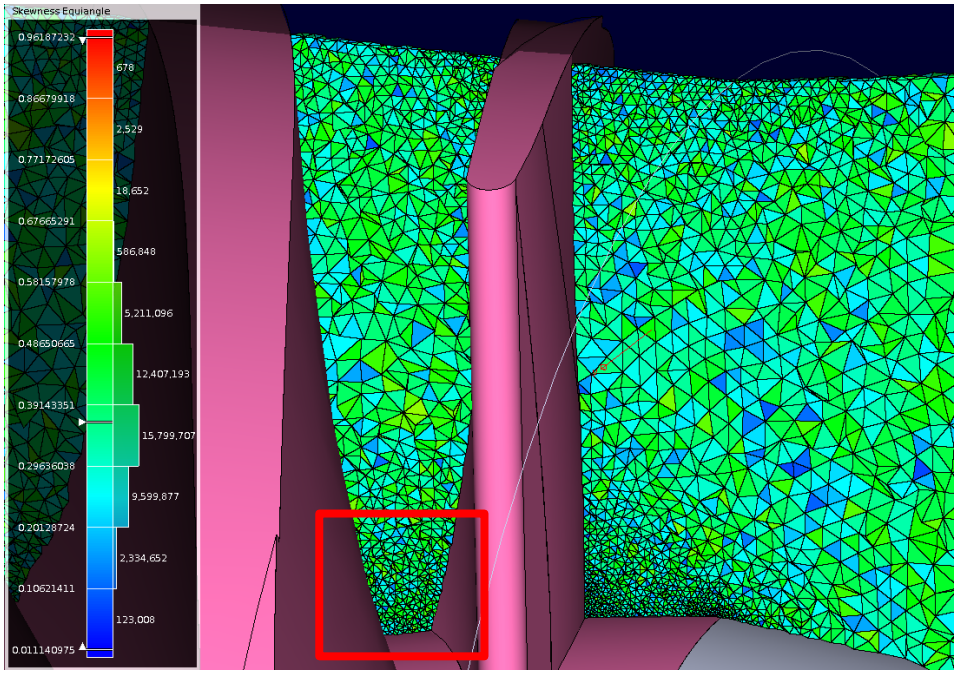

Figure 3.55: Sample fully-unstructured grid volume at the HGV trailing edge

3.4.1.2. Grid Independence Method

An important aspect to any CFD study is verification of grid independence. If a solution changes with grid resolution, then it is said to be grid-dependent and is not considered reliable. Grid independence studies typically examine a parameter, a line, or a surface of interest for changes with varying grid densities. As soon as variation of the parameter of interest is within a specified tolerance, the solution is deemed grid independent.

The independence analysis follows the recommendation of Celik, *et al.* [104] that, in turn, follows a procedure known as the Grid Convergence Index (GCI) method based on the Richardson Extrapolation. The above reference is brief, but provides numerous additional

references to research and examples in the literature, so no further introduction will be provided here. A full description of the procedure follows.

Three different grids must be generated, each with some representative size parameter h, total number of cells N, and incremental volume ΔV_i (or area for 2D grids). The size parameter could be defined in a number of ways, but one method is expressed simply as

$$h = \left[\frac{1}{N}\sum_{i=1}^{N}(\Delta V_i)\right]^{1/3} \tag{74}$$

The summation of the incremental volume is the total volume (or area) of the grid region. The differences in size between each of the three grids should be at least $h_i = 1.3h_j$. Experience from this study revealed that values close to or under the threshold $h_i = 1.2h_j$ will fail to converge properly. After generation of the proper grids, a figure of merit should be defined. It should be a performance factor of interest to the study; point values of field variables – such as velocities, pressures, or temperatures – are acceptable. For each grid size $h = \{h_1, h_2, h_3\}$, the figures of merit should be defined as $f = \{f_1, f_2, f_3\}$, and $h_1 < h_2 < h_3$. Ratios should be then be determined as

$$r_{21} = \frac{h_2}{h_1}, \qquad r_{32} = \frac{h_3}{h_2} \tag{75}$$

The apparent order p must then be calculated iteratively using the following expressions. The initial guess for p should correspond to the lowest-order spatial discretization being utilized in the flow solution.

$$\varepsilon_{32} = f_3 - f_2, \qquad \varepsilon_{21} = f_2 - f_1 \tag{76}$$

$$s = 1 \cdot \mathrm{sgn}\left(\frac{\varepsilon_{32}}{\varepsilon_{21}}\right) \tag{77}$$

$$q(p) = \ln\left(\frac{r_{21}^{p} - s}{r_{32}^{p} - s}\right) \tag{78}$$

$$p = \frac{1}{\ln(r_{21})} |\ln|\varepsilon_{32}/\varepsilon_{21}| + q(p)| \tag{79}$$

Extrapolated error values are then found by

$$f_{ext}^{21} = \frac{f_1 r_{21}^p - f_2}{r_{21}^p - 1} \tag{80}$$

Estimates for the approximate relative error and the extrapolated relative error (using the fine-grid case as an example) are then found by

$$e_a^{21} = \left|\frac{f_1 - f_2}{f_1}\right|, \qquad e_{ext}^{21} = \left|\frac{f_{ext}^{21} - f_1}{f_{ext}^{21}}\right| \tag{81}$$

Finally, the Grid Convergence Index (GCI) is defined as

$$GCI_{fine} = \frac{1.25 e_a^{21}}{r_{21}^p - 1} \tag{82}$$

3.4.1.3. Grid Independence Results

Two primary grid independence studies were conducted. The first major grid version was generated in conjunction with accomplishment of Research Objective 1 and the hybrid grid layout illustrated in Figure 3.50; it supports all results presented in Chapter 4. In the grid for this case, as the performance of the diffuser was the primary factor of interest, the diffuser aerodynamics served as the figures of merit. In particular, it was decided to examine the outer flow path where the recirculation region had been identified. Four grid cases were created: one utilized the T-Rex technique for boundary-layer resolution, while the other three were fully unstructured volumes of varying sizes. For the first study, the axial reference locations in Figure 3.56 were utilized.

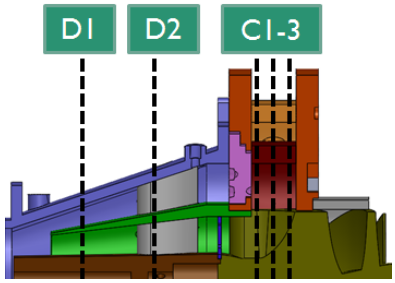

Figure 3.56: Axial reference labels

Figure 3.57 shows radial profiles of axial velocity in the diffuser outer flow path at axial reference location D1. Operating conditions for those data were $\lambda = 5.0$, "in-passage", $\dot{m}_{in} = 0.12$ kg/s, and $\phi_{cav} = 1.37$. Qualitatively, all four grids demonstrate very similar behavior. The peak velocity occurs at roughly 10% of the radial height of the outer channel and tapers steadily. Negative axial velocity is observed at about 90% of the channel height at a magnitude of about -1 m/s. The four curves almost collapse together during the steady slope within the central passage; the most substantial differences may be observed at the peak inner region. Notably, the T-Rex grid resolves higher velocities closer to the wall due to increased node density at the walls. However, the bulk qualities are very similar to the fully unstructured grids. As discussed previously, the marginal gain of boundary-layer resolution was not sufficient to offset the complications presented by highly-skewed T-Rex volumes; the evidence provided by data such as Figure 3.57 was therefore sufficient support for the decision to forego future grid development with T-Rex cells. Thus, for the quantitative grid independence calculations, only the three unstructured grids were examined with respective cell counts as listed in Figure 3.57. The maximum velocity of each curve was chosen as a quantitative figure of merit, f. The absolute cell counts for the three grid sizes were $N = \{55,\ 45,\ 30\}$ in millions of cells; the resulting representative grid sizes and corresponding figures of merit were $h_{1,2,3} = \{0.0263, 0.0317, 0.0466\}$ [mm] and $f_{1,2,3} = \{12.3, 13.0, 11.3\}$ [m/s] for the fine, medium, and coarse cases, respectively. The apparent order was found to be $p = 3.1$. In the fine-grid case,

the relative error, extrapolated relative error, and fine-grid convergence index were found to be $e_a^{21} = 5.0\%$, $e_{ext}^{21} = 7.1\%$, and $GCI_{fine}^{21} = 8.3\%$

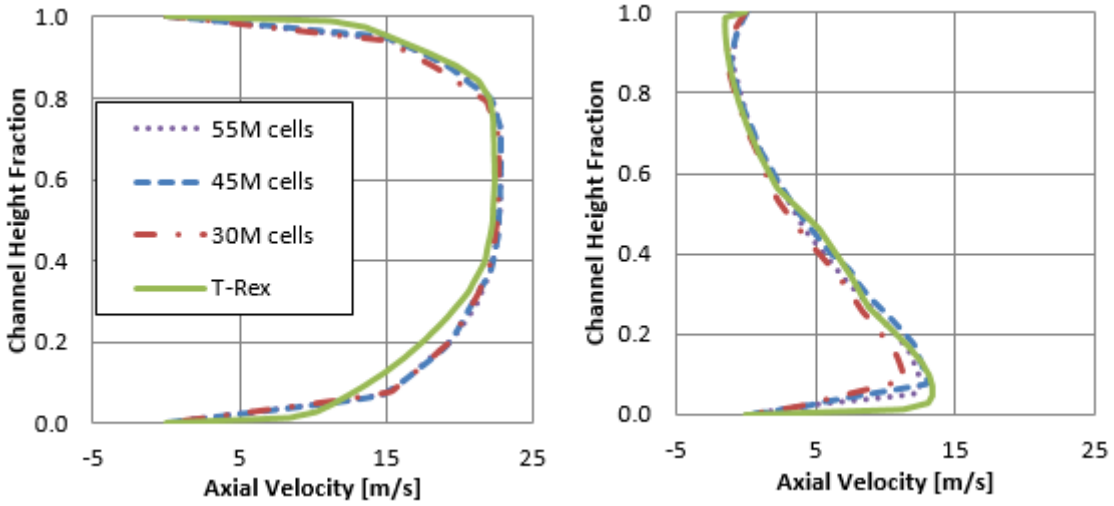

Figure 3.57: Demonstrating aerodynamic grid independence at axial location D1, core path (left); and D1, outer path (right)

The second grid independence study was conducted after the configuration was altered to that reflected in Figure 3.54 in support of both Objectives 2 and 3; it corresponds to the results presented in Chapters 5 and 6. As the general focus of the objectives had shifted from aerodynamic to thermodynamic performance, the selected figure of merit was therefore the exit temperature profile. The RVC geometry was selected to represent the other major configurations as it represented a "worst case" in terms of geometric complexity; all other aspects of the grids of the alternate geometries were equivalent. The independence analysis was conducted upon the RVC configuration with three grids of sizes $N = \{88.8, 66.2, 45.3\}$ in millions of cells. All surfaces and volumes were composed of unstructured triangles and tetrahedra, respectively. The exit temperature profiles of the three grids were examined as shown in Figure 3.58. These profiles were one-dimensional radial profiles spanning from the inner diameter ($r/R = 0$) to the outer diameter at the lateral midpoint of the HGV exit plane.

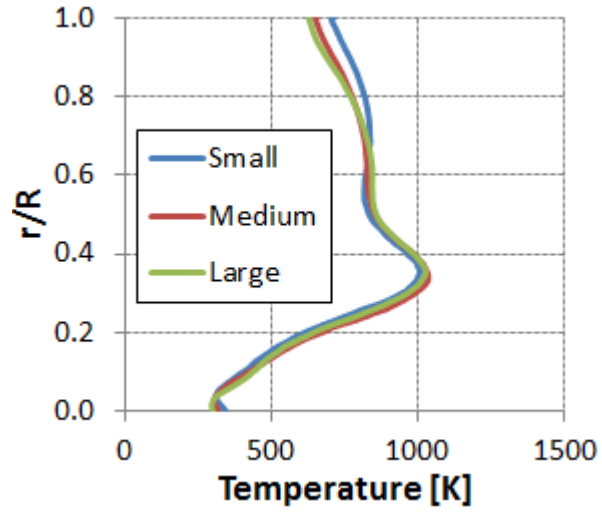

Figure 3.58: Exit temperature profiles for grid independence

As a variation on the first procedure, the independence analysis was applied to six separate points of constant r/R rather than only the peak location. Thus, the apparent order p, the relative error e_a^{21}, relative extrapolated error e_{ext}^{21}, and grid convergence index GCI were reported at multiple locations. The representative grid sizes were common between all points, $h_{1,2,3} = \{1.42, 1.56, 1.77\}$, as were the resulting grid refinement ratios, $r_{21} = 1.10$, $r_{32} = 1.13$. This approach proved instructive, because while locations in the bulk region between $0.37 \leq r/R \leq 0.8$ saw very little error, the regions at the outer wall and near the inner wall both demonstrated relatively high error. The point at $r/R = 0.0$ was not included as it failed to converge properly. The high error near the wall regions could be attributed to relatively poor near-wall resolution, as the boundary layers were deliberately not modeled, per the discussion in the preceding paragraphs. However, the reported grid refinement ratios were in fact lower than the recommended value of $r = 1.3$, and past experience within this research has demonstrated the extreme sensitivity of this grid independence approach to those ratios. Thus, some improvement to the large error near the walls would likely arise if the range of grid sizes, and therefore the values of the refinement ratios, were increased.

Table 3.6: Grid independence data for exit temperature profiles

r/R	f1	f2	f3	e21	e32	s	f21ext	ea21	eext21	GCI
1.00	627.4	653.1	709.4	25.71	56.28	1	583.1	4.10%	7.60%	8.83%
0.80	770.7	774.7	817.3	3.99	42.59	1	769.9	0.52%	0.11%	0.13%
0.60	843.9	826.9	820.8	-17.00	-6.10	1	848.4	2.01%	0.53%	0.66%
0.40	983.6	985.0	960.9	1.47	-24.15	-1	983.4	0.15%	0.02%	0.02%
0.37	1016.9	1019.7	997.2	2.74	-22.52	-1	1016.3	0.27%	0.06%	0.08%
0.20	645.1	675.8	615.9	30.78	-60.00	-1	604.2	4.77%	6.77%	7.92%
						AVG:	800.9	1.97%	2.51%	2.94%

3.4.1.4. Flow Solutions

Fluent versions 14.7 and 16.2 were utilized for the flow solutions. Fluent has a wide range of capability, much of which has been documented in the literature review (Section 2.2). For all applications, the realizable $k-\varepsilon$ turbulence model with enhanced wall functions was utilized with success based on recommendations from Vogiatzis [105] as well as Mongia [14]. A steady, pressure-based solver was invoked in conjunction with the "coupled" pressure-velocity scheme. Spatial discretization remained relatively constant throughout the research based again on Vogiatzis [105]: the pressure scheme was set to "second-order," the third-order "MUSCL" scheme was invoked for the momentum term, and the third-order "QUICK" scheme was set for the turbulent kinetic energy and dissipation terms. In early research, reactions were defined by volumetric (bulk phase) species transport models with both single-step and two-step global chemistry. The former utilized a standard five-species model shown by Eqn. (83), while the latter utilized six species as shown by Eqn. (84)

$$C_3H_8 + 5O_2 + 18.8N_2 \rightarrow 3CO_2 + 4H_2O + 18.8N_2 \tag{83}$$

$$\begin{gathered} C_3H_8 + 3.5O_2 + 13.2N_2 \rightarrow 3CO + 4H_2O + 13.2N_2 \\ CO + 0.5O_2 \rightarrow CO_2 \end{gathered} \tag{84}$$

The eddy-dissipation model was invoked for turbulence-chemistry interactions, and the option for a diffusion energy source was maintained. The inlet boundary condition was set as "mass flow inlet," while the outlet is set to "outflow." Walls were standard, no-slip, adiabatic walls,

with the exception of the expansion cone at the exit (Figure 3.50), which was set to either "slip" or "symmetry" in order to simulate a far-field condition (in other words, either condition results in no velocity component normal to the surface). Importantly, as a consequence of the assumption of adiabatic walls, the model was not expected to accurately capture the effects of any condition that involves significant thermal radiation to or from the walls. Nonetheless, the model was still expected to serve as a reasonable basis for comparison to the experiment given the typical temperatures in the test rig.

Based on data and recommendations from Briones [106] as well as the work of Briones *et al.* [25], a flamelet combustion model was implemented in later phases of the research. A partially-premixed approach was selected due to its more accurate representation of real-world behaviors, not only in the UCC but in general combustion problems. For the bulk of the late-phase work, adiabatic diffusion flamelets were utilized, and the flamelet-generated manifold was invoked; more detail on the theory behind that method is provided in Appendix A. Detailed chemistry models are required for such an approach; the GRI 3.0 mechanism was utilized most successfully. The GRI 3.0 mechanism contains 53 species; complete details are given again in Appendix A. Finally, in order to provide more direct comparability with Briones [25], the premix variance was set to algebraic (default parameter value) and the source term closure was set to finite-rate only.

Other evolutions to the solver parameters included – as mentioned in the prior section – changing the exhaust outer cowling from a 'symmetry' condition to a 'wall' boundary condition. The other boundary conditions also evolved; to more closely match the work at AFRL, the inlet was modeled as a pressure inlet, while the outlet was set as "mass flow inlet", but with the mass flow component directed outward. The fuel inlet remained a traditional mass flow inlet for the duration of the research. Table 3.7 provides a sample set of boundary conditions for one of these typical late-phase flow solutions. In that case, the target inlet mass flow rate is 0.108 kg/s, and the partially-premixed combustion model is being utilized. Inlet pressure settings are based on

pressure measurements from early experiments at the desired mass flow. The mixture fraction is defined such that $f = 1$ corresponds to 100% propane, and $f = 0$ corresponds to 100% air. The definition of the flow components at the outlet boundary accounts for the high degree of swirl still present in the exit flow; the axial component is positive in the outward direction at the outlet boundary. The locations of the boundaries are displayed by Figure 3.59; the inlet is shown in yellow, the outlet in bright green, and the fuel injection points are visible around the cavity outer diameter as sets of eight red holes. All default residual quantities were monitored for quality of convergence with the addition of a monitor of the area-averaged temperature at the cavity axial midplane. Continuity residuals were generally $\mathcal{O}\sim10^{-3}$, cavity temperature residuals were $\mathcal{O}\sim10^{-2}$ and all remaining residual values were lower. The solution was considered converged when the residuals leveled off with minor oscillations. Convergence was further monitored through examination of various field variable profiles; the full details are presented in Appendix G.

Table 3.7. Example boundary condition setup

Inlet		Fuel Inlet		Outlet	
Initial Total Pressure [Pa]	5200	Mass Flow Rate [kg/s]	0.00185	Mass Flow Rate [kg/s]	0.10985
Initial Gauge Pressure [Pa]	4800	Initial Gauge Pressure [Pa]	6500	Initial Gauge Pressure [Pa]	0
Turbulence Intensity [%]	5	Turbulence Intensity [%]	5	Radial Flow Component	0
Hydraulic Diameter [in]	3	Hydraulic Diameter [in]	0.5	Tangential Flow Component	1
Progress Variable	0	Progress Variable	0	Axial Flow Component	1
Mixture Fraction	0	Mixture Fraction	1	Turublence Intensity	5
				Hydrualic Diameter	3
				Progress Variable	0
				Mixture Fraction	0

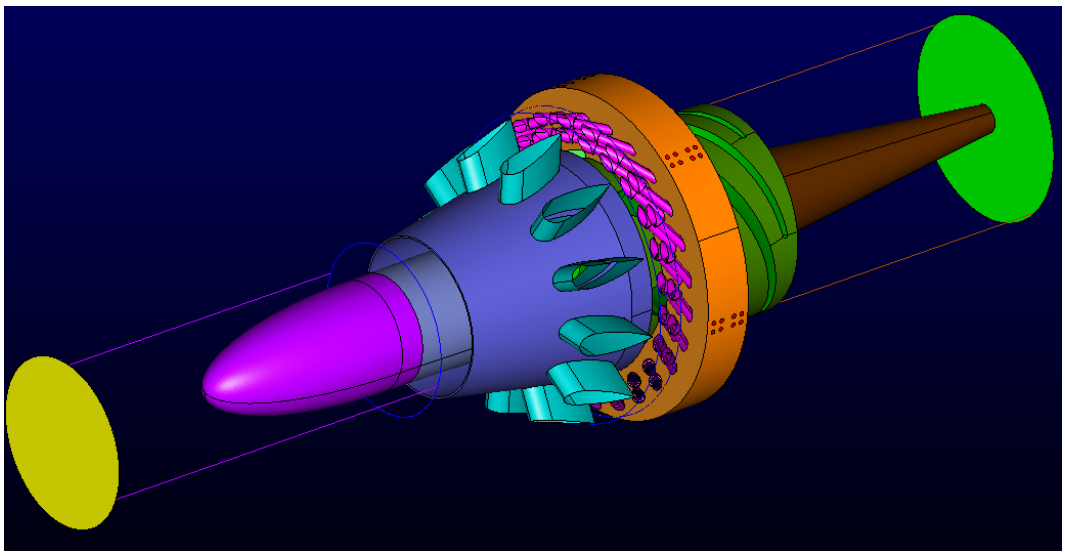

Figure 3.59: Boundary conditions

3.4.1.5. Mach Number Calculation

In the particular solver methods that were selected, Mach number was not a default field variable computed as part of the solution. Therefore, in order to present those results, the Mach number had to be derived from the isentropic relations. In non-reacting cases, the formula was defined by Eq. (85) where $\gamma = 1.4$. In the reacting cases the value for γ had to be manually defined as $\gamma = c_p/c_v$. The value for c_v was also not a default output in the selected solution schemes, so it was derived as a function of the product of the molar mass of the five most prominent species and the gas constant R as shown in Eq. (86),

$$M = \sqrt{\left(\frac{P_t}{P}\right)^{\left(\frac{\gamma-1}{\gamma}-1\right)/(\gamma-1)}} \tag{85}$$

$$\begin{aligned} M(\text{mixture}) = {} & M(C_3H_8) * 44.1 + M(O_2) * 32 + M(N_2) * 56 + M(H_2O) \\ & * 33 + M(CO_2) * 44 \\ c_v = {} & c_p - \frac{R}{M(\text{mixture})} \end{aligned} \tag{86}$$

3.4.2. Workstation

A dedicated HP Z820 desktop workstation was available for early computational work. It was configured with two Intel Xeon E5-2690 v2 processors, each of which contained ten cores with two threads per core; thus 40 total threads were available for parallel processing. Installed memory consisted of 128 gigabytes of 8-channel ECC DDR3, and graphics were handled by a NVIDIA Quadro K6000 card. That workstation alone was sufficient for all early computational work where typical case sizes were on the order of 20 million cells. However, as discussed in prior sections, (1) the grid grew in density, and (2) the combustion model grew from global to detailed chemistry (the number of species modeled increases from five to 53). The workstation was able to load case files for those later projects, but the installed memory was insufficient to run them. Near the end of this research – in preparation for subsequent students – the workstation memory was upgraded from 128 GB to 256 GB; initial trials with the more complex

cases were successful – memory usage for a 66 M cell case with complex chemistry was ~210 GB.

For the latter phases of this research, the large-scale computational problems were facilitated by the Department of Defense (DoD) Supercomputing Resource Center (DSRC), located at Wright-Patterson AFB and managed by the Air Force Research Laboratory (AFRL). Much of that initial work was performed on the computing cluster named "Sprit." Sprit is an ICE X system produced by Silicon Graphic International (SGI); further technical system details can be found in the online documentation [107]. Typical cases of 20M cells were submitted to Spirit with resource requests in a range between 128 and 320 processing cores; the number of requested cores represented a balance between solution speed and queuing speed (larger requests waited longer in the queue). Generally, satisfactory results were obtained using ~150 cores on a 20M cell case in about four hours of wall clock time. Notably, when compared to the performance of the desktop workstation, that metric implied that the problems generated for this work scaled well on the range of processing cores tested.

The DSRC deployed a new system dubbed "Thunder" in the fall of 2015, and the work for this study subsequently shifted to that system. Again, full technical details are documented online [107]. Notably, the more complex cases represented by the final phases of research required substantially more computing time – at 180 cores, a typical case running for 9000 iterations would take approximately 24 hours of wall clock time. In total, the effort represented by this work required approximately 550,000 CPU hours on the DSRC systems in addition to an estimated 50,000 CPU hours on local AFIT hardware.

IV. Common Source Flow Delivery

This chapter presents results and analyses relevant to the first objective: to develop the aerodynamic mechanisms to deliver the proper air and fuel to the high-g cavity from a common flow source. It is organized into two major sections. Section 4.1 presents data from initial cold-flow experimental and numerical testing performed in order to gain better understanding of the diffuser performance and optimize the instrumentation. Initial designs for the core channel plate were simulated, produced, and tested, and a parametric fit was found that guided the work of the second phase. In Section 4.2, cold-flow and reacting tests were performed on new variations of the channel plate, and an optimum configuration was established for subsequent research upon the UCC v2 geometry.

4.1. Initial Testing and Channel Design

The first research objective was founded on attaining satisfactory operation with the common-source diffuser; completion of Objective 1 was a requirement for the commencement of work on Objectives 2 and 3. The mass flow ratio between the core path and the combustion cavity had been demonstrated to be an important performance parameter throughout the literature. For the AFIT UCC in particular, Section 2.5.3 documents the establishment of a 70/30 core/cavity ratio as being an optimum set point. Thus, the initial design of the diffuser was such that, with the middle diameter (MD) in the "Middle" configuration (see Figure 3.3), a 70/30 mass flow split – or a Core Flow Fraction (CFF) of 70% – could be realized. As outlined in Section 2.5.4, Miranda [98] concluded his research by describing several issues with the design of the common source diffuser related to attainment of that goal.

The discussion in this section picked up where Miranda left off by examining the CFF. It was founded upon the initial hypothesis regarding the air injection scheme employed by the

diffuser. The diffuser air injection panels were intended to replicate the radial air injection schemes of past work in terms of jet diameter and injection angle. However, the previous work used two separate flow sources to deliver the cavity air and the core air, and measurements at that time had shown that the cavity required a larger supply pressure. In a common source configuration, there was only one pressure supply by design. The additional pressure drop due to the air injection holes disproportionately affected the inlet air and therefore resulted in an inadequate flow split. As a result, measurements of mass flow within the outer diffuser path by Miranda [98] revealed negligible flow – and at times adverse pressure gradients were measured between the outer path and the combustion cavity.

To balance the pressure drop presented by the air drivers, the core channel restrictor plate was designed as described in Section 3.3.1. The designs were then concurrently evaluated experimentally and numerically. Three initial channel plate design variants with $\lambda = 0.7, 1.0, 1.3$ were fabricated; recall that the equivalent channel size parameter for the baseline unrestricted case was $\lambda = 8$. The inlet mass flow was varied in cold-flow testing and modeling over the set points $\dot{m}_{in} = \{0.06, 0.12, 0.18, 0.24\}$ kg/s.

In the forthcoming discussion, the first matter to be addressed in Section 4.1.1 was a discovery by way of CFD analysis of more complicated aerodynamic fields than anticipated in the diffuser. That analysis provided important context to the diffuser characterization, particularly regarding choices of instrumentation and measurement strategy. Subsequently, cold-flow experimental results are presented with corresponding CFD in Section 4.1.2. Section 4.1.3 then presents the first series of reacting CFD analyses that were performed to understand the effects of combustion on the mass flow splits in the diffuser and the corresponding effects of the channel plate. An important modeling development will be discussed in Section 4.1.6, which then sets the stage for transition to Section 4.2.

4.1.1. Diffuser Recirculation

This section presents a subset of results from a range of test cases, many of which will be discussed in more detail in subsequent sections. The goal here, however, is to illustrate the recirculation phenomena within the diffuser outer flow path.

Contours of velocity magnitude for the baseline $\lambda = 8$ and $\lambda = 4.6$ cases are shown in Figure 4.1. From that figure several qualitative observations may be made. First, the effect of inserting blockage into the core flow is apparent in terms of increased velocity of the cavity air injection. The solid surfaces of the channel plate were observed to induce several regions of low velocity at the inner and outer walls of the core flow path. Furthermore, the acceleration of the flow through the diffuser support vanes was non-trivial in the core flow. Not only was the bulk of the flow present in the core, but the spacing between the support vanes was also narrowest at that interior location. Such an effect was not a design consideration for the support vanes: their primary purpose was structural support with minimal associated pressure loss. Finally, and most importantly, a substantial low-velocity region was observed at the outer diameter of the cavity flow path. If the values of axial velocity were examined at that point, the presence of a recirculation region was revealed where the axial velocity at the outer wall was on the order of -2 m/s.

That result is shown by the one-dimensional axial velocity profiles in Figure 4.2. The profiles were obtained from the axial location indicated by the dashed black line in Figure 4.1. The normalized radial coordinate is given in terms of the overall diffuser height from inner to outer diameter. Profiles from both the inner and outer passages are shown at two different inlet mass flow rates and two different levels of core restriction. While the core path demonstrated a velocity profile typical of canonical channel flow, the outer path velocity profile was highly skewed toward the inner cavity wall (synonymous with the diffuser middle diameter). The peak velocities remained closely attached to the wall of the flow splitter, while at the outer diameter the minimum axial velocity reached about -2 m/s – thus the flow had

reversed and was circulating upstream. The effect was more pronounced at higher mass flow rates. The level of core blockage did not greatly influence the recirculation region; however, increased blockage caused higher peak velocities in the outer path and correspondingly lower peak velocities in the inner path.

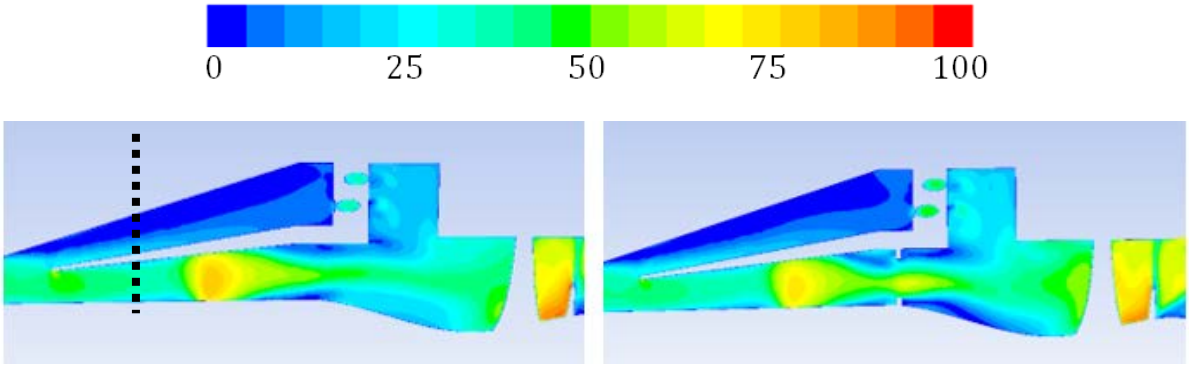

Figure 4.1: Longitudinal planes colored by contours of velocity magnitude [m/s] demonstrating the effects of no flow blockage (left) and the "optimal" flow blockage, $\lambda = 4.6$ (right) at $\dot{m}_{in} = 0.18$ kg/s

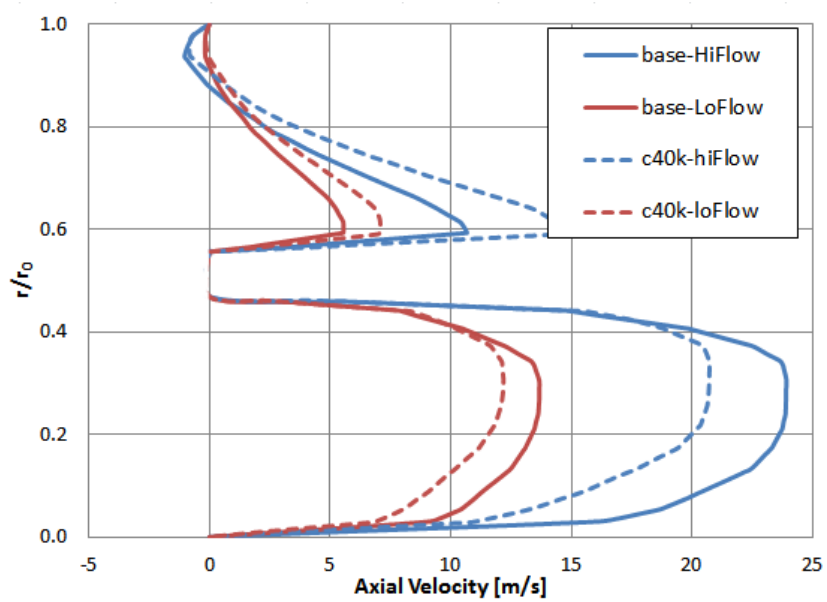

Figure 4.2: Profiles of axial velocity within the diffuser at two mass flow rates and two levels of flow blockage

In an attempt to account for the simulated radial variability, a rake of pitot-static probes was installed in the outer flow path as was shown in Figure 3.30. Results from cold-flow testing with the probes are shown in Table 4.1. Rake 1 was installed closest to the middle diameter – it

was radially the lowest of the three at a point within the first 10% of the outer passage height. Rake 2 was meant to be centered but the final installation ended up with it being closer to Rake 1 at a point about 25% of the passage height. Rake 3 was outboard at about 90%. The result was that Rake 1 captured the peak pressure differential and the resulting peak velocity in the outer passage, while Rake 2 captured velocities that were slightly lower. The pressure deltas at Rake 3 were all negative; it was oriented identically to the other two probes so it was, in effect, facing directly away from the local flow instead of into it. Therefore, the negative pressures measured at Rake 3 were indicators of the reverse flow only; the magnitude of that flow could not be quantified.

Table 4.1. Cold-flow test results from the diffuser probe rake

	Rake1		Rake2		Rake3	
Inlet Mass Flow [kg/s]	Pt - Ps	Velocity	Pt - Ps	Velocity	Pt - Ps	Velocity
0.11	150.14	15.79	79.88	11.52	-18.92	--
0.12	183.49	17.46	101.67	13.00	-16.41	--
0.18	382.07	25.19	237.22	19.85	-34.47	--
0.24	455.53	27.51	424.79	26.56	-73.96	--

There were two major implications to those collected observations: (1) the diffuser flow splitter and outer casing were not optimal for the operating flow environment, (2) estimates of the mass flow rate in the outer path from point measurements of pressure drop would be erroneous due to the nonuniformity of the velocity profile. At a minimum, the estimate would have to account for the velocity as a function of radial coordinate, $\dot{m}_{outer} = \rho A \int v(r) dr$. However, the predicted velocity field in the core flow was better suited to such estimates as a point measurement within its radial span would allow a reasonable approximation of the remaining profile. Therefore, in the remaining discussions, any calculations of the diffuser mass flow rate and the core flow fraction (CFF) were performed with data from the diffuser entrance and the core flow path only. Those locations are illustrated by Figure 3.25. While the

diffuser inlet measurement was accomplished with a pitot-static probe, the geometry at the core location precluded installation of the dedicated pitot-static probes (excessive bending would have been required), thus the traditional approach of discrete total and static measurements was taken in the core.

4.1.2. Cold-Flow Testing

Initial measurements of pressure "deltas" are reported in gauge values in the four rows of Table 4.2 between four locations. These locations are: (1) the total probes in the diffuser inlet and HGV exit, (2) the total and static ports in the outer path, (3) the total and static ports in the core (inner) path, and (4) the total probes in the outer path and the CC. The columns in the table are ordered by decreasing λ – ie, increasing blockage. In the first row, an increase in the total system pressure loss is shown as the level of core blockage increases. In absolute terms, the system total loss with the core open geometry was measured at 1.1% in the baseline case; with channel sizes of 1.3, 1, and 0.7 the total losses were 4.1%, 4.5%, and 4.5%, respectively. In the outer path, no differential between the total and static measurements was found. However, the application of the core restriction induced a differential in the outer path that increased with increasing blockage. Conversely, the total-static differential was very high in the core passage in the baseline case due to its acceptance of nearly all of the incoming flow. That value decreased dramatically with the onset of core blockage, although its trend with λ was not consistent. Finally, a pressure drop was observed in the baseline case across the air injection panels as represented by the delta between the diffuser outer path and the cavity. That point implied that, although the outer diffuser total/static probes did not register any readable flow, there was in fact some flow as evidenced by the pressure drop across the air drivers. A more detailed examination of the air injector pressure drops is given by Figure 4.3 with variance in both λ and $\dot{m}_{in}$. As expected, the air driver pressure drop depended on both factors with increasing $\dot{m}_{in}$ and decreasing λ driving more pressure into the outer path. Notably, at the

lower flow rate of $\dot{m}_{in} = 0.12$ kg/s and $\lambda = 8$ the pressure drop across the panels was effectively zero.

Table 4.2. Observed pressure deltas [Pa-g], $\dot{m}_{in} = 0.18$ kg/s, Core Open

Delta	Baseline	λ = 1.3	λ = 1.0	λ = 0.7
Inlet to Exit	1201	4478	5021	4989
Diffuser Outer Path, Total-Static	---	11	173	222
Diffuser Core Path, Total-Static	801	184	122	153
Diffuser Outer Path to Cavity	659	3491	3992	4265

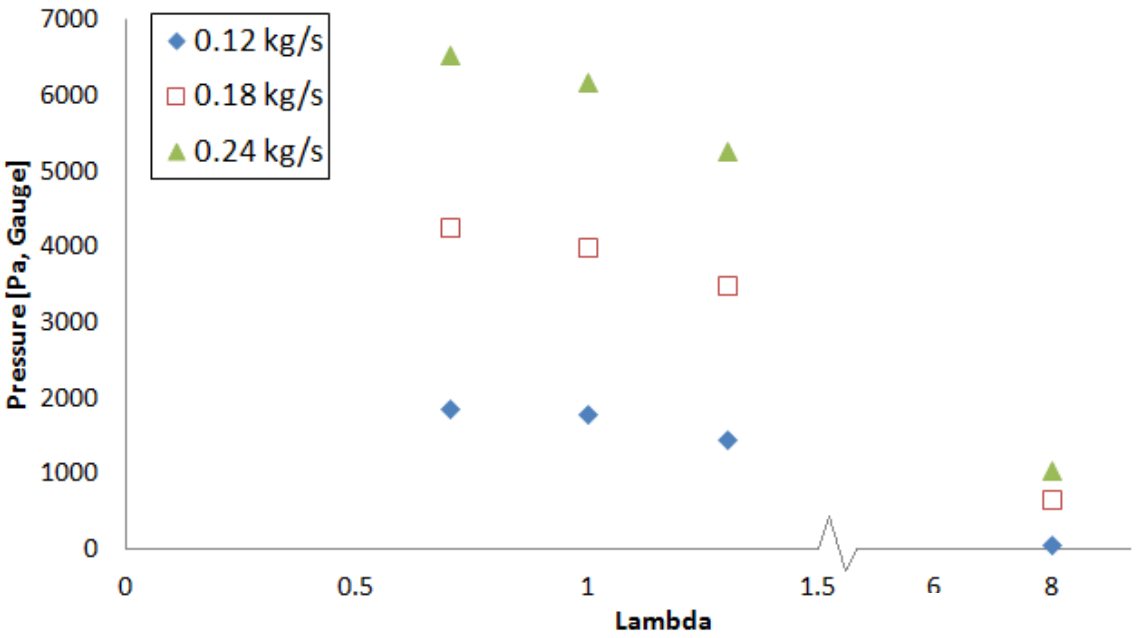

Figure 4.3: Pressure drop across the air injection panels, Core Open

Processing the measured pressures into estimates of mass flow rate was accomplished with a simple incompressible Bernoulli relation as presented in Section 3.1.3. Table 4.3 compares results across inlet mass flow levels and channel sizes. Those results demonstrated that even with the largest channel size, values of the CFF were well below the target of 70%. In

the numerical model, the CFF was determined with a surface integral of mass flow within the core area at an axial location about 2 cm downstream of the middle diameter flow split; that location is highlighted in Figure 4.1. The CFD results at corresponding experimental conditions are shown as well in the table. The points at $\lambda = 0.7, 1.0, 1.3$, and 8.0 were simulated at all three of the experimental mass flow rates; findings from the model matched the experiment in that that the CFF was a strong function of λ while being substantially less sensitive to $\dot{m}_{in}$. However, quantitative agreement with the experiment was inconsistent. In the baseline case the CFD was shown to greatly under-predict the measured values; however when the channel plate was installed the CFD was closer – usually within 10% of the experiment with the exception being at $\lambda = 1$ where the CFD over-predicted the CFF by about 30%.

In addition to the tested channel sizes, the computational model was extended in a parametric study over a selected range of channel sizes and mass flow rates as documented in Figure 4.4. Utilizing the extended parametric CFD results at $\lambda = \{2, 2.5, 5\}$, a logarithmic trend was found to describe the resultant relationship as defined by Equation (87) with a fit quality of $R^2 = 0.998$.

$$CFF = 23.7 \ln \lambda + 33.6 \tag{87}$$

Thus, a solution for lambda at the desired level of $CFF = 0.7$ yielded $\lambda_{70} = 4.65$. A computational case with a channel plate defined by $\lambda = 4.6$ was subsequently generated and solved with a calculated value of $CFF = 0.71$, therefore indicating that the prediction was correct. Given that the CFD was shown to under-predict the CFF at higher λ, a conservative estimate for the required blockage for new experimental hardware was determined to be $\lambda_{70e} = 4.0$.

Table 4.3. Numerical and experimental cold-flow results

λ	Inlet [kg/s]	EXP CFF	CFD CFF
0.7	0.12	23.7	26.4
0.7	0.18	27.0	24.5
0.7	0.24	27.5	24.3
1	0.12	24.0	34.3
1	0.18	26.0	34.3
1	0.24	26.8	34.2
1.3	0.12	34.9	39.6
1.3	0.18	38.3	40.5
1.3	0.24	39.7	38.0
8	0.12	100.0	82.6
8	0.18	100.0	82.8
8	0.24	100.0	82.9

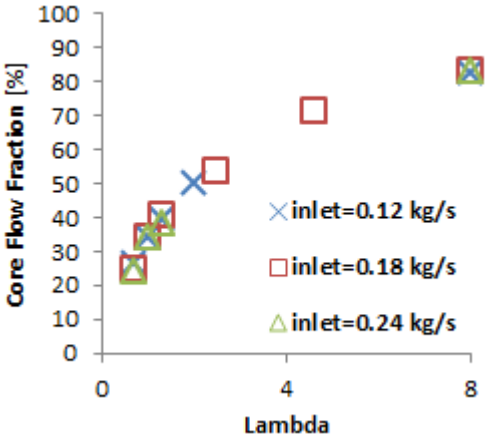

Figure 4.4: CFD parametric study of core blockage versus core flow fraction

As the research expanded a more compact nomenclature was developed. Cases were referenced as c## where ## indicated the channel size. Furthermore, investigations were initiated into the effect of the channel orientation with respect to the HGV. As illustrated by Figure 3.2, the channel openings could be positioned either "in-passage" or "on-vane." A "k" suffix was added to a case label to indicate an "on-vane" orientation. For example, case c50k was configured with $\lambda = 5.0$ "on-vane."

Figure 4.5 presents static pressure contours for the baseline and c50k cases. As implied by the data in Table 4.3, the CFD did not predict adverse pressure gradients in the outer path of the diffuser. A quantitative comparison between four channel configurations was implemented by taking area-weighted averages of the pressure on annular surfaces within the inner and outer flow paths just upstream of the channel plate location and the air drivers, respectively, and comparing against similarly computed averages just downstream of those same features. The results were representative pressure drop values for both the core and cavity flow paths as shown in Table 4.4. A positive pressure drop was certainly present in the cavity path; more

notably, it was nearly ten times the drop in the core in the baseline case. The resulting flow field would be strongly biased toward the lower-resistance path of the core, thereby affecting the ability of the diffuser to split the inlet air as designed. The pressure drop increased across both features upon installation of the channel plate. Upon observation of the contours, it was noted that a significant reduction in pressure in the core had a second-order effect of diminishing the pressure in the cavity. However, the ratio between the core and cavity pressure drops increased, thus indicating that the flow bias toward the core was reduced. The core pressure drop again increased by a substantial margin upon "clocking" the channel openings. This was the result of the HGV leading edges becoming influential upon the flow, whereas in the in-passage orientation the leading edges were "hidden" from the upstream flow by the channel plate blockage. Again, the cavity drop increased as well, but at a reduced rate – thus the core/cavity pressure drop ratio increased. In a similar fashion, the c40k case increased the pressure drops as well as the value of the core/cavity ratio.

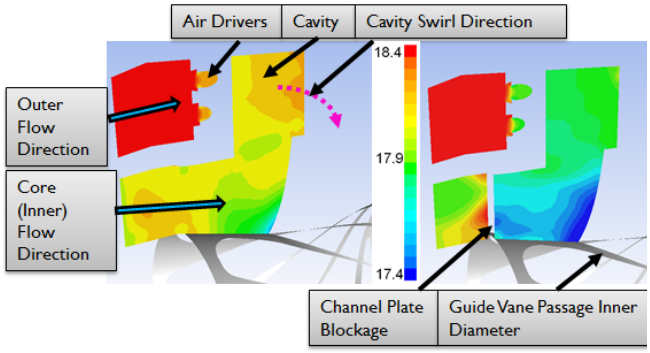

Figure 4.5: CFD contours of pressure [kPa-g] of the baseline (left) and c50k cases

Table 4.4. Passage pressure drop weighted averages [Pa-g]

Case	Cavity Pressure Drop	Core Pressure Drop	Core/Cavity
Baseline	368.9	48.0	0.130
c50	467.0	185.9	0.398
c50k	532.9	328.5	0.616
c40k	771.4	617.8	0.801

4.1.3. Initial reacting tests

Subsequent to the cold-flow test and simulation campaign, efforts were focused on reacting-flow variants of the same. Initial CFD was relegated to very simple combustion models as introduced in Section 3.4.1.4 in order to facilitate successful runs with relatively minimal sources of error. A set of calculations were performed at the moderate scale mass flow rate,

$\dot{m}_{in} = 0.18$ kg/s and with the channel plate at its predicted numerically-optimum sizing of $\lambda = 4.6$. Thus, the mass flow rate into the cavity was $\dot{m}_{cav} = (1 - CFF)\dot{m}_{in} = 0.054$ kg/s. The cavity equivalence ratio was then defined by Eqn. (88) with the stoichiometric air-fuel ratio for propane-air combustion is $A/F|_{stoich} = 15.64$. For example, the fuel flow rate to achieve $\phi = 1.0$ would be $\dot{m}_{fuel} = 0.00345$ kg/s.

$$\phi_{cav} = \frac{\dot{m}_{fuel}(15.64)}{\dot{m}_{cav}} \tag{88}$$

Furthermore, as implied by the cold flow results in Table 4.4, it was hypothesized that the orientation of the channel opening with respect to the hybrid guide vane (HGV) leading edges might have some effect on the combustion process. Thus, numerical contours of temperature are shown in Figure 4.6 from three configurations: the baseline case with no channel plate (top), and then two variations of the $\lambda = 4.6$ plate in the two different orientations. The axial extents of the cut begin downstream of the diffuser flow splitter, and end just downstream of the HGV trailing edge. The angle of the cut was defined such that the plane passed through the center of one of the HGV passage; consequently, one of the diffuser support vanes was intersected at an odd angle, thereby producing the asymmetric shape visible in the images. The first conclusion was that the differences between the unrestricted and the "in-channel" case were subtle, but notable. It has already been noted that the added restriction increased the velocity of the air injected into the cavity and the result in the reacting scenario was that the temperatures were slightly higher, and the hot mixture appeared to be better distributed throughout the cavity cross-section. The second observation was that, in the "in-channel" case, the hot gases from the cavity are drawn into the low-velocity region downstream of the channel blockage, but upstream of the cavity front wall. The low-velocity region therefore acted as a flameholder, locally facilitating hot-gas migration.

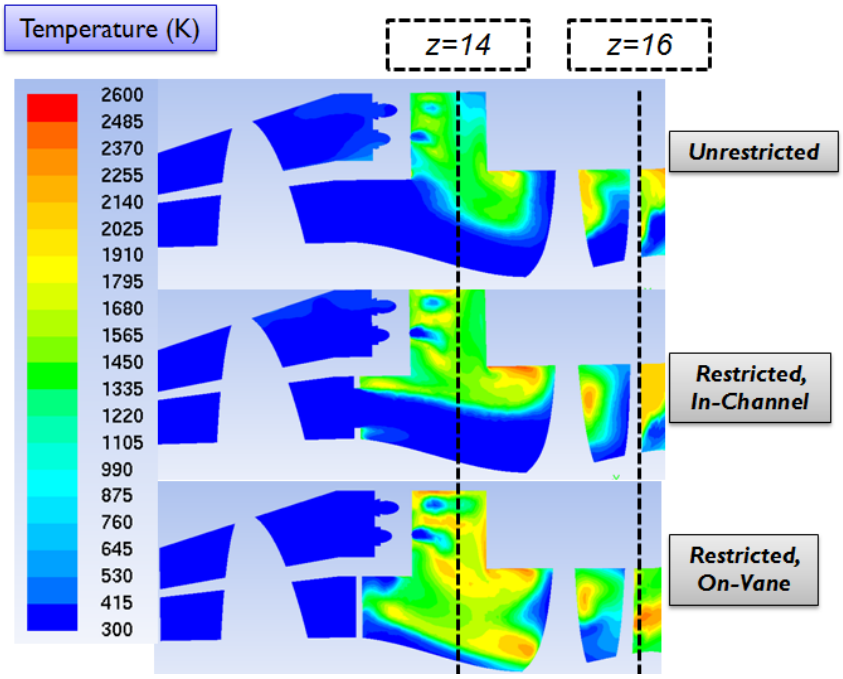

Figure 4.6: Longitudinal planes of temperature contours for the three channel-restriction orientations

The final and most notable observation was that, in the "on-vane" case, the flameholding behavior of the channel plate was magnified. In that case, the channel opening was centered on the HGV leading edge while the channel blockage was centered on the HGV passage. Thus, the low-velocity (and low-pressure) region downstream of the blockage had the desirable effect of drawing the hot cavity products down nearly the entire radial height of the HGV passage. This was a significant finding as most prior work had documented the propensity of the hot gas to remain biased toward the outer diameter. Included in Figure 4.6 are dashed black lines describing axial (z-coordinate) reference locations. Cutting planes of constant axial coordinate corresponding to those positions are shown in Figure 4.7 and Figure 4.8; the contours are similarly colored by temperature [K]. Figure 4.7 also includes transparent hole patterns representing the position of the cavity air driver injection points.

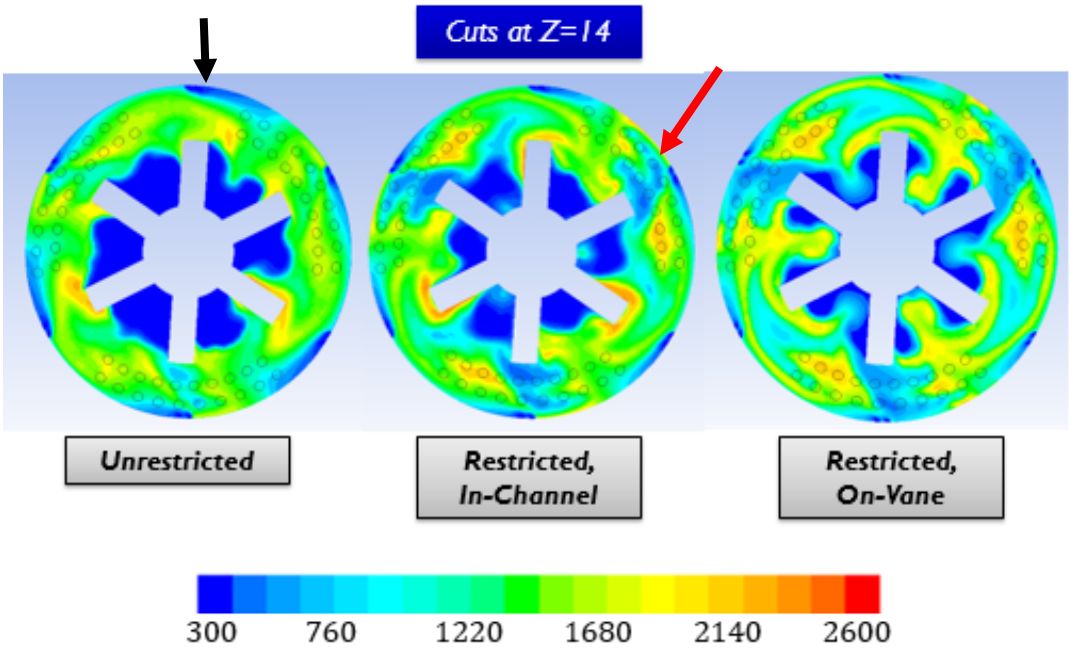

Figure 4.7: Axial planes through the combustion cavity of temperature contours for the three channel-restriction orientations

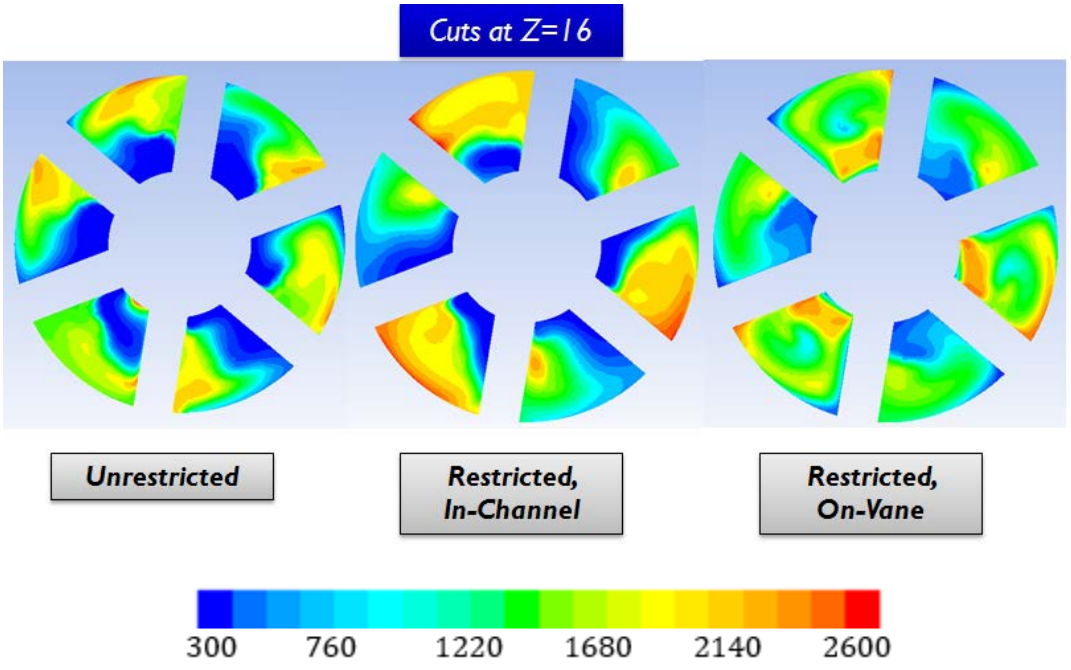

Figure 4.8: Axial cuts at the exit plane of temperature contours for the three channel-restriction orientations

The first observation to address, common to both figures, was the presence of semi-periodic asymmetry. Patterns of behavior tended to correspond to the HGV airfoils and

passages; similarity was found in patterns of every other passage. That is, the contours within the passages at the (approximately) 1, 5, and 9 o'clock positions were similar; likewise, similarity was found in the 3, 7, and 11 o'clock passages. It was found that the combustion dynamics within the cavity were closely coupled to the presence – or lack thereof – of the upstream air driver jets. The jets in the UCC v2 configuration represented here were restricted to the three discrete panels as illustrated in Figure 4.7. The panels were oriented such that they were centered over every other HGV airfoil, thus inducing the observed semi-periodic behavior.

The second observation was that the effects of the core restriction relative to the baseline case were again qualitatively evident. Comparing the left (baseline) image with the center image of Figure 4.7, the fuel plume along the outer diameter (indicated by the black arrow) was more disbursed and the cold regions (corresponding to the propagating cores of the air drivers and indicated by the red arrow) were more concentrated. This indicated that the air was being injected more forcefully and thereby applying more turbulence to the cavity bulk motion. The inward extent of the hot gas migration was also greater in the restricted case than in the unrestricted case due to the higher cavity velocities brought about by a more balanced pressure gradient between the core and the outer diffusion paths.

The third observation regarded the relatively dramatic increase in the inward radial extent of the flow migration in the "on-vane" case compared to the "in-passage" case. This supported earlier assertions that the solid portion of the channel plate acted as a flameholder and drew the hot products into the induced low-pressure regions. In Figure 4.8 this effect is shown to propagate through the HGV passages. The temperature distribution in the in-channel case was already improved over the unrestricted case with increased uniformity across the span of the exit plane. The on-vane case improves the temperature distribution further by allowing hot gas migration almost all the way to the inner diameter – though only in three of the six passages. Achieving hot gas migration to the inner diameter was an important

accomplishment, however it should be noted that the temperature profile was still not ideal. In those passages with the greatest inward migration, the peak temperatures also tended to be concentrated toward the inner diameter while cores of cooler air remained present in the central portion of the span.

4.1.4. Exit Temperature Profiles

Initial investigation into the exit temperature profiles was accomplished utilizing the averaging procedure outlined in Appendix F; that procedure is invoked and discussed at greater length in Sections 6.1.3 and 6.3.2. The profiles span from the inner diameter ($r/R = 0$) to the outer diameter ($r/R = 1$) of the exit plane. A representative depiction of the exit plane location is shown by Figure 4.9; it was positioned such that it was approximately normal to each of the vane walls and immediately upstream of the trailing edge of the pressure-side vane. Each profile was averaged first laterally at defined radial intervals along each exit plane, then the profiles from each of the six exit planes were themselves averaged into a single curve. Data were examined after the method of Section 4.1.3 with three cases under consideration: the baseline, the restricted in-passage, and the restricted on-vane. In all three cases the operating conditions were $\dot{m}_{in} = 0.18$ kg/s and $\phi_{cav} = 1.37$. The results from those three cases appear together in Figure 4.10. The peak temperatures in each profile range between 1400 and 1750 K, while the minima all occurred at the inner diameter. The overall mean exit temperatures for the baseline and on-vane configurations were similar at 1080 and 1060 K, respectively; the mean for the in-passage case, however, was substantially greater at 1320 K. All three cases demonstrated the previously-observed tendency of the hot gases to remain biased toward the outer diameter, while the on-vane case demonstrated a uniquely-shaped profile that involved a nearly linear change from the hottest ID temperature among the three cases to the coldest OD. This quantitative evidence supports the qualitative observations of Section 4.1.3. Further discussion and analysis of this issue are the primary topics of Chapter 6.

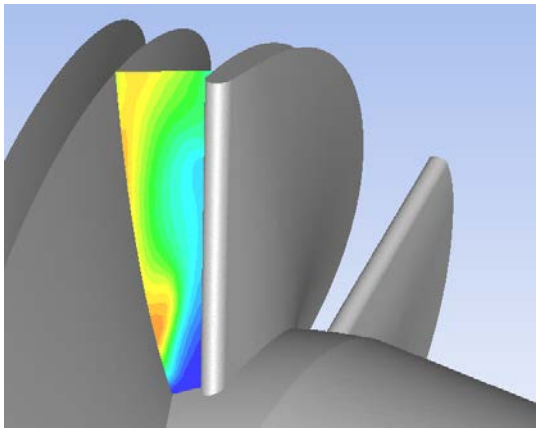

Figure 4.9: Location of the HGV exit plane as defined for this research

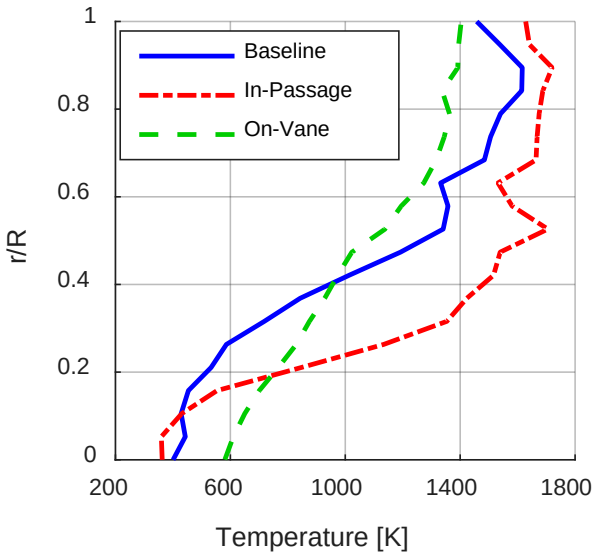

Figure 4.10: Averaged exit temperature profiles of the baseline, in-passage, and on-vane configurations

4.1.5. Mach Number Distribution

As the selected Fluent solver method did not directly produce Mach number as a field variable, a user-defined function was programmed as detailed in Section 3.4.1.5. A non-reacting case of the c40k configuration is shown on the top of Figure 4.11 while its reacting counterpart is shown on the bottom. For context, the contours of velocity magnitude from the same two cases are shown in Figure 4.12. The presence of reactions in the system had the anticipated effect of increasing acceleration of flow through the HGV passages due to expansion induced by heat release. Mach numbers at the exit plane approached values of $\sim M = 0.6$ in the bulk flow and were generally higher near the walls. The latter observation was explained by the contraction of the HGV passage at the inner diameter that induced greater acceleration than at the comparatively wide OD. The speed of the flow decreased downstream of the exit plane though it remained concentrated largely at the OD due to its strong residual circumferential motion. The symmetry condition imposed by the outer exhaust "wall" served to remove any radial components, thereby approximating the behavior of exhausting into ambient conditions.

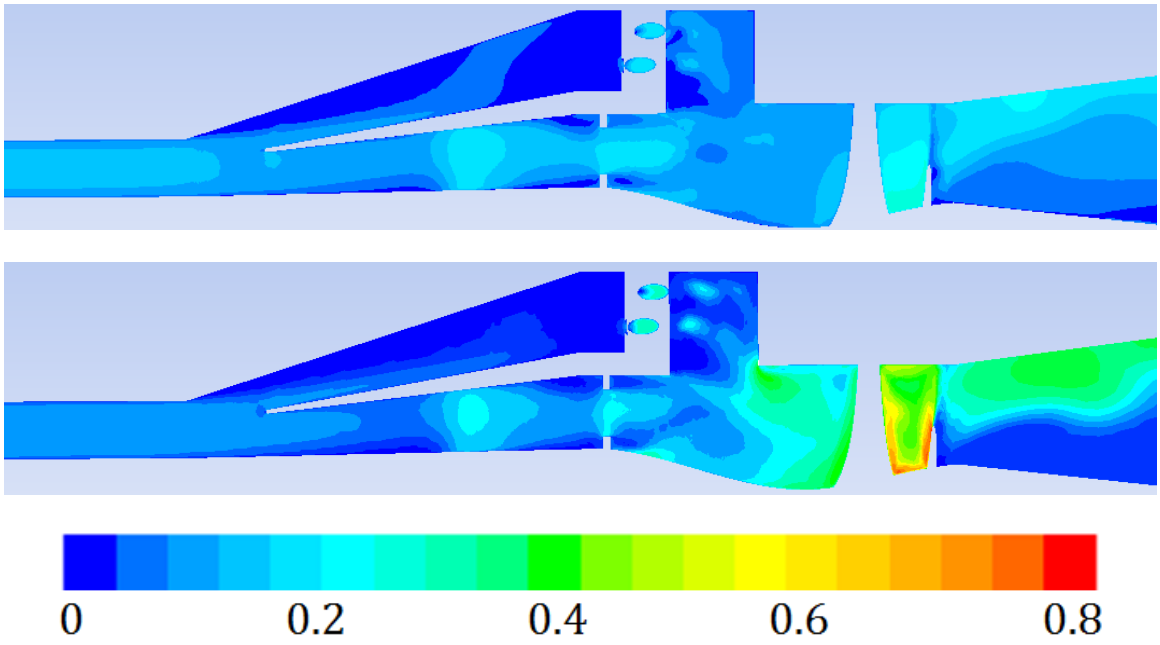

Figure 4.11: Longitudinal planes of Mach number at $\dot{m}_{in} = 0.18$, case c40k, non-reacting (top) and reacting (bottom, $\phi_{cav} = 1.37$)

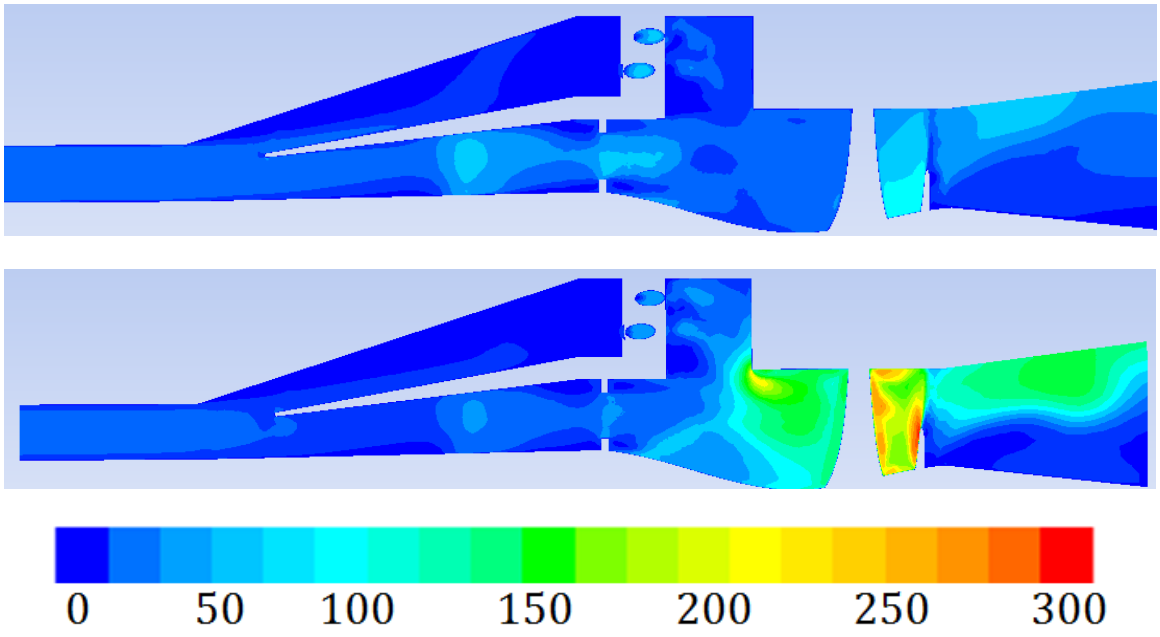

Figure 4.12: Longitudinal planes of velocity magnitude at $\dot{m}_{in} = 0.18$, case c40k, non-reacting (top) and reacting (bottom, $\phi_{cav} = 1.37$)

4.1.6. HGV Modification

To present a complete accounting, an important detail of the foregoing section must now be separately addressed. Due to an oversight, the CFD model utilized for all of the initial UCC simulations was integrated with the Miranda HGV centerbody design. The Miranda design was a concept only – it had never been produced. The actual hardware present in the UCC up to that point had been the original straight-inlet Wilson LLCB design. The distinction between the two was described in part by Section 3.3.4; exact details on the solid model construction parameters that led to the distinction are provided by Appendix B. For this current discussion, cutaway views of the two designs are shown in Figure 4.13. The cutting plane in the images is oriented such that it passes through the midpoint of the leading edge of an airfoil in each case. The Miranda design was intended to remain as axially straight as possible as it passed beneath the circumferential cavity. As a result, though the trailing edge exit angles were similar in magnitude, the construction was performed such that the exit area of the Miranda design was nearly double that of the Wilson design. This was a consequence of the delayed pitching of the Miranda airfoils: since their turning began later than the Wilson design, they completed fewer degrees of revolution and were thereby shorter in overall length. Wilson's vanes were longer, so they completed more revolutions over the same axial distance, and they were therefore closer together. The passage widths at the exit plane of the Wilson and Miranda designs were 0.92 and 1.53 cm, respectively. The implications of these differences will become more clear in forthcoming discussion, but it must be clarified that all of the numerical results of Sections 4.1.2 and 4.1.3 were performed using the Miranda vane, while the corresponding experimental rig had the Wilson LLCB vane installed. All CFD described in the Section 4.2 was performed with the Wilson vane properly modeled.

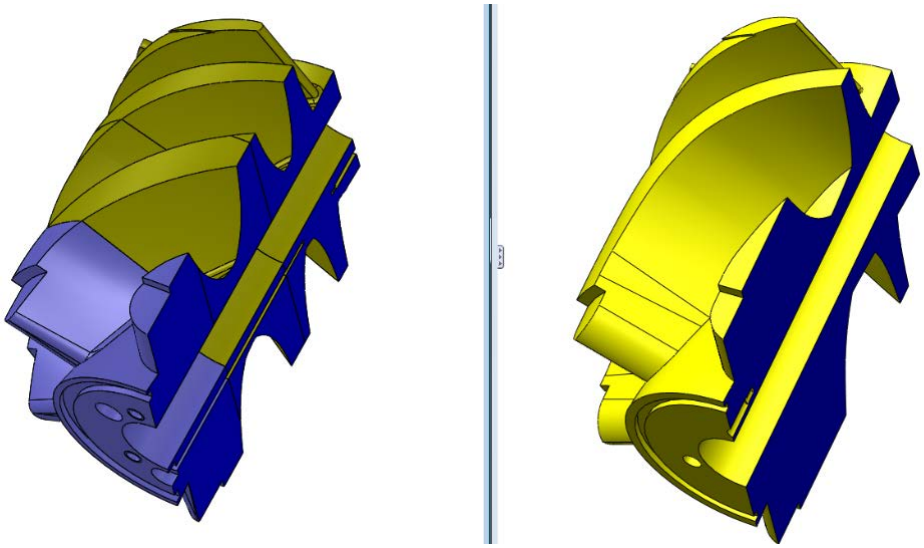

Figure 4.13: Axial cutaway views of the Wilson centerbody (left) and the Miranda centerbody (right)

The differences between the two designs were evaluated by examining contours of Mach number utilizing cases from the current section (that integrated the Miranda centerbody) as well as cases from Section 4.2 (that correctly integrated the Wilson centerbody). The two were compared in Figure 4.14 with an "in-passage" channel configuration at $\dot{m}_{in} = 0.12$ and $\phi_{cav} = 1.37$. The first observation was the increased vane turning made manifest by the number of "cutouts" in the longitudinal contour. There is one full and one partial cutout created by the solid vane surface in the case of the Miranda geometry; in contrast, the Wilson vane contour demonstrated three full cutouts, a result of the increased number of turns created by the increased helix pitch. Furthermore, the exit Mach number was slightly higher in the Wilson configuration on average, but significantly higher at the ID. As discussed in Section 4.1.5, the contraction at the inner diameter contributed to increased acceleration. The influence on the exit temperature profiles was examined by Figure 4.15. Notably, while the ID and peak values are similar, the OD temperatures were substantially different between the two. This was a result of increased dissimilarity between neighboring exit passages as will be discussed in Section 4.2.2.2.

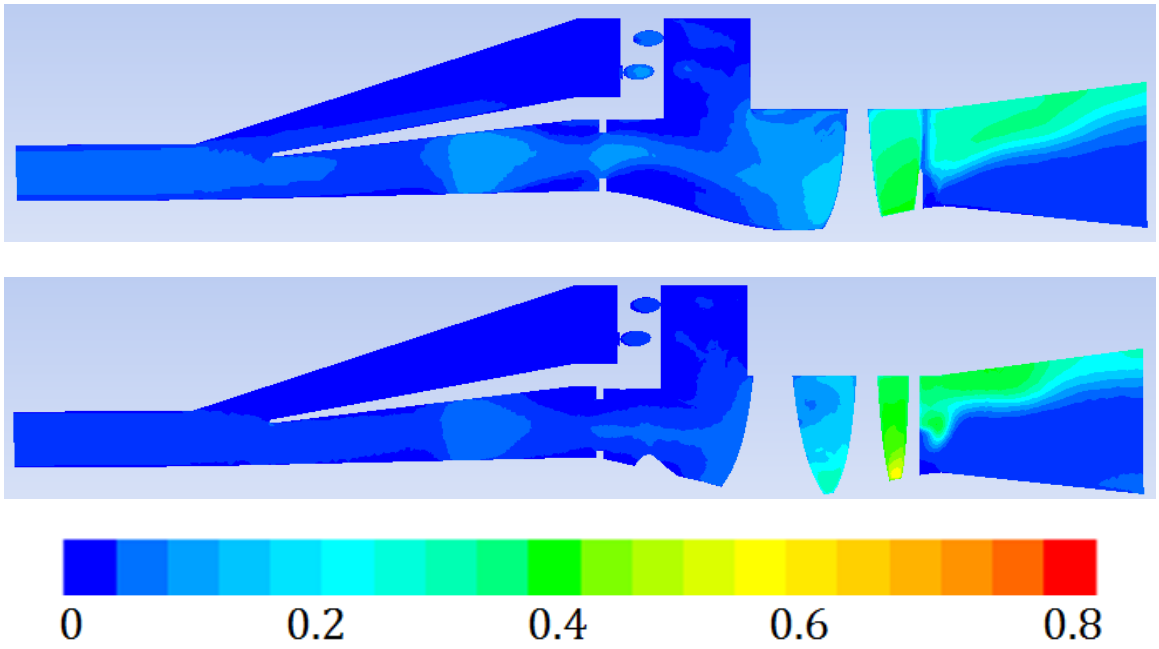

Figure 4.14: Comparing Mach number contours in a reacting case in c40 configuration at $\dot{m}_{in} = 0.12$ kg/s and $\phi_{cav} = 1.37$ with the Miranda vane (top) and the Wilson vane (bottom).

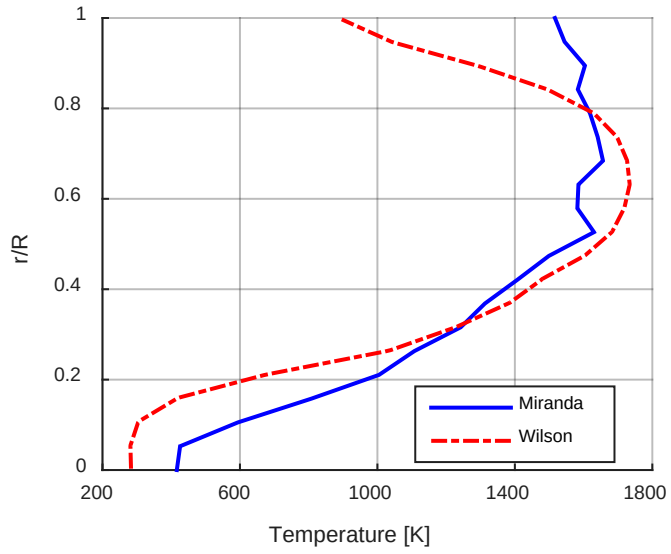

Figure 4.15: Comparing exit temperature profiles in a reacting case with channel configuration c40 at $\dot{m}_{in} = 0.12$ kg/s and $\phi_{cav} = 1.37$

4.2. Common-Source Reacting Flow Analysis

The campaign following the initial cold-flow testing featured the first successful reacting tests of the AFIT UCC with the common-source diffuser installed. Based on the cold-flow experience, the decision was made to reduce the target levels of inlet mass flow rate. Specifically, the COAL Lab compressor was capable of providing flow to the UCC at rates up to 0.24 kg/s but that peak point in particular could only be sustained for ten to fifteen seconds before the pressure reservoir was depleted. Points at 0.18 kg/s could be sustained only for 30 to 45 seconds. The peak long-duration sustainable flow rate was found to be right around 0.108 kg/s. The reservoir still depleted, albeit very slowly – run times up to an hour were routinely executed at that condition without incident. Run times at a slightly increased rate of 0.12 kg/s (20 SLPM) could be executed but were typically limited to about 30 minutes. Thus – as relatively long-term stability was required for combusting tests – much of the campaign described here and in subsequent chapters was restricted to peak inlet flow rates of 0.120 kg/s. An example of the resulting change in Mach distribution was given by comparison of the contours in Figure 4.11 and Figure 4.14. With the Miranda centerbody, changing from 0.18 to 0.12 kg/s inlet mass flow yielded a decrease in exit Mach from 0.6 to 0.4, on average. The same could then be inferred about the Wilson geometry utilized in this section as the comparisons between the two in Figure 4.14 demonstrated that they were similar overall in Mach distribution.

4.2.1. Experimental reacting flow results

Additional channel plates were produced with $\lambda = 4$ and 5 and the baseline case, $\lambda = 8$, remained a part of the test matrix. Table 4.5 summarizes the levels of the operating parameters that were examined during the reacting-flow common-source test block. Axial reference locations area again defined within the computational geometry to facilitate discussion; these are shown in Figure 4.16.

Table 4.5. Primary test condition matrix for common-source reacting-flow tests

Channel Size (λ)	Channel Orientation	Total Air Flow [kg/s]	Equivalence Ratio
4, 5, 8	on-vane, in-passage	0.06, 0.108, 0.120	0.80, 1.37

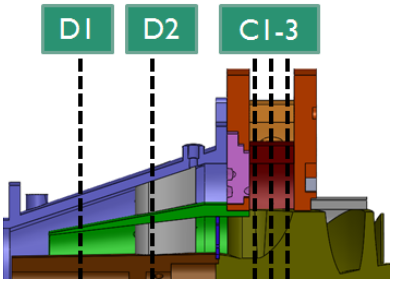

Figure 4.16: Axial reference labels

As in earlier tests, the primary performance metric of interest was the core flow fraction (CFF). In Figure 4.17, the cold-flow data from Section 4.1 are repeated alongside updated cold-flow results utilizing the second-iteration channel plates. Separate logarithmic trend lines were generated for the experimental and numerical results to highlight the differences between the two. The CFD data for $\lambda = 4.6$ and 8 were recreated using the proper centerbody. Repeated points for a given channel size again represent variations in mass flow. Incorporating the proper vane geometry led the CFD to more consistently over predict the CFF; the discrepancy was fairly constant throughout the range of λ with a difference of about 7%. Notably, testing with the baseline unrestricted configuration ($\lambda = 8$) revealed a value of CFF not far from the desired point $CFF = 0.70$. This was contrary to earlier results both in Miranda [98] and in Section 4.1. The new result most likely arose from an improvement in instrumentation (as discussed in Section 3.1.3) and, more importantly, post-processing based on the lessons learned from the initial cold-flow tests. Accounting for some of the finer details of the diffuser aerodynamics – such as the predicted shape of the core velocity profile – changed many of the assumptions that went into estimating the mass flow rate based on the point pressure probe results. Specifically, estimates of the total area at the point of the core probe measurement were revised to reflect the presence of a boundary layer.

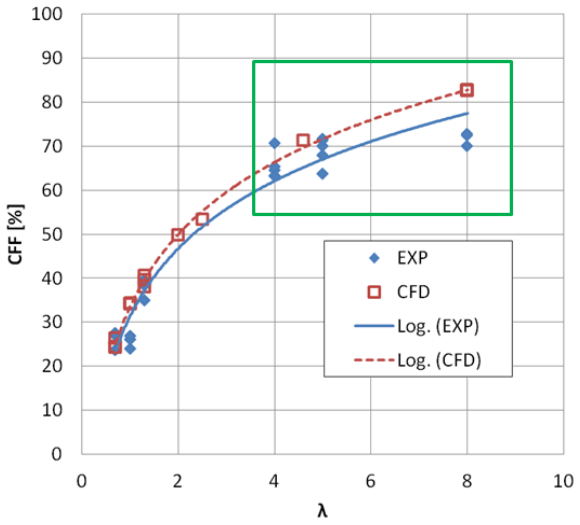

Figure 4.17: Cold-flow experimental and numerical variation of CFF with λ

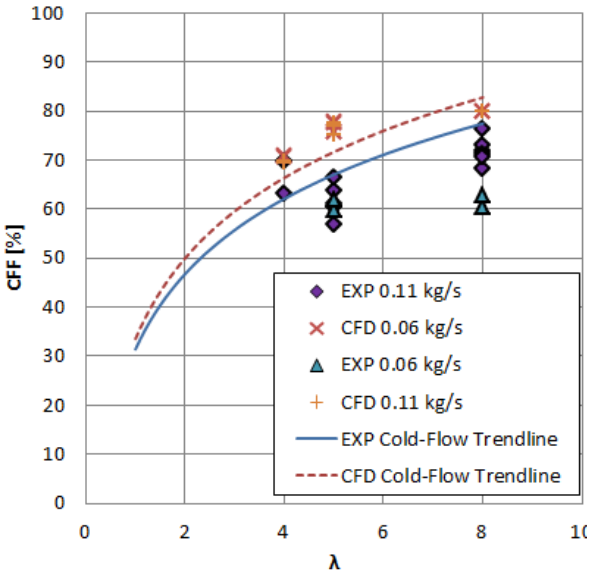

Figure 4.18: Reacting flow experimental and numerical data overlaid with corresponding cold-flow trend lines

Accompanying the cold-flow results were similar reacting-flow test results shown in Figure 4.18. Reacting tests were only run at the conditions of Table 4.5; no effort was made to combust with the early-version channel plates. However, the trend lines from the cold-flow data were transcribed to Figure 4.18 in order to illustrate the impact of combustion on the flow distribution. Experimental results provided two observations: (1) there was substantially increased variability with respect to mass flow, and (2) the general trend indicated that CFF decreased at a given condition relative to its cold-flow counterpart. The general conclusion was mixed: the variability of the data made it difficult to determine, in reacting flow, whether or not there was an optimal channel size. The implication of the baseline results was that, in some cases, the desired flow split was attained without any core blockage at all. The final design decision that resulted from these tests, however, was to keep the channel plate with $\lambda = 5$ installed in the "on-vane" configuration based on (1) the potential for enhanced inward flow migration, and (2) the vision of future HGV designs incorporating cooling schemes that would utilize the cold core flow from the channel openings.

4.2.2. Extended Numerical Analysis with v2 Geometry

This section documents the first detailed CFD insight into the highly complex nature of the combustion environment. The results discussed in Section 4.1.3 were instructive and the CFD analysis proved critical to that early phase of research by way of identifying the proper channel plate design and generating more informed decisions about how to instrument, measure, and process data from the diffuser. However, as discussed in Section 4.1.6, it was discovered that those CFD models contained the incorrect geometry to compare against the experiments. Various other incremental changes to the numerical grid and the solver strategy were incorporated as well from the lessons learned from those first results. Grid refinement increased substantially; as discussed in Section 3.4.1, a move was made away from the "T-Rex" style grid to a purely unstructured grid that led to higher cell quality. Additionally, the transition from the CFD of Section 4.1 to 4.2 was accompanied by the transition from the grid design shown in Figure 3.50 to Figure 3.54 where the latter incorporated the full inlet (vs. an annulus) and a walled outlet cowling (vs the "symmetry" approximation employed early on). For those reasons, the work in this section contains the more thorough examination of the UCC. Several important characteristics of the general circumferential cavity (CC) flow field are discussed, and three broad perspectives are given in terms of the distribution of temperature, the tangential velocity and residence time, and the radial velocity and flow migration patterns.

4.2.2.1. Mach Number Distribution

The Mach number distribution was recorded for the reacting CFD cases for several axial locations. For each measurement, a surface of constant axial coordinate was defined, and the values of Mach number were subsequently integrated across the surface on a Mass-averaged basis (see Appendix A.4) with the results recorded in Table 4.6. Seven axial locations were defined from the inlet upstream of the diffuser to the HGV exit plane. Note that two axial surfaces within the diffuser were per the procedure of this chapter, including an inner (core)

annular region and an outer annular region. The HGV Inlet surface was defined immediately downstream of the HGV leading edges to document the velocity of the incoming core flow, while the Cavity Midpoint was defined at the axial center of the circumferential cavity. The HGV Max Area location was defined part-way through the HGV passage at the point where its inner diameter reached a minimum per the reduced-Rayleigh-loss design.

Table 4.6. Mass-averaged Mach number values for varying $\dot{m}_{in}$ and varying axial position

z/L		$\dot{m}_{in}$ [g/s]	60	108	150
0.13	Inlet		0.00	0.04	0.04
0.43	Inner Diffuser		0.03	0.05	0.06
0.43	Outer Diffuser		0.00	0.01	0.02
0.58	HGV Inlet		0.03	0.06	0.08
0.60	Cavity Midpoint		0.03	0.06	0.07
0.64	HGV Max Area		0.07	0.13	0.17
0.70	HGV Exit Plane		0.17	0.31	0.42

Note that at the lowest mass flow rate, $\dot{m}_{in} = 0.060$ kg/s, some axial locations demonstrated values of $M < 0.01$, which appear as zero in the table, specifically the inlet and the outer diffuser path. Minimum Mach numbers were observed at both of those locations regardless of mass flow rate due to (1) the relatively large duct diameter of the upstream inlet, and (2) the recirculation zone in the outer diffuser. Mach numbers in the primary combustion zone at Cavity Midpoint were relatively low; that trait is generally desirable in gas turbine combustion in order to promote optimal mixing and residence time with minimal losses. The Mach number at the exit plane, however, was somewhat lower than desired. Although the velocity magnitudes at the exit were estimated to exceed 400 m/s at some points, the thermal expansion and the resulting density reduction had the anticipated of reducing the Mach number. Modern gas turbine combustor design generally calls for high subsonic conditions – M~0.8 – at the entrance to the high-pressure turbine rotor. Two observations resulted from this analysis: first, the design of the AFIT UCC may need to incorporate work in the future to obtain

higher exit Mach numbers; second, however, higher exit Mach numbers may fall naturally from future work dedicated to operating the AFIT UCC at higher overall pressure ratios.

4.2.2.2. Temperature and Stream Distribution

In Figure 4.19, planes of constant axial coordinate at reference locations C1 and C3, as defined by Figure 3.56, are shown colored by temperature [K]. Portions of the HGV geometry are included and appear in shaded grey color. Important features of the cavity flow environment are highlighted: the cold cores of the air driver jets are clearly visible in the front portion of the cavity (C1 – left column of images). Those effects were absent at location C3. Similarly, the six fuel injection locations are also made visible as cold jets. By design, three of the fuel injection locations were centered upon cavity air injection plates while the three other fuel injectors were centered between the plates. The results of that semi-symmetrical arrangement were semi-periodic patterns to the flow field. Those fuel streams that met the air drivers were thoroughly mixed, and heat release followed as indicated by the high-temperature regions just downstream (clockwise). Conversely, the fuel streams that were not mixed by the air drivers spanned nearly the entire radial height of the combustion cavity. Notably, all six fuel injectors were positioned directly above the top surfaces of the HGV airfoils. Thus, the momentum of the unmixed fuel streams carried them directly to those HGV surfaces at which point they were diverted to the core passages on either side. The bulk circumferential swirl of the cavity was interrupted by the unmixed fuel jets thereby reducing the effective residence time of the partially-combusted mixture within the cavity. Finally, minimal qualitative distinctions are observable when comparing the $\phi = 0.8$ and $\phi = 1.37$ cases (the top and bottom rows, respectively) (cases as defined in Table 4.5). Temperatures appeared slightly higher at low-ϕ. For context, the calculated adiabatic flame temperatures at ambient pressure and temperature at $\phi = 0.8$ is 2025 K; similarly, at $\phi = 1.37$ it is 2053 K. Thus, the trend observed in Figure 4.19 is opposite of what might be expected from a well-mixed system, although the

intent of the UCC was not necessarily to mix and burn entirely in the cavity. The high-ϕ condition was indeed shown to encourage more burning in the HGV passage in the discussion presented in Chapter 6.

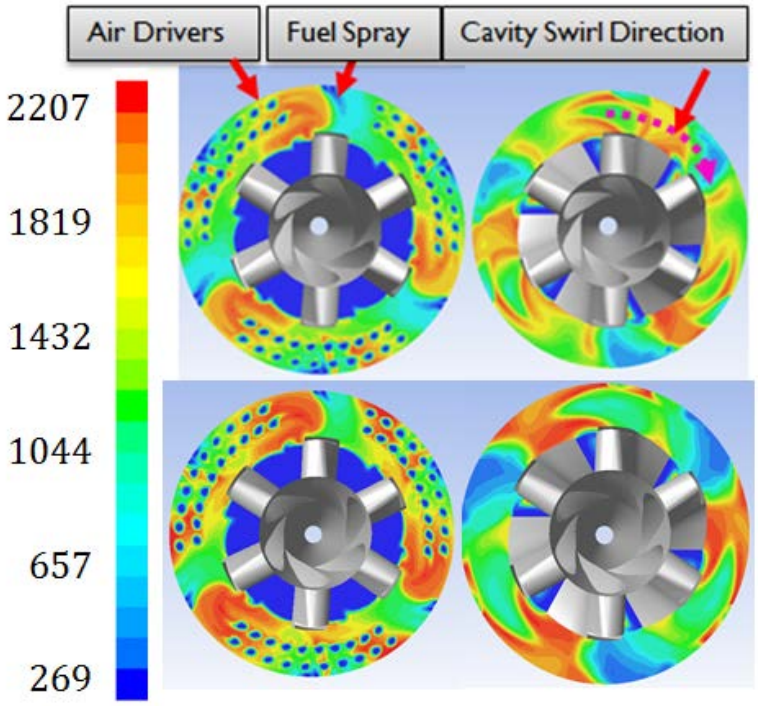

Figure 4.19: Computational axial cuts of temperature [K] contours in the high-g cavity at high ϕ, planes C1 and C3 (top left and right), and low ϕ, planes C1 and C3 (bottom left and right)

Additional temperature analysis was performed by examining the mass-averaged temperature "exiting" the circumferential cavity interface with the core flow, $\bar{T}_{int}$. A computational surface was defined at a constant radial coordinate representing that interface: the outer diameter of the core and the inner diameter of the cavity were both defined by the radial value $r = 2.1$ that also corresponded to the radial height of the HGV airfoils. An illustration of that computational plane, colored by temperature, is provided by Figure 4.20 (note that the actual radial coordinate of the surface was set to 2.05 in order to exclude the vane OD wall surfaces from the averaging calculations). Qualitatively, every case presented behavior similar to that depicted by the contours: high-temperature migration tended to adhere to the HGV suction-side, while the pressure-side temperatures were dominated by the relatively high-

velocity cold core flow. The mass-averaged temperatures at that interface are shown in Table 4.7 for eight cases with varying mass flow, fuel flow, and channel blockage. Using the tabulated data – with the "Channel" column mapped to a binary indicator variable C – a simple regression analysis may be accomplished. It is important to note the limitations of such a procedure: all dependent variables below are represented by only two levels each, so only estimates of potential linear relationships may be derived. With that in mind, thought, the mass-averaged interface temperature was modeled with the formula shown by Equation (89). That model provides estimates as to the relative effects of the UCC operating conditions upon the mass-averaged temperatures at the interface: $\bar{T}_{int}$ is a positive function of all three – meaning that as any of the variables are increased, an increase in the temperature can be expected. It was noted based on the contours of Figure 4.20 that even at that interface the cold core flow was influential; therefore it was not expected that average temperatures would approach the theoretical adiabatic flame temperatures represented by ϕ_{cav} alone. As will be discussed further in Chapter 6, a system-level metric becomes more appropriate at that stage.

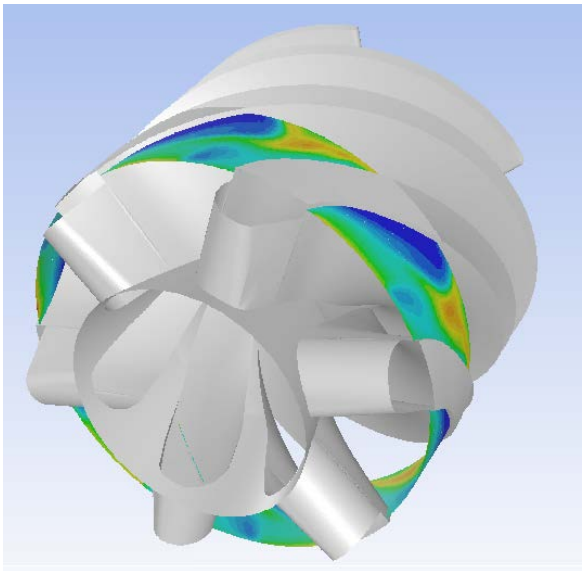

Figure 4.20: Computational interface between the CC and the core

Table 4.7. Mass-averaged temperature calculations at the CC/core interface

$\dot{m}_{in}$	ϕ_{cav}	Channel	$\bar{T}_{int}$
0.06	0.80	base	869.4
0.06	0.80	c50k	1109
0.06	1.37	base	890.5
0.06	1.37	c50k	1170
0.12	0.80	base	901.6
0.12	0.80	c50k	1127
0.12	1.37	base	944.7
0.12	1.37	c50k	1231

$$\bar{T}_{int} = 730 + 688\dot{m}_{in} + 101\phi_{cav} + 258C \tag{89}$$

Three-dimensional stream traces were generated to illustrate the cavity temperature field behavior with some added spatial context. The qualities of greatest interest were (1) how the heat is distributed and (2) how long the fuel remained in the circumferential cavity. In Figure 4.21, the condition $\dot{m} = 0.120$ kg/s and $\phi_{cav} = 1.37$ was considered (high phi, high flow) where the streams were colored by temperature with the same contour levels as in Figure 4.19. The stream traces originated at each of the six fuel injection locations – thus they provided a good representation for the path of notional fuel "streams" (they don't track the fuel particles themselves) as they were injected and combusted. As discussed in Section 3.1.1, the fuel baffles were designed to distribute the gaseous propane evenly among four axially-spaced pairs of holes; thus the fuel stream traces originated from a variety of axial locations. Each of the four experimental core restriction cases was shown to highlight the influence of the channel plate on the fuel distribution. In the upper left image, the baseline case reinforced the previous conclusions regarding the semi-periodic behavior induced by the three cavity air injection plates. The fuel streams that were well-mixed with the incoming air were evident as they spread fairly evenly across the radial height of the CC; conversely, those streams that were poorly mixed were also evident as they traversed the radial height of the cavity with almost no circumferential rotation. The highest temperature regions within the cavity corresponded to those where the fuel was well-mixed, while the poorly-mixed streams see little to no heating before they encounter the HGV centerbody. When the $\lambda = 5.0$ restrictor plate was installed in the "in-passage" configuration (Case c50, top-right), no significant difference in the streamline distribution was observed.

However, a greater impact to the fuel stream distribution was achieved in the "on-vane" configuration (Case c50k, bottom-left). There, all fuel streams were engaged by the bulk flow, and the streams originating from the unmixed fuel injectors begin to carry over to the next HGV

passage rather than migrating immediately. Similar patterns were seen in the $\lambda = 4.0$ case: impact in the "in-passage" (not shown) orientation was less than "on-vane." Furthermore, minimal differences were observed between the c50k and the c40k cases: the primary influence was the orientation of the channel plate rather than the size of the channels. As the goal of the CC is to act as a primary combustion zone, increasing the amount of time that the fuel streams spend within the CC was a high priority, thereby making cases such as c50k and c40k desirable. To fully develop those qualitative observations into more quantitative comparisons, however, it was necessary to analyze the cavity velocity field as presented in the next section.

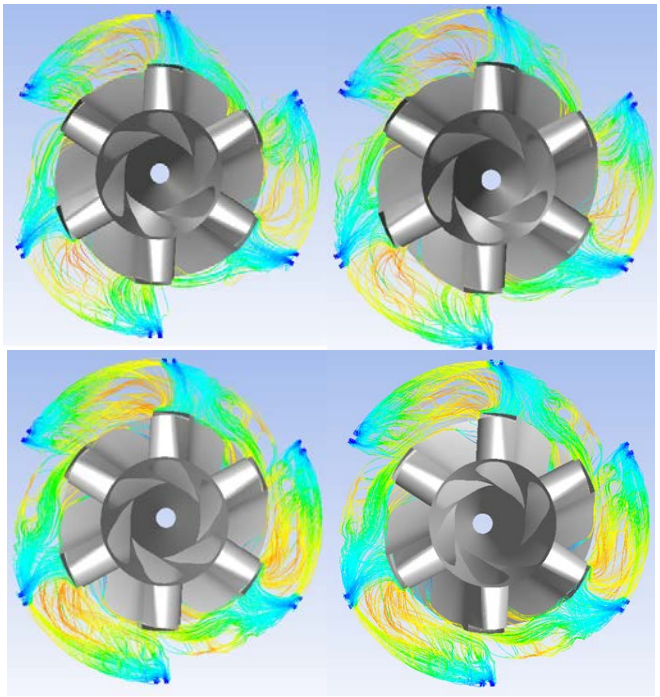

Figure 4.21: 3D stream traces from the fuel injectors colored by temperature for the baseline (top left), c50 (top right), c50k (bottom left) and c40k (bottom right) cases at high phi/high flow

4.2.2.3. Velocity Field and Residence Time

The longevity of the fuel streams within the cavity as shown in Figure 4.21 provides insights into cavity residence time. In order to perform that calculation, however, the local velocity field must first be understood. For this initial analysis, a single geometry configuration – case c50k – was examined at four different operating conditions in order to discern the

influence of $\dot{m}_{in}$ and ϕ_{cav} on the velocity magnitudes. Figure 4.22 presents contour plots at axial location C2 of the tangential velocity at low and high levels of $\dot{m}_{in} = \{0.06, 0.12\}$ and $\phi_{cav} = \{0.80, 1.37\}$. The influence of increased mass flow was clear, as was the disrupting influence of the fuel injection. Intuitively, regions of sharp increase in tangential velocity fell nearly directly between the fuel injection locations (noted by black circles in the upper-left image), each of which are followed by a sharp decrease caused by one of the fuel plumes traversing the full radial height of the cavity. Regions of high tangential velocity were also observed entering the HGV passage on the vane suction-side (one example is circled in pink). This behavior was the result of two primary influences: first, the tangential component of the velocity in the CC is maintained by the tangentially-turning HGV passages – at location C2 the vane angle is already nearly 45° to the axial direction; second, the HGV passages contract as they turn thus accelerating both the migrating cavity flow and the upstream core flow. This pattern was observed experimentally as well as discussed in Chapter 5.

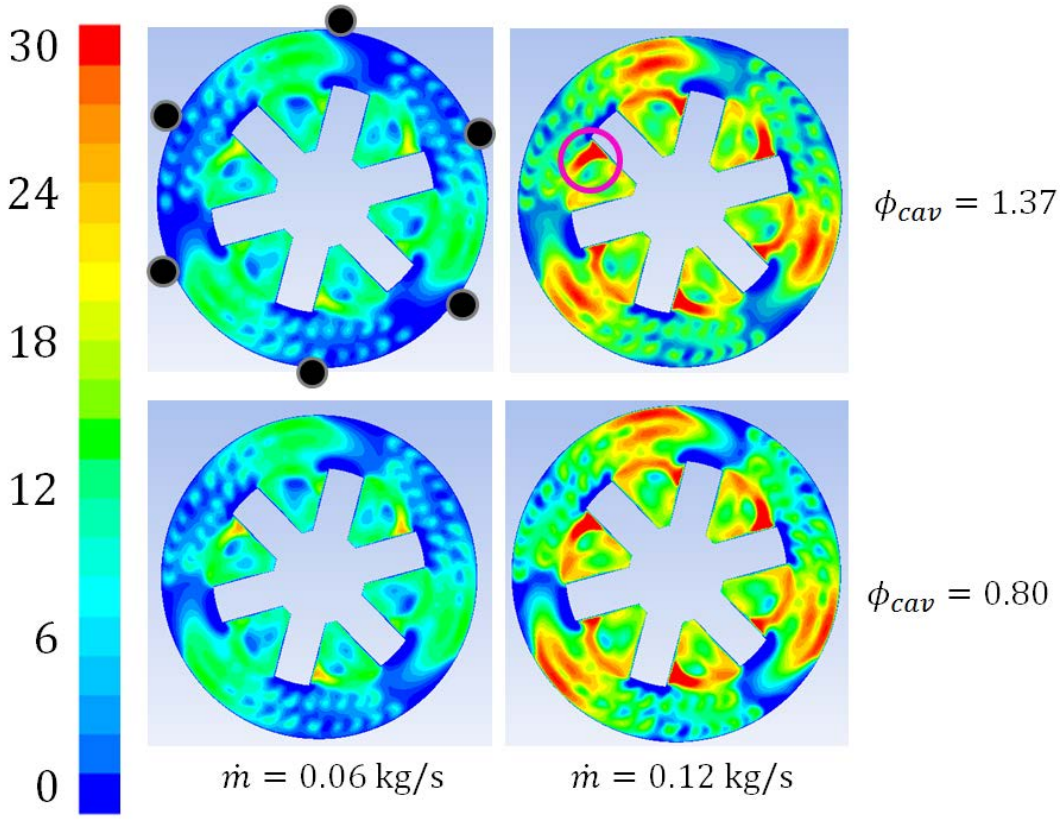

Figure 4.22: Tangential velocity contours [m/s] at four conditions

To gain useful inputs into an estimate of fuel stream residence time, a more quantitative analysis was implemented by extracting a set of one-dimensional concentric circles at each of the three cavity locations, C1-3. The node values of each circle were arithmetically averaged thereby producing radial profiles spanning the height of the CC; the cavity height was normalized by the parameters $h = r - r_v$ and the cavity radial height h_0. (As a matter of note, the technique of vertex-averaging was deemed appropriate for use in this case due to the fact that the points that were being averaged originated from an effectively one-dimensional curve. Trials data were collected using mass-weighted averaging, but that technique resulted in zero values. When area-weighted averaged was used, the profiles were exactly the same shape with some minor deviations of not more than 0.3% from the vertex-averaged result.)

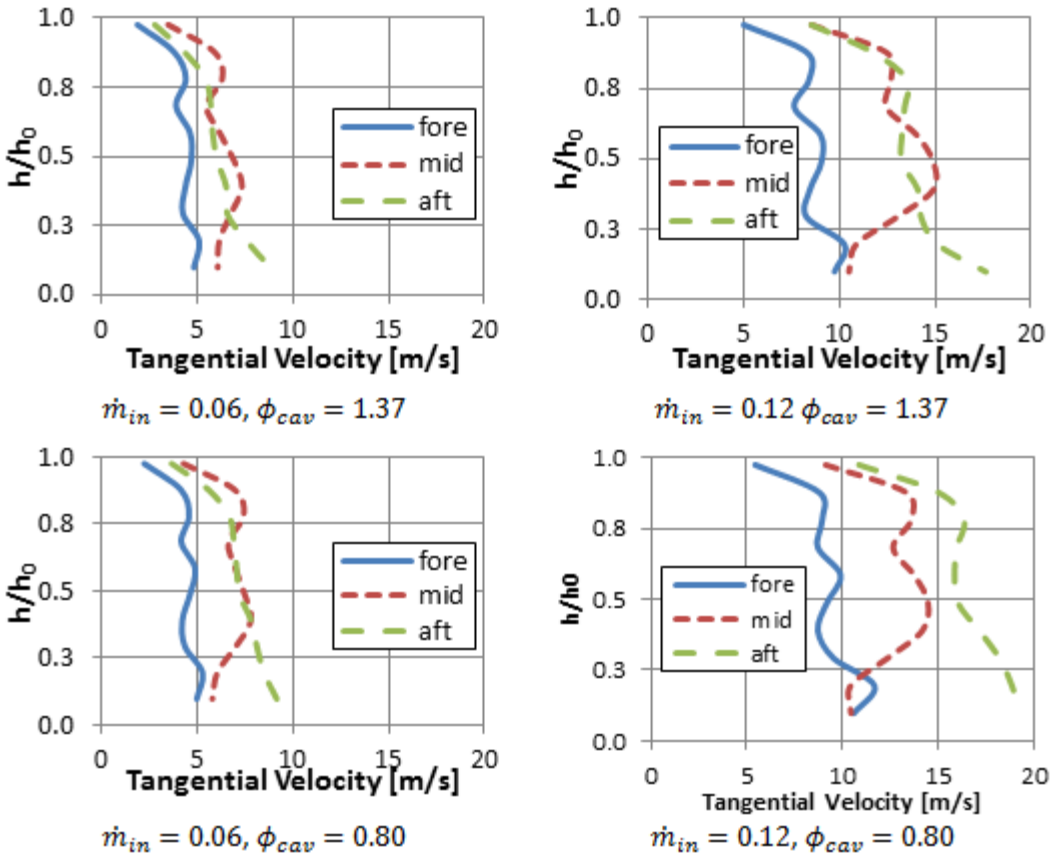

Figure 4.23: Radial profiles of circumferentially-averaged tangential velocity at the same conditions as Fig. 4.15

The profiles are shown in Figure 4.23 where the pattern of operating conditions shown in Figure 4.22 is again repeated. At each condition a radial profile is shown at the fore (C1), middle (C2) and aft (C3) axial locations. The velocity was shown to increase substantially with increasing $\dot{m}_{in}$ as expected from the qualitative analysis. Furthermore, the axial gradient of the velocity was shown to be increasing fore to aft, with the most significant increase happening between the fore and middle positions in all cases. Finally, the influence of ϕ_{cav} was shown to be somewhat less than that of $\dot{m}_{in}$. In all cases and at all locations the influence of the air drivers is notable from the local maxima at $h/h_0 \cong 0.85, 0.5$, while the precise location of the peaks decreases from fore to aft due to the inward-radial gradients that are present as well; more on that topic will be discussed in Section 4.2.2.4.

While no specific goal for residence time was set for this research, generally speaking, higher residence time within the cavity would imply more complete and efficient combustion

overall. Given quantitative knowledge of the velocity distribution, residence time within the cavity can be estimated in combination with the earlier qualitative observation of the fuel streamlines. Average residence length of a fuel stream was determined by the distance from injection point to the point of migration into the HGV passage. In all cases, the boundary between the CC and the HGV passages is defined as the outer radius of the HGV vanes (r_v = 5.33 cm). In the images of Figure 4.21 that boundary is traced by the outer edges of the solid vane bodies as shown. In the baseline (upper-left) case, the maximum residence length of a fuel stream is no more than a single HGV passage – or about 60° – while some streams are present for no more than the radial height of the cavity; an estimate of the average angular travel of the fuel streams therefore becomes equal to about half of a vane passage, or 30°.

To facilitate consistent comparisons, the arc length was computed using the radial midpoint of the CC, $r_m = r_v + 0.5h_0 = 6.64$ cm. Thus, the average residence length was found by $l_{res} = (30/360)(\pi 2 r_m) = 3.48$ cm. To account for axial gradients, the reference tangential velocity was taken as the average of the values at $h/h_0 = 0.5$ at all three axial positions from the upper-right image of Figure 4.23 (recalling that the conditions of all the images in Figure 4.21 were "high/high"); thus $v_{t,ref} = 1/3\,(9.0 + 13 + 15) = 12$ m/s. Therefore, the estimated residence time at the conditions of Figure 4.21 was found to be $t_{res} = l_{res}/v_{t,ref} = 2.8$ ms. The change between the baseline and the case c50 streamlines is minimal; slightly more streams are disbursed outward within the cavity, however there is insufficient information to warrant a change in the estimated average angular travel, so the estimated residence time of case c50 appears equal to the baseline. In contrast, the streams in case c50k (bottom left) are much more broadly disbursed within the cavity and remain circulating for substantially greater angular distances. Most streams appear to be carried across the span of one full HGV passage, so the estimated average angular travel of case c50k was taken as 60°. Thus, the estimated residence time was found to be double that of the baseline, or $t_{res} = 5.6$ ms. In other words, the effect of

'clocking' the channel opening from in-passage to on-vane was to increase the average fuel stream residence time by nearly 100% (or 2x).

In contrast, the effect of an increase in the inlet mass flow rate given either channel orientation on the average cavity residence time was negligible. The explanation for that result is that the increasing mass flow rate has two effects: (1) it causes an increase in the tangential velocity while concurrently (2) causing an increase in the average residence length. That is, fuel streams are resident in the cavity for longer distances, but they are also traveling at increased speeds. It was found that the proportional increase in tangential velocity was nearly equivalent to the proportional increase in residence length, and therefore the two effects balance each other out. This observation was also noted in the analysis of Section 5.2.4.

4.2.2.4. Radial Velocity Fields

The migration patterns of the cavity flow into the core are additional parameters of interest. Qualitative observations are again facilitated by observation of axial planes as shown by Figure 4.24; the axial position for both images is at the center of the circumferential cavity or location C2. The contours are of radial velocity [m/s], where positive values indicate a component outward from the center, and negative values indicate inward components. The design of the cavity is such that planes cutting through its axial midpoint are centered between two rows of fuel injection holes – thus the inward components of the fuel injectors are not visible immediately at the outer diameter. Rather, the influence of the fuel jets is manifest in the regions above the HGV airfoils, one example of which is highlighted by the black dashed circle.

One other important contextual note is that the two-dimensional cross-section of the HGV airfoil can be somewhat deceptive in this view – the airfoils are turning at this location at an angle that is already nearly 45° to the engine axis. Migration from the circumferential passage tends to impact the vane suction-side (the left edge of each airfoil as viewed from the front): hence, the greatest inward-radial components fall on that side of the HGV passage.

Concurrently, the strong axial components of the core flow meet the vane pressure-side (the right edge of each airfoil) and tend to be pulled outward, or "up" the vane wall: hence the greatest outward-radial components are observable on that side. In the left image of Figure 4.24 of the c50 case those effects are prominent. However, in the right image where the c50k case is shown, those effects are greatly diminished. When the channel plate opening is oriented on-vane, the solid portion of the plate blocks the upstream core flow from entering the passage direction and instead redirects it to the vane leading edge. The zone immediately downstream of the blockage is therefore characterized by a recirculation region that serves to draw the outer cavity flow more strongly than when the channel opening allows the core flow into the passage unimpeded.

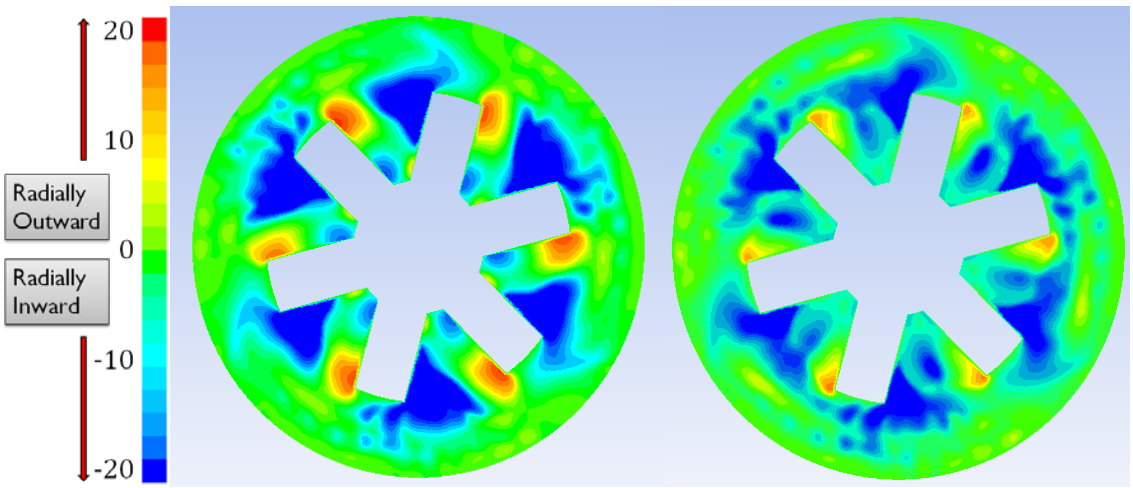

Figure 4.24: Radial velocity contours of the combustion cavity for cases c50 (left) and c50k (right)

Those conclusions are reinforced by examining stream traces as shown in Figure 4.25. The traces originate from a single channel passage opening in both cases; in the left image representing the c50 case the opening is centered in the passage, and in the right image from c50k it is centered on the vane leading edge. Case c50 presents several features, the most notable of which is the stray trace that migrated completely up into the cavity to circulate before returning back into the core flow. Furthermore, although the channel is centered on the passage opening, many of its streams still transition to the next passage over. The point from

the prior discussion where the streams meet the pressure-side wall and are pulled upward is highlighted by the red box. That same behavior was observed in the c50k case, again as highlighted by the box; however its magnitude was less. The streams from the channel met the leading edge and then became relatively evenly split between the passages on either side. The low-pressure recirculation region was observed as highlighted by the red circle.

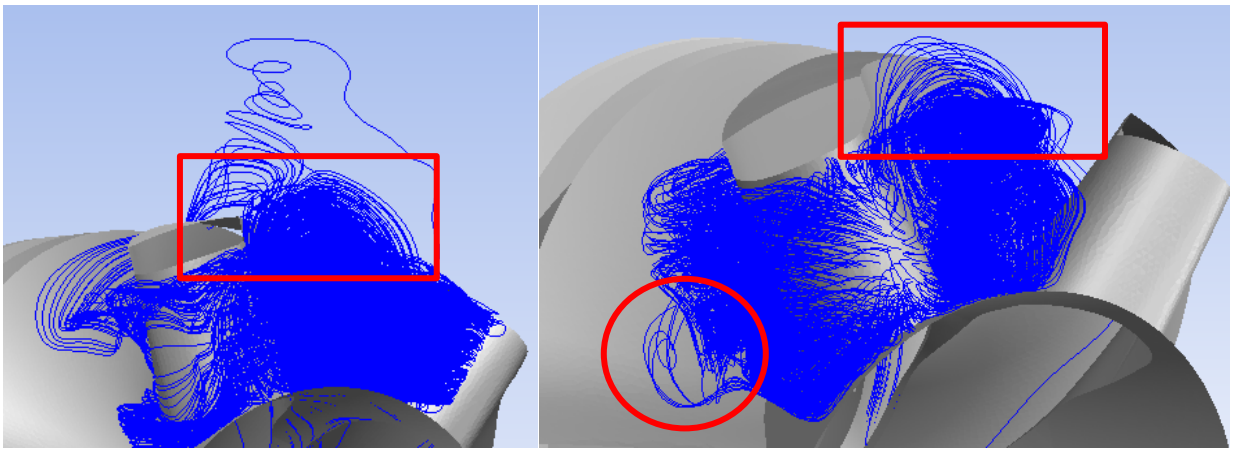

Figure 4.25: Stream traces originating from the channel opening for cases c50 (left) and c50k (right)

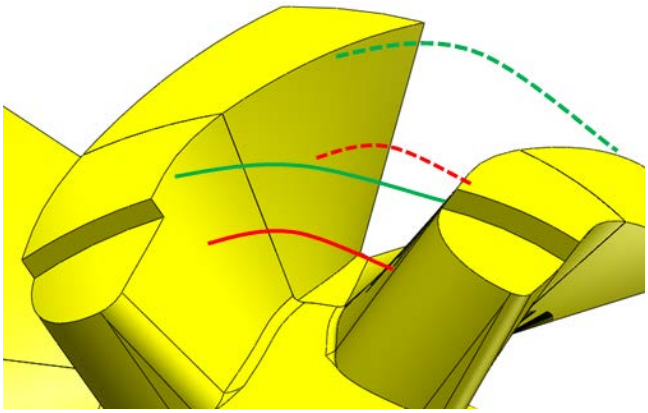

Figure 4.26: Fore (solid), aft (dashed), mid-height (red) and upper-height (green) radial velocity profile locations

A more quantitative examination of the radial flow migration was performed by examining one-dimensional profiles of radial velocity across the span of a single HGV passage. Axial reference locations C1 and C3 were considered as were radial heights corresponding to 50% ("mid-height") and 90% ("upper"). The approximate placement of those four locations

relative to the HGV passage is illustrated by Figure 4.26. The velocity profiles are shown in Figure 4.27 for a variety of configurations at the operating condition characterized by $\dot{m}_{in}$ = 0.120 kg/s and ϕ_{cav} = 1.37 at the mid-height position. The x-axis is defined by a "channel span fraction" that ranges from zero on the pressure-side of the first vane to one at the suction-side of the next vane; in reference to Figure 4.26, the channel span fraction is defined as zero on the left side of the passage.

In the left image of Figure 4.27, while minimal distinction is observable between the baseline and c50 cases, a substantial difference was noted between the in-passage and on-vane configurations. As seen in the contour plots of Figure 4.24, the presence of a blockage centered on the HGV passage in the on-vane configuration induced a substantial increase in the cavity flow entrainment into the center of the passage. The right image examines the difference between cases c50 and c50k more closely by displaying results from both axial locations C1 and C3. The strong inward-radial components were more prevalent near the aft of the cavity in both cases. In the front of the cavity there was minimal distinction between cases c50 and c50k, but at the aft position the substantial inward component at the center of the passage in case c50k is again visible.

The analysis is repeated in Figure 4.28 at the upper-height locations. The radial velocity magnitudes in general were greater for all cases: there was a significant positive component on the pressure side indicating core flow entrainment into the cavity. This was expected based on the observations of the contours in Figure 4.24. The driver of that behavior was likely a function of the axial inertia of the core flow sweeping up the surface of the circumferentially-turning vane. The negative radial velocity components at the suction side were also greater than in Figure 4.27; again, those effects were more prevalent at the aft position. In the image of Figure 4.28 the baseline and c50 profiles were again similar; the main difference was observed from the "on-vane" configurations. Furthermore, the c40k case again induced greater inward radial motion than the c50k case. In the right image, the effect of changing the channel

orientation was again clear: both c50k profiles were lower than their counterparts at almost all locations.

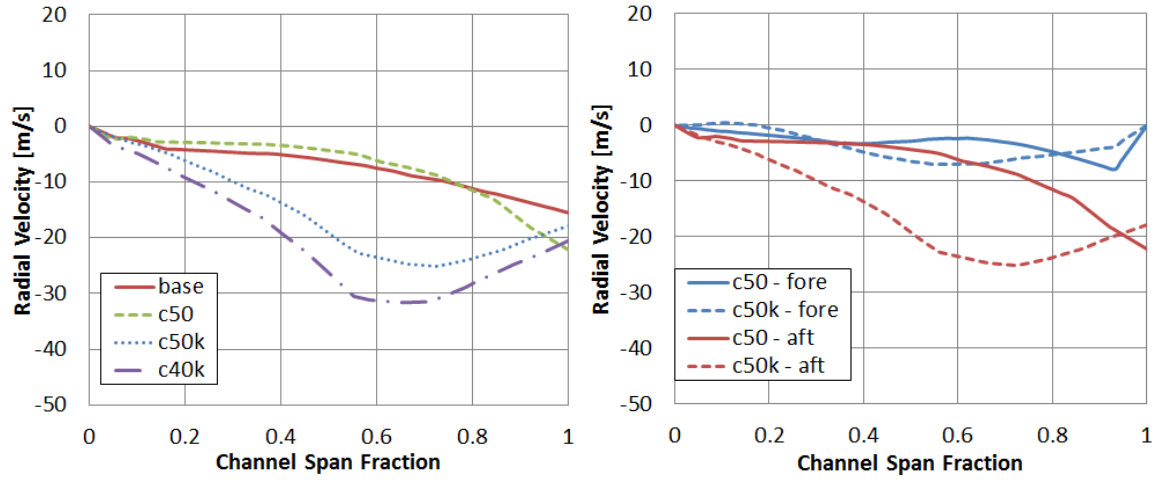

Figure 4.27: Numerical radial velocity profiles at 50% of HGV height; comparisons of all four configurations at location C3 (left), and comparisons of two configurations at locations C1 and C3 (right)

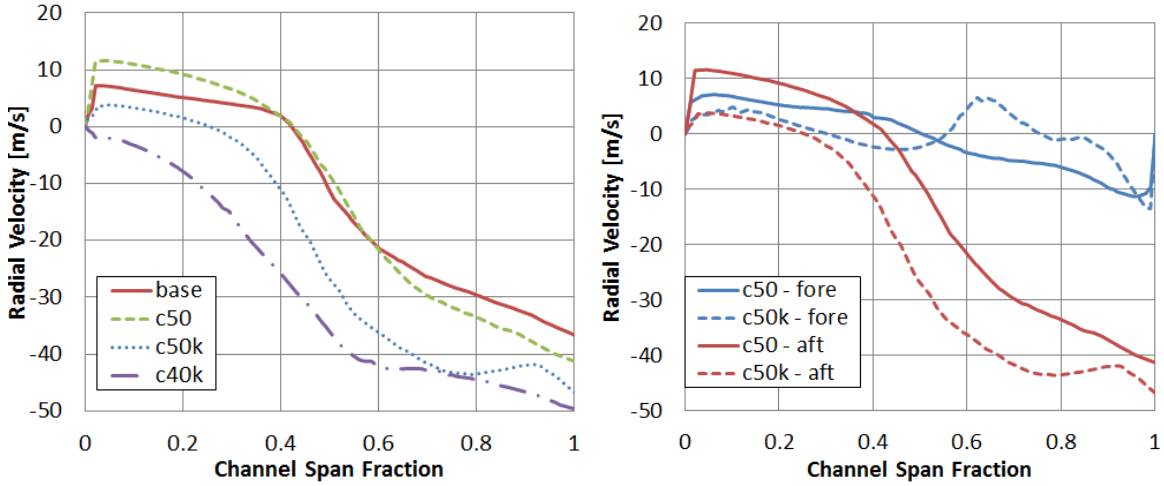

Figure 4.28: Numerical radial velocity profiles at 90% of HGV height; comparisons of all four configurations at location C3 (left), and comparisons of two configurations at locations C1 and C3 (right)

In Figure 4.29 similar results are presented comparing configurations c50 and c50k at the aft reference location C3 with respect to changes in ϕ_{cav} (left) and $\dot{m}_{in}$ (right). The left image demonstrates that the observations are fairly independent of ϕ_{cav} with constant $\dot{m}_{in} = 0.12$, and the right image demonstrates that the effects are similar but more pronounced with increasing $\dot{m}_{in}$ and constant $\phi_{cav} = 0.80$. The same analysis is shown in Figure 4.30 at the

upper-height locations. Some sensitivity with ϕ_{cav} was observed near the suction side of both configurations in the left image. This was likely due to the nearer proximity to the combustion cavity that was itself directly influenced by ϕ_{cav}. The right image demonstrated again that increased $\dot{m}_{in}$ led to relatively greater inward motion in the c50k case. In the c50 profile, however, increasing $\dot{m}_{in}$ led to dual effects: (1) increased outward motion at the pressure side, and (2) increased inward motion at the suction side.

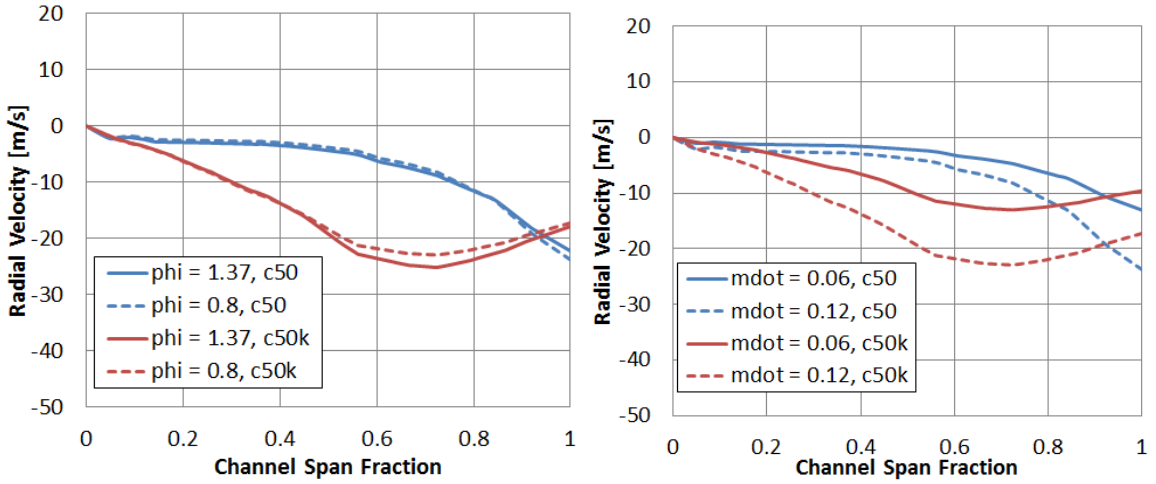

Figure 4.29: Numerical radial velocity profiles at 50% of HGV height at axial location C3; at constant $\dot{m}_{in} = 0.12$ kg/s (left) and constant $\phi_{cav} = 0.80$ (right)

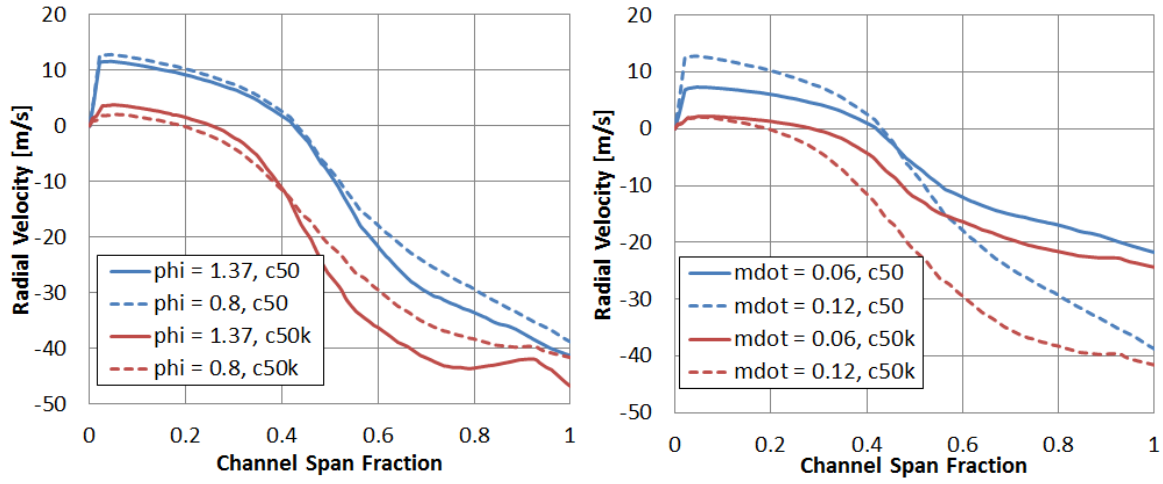

Figure 4.30: Numerical radial velocity profiles at 90% of HGV height at axial location C3; at constant $\dot{m}_{in} = 0.12$ kg/s (left) and constant $\phi_{cav} = 0.80$ (right)

4.3. Chapter Summary

The objective addressed by the chapter was Objective 1: to develop the aerodynamic mechanisms to deliver the proper air and fuel to the high-g cavity from a common flow source. To that end, this chapter was comprised of both experimental and computational results from a study of the AFIT UCC in two distinct phases. In Section 4.1, early computational results accompanied preliminary cold-flow experimental results. The objective was to resolve the performance issues observed with the common-source diffuser that were observed by previous workers. With a combination of the new CFD model and refined instrumentation, Section 4.1 validated the diffuser performance issues and presented a solution in the form of the core channel restrictor plate. Cold-flow testing demonstrated that the size of the core channel was an effective variable with which the core flow fraction (CFF) could be controlled. CFD further verified that result and extensions of the CFD study revealed an optimum channel size of $\lambda = 4.6$ in order to achieve the desired value of $CFF = 0.70$. Furthermore, CFD extensions identified the potential benefits of controlling the orientation of the core channel opening with respect to the HGV leading edge. When the opening was centered on a leading edge, CFD predictions indicated that hot gas migration from the circumferential cavity (CC) would be enhanced.

In Section 4.2, the first test results documenting the performance of the AFIT UCC with a common upstream flow source under reacting conditions were presented. Based on the prior section, new channel plates were tested, and they demonstrated the ability to effectively control the CFF. By way of enhanced instrumentation, it was found that the diffuser performance was not as detrimental as previously reported by Miranda [98], nor even as demonstrated in Section 4.1. However, experimental results demonstrated that the core channel plate was still effective in controlling the CFF to its desired value. The successful operation of the UCC at its design conditions was sufficient to satisfy the completion of Objective 1; those conditions comprised

inlet mass flow rates between 0.06 and 0.12 kg/s and cavity equivalence ratios between 0.8 and 1.37. In general, operating at higher mass flow rates was considered desirable; however, the evidence and the full discussion for that assertion will be documented in Chapter 5.

The development and refinement of the CFD model that accompanied the experiments provided unique opportunities to dive deeper into the UCC performance as a supplement to the initial objective. CFD results were shown to confirm the experimental trends, and CFD extensions offered the first insight into the complex reacting flow environment of the UCC. Specifically, the presence of semi-periodic patterns was observed as a result of the arrangement of the cavity air driver panels. Consequently, half of the fuel injected into the CC tended to escape into the core flow before it could be properly circulated and burned. Installation of the core channel plate was found to alleviate that problem to a limited degree; orienting the channels "on-vane" was shown to have more desirable influence on the cavity flow – residence times of fuel streams within the cavity were improved from 2.8 ms in the baseline configuration to 5.6 ms in both cases of channel size $\lambda = 4$ and 5, oriented "on-vane."

Radial velocity trends were examined in detail by the CFD to investigate the hypothesis that the channel orientation played a significant role in the radial migration patterns from the circumferential cavity. The hypothesis was proven by examination of radial velocity contours, streamlines emanating from the channel openings, and radial velocity profiles within the HGV passages. Increased inward-radial flow was demonstrated in the "on-vane" cases.

V. Cavity Flame Dynamics

This chapter presents all results and analyses related to the second research objective: to determine the effects of the complex flow environment on flame dynamics within the high-g combustion cavity. The objective was focused on the response of the cavity g-load by examining velocity distribution in Section 5.2, reaction dynamics by examining equivalence ratio in Section 5.3, and heat distribution by examining temperature in Section 5.4. The primary experimental tools invoked to measure velocity were particle image velocimetry (PIV) and particle streak emission velocimetry (PSEV). The former provided a more precise evaluation with a limited field of view, while the latter provided a wider field of view but with qualified interpretation. To measure the equivalence ratio, the laser-induced breakdown spectroscopy (LIBS) method was utilized. For temperature measurements, the technique of thin-filament pyrometry (TFP) was invoked. In all cases, the computational fluid dynamics (CFD) model was analyzed in analogous fashion to the experiment. It was as well extended beyond experimental conditions to provide complementary insight into UCC behavior that was not attainable with the experimental measurements. First, and most importantly, in Section 5.1 a discussion is presented regarding the transition from UCC v2 to the v3 hardware. The UCC behavior was evaluated based on its response to the changes in cavity size and air delivery mechanism.

5.1. Impact of Changing Cavity Geometry

The first investigation regarded the effects of transitioning from the v2 to the v3 hardware. Recall that the primary two differences were (1) replacement of the three discrete cavity air-driver panels with a single uniformly-distributed plate of air drivers, and (2) increasing the outer dimeter of the cavity; refer to Section 3.1.1.2 for full details. Since both of these changes were made at the same time, the independent effects of each change could not be

separated. However, certain results can be expected to be the fall out of one of these changes versus the other as will be discussed. Axial reference locations were again utilized to facilitate discussion similar to Chapter 4. Those locations are illustrated in Figure 5.1. The location labels C1, C2, and C3 were referenced interchangeably with the labels "fore," "mid," and "aft," respectively.

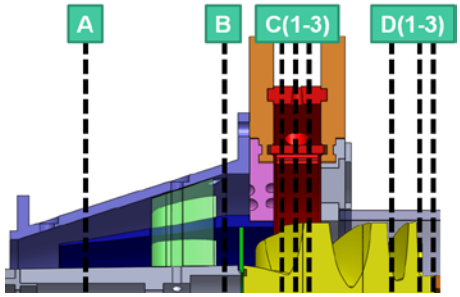

Figure 5.1: Axial reference locations (Ch. 5)

In Figure 5.2, the two configurations are compared in two ways at an identical operating condition of $\dot{m}_{in} = 0.108$ kg/s and $\phi_{cav} = 1.37$. The top row shows temperature contours at axial location C2 while the bottom row shows the fuel streamlines at the same location. The cavity height of configuration v2, h_0, is shown, and the v3 value $h_1 = 1.21h_0$ is shown in a corresponding location; the volume of the cavity in the v3 configuration, V_1, is also shown in relation to V_0. The diameter of the HGV centerbody did not change and the images in the figure are scaled appropriately – to emphasize this, the dashed black lines trace the outer edge of the centerbody from one configuration to the other.

The temperature contours in Figure 5.2 illustrated a significant difference in the distribution of the hot regions at the cavity midpoint. In v2, those regions are very uneven and are heavily influenced by the air drivers and the fuel streams. The patterns are semi-periodic due to the orientation of the cavity air driver panels. As discussed in Chapter 4, those fuel streams that were injected between air driver panels traversed the entire radial height of the cavity without any circumferential distribution, thereby severely disrupting the circumferential

flow of the neighboring air injection holes. The modifications of the v3 geometry largely resolved that issue: the hot regions were much more uniformly distributed in a circular band within the inner half of the circumferential cavity (CC); the patterns were nearly symmetric in 60° arcs, thus satisfying one of the original intents of the UCC design. The influence of the air drivers was less apparent due in large part to the "flattening" of the fuel streams. In all cases, the fuel plume was turned by the circumferential flow almost immediately upon injection, thus enabling the use of the increased outer volume of the cavity for preliminary fuel diffusion and mixing.

That behavior was even more apparent in the three-dimensional fuel traces shown by the images in the bottom row of Figure 5.2. The fuel traces were again colored by temperature with the same levels as the temperature contours. Comparing volumetric behaviors alone, the streamlines in the v3 configuration clearly disburse evenly around the full outer diameter of the cavity before mixing and experiencing even heating toward the cavity inner diameter and the migration points. An examination of the computed values of local equivalence ratio was also performed, and representative results are shown in Figure 5.3. Two conclusions were drawn: first, in support of the previous discussion, the issue of fuel exiting the cavity prematurely was resolved. Second, the "layer" of fuel around the cavity outer diameter was substantial. Nearly 50% of the cavity volume was therefore essentially behaving as a fuel plenum rather than hosting the desired mixing and combustion processes. This result motivated the changes to the angle of the cavity air drivers as described in Chapter 3. The results of those changes will be discussed fully in Chapter 6.

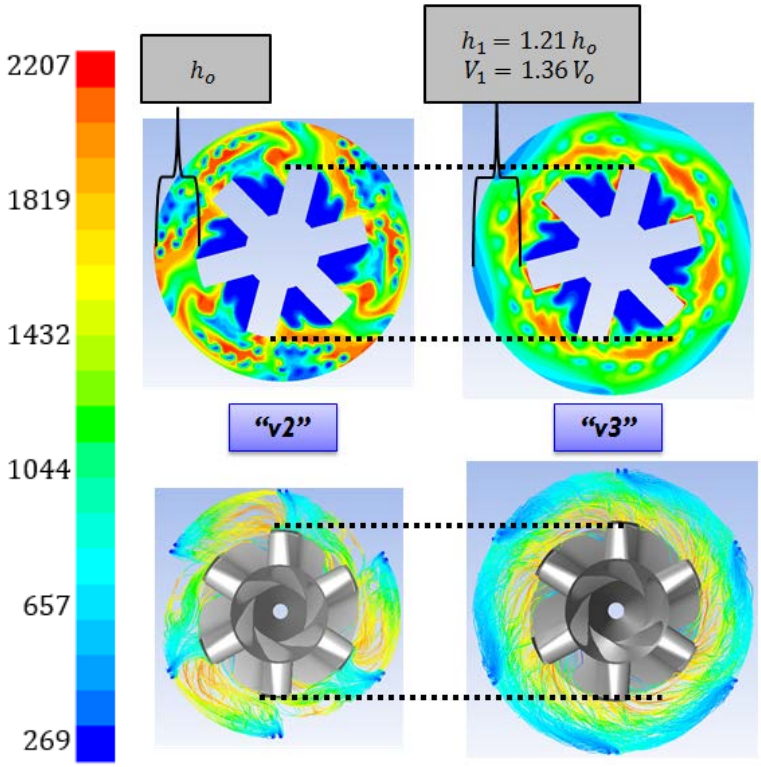

Figure 5.2: CFD temperature distribution (top) and fuel streamline (bottom) comparison between the v2 and the v3 UCC hardware

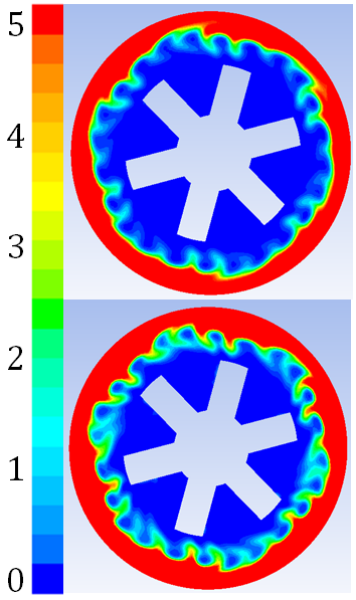

Figure 5.3: Sample CFD predicted local equivalence ratio field

5.2. Impact of Operating Conditions on g-Load and Residence Time

The first goal of research Objective 2 was to understand how the flow in the CC responded to operating conditions. In keeping with the pattern of analysis presented in Chapter 4, the first response variables selected for study were the cavity g-load and residence time. As those parameters were velocity-driven, the optical velocity-measurement tools were ideal for integration with the investigation. The "v3" hardware was designed specifically to accept a variety of optical diagnostics of the velocity field including Particle Image Velocimetry (PIV) and Particle Streak Emission Velocimetry (PSEV). With those velocity measurements, the g-load in the cavity was effectively measured and its impact on the overall reaction dynamics and residence time was analyzed.

5.2.1. Experimental Setup Summary

The experiments summarized in this section were completed within a single test campaign utilizing the "v3" UCC hardware as described in Section 3.1.1.2. Test conditions were limited due to the requirement to maintain steady operating conditions while minimizing the amount of seed particles needed to obtain usable signal as discussed in Section 3.2.1. Thus, for both PIV and PSEV experiments, only two inlet mass flow conditions were evaluated: $\dot{m}_{in} = \{0.060, 0.108\}$ kg/s. In the computational model, an additional test condition at $\dot{m}_{in} = 0.15$ kg/s was considered. At each experimental condition, cavity equivalence ratios of $\phi_{cav} = \{0.80, 1.37\}$ were included, while the computational study again extended to additional equivalence ratios at each inlet flow setting.

5.2.2. Experimental Impacts of Operating Conditions on Velocity

Measurements of the velocity field via PIV and PSEV were pursued primarily to determine mixing characteristics and potential g-loading effects within the cavity flow. The PIV measurements were subject to significant geometric and operational constraints as outlined in Section 3.2.1, more so even than the PSEV. Consequently, usable PIV data were only obtained at three operating conditions. Conditions 1 and 2 were both at an inlet mass flow rate of $\dot{m}_{in} = 0.060$ kg/s with cavity equivalence ratios of 0.80 and 1.37, respectively. Both conditions utilized at least 150 image pairs for the analysis. Condition 3 was taken at $\dot{m}_{in} = 0.108$ kg/s and $\phi_{cav} = 0.79$, though only 20 image pairs were captured due to the rapid buildup of seed particles on the viewing window. The laser sheet was positioned axially at the center of the circumferential cavity (CC) – corresponding to reference location C2 from Figure 5.1; an illustration of the beam optics and beam path were provided by Figure 3.12 and Figure 3.34, respectively.

Figure 5.4 displays the PIV measurements at each of the three test conditions along the top row. The axes are labeled by spatial coordinate – thus the scale of the field-of-view may be

appreciated. The images are in order from conditions 1 to 3 left to right; the view is aft looking forward – thus the direction of the cavity bulk flow rotation is counter-clockwise. Each PIV image is accompanied by a corresponding CFD contour plot colored with levels identical to those of the PIV and at an identical axial position. The CFD results were interrogated as to be analogous to the PIV measurements in that they were two-dimensional representations of the tangential velocity at axial location C2. The left-most PIV image is highlighted by a black trapezoid, which is then transcribed to the CFD image below; this denotes the approximate location of the PIV field-of-view with respect to the CFD geometry shown.

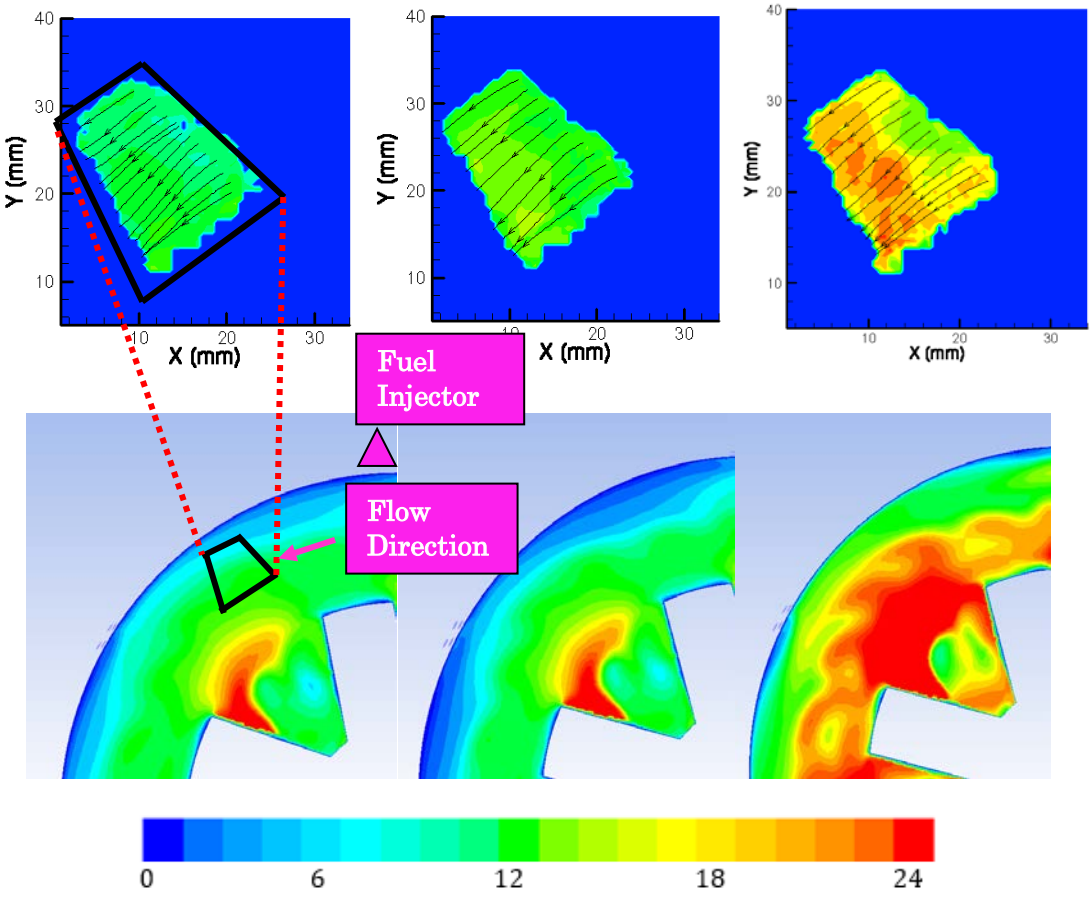

Figure 5.4: Top row: PIV results showing tangential velocity [m/s] for Conditions 1 (left), 2, and 3. Bottom row: corresponding CFD results with approximate matching region highlighted (identical contour levels)

The overall agreement between the PIV and the CFD is good. At the lower mass flow rates the PIV measurements indicated tangential velocities of about 12 m/s, as did the CFD. At

the higher mass flow rate, the measured tangential velocity varies between 18 and 22 m/s, while the CFD calculated between 16 and 23 m/s in the same region. Notably, the measurements capture the region of slightly reduced velocity that follows the top surface of the HGV airfoil. The peak velocities of the measurement appear in the lower-left corner corresponding to the beginning of the core entrainment phenomena – i.e., the rapid acceleration of the flow induced by the turning and contraction of the HGV passages.

The PIV field-of-view was insufficient to capture the more important CC field characteristics, however, such as the fuel injection and the full core entrainment. The former would have been observed as a distinct low-velocity region along the outer diameter and the latter would have been a distinct high-velocity region at the inner diameter. The computational results clearly demonstrate the increase in the low-velocity layer about the outer diameter corresponding to the perpendicular injection of the gaseous propane from the fuel baffles. Observing the way in which the fuel disburses at the outer diameter provides cues as to where the primary fuel-air mixing is occurring and where the initial flame fronts are located. Furthermore, the computational results demonstrate the rapid acceleration of the fluid as it turns and is entrained inward by the HGV passages; this was observed in the images as spreading high-velocity regions attached to the vane surfaces. At the axial location C2, the turning angle of the hybrid vanes is already nearly 45° relative to the axial direction and increasing, thus the tangential flow from the CC encounters little turning resistance. Furthermore, the HGV passages are contracting, thereby effecting the acceleration of both the entrained cavity flow and the already fast core flow.

The mechanisms driving the flow through the HGV passages to the exit will be examined more closely in Chapter 6; however the interaction between the core and the cavity flow, particularly the strength of acceleration, carry implications about how combustion in the cavity develops. Acceleration is generally desirable from a combustor as one of the goals is to achieve high Mach number at the exit plane. In the case of the UCC, however, accelerating

products from the cavity too quickly could potentially quench the reactions that are already in progress (as illustrated in Section 6.1.1). Additionally, the tangential velocity component is increasing in conjunction with a decrease in the radial height – therefore the impact on g-load becomes dramatic. While high g-load in the cavity is desirable, as will be discussed in Section 5.2.5, the primary risk of excess acceleration is loading the flow up to and beyond the threshold where g-load is predicted to begin over-stretching the flame as discussed in Section 2.4.5.1.

PSEV data was more easily obtainable as the required density of seed particles was substantially less than that of the PIV. Data were reported at six conditions, and all observations were made with at least 500 image pairs. However, as previously discussed, the PSEV measurements were strictly *bulk velocity* measurements due to a lack of ability to resolve the axial (z) component. Consequently, no direct CFD comparisons were made with the PSEV measurements, although the measured values were fairly close to the tangential velocity calculations at the same conditions.

The PSEV data are shown in Figure 5.5. The top row consists of results at constant cavity equivalence ratio with varying inlet mass flow. As the mass flow was increased, the induced velocity in the cavity was observed to increase proportionally. Notably, in the high-flow case (top right), evidence was present of the influence of the fuel injection at the locations highlighted by the pink triangles (note that the nearby horizontal streak of blue is only an anomaly in the signal). While the aft viewing window did not extend to the outermost radial height of the CC, at the fuel injection locations the jets penetrated just enough to exert influence within the PSEV data. The impact of the fuel injection was apparent in the bottom row of images as well. With constant inlet mass flow, as the fuel flow was increased, the bulk cavity velocity appeared to diminish. One explanation was that the reduction occurred due to the interruption of the bulk momentum by the transverse fuel injection jets, similar to the behavior discussed in Chapter 4. In the current case, however, the fuel momentum is dispersed within an extended outer volume as well as being more evenly mixed by the cavity air drivers so no

dramatic interruption of the circumferential motion was observed. The explanation for the diminishing velocity in the lower row of images was frustrated by the upper-right image at the condition $\dot{m}_{in} = 0.15$ kg/s and $\phi_{cav} = 0.80$. It would notionally fit as well in the bottom row between the 0.66 and 1.0 ϕ_{cav} conditions, however its results do not fit within the monotonic decrease otherwise observed. There was, therefore, some other effect that changed between the two test conditions and that was not captured by the air and fuel flow rates.

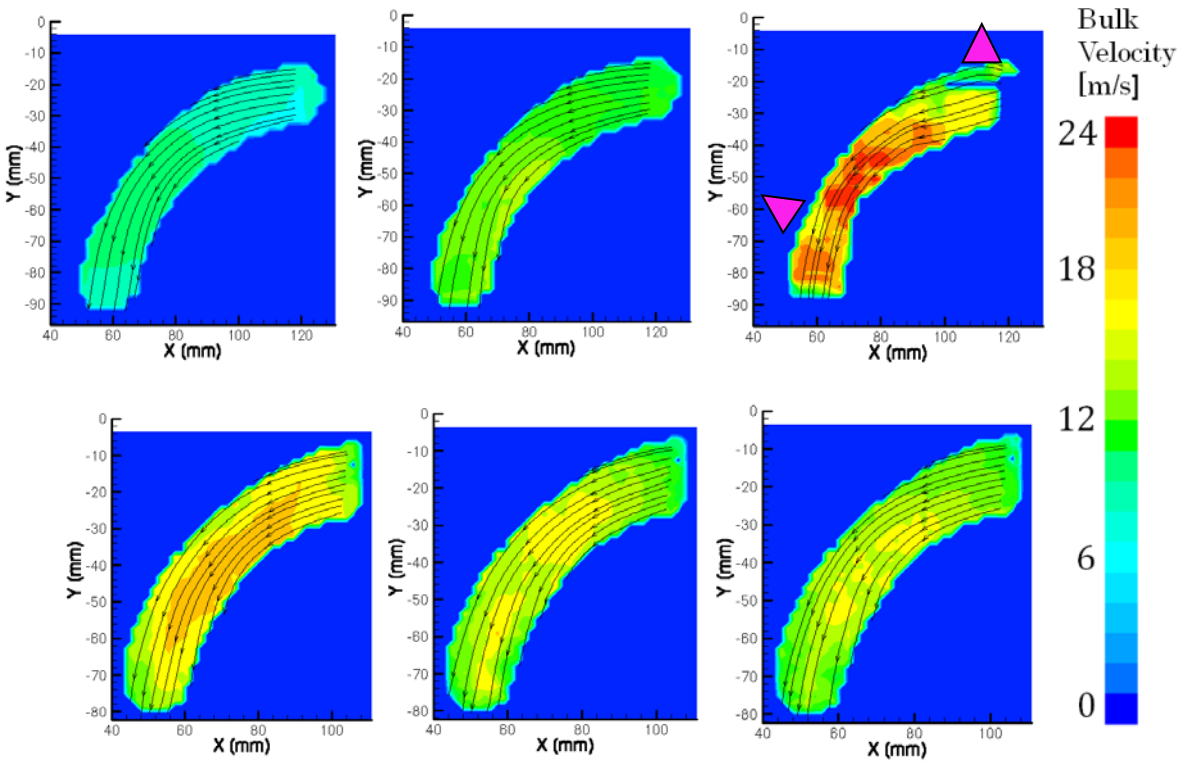

Figure 5.5: PSEV results of bulk velocity magnitude [m/s] for constant $\phi_{cav} = 0.80$ (top row) and $\dot{m}_{in} = \{0.06, 0.108, 0.15\}$ kg/s; and at constant $\dot{m}_{in} = 0.15$ kg/s (bottom row) at $\phi_{cav} = \{0.66, 1.0, 1.2\}$

In quantitative terms, the net effect of increasing the mass flow rate from 0.06 to 0.15 kg/s amounted to an increase in the average cavity bulk velocity from 10 to 22 m/s – that is, every unit mass flow increase induced an increase in cavity velocity of about 1.3 m/s. The inverse effect of equivalence ratio could be similarly quantified based only on the images in the bottom row: each unit increase in ϕ_{cav} resulted in a cavity velocity decrease of about 1 m/s. The issue of the upper-right image indicated some potential nonlinear effects, however insufficient

information was available to support further conclusions. Inferences about the tangential velocity from the bulk velocity measurements were difficult as the contribution of the z-component at any given point in the field of view was unknown; it will be shown in the upcoming CFD results in Section 5.2.3 that the axial velocity gradients, especially in the radially-lower portions of the cavity, were significant.

To place the experimental results in the context of g-load, levels of *tangential* velocity on the order of 10 m/s, considering a mean radius of about 7 cm (appropriate for the UCC v3 cavity), equate to g-loading of only $150g_0$. The tangential velocity in the PSEV data could be no greater than the bulk values, and it was likely slightly less; therefore the low flow condition in the upper-left image would likely have tangential velocities in that range. Similarly, the high flow condition likely had tangential velocities in the range of 20 m/s; at the centerline the corresponding g-loading would be $590g_0$. More discussion on the nature of the g-load gradients in the cavity is given in Section 5.2.3, however the PIV and PSEV results appear to indicated that most current UCC operating conditions fall at the lower range of the "g-effect" window, $350 < g < 3000$. It is desirable to be as near as possible to the upper limit in order to attain the highest potential effect from circumferential loading, however it appears that the operational range of the AFIT UCC is insufficient to reach those levels of loading at this time.

5.2.3. Computational Impact of Operating Conditions on Velocity

Vector analyses were undertaken to provide another view with which to present the complex interactions present in the CC. Computational images were extracted in such a way as to match the view of the experimental setup from Section 5.2.1 with the eventual goal of matching two-dimensional experimental vector fields. While the experimental results did not end up lending themselves to such use for a variety of reasons, the numerical vector images were still useful in highlighting various aspects of the cavity flow.

Figure 5.6 shows velocity vectors colored by tangential velocity. The view matched the experimental hardware: the CFD "window" was 1.9 cm in height, spanned an arc of 80°, and the perspective was aft-looking-forward – that is, the bulk motion was counterclockwise. Four primary cases were represented at levels of ϕ_{cav} = 0.80 and 1.37 ("lean" and "rich") and at levels of $\dot{m}_{in}$ = 0.108 and 0.15 kg/s ("med" and "high"). In the top image the location of one fuel injection baffle was highlighted by a pink triangle. Another injection baffle was located just off the right edge of the image, and the HGV passage occurred below the center-third of each image. The differences between the rich and lean cases for both levels of $\dot{m}_{in}$ included an increase in the region of low-velocity at the outer diameter, corresponding with the trends in temperature and g-load discussed in Section 5.4.1. Differences between the levels of $\dot{m}_{in}$ were reflected by increases in overall bulk velocity while the distribution of the low-speed fuel flow was left relatively unchanged. In all cases there was consistent inward-radial motion in the lower half of the view plane with the largest radial components appearing nearly directly above the HGV passage at the point indicated by the white arrow. This was a consequence of the strong entrainment mechanisms, which have been discussed in several prior sections, attributed to the vane turning and passage contraction.

In Figure 5.7 vectors from the high-flow lean-ϕ case are shown at each of the three axial reference locations. The high-temperature region was most prevalent at the aft plane as has been observed previously. More notably, the flow patterns around the air injection jets demonstrated helical patterns through which the fuel and partially-reacted fluid from the outer diameter became entrained between the cold cores, thereby enabling the flame fronts observed in Section 5.4.1. The helical entrainment diminishes by the middle plane and is replaced instead by an arcing path that resembles very closely the composite PSEV image shown in Figure 3.35. The inward-radial turning developed from fore to aft as entrainment from the HGV passage became more pronounced such that, in the aft image, some vectors are only about 10° off from the radial direction.

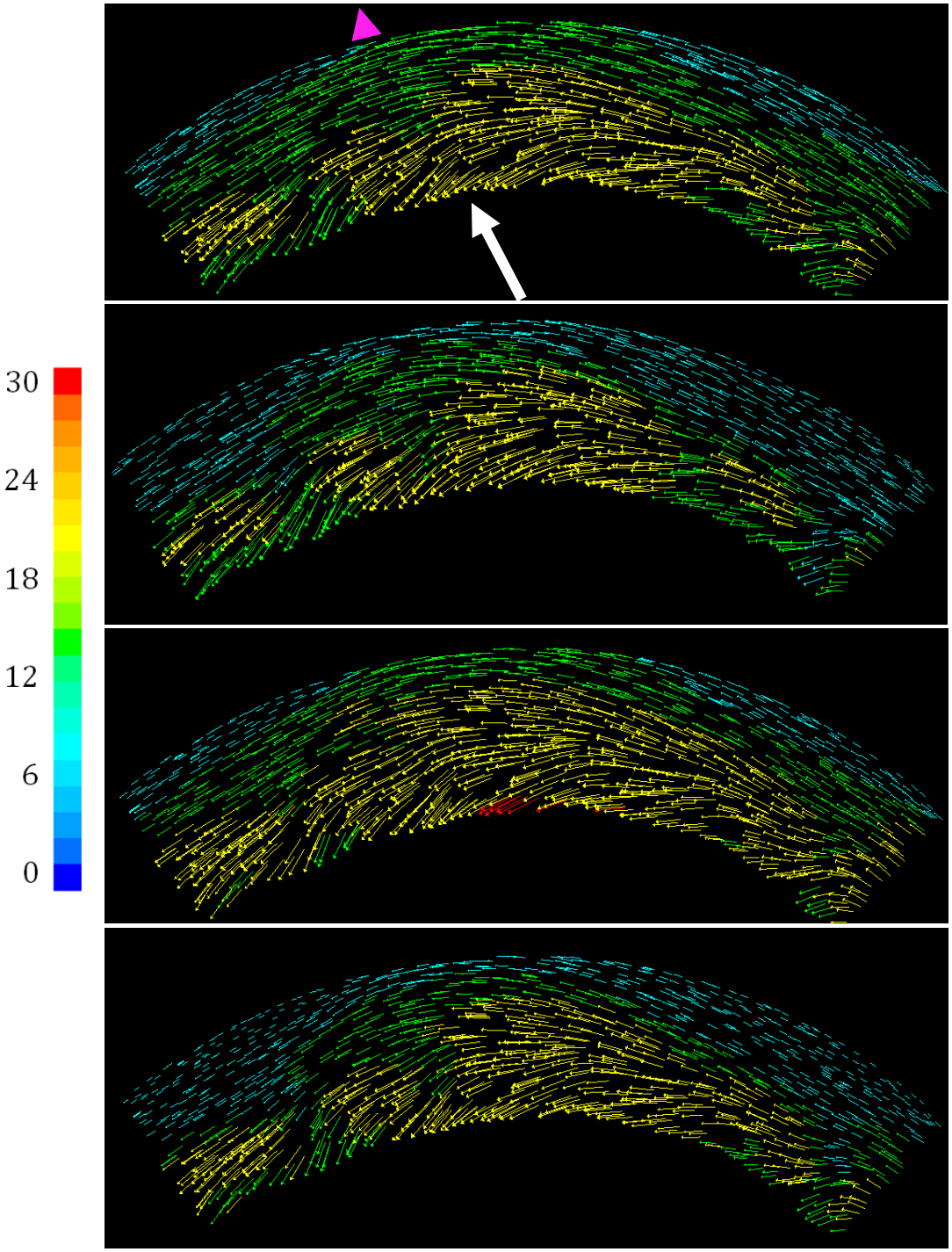

Figure 5.6: Velocity vectors colored by tangential velocity [m/s] for, from top to bottom, cases med-lean, med-rich, high-lean, high-rich

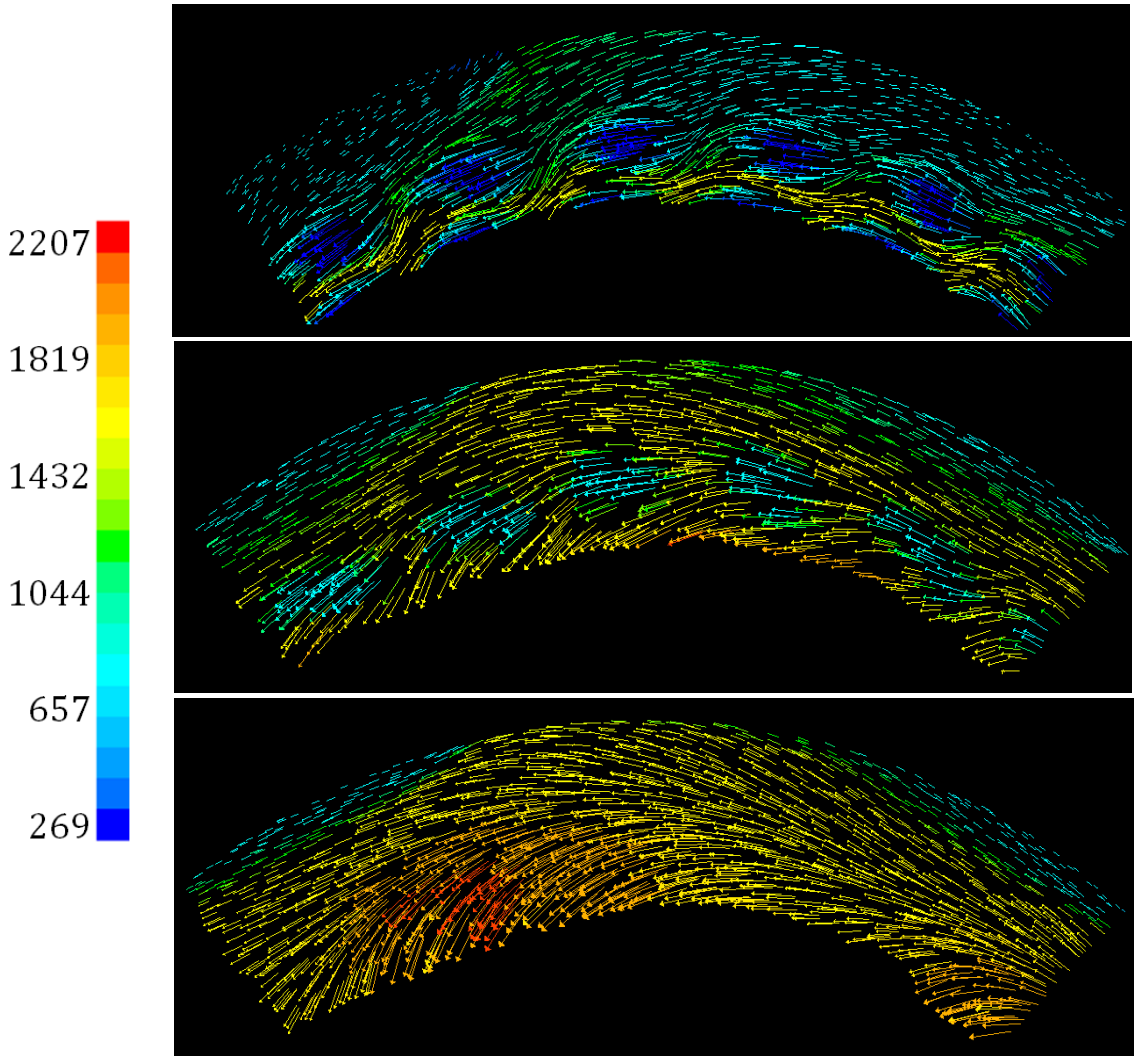

Figure 5.7: Velocity vectors colored by temperature [K] at three axial positions.

Additionally, though not observable in Figure 5.7, the inward turning included a strong axial component of nearly equal magnitude. Thus, while tangential velocity is the only component affecting the computation of the cavity g-loading, near the cavity-core interface strong axial velocities begin to appear as well. This turning has not yet been accounted for though it may have an impact on the development of the flame in the aft of the cavity and as it migrates into the HGV passage. The primary benefit to the vector analysis was a qualitative appreciation for the complexity of the motion within the cavity and particularly within the view

of the optical experiments of the previous section. Influence of the velocity gradients will be analyzed in more detail in Sections 5.2.4 and 5.2.5.

5.2.4. Residence Time Analysis

With an understanding of the cavity velocity field, these measurements can now be used to obtain estimates of residence time. Contours of tangential velocity at axial location C2 and at four operating conditions are shown in Figure 5.8. The 60° patterns remain, although the velocity gradients are not as uniform in the circumferential direction as were the temperatures. The velocities are more strongly influenced by the HGV geometry for the same reasons discussed in Chapter 4: the tangential turning and the passage contraction. Furthermore, the variance with ϕ_{cav} is minimal, similar to Figure 4.22, although the change is more pronounced at the medium-flow conditions. In those cases, the increasing fuel flow does not meet as much resistance from the cavity air drivers and therefore diffuses through a larger region at the outer diameter.

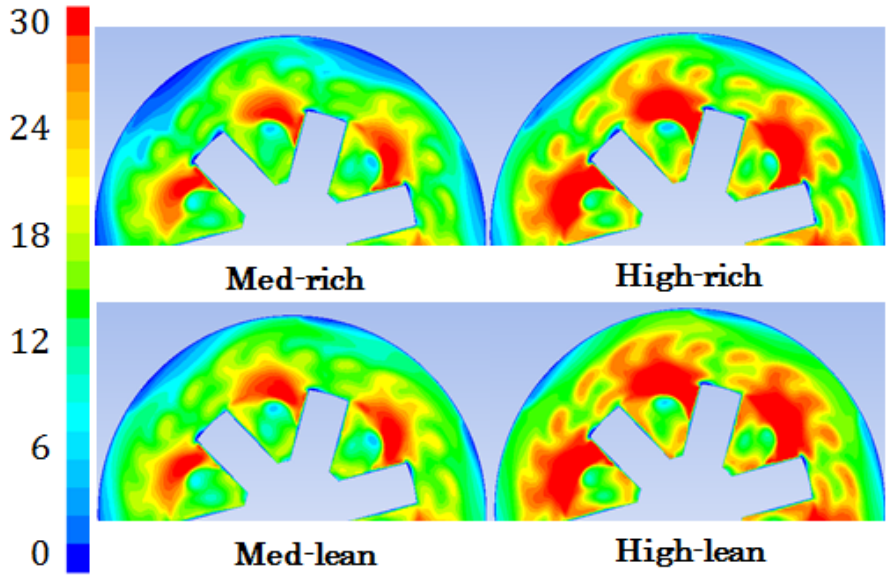

Figure 5.8: Contours of tangential velocity [m/s] at four conditions at axial location C2

Circumferentially-averaged radial profiles of tangential velocity are shown in Figure 5.9. Patterns were observed similar to those discussed in Chapter 4 – air driver cores correspond to

local maxima, and those cores were observed to decrease slightly in radial height while also diminishing from fore to aft. Indeed, the velocity profiles in all cases were fully smooth at the aft location. Additionally, the patterns seen in the profiles were all fairly similar. Increasing the level of $\dot{m}_{in}$ increased velocities throughout – specifically, a 40% increase (from medium (0.108 kg/s) to high (0.15 kg/s)) led to a corresponding 27% increase in axially-averaged centerline tangential velocity (from 15 m/s to 19 m/s) in the rich case and a 24% increase (17 to 21 m/s) in the lean case. The effect of fuel flow was evident as well: a 75% increase in ϕ_{cav} led to 12% and 9% decreases in average tangential velocity in the med-flow and high-flow conditions, respectively.

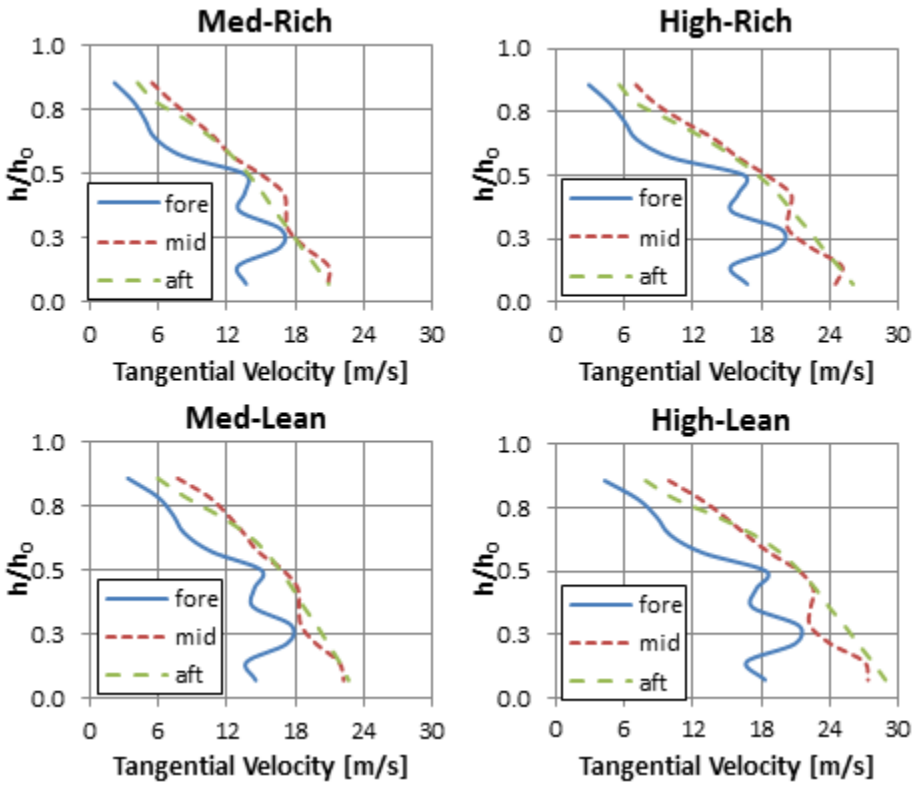

Figure 5.9: Radial profiles of circumferentially-averaged tangential velocity at the same conditions as Fig. 4.14

To complete the analysis, Figure 5.10 shows 3D fuel traces from a single fuel injection location at the same four operating conditions. Notably, lower total flow rates (left column) appeared to allow increased circulation of the fuel streams whereas the high flow conditions (right column) appeared to impose earlier migration of the fuel streams into the core flow. Rich

levels of ϕ_{cav} led to more, colder streams residing for increased durations within the CC and therefore an increased radial thickness of the cold-fuel layer along the outer dimeter. In contrast to the v2 results in Section 4.2.2.3, the majority of the fuel traces in the v3 case remained in the cavity for a length corresponding to at least one HGV passage, while many streams traversed at least two passages and some streams made a complete rotation before migrating. Thus, estimates of the average angular travel for the med-rich, high-rich, med-lean, and high-lean cases were respectively 135, 120, 135, and 120°.

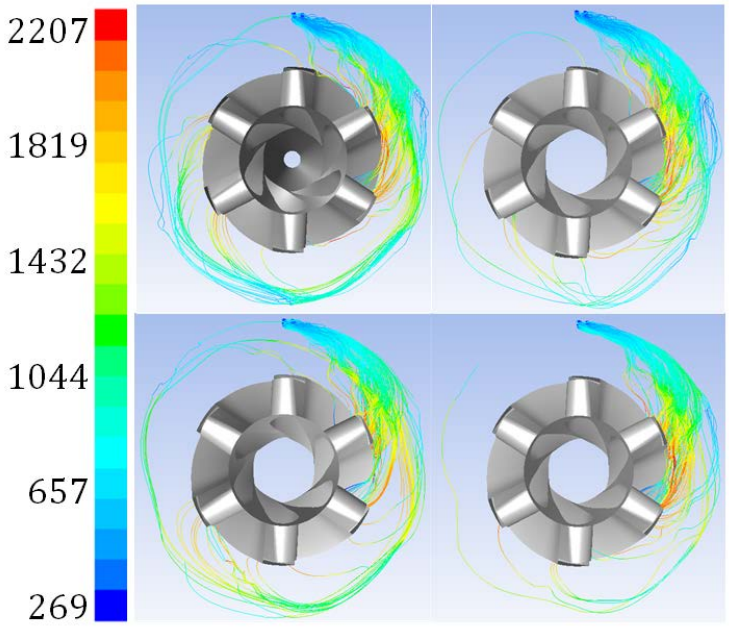

Figure 5.10: Single-point fuel injection stream traces colored by temperature [K]; med-rich (top left), high-rich (top right), med-lean (bottom left), high-lean (bottom right)

The radius at the midpoint is $r_m = 3.17$ cm, and the reference tangential velocities for the four cases were respectively $v_{t,ref} = \{15, 19, 17, 21\}$ m/s. The resulting estimates of residence time were therefore $t_{res} = \{11, 7.8, 9.8, 6.8\}$ ms. For comparison, the maximum residence time observed in the UCC v2 configuration was 5.6 ms. A basic regression analysis was performed to determine the parametric relationship between the dependent (t_{res}) and independent ($\dot{m}_{in}$, ϕ_{cav}) variables. As only two levels of the independent variables were recorded, the regression should be interpreted with care as it will not account for any potential non-linear relationships. The

derived formula for the residence time of the AFIT UCC v3 test hardware was found in the form shown by (90).

$$t_{res} = 18 - 77\dot{m}_{in} + 0.83\phi_{cav} \tag{90}$$

Therefore, again as observed in Chapter 4, residence times were negative functions of mass flow; that is, they were higher in lower-flow cases due to the lower tangential velocity over similar resident lengths. Residence times were higher in the richer cases as well, again due to the resultant lower tangential velocities. As previously stated, no firm goal for residence time has yet been set, therefore opening a trade space for further examination. Future work will be required to better understand the precise effects of certain residence-time targets to affect such a trade study.

5.2.5. Model g-loading

The g-loading within the CC was a metric of particular interest to this work. Figure 5.11 presents the first detailed numerical examination of that quantity, based on Eqn. (55) in Section 2.4.6, and calculated on a per-cell basis before being averaged. The top image shows the four primary cases, which have been referenced in previous discussion. In all, the loading at the outer diameter was low as expected due to the limited flow in the outer 25% cavity height as shown in Figure 5.9 and the large radial coordinate. The trends in all cases were increasing g-load inward due to increased tangential velocity and decreased radial coordinate. The profiles were observed to shift higher in response to both increasing air mass flow and decreasing fuel flow; that latter effect was likely due to the same mechanism discussed in the previous paragraph – the increased fuel flow not only cooled the surrounding regions but also added resistance to the bulk circumferential flow. The upper-right image of Figure 5.11 reinforces the proportional behavior of the g-load with respect to mass flow. Importantly, the lower flow rates indicate g-loads well below the theoretical threshold at which flame-front effects could be expected based on the Lewis standard [53] of $g \geq 350$. At the inner diameter, as the flow was

entrained into the HGV passages, the turning of the vanes maintained and accelerated the tangential component while the radial coordinate continued to decrease. Thus, local g-load in the HGV passages increased dramatically to $\mathcal{O}{\sim}10^4$. The onset of that behavior is evident in the lower image of Figure 5.11 where three axial positions are plotted at the high-flow lean-ϕ condition.

The threshold at which the "g-effect" occurs is not fully understood and its definitions can vary. Per Lewis [53] loading as low as $350g_0$ can begin to influence flame dynamics, whereas Lapsa and Dahm [57] noted the onset of such influence near $1000g_0$. From the observations in this chapter, the primary flame location in the AFIT UCC was generally in the lower 50% of the radial span of its combustion cavity. Thus, as shown in the center image of Figure 5.11, the Lewis threshold was attained by all but the lowest ($\dot{m}_{in} = 0.06$ kg/s) flow condition for the entire flame region. However, if the more stringent Lapsa criteria is applied, then only the two highest flow conditions may realize such behavior, and then only in the lower portions of the flame front. The implications are that, were a g-effect to exist in the current test rig, it would likely be localized and the resulting influence would depend very much on the structure of the flow at those locations.

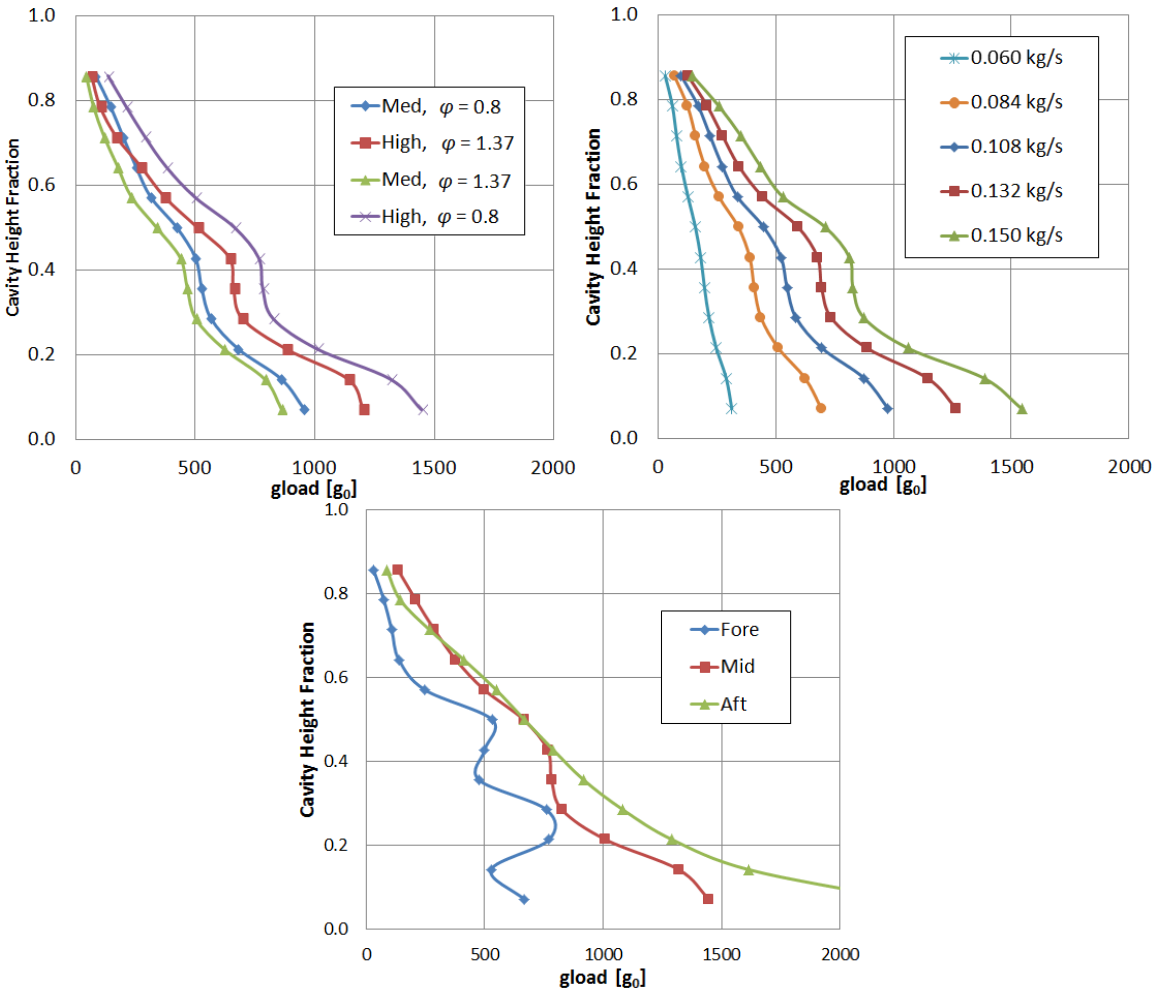

Figure 5.11: Radial profiles of circumferentially-averaged g-loads in the cavity

5.3. Impact of Equivalence Ratio on Mixing and Reactions in Cavity

Gaining an understanding to the combustion process – specifically temperature distributions, flame locations, and fuel/air mixing – was another fundamental goal of the second research objective. As outlined in Chapters 2 and 3, a particular technique was made available with the capability to provide nonintrusive measurements of the local equivalence ratio within highly turbulent, complex flow regimes such as represented by the UCC. Thus, the following section presents results from a distinct campaign with the goal of obtaining high-fidelity characterization of the mixing qualities of the combustion cavity to further the goals of

Objective 2. The LIBS experimental technique was coupled with complementary CFD results to compare value of local equivalence ratio against UCC operating conditions. Importantly, the CFD in this section differed from that of Sections 5.1 and 5.2 as well as all of Chapter 4. Whereas global chemistry had been relied upon in those previous discussions, in Section 5.3, 5.4, and 5.5 the refined numerical procedure utilizing flamelet combustion modeling was employed as detailed by Section 3.4.1.4. Furthermore, the updated grid topology illustrated by Figure 3.54 was utilized.

The LIBS measurement was taken at the axial midpoint of the cavity, circumferentially 15° counter-clockwise from one of the fuel injection baffles at approximately 75% of the cavity radial height ($h/h_0 = 0.75$). The location was determined primarily by ease of access by the beam-forming optics. As discussed in Section 3.2.3, variation in the axial direction was not possible due to (1) potential damage to the quartz window and (2) reflection from the forward cavity wall. Variation in the circumferential and radial directions would have been possible; however they would have required substantial labor to reposition the optical hardware and cameras. Thus, only a single position was analyzed; as the forthcoming data will show, however, that location ended up being a good choice for the phenomena being measured.

The collection rate matched the 10 Hz pulse of the laser, yielding signals at every "shot;" however, not every signal was usable. The experimental procedure was beset by similar difficulties as in the PSEV and the TFP methods: there were limitations based on the condition of the flow to where useable signals could be collected. Since the overall LIBS signal scales with the density of the gases, low temperature high density gases yield much stronger emissions that those at high temperature and low density. In these tests, the spectrometer and the laser power were adjusted for the low-signal high-temperature regime in order to capture effects of primary interest in the hot cavity regions. Consequently, high-density low-temperature gases saturated the detection system and were not measured. The measurement was further limited by the

range of the calibration, which was discussed in Section 3.2.3. The result was that no values below $\phi_l = 0.6$ could be measured.

The actual number of shots and the number of usable data points at each test condition are shown in Table 5.1; there did not appear to be any trend or consistency to the ratio of usable points to total number of shots based on operating condition. The end result was a bias of the data to the exclusion of equivalence ratios that were not within the flammability limits of the propane-air flame. In other words: the measurements obtained were not measures of the equivalence ratio of all gas in the cavity – they were only measures of the equivalence ratio of the hot gas. Another parameter is given in the table, $\hat{\phi}$, which will be the topic of an upcoming discussion.

Table 5.1: Test conditions and usable shot fraction

Condition	$\dot{m}_{in}$	φ_{cav}	Shots	Points	Ratio	φ_{hat}
1	0.108	0.60	607	156	26%	46%
2	0.108	0.80	436	97	22%	66%
3	0.108	1.05	578	239	41%	13%
4	0.150	0.60	822	124	15%	60%
5	0.150	0.80	668	203	30%	27%

As introduced by Table 5.1, results were collected at five conditions over a range of cavity equivalence ratios, ϕ_{cav}, and inlet mass flow rates, $\dot{m}_{in}$. The test conditions, corresponding time-averaged LIBS results, and CFD results from the same location are shown by Table 5.2. The full set of time-resolved data is also shown in Figure 5.12 to aid the discussion. Each time-averaged result was the collection of at least 100 samples. Notably, all measured averaged values fell within the range $0.68 < \bar{\phi}_{LIBS} < 0.83$, thereby indicating that any burning at that location was occurring – on average – at relatively lean conditions regardless of the overall level of ϕ_{cav}.

Table 5.2: Test conditions and time-averaged LIBS results

Condition	$\dot{m}_{in}$	ϕ_{cav}	ϕ_{LIBS}	ϕ_{CFD}
1	0.108	0.60	0.719	0.600
2	0.108	0.80	0.714	0.615
3	0.108	1.05	0.677	0.853
4	0.150	0.60	0.825	0.540
5	0.150	0.80	0.677	1.032

There was inconsistency in the trends as the mass and fuel flow rates were changed. An increase in $\bar{\phi}_{LIBS}$ accompanied an increase in mass flow at $\phi_{cav} = 0.6$, although the same trend was not seen at $\phi_{cav} = 0.8$. That could have been due to the radial penetration of the fuel jet, which was a more prominent influence at that particular location. At both levels of mass flow, however, the effect of increasing ϕ_{cav} was to decrease the local value of $\bar{\phi}_{LIBS}$.

Figure 5.12 provides the instantaneous time-resolved results of every resolvable measurement from the five tested conditions. Condition 3 is highlighted in the top row with an extended axis for better detail; it was chosen as it had the highest percentage of usable shot. Examining the time-resolved data illuminates one important aspect of the measurement. While the measured values themselves are highly accurate outside of the noted biases, the actual conditions within the cavity were highly unstable. Figure 5.12 demonstrates variation at the location of the instantaneous LIBS measurement in a range of $0.6 < \phi'_{LIBS} < 2.3$ (the value of 2.3 was observed in the lone out-of-range peak in the plot from Condition 4). Furthermore, the data represented by Figure 5.12 consist of 819 usable points out of 3111 shots over the respective time spans (about 25% usable data). Thus, further fluctuations in the actual value of ϕ at that point were very likely occurring, but the resultant signals were unusable due to the limitations discussed previously.

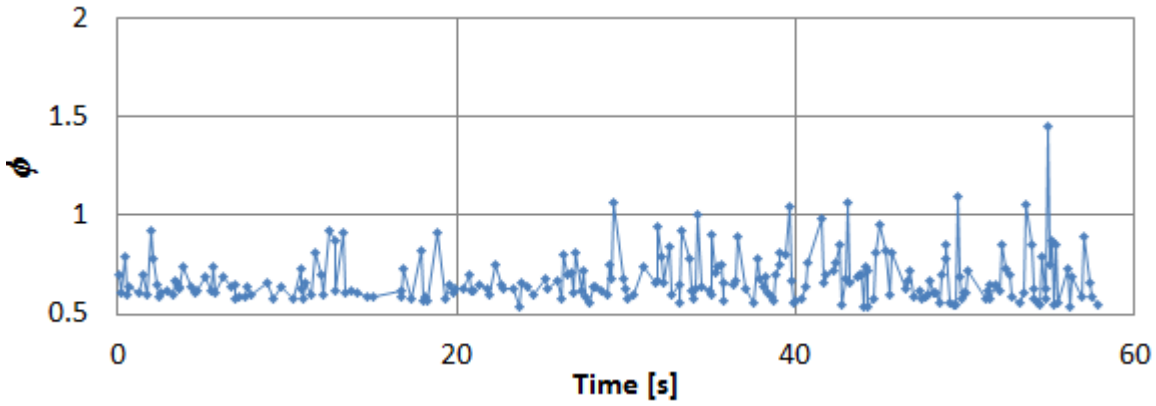

Condition 3

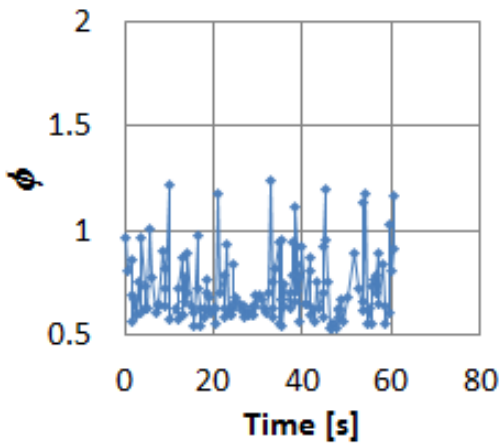

Condition 1

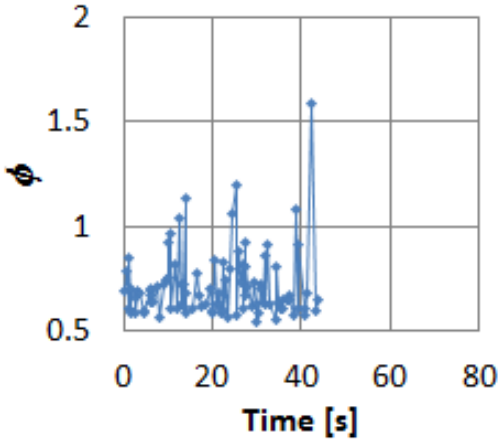

Condition 2

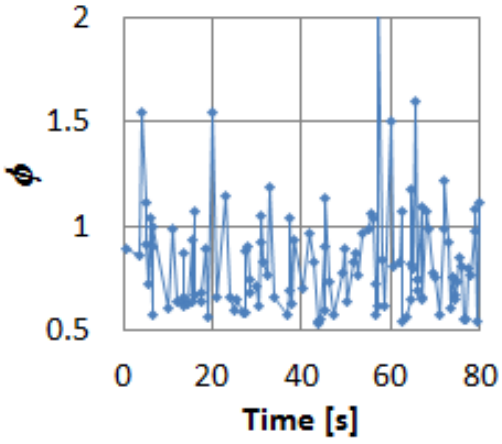

Condition 4

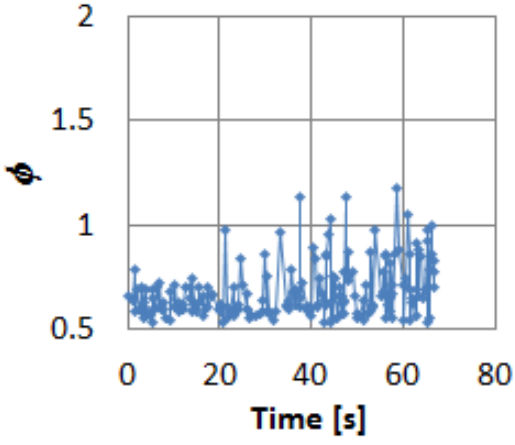

Condition 5

Figure 5.12: Time-resolved LIBS equivalence ratio calculations

Some trends were observed in the fluctuations themselves as conditions were compared. First, the ratio of usable point to number of shots as shown in Table 5.1 appeared to increase consistently with ϕ_{cav}. This was logical as such an increase would notionally push more cavity fluid conditions within the measureable range. To obtain further quantification, a parameter was introduced to account for the magnitude of the fluctuating component with respect to the overall mean, $\hat{\phi} = \phi'/\bar{\phi}$ where $\phi' = |\phi - \bar{\phi}|$. Values of $\hat{\phi}$ were averaged for each case and reported alongside the data in Table 5.1 to help explain the shapes of the profiles in Figure 5.12. As expected, the fluctuations decreased substantially between Conditions 4 and 5, thereby suggesting further dependence of the measurement unsteadiness on the level of ϕ_{cav}. The comparison of Conditions 1, 2, and 3 was less consistent, although the highest level of ϕ_{cav} represented by Condition 3 did see the lowest value of $\hat{\phi}$.

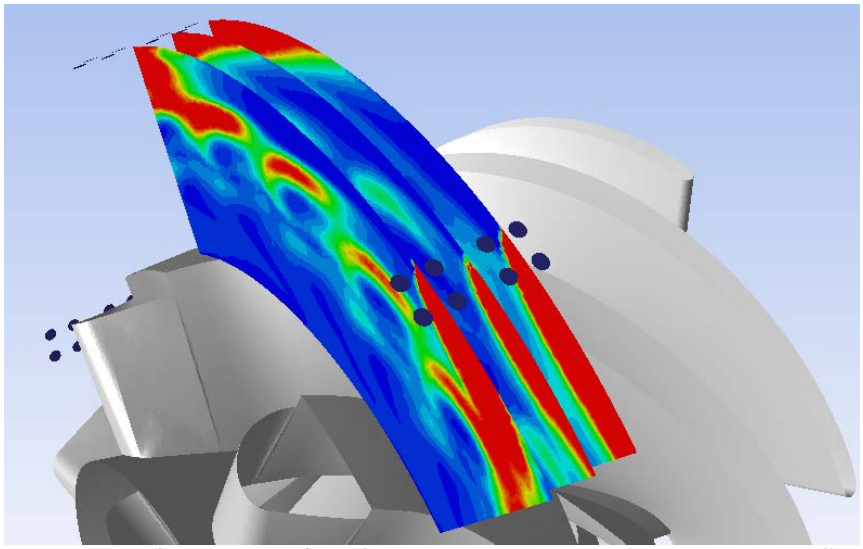

Figure 5.13: Orientation of LIBS computational planes with respect to HGV geometry and fuel injection baffles

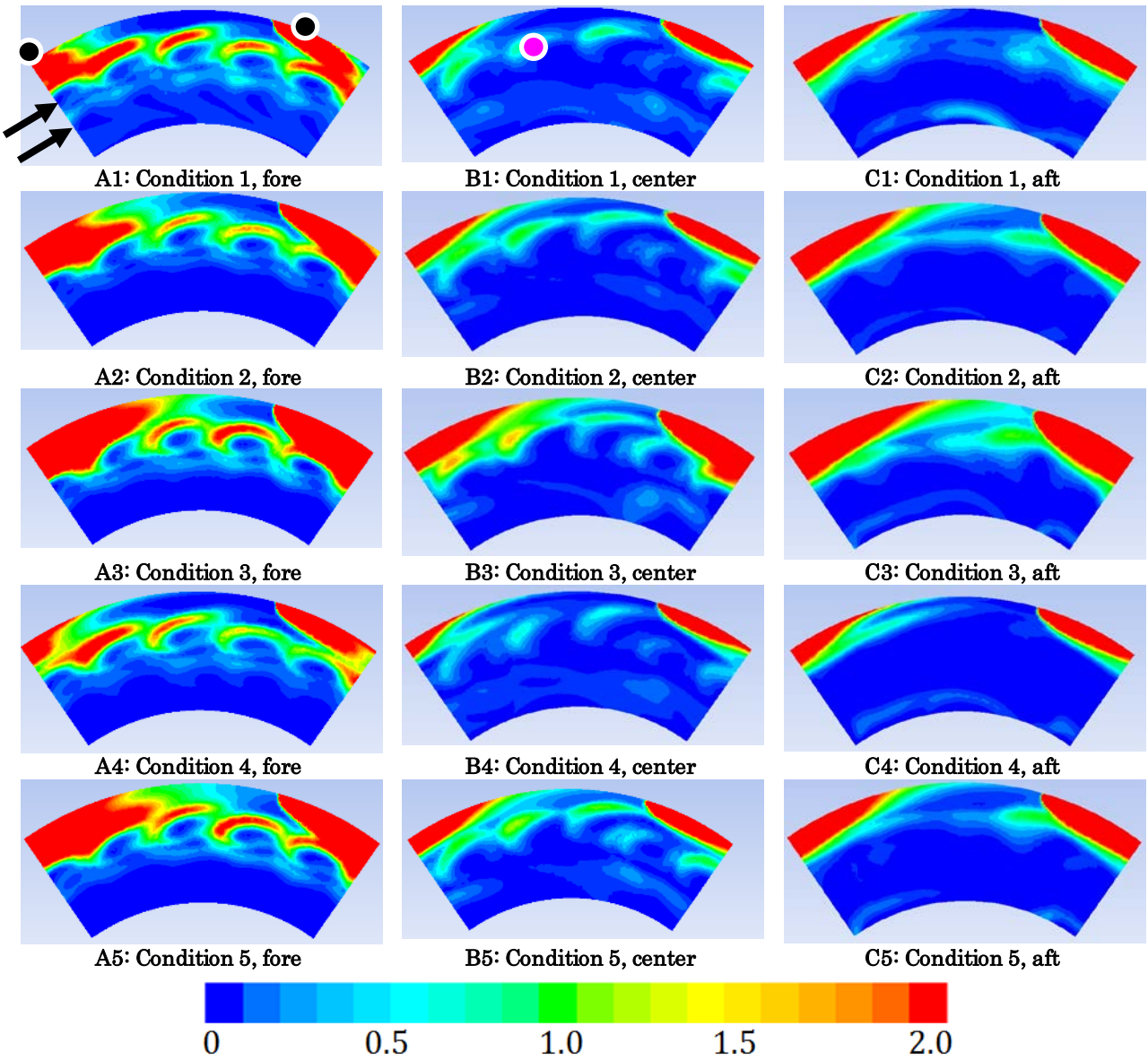

Figure 5.14: CFD contours of ϕ_l

Added insight was obtained through CFD contours at three axial planes positioned at ¼, ½, and ¾ of the cavity axial length and dubbed "fore," "center," and "aft," respectively. Figure 5.13 illustrates the placement of the computational planes relative to the hybrid guide vane (HGV) geometry (in gray) and the fuel injection baffles (dark blue). The numerical results – while temporally averaged – revealed a very complex flow field particularly in the region of the LIBS measurement with significant gradients in all directions – radial, tangential, and axial. In Figure 5.14, contours from all five of the test conditions are shown at each of the three axial

positions. The fuel injection jets are highlighted by black and white circles in image **A1** and are marked by large regions of high (beyond contour range) ϕ_l along the outer diameter. The radial positions of the rows of tangential cavity air drivers are noted by the black arrows in image **A1** and may be observed in both columns **A** and **B** by the distinct cores of low ϕ.

One general conclusion was that increasing ϕ_{cav} at a given mass flow rate correspondingly increased the size of the fuel-rich regions. The differences between conditions of equal ϕ_{cav} but different $\dot{m}_{in}$ (that is, Conditions 1 vs. 4 and 2 vs. 5) are not substantial. Overall, the fuel was shown to interact strongly with the circular air inlets producing regions of relatively high ϕ_l above and within the air jets, especially at the forward location. It was revealed through analysis of the velocity vectors in Section 5.2.3 that a helical flow pattern existed within the air driver cores that served to draw fluid from the outer volume of the cavity. Consequently, the severity of the gradients implied that substantial differentials should be expected with any spatial variation in any direction. The approximate location of the LIBS measurement is highlighted in image **B1** by the pink and white circle. While the measurement is effectively a point value at the center of that circle, spatial uncertainty was about +/-0.5 mm in the radial and tangential directions and +/-0.1 mm in the axial direction. Thus, the contours did in fact indicate the presence of regions that fell within the range of the LIBS measurement and within the range of spatial uncertainty. However, the potential variability in the values of ϕ_l with even modest uncertainty in the exact location of the measurement was an issue that could not be reconciled with the available data.

To illustrate the relative regions of heat release, Figure 5.15 compares image **A2** with a contour of temperature at the same location. Peak heat release in all simulated cases tended to occur in the inner half of the CC and was shown to increase toward the aft (more detail will be given in 5.4). Notably, the peak temperature occurs in very fuel-lean regions, indicating that much of what might characterize primary-zone burning has already occurred above and around

the first row of air driver jets. The second row of jets appears to dilute and mix the intermediate products as they circulate and proceed inward.

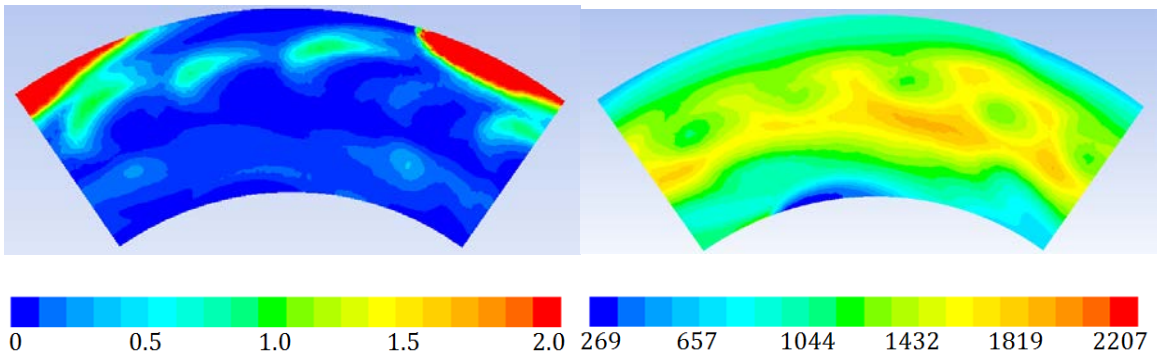

Figure 5.15: Comparing the equivalence ratio (left) and temperature contours (right) for Condition 1, center

To better quantify the effects of spatial variability, the technique of generating circumferentially-averaged radial profiles was employed with the results shown in Figure 5.16 and Figure 5.17. Figure 5.16 examines a single flow condition, $\dot{m}_{in} = 0.108$ kg/s, at the three tested levels of ϕ_{cav} and at the three axial positions examined by the CFD contour planes. The LIBS measurement location at $h/h_0 = 0.75$ is highlighted by the orange line. In all the results, there is a certain value of h/h_0 at which ϕ_l begins to increase asymptotically; this corresponds to the lower limit of the fuel injection plume (where technically $\phi_l = \infty$). The effect of increasing the fuel flow was to decrease the value of h/h_0 at which that steep gradient began; the outer "fuel layer" was effectively made thicker and cooler. The fuel layer was thicker at the front of the cavity as it was in a region of relatively lower velocity; the air drivers fed the cavity from only one side, thus the outer forward corner did not see as much impact from the driver cores as did the remainder of the CC volume. Finally, Figure 5.17 demonstrated that the impact of $\dot{m}_{in}$ on the distribution of ϕ_l was negligible, as upheld by the contours in Figure 5.14.

Importantly, the values at $h/h_0 = 0.7$ were not expected to match the LIBS measurements as they were spatially-averaged, however they did provide insight into the structure of the cavity at the approximate region of the measurement. That radial location was effectively a transition region. The outer cavity volume – outside the top row of air drivers –

appeared to serve effectively as a primary combustion zone. The fuel was introduced, subjected to initial mixing, and began burning at relatively moderate temperatures. The interaction with the air drivers served to rapidly transport the intermediate products inward in highly complex flow patterns, rapidly diluting the mixture in the process. (Those flow patterns have come to light largely through examination of the vector field as in Figure 5.6 and the streamlines as in Figure 5.10.)

The LIBS measurement was taken at a radial location that was nearly level with the top edge of the top row of air drivers; thus it was precisely in the midst of one of the more complex flow regions in the CC and at the site of potentially severe gradients, even relative to the remaining flow field. Furthermore, the transient nature of the data in Figure 5.12 implied that there are likely extreme temporal gradients accompanying the spatial gradients illustrated by Figure 5.14. The CFD solution is steady-state, but that does not necessarily guarantee a match to time-averaged measurements of a highly transient event. The likely reality is that the spatial gradients exist as shown by the CFD, but they are also in motion temporally; that is, the "pockets" of alternating high and low ϕ likely ebb and flow about the air drivers. If the time-resolved data are to be taken as an indication, then that ebb-and-flow also appears to occur without any resolvable pattern. A scale-resolved transient numerical solution will be required to obtain a more reliable comparison with this and other experimental measurements.

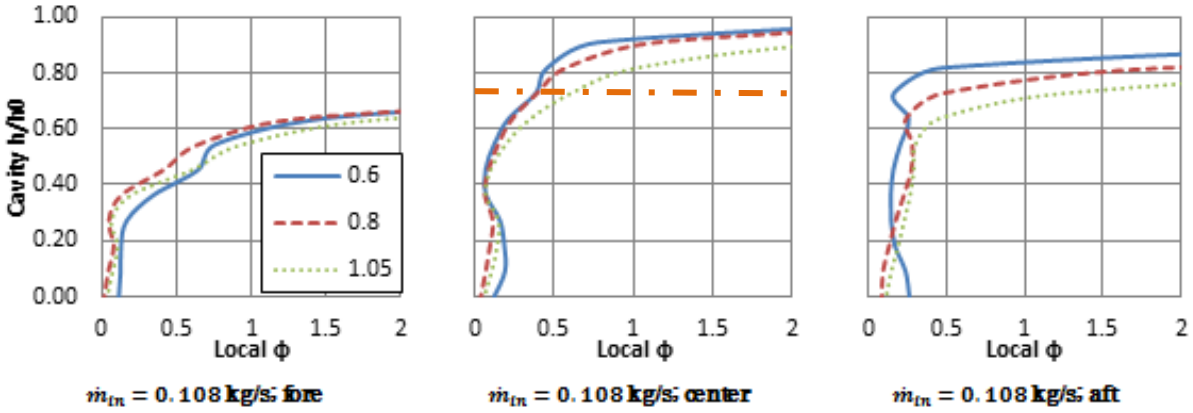

Figure 5.16: CFD circumferentially-averaged profiles of ϕ_l comparing levels of ϕ_{cav} at fore, center, and aft axial positions

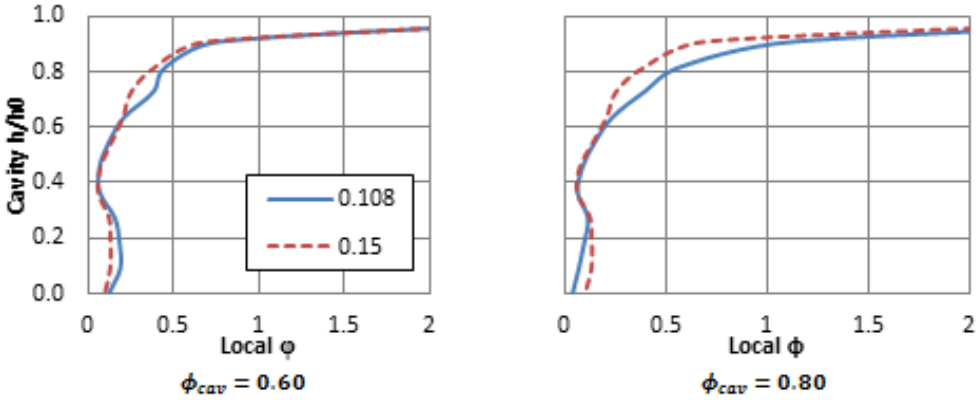

Figure 5.17: CFD circumferentially-averaged profiles of ϕ_l comparing low (0.108 kg/s) and high (0.150 kg/s) levels of $\dot{m}_{in}$

5.4. Impact of Operating Conditions on Temperature

As stated at the introduction to Section 5.3, resolution of Objective 2 requires knowledge of the numerous aspects of the combustion process within the circumferential cavity. Central to that understanding is the resultant temperature patterns. Therefore, this section presents a discussion of the distribution of the cavity temperature field and its response to various operating conditions. The TFP measurement technique is combined with corresponding CFD analysis to provide insight into spatial and temporal temperature gradients; extended CFD results are also discussed. The ultimate goals of the temperature analysis were to bolster prior

evidence and understanding of fuel/air mixing and the progression of the reactions within the cavity.

5.4.1. Temperature Profiles

One-dimensional temperature profiles were experimentally facilitated by TFP measurements that were collected using the methods outlined in Section 3.2.4. There, the filament placement was shown at four position mounted to the top surface of an HGV vane and spanning the radial height of the cavity; mounting requirements led to the filament position varying both axially and circumferentially as shown by Figure 3.41. Recall that the filaments were labeled according to their relative axial location: the fore wall of the cavity was at "0%", and the "13% filament" was mounted at 13% of the cavity axial length and was thus fore-most of the set comprised of the 13%, 31%, 61%, and 88% filaments.

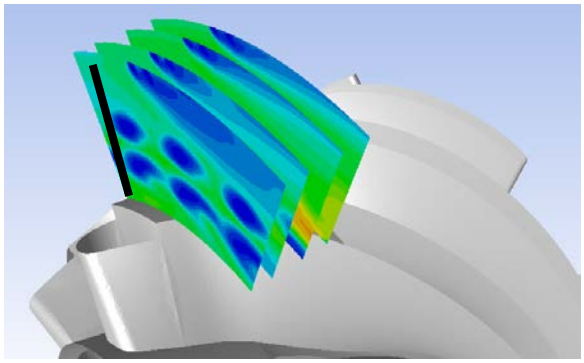

Figure 5.18: Orientation of TFP computational planes with respect to HGV geometry

Test conditions for these experiments were dictated primarily by alignment with the work of Gilbert [100]. They therefore consisted of a single level of inlet mass flow, $\dot{m}_{in} = 0.108$ kg/s, and three levels of cavity equivalence ratio $\phi_{cav} = \{0.99, 1.1, 1.3\}$. The numerical model was also processed to replicate the filament placement through the generation of contour planes at axial positions matching those of the filaments. The four numerical planes are illustrated in Figure 5.18 with the HGV centerbody geometry shown for reference. The approximate location of the 13% filament is highlighted on the foremost plane by a black line.

To first gain an appreciation for the characteristics of the experimental region, numerical temperature contours at the three tested conditions were examined in Figure 5.19 for all four axial positions. In row **A** the approximate location of each corresponding filament is shown with a black line. The view is front-looking-aft, so the bulk circumferential rotation is clockwise. One HGV surface is also visible in the lower portions of the images for further reference. Common features included the cold cores produced by the cavity air drivers, the cold plume of fuel from the injection baffle at the top, and the increase in the size of the hot regions from front to back. A semi-uniform high-temperature band was present in the 61% position in all conditions, and the hot region at the 88% was shaped largely by the HGV passage beneath it due to the sustained turning and contraction therein. The variance due to ϕ_{cav} was most prevalent in the shape of the fuel plume that increased in size with increased fuel flow; otherwise the remainder of the field was negligibly affected at these conditions.

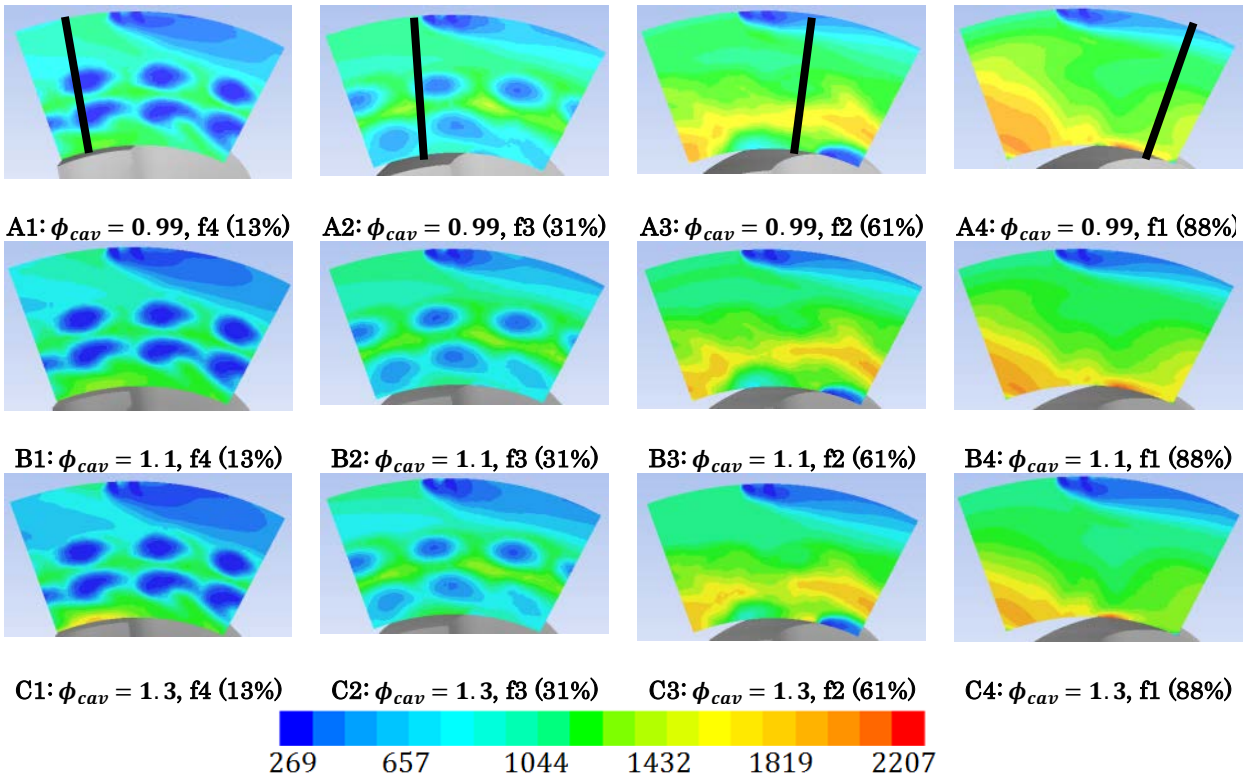

Figure 5.19. Temperature [K] contours at axial locations matching filament placement

As the gap between filaments f3 and f2 was relatively large, another CFD contour was generated at a position centered between the two (roughly 45% of the cavity width, or $z = 13.85$) and shown in Figure 5.20. On average, the temperature increase within the cavity will be demonstrated to trend linearly in Chapter 6. However in Figure 5.20 the axial gradients were observed to be substantially more complex. The transition is characterized by the gradual dissipation of the cold air jet cores and the growth of the inner high-temperature band. As demonstrated by Figure 5.7, the reaction zones tended to anchor in the midst of the air driver cores. The CFD predictions indicate that those anchored reaction zones served propagated and fed the regions of peak heat release near the cavity aft wall.

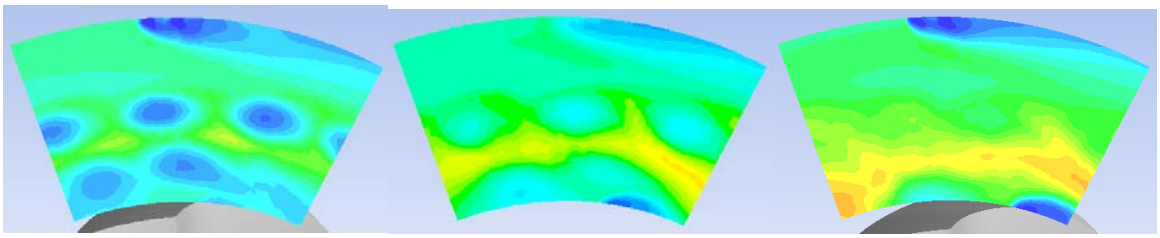

Figure 5.20: CFD contours demonstrating the transition from the 31% location (left), to an intermediate 45% location (center) and on to the 61% location (right)

The experimental data were analyzed together with the analogous numerical profiles as shown in Figure 5.21; the CFD profiles were un-averaged – they represented the same discrete one-dimensional profiles as did the filaments. For clarity, the results were divided such that the charts in the left column presented the results from the front two filaments and the right column presented the back two filaments. To interpret the filament results clearly, two elements were crucial to recognize. First, the filament data did not represent the full radial span of the cavity as the field of view was limited by the size of the quartz window. Second, as discussed in Section 3.2.4, the filaments were unable to resolve any data below 980 K. That is, the filament signal would translate into 980 K in the presence of any real gas temperature at or below that value. Therefore, all data in Figure 5.21 at 980 K can be assumed to represent lower-temperature flow. Thus, when examining the behavior at the 13% location, it was

reasonable to expect little – if any – usable signal from the filaments. As illustrated by the temperature contours, the bulk of that region consisted of cold air driver cores. Those cores were clearly visible as local minima in the CFD profiles while the experimental filament data registered no signal. However, the filament data also indicated the presence of a substantial hot region at the outer diameter in both the 13% and 31% locations and at all three tested conditions that were not predicted by the CFD. The hot region appeared at the 13% position and expanded significantly at the 31% position. Conversely, the CFD predicted relatively cool temperatures at the outer diameter, followed by a sharp spike in temperature at the inner diameter (which was beyond the field of view of the filament data). In the aft positions, the filament data showed fairly smooth and uniform temperature profiles. The CFD, however, continued to predict residual influence from the cold driver cores at the 61% location that diminished almost entirely by the 81% location. In both locations the temperature increased linearly from the outer to the inner diameter.

To verify that the one-dimensional profiles extracted from the CFD results were representative of the predicted temperatures throughout the cavity, they were compared with circumferentially-averaged profiles in Figure 5.22 for three axial locations. In all cases the agreement is good: thus, the one-dimensional profiles did not belie any substantial asymmetry or other such behavior within the cavity. It was reasonably expected that the same conclusion could be stated for the one-dimensional TFP measurements, although such an assertion would require validation.

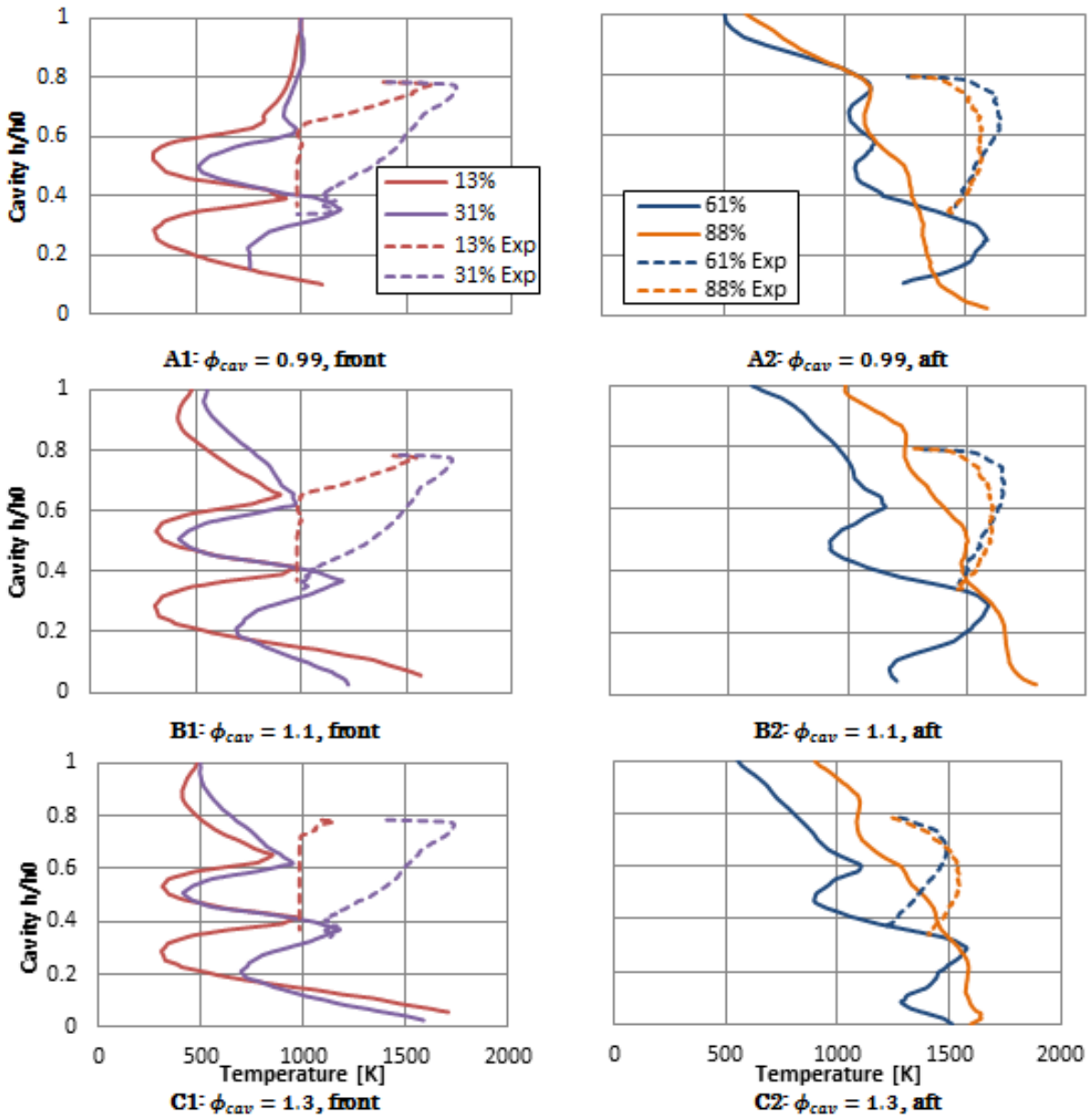

Figure 5.21: Experimental and numerical TFP results for the front two filaments (left column) and the aft filaments (right)

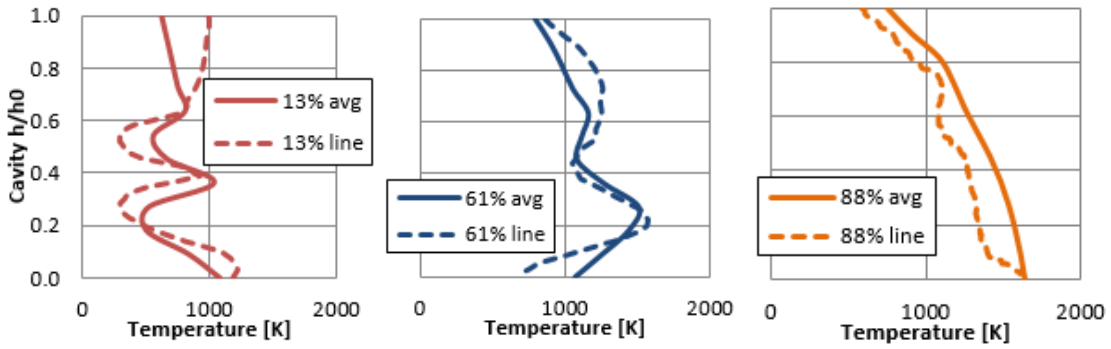

Figure 5.22: Comparing CFD results: one-dimensional vs. circumferentially averaged profiles

In terms of the operation of the AFIT UCC, it is not desirable to impart peak heat release too far inboard as challenging cooling requirements for the HGV would thereby result. From that perspective, the experimental TFP produced fundamentally optimistic results. However, the CFD predictions were more mixed. That discrepancy was expected, primarily due to the steady-state assumption of the CFD model. However, to explain the regions of more substantial variation, two explanatory hypotheses were developed. First, the reality of the interaction between the fuel and the air drivers was highly complex; significant mixing was occurring concurrently with chemical reactions within multiple layers of shear and turbulent effects. The spacing of the grid in those regions was likely insufficient to fully resolve those behaviors, therefore resulting in the loss of information on a large portion of flame development. The losses were most likely with respect turbulent interactions and mixing scales in particular – assumptions of fast chemistry should still be valid for the conditions within the UCC. The consequence of such shortcomings would logically be colder regions and slower chemistry than observed experimentally. Second, as previously discussed, experimental observations and measurements have continually supported the conclusion that the AFIT UCC is unsteady. The TFP data were obtained similarly to the LIBS data as time-averaged results from real-time measurements. Thus, to aid that discussion, a similar examination of the transient TFP data was accomplished.

The TFP imagery was collected at a rate of 53 Hz, therefore making them theoretically better-resolved in time than the LIBS data. However the TFP process also encountered issues with dropped data issues: some of the collected frames did not contain any usable signal. In the case of the conditions at $\phi_{cav} = 0.99$ and $\phi_{cav} = 1.1$, the ratio of usable frames to total frames was comparatively good at 61% and 60%, respectively. For unexplained reasons, however, the data at $\phi_{cav} = 1.3$ saw a success ratio of only 16%. Figure 5.23 presents a subset of time-resolved data at the $\phi_{cav} = 0.99$ condition. In the top row, instantaneous temperature profiles are given for the 13% (left) and the 88% (right) filaments. In the bottom row, a single radial location was sampled over the duration of the signal, again for the 13% (left) and 88% (right) filaments. The instantaneous profiles were selected in order to demonstrate the lowest and highest profiles as well as one roughly central. Furthermore, the radial location for the signal duration sample was selected at a point corresponding to the approximate radial center of the instantaneous profiles that varied based on profile shape. Figure 5.24 presents the same data for the $\phi_{cav} = 1.3$ condition.

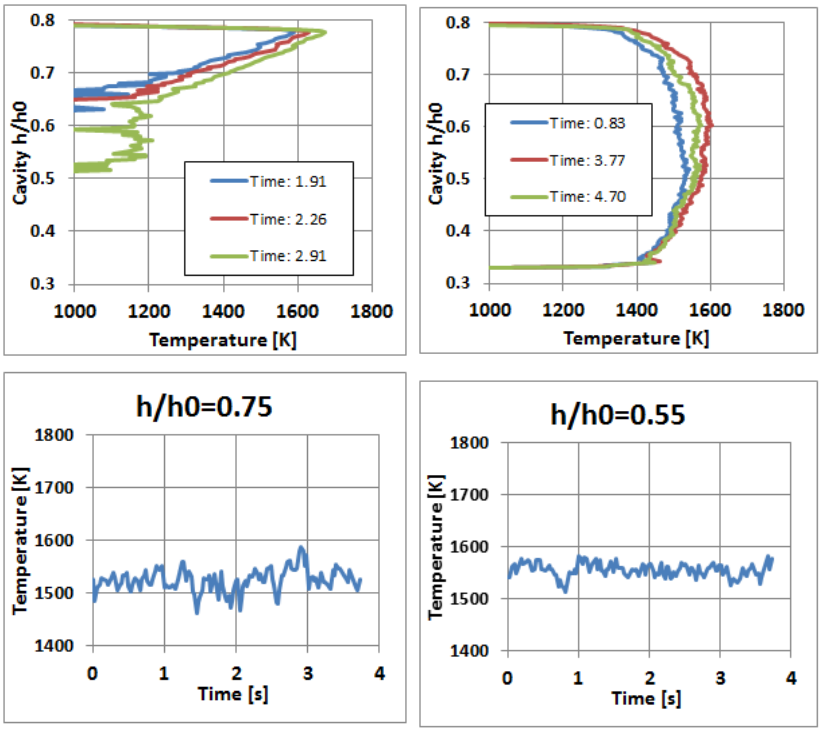

Figure 5.23: Experimental TFP data for the 13% (left) and 81% (right) filaments showing instantaneous radial profiles (top) and transient data from a single radial location (bottom); condition is $\phi_{cav} = 0.99$

First, the instantaneous observations were validated against the averaged results presented in Figure 5.21. As expected, the differences between the $\phi = 0.99$ and $\phi = 1.3$ conditions for the 13% filament profiles were substantial. Note as well that the axes for the 13% filament single-point duration sample in the lower-left of Figure 5.24 had to be adjusted to account for lower temperature at this location. In broader terms, the variability appeared to increase between the lower and the higher fuel set points; it ranged about 50 K in the former, and about 100 K in the latter for the 88% filament (recall from Section 3.2.4 that the TFP accuracy was computed to be about 30 K). The duration sample for the 13% filament in Figure 5.24 was comparatively dramatic and could not be explained. It was considered possible that the low 16% ratio of usable to total frames was another symptom of a potential outlier condition that might have led to erroneous behavior, but no further evidence was collected to support that conclusion.

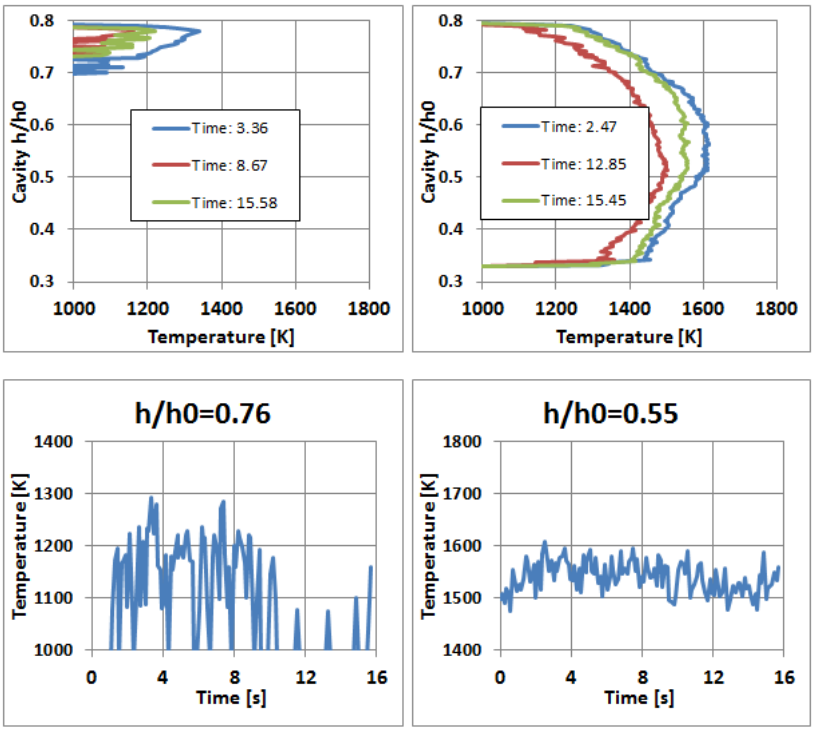

Figure 5.24: Experimental TFP data for the 13% (left) and 81% (right) filaments showing instantaneous radial profiles (top) and transient data from a single radial location (bottom); condition is $\phi_{cav} = 1.3$

The transient data were statistically sampled to produce the results in Table 5.3. The mean values were calculated considering only those points that indicated a viable signal (i.e. – those temperatures greater than 980 K); the standard deviation was similarly constrained. As supported by the previous plots, the variability appeared most substantially at the fuel-rich condition. Furthermore, at all conditions, variability was greater in the front two filaments where the temperatures were correspondingly cooler as seen is in Figure 5.25. A clear trend was characterized by an exponential function as displayed on the figure. An exponential fit was deliberately selected because it yielded physically logical behavior of converging on a small positive value as temperature increased toward reasonable values (i.e. – approaching adiabatic flame temperature).

Table 5.3: Characterization of transient variability in TFP data

ϕ_{cav}	Filament	Mean [K]	StdDev [K]
0.99	88	1513.7	17.39
	61	1562.0	16.12
	31	1413.6	33.38
	13	1309.8	36.34
1.1	88	1549.3	22.01
	61	1572.3	18.77
	31	1384.9	39.54
	13	1269.7	37.25
1.3	88	1462.7	35.58
	61	1379.8	44.57
	31	1229.0	59.66
	13	1071.9	56.54

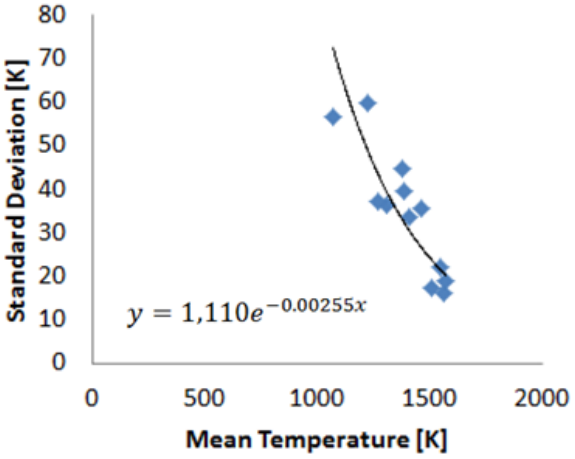

Figure 5.25: Experimental TFP deviation as a function of mean temperature

The fundamental conclusion was a counterpoint to previous discussions with the LIBS data. Whereas the broad theme that developed in Section 5.3 and in most of this current section was that the UCC was itself unstable, on interpretation of the data in Figure 5.25 is that, if the UCC were operated in such a way to attain higher temperatures, more stable operation might be possible. It was acknowledged that the operating conditions of the UCC – atmospheric pressure with gaseous fuel – were not expected to generate behaviors representative of a traditional high-pressure combustor experiment. These results support that understanding and further indicate that the performance of the current UCC design could very likely be improved if its conditions changed. Increasing operating pressure would certainly yield better mixing and more complete combustion, which would in turn increase efficiency and stability.

Another interpretation of the above results, however, is that the TFP measurement itself is more subject to variation at lower temperatures, particularly those which correspond to its lower limit. As the CFD demonstrated in Figure 5.21, the predicted spatial gradients in temperature are the most severe at the 13% filament location due to the interaction of cavity combustion with freshly introduced cold cavity air. Those gradients spanned a range of nearly 700K: from temperature peaks of about 1000 K to jet core temperatures at inlet conditions of

300 K. The strongest gradients manifest in the 1-D CFD profiles was about 150 K/mm as compared to the strongest observed gradients in the experimental data of 130 K/mm. Thus, it was hypothesized that, were the TFP measurements able to extend into lower temperature regimes, the profiles shapes might take forms similar to those predicted by the CFD. However, given its limited signal range, the presence of the strong spatial gradients in conjunction with temperatures beyond signal range may have contributed significantly to increased variability in the TFP data.

The best path to deconflict those two interpretations would be to collect new experimental TFP data using an infrared (IR) camera as opposed to the visible-spectrum camera currently in use. In the IR range, the effective lower limit to the TFP signal is hypothesized to be approximately 700 K; thus, IR data could be compared to visible-range data to determine whether or not the variability was due to signal quality or if it was actually a function of the combustor operating condition.

5.4.2. Computational Effects of Mass Flow and Equivalence Ratio

The cavity temperatures were examined in detail in the computational model to gain a better understanding of the nature of the structures that characterized the circumferential flow. Temperature contours were examined at the four conditions: medium and high inlet flow ($\dot{m}_{in} = \{0.11, 0.15\}$ kg/s) and lean and rich cavity equivalence ratio ($\phi_{cav} = \{0.80, 1.37\}$. Also represented are the three axial positions with which this section has focused, shown in Figure 5.26. The center column demonstrated the familiar behavior that was previously discussed in Section 5.4.1: the relatively consistent high-temperature region was anchored in the inner portion of the CC while the outer cavity diameter contained uniformly cooler regions of initial fuel mixing and burning. Variation with air and fuel flow rates was subtle and difficult to discern from the contours alone. However, variation with axial position was substantial and consistent at all operating conditions. In the forward position, a very hot region anchored at the

inner corner below the inner row of cavity air drivers. Its shape was consistent between all run conditions, being defined by the high-velocity air driver cores as well as the HGV surfaces. Reading the plots from left to right, that high-temperature region was observed to migrate into its "lifted" position in the center, then spread and encompass the bulk of the cavity in the aft. In the aft position, unlike at the other two locations, a discernable effect occurred due to variation in fuel flow.

The lean cases contained notably larger hot regions than their rich counterparts; in terms of the last five contour levels (1819 K and above), they occupied about 15% of the cavity area in the rich cases versus about 90% of the cavity area in the lean. Furthermore, in the rich cases the hot regions were confined to the inner diameter and were observed to attach to the HGV outer and suction-side surfaces. Again, the adiabatic flame temperatures for propane-air combustion at the lean and rich operating conditions were calculated to be 2025 K and 2053 K, respectively; however, temperature calculations revealed a contrary trend with hotter temperatures at leaner set points. The physics explaining that difference were unclear; it was believed to not be a simple matter of combustion efficiency. Indeed, the intent of the circumferential cavity was never to attain fully complete combustion, therefore comparing against adiabatic flame temperatures within the cavity along would be erroneous.

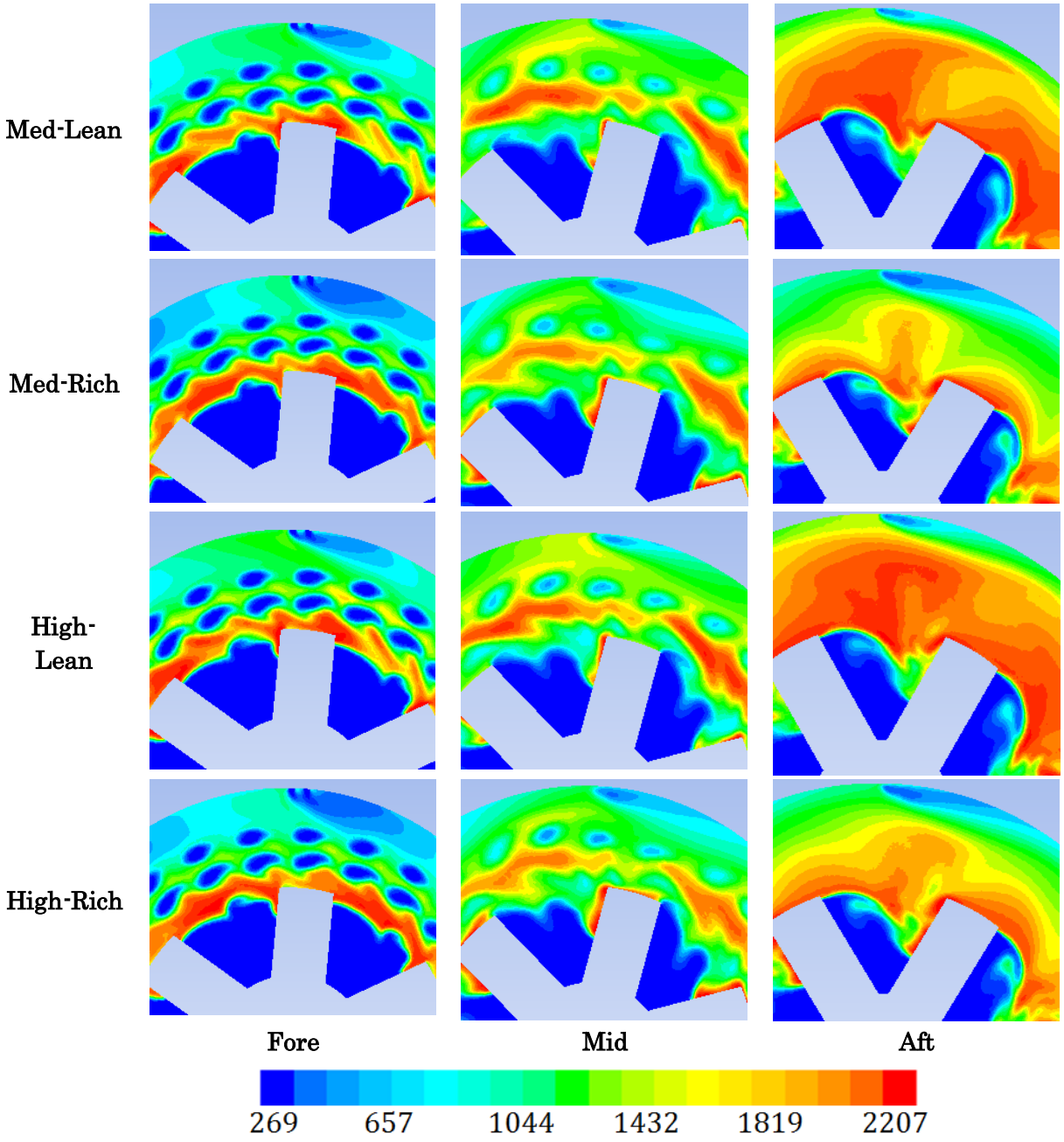

Figure 5.26: Temperature [K] contours at four operating conditions and three axial positions

To better understand the mechanisms driving the cavity temperature distribution, as in Section 4.2.2.2, mass-averaged data were tabulated at the interface between the CC and the core in order to quantify the state of the flow as it transitioned between the two regions. However in this case, as opposed to the Chapter 4 data, one additional level of the mass flow rate was available for regression analysis (while the channel size was constant and was

therefore not considered). Furthermore, other independent variables were included in the data extraction: mass-averaged concentrations (as mass fractions) of C_3H_8, CO_2, and CO, as well as the mass-averaged equivalence ratio at the interface. A model was again generated as shown by Equation (91). While similar caveats to the interpretation of the model apply as outlined in Chapter 4 due to the limited number of independent variable levels, the confidence metrics of the model were still fairly high (p-value < 0.02 for both factors) even with the inclusion of a third level to $\dot{m}_{in}$. Therefore, the mass-averaged temperature at the interface was again demonstrated to be positively affected by both $\dot{m}_{in}$ and ϕ_{cav}. Furthermore, as demonstrated by the model from Section 4.2.2.2, the influence of mass flow is much greater (an order of magnitude) than equivalence ratio. Models for the other quantities were similarly examined although they will only be summarized here: the average ϕ at the interface was positively influenced by both $\dot{m}_{in}$ and ϕ_{cav} in nearly equal proportions (i.e. – increasing either factor contributed to an increase in the local ϕ at the interface). The mass fractions of both C_3H_8 and CO_2 were positively influenced by both $\dot{m}_{in}$ and ϕ_{cav} as well. However, CO was a positive factor of ϕ_{cav} but a negative factor of $\dot{m}_{in}$. Increasing fuel flow led to increasing CO as expected, but increasing mass flow led to decreasing CO. Notably, the residence time analysis indicated that increased mass flow also led to decreased cavity residence time. However, the average temperatures were also observed to increase. As CO was an intermediate species in the combustion model utilized for this section, decreasing CO in conjunction with increasing temperatures implied more complete combustion. Therefore, it appeared that – in spite of a predicted decrease in residence time – the combustion process was enhanced by the increased mass flow. That was likely due to increased turbulent mixing and corrugation of the flame fronts, which would logically provide the propensity for more efficient combustion more quickly.

Table 5.4. Mass-averaged field calculations at the CC/core interface for Ch. 5

$\dot{m}_{in}$	ϕ_{cav}	$\bar{T}_{int}$	c3h8	co2	co	$\bar{\phi}_{int}$
0.06	0.80	1224	0.0094	0.0692	0.0069	0.1978
0.06	1.37	1313	0.0271	0.0783	0.0091	0.6026
0.11	0.80	1328	0.0085	0.0795	0.0063	0.1803
0.11	1.37	1435	0.0322	0.0916	0.0083	0.7315
0.15	0.80	1353	0.0098	0.0816	0.0063	0.2086
0.15	1.37	1459	0.0328	0.0933	0.0085	0.7317

$$\bar{T}_{int} = 996 + 1550\dot{m}_{in} + 178\phi_{cav} \tag{91}$$

Circumferentially-averaged profiles were utilized to provide further quantitative characterization of the cavity dynamics. In Figure 5.27, radial profiles of temperature are given with a number of variations. In the top-left image the radial trends are plotted at each of the four reference operating conditions at axial location C2 (mid). The profile shapes at all conditions were similar, and indeed all four lines nearly collapsed onto each other below $h/h_0 = 0.5$. However, the temperatures in both lean cases still exceeded the rich cases at almost every point; the effect was more pronounced above $h/h_0 = 0.5$. There were negligible differences at conditions of equal ϕ_{cav} but different mass flow. In the top-right image, a range of ϕ_{cav} results are shown at axial location C2 (mid). The trend demonstrated a consistent decrease in overall temperatures with increasing ϕ_{cav} almost exclusively in the outer portion of the cavity. One mechanism identified to explain the temperature trends in the outer diameter was the presence of the outer layer of diffusing fuel. As the fuel flow rate increases, the radial thickness of the cold (300 K) fuel layer increases as well. The surface area at which the fuel and the air interact is not altered, rather it is shifted inward. Thus, any newly-introduced fuel interacts only with the fuel layer until it has had time to circulate and migrate radially inward. This trend was observed as well in the temperature contours of Figure 5.26. Thus, the introduction of stronger cold fuel streams tends to cool the outer volume and, as observed in images Aft2 and Aft4 of Figure 5.26, it tends to force the regions of peak heat release and peak reaction rates

inward into the HGV passages. While some reactions in the HGV are expected, qualitative observations during UCC testing indicated that HGV reactions became excessive to the point of visible flame extending beyond the HGV exit plane. Therefore, controlling ϕ_{cav} by increasing the fuel flow rate may not be an optimal design philosophy if it serves only to force more reactions out of the cavity. Alternatively, controlling the cavity air inlet mass flow rate, $\dot{m}_{cav} = 1 - CFF$, could yield better distribution of the reactions within the cavity itself without requiring excess volume around the outer diameter for the diffusion of the outer fuel layer.

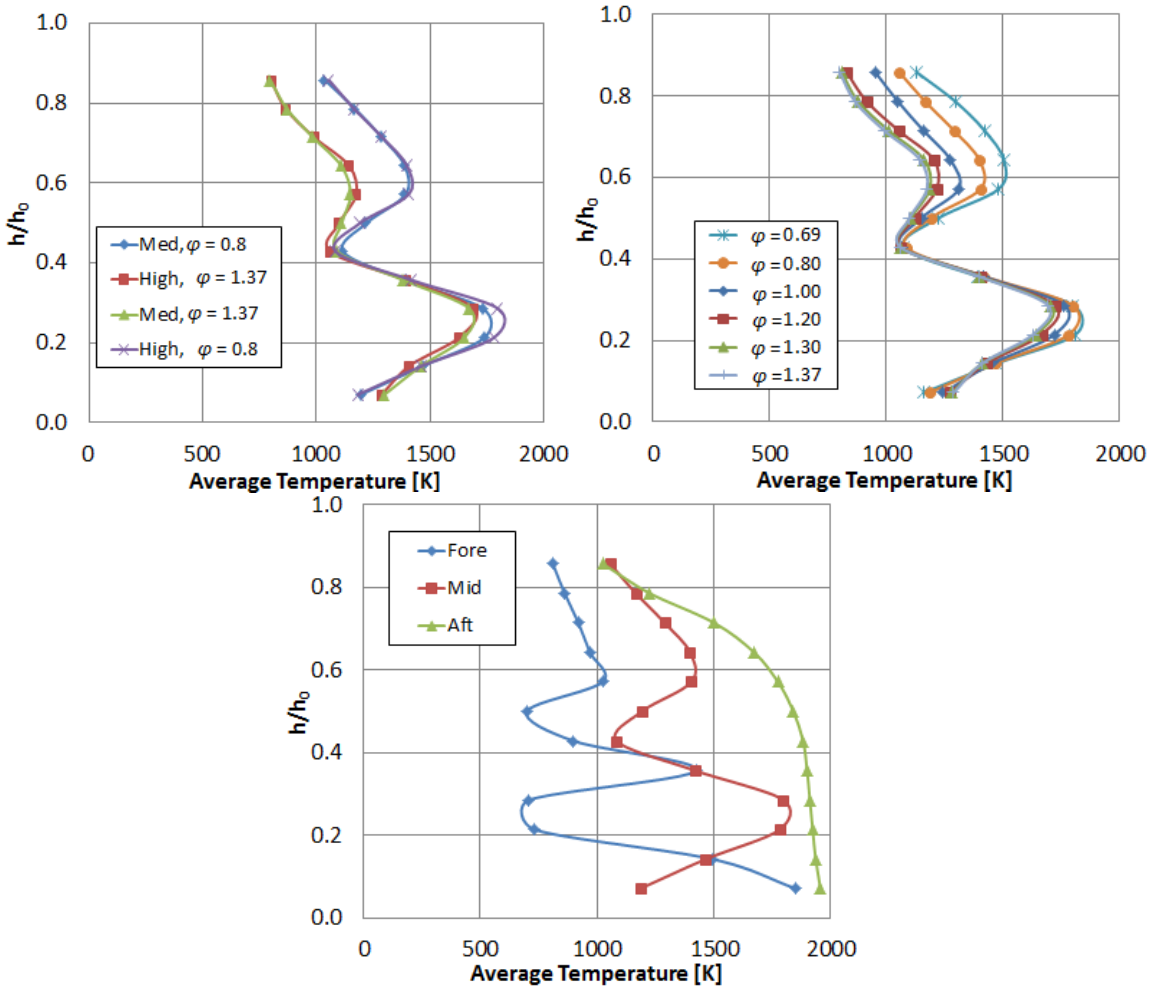

Figure 5.27: Radial profiles of circumferentially-averaged temperatures in the cavity

In the bottom image profiles are shown at axial locations C1, C2, and C3 at an operating condition of $\dot{m}_{in} = 0.12$ kg/s and $\phi_{cav} = 1.37$. The quantitative profiles corroborated the

qualitative observations from the contour plots. The local temperature minima corresponding to the air driver jets persisted from the forward to the center position and were absent at the aft position. Notably, the temperature at the inner diameter of the forward profile increased substantially until it nearly reached the level of the aft profile. This was attributed to hot regions stabilizing at the corner formed by the HGV top surface and the air driver plate.

5.5. Impact of Air Driver and HGV Geometry Changes

In Chapter 6 a detailed examination of the influence of four major design alternatives will be presented. However, an explanation of the details of those changes as they affect the circumferential cavity (CC) will be given as a component of the current discussion. The goal of the examination was added understanding of the parameters that influenced cavity reactions and g-loading. The specifics of each tested design were addressed in Section 3.3. To discuss the results, the nomenclature adopted for each of the four geometry cases was as follows: (1) the smooth-surface low-loss centerbody case was dubbed "LLB," (2) the case that implemented the new radial-vane cavity was dubbed "RVC," (3) the case that implemented the compound-angle cavity air drivers was "CPD," and (4) the case that implemented the combination of the radial-vane cavity and the compound-angle drivers was "CMB."

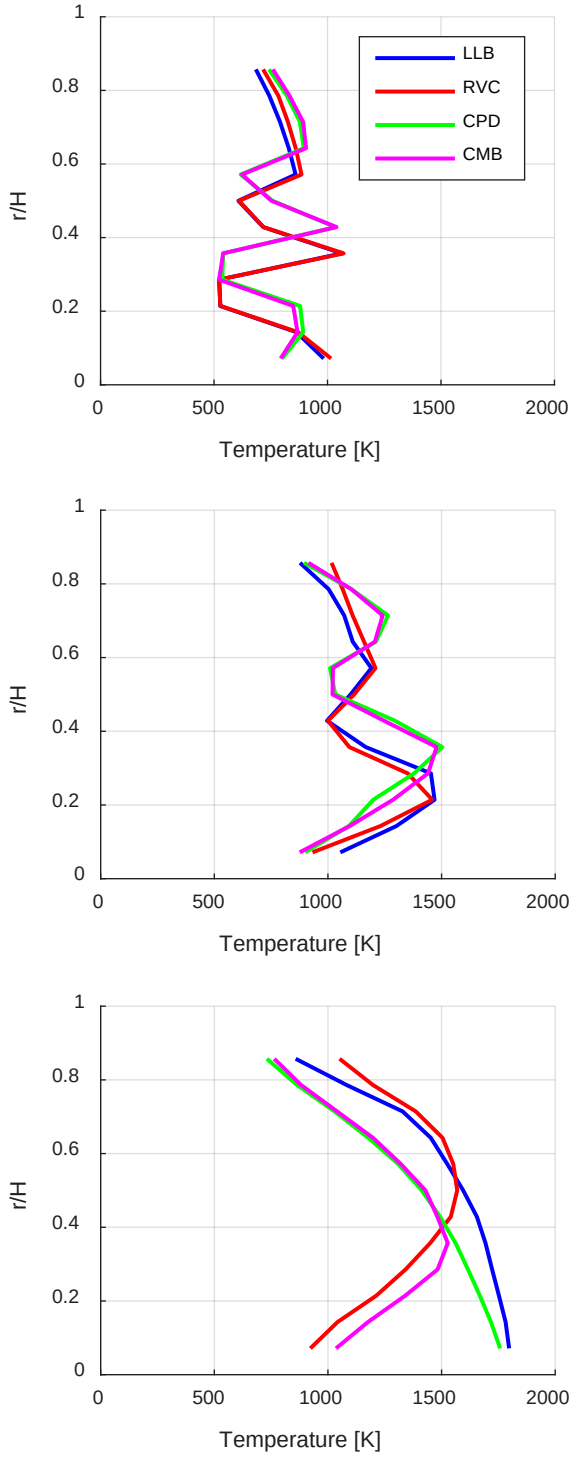

Figure 5.28: Circumferentially-averaged CC temperature at locations C1, C2, and C3, lean

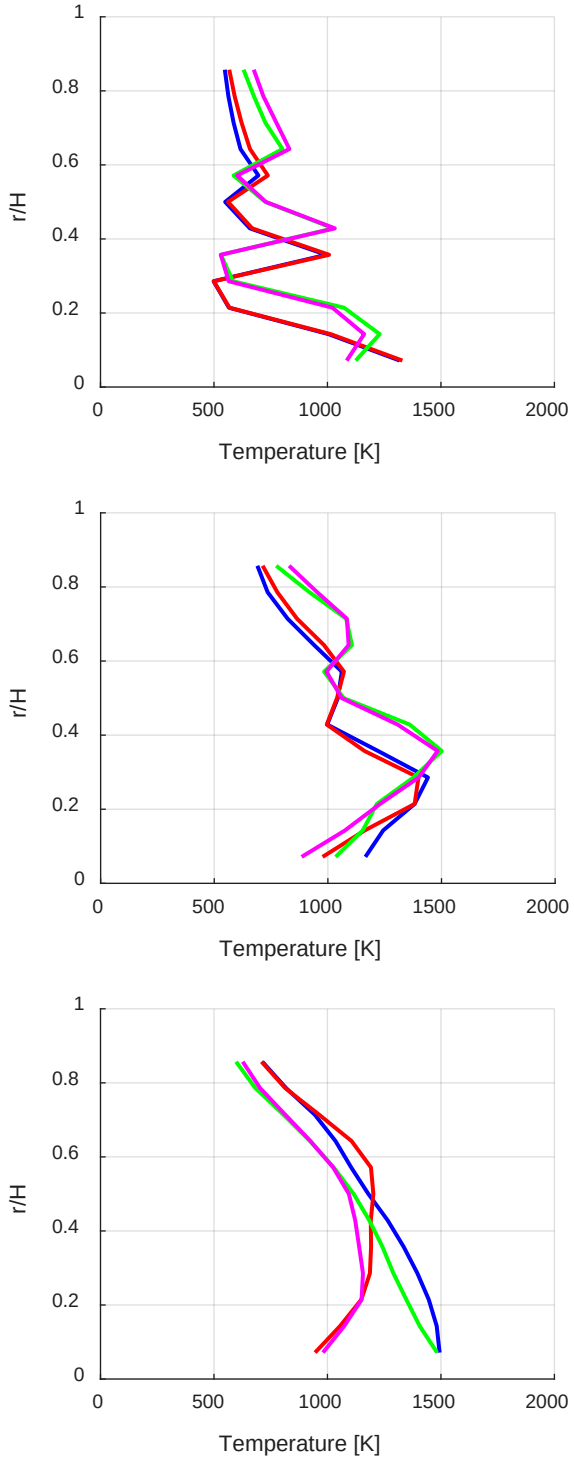

Figure 5.29: Circumferentially-averaged CC temperature at locations C1, C2, and C3, rich

To assess the impact of the geometry changes on the cavity in detail, computational circumferentially-averaged radial profiles were again employed as presented previously in

Section 5.4.2. The radial profiles were computed at the three cavity axial locations C1, C2, and C3. In Figure 5.28 temperature data are presented for the lean condition, while the rich condition temperatures are given in Figure 5.29. At the front of the cavity, and somewhat at the center, the air driver cores were manifested as local temperature minima. The CPD and CMB cases both demonstrated the immediate effects of the air driver angle change as radially-outboard shifts in those minima; the effect of the RVC geometry on the temperature profiles at those same locations was negligible. Conversely, at location C3, the influence of the air drivers was completely absent. Instead, the RVC geometry had the notable effect of sharply diminishing the temperature at the inner diameter of the cavity whereas the temperature profile increased continuously in the LLB and CPD cases. Thus, the earlier hypothesis regarding the premature quenching of the hot cavity products by way of the RVC entrainment mechanisms was reinforced. In both lean and rich conditions, the RVC creates much stronger mixing between the hot gas and the cold core due to the vortex shed from the front-facing step as will be discussed further in Section 6.1.1. The effects of the compound drivers were less dramatic at position C3 but still observable. Both the CPD and the CMB profiles were generally cooler than their LLB and RVC case counterparts. This was a result of the improved mixing within the CC between the reacting fluid and the incoming cold air and fuel.

Finally, a similar method was employed to examine the effects on the cavity velocity distribution by way of the g-load parameter. Figure 5.30 and Figure 5.31 present that data in a format similar to the prior discussion. However, the effects of ϕ_{cav} upon the cavity g-load were generally negligible, so the profiles in the two figures were fairly similar. The differences among the geometries were also somewhat similar at locations C1 and C2; the compound driver cases appeared to increase the velocity at the outer diameter slightly. At position C3, however, the differences again become more pronounced. As will be discussed in Section 6.1.1, one major effect of the radial vane cavity design was to resist the tangential acceleration of the flow as it migrated into the turning, contracting HGV passage. The velocity vector results in Figure 6.5

demonstrated that the tangential components that were present in the LLB case were shifted into the axial direction in the RVC case by the tapering of the RVC inner wall. That effect was notable in the bottom images of Figure 5.30 and Figure 5.31. While the LLB and CPD g-load profiles were seen to transition from a linear increase to an exponential increase, those of the RVC and CMB cases continued the linear increase as in the CC outer diameter. The net effect of that reduction in g-load was uncertain as it was confounded with a multitude of additional effects within the RVC geometry. Furthermore, the g-load as defined in this study was based only on the tangential velocity and it did not account for the loading that might have been imposed by strong vorticity as induced by the RVC. Deconflicting these numerous effects is an important area for future work in order to better understand the influence of g-load on the combustion process. The takeaways from the cavity analyses were therefore that, at the interface between the CC and the core, addition of a radial vane cavity causes migration to occur (1) at slightly lower average velocity and (2) as substantially lower temperatures.

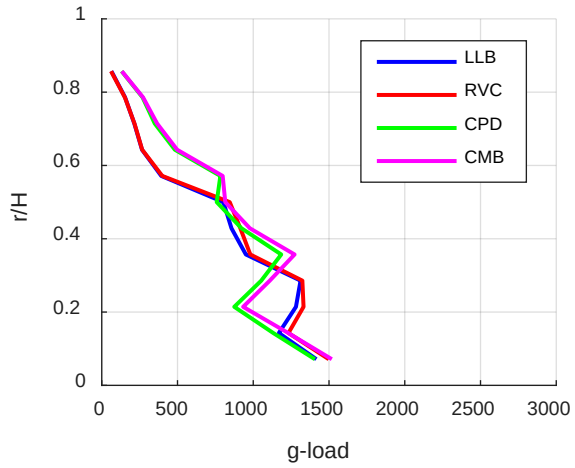

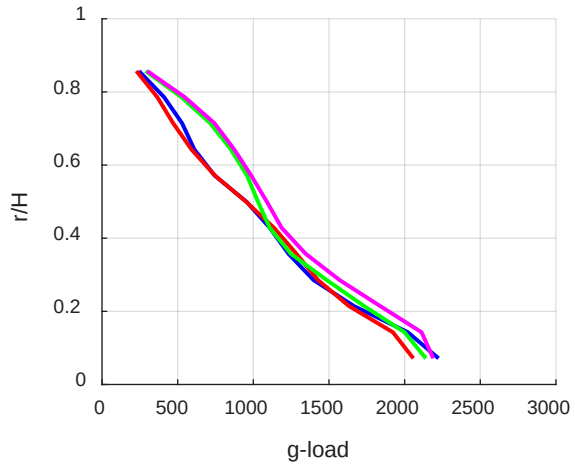

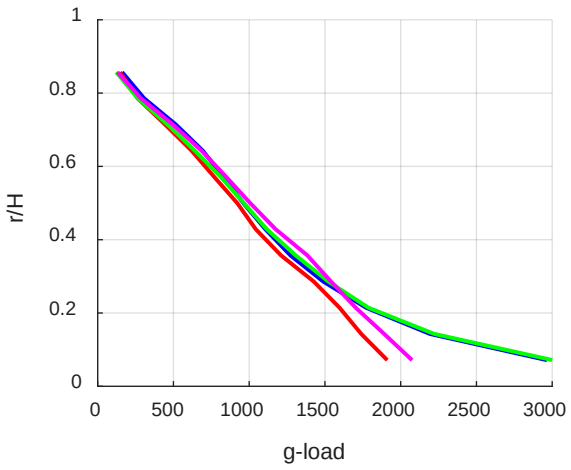

Figure 5.30: Circumferentially-averaged CC g-load at locations C1, C2, and C3, lean

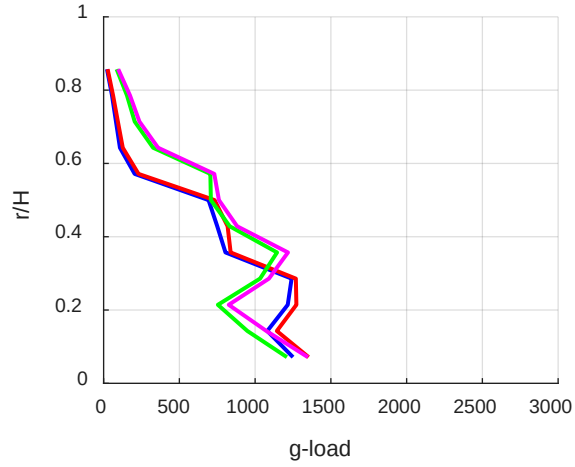

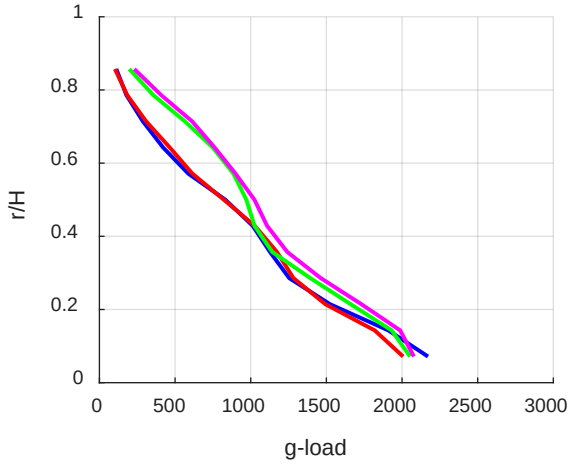

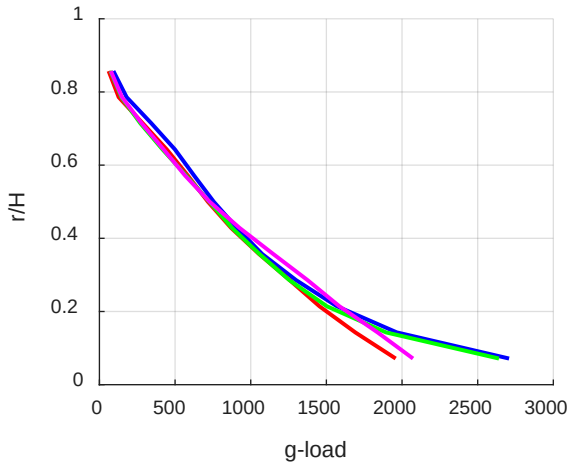

Figure 5.31: Circumferentially-averaged CC g-load at locations C1, C2, and C3, rich

5.6. Chapter Summary

This chapter presented results and discussion related to the resolution of Objective 2: to determine the effects of the complex flow environment on flame dynamics within the high-g combustion cavity. The goals of the objective involved the measurement and analysis of velocity, equivalence ratio, and temperature within the cavity to facilitate understanding of the cavity g-load, residence time, fuel/air mixing, and heat release characteristics. Initially, results were presented that summarized the effects of transitioning from the "v2" to the "v3" geometry. The unique design of the "v3" cavity subsequently permitted the use of a variety of advanced optical diagnostic tools to collect data on cavity velocity, equivalence ratio, and temperature, while CFD continued to play a complementary role in explaining and elaborating on the experimental observations.

5.6.1. Comparing v2 and v3 Geometries

The biggest observed effect of the transition from the v2 to the v3 hardware was the uniformity of the flow field. The hypothesis of Chapter 4 was that the cavity field was highly dependent on the distribution of the cavity air drivers, and the evidence in this chapter corroborated that theory. Uniformly-distributed air drivers led to comparatively uniformly-distributed cavity fields, and more importantly, to an increase in peak estimated fuel stream residence time from 5.6 ms to 11 ms.

5.6.2. Velocity

Velocity data were collected by way of the PIV and PSEV techniques. Due to operating constraints, the breadth of PIV data was far less than desired with only three operating conditions characterized. However, the agreement between those three measurements and the CFD was good – deviations between the two did not exceed 10%. The PSEV data were limited to somewhat qualitative analyses due to the inherent inability to resolve the z-components.

However, it was observed that there was a dependence of the velocity on both the cavity air mass flow rate and the fuel injection rate. As expected, increasing inlet flow rate led to increased velocity; however, some data indicated that velocity also tended to decrease in response to increased fuel injection.

The CFD model was used to extend the analysis by analyzing the tangential velocity gradients within the cavity. The residence time analysis of Chapter 4 was repeated with the new geometry. It was found that residence times were lower at higher flow rates. The high flow rates caused an expected increase in the tangential velocity, but the observed residence length did not increase proportionally; instead the bulk of the fuel streams traversed similar residence lengths at higher velocities. Observed residences times were also higher in fuel-rich conditions; this was postulated to result from the tendency of the fuel flow to reduce the velocity of the cavity tangential motion.

The analysis of cavity tangential velocity transitioned to computation of g-load profiles. The primary observation was that many of the UCC operating conditions were insufficient to attain the theoretical lower limit at which the g-effect could be observed: $g = 350g_o$. Furthermore, significant gradients were observed in both radial and axial directions. As the cavity flow migrated into the guide vane passages, the combination of acceleration and reduction of radial coordinate led to dramatic increases in g-load, especially at the aft of the cavity. Within the vane passage, then, the issue becomes too much loading rather than too little, as exceeding the limit of $g \approx 3{,}500g_0$ was hypothesized by Lewis [53] to result in a "bluff-body blowout" scenario.

5.6.3. Equivalence Ratio

The cavity equivalence ratio was analyzed to aid understanding of the fuel/air mixing and the primary reaction locations. The LIBS technique was employed to obtain the requisite experimental measurements. The results were complex trends that eluded consistent

characterization. Furthermore, the comparison against the CFD was largely unsatisfactory. However, examination of the CFD data revealed the presence of substantial gradients in all three directions. Examination of the time-resolved LIBS data subsequently revealed the presence of relatively dramatic temporal unsteadiness that was not reflected by the initial time-averaged results. The reality was therefore postulated to involve a combination of the strong spatial gradients predicted by the steady-state CFD solutions and the transient effects demonstrated by the experimental measurements.

5.6.4. Temperature

Arguably the most crucial piece of the objective was an appreciation for the behavior of the cavity temperatures in response to operating conditions. An optical diagnostic approach was again employed to collect experimental data to compare against the model. The TFP technique was utilized to obtain high-fidelity temperature profiles within the cavity. Similar to the LIBS, the trends in the experimental data were difficult to interpret; furthermore, their agreement with the CFD was lacking. Notably, the TFP consistently demonstrated a distinct high-temperature region in the front-outer portion of the cavity that was nowhere shown by the CFD. However, again, close examination of the CFD revealed strong spatial gradients. The time-resolved TFP data were also examined. They revealed fairly wide variation and one particular case that demonstrated potential outlier issues. Computing statistics from the data produced a trend indicating that variability decreased with increasing temperature; that result was promising in one aspect as it proved that the current UCC design could attain stable operation with improvements to operating pressure capabilities. Alternatively, that result could indicate that it is variability in the TFP measurement itself, rather than the UCC, which is a function of temperature. In future work, the variance of the TFP signal at its lower limits will need to be validated with alternate collection techniques.

Importantly, the results of the section as a whole also produced two firm recommendations were made for future work: (1) a transient CFD model must be developed to validate the unsteady UCC effects, and (2) the presence of the high-temperature regions identified by the front filaments must be verified. The latter task could be a simple matter, as cameras could be repositioned to afford the required views.

5.6.5. Geometry Changes

Finally, the response of the cavity to some fundamental geometry changes was shown. The impact of the installation of a new compound-angle air driver was shown to be minimal. Aside from the observed increase in the radial height of the cold cores of the air jets, no other significant differences were noted. However, significant deviations were observed as an effect of the installation of a new radial vane cavity (RVC). The RVC effectively opened up a new volume to accept the migrating cavity flow. At the aft of the circumferential cavity, a marked decrease in temperature occurred at the location of its interface with the radial cavity.

VI. Hot Gas Migration

This chapter addresses the goal of Objective Three: to investigate the parameters that influence and promote hot gas migration into the core flow to enable control over the exit temperature distribution. For the entirety of UCC development, the fundamental vision has comprised some outer-diameter cavity encircling a form of airfoil or guide-vane geometry. While the research at AFRL focused on straight guide vanes (Section 2.4.6.2), the inception of the current AFIT design began with the concept of a curved vane that would serve the purposes of both a compressor exit guide vane and a turbine inlet guide vane (Section 2.5.3). That component was therefore dubbed the hybrid guide vane (HGV) and it became central to all AFIT testing from that point to the present.

Fundamentally, exit temperature profiles have been the metric of choice to describe gas turbine combustor trade spaces as was discussed in Section 2.1.2.4. Thus, measurements of the HGV exit temperature for the AFIT rig were documented on the UCC v1 geometry by Damele *et al.* [94] with the results as reproduced by Figure 2.67 and Figure 2.68; the conclusion was that the UCC operated with high temperature regions strongly biased toward the outer diameter. The motivation for Objective Three of this research was to investigate the causes for that bias and to explore potential design changes to effect a more optimal distribution; however in this case the UCC v3 geometry would be tested. To summarize the associated discussion in Chapter 3, the fundamental differences in those geometries was the incorporation of the diffuser (UCC v2), and the incorporation of uniform air drivers combined with an increased cavity outer diameter (UCC v3). Thus, while the HGV geometry has remained consistent, many other changes have already been made that have influenced the UCC performance as discussed in Chapters 4 and 5. The core of this Chapter is therefore to demonstrate and overall

improvement over the conditions observed by Damele while also examining the traits of the UCC v3 configuration that lead to optimal system and exit conditions.

As demonstrated by Damele, examination of the behavior within the HGV was inherently difficult due to the complexity of the geometry. Thus, for the current research, it was necessary to expand the available toolset in order to rigorously evaluate the impact of UCC design and operational characteristics upon the flow through the HGV. Experimental data at the HGV exit plane was collected as one important indicator of the performance of the HGV as a whole, while substantial analysis into the behavior of the flow between the cavity/core interface and the exit plane was performed using the computational fluid dynamics (CFD) model developed as part of this research program. Much of the experimental data collected for this chapter was obtained in a collaborative effort with Gilbert [100]. Per Gilbert's test design and execution, the dependent variables were operating conditions ($\dot{m}_{in}, \phi_{cav}$) and geometric configurations. Two variations involving the cavity air delivery and the HGV surface respectively were explored; the details of those variations were discussed in Sections 3.3.2 and 3.3.3. Each variation was tested independently as were the baseline configuration and the case of both variations combined. The effects of those variations on the UCC system as a whole are presented and discussed in 6.1 with the ultimate goal of identifying which parameters had the greatest influence on the dynamics and composition of the migrating flow. As the distribution of the temperature at the exit plane is of special interest to this research and to gas turbine engine combustion in general, it is presented as the focus of Section 6.1.3. Finally, Section 6.2 expands the trade space established by Section 6.1 in order to select a geometry that yields optimum flow migration and exit temperature distribution within the HGV.

6.1. System Response to Geometry Changes

In this section, the baseline geometry was considered to be the UCC v3 configuration as introduced in Section 3.1.1.2 and evaluated in Chapter 5. Four geometry cases were defined

from that baseline as detailed in Sections 3.3.2 and 3.3.3, and they were evaluated at the system level from the circumferential cavity (CC) to the exit of the hybrid guide vanes (HGVs). The primary goal was to evaluate the distribution of temperature as the flow migrated through the HGV passages up to the HGV exit plane. At the exit plane, both experimental and computational data were available; the distribution of temperature and other field variables throughout the remainder of the UCC were examined computationally.

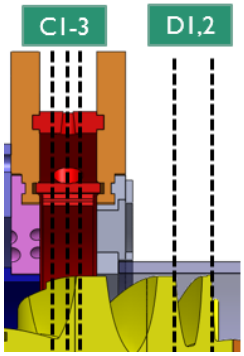

Figure 6.1: Section 6.2 CFD axial reference locations

The nomenclature adopted for each of the four geometry cases was as follows: (1) the baseline smooth-surface low-loss centerbody case (using the same HGV hardware as Wilson [91]) was dubbed "LLB," (2) the case that implemented the new radial-vane cavity was dubbed "RVC," (3) the case that implemented the compound-angle cavity air drivers was "CPD," and (4) the case that implemented the combination of the radial-vane cavity and the compound-angle drivers was "CMB." As the incorporation of the RVC was predicted to have the greatest impact, Section 6.1.1 presents system-level computational comparisons between the LLB and the RVC cases. Section 6.1.2 then introduces similar results from the CPD and CMB cases. Finally, Section 6.1.3 presents detailed computational and experimental results from the HGV exit plane. As in previous discussions, common reference locations will be utilized as illustrated in Figure 6.1. The first three of those were defined as fore, center, and aft locations within the circumferential cavity (CC). The fourth point (D1) occurred midway between the cavity aft wall

and the exit plane, while the fifth point (D2) was placed at the HGV exit plane, immediately upstream of the HGV trailing edges.

6.1.1. Effects of the Radial Vane Cavity

The UCC v3 radial vane cavity (RVC) was the first subject of investigation for its influence upon the flow patterns induced. The hypothesis was that the shape of the cavity as illustrated in Section 3.3.3 would work to transport more of the hot products from the circumferential cavity (CC) further inward toward the HGV centerbody inner diameter. This would resolve the outward biases observed previously by Damele [94] as shown in Figure 6.2. In those results, Damele took experimental thermocouple measurements that demonstrated peak temperatures at the outer diameter followed by a fairly steady decrease toward the inner diameter.

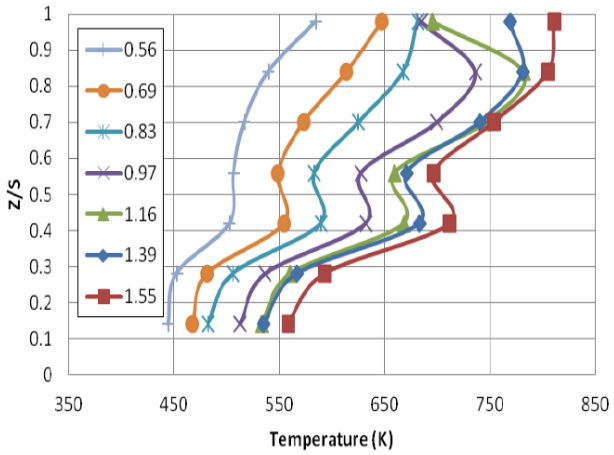

Figure 6.2: Thermocouple temperature profiles at various levels of ϕ_{cav} from Damele at $\dot{m}_{in}$ = 0.108 kg/s

In Figure 6.3, steady-state CFD solutions are shown through axial cross-sections at each of the five axial reference locations identified in Figure 6.1. The contours are colored by temperature and they represent flow conditions at one level of $\dot{m}_{in} = 0.150$ kg/s and two levels of $\phi_{cav} = \{0.80, 1.37\}$ for each of the LLB and RVC geometry cases. As the view is forward looking aft, the bulk circulation in the CC is clockwise.

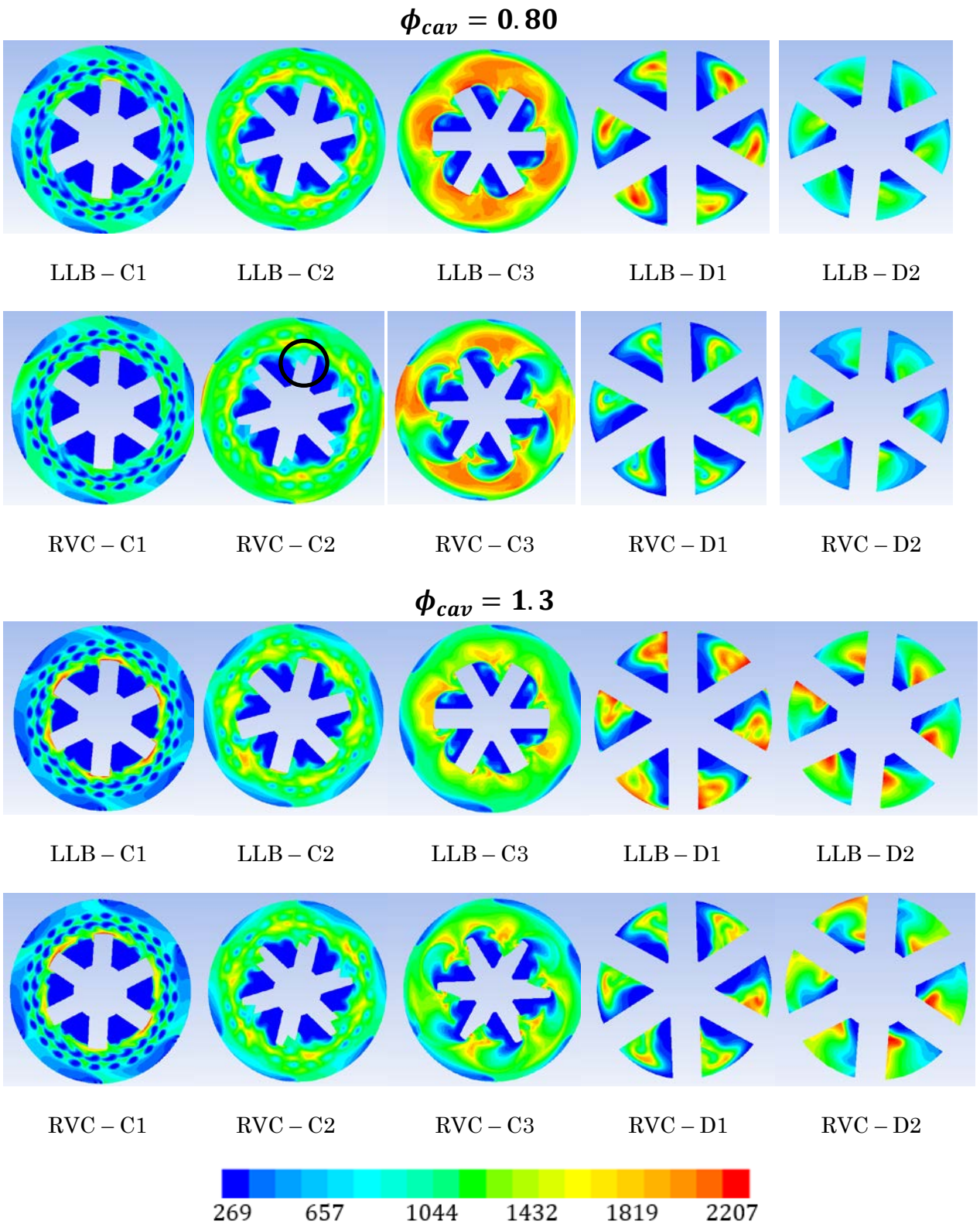

Figure 6.3: CFD axial cross-sections colored by temperature at varying axial locations; constant $\dot{m}_{in} = 0.150$

Each column of Figure 6.3 represents one of the five axial reference locations. At location C1, the cold cores of the cavity air drivers were clearly visible, as shown similarly in section 5.2.3, while at all three cavity locations the fuel injectors were marked by cold plumes hugging the outer diameter. In both geometries, a high-temperature band stabilized beneath the level of the air drivers at location C2. In the RVC case, the beginning of the RVC cutout was also visible at location C2 as highlighted by the black circle on image RVC-C2. It was observed that the initial cutout provided more volume to accept the intermediate gas products from the CC; this was in contrast to the LLB case where migrating gasses met only a smooth wall that permitted the formation of only a thin migration layer along the wall surface.

By location C3, the cavity flow was dominated by regions of peak heat release as the influence from the cavity air drivers diminished entirely. Again in the LLB case the migrating gasses continued to cling tightly to the HGV suction-side wall. Conversely, the RVC contour demonstrated more dynamic motion of the hot products as they entered the core air flow in the form of apparent helical motion into and then away from the radial cavity. This apparent motion was also present at location D1 where the concentrated hot spot visible in the LLB case was instead disbursed and relatively cooler. However, the hot flow did not appear to occupy a greater portion of the HGV passage in the RVC case compared to the LLB geometry as it neither approached the pressure-side wall nor did it spread fully to the inner diameter. The same conclusion was drawn at location D2: while the apparent circulation induced by the RVC appeared to disburse and cool the hotter regions of the migrating gasses, the overall effect was not substantially changed from the LLB case. Notably, the CFD results indicated that the regions of peak temperature were not biased exclusively to the outer diameter as demonstrated by Damele; rather, by the exit plane D2, they occupied areas that varied from 20% to 100% of the passage radial height. Furthermore, the CFD solutions were not consistently symmetric between the six HGV passages. For example, in the bottom-right image, RVC-D2, the hot regions were primarily focused along the inner suction-side, however in some cases they were

partially dispersed outward and even spread circumferentially around the outer diameter. Similar non-uniformity was observed to lesser extents in nearly every other image in the figure. As expected, and as already highlighted in the Chapter 5 discussion, the steady CFD model was not an ideal solution to the notoriously unsteady UCC problem. However, the results permit an examination of the interior flow field in response to geometry and operating conditions, which has heretofore been unavailable.

Notable changes were observed when comparing the lean- versus the rich-cavity cases: primarily, the cavity temperatures in both geometries were somewhat cooler, while the passage temperatures were conversely hotter. This was a result of additional reactions taking place within the vane passage as will be illustrated further later in this section. Additionally, asymmetric patterns were more prevalent in the rich passages, particularly in the hot regions. The general distinction between the LLB and RVC cases persisted, however: the hot gases, rather than transitioning smoothly, were instead subject to increased circulation and helical motion within the HGV passages that resulted in relatively cooler regions in the RVC geometry.

Stream traces were computed and utilized to illustrate the complex dynamics of the flow induced by the two geometries. The desire was to identify where each point of the exit temperature profile originated and how it traveled through the vane. Thus, 'reversed' stream traces were generated from a one-dimensional radial profile centered in the HGV exit plane for the LLB and the RVC configurations as shown in Figure 6.4. The view in Figure 6.4 is from the aft quarter looking forward. Visible geometry features include the outer and forward cavity walls, one HGV airfoil, the HGV inner diameter, the exit exhaust cone, and the diffuser inner and middle diameter components. Two of the fuel injection baffle locations are visible as well. The stream traces are colored by temperature with the same contour levels as shown in Figure 6.3.

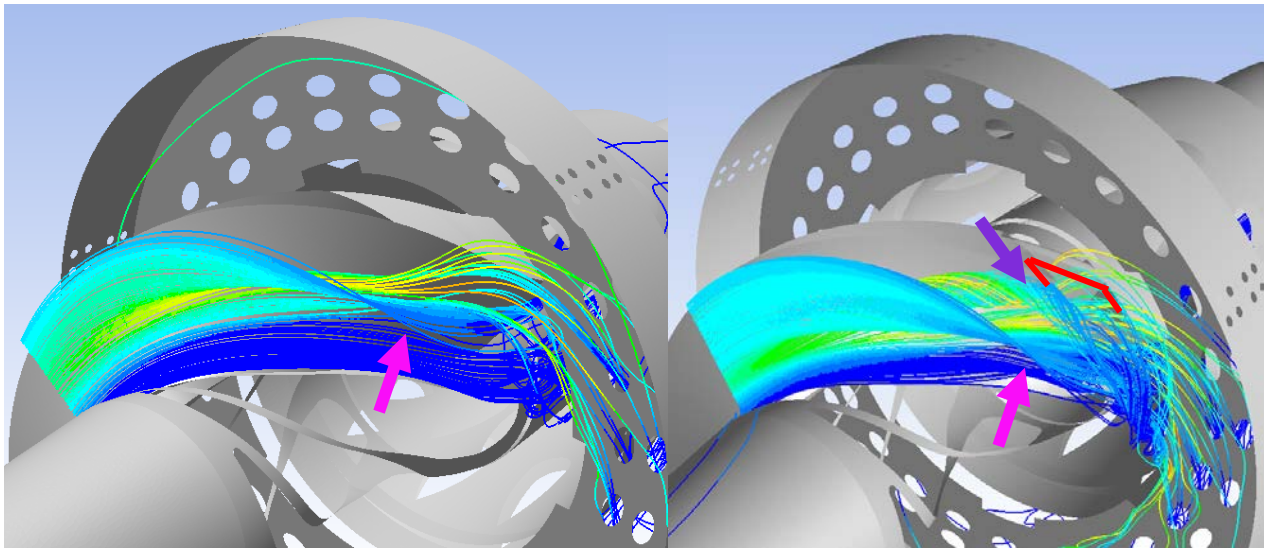

Figure 6.4: "Reversed" stream traces originating at the exit plane for case LLB (left) and RVC (right)

The upstream sources of the stream traces could be delineated by their initial temperatures: all cold (blue) traces originated from the inner core flow, while all traces at any warmer temperature originated from the cavity. In both cases, the hot temperatures originating from the cavity were forced to interact with both the HGV surface and the comparatively fast core flow; the nature of those interactions governed the path of each trace. In the LLB case, as mentioned previously, the migrating gasses met the smooth HGV surface and remained attached relatively closely through the duration of the passage.

In both cases, the cold core air mixed with the migrating flow through two primary mechanisms. First, the pink arrow indicates the point at which a sheet of traces folded up toward the passage outer diameter, rotating around the hot migrating gases and traversing the passage from pressure-side to suction side. Second, a layer of cold core air remained unmixed at the inner diameter. The temperature of that inner layer was shown to increase slowly in both images of Figure 6.4 although the high temperatures never expanded fully to the inner diameter. The radial vane cavity (RVC) is visible in the right image of the figure on the top surface of the displayed HGV airfoil; its radially-outboard edges are highlighted in red. Its

primary effect was the division of the hot migrating gasses into two disparate flows. One set of streams passed into the RVC and was subsequently guided by that geometry, while the other set of streams impacted the smooth portion of the HGV suction-side surface. The flow being guided by the RVC was tapered back into the primary core, thereby inducing motion away from the HGV surface. The tapered flow interacted with the direct-impact flow in such a way that a secondary vortex was generated within roughly the outer 25% of the vane passage volume; that vortex is indicated in the figure by the purple arrow. In addition to the primary rotation of the core air indicated by the pink arrow, some core air became entrained either into the RVC or into the subsequent secondary vortex and was thus more thoroughly mixed with the hot CC products. Therefore, while the RVC did little to improve the radial dispersion of the migrating flow within the HGV passage, it did enhance the dilution process, thereby reducing the occurrence of excessive hot spots within the flow and at the walls. More discussion regarding the resultant impact on the exit temperature distribution will be provided in Section 6.1.3.

Velocity vector plots provided further insight into the interaction between the cavity and core flows as shown by Figure 6.5. They were generated at axial locations C2 and C3 and at the condition $\phi_{cav} = 0.80$ and were colored by temperature at the same contour levels as used in Figure 6.3. In the baseline LLB images (**a** and **b**), the strongest velocity vectors appeared where the flow impacted the HGV suction-side wall the edge of which is highlighted in red (note that the effect of the vectors extending "into" the wall is simply the product of the cut itself – the wall geometry is not present to block visibility of those vectors from the defined view). Those vectors were indicative of the strong acceleration imposed by the HGV turning in combination with the contraction of the passage; the great majority of the high-velocity vectors were oriented in a direction approximately parallel to the LLB surface. The acceleration effect is more notable in image **b** near the aft cavity wall as the continued vane turning and passage contraction are met with points of peak heat release. In contrast, the same regions in images **c** and **d** depicted vectors with components more axial than tangential due to the taper of the RVC inner wall; the

approximate location of the RVC cutout is again highlighted in red. Furthermore, in the LLB case, a stagnation region appeared near the center of the top surface of the HGV airfoil. Streamlines with radially-inward components induced by neighboring gradients encounter the relatively large top surface and effectively terminate. This region was not present in the RVC geometry due to (1) the narrower width of that top surface due to the RVC cut, (2) the consequent increased rate of capture of the CC streamlines, and (3) the effect of the fillet on the pressure side of the airfoil; the approximate filet edge location is highlighted in pink in the figure. The net effect was less flat surface area upon which radially-inward components could be resisted.

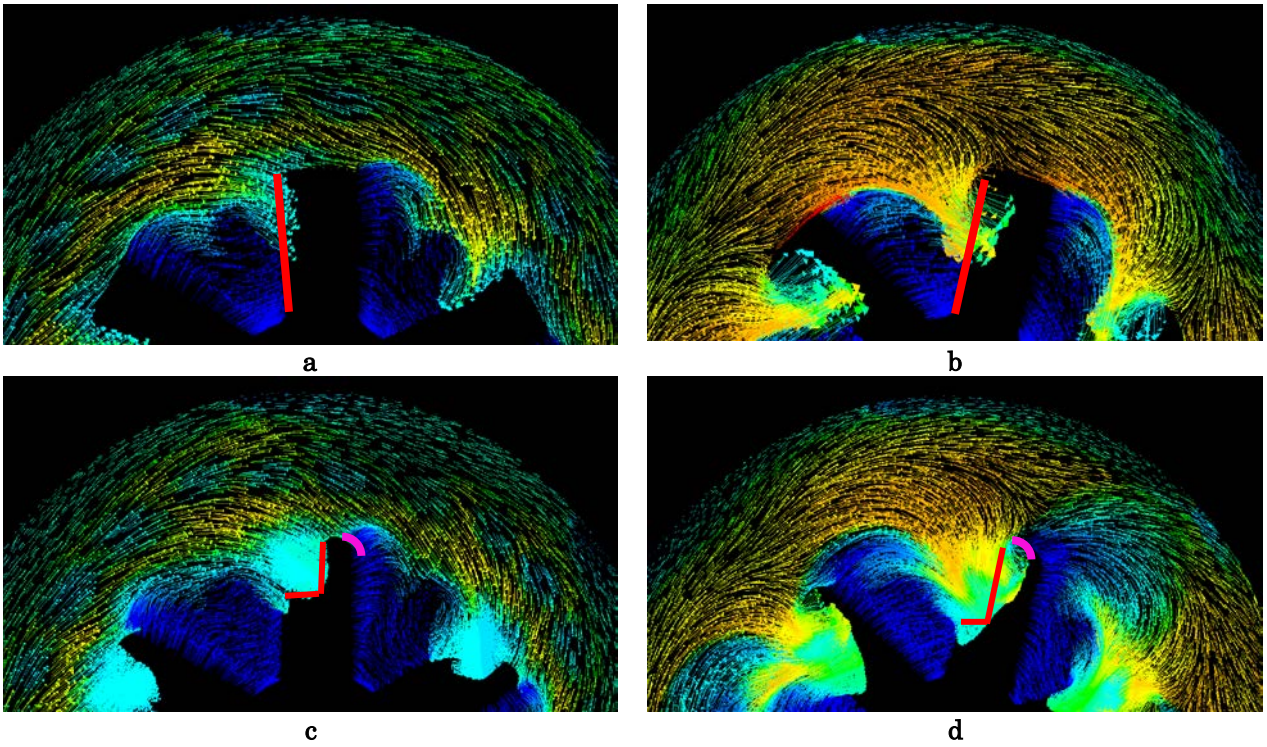

Figure 6.5: CFD velocity vectors colored by temperature at locations C2 (left) and C3, case LLB (top) and RVC

To facilitate a more quantitative analysis using the CFD data, axial planes were generated in increments of 2.54 mm beginning just upstream of the CC and ending at the exit plane. Field variables within those planes were then mass-averaged, thereby allowing the generation of longitudinal profiles along the axial length of the domain where each point in the

profile corresponds to the mass-averaged quantity from a 2-D plane at the given location. Figure 6.6 presents four such profiles of the LLB and RVC geometries at lean ($\phi_{cav} = 0.80$) and rich ($\phi_{cav} = 1.37$) cavity equivalence ratios. The chosen quantities were temperature, product formation rate, mass fraction of unburned hydrocarbons, and mass fraction of carbon monoxide. While the emissions model in this study was relatively coarse, the latter two quantities were useful for comparing relative combustion quality between the configurations. The temperature and the product formation rate were chosen as primary indicators of heat release and combustion activity, respectively. The images each also include two vertical dashed black lines that correspond to the location of the CC front and aft walls. The x-axis is defined by a normalized z-coordinate defined by the absolute value of z and the overall domain length, L. Note as well that the y-axes for the UHC and CO figures are logarithmic.

The differences between the two geometries are subtle in terms of temperature. Both cases were observed to demonstrate nearly identical mass-averaged temperature rise over the axial length of the cavity. Similarly, both cases demonstrated continued nearly-linear temperature rise through the HGV passage to the HGV exit plane at $z/L = 0.7$. At the condition of $\phi_{cav} = 0.8$, the average temperature was slightly greater in the LLB case compared to the RVC case; however the trend was reversed at $\phi_{cav} = 1.37$. Examination of the mass-averaged product formation rates provided greater insight into the mechanisms behind the temperature trends. Theoretically, product formation indicates reaction progression and associated heat release; the more products being formed, the greater the amount of fuel being combusted, and the greater the resulting temperature rise. As shown in image **b** of Figure 6.6, at lean cavity fuel flow, both the LLB and the RVC geometry demonstrated a peak in product formation at the axial midpoint of the cavity. Further downstream, the LLB geometry demonstrated a secondary peak within the HGV passage indicating that reactions were continuing to occur (as expected). However, the trend for the RVC geometry was markedly diminished in comparison. A substantially different pattern was observed in the rich cavity case: while the cavity-midpoint

peaks were still present (at greater magnitudes), the LLB geometry demonstrated two additional peaks within the HGV passages indicating two regions of intermediate/dilution combustion events. Furthermore, in stark contrast to the lean case, the rich case of the RVC geometry demonstrated a single secondary peak in product formation rate that exceeded even the rate of reactions in the circumferential cavity. Those trends explained why the RVC temperatures exceeded those of the LLB geometry at rich conditions versus the converse at lean conditions.

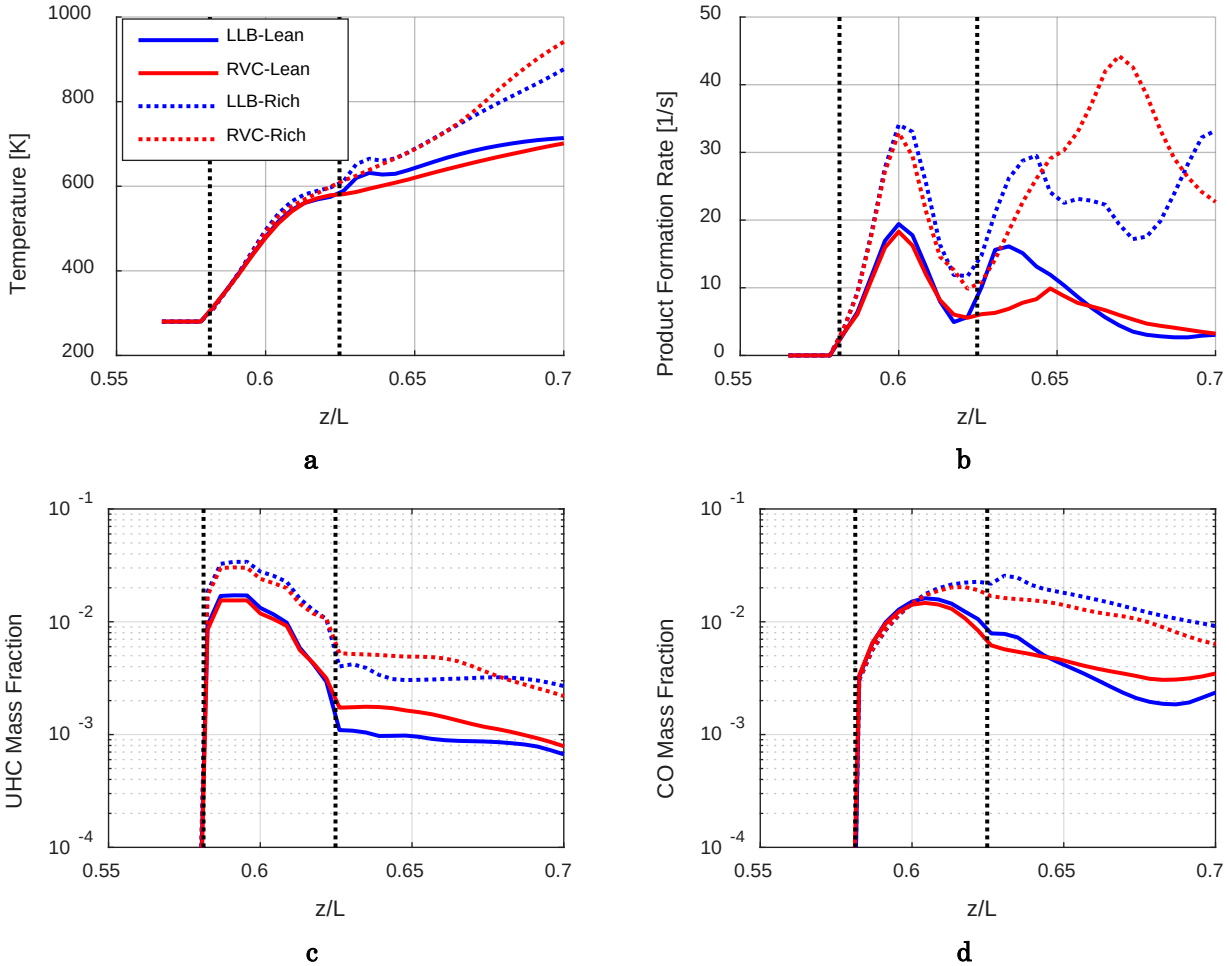

Figure 6.6: Axial mass-weighted average profiles for various quantities at lean and rich cavity equivalence ratios

Trends in pollutant emissions reflected those demonstrated by the temperatures and product formation rates. As anticipated, increasing the setting of ϕ_{cav} led to overall increased

emissions. It was observed that the higher exit temperatures corresponded to lower UHC concentrations, which again met with expectations: increased temperatures resulted from increased efficiency in consuming the injected fuel, which would therefore lead to a reduction in the presence of UHC. Those trends held again upon observation of the CO concentrations.

To put the predicted temperature distribution into context, it is helpful to evaluate the ideal condition represented by the adiabatic flame temperature (AF). Earlier discussion established that the adiabatic flame temperatures for propane-air at levels of $\phi_{cav} = \{0.80, 1.37\}$ were $T_{ad} = \{2025, 2053\}$ K. However, as the analysis of Figure 6.6 involves averaging over the entire UCC versus only the cavity, it is more appropriate to consider the value of $\phi_{ucc} = (1 - CFF)\phi_{cav}$ (see Appendix E). Thus, the adiabatic flame temperature at a given overall value of ϕ_{ucc} represents the peak theoretical temperature attainable by a system in which the given amount of fuel was ideally mixed and combusted with the given amount of air. The calculations presented in Table 6.1 present a comparison between the adiabatic flame temperatures at ϕ_{cav} versus ϕ_{ucc}. This is a theoretical notion only, however, it can be a useful metric with which to evaluate the relative merits of each geometry. An efficiency estimate can be calculated by taking the ratio of the mass-averaged temperature at the exit plane over the theoretical value of AF_{ucc}. In the case of $\phi_{cav} = 0.8$ ($\phi_{ucc} = 0.21$) the exit temperatures for the LLB and RVC case were 711.8 K and 695.5 K, respectively, yielding efficiency estimates of 0.82 and 0.80. In the rich case ($\phi_{ucc} = 0.36$) the efficiency estimates for the LLB and RVC case were 0.71 and 0.76. Thus, while the RVC performed relatively better, the overall efficiency estimates for both configurations were worse at the higher level of fuel flow. It was again acknowledged that operation of the AFIT UCC at more representative pressure ratios would likely lead to a substantial increase in those efficiency estimates.

Table 6.1: Comparing cavity vs. overall equivalence ratios

ϕ_cav	AF_cav	ϕ_ucc	AF_ucc
0.60	1701	0.16	734
0.70	1880	0.18	800
0.75	1964	0.20	845
0.80	2043	0.21	865
0.90	2179	0.23	928
1.00	2267	0.26	990
1.10	2265	0.29	1051
1.20	2201	0.31	1110
1.30	2124	0.34	1169
1.37	2071	0.36	1209

The working hypothesis to explain the differences between the LLB and the RVC cases is founded upon the intermediate reactions that take place in the HGV passages downstream of the cavity. As demonstrated by the stream traces in Figure 6.4, the mixing between the cavity and core flow streams was strongly influenced by the presence of the radial vane cavity. The qualitative assessment was that the secondary vortex increased the intensity of the mixing process, thereby resulting in a quenching effect upon the hot gases migrating from the cavity. In the lean case with $\phi_{cav} = 0.8$, whereas reactions continued in the passage with the smooth vane, the quenching effect of the RVC configuration was sufficient to significantly dampen those secondary reactions. In contrast, when the fuel flow rate was increased, the increased intensity of the reactions was sufficient to overcome the quenching effect and, conversely, the increased mixing had a constructive effect upon the intermediate reactions leading to an overall increase in the combustion efficiency at the exit plane. The reduction in relative efficiency between the lean and rich configurations, however, indicates that the current design of the UCC may not be ideal for cases with higher vs. lower fuel flow.

6.1.2. Effects of the Compound Angle Drivers

The hypothesis motivating the incorporation of the compound-angle air drivers centered on the observation that reactions were not satisfactorily completed within the CC even at lean operating conditions. The layer of unburnt fuel that developed about the outer diameter was demonstrated to be fairly substantial in Figure 5.14 and it was consequently surmised that the injection angle of the cavity air drivers was not sufficient to mix that outer fuel layer and promote more uniform combustion. Thus, as discussed in Section 3.3.2, the air drivers were modified to incorporate a 10° radially-outboard angle in addition to the 55° angle relative to the engine centerline. The theory was that injecting the air up into this region would start reactions sooner and ensure combustion within the complete CC volume to the maximum extent possible. As in Chapter 5, stream traces were utilized as an initial qualitative assessment of the flow field response as shown in Figure 6.7 at flow conditions $\dot{m}_{in} = 0.150$ kg/s and $\phi_{cav} = 0.80$.

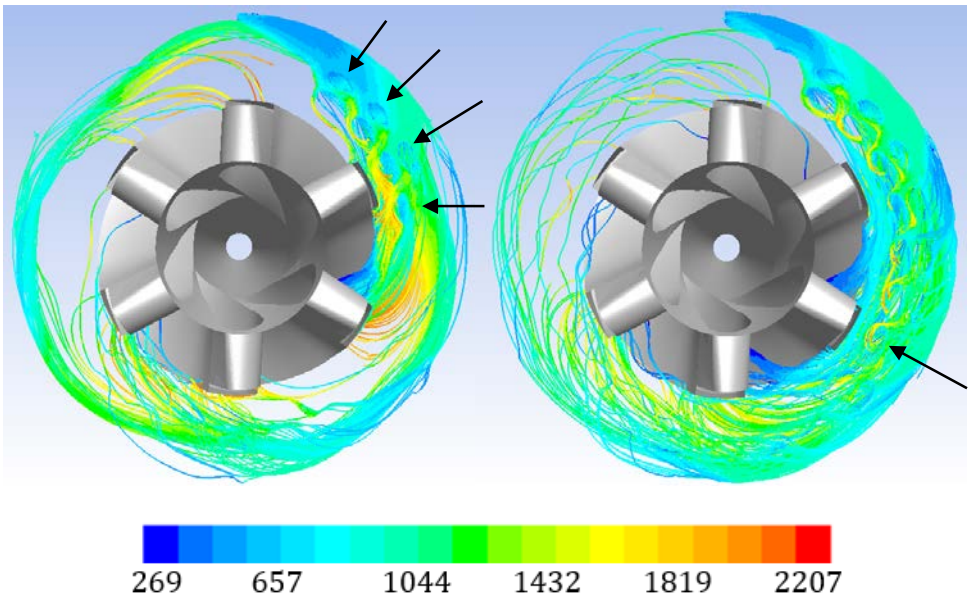

Figure 6.7: 3D stream traces colored by temperature from a single fuel injector; case LLB (left) and CPD (right)

The differences in streamline distribution within the cavity between the LLB and the CPD cases were significant. Where roughly half of the streams had migrated from the cavity by

the second passage downstream from the fuel injector in the LLB case, the patterns in the CPD case indicated a fairly even distribution of traces between the second and third passages with many streams continuing even further around the circumference. Additionally, the streams that circulated further appeared to be more evenly distributed in the CPD case. In contrast, the circulating streams in the LLB case were more densely packed and left substantial regions within the CC unoccupied. Furthermore, in the LLB case the influence of the air driver jets upon the stream traces was observable over the length of about one vane passage. In the image, the streams were seen to weave between about four pairs of air driver jets as indicated by the four black arrows. In the CPD case, the air driver cores were visible well into the third vane passage, the final pair of which is notated with a single black arrow. This behavior indicated that the fuel streams spent a greater span of the CC interacting and mixing with the incoming air in the CPD case as compared to the LLB case. Finally, a residence time analysis was conducted as developed in Chapter 4. To that end, the tangential velocity profiles within the cavity were compared in Figure 6.8. The mean tangential velocities at the cavity center were taken to be 25 m/s for both cases, while the approximate residence arc lengths (from examination of the streams in Figure 6.7) were taken as 180° and 210° for the LLB and CPD cases, respectively. The resulting residence time estimates were then 8.8 ms and 10.2 ms – the compound drivers thus had the effect of increasing residence time by about 16%. Notably, the lack of change in the mean tangential velocity also implies that the compound drivers have no appreciable effect on cavity g-loading.

As further illustration of the improved mixing characteristics of the CPD geometry, the local equivalence ratios were compared in Figure 6.9 at an axial plane at location C2 and at the same operating conditions as for Figure 6.7. The relatively thick fuel-rich region at the outer dimeter of the LLB case was observed to occupy nearly 50% of the CC area. This was contrasted by the CPD case in which the fuel-rich region was diminished by a substantial fraction by the outward-angled driver jets; it was estimated to occupy about 25% of the CC area.

Thus, increasing the outboard component of the injection angle decreased the fuel-rich volume by about half.

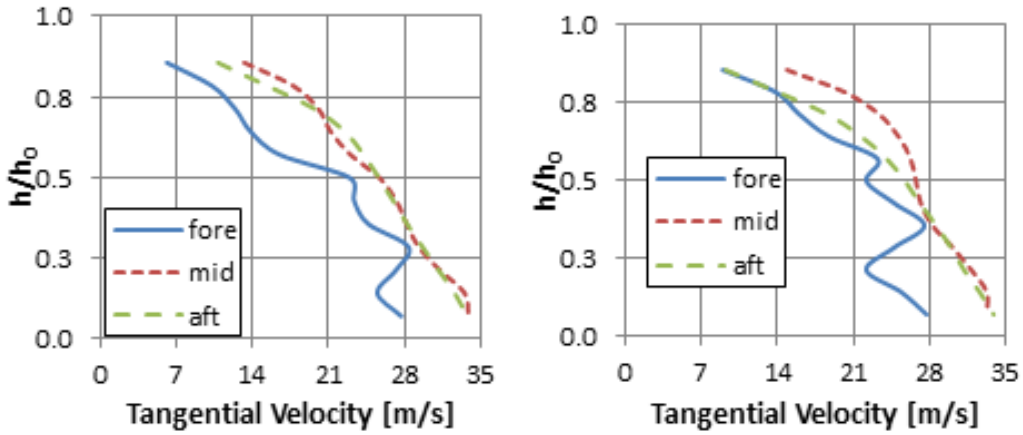

Figure 6.8: Comparing tangential velocity profiles between the LLB (left) and CPD (right) cases

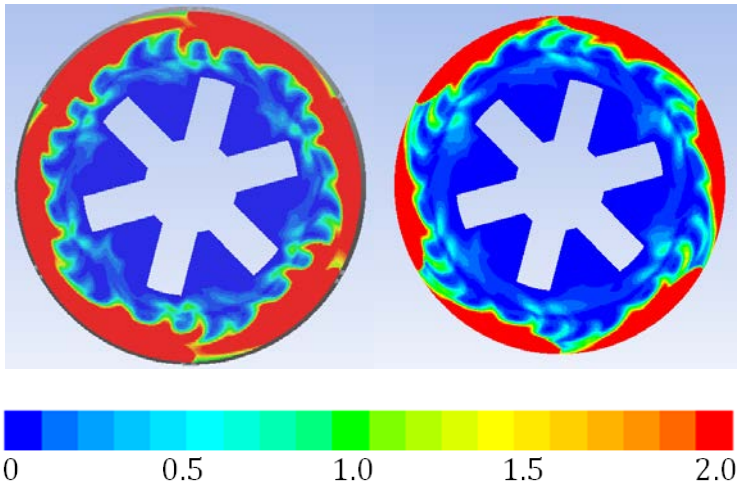

Figure 6.9: Contours of local equivalence ratio, LLB (left) and CPD (right)

In Figure 6.10, axial mass-averaged profiles are presented for all four geometries at lean (left) and rich (right) levels of ϕ_{cav} and at the same level of $\dot{m}_{in} = 0.15$ kg/s. Within the bounds of the circumferential cavity (CC), again as indicated by the vertical dashed black lines, the curves representing the compound-driver case (CPD) and the combined case (CMB) fell nearly on top of each other in both lean and rich conditions. That trend mirrored the relationship between the LLB and RVC cases, thereby indicating that the configuration of the air drivers

was the dominant feature within the CC, as expected. The impact of the introduction of the compound drivers was to slightly reduce the average temperature within the CC. The implication of that result is that, while mixing was improved as demonstrated previously in this section, the cavity configuration was in some way insufficient to allow additional heat generation within the cavity as a result of that improved mixing.

Further evidence for that conclusion was provided by the profiles of product formation rate where the CPD and CMB cases both demonstrated reduced production within the CC as compared to the LLB and RVC cases. Notably, however, the combination of the compound drivers with the radial vane cavity was able to overcome the lack of production within the HGV passages as demonstrated by image **c** in Figure 6.10. Whereas the RVC profile peak at $z/L \sim 0.65$ did not reach similar peaks in the LLB case, the CMB peak at the same location demonstrated that any quenching effect of the RVC geometry was compensated by the improved CC mixing induced by the compound drivers. Examining image **d** revealed similar trends. Within the CC, both the CPD and CMB cases produced lower average temperatures. Within the HGV passage, the CPD profile subsequently took a shape that was similar to the LLB profile; however the CMB curve demonstrated a unique shape that indicated substantially increased production compared to the CPD case. The CMB production peak exceeded the RVC peak as well, thereby implying that the CMB geometry resulted in the greatest amount of HGV passage burning. That conclusion is borne out again by referencing image **b**: the temperatures for both the RVC and the CMB cases increase over their smooth-vane counterparts within the HGV passage as a result of increased incidence of combustion within the vanes. Interestingly, in the fuel-rich condition of image **d**, the production rates for the LLB and CPD cases began to increase at the HGV exit plane while those of the RVC and CMB cases were decreasing. A potential implication of that result is that the LLB and CPD cases could induce further reactions at the transition point between the HGV and a theoretical downstream turbine rotor. Burning within the rotor is considered a very undesirable condition.

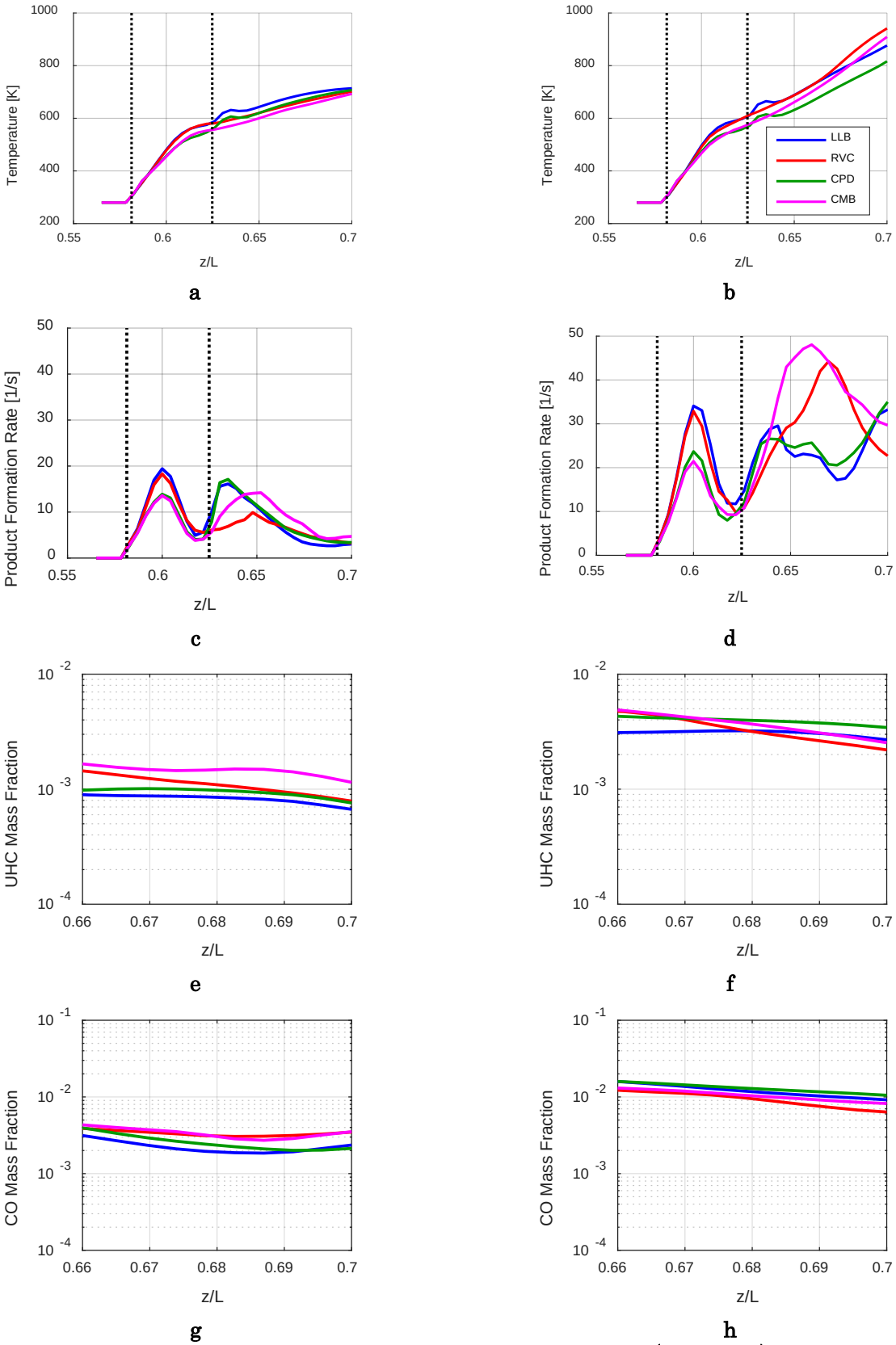

Figure 6.10: Mass-averaged axial profiles for various quantities at $\phi = 0.8$ (left column) and $\phi = 1.37$ (right column)

Examination of the trends in predicted emission in Figure 6.10 was again accomplished by calculating concentrations of unburned hydrocarbons (UHC) and carbon monoxide (CO). However in this analysis the horizontal axes were adjusted to focus in the region closest to the exit plane ($0.66 < z/L < 0.7$). At the lean operating condition, there was minimal distinction in terms of UHC between the LLB, CPD, and RVC cases, while the CMB case resulted in markedly increased UHC; that was an unexpected conclusion as the increased HGV production rate demonstrated by image **c** should have produced a complementary reduction in the amount of unburnt fuel species. Conversely, in image **f** the CMB case demonstrated an expected decrease in UHC concentration, which logically resulted from the increase passage production rate. In both images **e** and **f** the CPD configuration demonstrated increased UHC concentrations over the baseline LLB. The same was true for CO concentrations although the differences were less distinct. This was again likely the result of a CC design that was unable to fully capitalize on the increased potential from improved fuel/air mixing. Overall, as expected, the concentrations of pollutants were greater at the fuel-rich operating condition.

Examination of the trends at the cavity/core interface was accomplished as in Chapters 4 and 5 to better illuminate some of the differences between the geometries and potentially explain some of the driving mechanisms behind the hot gas distribution. Data from a subset of cases at constant $\dot{m}_{in} = 0.15$ kg/s are presented in Table 6.2. First: when compared to earlier analyses in Table 4.7 and Table 5.4, the average temperatures are notably cooler. This was a result of the implementation of a higher-fidelity combustion model with complex chemistry. The overall heat release was diminished as energy was consumed within a substantially increased number of chemical reactions. Second: as previously observed, increased ϕ_{cav} led to increased $\bar{T}_{int}$ in all cases. It also led to higher mass fractions of all three pollutant species as well as increased $\bar{\phi}_{int}$. And third: implementation of both the RVC and the CPD geometries led to decreased temepratures at the interface – more so for the latter. Clearly, then, combining the two features in the CMB configuration led to the largest observed drop in temperature relative

to the baseline. The RVC configuration also demonstrated an increase in the average concentration of fuel particles at the interface; in conjunction with the reduced temperature, that observation supported the conclusions from earlier discussion in Chapter 6 that the combustion processes were delayed by the RVC relative to the LLB at the cavity/core migration point. The CPD configuration, on the other hand, demonstrated both reduced temperatures and reduced concentrations of all three tracked species regardless of ϕ_{cav}. This was a counter-intuitive result as, based on analysis of Figure 6.7, it was expected that the compound-angle air drivers led to improved mixing and residence time within the cavity; those traits should theoretically lead to more complete combustion and higher heat release. Based on the data of Table 6.2, it did indeed appear that more combustion was occurring (based on the reduced pollutants at the interface), however there was not any evidence of increased heat release that should have resulted. The underlying implication is therefore that additional factors are affecting the cavity temperatures that have not yet been accounted for.

Table 6.2. Mass-averaged field calculations at the CC/core interface for various geometries

CFG	ϕ_{cav}	$\bar{T}_{int}$	c3h8	co2	co	$\bar{\phi}_{int}$
LLB	0.8	953	0.0026	0.046	0.016	0.049
RVC	0.8	933	0.0037	0.045	0.015	0.069
CPD	0.8	874	0.0019	0.041	0.014	0.035
CMB	0.8	804	0.0026	0.036	0.012	0.049
LLB	1.37	1095	0.0059	0.051	0.049	0.117
RVC	1.37	1044	0.0087	0.048	0.043	0.174
CPD	1.37	978	0.0046	0.044	0.038	0.092
CMB	1.37	894	0.0081	0.039	0.031	0.161

As the final component of this analysis, efficiency estimates were generated following the procedure introduced in Section 6.1.1 and supported by Table 6.1. Table 6.3 and Table 6.4 list the resulting calculations at $\dot{m}_{in} = 0.11$ and 0.15, respectively, for each configuration at two levels of ϕ_{cav}. From those estimates, it was observed that the LLB case was the most efficient at low ϕ_{cav} while the RVC case was the most efficient at high ϕ_{cav}; that conclusion held

regardless of inlet mass flow rate. In all cases, increasing ϕ_{cav} decreased relative efficiency. Notably, both the LLB and CPD cases were more efficient than the RVC and CMB cases at low ϕ while the reverse was true at high ϕ. Interestingly, an increase in inlet mass flow had the effect of decreasing efficiency at low ϕ_{cav}, and increasing efficiency at high ϕ_{cav} (with the exception of the CPD cases, which were nearly identical between the two mass flow rates at high ϕ_{cav}).

Table 6.3: Efficiency estimates for the four experimental geometry configurations, $\dot{m}_{in} = 0.108$ kg/s

ϕ_{cav}	ϕ_{ucc}	AF_{ucc}	Case	T_{ma}	η_{ma}
0.80	0.21	865	LLB - Lean	744.6	0.861
			RVC - Lean	724.6	0.838
			CPD - Lean	737.6	0.853
			CMB - Lean	723.2	0.836
1.37	0.36	1169	LLB - Rich	864.6	0.740
			RVC - Rich	929.8	0.795
			CPD - Rich	820.2	0.702
			CMB - Rich	881.9	0.754

Table 6.4: Efficiency estimates for the four experimental geometry configurations, $\dot{m}_{in} = 0.15$ kg/s

ϕ_{cav}	ϕ_{ucc}	AF_{ucc}	Case	T_{ma}	η_{ma}
0.80	0.21	865	LLB - Lean	714.0	0.825
			RVC - Lean	701.3	0.811
			CPD - Lean	707.2	0.818
			CMB - Lean	692.7	0.801
1.37	0.36	1169	LLB - Rich	876.4	0.750
			RVC - Rich	941.4	0.805
			CPD - Rich	816.4	0.698
			CMB - Rich	909.1	0.778

The overall conclusions based on examination of the temperatures and product formation rates were that (1) intermediate burning within the HGV passage was occurring in all cases, however it was sensitive to ϕ_{cav}, (2) the incorporation of the RVC increased that

sensitivity dramatically, and (3) in the lean condition and in the LLB and CPD cases it appeared that more reactions were occurring, which therefore generated relatively higher amounts of heat release overall within the HGV passage. The simulated emissions demonstrated trends that, for the most part, corresponded with the indicated temperature/production behaviors. In the rich condition, the RVC and CMB geometries generated less of both UHC and CO as compared to the LLB and CPD configurations. The results at the lean condition were somewhat less conclusive, although at the exit plane the concentrations of CO were actually higher for the RVC and CMB geometries.

6.1.3. Exit Temperature Analyses

In this subsection, the discussion is focused on the distribution of the hot gases at the HGV exit plane. The exit temperature profiles of the AFIT UCC are examined experimentally using the thin-filament pyrometry (TFP) technique and supplemented with the CFD model. Unique issues arose during processing of the TFP test results that affected interpretation of the resulting data; those discussions were presented in Section 3.2.5. The TFP results and accompanying CFD analysis are then presented for one geometry case – the LLB – in Section 6.1.3.1 in introduce and orient the reader to the nature of the TFP data and the strategy for its display. Subsequently, the remaining three geometry cases are added to the discussion in Section 6.1.3.2.

6.1.3.1. Baseline Exit Temperatures

To properly interpret the exit-plane TFP data, the relative position of each experimentally viable filament length had to be determined on a case-by-case basis. As discussed in Chapter 3, the actual spans had to account for the visible portion of the wire and the amount not coated in adhesive. A summary is provided by Table 3.3. Note that the exit passage span is defined by the variable s where $s = 0$ at the inner wall and $s = s_0$ at the outer wall. The spatial extend of each filament for each test case was defined by a starting and

ending value of the normalized variable s/s_0. Note that in all experimental cases, no data were available at the inner filament, F1. In the RVC case, data were unavailable at filament F2 as well (as observable in Figure 3.44 by the absence of signal at the F2 location), and in the LLB, CPD, and CMB cases no data were available at the F7 location.

Table 6.5: Summary filament span values

Case	Filament	Start s/s0	End s/s0	Case	Filament	Start s/s0	End s/s0
LLB	2	0.15	1.00	CPD	2	0.31	1.00
	3	0.26	1.00		3	0.50	1.00
	4	0.27	1.00		4	0.40	1.00
	5	0.24	1.00		5	0.32	1.00
	6	0.03	1.00		6	0.29	1.00
RVC	3	0.37	1.00	CMB	2	0.00	0.94
	4	0.31	1.00		3	0.03	0.93
	5	0.24	0.95		4	0.23	0.95
	6	0.36	0.87		5	0.31	0.96
	7	0.29	0.74		6	0.53	1.00

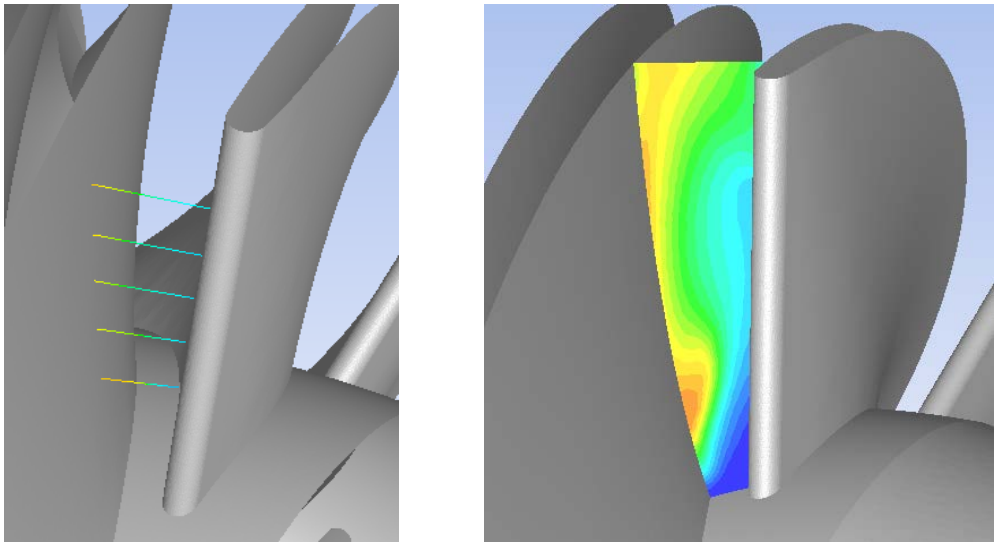

Figure 6.11: CFD/Experimental placement location (left) and CFD contour analysis plane (right)

In this section the TFP experimental measurements and corresponding CFD are presented only for the LLB case in order to introduce a very complex data set. In all cases, the CFD results were processed in such a way as to match the experimental setup as closely as possible. The filament placement in the exit passage for the CFD cases is illustrated in the left

image of Figure 6.11, while a sample two-dimensional contour plane is illustrated in the right image. The contour plane represents the definition of the UCC exit plane for the purpose of this discussion. The view is similar to the experimental field of view: cameras were positioned radially outboard from the passage of interest in order to capture as much of the lateral span as possible.

The profiles in Figure 6.12 present data from the LLB case at an air flow level of $\dot{m}_{in} = 0.108$ kg/s and a fuel flow setting of $\phi_{cav} = 1.0$. Solid lines represent CFD data that approximately match the placement of the filaments, while the dashed lines represent corresponding experimental filament data taking into account their relative spatial locations as described by Table 3.3; each CFD filament is labeled in the legend as f# while the corresponding experimental filament is labeled f#e. The CFD results illustrated complicated trends in span-wise and radial directions. On the outer surface ($s/s_0 = 1$), temperatures at the wall increased nearly monotonically until reversing between F6 and F7. On the other side of the span at the inner wall, the temperature stratification between the filaments reversed such that the peak temperatures occurred at F3 and decreased monotonically from there to F7; the F2 temperature at the inner wall remained below F3. The trend in the outer half of the cavity of increasing temperatures from F2 to F6 was upheld by the experimental data; although the profile shapes differed in some points, in the case of F6 at least the profiles in both the CFD and the experiment were fairly uniformly parabolic. The CFD results under-predicted the experimental data by as much as 500K at the pressure side; furthermore, while no test data were obtained at the suction side ($s/s_0 = 0$), the trends from F5 and F6 appeared to indicate a decrease toward the inner wall as opposed to the sharp increases predicted by the model. It was uncertain how much of that mismatch was due to the presence of the filament; the local flow at the wall would certainly have responded to the expanding adhesive, but the end result of that interaction could not be hypothesized.

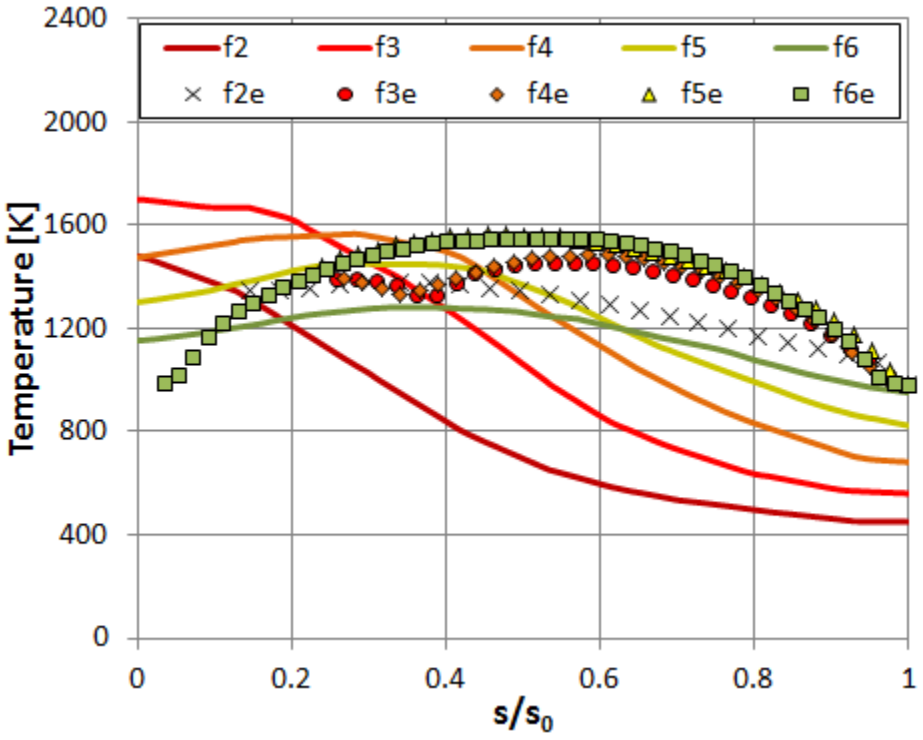

Figure 6.12: Span-wise profiles of temperature for the LLB case, $\phi_{cav} = 1.0$; colors are contour-order from "hot" (f2) to "cold" (f6)

In more compact form, the LLB experimental and CFD results are presented by Figure 6.13; results from filaments F3, and F5 were omitted for simplicity, as the primary observation was the change in the profiles with varied equivalence ratio. The profiles of F4 and F6 maintained shape but increased consistently from low to high settings of ϕ_{cav} in the CFD results; the experimental profiles do so in similar fashion. The experimental profile of F2 saw similar increases although its values in the inner span created an odd shape and might have been attributable to expanding filament adhesive. The CFD profile for F2 indicates fairly steady temperature at the outer wall, uneven shifting at the center of the passage, and near-steady temperature at the inner wall after an initial increase between the $\phi_{cav} = 0.7$ and $\phi_{cav} = 0.8$ cases. The F6 CFD profile maintained fairly uniform curvature while the experimental F6 profile became increasingly bowed; it was unclear whether that effect might have been in response to actual cool temperatures at the wall or some confounding effect of the

expanding adhesive. This, in conjunction with the behavior of the F2E profile, illustrated the complexity of interpreting the experimental results in the face of wholly uncertain conditions at the walls.

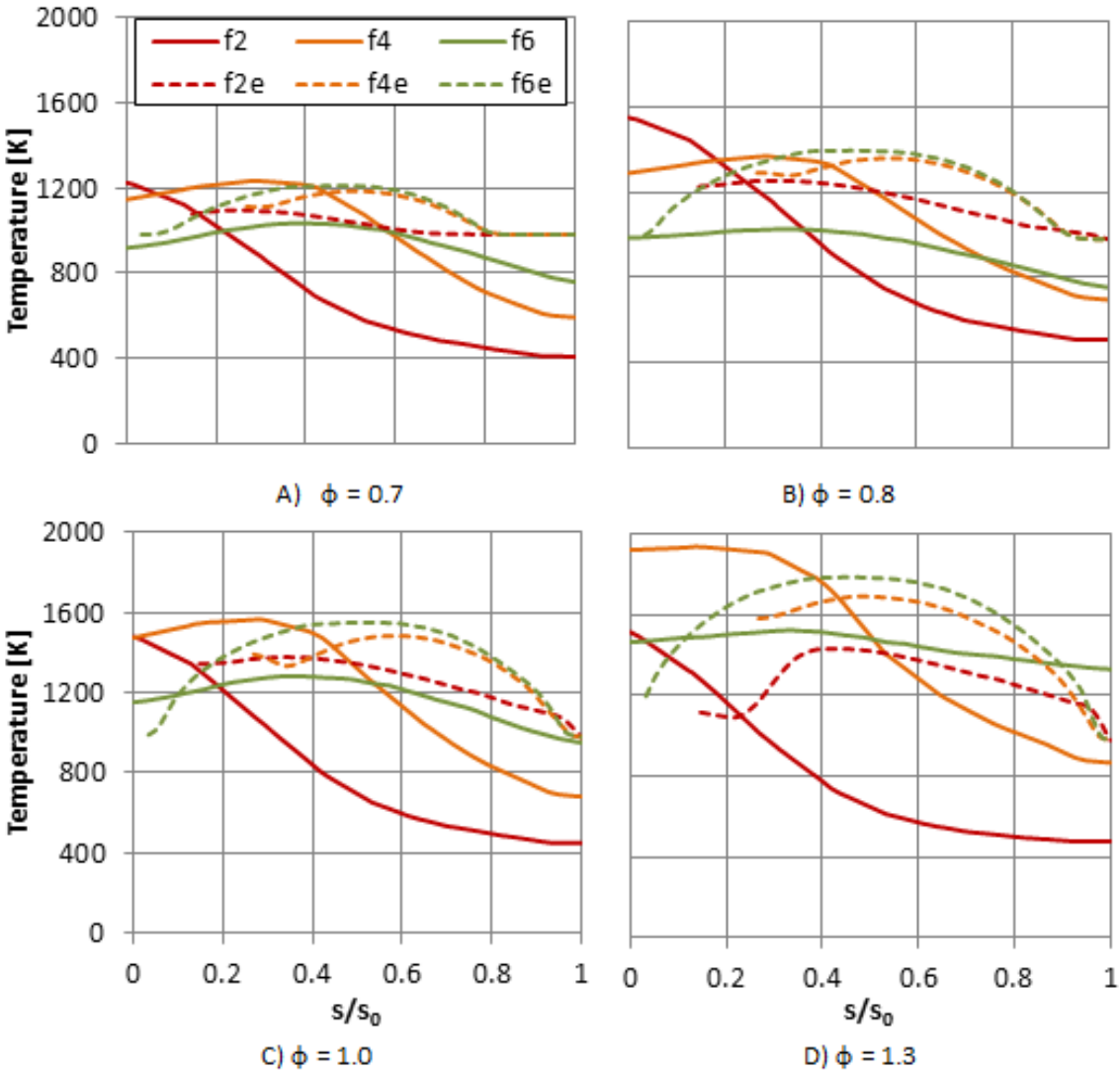

Figure 6.13: Experimental and numerical span-wise temperature profiles for the LLB case at $\phi_{cav} = \{0.70, 0.80, 1.0, 1.3\}$

Further insight into the complexity of the field at the exit plane was gained through examination of two-dimensional CFD contours as shown by Figure 6.14. The approximate span location of the experimental/numerical filament profiles is highlighted in the leftmost image by black lines. The LLB case is shown at four levels of ϕ_{cav}. Observation of the contours

demonstrated two important characteristics: first, the hot gas migrating from the circumferential cavity (CC) did not ever reach the inner diameter of the HGV passage, and second, the hot gas remained in large part attached to the suction-side wall (the left wall in the images) of each HGV airfoil. The result was that by the exit plane a hot spot developed at roughly 1/3 the radial height of the suction-side surface. The hot spot grew larger with increased ϕ_{cav}; therefore, the increasing temperatures observed in the TFP measurements were explained.

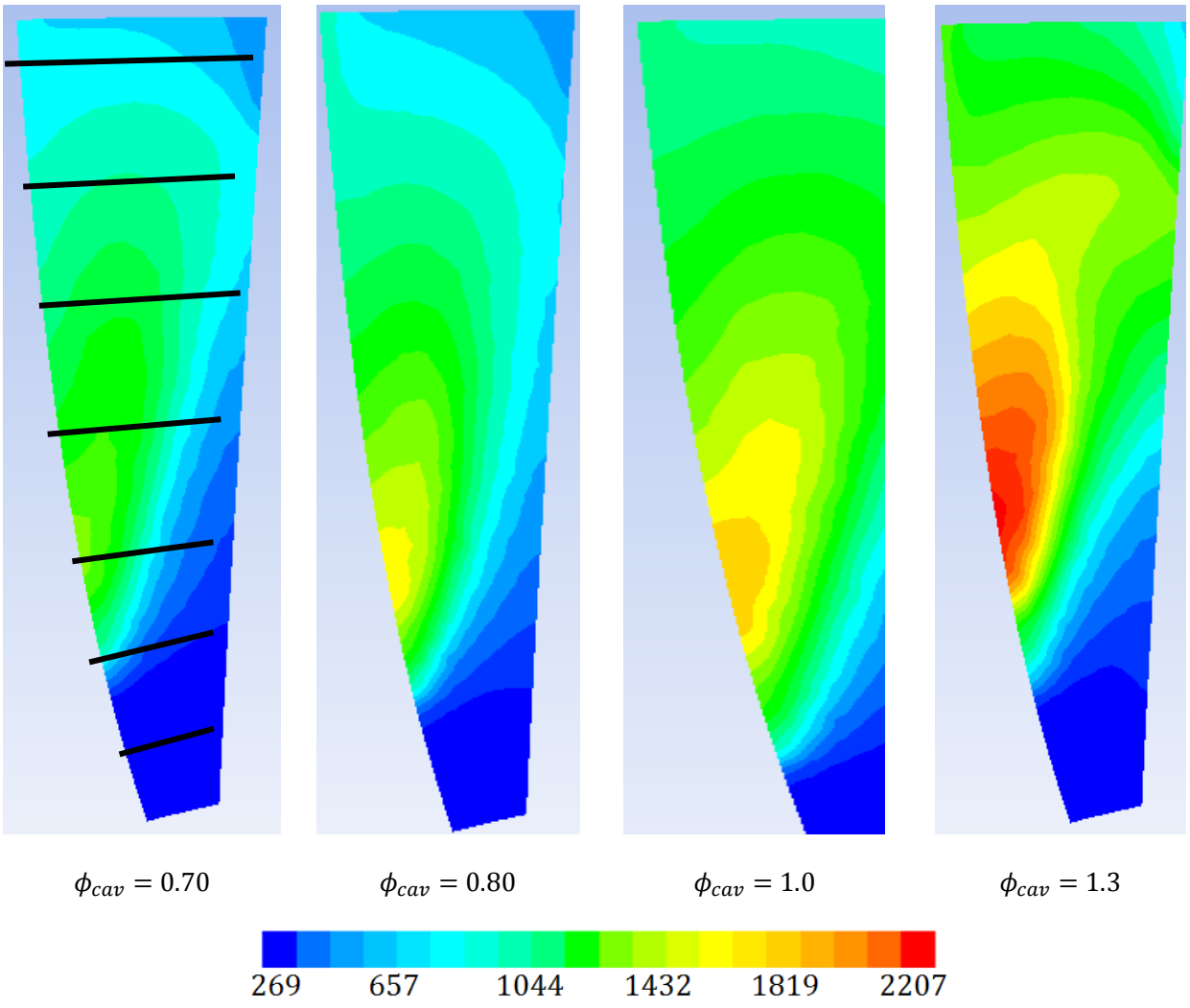

Figure 6.14: 2D CFD contours of temperature for the LLB case at settings of $\phi_{cav} = \{0.70, 0.80, 1.0, 1.3\}$; approximate orientation of the lateral filaments are also shown

As the CFD wall boundaries were set as adiabatic, temperatures at the wall were not expected to provide accurate representation of the real wall temperatures during rig operation; however, the temperatures at the wall in the CFD did provide a reliable measure of the gas temperature in that vicinity, and they were therefore useful for the purpose of identifying the heat release patterns within the vane passage that led to the conditions at the exit plane. For a baseline analysis, temperature contours along a single vane suction-side and pressure-side were generated at conditions $\dot{m}_{in} = 0.15$ kg/s and $\phi_{cav} = 0.80$ for the LLB geometry. Several notable features were highlighted. As expected, CFD predicted that the suction side was substantially hotter than the pressure side due to the impingement of the clockwise-rotating circumferential cavity flow. However, inspection of the suction-side image revealed hot spots at the fore and aft outer vane surface, which had not previously been fully recognized. It appeared that the forward hot spot represented some initial complete reaction that subsequently comprised a preliminary migration of hot products along the vane surface into the core flow. Hot gasses subsequently spread from the aft vane hot spot and generated significant heating along the suction-side surface. Hot gases from the forward migration point merged with the aft migration into a single hot band that remained isolated to the approximate radial midpoint of the vane surface with comparatively warm products outboard and ambient-temperature core flow inboard. As illustrated by Figure 6.16, that phenomenon was exacerbated tremendously at the rich cavity condition of $\phi_{cav} = 1.37$, although the total surface area of the vane exposed to the hot gasses remained realtively constant. In other words, while increased fuel flow increased the temperatures encountered by the vane surface, the influence of the cold core flow was unaltered, and the approximate radial distribution of the temperatures remained fairly similar.

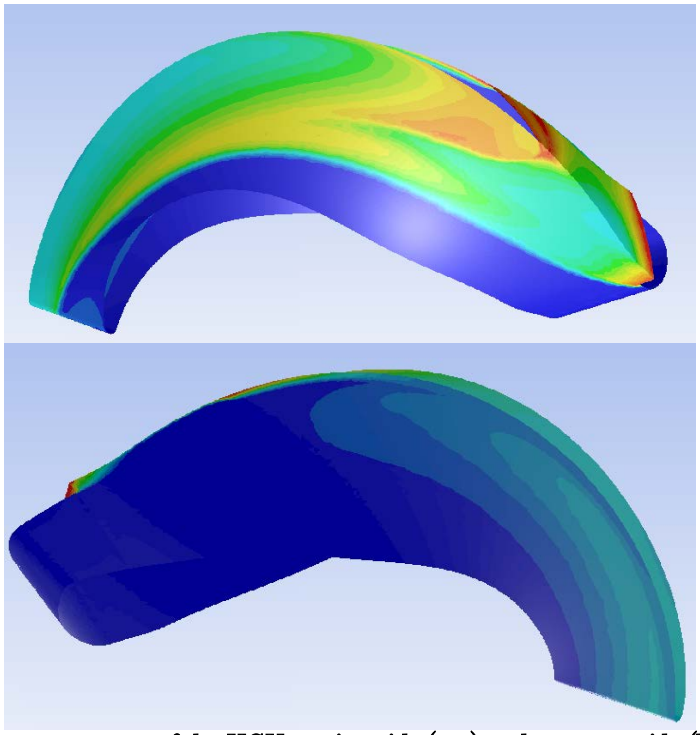

Figure 6.15: CFD wall temperatures of the HGV suction side (top) and pressure side (bottom) beneath a lean cavity

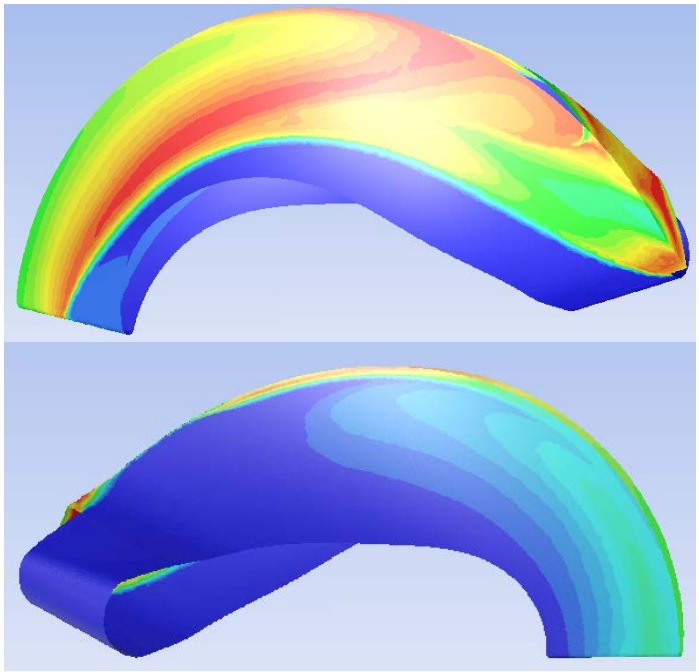

Figure 6.16: CFD wall temperatures of the HGV suction side (top) and pressure side (bottom) beneath a rich cavity

The wall temperatures helped to explain the formation of the hot spot at the exit plane. In conjunction with upcoming evidence in Section 6.1.3.2, the fundamental hypothesis explaining the formation of the suction-side hot spot was formulated: it was likely the product of increased burning within the HGV passage due to excess unburnt fuel and intermediate products being forced from the CC to mix with the core flow. Importantly, the presence of a suction-side hot spot provided another logical explanation for the tendency of the filament adhesive to expand on that side. While the adhesive prevented collection of explicit data, implicit conclusions were drawn that on the inner passage wall the temperatures must have approached and exceeded the adhesive maximum continuous operating temperature of 1530 K [108] while temperatures on the outer wall remained relatively cool. Indeed, predicted temperatures at the suction-side surface ranged from 1000 to 2200 K. As demonstrated in the previous discussion, the model tended to under-predict the data in the range $0.5 < s/s_0 < 1.0$, while experimental data in the range $s/s_0 < 0.5$ was generally suspect. The adiabatic flame temperature of propane in air is 2253 K, however; thus it is reasonable to hypothesize that hot spots approaching that temperature do exist in the real test system. This would provide sufficient conditions for the adhesive to become susceptible to the expansion phenomena originating from the expansion of trapped hot gas in the pilot mounting holes.

The exit temperatures were examined by way of temperature profile analysis to determine the precise nature of the influence of equivalence ratio on peak temperatures and pattern factors. The profiles were generated through two fundamental steps: first, circumferential averages were computed at discrete radial positions for each of the six exit passages to generate individual profiles for each passage. Then, the results from each passage were then averaged together to obtain a single profile representing all six passages. Further detail on the averaging process is given in Appendix F. In Figure 6.17, radial temperature profiles are presented for the LLB configuration at four levels of ϕ_{cav}. The peak temperatures increased continuously with phi. Increasing to $\phi_{cav} = 0.80$ resulted in a 9% increase in peak

temperature, with increases of 21% and 11% at 1.0 and 1.3, respectively. The outer wall temperatures increased in a similar fashion by 11%, 16%, and 11%. However, on average, the temperature increases were not commensurate with the amount of increased energy potential represented by the increased fuel. Thus, as detailed by the discussion surrounding Table 6.3 and Table 6.4, overall efficiency estimates decreased with increasing fuel flow.

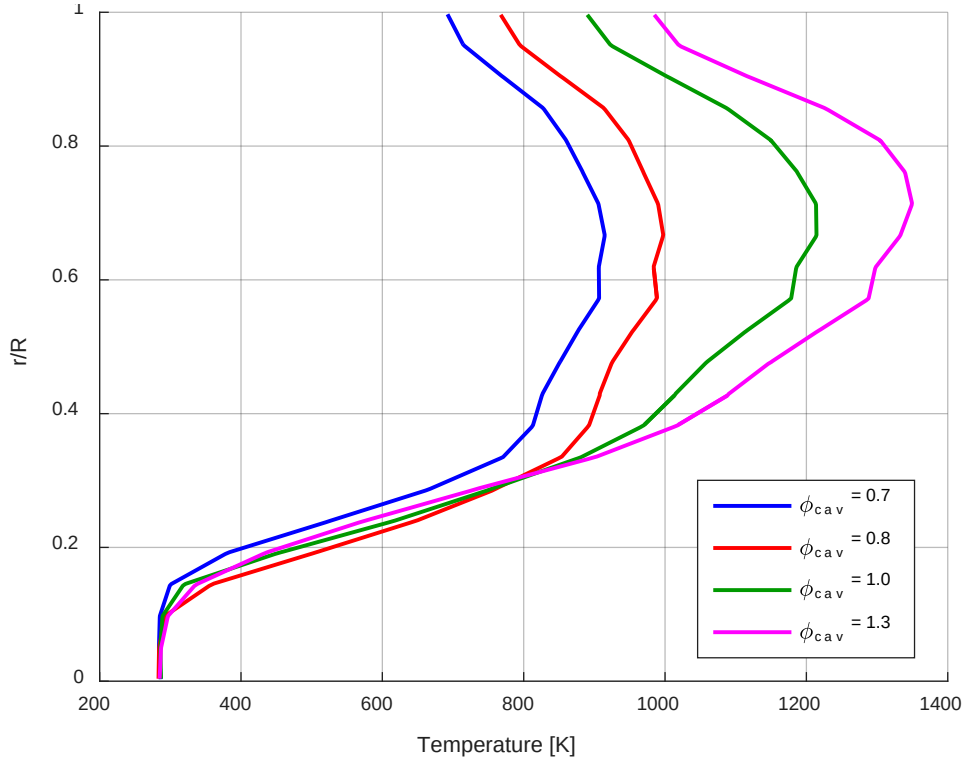

Figure 6.17: Radial temperature profiles for the LLB geometry at four levels of ϕ_{cav}

Pattern factors were computed according to Equation (24) where the value for T_4 corresponds to the average over the temperature profile; results are shown in Table 6.6. Recall that pattern factors do not generally describe the desired shape of the profile; such is usually prescribed by individual engine designers. However, values of the pattern factor in the range from 0.15 to 0.25 have been found to correspond to desirable temperature distributions in modern gas turbine engines. Notably, the computed pattern factors in Table 6.6 are somewhat greater than the modern standard. This was a consequence of two likely factors: (1) operating

at atmospheric inlet pressure and (2) the presence of cold inlet-temperature air at the exit plane. The values for pattern factor did not increase monotonically due to the inconsistent increase in the numerator term $T_{max} - T_{avg}$; the increasing values of T_{max} were offset by the disproportionately low T_{avg} induced by the cold flow at the inner diameter. However, the increase was steady between $0.80 \leq \phi_{cav} \leq 1.3$. The reasons for the overall increases in peak temperature and pattern factor were likely increased reactions in the HGV passages, which in turn led to higher peak temperatures while the ID temperature remained constant. The same trend was illustrated in Figure 6.10. The net effect of increased fuel injection into the cavity was to increase the volume occupied by the fuel layer in the outer diameter. There was simply more fuel present, but as a consequence there was less space available in the cavity for complete mixing. Figure 6.10 demonstrated that as ϕ_{cav} increased, the average product formation rate in the cavity increased while the average temperature decreased. It appeared through prior analysis in Section 5.3 that the regions of peak heat release occurred in the final stages of combustion corresponding to regions of relatively low local ϕ. An altenative perspective was that the average tempature gains in the axial profiles of Figure 6.10 always followed peaks in the product formation rate. Therefore, the final dilution stage of combustion at any given region of the cavity volume was characterized by (1) a peak-then-decrease in product formation rate and (2) the resultant increase in temperature.

With regard to UCC operation, the fundamental hypothesis was that all three combustion stages – primary, intermediate, dilution – were influential in the circumferential cavity at lean values of ϕ_{cav}. Conversely, increased fuel flow led to an absolute increase in production of intermediate species and a concurrent decrease of the available volume to complete intermediate burning. Thus, any residual intermediate burning – as well as the bulk of the dilution process – would consequently be relegated to the HGV passage.

Table 6.6: LLB pattern factors with respect to ϕ_{cav}

φ	T_{max}	T_{avg}	Pattern
0.70	914	709	0.479
0.80	997	784	0.423
1.00	1214	890	0.532
1.30	1349	960	0.573

6.1.3.2. Exit Temperature Effects Due to Geometry

Whereas the prior section was dedicated to an understanding the effects of operating conditions on the exit temperatures of a single UCC geometry configuration, this section returns to the objective of quantifying the effects of geometry changes. The focus will again be on exit temperatures with both experimental TFP data and computational analysis. As a reminder, the geometry configurations being evaluated are the low-loss centerbody (LLB), the radial-vane cavity (RVC), the compound air drivers (CPD), and the combination of the RVC and CPD (CMB).

For the geometry effect analysis, the comparisons were performed at operating conditions $\dot{m}_{in}$ = 0.108 kg/s and ϕ_{cav} = 0.80; both set points were generally preferred due to the relative stability of the test rig at those conditions. The effects upon a single filament – number f4 – were first compared across all four geometric configurations from both the experimental and the CFD results in Figure 6.18. Relative to the baseline LLB case of filament f4, which represents the approximate radial midpoint of the exit passage, the profiles in Figure 6.18 indicate that the primary effect of the RVC geometry was to generate an overall decrease in temperature. As the analysis of Figure 6.27 and Figure 6.28 will demonstrate, this was due to the CFD prediction that the RVC caused the local temperature maximum to shift radially inward, therefore leading to reduced temperatures elsewhere. The influence of the CPD geometry was a similar, though less substantial temperature decrease. This observation was counterintuitive as previous analysis in Section 5.1 indicated that the fuel streams were mixing

and residing longer in the circumferential cavity that should have resulted in more complete combustion and, therefore, higher overall exit temperatures. The CFD-predicted influence of the CMB geometry at the f4 location entailed higher temperature at the pressure-side of the passage and the lowest overall temperature of the four geometries at the suction side. The experimental data depicted different trends: the RVC data demonstrated lower pressure-side temperature but higher temperature near the mid-span. The CPD geometry yielded a temperature profile very similar to the LLB on the pressure-side but markedly lower at the midspan. The CMB data revealed a substantial departure from the other experimental results that prompted the hypothesis that it may have been erroneous. Further evidence to that end is presented later in this section.

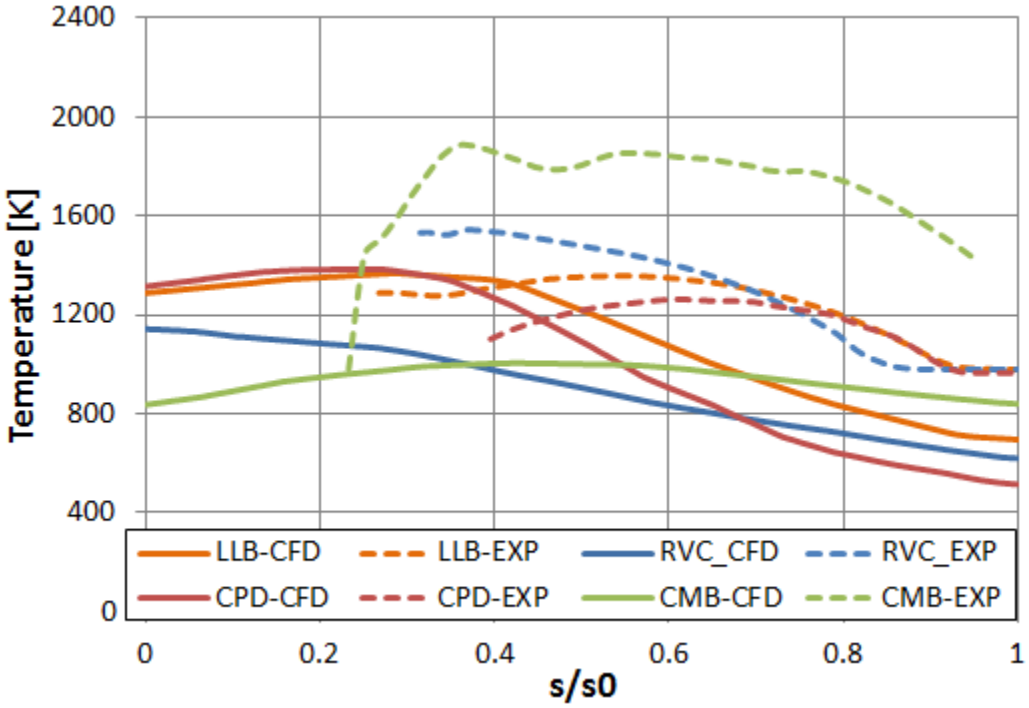

Figure 6.18: Experimental and numerical span-wise exit temperature profiles for filament f4

The complete data for the four geometry configurations are shown in each of Figure 6.19, Figure 6.20, Figure 6.21, and Figure 6.22. The first observation of the experimental data was that the differences between the LLB (Figure 6.19) and the RVC (Figure 6.20) cases included

substantially restricted passage span of usable experimental data. In fact, the RVC case was represented in the initial illustration of the adhesive expansion in Figure 3.44; thus, between 25 to 50% of the HGV passage was not represented in the RVC filament data. The next observation was that while the F3E and F6E lines were relatively close in the LLB case, in the RVC case the F3E line was substantially hotter than F6E, thus indicating an increase in the relative temperature in the inner channel passage as compared to the outer. The CFD results do not reflect that trend precisely, and in fact an overall decrease in temperature along all of the profiles was observed upon introduction of the RVC geometry. The exception was the CFD F2 line that increased along its span by as much as 360 K; however at the inner wall it, too, saw a slight decrease. In the RVC case the experimental profiles at lines F6E and F7E fell nearly on top of each other, while the analogous CFD profiles maintained similar shapes within about 70 K of each other. Those behaviors indicated relatively uniform temperature distribution within the radially outboard half of the channel passage, a trend that was supported by the model. Comparing the CFD curves between the LLB and RVC cases, some pattern was observed in the inflection points of the profiles as the hot spot on the inner wall began to exert its influence. The F2 line crossed the F3 line at $s/s_0 = 0.09$ in case LLB and at $s/s_0 = 0.45$ in case RVC; this implied a hot region on the wall that occupied a substantially greater portion of the channel passage. While the RVC geometry had the bulk effect of lowering the modeled temperatures at the exit plane, the CPD geometry concept had marginal impact upon the temperature profiles as observed through comparison of Figure 6.19 and Figure 6.21. Numerical profiles are very similar between the cases with the exception of slightly increased temperatures at the suction side in curves F2 and F3. The experimental data suffered from reduced spatial span as compared to the LLB case and the temperatures were slightly reduced. The experimental temperature peaks of the CPD case reach maximum values of about 1350 K compared to 1390 K in the LLB and 1520 K in the RVC cases.

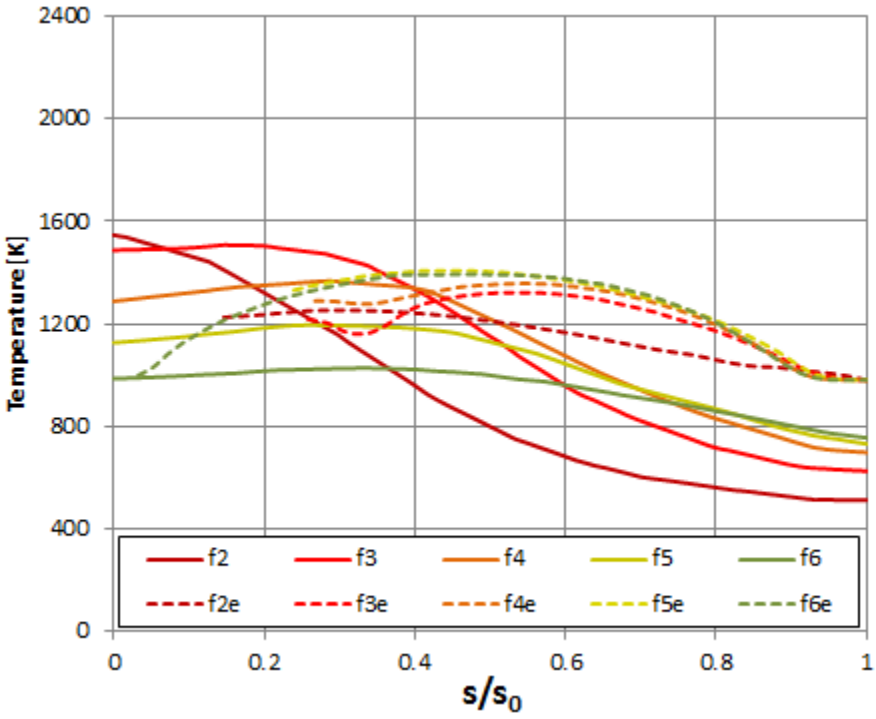

Figure 6.19: Experimental and numerical span-wise exit temperature profiles for the LLB case, $\phi_{cav} = 0.80$

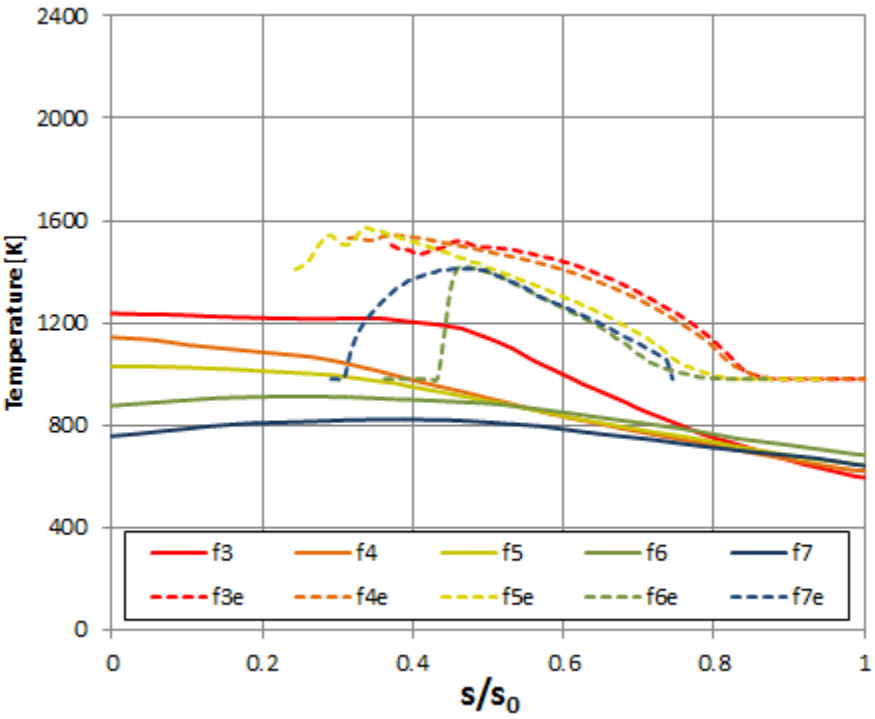

Figure 6.20: Experimental and numerical span-wise exit temperature profiles for the RVC case, $\phi_{cav} = 0.80$

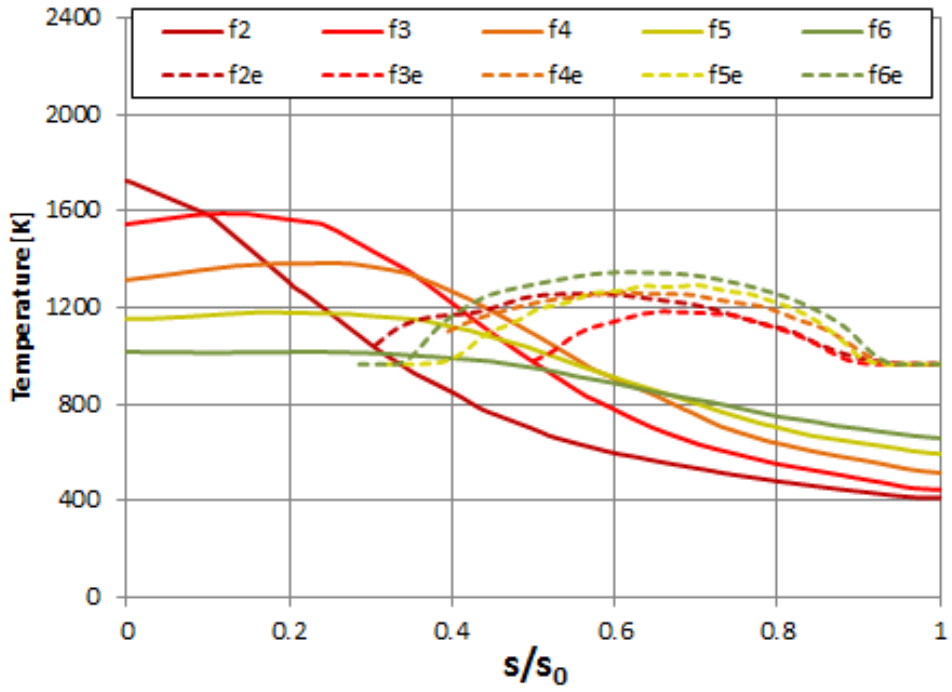

Figure 6.21: Experimental and numerical span-wise exit temperature profiles for the CPD case, $\phi_{cav} = 0.80$

A separate discussion is required to address the test data from the CMB experimental case. The profiles are shown in Figure 6.22, and, as noted in the discussion of Figure 6.18, the observed temperatures from that data were markedly increased over all three prior cases. The modeled results indicate increased temperatures on the pressure-side for filaments F2 through F5 while F6 is similar and F7 is slightly reduced. In contrast, the predicted temperatures on the suction side are relatively low compared to the other three cases. The inflection points between the profiles more closely resembled the data from the RVC case where filament F2 peaked near the center of the span; that was in contrast to the LLB and CPD cases where F2 peaked at the suction-side wall. The experimental data show a dramatic increase in temperature in addition to some abnormal features as compared to the other cases.

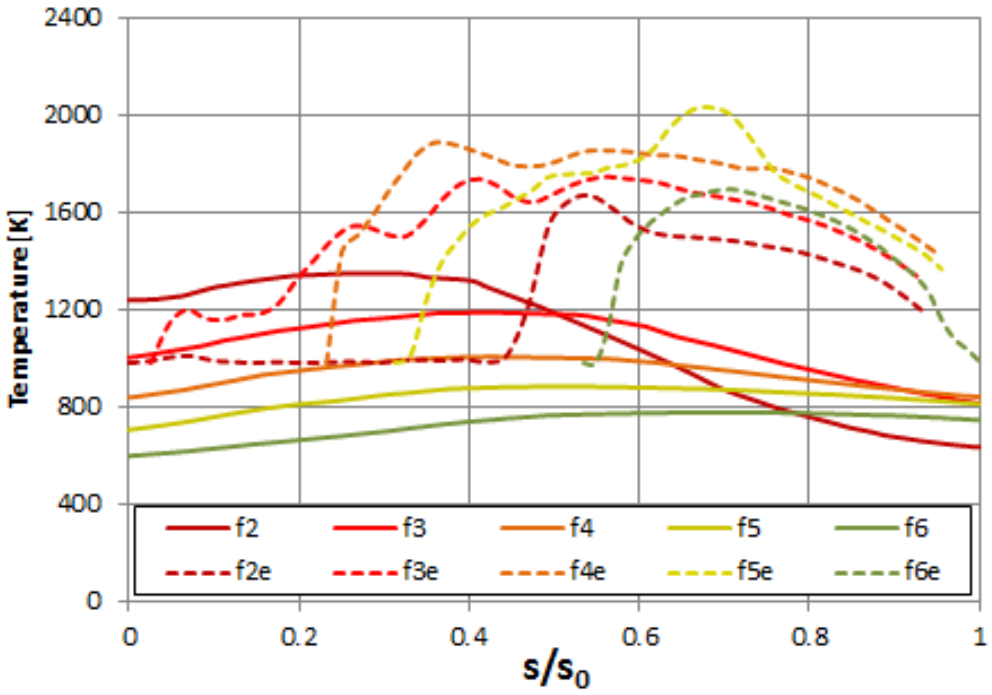

Figure 6.22: Experimental and numerical span-wise exit temperature profiles for the CMB case, $\phi_{cav} = 0.80$

The cause for this behavior was identified by examining (1) an unfiltered image of the test plane and (2) the individual images that were used to define the extracted data. The former appears in Figure 6.23. Note that the view angle is such that the outer, or pressure-side wall, is toward the top of the image. The left-most visible filament is F6 (filament F7 is obscured by the aft instrumentation ring). Observations from that figure were centered upon the notable impurities affecting the filaments themselves; these were very likely adhesive contaminants resulting either from installation or from the expansion phenomena. The adhesive likely had some influence upon the results, and one strong piece of evidence is the protruding temperature peak observed in the F5E line at $s/s_0 = 0.69$.

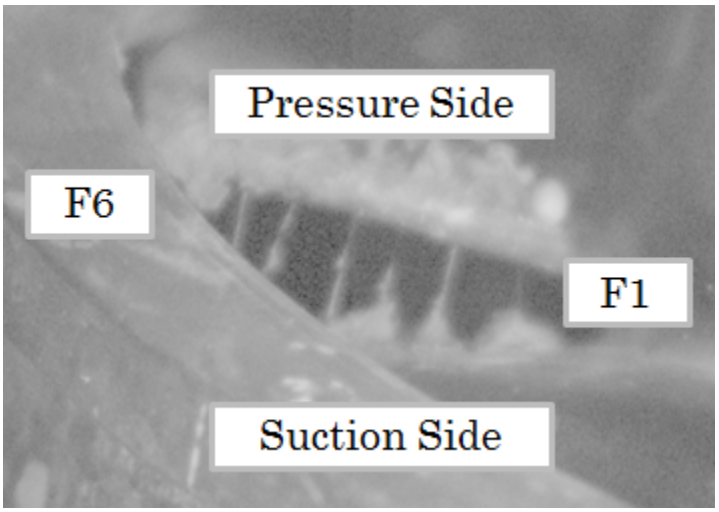

Figure 6.23: Unfiltered image of the CMB test

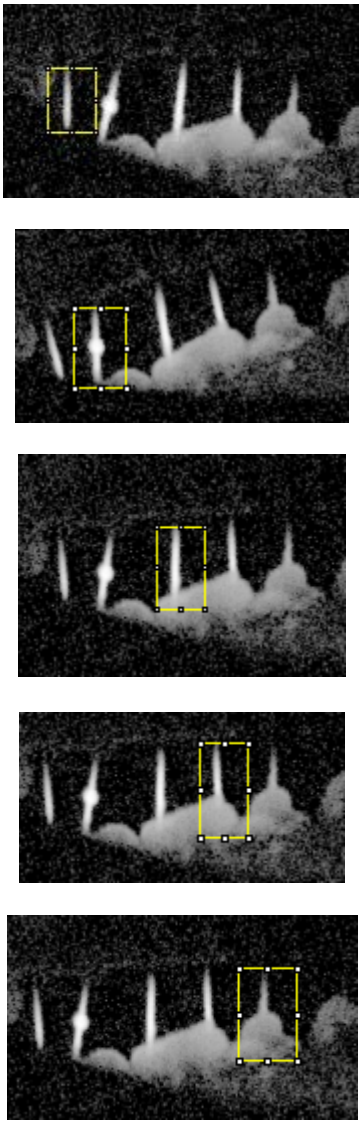

Figure 6.24: Sampled pixels for filament F6 (top) through F2 (bottom)

In Figure 6.24, the actual image used to sample the data for filament F5 appears as the second from the top. In that and all accompanying images, the sample region was defined by the yellow dashed box. While typical filament radiation appeared nearly linear, F5 was afflicted by a bright spherical luminescence that was attributed to a particularly large buildup of adhesive. Furthermore, the images of Figure 6.24 accurately reflected the sample space for each filament; thus, it was observed that the sample spaces in this case included portions of the expanding filament adhesive for filaments F4, F3, and F2.

Thus, the data in Figure 6.22 included erroneously-converted temperature measurements from the adhesive itself in an approximate range of $0 < s/s_0 < 0.6$ for those three filaments. As to the presumably good data in the remainder of the span, it was inconclusive whether or not smaller contaminated regions along the filaments might have been present; thus, it was unclear whether or not the dramatic temperature increases were a reflection of reality. It will be an important matter of future work to rerun these data – and likely all exit plane data – with particular care to avoid adhesive contamination through installation or expansion. The next discussion will provide complementary CFD results to aid understanding of what might be occurring at the HGV exit plane.

As in the previous section, to help explain the distribution of the hot gases that led to the conditions at the exit plane, a CFD analysis of the adiabatic wall temperatures of a representative HGV was conducted. Each of the four geometries are represented in Figure 6.25 at $\dot{m}_{in} = 0.15$ kg/s and $\phi_{cav} = 0.80$. The LLB image is identical to that shown in Figure 6.16. In comparison, the RVC vane demonstrated a notable dispersion of the suction-side hot spot; furthermore, the hot spots on the outer vane surface at the fore and aft cavity locations were also absent. The hot gases were instead concentrated to a location roughly centered upon the RVC channel at the point where it rejoins the primary vane surface. Additionally, the inward radial extent of the hot gasses at that axial location was markedly greater than in the case of the LLB; however, that gain was offset by the time the flow reached the trailing edge, and the resultant exit distribution did not exhibit any substantially improved inward radial migration as compare to the baseline. Examining the CPD vane, the forward cavity hot spot was notably absent, and the entire OD vane surface beneath the cavity was cooler. However, the aft hot spot was still present and it grew in intensity. Interestingly, while the high-temperature region was greater, the conditions at the vane trailing edge yet resembled the LLB. The CMB vane demonstrated temperatures very similar to the RVC with the exception of a somewhat cooler

OD at the vane trailing edge. Examination of the RVC surface in detail helps explain its unique results in this context as well as in the results that have been presented earlier.

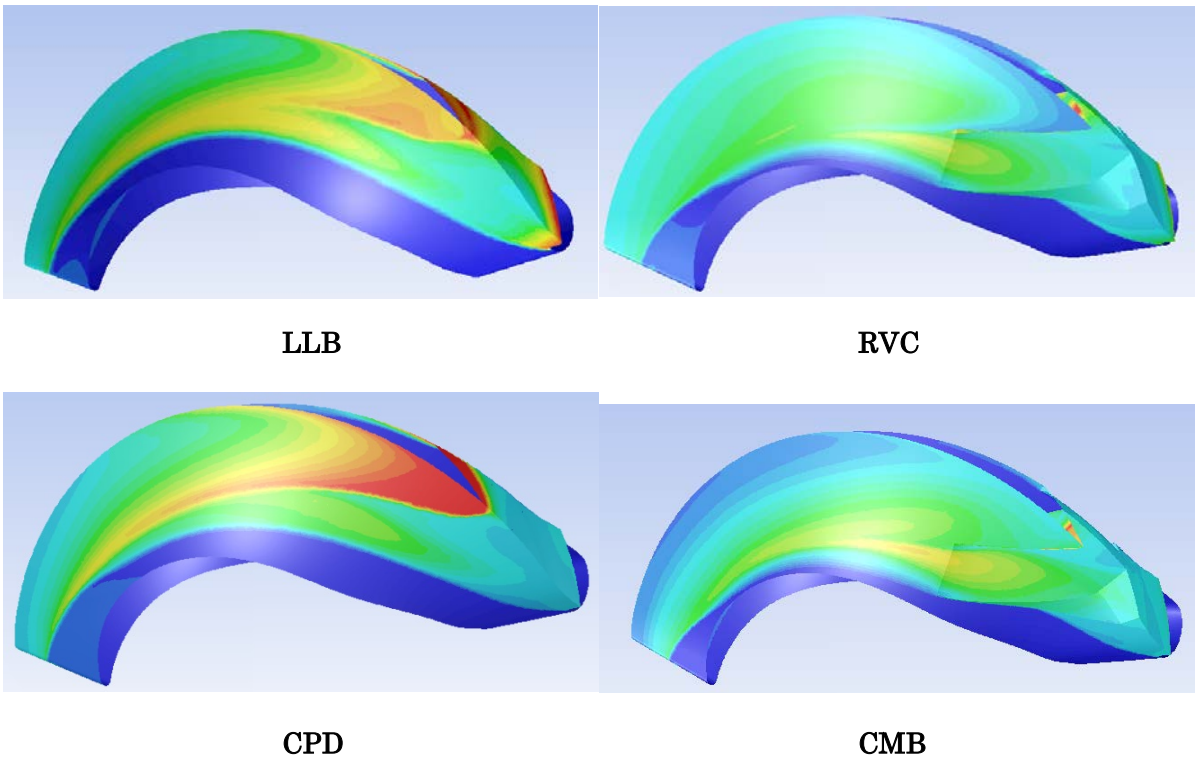

Figure 6.25: CFD wall temperatures of the HGV suction side for each of the four geometric configurations

In Figure 6.26, the adiabatic wall temperatures at the inner surface of the RVC are illustrated, and an aft hot spot is again visible as presented by the LLB and CPD configurations. However, instead of being guided by the suction-side vane surface, the hot gases are instead guided by the interior corner of the RVC. Consequently, they do not adhere to the vane but rather separate back out into the bulk core flow. That observation aligned with the discussion of the stream traces in Figure 6.4.

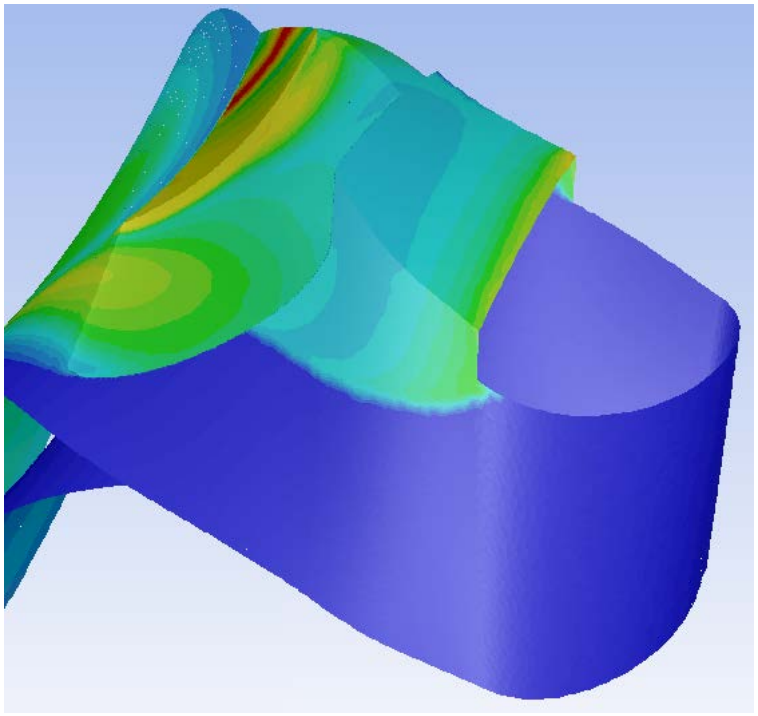

Figure 6.26: CFD wall temperatures showing the RVC cavity surface

The most complete picture of the temperature distribution at the HGV exit plane was provided by the CFD temperature contours shown in Figure 6.27. The fields were similar between the four geometries in several key aspects. First, all cases saw cold (inlet temperature) air at the inner diameter. Second, the highest temperature regions tended to remain attached to the left (suction-side) wall, while the pressure-side wall was relatively cool. Finally, as observed previously, the fuel-rich cases demonstrated substantially higher temperatures at the exit plane than their counterparts. As a result, the hot gases tended to occupy a greater area of the plane. The effect of the two cases that employed the radial cavity – RVC and CMB – was to shift the hot regions slightly radially inward relative to the other two geometries. That trend was more pronounced in the rich cases; additionally, the RVC geometry again had the effect of breaking up the focused hot spot observed in the LLB and CPD cases. The effect of the compound-air drivers was less substantial at the exit plane than in the cavity, as expected. (Note that a discussion of exit temperature profiles and corresponding profile factors will again appear as the final component of the current analysis).

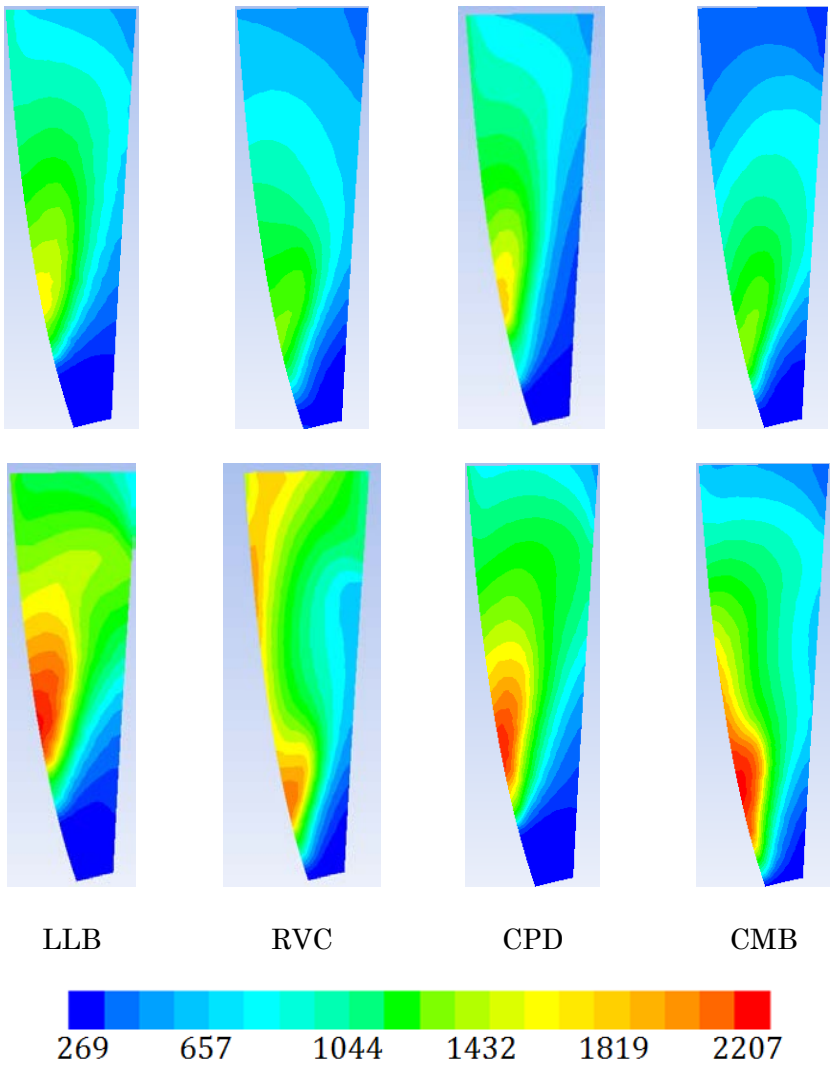

Figure 6.27: 2D temperature contours for the four geometries at $\phi_{cav} = 0.80$ (top row) and $\phi_{cav} = 1.3$ (bottom row) with constant $\dot{m}_{in} = 0.108$ kg/s

The same set of planes were collected at a higher inlet mass flow rate of $\dot{m}_{in} = 0.150$ kg/s as shown in Figure 6.28, and the same general trends were observed. As commented on in Figure 6.3, asymmetric patterns were present, and the computational planes in these figures represent single passages. Thus, flow patterns as observed in CPD case of Figure 6.28 were not necessarily representative of the patterns of neighboring planes. However, in general, the primary effect of the RVC geometry was an inward shift of the hot regions, and the primary effect of the compound-angle drivers at the exit plane was negligible.

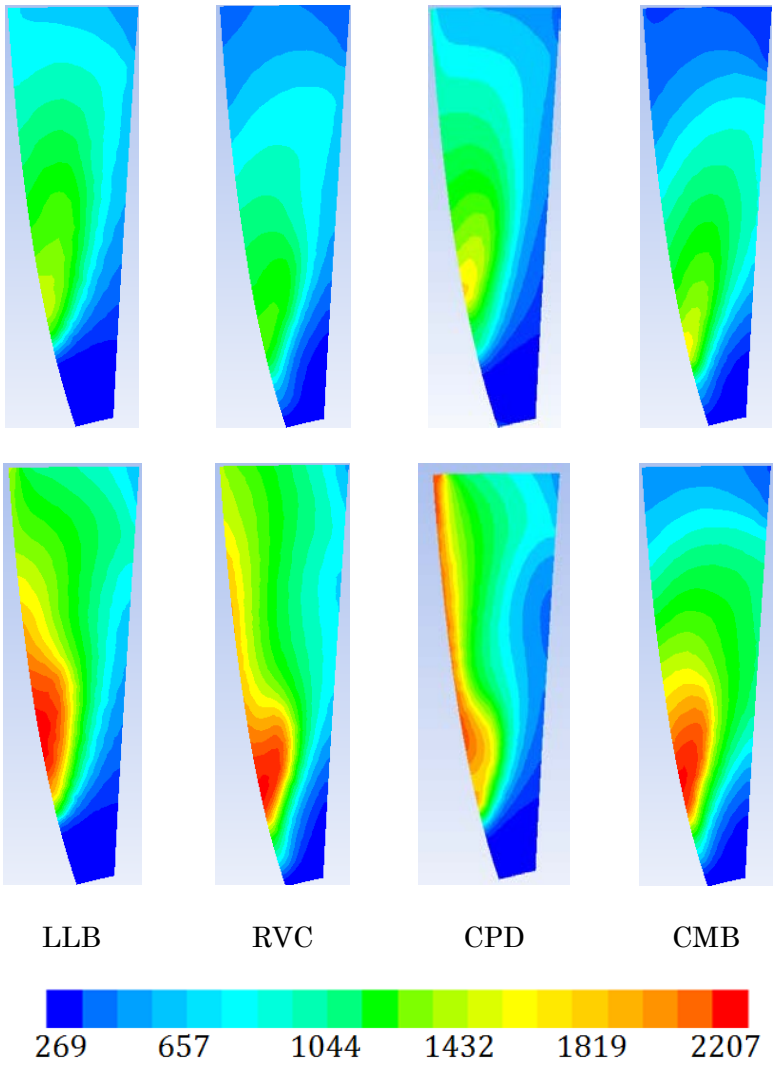

Figure 6.28: 2D temperature contours for the four geometries at $\phi_{cav} = 0.80$ (top row) and $\phi_{cav} = 1.3$ (bottom row) with constant $\dot{m}_{in} = 0.15$ kg/s

As the final step to the analysis of the exit temperatures, temperature profiles from the exit planes were calculated through the same procedure outlined in Section 6.1.3.1. It is important to note that the contours in Figure 6.28 and Figure 6.29 are views of single HGV exit passages in contrast to the passage-averaged profiles. Thus, the circumferential asymmetry between passages (observable for example in Figure 6.3) was accounted for in the profiles.

Profiles at $\dot{m}_{in} = 0.108$ kg/s and both levels of ϕ_{cav} are shown in Figure 6.29; similar profiles for $\dot{m}_{in} = 0.15$ kg/s are shown in Figure 6.30. The first general observation was that, in all four cases, the temperature at the inner diameter was nearly if not entirely equivalent to

that of the cold core air. Thus, none of the configurations were successful in migrating the hot gases fully inward. The second general observation was that all of the configurations had peak temperatures that were higher than the inner and outer wall temperatures except the rich RVC cases. In those instances, observed in the right-hand images of each figure, the average RVC profiles demonstrated unique behavior by actually increasing in temperature toward the OD to a point greater than their respective central peaks. The effects of total mass flow rate in general on the profiles were insubstantial in at the lean conditions but slightly more pronounce at the rich conditions. With the exception of the rich RVC case, all other CPD, CMB, and RVC profiles demonstrated reduced OD wall temperatures compared to the LLB baseline. The CMB case in particular created an average temperature difference of over 200 K at the outer wall. Such a difference is desirable as it implies a reduced wall cooling requirement at the given operating conditions. Furthermore, the CMB configuration accomplished the reduction in wall temperature without suffering from a reduction in peak temperature. That conclusion suggested that the reduced wall temperatures resulted from an improvement in the temperature distribution rather than a global reduction in combustion activity. Finally, both the RVC and CMB configurations were successful in accomplishing their primary goal of inducing inward-migration of the hot products. That success was evident by the shift of the temperatures peaks toward the ID as compared to the baseline. The LLB temperature peak occurred generally in the range of $0.6 < r/R < 0.75$, while the peaks of the RVC and CMB cases were found in the range of $0.3 < r/R < 0.4$.

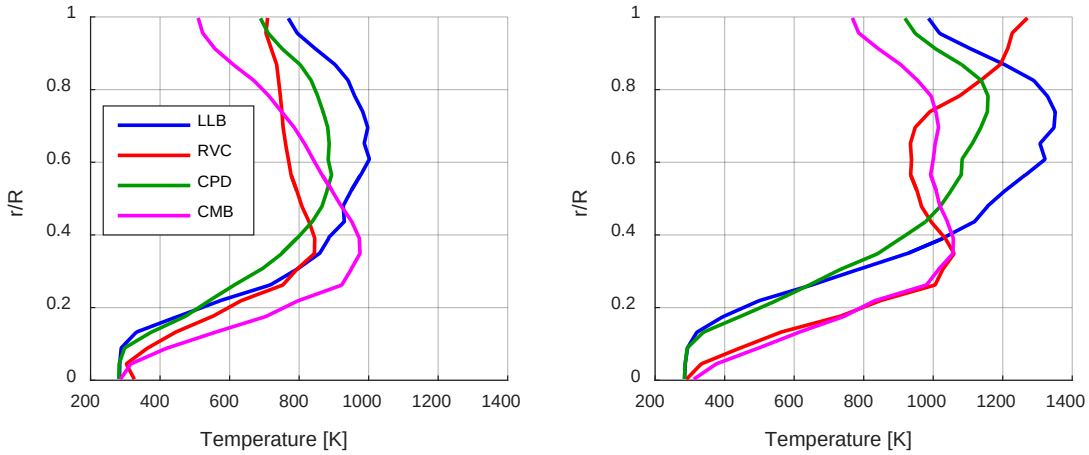

Figure 6.29: Radial temperature profiles for the all four geometries at $\dot{m}_{in} = 0.108$ kg/s and at lean (left) and rich (right) ϕ_{cav}

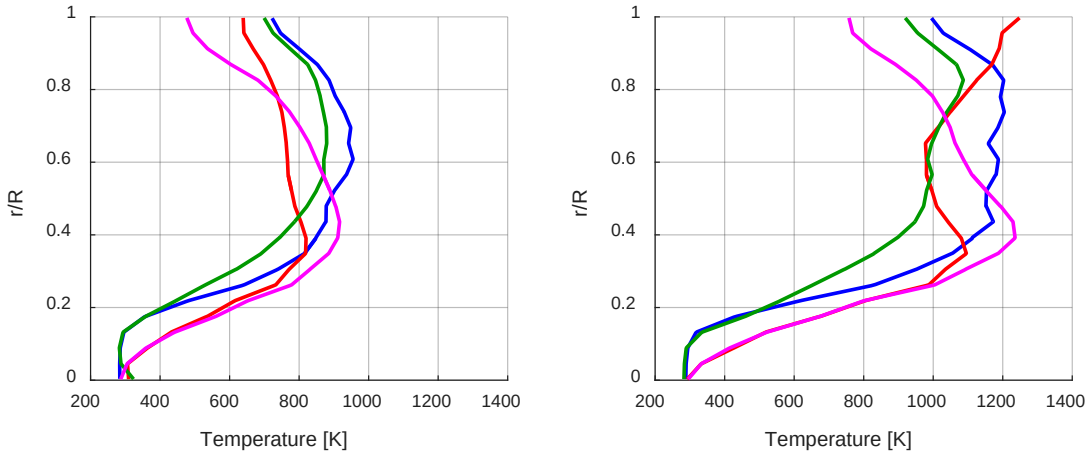

Figure 6.30: Radial temperature profiles for the all four geometries at $\dot{m}_{in} = 0.15$ kg/s and at lean (left) and rich (right) ϕ_{cav}

In all cases, the CPD profile shape was very similar to the LLB but at reduced temperatures. The differences at the lean condition were less than 100 K, however at the rich condition the delta was in excess of 200 K. The reason for this difference was alluded to in earlier discussion on the axial profiles of Figure 6.10 – the cavity design was most likely unable to facilitate the increased potential for heat release.

Values of the maximum and average temperatures along with estimated efficiencies (T_{avg}/AF_{ucc}) and computed pattern factors are given for all cases at $\dot{m}_{in} = 0.108$ kg/s in Table 6.7

and at $\dot{m}_{in}$ = 0.15 kg/s in Table 6.8. The first observation was that, as shown in Table 6.6, the pattern factor generally increased with increasing fuel flow except in the CMB case, which decreased in response to increasing ϕ_{cav} at both inlet flow rate conditions. The response of the pattern factor to $\dot{m}_{in}$ was less significant at low fuel flow and more pronounced at high fuel flow. At ϕ_{cav} = 1.37, increasing $\dot{m}_{in}$ led to decreased pattern factors in all configurations except the CMB case, which conversely increased.

The second observation was that the lowest pattern factor was found at the RVC-lean conditions. Referring back to Figure 6.29 and Figure 6.30, the low value for the pattern factor is a sensible result. The overall decrease in temperature is accompanied by a more substantial decrease in the peak temperature; thus the term $T_{max} - T_{avg}$ decreased in the RVC-lean case more than in any other. The result was a temperature profile that more closely matched a desirable shape; however it should be noted that the RVC case was shown in section 6.1.1 to be less desirable from a system perspective at low fuel flow due in part to its lower exit temperature. Notably, while the LLB and CPD profiles appeared nearly identical in the plots at lean conditions, their pattern factors were quite different due to (1) a slightly greater peak temperature and (2) a slightly lower average temperature in the LLB case as compared to the CPD. As expected after examining Figure 6.29, the rich case at $\dot{m}_{in}$ = 0.108 of the CMB design also yielded a low pattern factor as its value of $T_{max} - T_{avg}$ was lowest of that data set. That result was due to the effective "split" of the peak temperature into two local maxima as opposed to a single peak.

Finally, estimates of the relative combustion efficiency between the cases revealed that the lean LLB case at the moderate-flow rate of $\dot{m}_{in}$ = 0.108 generated the best performance with T_{avg}/AF_{ucc} = 0.86. The moderate-flow CPD case came in at a close second, while the RVC and the CMB cases were both somewhat further behind with T_{avg}/AF_{ucc} = 0.84. At lean conditions, the effect of increased mass flow appeared consisted of decreasing overall performance, while

the LLB continued to have the highest estimated efficiency. At rich conditions, however, the trend was more mixed; increased $\dot{m}_{in}$ led to increases in efficicney in the LLB, RVC, and CMB case but a slight decrease in the CPD case. However, at both levels of $\dot{m}_{in}$, the RVC geometry was the best performer at high ϕ_{cav}.

Table 6.7: Pattern factors for all geometry configurations at $\dot{m}_{in} = 0.108$ kg/s

Case	T_{max}	T_{avg}	T_{avg} / AF_{ucc}	Pattern	AF_{cav}	AF_{ucc}
LLB - Lean	1002	745	0.861	0.553	2043	865
RVC - Lean	845	725	0.838	0.271		
CPD - Lean	893	738	0.853	0.340		
CMB - Lean	975	723	0.836	0.569		
LLB - Rich	1351	865	0.740	0.832	2124	1169
RVC - Rich	1271	930	0.795	0.525		
CPD - Rich	1158	820	0.702	0.624		
CMB - Rich	1058	882	0.754	0.292		

Table 6.8: Pattern factors for all geometry configurations at $\dot{m}_{in} = 0.15$ kg/s

Case	T_{max}	T_{avg}	T_{avg} / AF_{ucc}	Pattern	AF_{cav}	AF_{ucc}
LLB - Lean	955	714	0.825	0.555	2043	865
RVC - Lean	820	701	0.811	0.282		
CPD - Lean	879	707	0.818	0.403		
CMB - Lean	916	693	0.801	0.542		
LLB - Rich	1204	876	0.750	0.549	2124	1169
RVC - Rich	1248	941	0.805	0.464		
CPD - Rich	1086	816	0.698	0.503		
CMB - Rich	1235	909	0.778	0.519		

The presence of peak temperatures exceeding AF_{ucc} – notably in the LLB-Rich case at $\dot{m}_{in} = 0.108$, indicated that some of the reactions in the HGV passage were continuing to progress at equivalence ratios between ϕ_{ucc} and ϕ_{cav}. However, the values of T_{avg} indicated that the majority of the reactions were either (1) occurring at or below ϕ_{ucc}, or (2) occurring at some value $\phi_{ucc} < \phi < \phi_{cav}$ before subsequently interacting with excess cold core air. The precise distribution of that equivalence ratio within the passages was difficult to quantify. Axial mass-

averaged profiles of local equivalence ratio are shown in Figure 6.31 for all four geometries at all four operating conditions. As illustrated in the axial and exit temperature CFD contours, the hot region occupies a fraction of the total passage area; the remainder is pure inlet air. Thus, the area-averaged values of ϕ were very low. Furthermore, the local ϕ was defined in the CFD on a cell-by-cell basis according to the local concentration of fuel (C_3H_8) and air; logically, equivalence ratios at the exit would be low as the vast majority of the fuel would have been consumed. However, as demonstrated by the temperature trends above and in the discussion of Section 6.1.1, heat release was still occurring and products were still forming; thus some fuel remained to perpetuate the combustion process. As for the profiles of Figure 6.31, trends were not discernable at either of the lean conditions. At the rich condition, the CPD profile was consistently greater than the LLB profile for both levels of $\dot{m}_{in}$, although the separation between the two was greater at $\dot{m}_{in} = 0.108$. The results from the RVC and CMB cases were mixed and inconclusive. Overall, any benefit of increased reaction rate that high-ϕ operation might provide would be offset by increased emissions as shown in Figure 6.10.

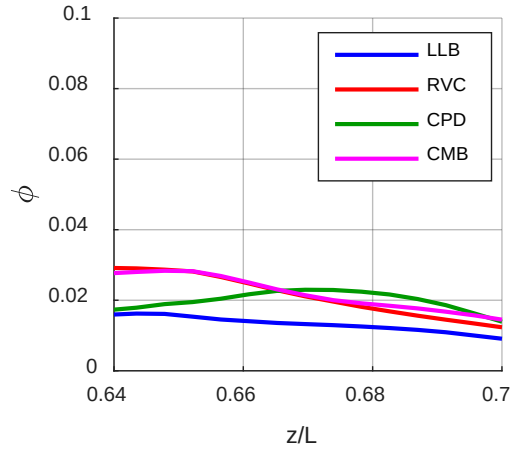

$\dot{m}_{in} = 0.108$, $\phi_{cav} = 0.8$

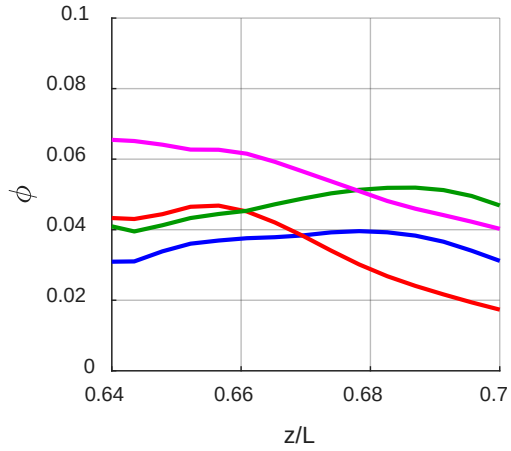

$\dot{m}_{in} = 0.108$, $\phi_{cav} = 1.3$

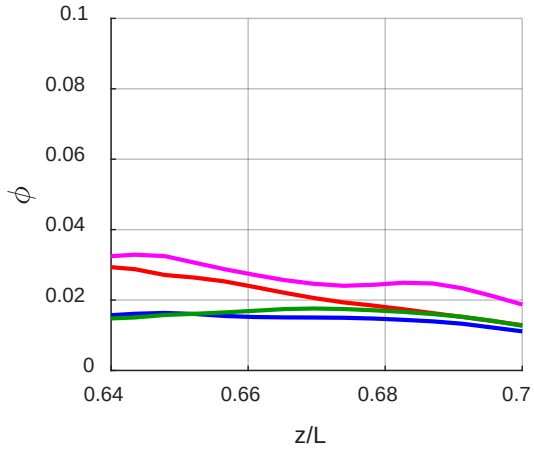

$\dot{m}_{in} = 0.15$, $\phi_{cav} = 0.8$

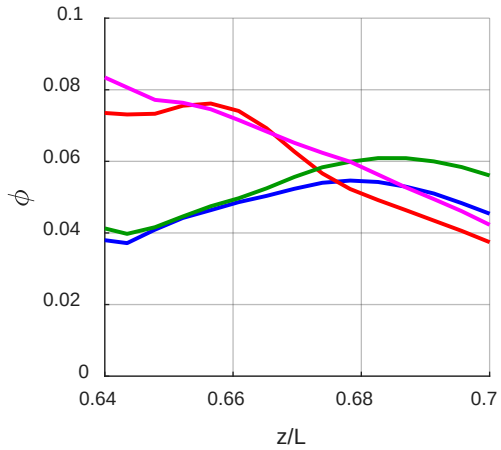

$\dot{m}_{in} = 0.15$, $\phi_{cav} = 1.3$

Figure 6.31: CFD axial profiles of mass-averaged local ϕ

In summary, of the four tested geometries, the RVC case did not appear to offer the desired benefit of producing a more desirable exit temperature distribution. While it did appear to increase mixing and circulation of the cavity products with the core flow, the end result remained non-uniform. The peak temperature was driven inward, but the hot products were not disbursed fully to the inner diameter. The CMB configuration appeared to gain the demonstrated benefits of the CPD case while also driving the peak temperature inward – and consequently reducing the outer wall temperatures. Upon examining the estimates of

efficiency, it was observed that, at low ϕ_{cav}, the baseline LLB design was most effective. At high ϕ_{cav}, however, the RVC design was shown to be the most effective of the four configurations. Peak efficiencies were realized at low $\dot{m}_{in}$ and low ϕ_{cav}; however it was also shown that, if high ϕ_{cav} was desired, then more efficiency was attained with high $\dot{m}_{in}$. Therefore, given all the accumulated evidence from this section, it was determined that the CMB configuration yielded the most desirable combination of features. Therefore, lacking any further analysis, it would be the best candidate to retain for future UCC testing.

Notably, in terms of estimated combustion efficiency alone, it appeared that the optimal operating conditions consisted of a lean cavity with the baseline LLB geometry. However, the problem was demonstrably more complex, particularly regarding the interaction between the cavity flow, the core flow, and the surface features of the HGV centerbody. The behaviors observed from the RVC were not well understood and it was therefore desired to undertake a more methodical analysis of the RVC and its design to better understand the parameters affecting flow migration and to make a more informed decision as to the next generation of HGV design. That trade study is the topic of the discussion in Section 6.2.

6.2. New Guide Vane Trade Analysis

The conclusion regarding the effect of the initial RVC design of Section 6.2 was that it had not performed as desired in terms of enhancing the distribution of the hot gas toward the inner and pressure-side walls of the HGV channels. Thus, to inform the next iteration of HGV design, a trade study was undertaken to discern which parameters of a vane cavity – or a vane in general – might yield the most desirable migration characteristics. Qualitatively, desirability was assessed by the distribution of the exit temperature within the defined exit plane; those designs that more evenly spread the temperatures across the entire area were judged superior. Quantitatively, the designs were assessed by (1) radial location of the peak temperature, (2) temperatures at the inner and outer walls, and (3) pattern factors. Preferred criteria were

considered as peak temperatures within the range of normalized radial height $0.25 \leq h/h_e \leq 0.75$, similar temperatures at the inner and outer walls, and relatively low pattern factor.

The design parameters of each case under consideration were presented in Table 3.4, which is reproduced below for reference. The reader may reference Section 3.3.4 for further details about parameter definitions and geometry illustrations. The operating conditions were held constant at $\dot{m}_{in} = 0.150$ kg/s and $\phi_{cav} = 0.75$; these choices were made due to the relative stability of the solutions. (While the results in this section are computational, it was also true that lean ϕ_{cav} was more stable experimentally.)

Table 3.4: Trade study cases and parameters

Case ID	Description	Parameters					Levels	
		B	E	Ca	Count		0	1
1	Smooth Vane	n/a				B/W	0.5	1
2	Baseline RVC	0	0	0	0	E/W	1.15	2.34
3	Full Cavity Span	1	0	0	0	Ca/W	0.46	0
4	Axially Extended	1	1	0	0	Count	1	2
5	Back Step Only	1	0	1	0			
6	Dual Back Steps	1	0	1	1			
7	Cresent	n/a						
8	Cut	n/a						

Analysis techniques of the prior two sections were employed in concert to assess the various geometries. In Figure 6.32, axial mass-averaged profiles of temperature and product formation rates are given for the length of the UCC, while mass-averaged profiles of UHC emissions are given for the HGV passage near the exit plane.

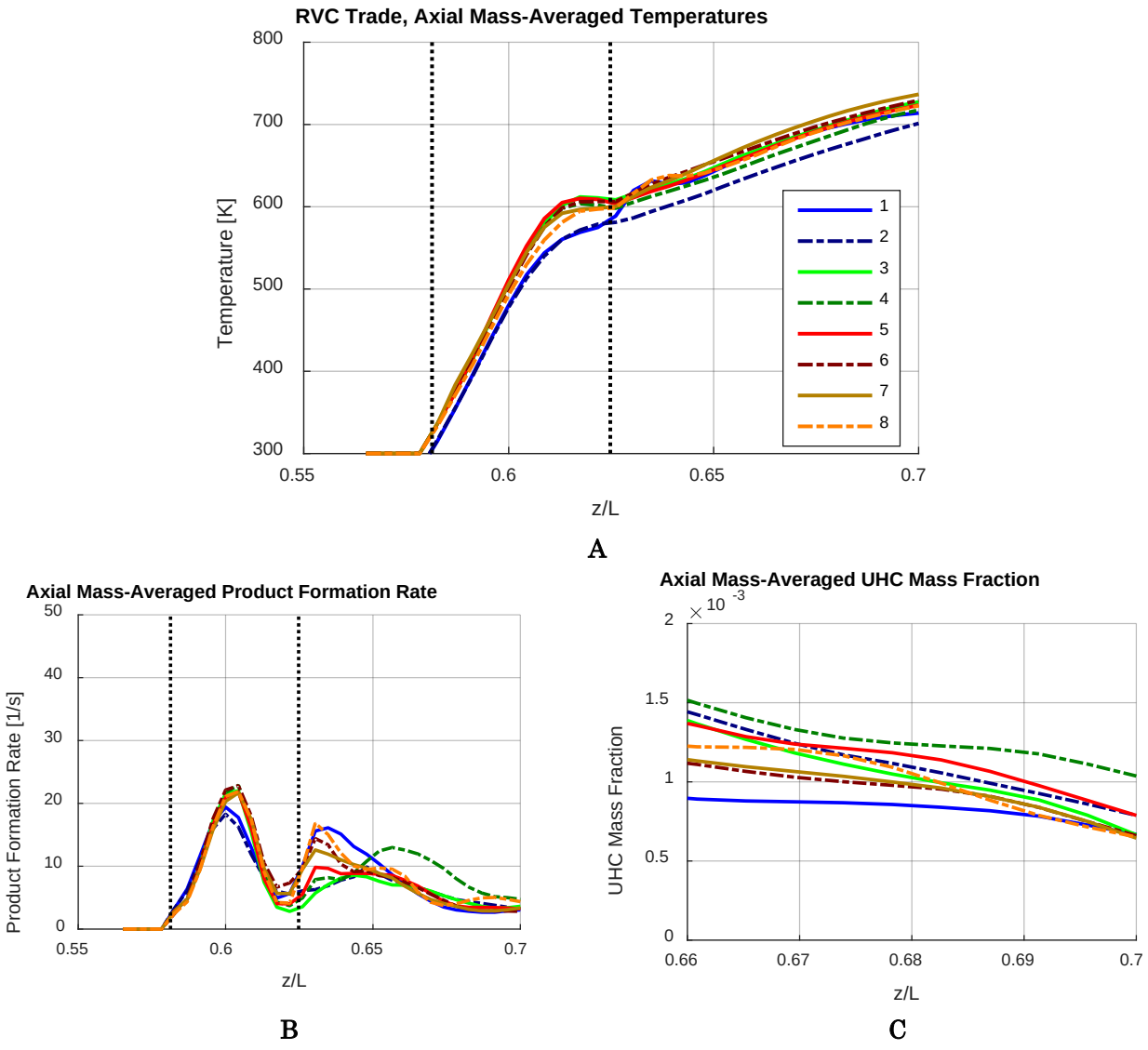

Figure 6.32: HGV trade study – CFD axial profiles of various quantities

The temperature trends indicated close correspondence among all of the modified geometries; the only substantial deviation is in Case 2 with the original RVC design presented in Section 6.1, which demonstrated, on average, lower temperatures than all the other cases. The explanation for that trend echoes the discussion from the prior section: examining the product formation rate reveals that Case 2 also demonstrated the lowest product formation and thus experienced the least amount of complete combustion. The "quenching" hypothesis was

again cited as the phenomena driving that behavior. The remaining RVC variants (Cases 3-6) were less affected as observed in both the temperatures and the product formation. Case 4 demonstrated concentrations of UHC that were relatively higher than the others; however, the overall range of the UHC values between all cases was only ~4e-4, which did not provide strong evidence for any definitive conclusions.

The cavity was also examined via circumferentially-averaged radial profiles of Temperature and g-load as presented in Figure 6.33 and Figure 6.34, respectively. Similar to the discussion in Section 6.1, minimal distinctions were present at the forward and center axial locations (the top and middle rows of figures, respectively). The primary differences were found at the aft location. The baseline Case 1 again demonstrated a continuous temperature increase toward the bottom of the circumferential cavity (CC), while all other cases with modified vane surfaces instead resulted in temperature decreases. The nature of those decreases was slightly different among each of the modified cases in terms of where the temperature peak settled and how low the temperature became at the inner diameter. The case with the highest peak and subsequently lowest inner temperature was Case 2 – the Gilbert RVC design – which peaked at a normalized radial height of 0.6. All other cases shifted the peak down to a height of about 0.2; the similarity of the shift between those cases was likely due to the fact that their respective surface modifications were performed across the entire axial span of the cavity. In contrast, the Case 2 cavity only occupied the aft half of the axial span. The case that most closely followed the baseline Case 1 profile was Case 8 – the "cut." This was due to the fact that the suction-side HGV surfaces were left unmodified; a temperature decrease was still present, however, due again to the increased volume. Finally, in terms of cavity g-load, no trends were observed that might influence design decisions.

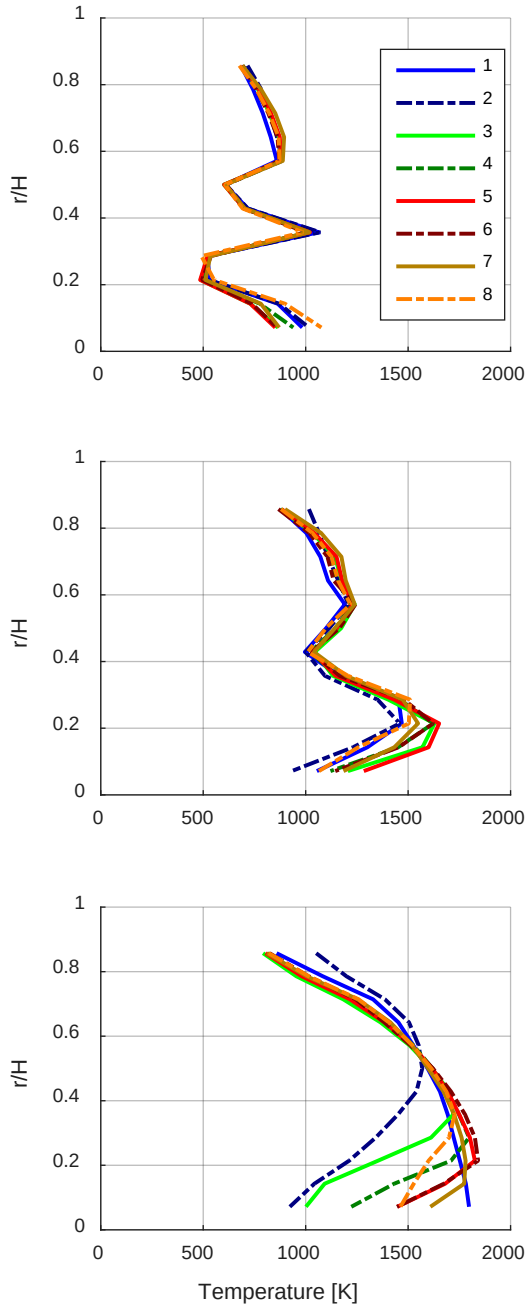

Figure 6.33: HGV trade study – CFD cavity temperatures at axial cuts C1 C2 C3

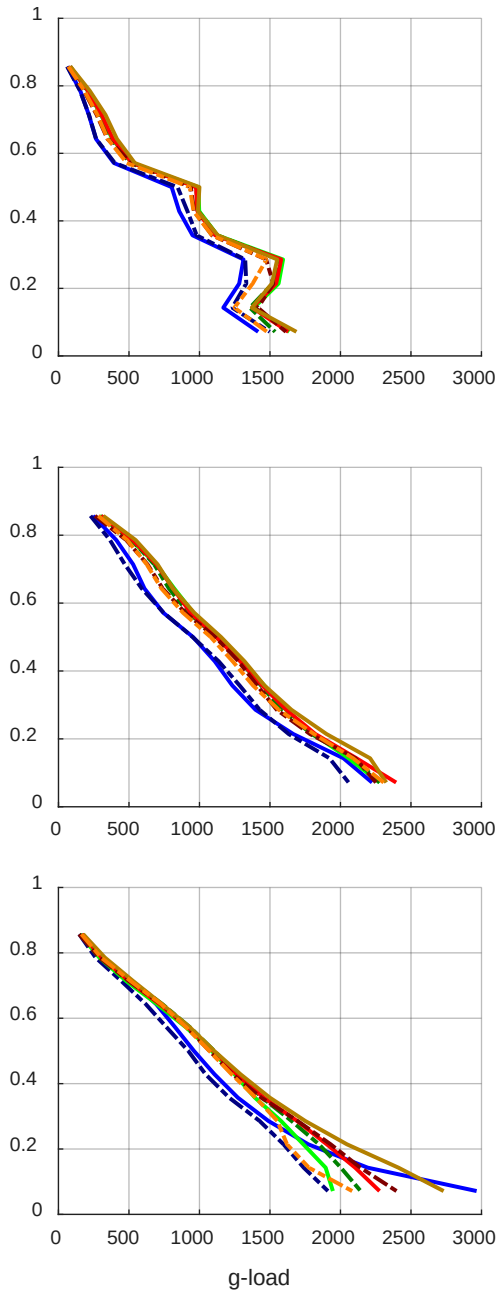

Figure 6.34: HGV trade study – CFD cavity g-load at axial cuts C1 C2 C3

A complete appreciation for the geometry effects was provided through examination of the temperature contours at the five axial reference positions for each case. Temperature contours for Cases one through four are shown in Figure 6.35, and five through eight are shown

in Figure 6.36. In all cases, in line with previous conclusions, the effects at the front of the cavity – location C1 – are negligible. Two minor exceptions were observed in Cases 7 and 8: the suction-side "crescent" and the pressure-side "cut", respectively, were both visible at location C1 and were both beginning to entrain hot flow. At location C2, all remaining suction-side surface modifications were visible, and all features began entraining hot flow from the cavity. Notably, the high-temperature "band" occupying the inner diameter in all cases appeared comparatively hotter in Cases 3-8. Returning to the center image of Figure 6.33 in the previous discussion that conclusion was quantitatively affirmed. The temperature peaks at the cavity midpoint occurred at $r/H = 0.21$; the bottom three values at that location were observed in Cases 2, 1, and 8 at 1460, 1470, and 1500 K, respectively. The maximum temperature was found in Case 5 at 1650 K while Cases 6 and 3 were very close. The common factor was again the presence of the surface features throughout the CC axial span as compared to the partial-span of Case 2 and the lack of features in Case 1.

The precise mechanism driving the hotter temperatures was hypothesized to be enhanced intermediate heat release through increased exposure to and mixing with entrained core flow within the surface features. At position C3 in Figure 6.35, the induced circulation within the HGV passages was visible in Cases 2 through 7 as streaks of hot gasses within the inner HGV passage. In Case 8, cold flow began to appear within the edge cut, replacing the hot contours that had been observed at location C2. Thus, the influence of the cut upon the CC migration flow appeared to diminish as it served instead to entrain excess cold core flow.

At locations D1 and D2, the flow patterns of Cases 1 and 8 became fairly similar. As the cut did not influence the migration of the hottest regions at the aft of the cavity, the behavior within the HGV passages reverted back to the baseline characteristics. Cases 3, 5, and 6 most successfully encouraged flow migration to the HGV inner diameter. However Case 7 most effectively disbursed the hot products across the circumferential span of the HGV passage. Notably, the hot gas was guided primarily within the region of the crescent cutout – it was

hypothesized that extending the cut completely to the inner diameter would improve the radial distribution as well. Finally, of all the cases, Case 6 appeared to fill the largest relative area of the cut at D2 with the lowest-temperature gas distribution.

Focusing on the exit plane in Figure 6.37, similar conclusions were drawn. Case 8 became similar to Case 1; Cases 3, 5, and 6 nearly reached the inner diameter; Case 7 disbursed the hot products most completely between the suction side and pressure side of the HGV passage; and Case 6 occupied the greatest overall proportion of the exit area. The most promising cases for further iteration were therefore determined to be Cases 6 and 7. While Cases 3, 5, and 6 performed similarly in the results presented here, operational experience with Case 2 revealed substantial material fatigue due to high temperatures on the front-facing step. Thus, if equivalent performance can be obtained without that step, then Cases 5 and 6 were considered better choices, and Case 6 outperformed Case 5 in terms of even distribution of the hot gases. The results of Case 7 were intriguing due to the relative magnitude of its lateral distribution between the suction and pressure side walls. Before committing to the Case 7 design, however, additional CFD would be required on a variation with the crescent cut all the way to the inner diameter in order to evaluate whether it could bring more products radially inward.

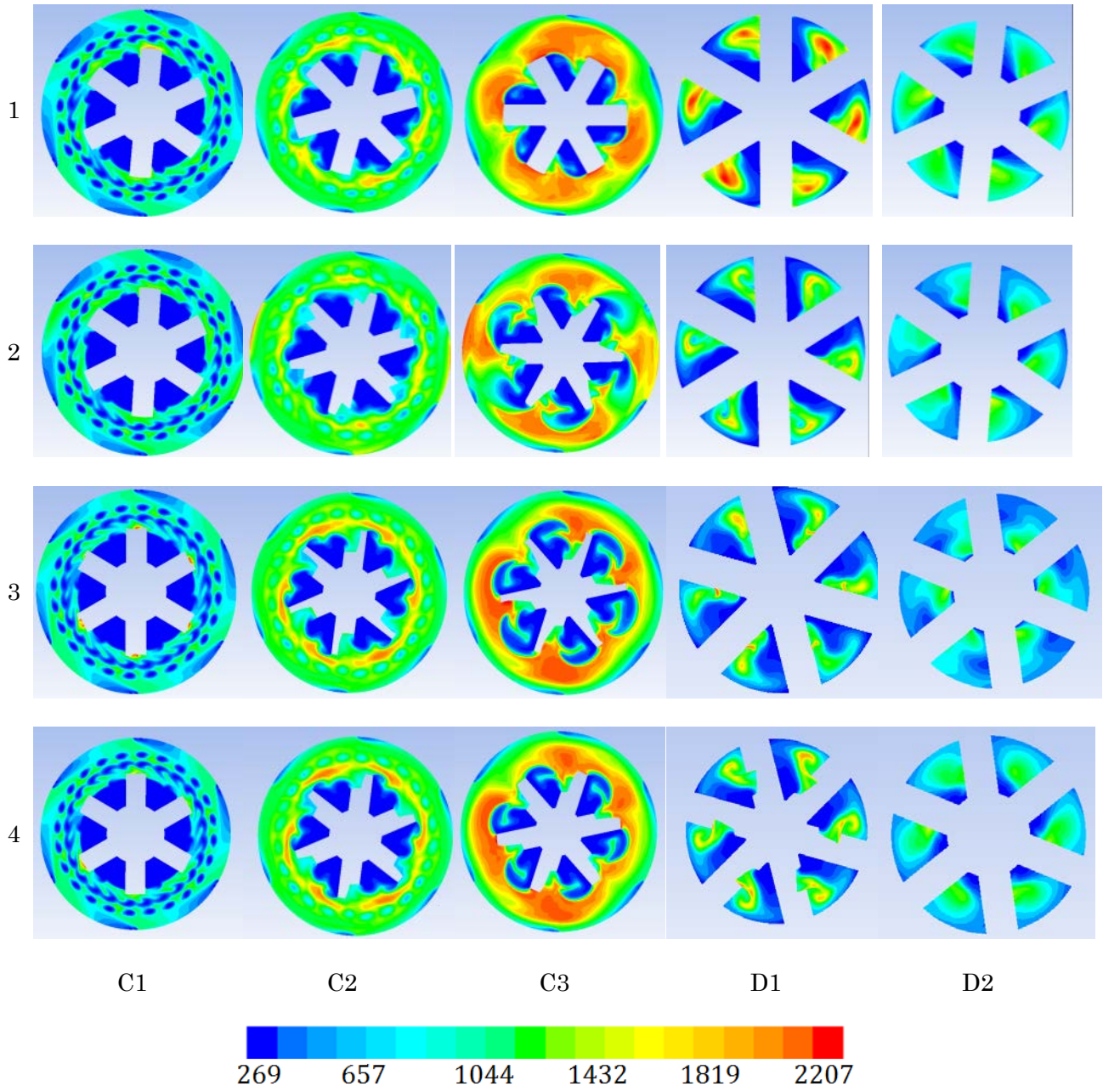

Figure 6.35: HGV trade study: CFD cavity and passage temperature contours, Cases one through four

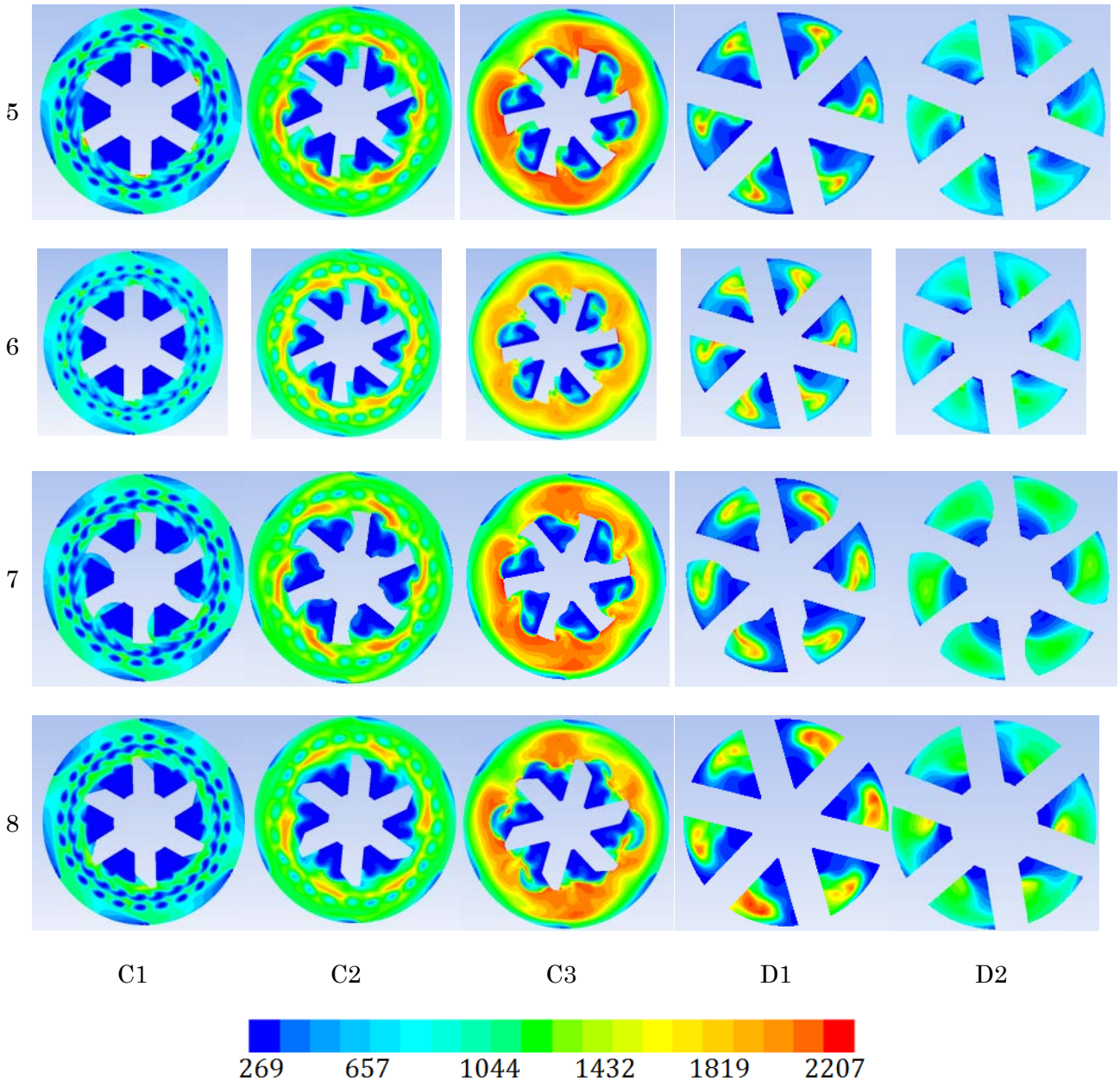

Figure 6.36: HGV trade study: CFD cavity and passage temperature contours, Cases five through eight

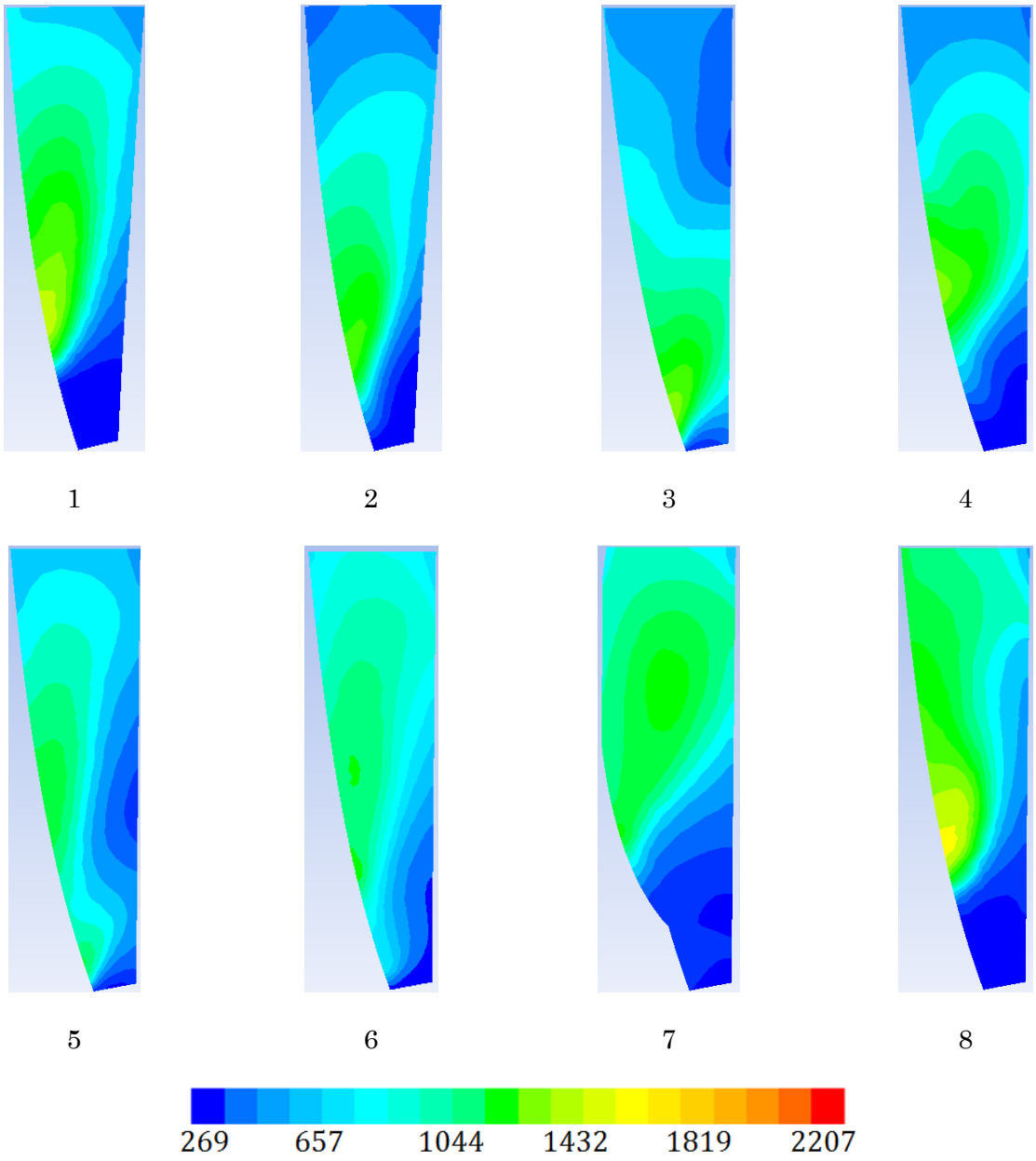

Figure 6.37: HGV trade study: CFD exit plane temperature contours

Adiabatic wall temperatures were also analyzed for these geometries as represented by Figure 6.38. All three cases with forward-facing cavity components – Cases 2, 3, and 4 – demonstrated similar propensity to capture the aft cavity hot spot and disburse it back into the bulk core. Similarly, all forward-facing cavities channeled the hot gases to a point roughly centered within their respective channels. In Case 3, that led to inward-migration that was more substantial than any other geometry; that was likely due to its effective capture of both

fore and aft cavity hot spots and subsequent delivery to the core at an early axial location. In contrast, while the outboard-facing geometry of Case 4 was identical to Case 3, its transition back to the core was more gradual due to its increased axial extent. Thus, while its termination points were at identical radial heights to Case 3, it was more strongly influenced by the core flow. Both Case 5 and Case 6 eschewed the front-facing step, and consequently they bore some resemblance to Case 1 in that the aft cavity hot spot attached to the vane suction side. In both cases, however, the edge of the radial cavity prevented those hot gases from entrenching in the outer corner of the HGV passage, and they were instead directed along the radial center of the vane surface. The "dual-mode" characteristic of Case 5 was observed to take shape shortly downstream of the radial cavity termination point, and was likely the result of an incomplete merger of the migrating gases from the fore- and aft-cavity hot spots. In contrast, those two migration patterns merged completely in Case 1 as well as Case 6. Case 7 demonstrated a similar ability to funnel the hot gases away from the outer corners. Case 8 was somewhat similar to Case 1 albeit with reduced suction-side temperatures. The pressure-side of Case 8 is not shown as it did not reveal any substantial pressure-side flow migration; indeed, the pressure-side cut of Case 8 was entirely at ambient temperatures, indicating that any cavity flow with which it interacted separated rather than following its guide. In all cases except for Case 1 and Case 8, the vane geometry demonstrated the important ability to preclude hot-gas attachment in the outer HGV passage corners. That result will be important when HGV cooling becomes a parameter of interest.

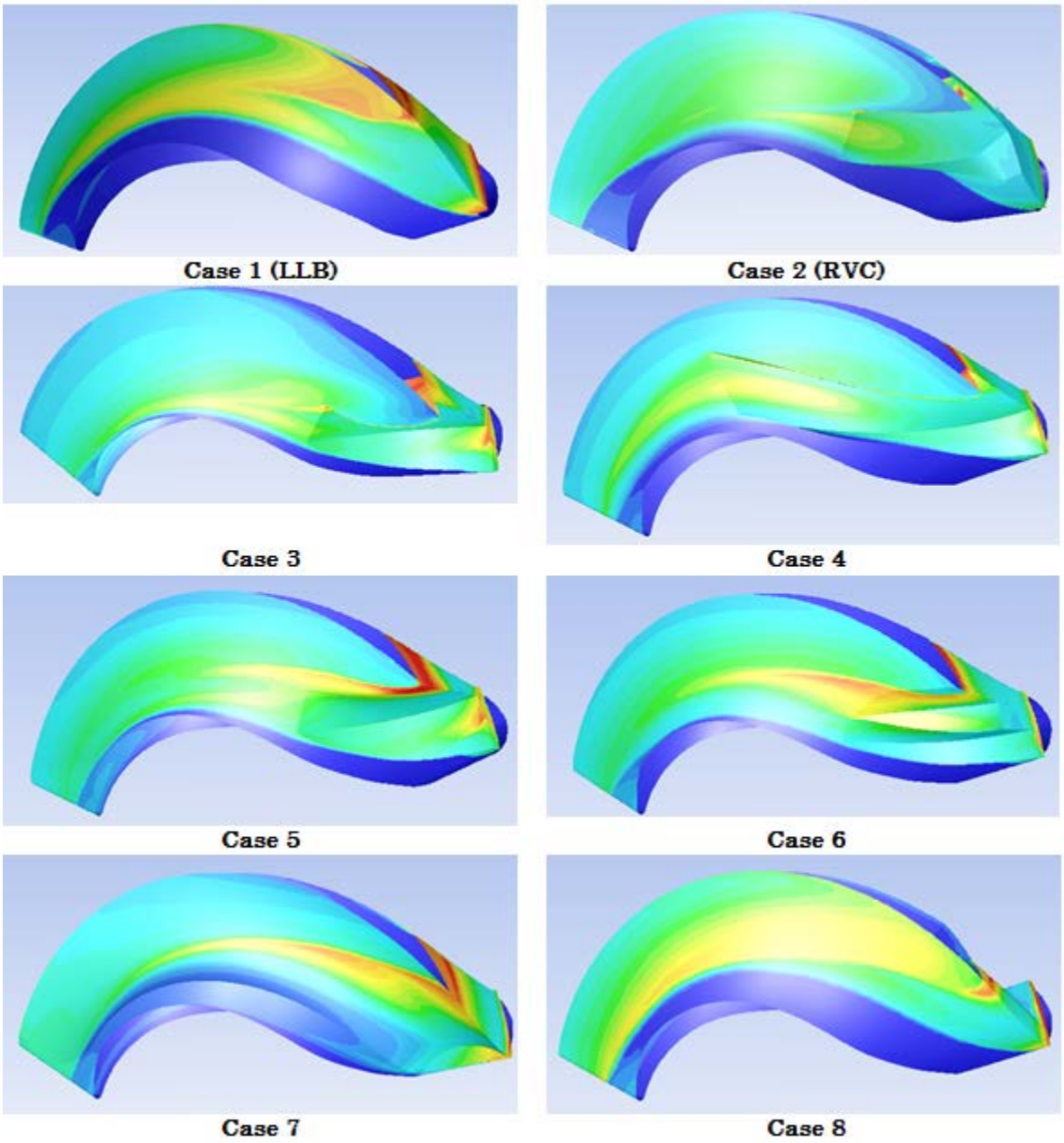

Figure 6.38: CFD wall temperatures for HGV trade study candidates

As in the previous section, quantitative analyses were facilitated by exit temperature profiles. The variations between cases were examined systematically in the following figures. The comparison between the baseline LLB (Case 1) and the initial RVC (Case 2) was examined in Section 6.1.3.2 but is repeated in Figure 6.39. The net effects were (1) a reduction in the radial location of the temperature peak from 60% to about 35% of the passage height, (2) an

overall reduction in the exit temperature, and (3) a decrease in the OD temperature of about 110 K. Changing from Case 2 to Case 3 involved changing the cavity axial width parameter B from 0.5 to 1.0. As seen in Figure 6.39, the result was further reduction of the radial height of the temperature peak from 35% to 20%. Notably, that shift was sufficient to begin influencing the cold flow at the ID by raising the temperature there by about 75 K. Furthermore, the peak temperature increased by over 100 K. Additionally, the average of the temperature profiles of Cases 1, 2, and 3 were 738, 679, and 738. While practically identical on the average, Cases 1 and 3 differed significantly in the magnitude and location of the temperature peak. Case 3 also demonstrated more significant gradients surrounding the peak, due in large part to the presence of a local temperature minimum at about 70% of the radial height. Case 3 also decreased the OD temperature below that of Case 2.

In Figure 6.40, Cases 4, 5, and 6 are compared. Case 4 maintained the parameter $B = 1.0$ as in Case 3 while increasing the axial extent variable ξ from 1.15 to 2.34 – approximately doubling its overall axial length. The result took a shape more resembling Case 1 although the location of the peak temperature was nearly at 50% height. That similarity was counter-intuitive given that Case 4 is geometrically more similar to Case 3 – however the profile results of Case 4 demonstrated a dramatic change from Case 3. Increasing the parameter ξ appeared to influence the location of the peak temperature radially outboard versus the inboard influence of increasing B. Case 5 was identical to Case 3 except the front-facing step was removed as expressed by the value of the variable C_a. Case 5 demonstrated a unique bimodal pattern with local maxima at 15% and 90% of the radial height. That dispersion of the hot gases led to increased temperatures at the ID and similar temperatures at the OD as compared to the baseline Case 1. Case 6 expanded on the Case 5 design by adding a second backward-facing stepped cavity; the results were similar ID/OD temperatures but with a smoother profile shape. A hint of a secondary temperature peak was observed at about 10% height, however it was not sufficient to classify as a true local maximum.

The curves in Figure 6.41 compare the baseline LLB case against the two variations that were not described by the standard RVC design parameters: the suction-side "crescent" (Case 7) and the large pressure-side cut (Case 8). Case 7 appeared to generate comparatively higher temperatures at the OD, ID, and peak; however, its profile intersected the baseline curve at 60% height leading to lower temperature in the range from 60% to 20%. Case 8 also demonstrated comparatively lower temperatures; however, two local temperature maxima were generated. The dual maxima did not appear to bear resemblance to those induced by Case 5.

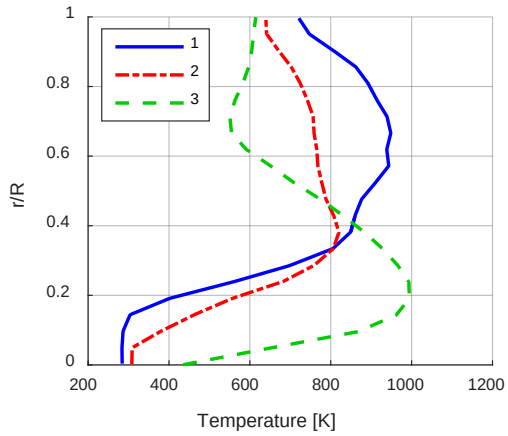

Figure 6.39: HGV trade study, comparing Cases 1-3

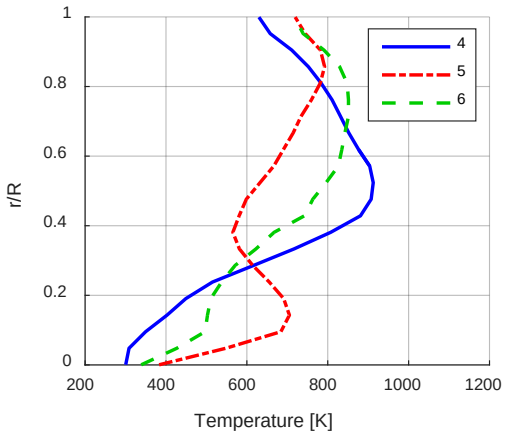

Figure 6.40: HGV trade study, comparing Cases 4-6

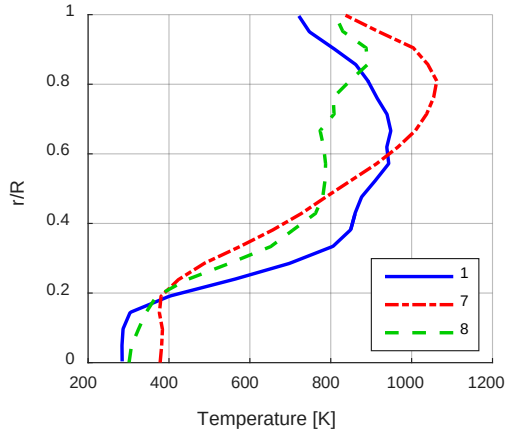

Figure 6.41: HGV trade study, comparing Cases 1, 7, and 8

Table 6.9: HGV trade study temperatures and pattern factors

Case ID	T_{max}	T_{avg}	Pattern
1	948	738	0.481
2	820	679	0.372
3	995	738	0.587
4	912	697	0.545
5	792	672	0.323
6	851	697	0.389
7	1062	748	0.701
8	891	669	0.602

The temperatures and pattern factors were computed from the radial profiles and presented in Table 6.9. The highest and lowest profile maximum temperatures appeared in Cases 7 (the crescent) and 5 (back-facing step only), respectively. Cases 5 and 6 demonstrated the lowest values of profile pattern factor; both were variations on the "backward-step-only" concept. The low pattern factors were due to the effective "splitting" of their temperature peaks into two comparatively lower local maxima, thereby reducing the numerator term $T_{max} - T_{avg}$ significantly. The highest pattern factor was found to be in Case 7 due to its high peak temperature.

To complete the trade-study, the mass-averaged temperatures at the exit (as in Figure 6.32) were compared against the theoretical adiabatic flame temperature as was done in Section 6.1. Based on an overall value of $\phi_{ucc} = 0.20$, the calculated efficiencies at the exit plane all fell within a range of $85\% < \eta < 87\%$. The highest and second-highest efficiency values were observed in Cases 7 and 6, respectively, while Case 2 demonstrated the lowest efficiency.

Table 6.10: HGV trade study efficiency estimates

ϕ_{cav}	ϕ_{ucc}	AF_{ucc}	Case	T_{ma}	η_{ma}
0.75	0.20	845	1	714.0	0.845
			2	701.3	0.830
			3	727.4	0.861
			4	717.5	0.849
			5	723.5	0.856
			6	729.4	0.863
			7	736.7	0.872
			8	722.8	0.855

The accumulated evidence of this section provides a wide variety of perspectives on the conditions at the HGV exit plane. Based on the a combination of qualitative temperature contour examination and quantitative pattern factor and efficiency calculations, Case 6 appeared to be the best of the tested designs. It presented the smoothest transition from OD to ID in terms of the temperature profile, avoiding the high peaks of other cases while maintaining

a relatively high average temperature. That resulted in a pattern factor that approached industry-standard values, thus making the design appealing from the perspective of the receiving high-pressure turbine (HPT) rotor. The high temperature also led to the second-highest efficiency estimate; the highest efficiency design – Case 7 – was subject to stronger gradients and consequently had the highest pattern factor, therefore making it overall less desirable. Finally, the temperature contours demonstrated that Case 6 had the ability to fill in the outer corner of the exit plane while also promoting radial dispersion nearly all the way to the ID, thus making the best use of the available exit area.

6.3. Chapter 6 Summary

The goal of this chapter was the accomplishment of research Objective 3: to investigate the parameters that influence and promote hot gas migration in to the core flow to enable control over the exit temperature profiles. The primary response variable of interest was the temperature; ultimately, the distribution of the temperature at the exit of a combustor can provide much information about its performance as a whole. The CFD model also permitted the examination of a variety of other parameters throughout the UCC system as they responded to various conditions.

6.3.1. Responses to Geometry Configuration Changes

The first investigation consisted of the evaluation of four major configuration changes: the baseline (Case LLB), the employment of compound-angle air drivers (Case CPD), the employment of a radial vane cavity (Case RVC), and the combination of both the new air drivers and the radial cavity (Case CMB). The RVC case had a complicated effect on the flow patterns characterized primarily by lower temperatures that were induced, in turn, with more aggressive mixing between the migrating cavity air and the cold core air. Stream traces were used to identify an additional vortex structure that formed as a result of interaction with the front-

facing step; this structure had the effect of stretching the high-temperature regions across the HGV passage lateral span, thereby increasing the surface area contact with the surrounding cold core flow. In lean cases the result of that behavior appeared to be premature quenching of the combustion process, but in rich cases the RVC induced significant levels of burning within the HGV passage in excess of the baseline case. It was not successful, however, in disbursing the hot products all the way to the inner diameter as was desired. The CPD case demonstrated more effective distribution of the cavity fuel by inducing more inlet air up into the cavity outer volume. The result was increased uniformity to the fuel stream traces and reduced thickness of the outer fuel-rich layer.

6.3.2. Exit Temperature Analysis

Specific focus was given to the temperature distribution at the exit plane. Experimental measurements were taken using the TFP technique, however due installation issues, the results were challenging to interpret. Overall the trends of the TFP measurements were in poor agreement with their corresponding CFD predictions. In general, the CFD results tended to under-predict the experimental measurements at the guide vane pressure-side wall while over-predicting at the suction-side. Notably, the CFD predicted that the highest-temperature regions would occur on the suction-side wall. However it was in that region, likely for that very reason, that the TFP measurements were unable to collect data. The CFD exit temperature profiles were examined in detail with regard to the four geometry configurations and it was shown that the CMB case resulted in a temperature distribution that was most desirable.

6.3.3. New Guide Vane Trade Study

As the original RVC case did not distribute the hot products radially inward as was initially desired, a CFD trade study was undertaken to examine a variety of surface feature modifications to the guide vane airfoils. Extending the opening of the radial-vane cavity concept so that it spanned the entire cavity – versus just half in the RVC design – demonstrated some

notable improvement in terms of inward-flow migration. Furthermore, radial cavity designs incorporating just a back-facing step performed well in terms of both radial and lateral hot gas distribution. A novel "crescent" concept was found to perform very well in terms of lateral distribution although it failed to distribute the products as well to the inner diameter. The final conclusion of the study was to that a dual-backward-step concept (Case 6) demonstrated the most desirable temperature distribution as manifested by the temperature contours, profiles, pattern factors, and efficiency estimates. That conclusion prompted the selection of the Case 6 design for production. As of this writing, the hardware has been received and is scheduled for experimental evaluation.

VII. Conclusion

In conclusion, this document presented investigations into the accomplishment of three research objectives:

1. Develop the aerodynamic mechanisms to deliver the proper air and fuel to the high-g cavity from a common flow source.
2. Determine the effects of the complex flow environment on flame dynamics within the high-g combustion cavity.
3. Investigate the parameters that influence and promote hot gas migration into the core flow to enable control over the exit temperature profiles

7.1. Common-Source Flow Delivery

To accomplish this objective, this program documented the first operational experience with the AFIT UCC configured with a common upstream flow source. Numerous challenges were met and resolved by way of computational and experimental analysis. The aerodynamic performance of the common-source flow diffuser was evaluated in terms of its ability to affect the required mass flow split between the core and cavity paths. A channel restrictor plate was designed to offset the observed pressure imbalance with the result of successful achievement of on-design operating conditions. A hypothesis with respect to channel orientation was developed and proven numerically; a configuration with the channel openings centered over the guide vane leading edges was demonstrated to have desirable effects on the migration patterns of the circumferential cavity products. Cavity residence times were evaluated; in the proposed optimal configuration they were found to reach 5.6 ms, which was an improvement over the baseline value of 2.8 ms.

7.2. High-G Combustion Cavity Flame Dynamics

Understanding the dynamics of the circumferential cavity (CC) was central to the research program. As a crucial first step, the lessons learned while accomplishing Objective 1 were translated into improved "v3" hardware to facilitate continued study of Objectives 2 and 3. The results were markedly superior in terms of cavity fuel circulation and resulting residence time; the predicted temperature and velocity fields were correspondingly more uniform. CC velocity characteristics were experimentally evaluated by way of PIV and PSEV measurements in concert with numerical analyses. Those results led to detailed analyses and discussion of the cavity residence time and g-loading. In the former, residence times were estimated to range up to 11 ms, representing a two-fold increase over the "v2" hardware. In the latter, the cavity g-load was demonstrated to be more sensitive to inlet mass flow than to cavity equivalence ratio. However, equivalence ratio – and therefore the fuel flow rate – was demonstrated to impact the cavity velocity in such a way that increased fuel flow cause a decrease in velocity. The theory for this interaction was that the perpendicular fuel jets contributed momentum to the flow that interrupted the larger circumferential motion, albeit slightly. Furthermore, it was revealed that, at the demonstrated operating conditions, the UCC cavity might not attain sufficient flow velocity to reach the threshold at which the influence of centrifugal loading might be observed.

To understand the characteristics of the CC flame fronts, the complementary measurement tools of LIBS and TFP were employed to evaluate the local equivalence ratio and profiles of temperature, respectively. The results included (1) substantial non-uniform temporal variation indicated by both measurements, and (2) substantial spatial gradients in both temperature and equivalence ratio predicted by the numerical solution. One important conclusion was that the cavity appeared to operate in two distinct zones: the volume above the air driver jets acted much as would be expected of a primary combustion zone with low temperatures and relatively rich local fuel concentrations. Interaction with the air drivers,

however, led to very complex behaviors while burning continued inward. Below the air drivers, and in the aft of the cavity where the influence of the air drivers was negligible, the highest-temperature regions were anchored in regions of correspondingly very low equivalence ratio. Thus, the combustion that continued in the cavity inner volume did so at very lean conditions as it began to migrate into the combustion cavity. It was shown that the temperatures at the aft of the cavity increased steadily for the LLB and CPD geometry configuration, whereas they peaked and then suddenly decreased in the RVC and CMB configurations.

7.3. Hot Gas Migration

In the study of the process of hot gas migration from the CC through the remainder of the system, the influence of the four major geometry configurations was again evaluated on the basis of computational axial profiles and the combination of computational and experimental analyses of the exit temperatures. Numerically, the temperature was evaluated as were the product formation rate and select pollutant species. The tendency of the RVC and CMB cases to produce cooler temperatures was reaffirmed in the cases of lean cavity equivalence ratios. However, at rich cavity equivalence ratios, the RVC and CMB cases were shown to induce a dramatic resurgence of reactions within the HGV passages as evidenced by increases in temperature, product formation rate, and emissions at the exit. While the intent of the RVC concept was to ultimately encourage more hot gas to migrate inward, the exit temperature contours and profiles indicated that it was unsuccessful at doing so, while also inducing undesirably large gradients between the temperature peak and the walls. In the rich case, the RVC configuration caused a temperature spike at the outer wall. While the CPD case was observed to improve the distribution of flow within the cavity, its influence on the remainder of the system was muted. However, in the CMB case, the incorporation of the CPD and RVC geometries together had the desirable effect of inducing the most uniform temperature profile of the four cases. Lateral profiles of temperature as measured by TFP were examined for similar

trends, although many experimental difficulties were encountered in the process. Thus, while some of the radial gradients were captured, the TFP measurements were unable to validate the presence of the peak temperature regions on the suction-side wall.

A trade study was undertaken to examine the effects of RVC-like geometries in more detail and to discern whether or not the relevant parameters could be adjusted to attain an even distribution of the hot products at the UCC exit. Improvements over the original RVC design were realized by increasing the cavity size, increasing its axial extent, and most of all by removing the front-facing step. By the criteria of exit plane temperature distribution, the most promising radial cavity design involved dual backward-facing cavities. That design was subsequently produced and schedule for experimental evaluation.

7.4. Recommendations for Future Work

The work embodied in this document represents substantial increases in the understanding of high-g combustor dynamics. This final section will outline three major recommendations that future UCC researchers are strongly encouraged to implement into their own programs. The author would go so far as to say that high-g combustion as a science may not progress without undertaking these three foundational tasks.

7.4.1. Improve Control and Measurement of the CFF

Pursuit of the first objective of this current research revealed many fundamental shortcomings to the existing inlet flow diffusion hardware. Most importantly, as demonstrated by the reacting flow results, it appeared that the CFF became sensitive to operating conditions. Therefore, in order to properly execute any future experiments with the AFIT UCC, the CFF needs to be measured reliably. Existing probe arrangements were suitable for coarse analyses, but proven, accurate, real-time feedback on the mass flow split within the UCC needs to be

designed and implemented. Furthermore, while the λ parameter was shown to be effective in controlling CFF, its execution in the form of discrete pieces of hardware was inflexible. Dynamic control of the flow through the inlet diffuser must be accomplished in order to operate in concert with the already-recommended dynamic feedback on the CFF variable. The end result will likely be analogous to adjusting the fuel mixture and propeller pitch in modern aircraft: different operating conditions will require different control set points in order to operate efficiently.

7.4.2. Develop and Refine Transient Analyses

Even without the experimental validation, the instability in the UCC was evident. Observers of test events often noted flickering flames from the exit plane, especially at fuel-rich set points. Strong acoustic modes were also present at all conditions, although their strength similarly increased with fuel flow. The experimental TFP and LIBS measurements confirmed this in no uncertain terms. Thus, the use of a RANS computational model is insufficient to fully account for the real-world behaviors. An exploration must be made of transient model options for the AFIT UCC. The computational grid will require significant refinement; resulting case sizes will be very large, however a re-look at periodic boundaries would also likely meet with success. Additionally, numerous modern adaptive-grid programs exist beyond those available in the current AFIT grid and flow solvers; it is possible that AFIT research would benefit from pursuit of modeling alternatives. The existing experimental data sets are prime candidates for evaluation against various unsteady solver schemes and grid strategies.

7.4.3. Understand Effects of Centrifugal Loading

The "g-effect" was one hopeful goal of this research program; however, as even outside researchers such as Briones [25] have found, the reality of centrifugally-loaded combustion systems is much more complex than Lewis may have realized. The task remains: the influence of centrifugal loading upon combustion dynamics must be isolated from the myriad other field

parameters that also serve to influence the development and completion of reactions. The task is itself one of fundamental physics, and therefore likely cannot be accomplished on the UCC test rig alone. The Lapsa and Dahm [57] experiment was a very promising approach, although to this author's knowledge they have not yet proceeded with any of the other variations that would be required: i.e., variations in the radius of the test piece, variations in fuel source, variations in flow turbulence, strong shear layers, etc. As of this writing, new efforts focused on this problem are beginning at the Air Force Research Laboratory; thus, opportunities for collaboration are ripe in that regard.

Appendices

A. Fluent

This section is devoted to some of the more technical details of the various aspects of Fluent that were important to my research. It's pretty much all based on the Theory Guide, which, if you don't have a copy, exists in the COAL LAB folder under References/Fluent. There's a copy of the User's Guide and an older Tutorial Guide in there as well.

1. Courant Number

The description of the role of the Courant (or CFL) number is somewhat hard to discern from the Fluent Theory Guide [12]. In transient solutions, it helps to determine the time step. In steady-state solutions, as applicable to the work in this document, it is simply a way for the algorithm to determine the level of implicit under-relaxation between iterations. As stated in [12], under-relaxation of variables is used in all cases for some material properties, and as well in the pressure-based coupled algorithm (which is used in Section 3.3.1) for momentum and pressure. For any variable in a given cell, its new value, ψ, is determined by the computed change, $\Delta\psi$, and the under-relaxation factor α. The CFL number is then a parameter that is defined in terms of α, and it is a discretely controlled setting in the pressure-based coupled algorithm.

$$\psi = \psi_{old} + \alpha\Delta\psi$$

$$\frac{1-\alpha}{\alpha} = \frac{1}{CFL}$$

A more complete description of the CFL number is found, at least initially, in the so-titled Wikipedia article. Therein, it is more clearly revealed that the Courant-Friedrichs-Lewy (CFL) condition is a necessary condition for convergence while solving certain partial differential equations numerically. However, it is described only in terms of transient solutions

as a control over the time step, not in the particular context as applied by Fluent to their steady-state pressure-based solver.

2. Turbulence Modeling

i. The Turbulent Viscosity Hypothesis

The turbulent viscosity hypothesis was an early approach to solve the closure problem introduced by Boussinesq in 1887, and is mathematically analogous to the stress-to-rate-of-strain relation for a Newtonian fluid. It is presented by ANSYS [12] simply as the "Boussinesq Approach" with notation as follows:

$$-\rho\overline{u_i'u_j'} = \mu_t\left(\frac{\partial u_i}{\partial x_j}+\frac{\partial u_j}{\partial x_i}\right)-\frac{2}{3}\left(\rho k+\mu_t\frac{\partial u_k}{\partial x_k}\right)\delta_{ij} \tag{92}$$

The turbulent viscosity hypothesis is a component of the Spalart-Allmaras one-equation model, as well as both two-equation models. Per ANSYS [12], a primary advantage of this approach is the relatively low computational cost associated with the computation of the turbulent viscosity, μ_t. In the case of the two-equation models, only two additional transport Equations are required, after which μ_t is computed as a function of k and ε or k and ω. ANSYS [12] proposes an alternative, termed the Reynolds stress transport model (RSM), in which transport Equations for each of the terms in the Reynolds stress tensor are solved. Thus, seven additional transport Equations must be solved for three-dimensional problems. In most cases the Boussinesq approach performs very well and the added computational cost of the RSM approach is unnecessary. It has been observed, however, that RSM is superior when anisotropic turbulent behavior is dominant [12].

ii. The $k-\varepsilon$ Model

The first of the most common two-equation turbulence models is the $k-\varepsilon$ model. It utilizes the turbulent kinetic energy and dissipation rate to derive a length scale $\left(L = k^{2/3}/\varepsilon\right)$, a

time scale ($\tau = k/\varepsilon$), and a quantity of dimension $\nu_T = C_\mu(k^2/\varepsilon)$. Thus, this model is considered complete, as it does not require any estimates of flow-dependent parameters. The model incorporates one transport equation for the kinetic energy, one transport equation for the dissipation rate, and the relation shown above for the turbulent viscosity in which $C_\mu = 0.09$ is one of the five model constants. Historically, the $k-\varepsilon$ model has been one of the simplest, and thus one of the most widely adopted models in the CFD discipline. Its capability to handle complex flows and near-wall behaviors, however, has been found to be lacking [11], and numerous modifications have been proposed over the years to adapt it to various classes of flows.

One such modification to the $k-\varepsilon$ model is the RNG $k-\varepsilon$ model derived using a statistical technique called renormalization group theory. It contains an additional term in the ε equation to improve accuracy for rapidly strained flows as well as a mechanism to account for the effect of swirl on turbulence [12]. Another variation is the realizable $k-\varepsilon$ model: the term "realizable" means that the model satisfies certain constraints on the Reynolds stresses consistent with the physics of turbulent flows. Specifically, it includes an alternative formulation of the turbulent viscosity and a modified transport equation for the dissipation rate.

iii. The $k-\omega$ Model

The second of the common two-equation models is the $k-\omega$ model. Its intent is to incorporate modifications for low-Reynolds number effects, compressibility, and shear flow spreading, such as may be found within shear layers and boundary layers. Thus, the performance of the $k-\omega$ model relative to the $k-\varepsilon$ model in such layers is superior. However, it is also sensitive to conditions in the free stream, making it perform poorly relative to the $k-\varepsilon$ model once no longer in a shear layer. Pope [11] and ANSYS [12] both present the modification to the $k-\omega$ model developed by Menter [109]. Therein the benefits of the $k-\omega$ and the $k-\varepsilon$ models were combined with various blending functions to obtain optimum performance both in

the shear layers and in the freestream. Specifically, ANSYS [12] references the shear-stress transport (SST) variation wherein a damped cross-diffusion derivative term is included in the ω equation in addition to the blending functions.

iv. The RSM Approach

ANSYS [12] notes that the RSM approach is subject to many of the same inaccuracies as other models, stemming from closure assumptions and scale equations. Consequently it may not always be worth the additional computation expense. However, it is highly recommended for conditions where the flow features of interest are the result of anisotropy in the Reynolds stresses, such as highly-swirled combustor flows and stress-induced secondary flows in ducts (both of those conditions are present in the Ultra-Compact Combustor).

Whereas the two-equation models operate with the intrinsic assumption that the Reynolds stresses are local functions of the mean velocity gradient, the RSM approach removes that assumption with an exact equation for the transport of the Reynolds stresses [11]. ANSYS [12] specifies that equation as a function of eight different terms describing (1) convection, (2) turbulent diffusion, (3) molecular diffusion, (4) stress production, (5) buoyancy production, (6) pressure strain, (7) dissipation, and (8) production by system rotation. Of these, terms 1, 3, 4, and 8 do not require any modeling. The remaining terms, however, need to be modeled to close the equations [12]. Pope [11] devotes substantial detail to the discussion of the modeling of those remaining terms, but that discourse is currently beyond the scope of this document.

v. Large Eddy Simulation

As mentioned previously, large eddy simulation (LES) offers a compromise between direct numerical simulation (DNS) and the simpler algebraic models. To preclude the intense computational time associated with resolving the smallest-scale motions, those small scales are modeled. As noted in Pope [11], the small-scale dynamics have some universal character that enables added confidence in the application of the simpler models. Conversely, the large-scale

motions are affected by the flow geometry, and are therefore not universal. Those dynamics are computed explicitly in LES just as they would be with a DNS approach, thereby attaining more accuracy and reliability in flows where large-scale unsteadiness is significant.

Conceptually, there are four steps in LES as outlined by Pope [11]. First, a filtering operation is used to decompose the velocity field into a filtered component and a residual (subgrid) component; the filtered component represents the large-scale eddy motion. Second, the Equations for the filtered velocity field are derived from the Navier-Stokes Equations. Third, closure is obtained by modeling the residual stress tensor. And finally, the model equations are solved numerically for one realization of the turbulent flow. Importantly, the filter width and the grid resolution are closely linked. If the LES solution is found to depend on the grid resolution, then the LES model is deemed incomplete. Thus, a grid-independent solution is required for a complete LES model application.

ANSYS [12] notes that a primary disadvantage of LES is its limited range of application. It is typically only useful when it can be applied to the entire computational domain, thereby limiting it to very low Reynolds number flows or flows where the boundary layers are not important. Otherwise, LES requires high resolution for wall bounded flows that become prohibitive in industrial applications. Thus, several alternatives are documented that blend LES with other models to attain high fidelity of the energy-containing flows while achieving sufficient resolution of the wall-bounded flows within reasonable computational expensed

The first of the LES alternatives is termed “Scale-Adaptive Simulation” (SAS). SAS allows resolution of the turbulent spectrum in unstable flow conditions based on the introduction of the von Karman length-scale into the turbulence scale equation. That information allows SAS models to adjust dynamically to resolve unsteady flow structures resulting in LES-like behavior in those unsteady regions; standard RANS capabilities are then recovered in the stable regions. A second LES alternative is “detached eddy simulation” (DES), known elsewhere as hybrid RANS/LES. LES filtering is rooted in grid scales, thereby leading to

high computational costs in boundary layers. In contrast, DES delineates the entire boundary-layer region as resolved by unsteady RANS computations, and it then applies LES to the separated regions. Thus, DES is somewhat less computationally expensive than LES, though still more so than a strictly RANS approach.

3. Combustion Modeling

i. Species Transport and Finite-Rate Chemistry

One method offered for implementing a turbulent reacting flame in Fluent is the Species Transport model. Mixing and transport of chemical species can be modeled by solving conservation equations describing convection, diffusion, and reaction sources for each component species. Reactions occur in the bulk phase, or in other words, the reactions are volumetric.

The local mass fractions for a given species are obtained through the solution of its specific convection-diffusion equation. The equation accounts for species production through reaction, addition from the dispersed phase, and any user-defined sources. Mass diffusion in turbulent flows is computed using the dilute approximation – also known as Fick's Law – modified with the addition of the turbulent Schmidt number and turbulent viscosity terms. Fluent also accounts for the transport of enthalpy due to species diffusion.

To compute reaction rates, Fluent relies on one of three models:

1) Laminar finite-rate model: effect of turbulent fluctuations are ignored
2) Eddy-dissipation model: reaction rates are assumed to be controlled by turbulence
3) Eddy-dissipation-concept (EDC) model: detailed Arrhenius chemical kinetics are incorporated

An important limitation to the eddy-dissipation model is that, for realistic results, only one or two-step heat release mechanisms are recommended. However, it is a useful model for flows

wherein the fuels are fast-burning relative to the turbulent mixing rate. In that case, the overall rate of reaction is controlled by the turbulence that slowly mixes fuel and oxidizer together into the reaction zones where they are quickly burned. Therefore, the chemical kinetic rates can be safely ignored. The net rate of production of a given species due to reaction is a function of the reactant and product mass fractions as well as the large-eddy mixing time scale k/ε. Combustion proceeds whenever turbulence is present ($k/\varepsilon > 0$) without requiring an ignition source for initiation.

ii. Non-Premixed Combustion

The crucial element of the non-premixed combustion model in Fluent is the reduction of the thermochemistry to a single parameter: the mixture fraction, or the local mass fraction of burnt and unburnt fuel stream elements in all the species. The mixture fraction is a conserved scalar quantity, and the combustion is thereby simplified to a mixing problem, after which the chemistry can be developed with various equilibrium models. Rather than solve Equations for individual species, concentrations are derived from the mixture fraction fields. Thermochemistry calculations are preprocessed and tabulated for lookup prior to solving the flow, and turbulence-chemistry interaction is accounted for with an assumed-shape probability density function (PDF).

iii. Premixed Combustion

In premixed combustion, fuel and oxidizer are mixed at the molecular level prior to ignition. Combustion then occurs as flame front propagating into the unburnt reactants. The modeling challenge is typically greater than that of non-premixed combustion since the flame front in a premixed regime is susceptible to turbulent effects. Flame propagation is determined by both the laminar flame speed and the turbulent eddies. Large turbulent eddies tend to corrugate the flame sheet while small eddies (smaller than the flame thickness) actually penetrate the flame and modify the internal structure. Furthermore, explicit knowledge of the

laminar flame speed would require detailed resolution of that internal flame structure, the requirements of which are largely unaffordable.

The premixed combustion model in Fluent is only suitable if the flame is perfectly premixed. In the current research, this condition is not anticipated as discrete fuel and oxidizer streams will be analyzed. There is the potential, though, for a partially premixed condition where a non-premixed diffusion flame lifts off the burner or is broken apart due to turbulent motions such that it propagates through premixed portions of the flow field. Thus, some knowledge of the premixed model is required.

The Fluent premixed model operates based on either a c-equation model or a G-equation model. In the former, c is a scalar variable representing the progress of reaction from burnt to unburnt, where c is defined as zero in the unburnt reactants. Note that c does not represent any intermediate reaction states, only a time-based migration from the unburnt zone to the burnt zone. A flame "brush" propagates upstream at a modeled turbulent flame speed. The laminar flame is assumed to be thin in comparison to the turbulent flame brush. Conversely, the G-equation is a flame-front tracking model governing the unsteady evolution of the flame interface.

Key to both premixed models is determination of the turbulent flame speed. Fluent accomplishes that through one of two models: the Zimont turbulent flame speed closure model, and the Peters flame speed model. For the former, the turbulent flame speed is calculated as a function of the RMS velocity, laminar flame speed, unburnt thermal diffusivity, and a turbulence length scale. It is based on the assumption of equilibrium small-scale turbulence inside the laminar flame, thereby allowing the expression of turbulent flame speed solely in terms of large-scale turbulent parameters. It is strictly applicable when the Kolmogorov scales are smaller than the flame thickness. The Peters model does not have that restriction, and instead models the turbulent flame speed as a function of the laminar flame thickness,

turbulent velocity scale, calculated flame brush thickness (which is different between the c- and G-equation models), and a set of empirical constants.

iv. Partially-Premixed Combustion

Three approaches are available for modeling partially-premixed combustion systems in Fluent: Chemical Equilibrium, Steady Diffusion Flamelet, and Steady Premixed Flamelet. The first two assume an infinitely-thin premixed flame front, and the flame-brush is indicated by a mean reaction progress variable $0 < \bar{c} < 1$. The Steady Premixed Flamelet model is based on the Flamelet Generated Manifold concept.

The partially-premixed combustion model is truly a combination of the two models previously discussed. It solves transport Equations for the mean reaction progress variable, $\bar{c}$, as well as the mixture fraction, $\bar{f}$, and the mixture fraction variance, $\overline{f'^2}$.

v. Emissions Modeling

Fluent has discrete modeling capability to predict the formation of NO_x, SO_x, and soot. Each will be briefly described in this section.

The Fluent NO_x model has the ability to predict thermal, prompt, and fuel NO_x formation, as well as NO_x consumption due to reburning. Thermal NO_x is formed by the oxidation of atmospheric nitrogen present in the combustion air. Prompt NO_x is produced by high-speed reactions at the flame front. Fuel NO_x results from oxidation of nitrogen contained in the fuel, and reburning mechanisms account for reaction of NO with hydrocarbons. To predict NO_x emissions, a transport equation for NO concentration is first solved. In the presence of fuel NO_x sources, additional transport Equations are solved for intermediate species. Importantly, NO_x is post-processed from an existing combustion simulation. That is, a given problem must be run to convergence before then initializing and implementing the additional NO_x model. ANSYS [12] notes, however, that the model should be used to evaluate trends only, as the NO_x quantity itself cannot be pinpointed.

Sulfur exists in liquid fuel mostly in organic form with mass fractions ranging from 0.5% to 3%. All SO_x emissions are produced because of the oxidation of fuel-bound sulfur. In Fluent, the assumption is made that liquid fuels release sulfur purely as H_2S. For low sulfur concentrations, a post-processing step may be implemented for solve the requisite transport equation.

There are four models provided for soot formation, and they may be coupled with radiation absorption with certain radiation models. The one-step Khan and Greeves model predicts soot formation based on a simple empirical rate. The two-step Tesner model predicts the formation of nuclei particles with soot formation on the nuclei. The Moss-Brooks model predicts soot formation for methane flames by solving transport Equations for normalized radical nuclei concentration and the soot mass fraction. Finally, the Moss-Brooks-Hall model extends the Moss-Brooks model to higher hydrocarbon fuels.

4. Surface Integral Methods

Fluent surfaces are sets of data points created for a given zone in the Fluent model, which may consist of internal cells, boundary cells, or both. For surfaces created during post-processing, the cell values (vs the face values) are used. Surface integrals are computed by summing the product of the facet area, A, and the facet value of the selected field variable, ψ. Two methods of integration were utilized over the course of this research. In early analysis, based in large part on the procedure of Briones [25], area-weighted averages were utilized for integration. Those values were computed based on the formula given in Equation (93). To compute the mass flow rate through a surface, the expression of Equation (94) is utilized. That expression is then incorporated into a second averaging method which was deferred to for much of the late-phase analysis of this research due to its better representation of the flow characteristics. The mass-weighted average of a field variable is defined by Equation (95).

$$\frac{1}{A}\int \psi dA = \frac{1}{A}\sum_{i=1}^{n} \psi_i \, |A_i| \tag{93}$$

$$\int \rho\vec{v} \cdot d\vec{A} = \sum_{i=1}^{n} \rho_i \vec{v}_i \cdot \vec{A}_i \tag{94}$$

$$\frac{\int \psi\rho\left|\vec{v} \cdot d\vec{A}\right|}{\int \rho\left|\vec{v} \cdot d\vec{A}\right|} = \frac{\sum_{i=1}^{n} \psi_i \rho_i \left|\vec{v}_i \cdot \vec{A}_i\right|}{\sum_{i=1}^{n} \rho_i \left|\vec{v}_i \cdot \vec{A}_i\right|} \tag{95}$$

B. Hybrid Guide Vane Design

This section will go through the process of creating the HGV in Solidworks. There's actually not a lot to it, but it can be pretty daunting to figure it out from the outside – particularly if you're not all that comfortable using Solidworks yet. I'll make it a step-by-step guide, but the steps are pretty broad and there'd plenty of room for improvisation/revision as the reader may require.

1. The initial body of revolution needs to be of the right diameter to match the adjoining pieces – the diffuser on the upstream side and the exhaust cone downstream. All of the current designs are also hollow since it was intended at one point to put cooling flow through the center, but that hasn't yet been operationally implemented.
2. There needs to be a revolved cut through this first body in the form dictated by Wilson [90] in order to reduce the Rayleigh loss; it's basically a "belly" at the center – you'd be best off copying the sketch from any other HGV file, but I wouldn't go so far as to say the precise shape has been optimized.
3. The vane airfoil itself is simply a rectangle tracing a helical sketch. Once you get to this point you've basically got it figured out – it was a substantial revelation to me at least. Just create a rectangular sketch on the plane where you want the vane leading edge – the only real requirement is that the whole leading edge be forward of the combustion cavity. A variety of helix settings are documented in the file below (should presumably be the same path – if not just search the COAL LAB directory and hopefully it'll turn up):

L:\Research\COAL LAB\Solidworks\CottleWorks\centerbody\helixSettings.xlsx

4. From there it's just a circular pattern of the helix, then creative application of edge filets. And you've got yourself an HGV. I might put some illustrations in here at some point, but if I forget and you're still reading this just use the "rollback" bar on one of the HGV Solidworks files and you can see the progression.

C. LIBS Hencken Calibration Data

The following figures summarize the data collected during calibration testing for the LIBS technique. Figure A.1 and Figure A.2 show observed emission intensities and ratios from the Hencken flame as function of the equivalence ratio for atomic hydrogen, oxygen, and nitrogen. Figure A.3 provides a correlation for equivalence ratio as a function of the H/N ratio – the inverse of that shown in Figure 3.38.

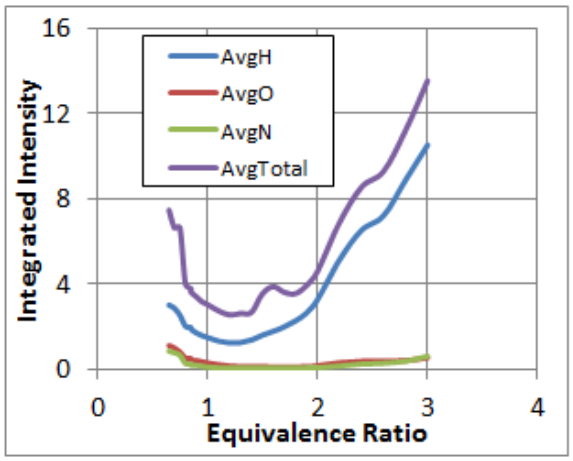

Figure A.1: Average observed emission intensities

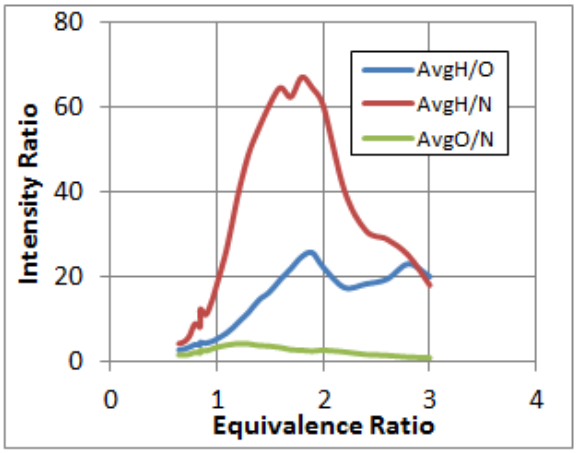

Figure A.2: Average observed emission ratios

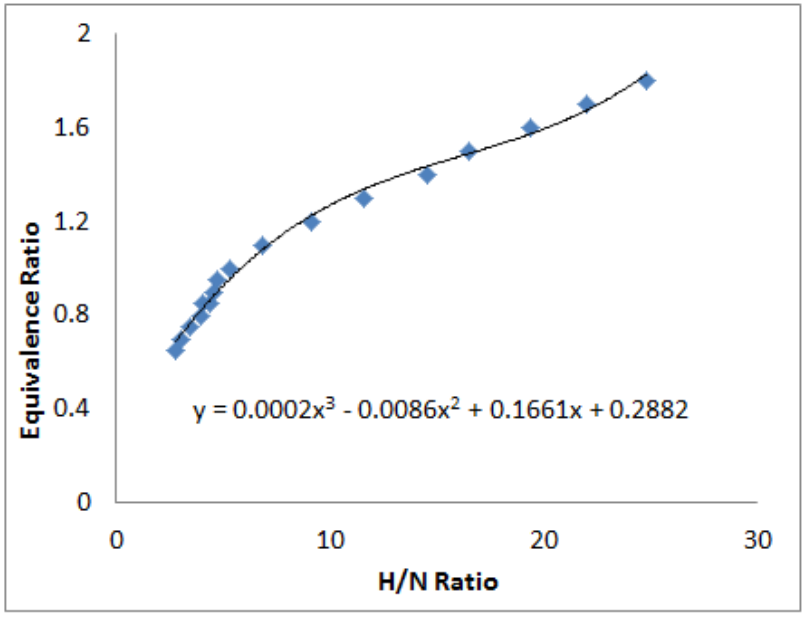

Figure A.3: Equivalence ratio as a function of H/N

D. Sample Codes

This section contains sample scripts for executing operations in Fluent both locally and remotely. I've also thrown in an MS Word macro that's become a staple for me in the composition of this and other documents.

1. Journal File

The code on the next page incorporates everything needed to run a Fluent job with an un-modified Pointwise export file. The only catch is that you need to know what your boundary labels are to appropriately define your boundary conditions. You also need to ensure that the lookup path for the initial .cas file is properly defined based on where you're executing. The script executes all of the setup and then solves for the defined number of iterations. After the final iteration, a number of post-processing steps are executed. Those consist of the definition of a number of computational planes and profiles and then the subsequent export of text data.

```
file/read /workspace/acottle/Data/125_53-150188.cas
mesh/check
mesh/scale .0254 .0254 .0254
define/units length in
mesh/reorder/reorder-domain
;mesh/quality
;mesh/ri/iq
define/models/viscous/ke-realizable yes
define/models/viscous/nwt/ewt yes
define/models/viscous/curvature-correction yes
define/models/species/partially-premixed-combustion yes no
       "/home/acottle/ChemicalMechanisms/v21c50k.pdf"
define/models/species/ppcp "algebraic" .1 0
;define/boundary-conditions/modify-zones/zone-type inlet pi
;define/boundary-conditions/modify-zones/zone-type outlet mfi
define/boundary-conditions/mfi 13 y y n 0.00188 n 4300 n y n n n y 5 .5 n 0 n 0 n 1 n
       0
define/boundary-conditions/pi 16 y n 4120 n 3820 n y n n n y 5 3 n 0 n 0 n 0 n 0
define/boundary-conditions/mfi 18 y y n .15188 n 3000 y n y n 0 n 1 n 1 n n n y 5 3 n
       0 n 0 n 0 n 0
solve/set/p-v-coupling 24
solve/set/gradient-scheme n y
solve/set/pseudo-transient y y 2 1 0 .012
solve/set/d-s/m 6
solve/set/d-s/k 4
solve/set/d-s/e 4
;solve/set/p-v-controls 15 .5 .5
solve/set/prf/density .95
solve/set/prf bf .95
solve/set/prf tv .95
solve/monitors/residual/convergence-criteria 1e-6 ,,,,,,,,
file/auto-save/cf/icim
file/auto-save/df 500
file/auto-save/rmrf y
file/auto-save/mf 2
solve/initialize/hyb-initialization
;solve/patch combustor outlet.1 , premixc 1
surface/iso-surface z-coordinate z13p9 () () 13.9 ()
solve/monitors/surface set-monitor cavity "Area-Weighted Average" total-temperature
       z13p9 () no yes no 1
solve/iterate 8001
define/custom-field-functions/define "gload"
       (tangential_velocity^2)/(9.81*radial_coordinate)
define/custom-field-functions/define "localphi" c3h8*15.64/(n2+o2)
define/custom-field-functions/define "otherhc" c2h2+c2h3+c2h4+c2h6+ch3
surface/iso-surface z-coordinate z13p0 () () 13.0 ()
surface/iso-surface z-coordinate z13p1 () () 13.1 ()
surface/iso-surface z-coordinate z13p2 () () 13.2 ()
surface/iso-surface z-coordinate z13p3 () () 13.3 ()
surface/iso-surface z-coordinate z13p4 () () 13.4 ()
surface/iso-surface z-coordinate z13p6 () () 13.6 ()
surface/iso-surface z-coordinate z13p7 () () 13.7 ()
surface/iso-surface z-coordinate z13p8 () () 13.8 ()
surface/iso-surface z-coordinate z14p0 () () 14.0 ()
surface/iso-surface z-coordinate z14p1 () () 14.1 ()
surface/iso-surface z-coordinate z14p2 () () 14.2 ()
surface/iso-surface z-coordinate z14p4 () () 14.4 ()
surface/iso-surface z-coordinate z14p5 () () 14.5 ()
surface/iso-surface z-coordinate z14p6 () () 14.6 ()
surface/iso-surface z-coordinate z14p7 () () 14.7 ()
surface/iso-surface z-coordinate z14p8 () () 14.8 ()
surface/iso-surface z-coordinate z14p9 () () 14.9 ()
surface/iso-surface z-coordinate z15p0 () () 15.0 ()
```

```
surface/iso-surface z-coordinate z15p1 () () 15.1 ()
surface/iso-surface z-coordinate z15p2 () () 15.2 ()
surface/iso-surface z-coordinate z15p3 () () 15.3 ()
surface/iso-surface z-coordinate z15p4 () () 15.4 ()
surface/iso-surface z-coordinate z15p5 () () 15.5 ()
surface/iso-surface z-coordinate z15p6 () () 15.6 ()
surface/iso-surface z-coordinate z15p7 () () 15.7 ()
surface/iso-surface z-coordinate z15p8 () () 15.8 ()
surface/iso-surface z-coordinate z15p9 () () 15.9 ()
surface/iso-surface z-coordinate z16p0 () () 16.0 ()
surface/iso-surface z-coordinate z16p1 () () 16.1 ()
surface/iso-surface z-coordinate z16p2 () () 16.2 ()
surface/iso-surface z-coordinate z16p3 () () 16.3 ()
surface/iso-surface z-coordinate z16p4 () () 16.4 ()
surface/iso-surface z-coordinate z16p5 () () 16.5 ()
surface/iso-surface z-coordinate z16p6 () () 16.6 ()
surface/iso-surface z-coordinate z16p7 () () 16.7 ()
surface/iso-surface z-coordinate z16p8 () () 16.8 ()
surface/iso-surface z-coordinate z16p9 () () 16.9 ()
surface/iso-surface z-coordinate z17p0 () () 17.0 ()
surface/iso-surface z-coordinate z17p1 () () 17.1 ()
surface/iso-surface z-coordinate z17p2 () () 17.2 ()
surface/iso-surface z-coordinate z17p3 () () 17.3 ()
surface/iso-surface z-coordinate z17p4 () () 17.4 ()
surface/iso-surface z-coordinate z17p5 () () 17.5 ()
surface/iso-surface z-coordinate z17p6 () () 17.6 ()
surface/iso-surface z-coordinate z17p7 () () 17.7 ()
surface/iso-surface z-coordinate z17p8 () () 17.8 ()
surface/iso-surface z-coordinate z17p9 () () 17.9 ()
surface/iso-surface z-coordinate z18p0 () () 18.0 ()
surface/iso-surface z-coordinate z18p1 () () 18.1 ()
surface/iso-surface z-coordinate z18p2 () () 18.2 ()
surface/iso-surface z-coordinate z18p3 () () 18.3 ()
surface/iso-surface z-coordinate z18p4 () () 18.4 ()
surface/iso-surface z-coordinate z18p5 () () 18.5 ()
surface/iso-surface z-coordinate z18p6 () () 18.6 ()
surface/iso-surface z-coordinate z18p7 () () 18.7 ()
surface/iso-surface z-coordinate z18p8 () () 18.8 ()
surface/iso-surface z-coordinate z18p9 () () 18.9 ()
surface/iso-surface z-coordinate z19p0 () () 19.0 ()
surface/iso-surface z-coordinate mid () () 13.9 ()
surface/iso-surface z-coordinate for () () 13.5 ()
surface/iso-surface z-coordinate aft () () 14.3 ()
surface/iso-surface radial-coordinate for_3p3 for () () 3.3 ()
surface/iso-surface radial-coordinate for_3p2 for () () 3.2 ()
surface/iso-surface radial-coordinate for_3p1 for () () 3.1 ()
surface/iso-surface radial-coordinate for_3p0 for () () 3.0 ()
surface/iso-surface radial-coordinate for_2p9 for () () 2.9 ()
surface/iso-surface radial-coordinate for_2p8 for () () 2.8 ()
surface/iso-surface radial-coordinate for_2p7 for () () 2.7 ()
surface/iso-surface radial-coordinate for_2p6 for () () 2.6 ()
surface/iso-surface radial-coordinate for_2p5 for () () 2.5 ()
surface/iso-surface radial-coordinate for_2p4 for () () 2.4 ()
surface/iso-surface radial-coordinate for_2p3 for () () 2.3 ()
surface/iso-surface radial-coordinate for_2p2 for () () 2.2 ()
surface/iso-surface radial-coordinate mid_3p3 mid () () 3.3 ()
surface/iso-surface radial-coordinate mid_3p2 mid () () 3.2 ()
surface/iso-surface radial-coordinate mid_3p1 mid () () 3.1 ()
surface/iso-surface radial-coordinate mid_3p0 mid () () 3.0 ()
surface/iso-surface radial-coordinate mid_2p9 mid () () 2.9 ()
surface/iso-surface radial-coordinate mid_2p8 mid () () 2.8 ()
surface/iso-surface radial-coordinate mid_2p7 mid () () 2.7 ()
surface/iso-surface radial-coordinate mid_2p6 mid () () 2.6 ()
```

```
surface/iso-surface radial-coordinate mid_2p5 mid () () 2.5 ()
surface/iso-surface radial-coordinate mid_2p4 mid () () 2.4 ()
surface/iso-surface radial-coordinate mid_2p3 mid () () 2.3 ()
surface/iso-surface radial-coordinate mid_2p2 mid () () 2.2 ()
surface/iso-surface radial-coordinate aft_3p3 aft () () 3.3 ()
surface/iso-surface radial-coordinate aft_3p2 aft () () 3.2 ()
surface/iso-surface radial-coordinate aft_3p1 aft () () 3.1 ()
surface/iso-surface radial-coordinate aft_3p0 aft () () 3.0 ()
surface/iso-surface radial-coordinate aft_2p9 aft () () 2.9 ()
surface/iso-surface radial-coordinate aft_2p8 aft () () 2.8 ()
surface/iso-surface radial-coordinate aft_2p7 aft () () 2.7 ()
surface/iso-surface radial-coordinate aft_2p6 aft () () 2.6 ()
surface/iso-surface radial-coordinate aft_2p5 aft () () 2.5 ()
surface/iso-surface radial-coordinate aft_2p4 aft () () 2.4 ()
surface/iso-surface radial-coordinate aft_2p3 aft () () 2.3 ()
surface/iso-surface radial-coordinate aft_2p2 aft () () 2.2 ()
surface/line-surface exitA -.028184 .94955 16.227 .41159 2.0574 16.104
surface/line-surface exitB .81769 .48095 16.227 1.9876 .67225 16.104
surface/line-surface exitC .83642 -.45036 16.227 1.5760 -1.3851 16.104
surface/line-surface exitD .028184 -.94955 16.227 -.41159 -2.0574 16.104
surface/line-surface exitE -.81769 -.48095 16.227 -1.9876 -.67225 16.104
surface/line-surface exitF -.83642 .45036 16.227 -1.5760 1.3851 16.104
surface/line-surface cavA -0.23078 2.08829 13.51208 -0.36809 3.33073 13.51208
surface/line-surface cavB -0.31708 2.07479 13.68751 -0.50592 3.31045 13.68751
surface/line-surface cavC -0.69544 1.98150 13.98592 -1.10940 3.16097 13.98592
surface/line-surface cavD -1.10557 1.78542 14.25068 -1.76364 2.84817 14.25068
plot/plot y 125_exitTempRadial.txt y n n radial-coordinate n n temperature exitA exitB
      exitC exitD exitE exitF ()
plot/plot y 125_cavTempRadial.txt y n n radial-coordinate n n temperature cavA cavB
      cavC cavD ()
report/surface-integrals/vertex-avg for_3p3 for_3p2 for_3p1 for_3p0 for_2p9 for_2p8
      for_2p7 for_2p6 for_2p5 for_2p4 for_2p3 for_2p2 mid_3p3 mid_3p2 mid_3p1 mid_3p0
      mid_2p9 mid_2p8 mid_2p7 mid_2p6 mid_2p5 mid_2p4 mid_2p3 mid_2p2 aft_3p3 aft_3p2
      aft_3p1 aft_3p0 aft_2p9 aft_2p8 aft_2p7 aft_2p6 aft_2p5 aft_2p4 aft_2p3 aft_2p2
      () gload yes "125_gload.txt"
report/surface-integrals/vertex-avg for_3p3 for_3p2 for_3p1 for_3p0 for_2p9 for_2p8
      for_2p7 for_2p6 for_2p5 for_2p4 for_2p3 for_2p2 mid_3p3 mid_3p2 mid_3p1 mid_3p0
      mid_2p9 mid_2p8 mid_2p7 mid_2p6 mid_2p5 mid_2p4 mid_2p3 mid_2p2 aft_3p3 aft_3p2
      aft_3p1 aft_3p0 aft_2p9 aft_2p8 aft_2p7 aft_2p6 aft_2p5 aft_2p4 aft_2p3 aft_2p2
      () localphi yes "125_localphi.txt"
report/surface-integrals/vertex-avg for_3p3 for_3p2 for_3p1 for_3p0 for_2p9 for_2p8
      for_2p7 for_2p6 for_2p5 for_2p4 for_2p3 for_2p2 mid_3p3 mid_3p2 mid_3p1 mid_3p0
      mid_2p9 mid_2p8 mid_2p7 mid_2p6 mid_2p5 mid_2p4 mid_2p3 mid_2p2 aft_3p3 aft_3p2
      aft_3p1 aft_3p0 aft_2p9 aft_2p8 aft_2p7 aft_2p6 aft_2p5 aft_2p4 aft_2p3 aft_2p2
      () fmean yes "125_fmean.txt"
report/surface-integrals/vertex-avg for_3p3 for_3p2 for_3p1 for_3p0 for_2p9 for_2p8
      for_2p7 for_2p6 for_2p5 for_2p4 for_2p3 for_2p2 mid_3p3 mid_3p2 mid_3p1 mid_3p0
      mid_2p9 mid_2p8 mid_2p7 mid_2p6 mid_2p5 mid_2p4 mid_2p3 mid_2p2 aft_3p3 aft_3p2
      aft_3p1 aft_3p0 aft_2p9 aft_2p8 aft_2p7 aft_2p6 aft_2p5 aft_2p4 aft_2p3 aft_2p2
      () temperature yes "125_temp.txt"
report/surface-integrals/vertex-avg for_3p3 for_3p2 for_3p1 for_3p0 for_2p9 for_2p8
      for_2p7 for_2p6 for_2p5 for_2p4 for_2p3 for_2p2 mid_3p3 mid_3p2 mid_3p1 mid_3p0
      mid_2p9 mid_2p8 mid_2p7 mid_2p6 mid_2p5 mid_2p4 mid_2p3 mid_2p2 aft_3p3 aft_3p2
      aft_3p1 aft_3p0 aft_2p9 aft_2p8 aft_2p7 aft_2p6 aft_2p5 aft_2p4 aft_2p3 aft_2p2
      () radial-velocity yes "125_radV.txt"
report/surface-integrals/vertex-avg for_3p3 for_3p2 for_3p1 for_3p0 for_2p9 for_2p8
      for_2p7 for_2p6 for_2p5 for_2p4 for_2p3 for_2p2 mid_3p3 mid_3p2 mid_3p1 mid_3p0
      mid_2p9 mid_2p8 mid_2p7 mid_2p6 mid_2p5 mid_2p4 mid_2p3 mid_2p2 aft_3p3 aft_3p2
      aft_3p1 aft_3p0 aft_2p9 aft_2p8 aft_2p7 aft_2p6 aft_2p5 aft_2p4 aft_2p3 aft_2p2
      () tangential-velocity yes "125_tanV.txt"
report/surface-integrals/area-weighted-avg z13p0 z13p1 z13p2 z13p3 z13p4 for z13p6
      z13p7 z13p8 mid z14p0 z14p1 z14p2 aft z14p4 z14p5 z14p6 z14p7 z14p8 z14p9 z15p0
      z15p1 z15p2 z15p3 z15p4 z15p5 z15p6 z15p7 z15p8 z15p9 z16p0 z16p1 z16p2 z16p3
```

```
      z16p4 z16p5 z16p6 z16p7 z16p8 z16p9 z17p0 z17p1 z17p2 z17p3 z17p4 z17p5 z17p6
      z17p7 z17p8 z17p9 z18p0 z18p1 z18p2 z18p3 z18p4 z18p5 z18p6 z18p7 z18p8 z18p9
      z19p0 () temperature yes "125_ax-Temp-AA.txt"
report/surface-integrals/mass-weighted-avg z13p0 z13p1 z13p2 z13p3 z13p4 for z13p6
      z13p7 z13p8 mid z14p0 z14p1 z14p2 aft z14p4 z14p5 z14p6 z14p7 z14p8 z14p9 z15p0
      z15p1 z15p2 z15p3 z15p4 z15p5 z15p6 z15p7 z15p8 z15p9 z16p0 z16p1 z16p2 z16p3
      z16p4 z16p5 z16p6 z16p7 z16p8 z16p9 z17p0 z17p1 z17p2 z17p3 z17p4 z17p5 z17p6
      z17p7 z17p8 z17p9 z18p0 z18p1 z18p2 z18p3 z18p4 z18p5 z18p6 z18p7 z18p8 z18p9
      z19p0 () temperature yes "125_ax-Temp-MA.txt"
report/surface-integrals/area-weighted-avg z13p0 z13p1 z13p2 z13p3 z13p4 for z13p6
      z13p7 z13p8 mid z14p0 z14p1 z14p2 aft z14p4 z14p5 z14p6 z14p7 z14p8 z14p9 z15p0
      z15p1 z15p2 z15p3 z15p4 z15p5 z15p6 z15p7 z15p8 z15p9 z16p0 z16p1 z16p2 z16p3
      z16p4 z16p5 z16p6 z16p7 z16p8 z16p9 z17p0 z17p1 z17p2 z17p3 z17p4 z17p5 z17p6
      z17p7 z17p8 z17p9 z18p0 z18p1 z18p2 z18p3 z18p4 z18p5 z18p6 z18p7 z18p8 z18p9
      z19p0 () premixc yes "125_ax-premixc.txt"
report/surface-integrals/area-weighted-avg z13p0 z13p1 z13p2 z13p3 z13p4 for z13p6
      z13p7 z13p8 mid z14p0 z14p1 z14p2 aft z14p4 z14p5 z14p6 z14p7 z14p8 z14p9 z15p0
      z15p1 z15p2 z15p3 z15p4 z15p5 z15p6 z15p7 z15p8 z15p9 z16p0 z16p1 z16p2 z16p3
      z16p4 z16p5 z16p6 z16p7 z16p8 z16p9 z17p0 z17p1 z17p2 z17p3 z17p4 z17p5 z17p6
      z17p7 z17p8 z17p9 z18p0 z18p1 z18p2 z18p3 z18p4 z18p5 z18p6 z18p7 z18p8 z18p9
      z19p0 () product-formation-rate yes "125_ax-prodform.txt"
report/surface-integrals/area-weighted-avg z13p0 z13p1 z13p2 z13p3 z13p4 for z13p6
      z13p7 z13p8 mid z14p0 z14p1 z14p2 aft z14p4 z14p5 z14p6 z14p7 z14p8 z14p9 z15p0
      z15p1 z15p2 z15p3 z15p4 z15p5 z15p6 z15p7 z15p8 z15p9 z16p0 z16p1 z16p2 z16p3
      z16p4 z16p5 z16p6 z16p7 z16p8 z16p9 z17p0 z17p1 z17p2 z17p3 z17p4 z17p5 z17p6
      z17p7 z17p8 z17p9 z18p0 z18p1 z18p2 z18p3 z18p4 z18p5 z18p6 z18p7 z18p8 z18p9
      z19p0 () localphi yes "125_ax-phi.txt"
report/surface-integrals/area-weighted-avg z13p0 z13p1 z13p2 z13p3 z13p4 for z13p6
      z13p7 z13p8 mid z14p0 z14p1 z14p2 aft z14p4 z14p5 z14p6 z14p7 z14p8 z14p9 z15p0
      z15p1 z15p2 z15p3 z15p4 z15p5 z15p6 z15p7 z15p8 z15p9 z16p0 z16p1 z16p2 z16p3
      z16p4 z16p5 z16p6 z16p7 z16p8 z16p9 z17p0 z17p1 z17p2 z17p3 z17p4 z17p5 z17p6
      z17p7 z17p8 z17p9 z18p0 z18p1 z18p2 z18p3 z18p4 z18p5 z18p6 z18p7 z18p8 z18p9
      z19p0 () fmean yes "125_ax-fmean.txt"
report/surface-integrals/area-weighted-avg z13p0 z13p1 z13p2 z13p3 z13p4 for z13p6
      z13p7 z13p8 mid z14p0 z14p1 z14p2 aft z14p4 z14p5 z14p6 z14p7 z14p8 z14p9 z15p0
      z15p1 z15p2 z15p3 z15p4 z15p5 z15p6 z15p7 z15p8 z15p9 z16p0 z16p1 z16p2 z16p3
      z16p4 z16p5 z16p6 z16p7 z16p8 z16p9 z17p0 z17p1 z17p2 z17p3 z17p4 z17p5 z17p6
      z17p7 z17p8 z17p9 z18p0 z18p1 z18p2 z18p3 z18p4 z18p5 z18p6 z18p7 z18p8 z18p9
      z19p0 () un-normalized-progress-variable yes "125_ax-unprogvar.txt"
report/surface-integrals/area-weighted-avg z13p0 z13p1 z13p2 z13p3 z13p4 for z13p6
      z13p7 z13p8 mid z14p0 z14p1 z14p2 aft z14p4 z14p5 z14p6 z14p7 z14p8 z14p9 z15p0
      z15p1 z15p2 z15p3 z15p4 z15p5 z15p6 z15p7 z15p8 z15p9 z16p0 z16p1 z16p2 z16p3
      z16p4 z16p5 z16p6 z16p7 z16p8 z16p9 z17p0 z17p1 z17p2 z17p3 z17p4 z17p5 z17p6
      z17p7 z17p8 z17p9 z18p0 z18p1 z18p2 z18p3 z18p4 z18p5 z18p6 z18p7 z18p8 z18p9
      z19p0 () premix-finite-rate-source yes "125_ax-premixSource.txt"
report/surface-integrals/area-weighted-avg z13p0 z13p1 z13p2 z13p3 z13p4 for z13p6
      z13p7 z13p8 mid z14p0 z14p1 z14p2 aft z14p4 z14p5 z14p6 z14p7 z14p8 z14p9 z15p0
      z15p1 z15p2 z15p3 z15p4 z15p5 z15p6 z15p7 z15p8 z15p9 z16p0 z16p1 z16p2 z16p3
      z16p4 z16p5 z16p6 z16p7 z16p8 z16p9 z17p0 z17p1 z17p2 z17p3 z17p4 z17p5 z17p6
      z17p7 z17p8 z17p9 z18p0 z18p1 z18p2 z18p3 z18p4 z18p5 z18p6 z18p7 z18p8 z18p9
      z19p0 () c3h8 yes "125_ax-c3h8.txt"
report/surface-integrals/area-weighted-avg z13p0 z13p1 z13p2 z13p3 z13p4 for z13p6
      z13p7 z13p8 mid z14p0 z14p1 z14p2 aft z14p4 z14p5 z14p6 z14p7 z14p8 z14p9 z15p0
      z15p1 z15p2 z15p3 z15p4 z15p5 z15p6 z15p7 z15p8 z15p9 z16p0 z16p1 z16p2 z16p3
      z16p4 z16p5 z16p6 z16p7 z16p8 z16p9 z17p0 z17p1 z17p2 z17p3 z17p4 z17p5 z17p6
      z17p7 z17p8 z17p9 z18p0 z18p1 z18p2 z18p3 z18p4 z18p5 z18p6 z18p7 z18p8 z18p9
      z19p0 () ch4 yes "125_ax-ch4.txt"
report/surface-integrals/area-weighted-avg z13p0 z13p1 z13p2 z13p3 z13p4 for z13p6
      z13p7 z13p8 mid z14p0 z14p1 z14p2 aft z14p4 z14p5 z14p6 z14p7 z14p8 z14p9 z15p0
      z15p1 z15p2 z15p3 z15p4 z15p5 z15p6 z15p7 z15p8 z15p9 z16p0 z16p1 z16p2 z16p3
      z16p4 z16p5 z16p6 z16p7 z16p8 z16p9 z17p0 z17p1 z17p2 z17p3 z17p4 z17p5 z17p6
      z17p7 z17p8 z17p9 z18p0 z18p1 z18p2 z18p3 z18p4 z18p5 z18p6 z18p7 z18p8 z18p9
      z19p0 () otherhc yes "125_ax-otherhc.txt"
```

```
report/surface-integrals/area-weighted-avg z13p0 z13p1 z13p2 z13p3 z13p4 for z13p6
      z13p7 z13p8 mid z14p0 z14p1 z14p2 aft z14p4 z14p5 z14p6 z14p7 z14p8 z14p9 z15p0
      z15p1 z15p2 z15p3 z15p4 z15p5 z15p6 z15p7 z15p8 z15p9 z16p0 z16p1 z16p2 z16p3
      z16p4 z16p5 z16p6 z16p7 z16p8 z16p9 z17p0 z17p1 z17p2 z17p3 z17p4 z17p5 z17p6
      z17p7 z17p8 z17p9 z18p0 z18p1 z18p2 z18p3 z18p4 z18p5 z18p6 z18p7 z18p8 z18p9
      z19p0 () co yes "125_ax-co.txt"
report/surface-integrals/area-weighted-avg z13p0 z13p1 z13p2 z13p3 z13p4 for z13p6
      z13p7 z13p8 mid z14p0 z14p1 z14p2 aft z14p4 z14p5 z14p6 z14p7 z14p8 z14p9 z15p0
      z15p1 z15p2 z15p3 z15p4 z15p5 z15p6 z15p7 z15p8 z15p9 z16p0 z16p1 z16p2 z16p3
      z16p4 z16p5 z16p6 z16p7 z16p8 z16p9 z17p0 z17p1 z17p2 z17p3 z17p4 z17p5 z17p6
      z17p7 z17p8 z17p9 z18p0 z18p1 z18p2 z18p3 z18p4 z18p5 z18p6 z18p7 z18p8 z18p9
      z19p0 () co2 yes "125_ax-co2.txt"
report/surface-integrals/mass-weighted-avg z13p0 z13p1 z13p2 z13p3 z13p4 for z13p6
      z13p7 z13p8 mid z14p0 z14p1 z14p2 aft z14p4 z14p5 z14p6 z14p7 z14p8 z14p9 z15p0
      z15p1 z15p2 z15p3 z15p4 z15p5 z15p6 z15p7 z15p8 z15p9 z16p0 z16p1 z16p2 z16p3
      z16p4 z16p5 z16p6 z16p7 z16p8 z16p9 z17p0 z17p1 z17p2 z17p3 z17p4 z17p5 z17p6
      z17p7 z17p8 z17p9 z18p0 z18p1 z18p2 z18p3 z18p4 z18p5 z18p6 z18p7 z18p8 z18p9
      z19p0 () premixc yes "125_ax-premixc-MA.txt"
report/surface-integrals/mass-weighted-avg z13p0 z13p1 z13p2 z13p3 z13p4 for z13p6
      z13p7 z13p8 mid z14p0 z14p1 z14p2 aft z14p4 z14p5 z14p6 z14p7 z14p8 z14p9 z15p0
      z15p1 z15p2 z15p3 z15p4 z15p5 z15p6 z15p7 z15p8 z15p9 z16p0 z16p1 z16p2 z16p3
      z16p4 z16p5 z16p6 z16p7 z16p8 z16p9 z17p0 z17p1 z17p2 z17p3 z17p4 z17p5 z17p6
      z17p7 z17p8 z17p9 z18p0 z18p1 z18p2 z18p3 z18p4 z18p5 z18p6 z18p7 z18p8 z18p9
      z19p0 () product-formation-rate yes "125_ax-prodform-MA.txt"
report/surface-integrals/mass-weighted-avg z13p0 z13p1 z13p2 z13p3 z13p4 for z13p6
      z13p7 z13p8 mid z14p0 z14p1 z14p2 aft z14p4 z14p5 z14p6 z14p7 z14p8 z14p9 z15p0
      z15p1 z15p2 z15p3 z15p4 z15p5 z15p6 z15p7 z15p8 z15p9 z16p0 z16p1 z16p2 z16p3
      z16p4 z16p5 z16p6 z16p7 z16p8 z16p9 z17p0 z17p1 z17p2 z17p3 z17p4 z17p5 z17p6
      z17p7 z17p8 z17p9 z18p0 z18p1 z18p2 z18p3 z18p4 z18p5 z18p6 z18p7 z18p8 z18p9
      z19p0 () localphi yes "125_ax-phi-MA.txt"
report/surface-integrals/mass-weighted-avg z13p0 z13p1 z13p2 z13p3 z13p4 for z13p6
      z13p7 z13p8 mid z14p0 z14p1 z14p2 aft z14p4 z14p5 z14p6 z14p7 z14p8 z14p9 z15p0
      z15p1 z15p2 z15p3 z15p4 z15p5 z15p6 z15p7 z15p8 z15p9 z16p0 z16p1 z16p2 z16p3
      z16p4 z16p5 z16p6 z16p7 z16p8 z16p9 z17p0 z17p1 z17p2 z17p3 z17p4 z17p5 z17p6
      z17p7 z17p8 z17p9 z18p0 z18p1 z18p2 z18p3 z18p4 z18p5 z18p6 z18p7 z18p8 z18p9
      z19p0 () fmean yes "125_ax-fmean-MA.txt"
report/surface-integrals/mass-weighted-avg z13p0 z13p1 z13p2 z13p3 z13p4 for z13p6
      z13p7 z13p8 mid z14p0 z14p1 z14p2 aft z14p4 z14p5 z14p6 z14p7 z14p8 z14p9 z15p0
      z15p1 z15p2 z15p3 z15p4 z15p5 z15p6 z15p7 z15p8 z15p9 z16p0 z16p1 z16p2 z16p3
      z16p4 z16p5 z16p6 z16p7 z16p8 z16p9 z17p0 z17p1 z17p2 z17p3 z17p4 z17p5 z17p6
      z17p7 z17p8 z17p9 z18p0 z18p1 z18p2 z18p3 z18p4 z18p5 z18p6 z18p7 z18p8 z18p9
      z19p0 () un-normalized-progress-variable yes "125_ax-unprogvar-MA.txt"
report/surface-integrals/mass-weighted-avg z13p0 z13p1 z13p2 z13p3 z13p4 for z13p6
      z13p7 z13p8 mid z14p0 z14p1 z14p2 aft z14p4 z14p5 z14p6 z14p7 z14p8 z14p9 z15p0
      z15p1 z15p2 z15p3 z15p4 z15p5 z15p6 z15p7 z15p8 z15p9 z16p0 z16p1 z16p2 z16p3
      z16p4 z16p5 z16p6 z16p7 z16p8 z16p9 z17p0 z17p1 z17p2 z17p3 z17p4 z17p5 z17p6
      z17p7 z17p8 z17p9 z18p0 z18p1 z18p2 z18p3 z18p4 z18p5 z18p6 z18p7 z18p8 z18p9
      z19p0 () premix-finite-rate-source yes "125_ax-premixSource-MA.txt"
report/surface-integrals/mass-weighted-avg z13p0 z13p1 z13p2 z13p3 z13p4 for z13p6
      z13p7 z13p8 mid z14p0 z14p1 z14p2 aft z14p4 z14p5 z14p6 z14p7 z14p8 z14p9 z15p0
      z15p1 z15p2 z15p3 z15p4 z15p5 z15p6 z15p7 z15p8 z15p9 z16p0 z16p1 z16p2 z16p3
      z16p4 z16p5 z16p6 z16p7 z16p8 z16p9 z17p0 z17p1 z17p2 z17p3 z17p4 z17p5 z17p6
      z17p7 z17p8 z17p9 z18p0 z18p1 z18p2 z18p3 z18p4 z18p5 z18p6 z18p7 z18p8 z18p9
      z19p0 () c3h8 yes "125_ax-c3h8-MA.txt"
report/surface-integrals/mass-weighted-avg z13p0 z13p1 z13p2 z13p3 z13p4 for z13p6
      z13p7 z13p8 mid z14p0 z14p1 z14p2 aft z14p4 z14p5 z14p6 z14p7 z14p8 z14p9 z15p0
      z15p1 z15p2 z15p3 z15p4 z15p5 z15p6 z15p7 z15p8 z15p9 z16p0 z16p1 z16p2 z16p3
      z16p4 z16p5 z16p6 z16p7 z16p8 z16p9 z17p0 z17p1 z17p2 z17p3 z17p4 z17p5 z17p6
      z17p7 z17p8 z17p9 z18p0 z18p1 z18p2 z18p3 z18p4 z18p5 z18p6 z18p7 z18p8 z18p9
      z19p0 () ch4 yes "125_ax-ch4-MA.txt"
report/surface-integrals/mass-weighted-avg z13p0 z13p1 z13p2 z13p3 z13p4 for z13p6
      z13p7 z13p8 mid z14p0 z14p1 z14p2 aft z14p4 z14p5 z14p6 z14p7 z14p8 z14p9 z15p0
      z15p1 z15p2 z15p3 z15p4 z15p5 z15p6 z15p7 z15p8 z15p9 z16p0 z16p1 z16p2 z16p3
```

```
      z16p4 z16p5 z16p6 z16p7 z16p8 z16p9 z17p0 z17p1 z17p2 z17p3 z17p4 z17p5 z17p6
      z17p7 z17p8 z17p9 z18p0 z18p1 z18p2 z18p3 z18p4 z18p5 z18p6 z18p7 z18p8 z18p9
      z19p0 () otherhc yes "125_ax-otherhc-MA.txt"
report/surface-integrals/mass-weighted-avg z13p0 z13p1 z13p2 z13p3 z13p4 for z13p6
      z13p7 z13p8 mid z14p0 z14p1 z14p2 aft z14p4 z14p5 z14p6 z14p7 z14p8 z14p9 z15p0
      z15p1 z15p2 z15p3 z15p4 z15p5 z15p6 z15p7 z15p8 z15p9 z16p0 z16p1 z16p2 z16p3
      z16p4 z16p5 z16p6 z16p7 z16p8 z16p9 z17p0 z17p1 z17p2 z17p3 z17p4 z17p5 z17p6
      z17p7 z17p8 z17p9 z18p0 z18p1 z18p2 z18p3 z18p4 z18p5 z18p6 z18p7 z18p8 z18p9
      z19p0 () co yes "125_ax-co-MA.txt"
report/surface-integrals/mass-weighted-avg z13p0 z13p1 z13p2 z13p3 z13p4 for z13p6
      z13p7 z13p8 mid z14p0 z14p1 z14p2 aft z14p4 z14p5 z14p6 z14p7 z14p8 z14p9 z15p0
      z15p1 z15p2 z15p3 z15p4 z15p5 z15p6 z15p7 z15p8 z15p9 z16p0 z16p1 z16p2 z16p3
      z16p4 z16p5 z16p6 z16p7 z16p8 z16p9 z17p0 z17p1 z17p2 z17p3 z17p4 z17p5 z17p6
      z17p7 z17p8 z17p9 z18p0 z18p1 z18p2 z18p3 z18p4 z18p5 z18p6 z18p7 z18p8 z18p9
      z19p0 () co2 yes "125_ax-co2-MA.txt"
exit y
```

2. AFRL – Thunder Batch Script

The following code comprises all the necessary commands to execute a batch job on the AFRL DSRC. Note that a journal file (as listed previously) is required. For more details on accessing and using the DSRC please reference https://centers.hpc.mil/.

```
#!/bin/csh
#PBS -N c111
#PBS -l walltime=025:00:00
#PBS -l job_type='MPI'
#PBS -l acfd_solver=1,anshpc=180
#PBS -l ncpus=180
#PBS -l application=fluent
#PBS -A WPTAFITO29212MAP
#PBS -q standard
#PBS -j oe
#PBS -V

# Environment Setup ----------------------------------------------
# Set location and name of journal file
set RUN_DIR = Journals
set JOURNAL = 111_50-150342
# Move to your scratch directory in Workspace
cd ${WORKDIR}
# Create a job-specific subdirectory based on JOBID and cd to it
set JOBID=`echo ${PBS_JOBID} | cut -d '.' -f 1`
cd ${JOBID}.THUNDER

# Launching ------------------------------------------------------
module load fluent/16.0.0
# Loaded to translate Intel MPI to SGI MPT.
module load perfboost
# Copy executable from $HOME and submit it (change -t to match ncpus!)
fluent 3ddp -pib -ssh -mpi=intel -cnf=$PBS_NODEFILE -g -t180 -i
${HOME}/${RUN_DIR}/${JOURNAL}.jou >& residuals.out

exit($status)
```

3. AFIT Batch Script

Batch execution on the local AFIT clusters requires a slightly different – and simpler – setup. As of this writing, there are exactly enough licenses to run on three of the large-memory (32-core) nodes.

```
#!/bin/bash
#PBS -l nodes=3:ppn=32
#PBS -j oe
#PBS -N c55
#PBS -S /bin/bash

cd $PBS_O_WORKDIR

# (change -t to match ncpus!)
fluent 3ddp -ssh -t96 -cnf=$PBS_NODEFILE -g -i j55_32-108235.jou >& 55residuals.out
```

4. MS Word Text Box Update Macro

This document was composed entirely in Microsoft Word 2010. For technical writing in Word, the author strongly recommends the following strategies:

- Become familiar and proficient with customized styles
- Become familiar and proficient with field usage and updating
- Take advantage of built-in equation-editing shortcuts
    - See L:\Research\COAL LAB\Students\Cottle\Data\TemplatesMacrosEtc\ "Equation Editor Shortcut Commands.pdf"
- Utilize the built-in reference manager
    - See L:\Research\COAL LAB\Students\Cottle\Data\TemplatesMacrosEtc\ "IEEE_Reference_mod.XSL"
    - Put that style sheet in the MS Word Bibliography directory if you can. Recently updated AFIT computers won't allow you access, but older ones – as well as your personal computer – will. Mine is at C:\Program Files (x86)\Microsoft Office\Office14\Bibliography\Style\
- Put all figures and their captions together in text boxes. That prevents them from being improperly separated during formatting. However, that also prevents them from being properly updated when you do a simple select-all + F9 to update the document fields. Thus, use the following macro to update your text box fields prior to updating the remaining document:

```
Sub UpdateTBFields()
  Dim shp As Shape

  For Each shp In ActiveDocument.Shapes
    With shp.TextFrame
      If .HasText Then
        .TextRange.Fields.Update
      End If
    End With
  Next
End Sub
```

E. Derivation of Overall Equivalence Ratio

$$\phi_{cav} = \frac{\dot{m}_{fuel} \cdot 15.64}{\dot{m}_{air,cav}}$$

$$\phi_{ucc} = \frac{\dot{m}_{fuel} \cdot 15.64}{\dot{m}_{air,total}} = \frac{\dot{m}_{fuel} \cdot 15.64}{\dot{m}_{air,total}} \left(\frac{\dot{m}_{air,cav}}{\dot{m}_{air,cav}} \right) = \frac{\dot{m}_{air,cav}}{\dot{m}_{air,total}} \phi_{cav}$$

$$CFF = \frac{\dot{m}_{air,core}}{\dot{m}_{air,total}} = \frac{\dot{m}_{air,total} - \dot{m}_{air,cav}}{\dot{m}_{air,total}} = 1 - \frac{\dot{m}_{air,cav}}{\dot{m}_{air,total}}$$

$$\frac{\dot{m}_{air,cav}}{\dot{m}_{air,total}} = 1 - CFF$$

$$\therefore \phi_{ucc} = (1 - CFF)\phi_{cav}$$

F. Exit Temperature Profile Averaging Process

This section will follow the averaging process for the case of the LLB geometry, $\dot{m}_{in} = 0.15$, $\phi_{cav} = 1.37$. For reference, temperature contours in the axial plane and in a single exit plane are shown in Figure A.4. The exit plane contour corresponds to the passage noted by the black arrow in the axial plane.

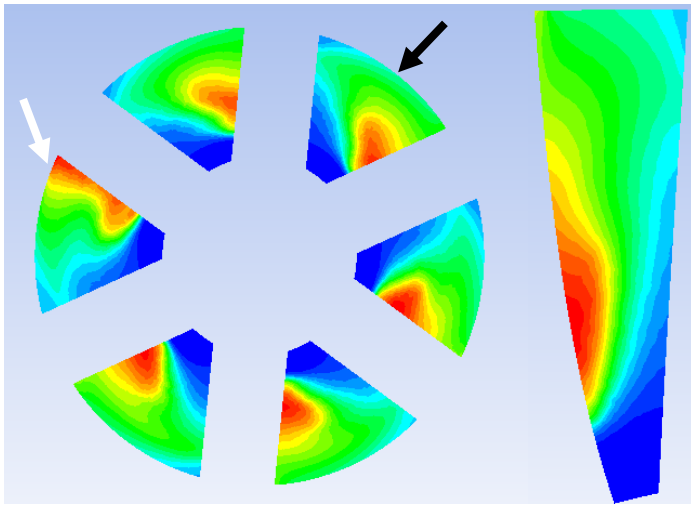

Figure A.4: Temperature contours of LLB geometry, high mass flow, rich fuel setpoint; axial plane (left) and exit plane (right)

The goal at the outset was to gain a more thorough understanding of the exit plane itself, since that's where the experimental data were taken. The complicating factor was that the exit plane was at a non-standard inclination with respect to the axial plane. Thus, the definition of each plane was accomplished in Fluent using three points in x-y-z space; those points were, in turn, extracted from the Pointwise mesh model (noting that the node coordinates from Pointwise carry over into Fluent during the export process). The precise coordinates are given in the file "ExitPlanesAndOtherData.xlsx" as currently stored in the folder below:

[L:\Research\COAL LAB\Students\Cottle\Data\CFD\Obj3\obj3-processing\ ]

It's important to note that the coordinate definitions were constant throughout all of the CFD cases EXCEPT those generated for the RVC trade study; thus there are two sets of results in

that file. After the planes were defined, the initial approach to the temperature profiles involved simply taking a one-dimensional line of points through the plane's lateral centerline. That procedure, however, did not satisfactorily account for the substantial lateral gradients in the temperature as illustrated by Figure A.4. Thus, the exit planes were re-visited. One alternative option might have been to define several dozen lateral profiles analogous to those defined for the TRP study; however, instead it was decided to simply extract parameter values for every computational node in the plane. For simplicity, only two values were extracted: temperature, and radial coordinate. By the end of this program that procedure had become fully automated; the journal code and PBS code shown below can be placed in the directory of any file (and modified to reflect the proper file name) and the exit plane data can be extracted.

----- Journal Code ------

```
file/read-case-data 60_108f185-1.cas
surface/plane aLP -.8326 -.4761 16.28 -.8027 -.4858 16.18 -1.973 -
     .7148 15.94
surface/iso-clip z-coordinate aLP2 aLP 15.9 16.3
surface/iso-clip x-coordinate _epa aLP2 -2 0
surface/plane bLP -.8286 .4830 16.28 -.8443 .4177 16.18 -1.605 1.351
     15.94
surface/iso-clip z-coordinate bLP2 bLP 15.9 16.3
surface/iso-clip x-coordinate _epb bLP2 -2 0
surface/plane cLP .0040 .9591 16.28 -.0604 .9340 16.18 .3674 2.066
     15.94
surface/iso-clip z-coordinate cLP2 cLP 15.9 16.3
surface/iso-clip y-coordinate _epc cLP2 0 2.1
surface/plane dLP .8326 .4761 16.28 .8027 .4858 16.18 1.973 .7148
     15.94
surface/iso-clip z-coordinate dLP2 dLP 15.9 16.3
surface/iso-clip x-coordinate _epd dLP2 0 2.1
surface/plane eLP .8286 -.4830 16.28 .8443 -.4177 16.18 1.605 -1.351
     15.94
surface/iso-clip z-coordinate eLP2 eLP 15.9 16.3
surface/iso-clip x-coordinate _epe eLP2 0 2
surface/plane fLP -.0040 -.9591 16.28 .0604 -.9340 16.18 -.3674 -2.066
     15.94
surface/iso-clip z-coordinate fLP2 fLP 15.9 16.3
surface/iso-clip y-coordinate _epf fLP2 -2.1 0
plot/plot y 60_exitTempAll.txt y n n radial-coordinate n n temperature
     _epa _epb _epc _epd _epe _epf ()

exit y
```

----- PBS Code ------

```
#!/bin/bash
#PBS -l nodes=2:ppn=16
#PBS -j oe
#PBS -N tempAll
#PBS -S /bin/bash

cd $PBS_O_WORKDIR

# (change -t to match ncpus!)
fluent 3ddp -ssh -t32 -cnf=$PBS_NODEFILE -g -i jTempAll.jou >&
     tresiduals.out
```

The resulting text files were then processed by MATLAB. In Figure A.5, plots are shown of temperature versus radial coordinate for two distinct exit passages; raw data are shown in blue, and the circumferentially-averaged profiles are shown in black. The averaged profiles were generated by "binning" the raw data around discrete radial coordinates; those points are indicated on the profiles with heavy black x's. Notably, the left image represents the passage indicated by the white arrow in Figure A.4 which displayed substantially non-uniform behavior by way of hot regions expanding nearly all the way to the outer diameter. That behavior was observed in many other results as shown in Ch. 6.

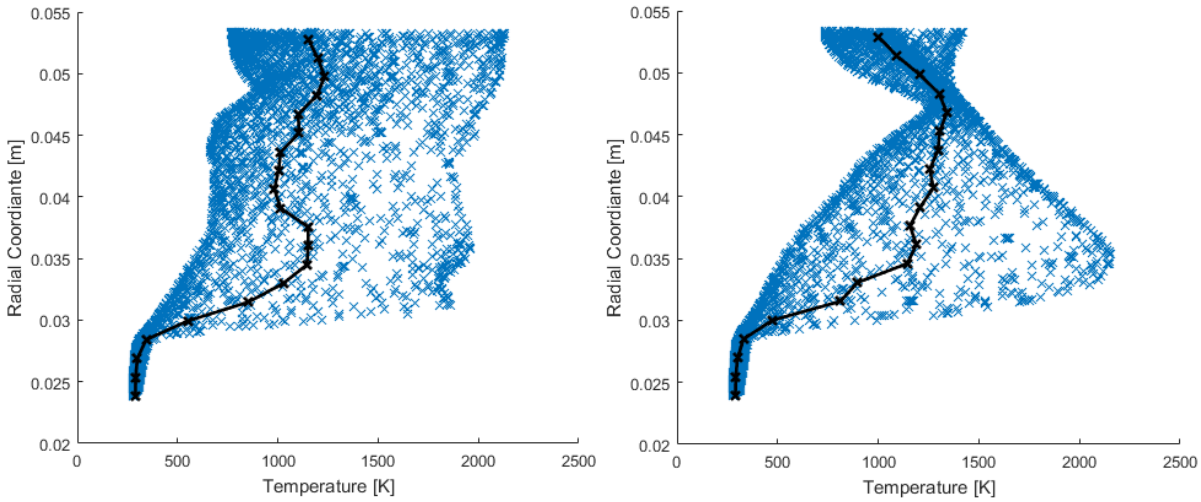

Figure A.5: Plots demonstrating the raw data (blue x's) and bin-averaged profiles (black line) for two separate exit planes

The profiles were very sensitive to the size of the bins, as illustrated in Figure A.6. If the bins were made too small then they were susceptible to increased variation due to the spacing of the grid points; however, if the bins were too large, then the procedure began to represent an area-average, and weighting the averages by area or by mass would have been required. To maintain the validity of the simple arithmetic averaging which was being implemented but to avoid the "noisy" trends of the small bins, the 1.27 mm bin size was selected. That bin size is reflected in Figure A.5 and as well in Figure A.7. In Figure A.7, the circumferentially-averaged profiles for each of the six exit passages are shown in conjunction with a single profile which represents the average of all six passages. That procedure was complicated by the fact that each of the six discreet profiles contained radial coordinate vectors which differed very slightly due to the unstructured grid volume. To overcome this dissimilarity, each individual profile was updated to include all radial coordinates represented by each of the other profiles. Temperature values at the updated coordinates were then interpolated. The result was six individual profiles with matching radial coordinate vectors; thus average temperatures could then be computed at each radial coordinate. The resulting average profile – represented by the solid line in Figure A.7, was utilized in the discussion on temperature profiles throughout Chapter 6.

As demonstrated by Figure A.4, Figure A.5, and Figure A.7, there was variability between the six passages which to this point has not been satisfactorily explained. As discussed in Section 3.4.1.3, and as will be further shown in Appendix G, the independence and convergence of the CFD solution was sound. Thus, since non-uniform fields presented themselves within an otherwise axisymmetric geometry, the probably explanation is a breakdown of the steady-state assumption upon which the CFD model is founded.

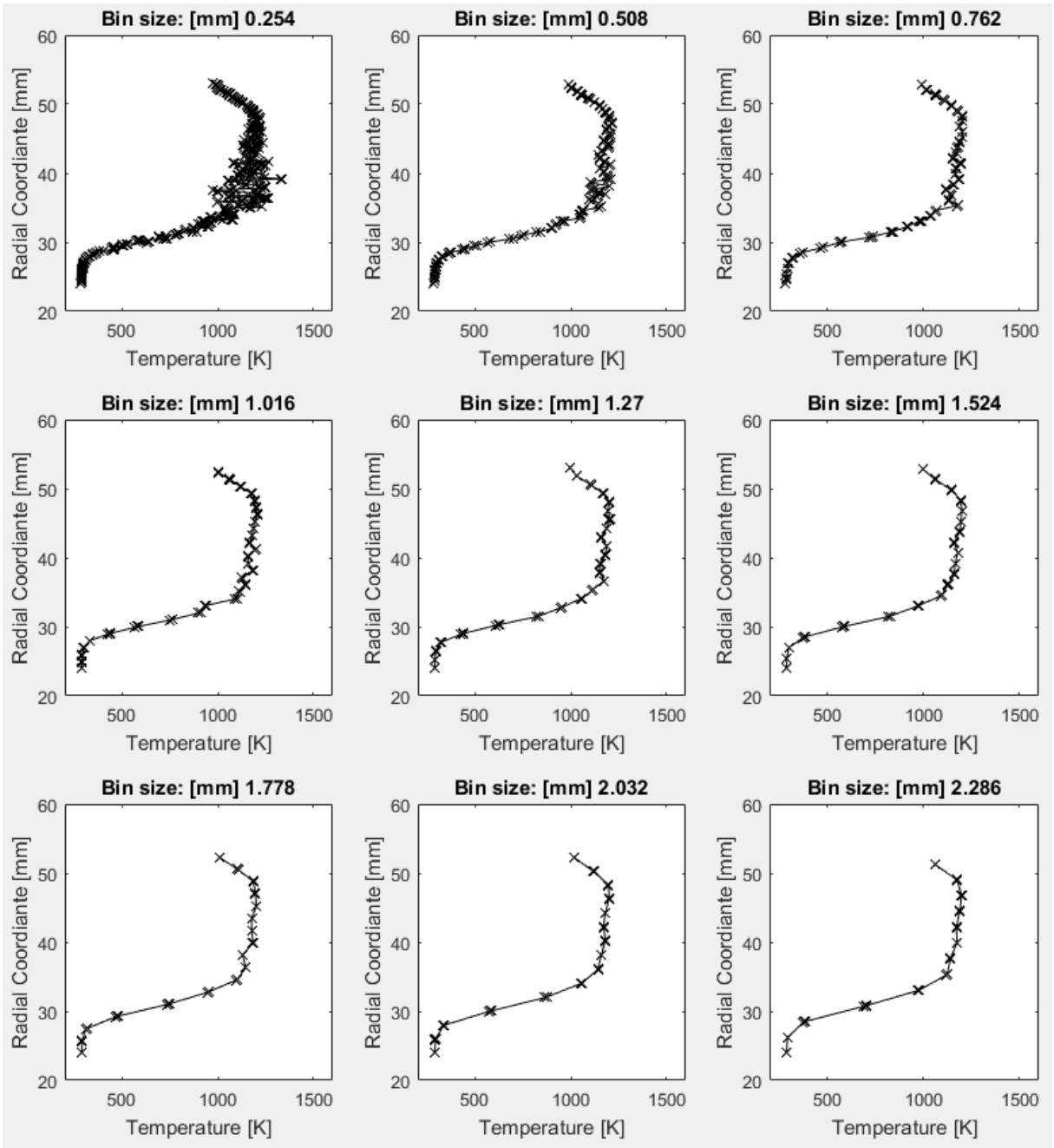

Figure A.6: Comparing nine options for bin sizes

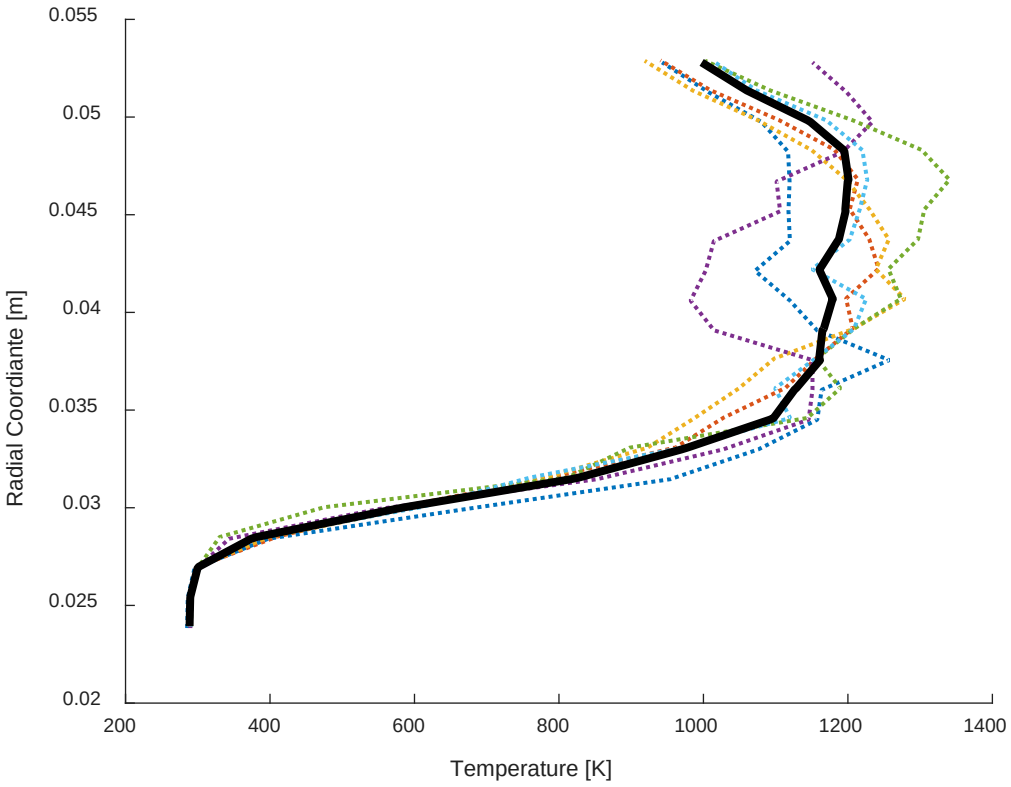

Figure A.7: Comparing the bin-averaged profiles for each of the six exit passages (dashed lines) to the interpolated-average of all six (solid line)

G. Additional Grid Convergence Data

This section documents CFD data from the case with the UCC v3, LLB configuration with $\dot{m}_{in} = 0.108$ kg/s and $\phi_{cav} = 0.8$. Data were extracted every 500 iterations, however the figures below highlight three specific cases at 3000, 5000, and 7000 iterations; most of the computations for this document were terminated at 7000 iterations. Figure A.8 and Figure A.9 show temperatures at the exit plane and as longitudinal averages, respectively. Figure A.10 shows longitudinal product formation rates, and Figure A.11 shows g-load in the circumferential cavity. In all four figures, the profiles at 5000 and 7000 iterations are exactly overlaid. The profiles at 3000 iterations are only slightly different as manifest, for example, at the OD wall temperature in Figure A.8, the second local maximum in Figure A.10, or the ID g-load in Figure A.11. These results verify the convergence of the CFD solutions while further indicating that such convergence was likely attained as early as 5000 iterations. Thus, future use of these models could realize potential savings in terms of CPU hours by way of this guidance.

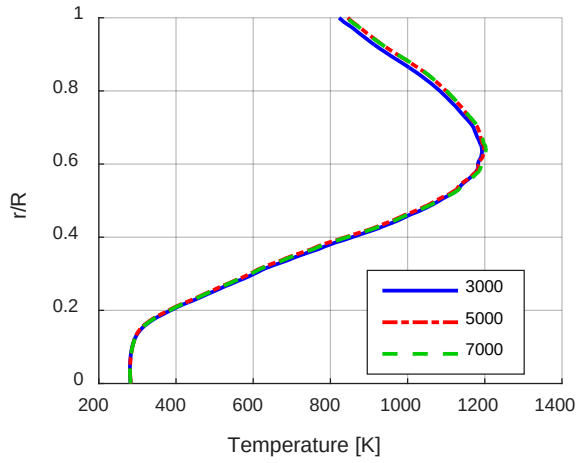

Figure A.8: One-dimensional exit temperature profiles at various iteration counts

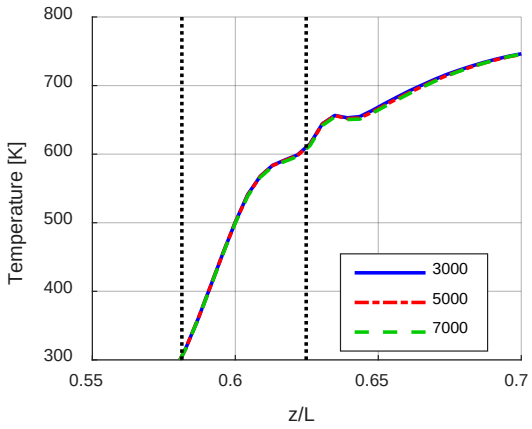

Figure A.9: Axial mass-averaged temperature profiles at various iteration counts

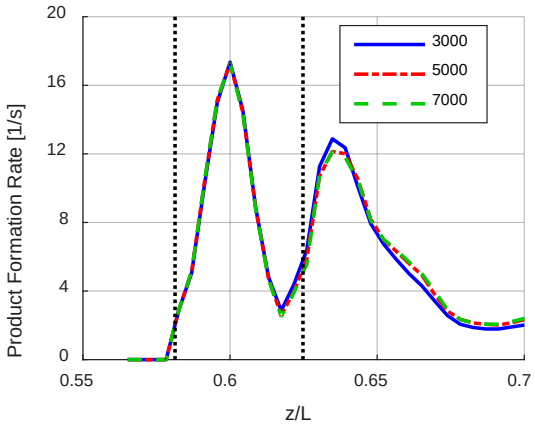

Figure A.10: Axial mass-averaged product formation rate profiles at various iteration counts

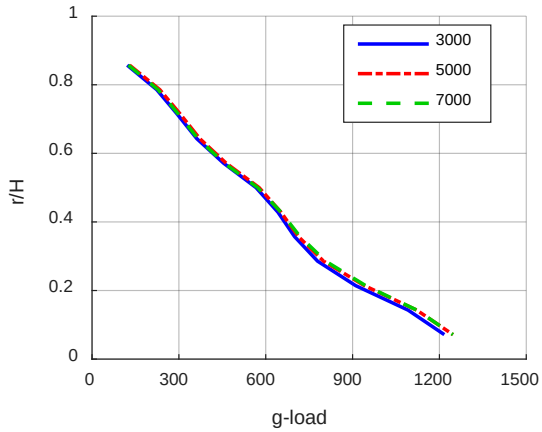

Figure A.11: Circumferentially-averaged profiles of cavity g-load at various iteration counts

H. References

[1] The White House, "National Security Strategy," 2015.

[2] B. T. Bohan and M. D. Polanka, "Analysis of Flow Migration in an Ultra-Compact Combustor," *Journal of Engineering for Gas Turbines and Power,* vol. 135, no. 5, pp. 1-11, 2013.

[3] J. Mattingly and H. von Ohain, Elements of Propulsion: Gas Turbines and Rockets, AIAA, 2006.

[4] M. P. Boyce, Gas Turbine Engineering Handbook, 4th ed., Butterworh-Heinemann, 2011.

[5] S. Turns, An Introduction to Combustion: Concepts and Applications, 3rd ed., McGraw-Hill, 2011.

[6] R. A. Anthenien and J. Zelina, "Experimental Results on the Turbulent Combustion Regimes within a Small-Scale Atmospheric Pressure High-g Combustor," in *Spring Technical Meeting of the Central States Section: Combustion Institute*, Cleveland, OH, 2006.

[7] A. H. Lefebvre and D. R. Ballal, Gas Turbine Combustion: Alternative Fuels and Emissions, 3rd ed., Boca Raton, FL: CRC Press, 2010, p. 537.

[8] R. A. Anthenien, R. A. Mantz, W. M. Roquemore and G. Sturgess, "Experimental Results for a Novel, High Swirl, Ultra Compact Combustor for Gas Turbine Engines," in *2nd Joint Meeting of the U.S. Sections of the Combustion Institute*, Oakland, CA, 2001.

[9] D. W. Bahr, "Aircraft Turbine Engine NOx Emission Limits: Status and Trends," in *ASME 1992 International Gas Turbine and Aeroengine Congress and Exposition*, Cologne, Germany, 1992.

[10] J. Zelina, D. T. Shouse and R. D. Hancock, "Ultra-Compact Combustors for Advanced Gas Turbine Engines," in *49th ASME International Gas Turbine and Aeroengine Congress and Exposition*, Vienna, Austria, 2004.

[11] S. B. Pope, Turbulent Flows, Cambridge: Cambridge University Press, 2000.

[12] ANSYS, Inc, Fluent v14.5 Theory Guide.

[13] G. K. Batchelor, An Introduction to Fluid Dynamics, Cambridge, England: Cambridge University Press, 1967.

[14] H. C. Mongia, "Recent Progress in Comprehensive Modeling of Gas Turbine Engine Combustion," in *46th AIAA Aerospace Sciences Meeting and Exhibit*, Reno, NV, 2008.

[15] H. C. Mongia, "Comprehensive Gas Turbine Combustion Modeling Methodology," in *International Aerospace CFD Conference*, Paris, 2007.

[16] J. Ehret, "Design Optimization of a High-G Loaded Ultra-Compact Combustor," Wright-State University, Dayton, OH, 2002.

[17] R. T. Greenwood, "Numerical Analysis and Optimization of the Ultra Compact Combustor," Air Force Institute of Technology, Wright-Patterson Air Force Base, OH, 2005.

[18] J. Anisko, "Numerical Investigation of Cavity-Vane Interactions within the Ultra Compact Combustor," Air Force Institute of Technology, Wright-Patterson Air Force Base, Ohio, 2006.

[19] D. S. Moenter, "Design and Numerical Simualtion of Two Dimensional Ultra Compact Combustor Model Sections for Experimental Observation of Cavity-Vane Flow Interactions," Air Force Institute of Technology, Wright-Patterson Air Force Base, Ohio, 2006.

[20] M. A. Mawid, T. W. Park, H. Thornburg, B. Sekar and J. Zelina, "Numerical Analysis of Inter-Turbine Burner (ITB) Concepts for Improved Gas Turbine Engine Performance," in *43rd AIAA Aerospace Sciences Meeting and Exhibit*, Reno, NV, 2005.

[21] M. A. Mawid, H. Thornburg, B. Sekar and J. Zelina, "Performance of an Inter-Turbine Burner (ITB) Concept with Three Different Vane Cavity Shapes," in *42nd AIAA/ASME/SAE/ASEE Joint Propulsion Conference and Exhibit*, Sacramento, CA, 2006.

[22] H. Thornburg, B. Sekar, J. Zelina and R. Greenwood, "Numerical Study of an Inter-Turbine Burner (ITB) Concept with Curved Radial Vane," in *45th AIAA Aerospace Sciences Meeting and Exhibit*, Reno, NV, 2007.

[23] A. M. Briones, B. Sekar, D. T. Shouse, D. L. Blunck, H. J. Thornburg and T. J. Erdmann, "Reacting Flows in Ultra-Compact Combustors with Combined-Diffuser Flameholder," *Journal of Propulsion and Power,* vol. 31, no. 1, pp. 238-252, 2015.

[24] A. M. Briones, B. Sekar and T. Erdmann, "Effect of Centrifugal Force on Turbulent Premixed Flames," *Journal of Engineering for Gas Turbines and Power,* vol. 137, no. 1, pp. 1-10, 2015.

[25] A. M. Briones, D. L. Burrus, T. J. Erdmann and D. T. Shouse, "Effect of Centrifugal Force on the Performance of High-G Ultra Compact Combustor," in *Proceedings of ASME Turbo Expo*, Montreal, Canada, 2015.

[26] Dantec Dynamics, August 2016. [Online]. Available: http://www.dantecdynamics.com/measurement-principles-of-piv.

[27] C. D. Slabaugh, I. Boxx, S. Werner, R. P. Lucht and W. Meier, "Structure and Dynamics of Premixed Swirl Flames at Elevated Power Density," *AIAA Journal,* vol. 54, no. 3, p. 946, March 2016.

[28] J. Meadows and A. K. Agrawal, "Time-resolved PIV of lean premixed combustion without and with porous inert media for acoustic control," *Combustion and Flame,* vol. 162, pp. 1063-1077, October 2015.

[29] V. Vilimpoc, L. P. Goss and B. Sarka, "Spatial Temperature-Profile Measurements by the Thin-Filament-Pyrometry Technique," *Optics Letters,* vol. 13, no. 2, February 1988.

[30] Innovative Scientific Solutions, Inc, "SABER-Rig Experimental Campaign," Wright-Patterson Air Force Base, 2014.

[31] B. Ma, G. Wang, G. Magnotti, R. S. Barlow and M. Long, "Intensity-ratio and color-ratio thin-filament pyrometry: Uncertanties and accuracy," *Combustion and Flame,* vol. 161, pp. 908-916, 2014.

[32] M. Reuter, S. Biasotti, D. Giorgi, G. Patane and M. Spagnuolo, "Discrete Laplace-Beltrami operators for shape analysis and segmentation," *Computers and Graphics,* vol. 33, no. 3, pp. 381-390, March 2009.

[33] R. Fisher, S. Perkins, A. Walker and E. Wolfart, 2003. [Online]. Available: http://homepages.inf.ed.ac.uk/rbf/HIPR2/log.htm.

[34] R. Noll, Laser-Induced Breakdown Spectroscopy, Springer, 2012.

[35] H. Do and C. Carter, "Hydrocarbon fuel concentration measurement in reacting flows using short-gated emission spectra of laser induced plasma," *Combustion and Flame,* vol. 160, pp. 601-609, 2013.

[36] M. Kotzagianni and S. Couris, "Femtosecond laser induced breakdown spectroscopy of air-methane mixtures," *Chemical Physics Letters,* Vols. 561-562, pp. 36-41, 2013.

[37] W. A. Sirignano, J.-P. Delplanque and F. Liu, "Selected Challenges in Jet and Rocket Engine Combustion Research," in *33rd Joint Propulsion Conference and Exhibit*, Seattle, WA, 1997.

[38] W. A. Sirignano and F. Liu, "Performance Increases for Gas-Turbine Engines Through Combustion Inside the Turbine," *Journal of Propulsion and Power,* vol. 15, pp. 111-118, 1999.

[39] W. A. Sirignano and I. Kim, "Diffusion Flame in a Two-Dimensional Accelerating Mixing Layer," *Physics of Fluids,* vol. 9, pp. 2617-2630, 1997.

[40] X. Fang, F. Liu and W. A. Sirignano, "Ignition and Flame Studies for an Accelerating Transonic Mixing Layer," *Journal of Propulsion and Power,* vol. 17, no. 5, pp. 1058-1066, 2001.

[41] C. Mehring, F. Liu and W. A. Sirignano, "Ignition and Flame Studies for a Turbulent Acceleration Transonic Mixing Layer," in *39th Aerospace Sciences Meeting*, Reno, NV, 2001.

[42] F. Cheng, F. Liu and W. A. Sirignano, "Reacting Mixing-Layer Computations in a Simulated Turbine-Stator Passage," *Journal of Propulsion and Power,* vol. 25, no. 2, pp. 322-334, 2009.

[43] B. J. Colcord and W. A. Sirignano, "Combustion Model with Fuel Injection into and Air Flow Past a Cavity," in *Proceedings of the Fall Meeting of the Western States Section of the Combustion Institute*, Livermore, CA, 2007.

[44] W. A. Sirignano, D. Dunn-Rankin, F. Liu, B. Colcord and S. Puranam, "Turbine Burners: Performance Improvement and Challenges of Flameholding," *AIAA Journal,* pp. 1645-1669, 2012.

[45] V. Puranam, J. Arici, N. Amade-Sarzi, D. Dunn-Rankin and W. A. Sirignano, "Turbulent Combustion in a Curving, Contracting Channel with a Cavity Stabilized Flame," *Proceedings of the Combustion Institute,* vol. 32, pp. 2973-2981, 2009.

[46] W. M. Roquemore, D. Shouse, D. Burrus, A. Johnson, C. Cooper, B. Duncan, K.-Y. Hsu, V. R. Katta, G. J. Sturgess and I. Vihinen, "Trapped Vortex Combustor Concept for Gas Turbine Engines," in *39th AIAA Aerospace Sciences Meeting and Exhibit*, Reno, NV, 2001.

[47] W. A. Mair, "The Effect of a Rear-Mounted disc on the Drag of a Blunt-Based Body of Revolution," *The Aeronautical Quarterly,* pp. 350-360, 1965.

[48] B. H. J. Little and R. R. Whipkey, "Locked Vortex Afterbodies," *Journal of Aircraft,* vol. 16, no. 5, pp. 296-302, 1979.

[49] V. R. Katta and W. M. Roquemore, "Numerical Studies on Trapped-Vortex Concepts for Stable Combustion," in *American Society of Mechanical Engineers Turbo Asia Conference*, Jakarta, Indonesia, 1996.

[50] T. J. Erdmann, D. L. Burrus, J. T. Gross, D. L. Blunck, A. Briones, B. Sekar, A. W. Caswell, C. Neuroth, A. Lynch and D. Shouse, "Experimental Characterization of the Reaction Zone in an Ultra-Compact Combustor," in *50th AIAA/ASME/SAE/ASEE Joint Propulsion Conference*, Cleveland, OH, 2014.

[51] D. L. Blunck, D. T. Shouse, C. Neruoth, A. Lynch, T. J. Erdmann, D. L. Burrus, J. Zelina, D. Richardson and A. Caswell, "Experimental Studies of Cavity and Core Flow Interactions with Applications to Ultra Compact Combustors," *Journal of Engineering for Gas Turbines and Power,* vol. 136, no. 9, pp. 1-8, 2014.

[52] G. D. Lewis, "Combustion in a Centrifugal-Force Field," *Symposium (International) on Combustion,* vol. 13, no. 1, pp. 625-629, 1971.

[53] G. D. Lewis, "Centrifugal-Force Effects on Combustion," *Symposium (International) on Combustion,* vol. 14, no. 1, pp. 413-419, 1973.

[54] G. D. Lewis, J. H. Shadowen and E. B. Thayer, "Swirling Flow Combustion," *Journal of Energy,* vol. 1, no. 4, pp. 201-205, 1977.

[55] J. Zelina, G. J. Sturgess and D. T. Shouse, "The Behavior of an Ultra-Compact Combustor (UCC) Based on Centrifugally-Enhanced Turbulent Burning Rates," in *40th AIAA/ASME/SAE/ASEE Joint Propulsion Conference and Exhibit*, Fort Lauderdale, FL, 2004.

[56] Y. Yonezawa, H. Toh, S. Goto and M. Obata, "Development of the Jet-Swirl High Loading Combustor," in *26th AIAA/SAE/ASME/ASEE Joint Propulsion Conference*, Orlando, FL, 1990.

[57] A. P. Lapsa and W. J. A. Dahm, "Hyperacceleration effects on turbulent combustion in premixed step-stabilized flames," *Proceedings of the Combustion Institute,* vol. 32, pp. 1731-1738, 2009.

[58] R. J. Quaale, R. A. Anthenien, J. Zelina and J. Ehret, "Flow Measurements Within a High Swirl Ultra Compact Combustor for Gas Turbine Engines," in *16th Meeting of the International Society for Airbreathing Engines*, Cleveland, OH, 2003.

[59] J. Zelina, J. Ehret, R. D. Hancock, D. T. Shouse and W. M. Roquemore, "Ultra-Compact Combustion Technology Using High Swirl for Enhanced Burning Rate," in *38th AIAA/ASME/SAE/ASEE Joint Propulsion Conference and Exhibit*, Indianapolis, IN, 2002.

[60] J. Zelina, G. J. Sturgess, A. Mansour and R. D. Hancock, "Fuel Injection Design Optimization for an Ultra-Compact Combustor," U. S. Air Force Research Laboratory, Wright-Patterson Air Force Base, Ohio, 2003.

[61] J. Zelina, D. T. Shouse and C. Neuroth, "High-Pressure Tests of a High-g, Ultra-Compact Combustor," in *41st AIAA/ASME/SAE/ASEE Joint Propulsion Conference and Exhibit*, Tucson, AZ, 2005.

[62] J. Zelina, R. T. Greenwood and D. T. Shouse, "Operability and Efficiency Performance of Ultra-Compact, High Gravity (g) Combustor Concepts," in *51st ASME International Gas Turbine and Aeroengine Congress and Exposition*, Barcelona, Spain, 2006.

[63] M. Hiddeman and P. Marx, "Operating Experience with the Latest Upgrade of Alstom's Sequential Combustion GT26 Gas Turbine," in *Proceedings of the ASME Turbo Expo*, Glasgow, UK, 2010.

[64] A. Ciani, A. Eroglu, F. Guthe and B. Paikert, "Full Scale Atmospheric Tests of Sequential Combustion," in *Proceedings of the ASME Turbo Expo*, Glasgow, UK, 2010.

[65] K. Vogeler, "Potential of Sequential Combustion for High Bypass Jet Engines," in *ASME Turbo Expo*, Stockholm, Sweden, 1998.

[66] K. H. Liew, E. Urip, S. L. Yang, J. D. Mattingly and C. J. Marek, "Performance Cycle Analysis of Turbofan Engine with Interstage Turbine Burner," *Journal of Propulsion and Power,* vol. 22, no. 2, p. 6, 2006.

[67] J. Zelina, D. T. Shouse, J. S. Stutrud, G. J. Sturgess and W. M. Roquemore, "Exploration of Compact Combustors for Reheat Cycle Aero Engine Applications," in *51st ASME International Gas Turbine and Aeroengine Congress and Exposition*, Barcelona, Spain, 2006.

[68] C. J. Spytek, "Application of an Inter-Turbine Burner using Core Driven Vitiated Air in a Gas Turbine Engine," in *Proceedings of the ASME Turbo Expo 2012*, Copenhagen, Denmark, 2012.

[69] R. J. Quaale, "Experimental Results for a High Swirl, Ultra Compact Combustor for Gas Turbine Engines," Air Force Institute of Technology, Wright-Patterson Air Force Base, OH, 2003.

[70] J. M. Armstrong, "Effect of Equivalence Ratio and G-loading on In-Situ Measurements of Chemiluminescence in an Ultra Compact Combustor," Wright-Patterson Air Force Base, OH, 2004.

[71] R. T. Greenwood, R. A. Anthenien and J. Zelina, "Computational Analysis of the Ultra Compact Combustor," in *43rd AIAA Aerospace Sciences Meeting and Exhibit*, Reno, NV, 2005.

[72] ANSYS, Inc, "Ch. 14.1: NOx Formation," in *Fluent v14.5 Theory Guide*.

[73] J. F. Anisko, R. A. Anthenien and J. Zelina, "Numerical Investigation of Cavity-Vane Interactions within the Ultra Compact Combustor," in *44th AIAA Aerospace Sciences Meeting and Exhibit*, Reno, NV, 2006.

[74] W. S. Anderson, J. T. Radtke, P. I. King, H. Thornburg, J. Zelina and B. Sekar, "Effects of Main Swirl Direction on High-g Combustion," in *44th AIAA/ASME/SAE/ASEE Joint Propulsion Conference and Exhibit*, Hartford, CT, 2008.

[75] J. T. Radtke, "Efficiency and Pressure Loss Characteristics of an Ultra-Compact Combustor with Bulk Swirl," Air Force Institute of Technology, Wright-Patterson Air Force Base, OH, 2007.

[76] E. R. Dittman, "Design, Build and Validation of a Small Scale Combustion Chamber Testing Facility," Air Force Institute of Technology, Wright-Patterson Air Force Base, Ohio, 2006.

[77] W. S. Anderson, "Design, Construction, and Validation of the AFIT Small Scale Combustion Facility and Sectional Model of the Ultra-Compact Combustor," Air Force Institute of Technology, Wright-Patterson Air Force Base, OH, 2007.

[78] S. J. Koether, "Validation of the AFIT Small Scale Combustion Facility and OH Laser-Induced Fluorescence of an Atmospheric Laminar Premixed Flame," Air Force Institute of Technology, Wright-Patterson Air Force Base, OH, 2007.

[79] P. J. Lakusta, "Laser-Induced Fluorescence and Performance Analysis of the Ultra-Compact Combustor," Air Force Institute of Technology, Wright-Patterson Air Force Base, OH, 2008.

[80] T. B. Hankins, "Laser Diagnostic System Validation and Ultra-Compact Combustor Characterization," Air Force Institute of Technology, Wright-Patterson Air Force Base, OH, 2008.

[81] A. C. Drenth, "Laser-Induced Fluorescence and Synthetic Jet Fuel Analysis in the Ultra Compact Combustor," Air Force Institute of Technology, Wright-Patterson Air Force Base, OH, 2009.

[82] L. M. Thomas, "Flow Measurements Using Particle Image Velocitmetry in the Ultra Compact Combustor," Air Force Institute of Technology, Wright-Patterson Air Force Base, OH, 2009.

[83] K. D. LeBay, A. C. Drenth, L. M. Thomas, M. D. Polanka, R. D. Branam and J. B. Schmidt, "Characterizing the Effects of G-loading in an Ultra Compact Combustor via Sectional Models," in *Proceedings of the ASME Turbo Expo*, Glasgow, Scotland, 2010.

[84] K. D. LeBay, M. D. Polanka, M. F. Reeder and R. D. Branam, "Time-Resolved Particle Image Velocimetry Investigations within a Sectional Ultra Compact Combustor," in *49th AIAA Aerospace Sciences Meeting*, Orlando, FL, 2011.

[85] K. D. LeBay, M. D. Polanka and R. D. Branam, "Characterizing the Effect of Radial Vane Height on Flame Migration in an Ultra Compact Combustor," in *Proceedings of the ASME Turbo Expo*, Vancouver, Canada, 2011.

[86] K. D. LeBay, "Characterization of Centrifugally-Loaded Flame Migration for Ultra-Compact Combustors," Air Force Institute of Technology, Wright-Patterson Air Force Base, OH, 2011.

[87] A. K. Parks, "Desensitizing Flame Structure and Exhaust Emissions to Flow Parameters in an Ultra-Compact Combustor," Air Force Institute of Technology, Wright-Patterson Air Force Base, OH, 2012.

[88] F. Benhassen, "Time Resolved Filtered Rayleigh Scattering Measurement of a Centrifugally Loaded Buoyant Jet," Air Force Institute of Technology, Wright-Patterson Air Force Base, OH, 2011.

[89] B. T. Bohan, "Analysis of Flow Migration in an Ultra-Compact Combustor," Air Force Institute of Technology, Wright-Patterson Air Force Base, Ohio, 2011.

[90] J. D. Wilson, "Characterizing g-Loading, Swirl Direction, and Rayleigh Losses in an Ultra Compact Combustor," Air Force Institute of Technology, Wright-Patterson Air Force Base, OH, 2013.

[91] J. D. Wilson and M. D. Polanka, "Reduction of Rayleigh Losses in a High G-Loaded Ultra Compact Combustor," in *Proceedings of the ASME Turbo Expo 2013*, San Antonio, TX, 2013.

[92] J. D. Wilson, C. J. Damele and M. D. Polanka, "Flame Structure Effects at High G-Loading," *Journal of Engineering for Gas Turbines and Power,* vol. 136, 2014.

[93] C. J. Damele, "Operational Characteristics of an Ultra Compact Combustor," Air Force Institute of Technology, Wright-Patterson Air Force Base, OH, 2014.

[94] C. J. Damele, M. D. Polanka, J. D. Wilson and J. L. Rutledge, "Characterizing Thermal Exit Conditions for an Ultra Compact Combustor," in *52nd Aerospace Sciences Meeting*, National Harbor, MD, 2014.

[95] M. M. Conrad, "Integration of an Inter Turbine Burner to a Jet Turbine Engine," Air Force Institute of Technology, Wright-Patterson Air Force Base, OH, 2013.

[96] M. M. Conrad, J. D. Wilson and M. D. Polanka, "Integration Issues of an Ultra-Compact Combustor to a Jet Turbine Engine," in *49th AIAA/ASME/SAE/ASEE Joint Propulsion Conference*, San Jose, CA, 2013.

[97] A. J. Brinker, "Liquid Spray Characterization in Flow Fields with Centripetal Acceleration," Air Force Institute of Technology, Wright-Patterson Air Force Base, OH, 2014.

[98] J. L. Miranda, "The Use of an Ultra-Compact Combustor as an Inter-Turbine Burner for Improved Engine Performance," Air Force Institute of Technology, Wright-Patterson Air Force Base, OH, 2014.

[99] National Institute for Occupational Safety and Health, April 2016. [Online]. Available: http://www.cdc.gov/niosh/npg/npgd0105.html.

[100] N. A. Gilbert, "Enhanced Flow Migration in a Full Annular Ultra Compact Combustor," Wright-Patterson AFB, 2016.

[101] N. A. Gilbert, A. E. Cottle, M. D. Polanka and L. P. Goss, "Enhancing Flow Migration in a Full Annular Ultra Compact Combustor," in *54th AIAA Aerospace Sciences Meeting*, San Diego, CA, 2016.

[102] J. P. Steinbrenner and J. P. Abelanet, "Anisotriopic Tetrehedral Meshing Based on Surface Deformation Techniques," in *45th AIAA Aerospace Sciences Meeting and Exhibit*, Reno, NV, 2007.

[103] F. M. White, Viscous Fluid Flow, 3rd ed., McGraw-Hill, 2005.

[104] I. B. Celik, U. Ghia, P. J. Roache, C. J. Freitas, H. Coleman and P. E. Raad, "Procedure for Estimation and Reporting of Uncertainty Due to Discretization in CFD Applications," *Journal of Fluids Engineering,* vol. 130, no. 7, 2008.

[105] K. Vogiatzis, *Personnal Correspondance,* Wright-Patterson Air Force Base, Ohio, Dec 2014.

[106] A. J. Briones, *Personal Correspondence,* Wright-Patterson Air Force Base, OH, January 2015.

[107] Air Force Research Laboratory, "AFRL HPC Hardware," 10 May 2016. [Online]. Available: https://www.afrl.hpc.mil/hardware/index.html. [Accessed 10 May 2016].

[108] Cotronics, July 2016. [Online]. Available: http://www.cotronics.com/catalog/30%20%207030%20%20907.pdf.

[109] F. R. Menter, "Two-equation eddy-viscosity turbulence models for engineering applications," *AIAA Journal,* vol. 32, no. 8, pp. 1598-1605, 1994.

[110] A. E. Cottle and M. D. Polanka, "Common Flow Source for a Full Annular Ultra Compact Combustor," in *53rd AIAA Aerospace Sciences Meeting*, Kissimmee, FL, 2015.

[111] A. E. Cottle and M. D. Polanka, "Numerical and Experimental Results from a Common-Source High-G Ultra-Compact Combustor," in *Proceedings of ASME Turbo Expo*, Seoul, South Korea, 2016.

[112] A. E. Cottle, N. A. Gilbert and M. D. Polanka, "Mechanisms for Enhanced Flow Migration from an Annular, High-g Ultra Compact Combustor," in *54th AIAA Aerospace Sciences Meeting*, San Diego, CA, 2016.

[113] A. E. Cottle, M. D. Polanka, L. P. Goss and C. Z. Goss, "Detailed Combustion Velocities and Temperatures under High-G Loading," in *Proceedings of ASME Turbo Expo*, Seoul, South Korea, 2016.

[114] S. Kostka, S. Roy, P. J. Lakusta, T. R. Meyer, M. W. Renfro, J. R. Gord and R. Branam, "Comparison of line-peak and line-scanning excitation in two-color laser-induced fluorescence thermometry of OH," *Optical Society of America,* vol. 48, no. 32, pp. 6332-6343, November 2009.

REPORT DOCUMENTATION PAGE

Form Approved
OMB No. 0704-0188

1. REPORT DATE *(DD-MM-YYYY)*	2. REPORT TYPE	3. DATES COVERED *(From - To)*
22-12-2016	Dissertation	Sept. 2013 – Dec. 2016

4. TITLE AND SUBTITLE

Flow Field Dynamics in a High-g Ultra-Compact Combustor

5a. CONTRACT NUMBER

5b. GRANT NUMBER

5c. PROGRAM ELEMENT NUMBER

6. AUTHOR(S)

Cottle, Andrew E., Captain, USAF

5d. PROJECT NUMBER

5e. TASK NUMBER

5f. WORK UNIT NUMBER

7. PERFORMING ORGANIZATION NAME(S) AND ADDRESS(ES)

Air Force Institute of Technology
Graduate School of Engineering and Management (AFIT/ENY)
2950 Hobson Way, Building 640
WPAFB, OH 45433-8865

8. PERFORMING ORGANIZATION REPORT NUMBER

AFIT-ENY-DS-16-D-037

9. SPONSORING / MONITORING AGENCY NAME(S) AND ADDRESS(ES)

Dr. Chiping Li, Program Manager
Air Force Office of Scientific Research
875 N. Randolph, Ste. 325
Arlington, VA 22203

10. SPONSOR/MONITOR'S ACRONYM(S)

AFOSR/RTE

11. SPONSOR/MONITOR'S REPORT NUMBER(S)

12. DISTRIBUTION / AVAILABILITY STATEMENT

Distribution Statement A. Approved for public release; distribution unlimited.

13. SUPPLEMENTARY NOTES

14. ABSTRACT

The Ultra Compact Combustor (UCC) presents a novel solution to the advancement of aircraft gas turbine engine performance. A "high-g" UCC design operates by diverting a portion of the axial compressor flow into a circumferential combustion cavity positioned about the engine outer diameter. The circumferential cavity (CC) provides the necessary residence length and time for combustion within reduced axial lengths; furthermore, high rates of centrifugal acceleration – termed "high-g loading" – are imposed upon the swirling cavity flow. These high-g conditions are hypothesized to increase flame speed, reduce flame length, and improve lean blow-out performance. Work at AFIT was sponsored by the Air Force Office of Scientific Research to study high-g combustion. This research capitalized on the availability of advanced flow diagnostic data coupled with a computational fluid dynamics (CFD) model to provide detailed insight into the high-g flow field and combustion dynamics. Results indicated that combustion could be sustained and controlled in a manner suitable for integration into modern gas turbine engine architecture.

15. SUBJECT TERMS

Gas turbine engine, high-g combustion, combustion modeling, particle image velocimetry, thin-filament pyrometry, laser spectroscopy

16. SECURITY CLASSIFICATION OF:			17. LIMITATION OF ABSTRACT	18. NUMBER OF PAGES	19a. NAME OF RESPONSIBLE PERSON
					Marc D. Polanka, AFIT/ENY
a. REPORT	b. ABSTRACT	c. THIS PAGE	UU	423	19b. TELEPHONE NUMBER *(include area code)*
U	U	U			(937)255-6565x4714 marc.polanka@afit.edu

Standard Form 298 (Rev. 8-98)
Prescribed by ANSI Std. Z39.18